Petrology and geochemistry of the tapira alkaline complex, minas gerais state, Brazil

Brod, José Affonso

Brod, José Affonso (1999) *Petrology and geochemistry of the tapira alkaline complex, minas gerais state, Brazil*, Durham theses, Durham University. Available at Durham E-Theses Online: http://etheses.dur.ac.uk/4971/

Petrology and Geochemistry of the Tapira Alkaline Complex, Minas Gerais State, Brazil

By

José Affonso Brod

**A thesis submitted in partial fulfilment of
the requirements for the degree of
Doctor of Philosophy**

**Department of Geological Sciences
University of Durham
February 1999**

This thesis is dedicated to

Seu Gilberto and Dona Julce
Your love and wisdom gave me the inspiration, the strength
and the confidence to keep going on the long road to here
(Zeca)

Tereza
"As the wild mountain thyme
goes around the purple heather"
(Mc Peake Family)

Daniel and Heloíza
"Feed them on your dreams,
the one they pick is the one you'll go by"
(Graham Nash)

Declaration

I declare that this thesis, which I submit for the degree of Doctor of Philosophy at the University of Durham, is my own work and not substantially the same as any which has previously been submitted at this or another university.

José Affonso Brod

University of Durham

February 1999

Petrology and Geochemistry of the Tapira Alkaline Complex, Minas Gerais State, Brazil

José Affonso Brod

ABSTRACT

The Tapira alkaline complex is the southernmost of a series of carbonatite-bearing intrusions occurring in the Alto Paranaíba region, western Minas Gerais State, Brazil. Together with kamafugites, lamproites and kimberlites, these complexes form part of the Late-Cretaceous Alto Paranaíba Igneous Province (APIP). The Tapira igneous complex is emplaced into rocks of the Late-Proterozoic Brasília mobile belt, adjacent to a major cratonic area (the São Francisco craton).

The complex is formed by the amalgamation of several intrusions, comprising mainly ultramafic rocks (wehrlites and bebedourites), with subordinate syenite, carbonatite and melilitolite. At least two separate units of ultramafic rocks (B1 and B2) and five episodes of carbonatite intrusion (C1 to C5) are recognised. The plutonic rocks are crosscut by fine-grained ultramafic and carbonatite dykes. Two varieties of ultramafic dykes are recognised: phlogopite-picrites are the most primitive rocks in the complex; low-Cr dykes are more evolved, and typically lack olivine. The ultramafic dykes are carbonate-rich, and may contain carbonate ocelli, indicating that immiscibility of carbonatite liquid occurred early in the evolution of the complex. The ultramafic dykes are chemically similar to the APIP kamafugites.

The primitive Tapira magmas underwent some differentiation in the crust, before their final emplacement. Crystal fractionation from the phlogopite-picrite magma may have produced olivine and chromite-rich cumulates, but these rocks are under-represented in the complex. Crystal fractionation from low-Cr dykes may have produced the bebedourites. The Tapira complex contains examples of carbonatites that originated by either liquid immiscibility or crystal fractionation. These contrasting petrogenetic mechanisms have produced distinct geochemical and mineralogical signatures, which have been used to pinpoint specific events in the evolution of the complex, and to test the consanguinity of carbonatites and associated silicate rocks.

ACKNOWLEDGEMENTS

I would like to express my heartfelt gratitude to the following people and institutions:

First to my supervisors, Prof. R.N. Thompson and Dr. S.A. Gibson, for their encouragement and support throughout the project. Needless to say that this work would not have been possible without their constant help and invaluable advice. They went through every chapter in great detail, and the text was much improved by their comments. Their inspiring feedback, enthusiasm and extreme patience all played a vital role in leading to the successful conclusion of this thesis. Finally, Bob and Sally, many thanks for this great friendship over the years.

The Conselho Nacional de Desenvolvimento Científico e Tecnológico (CNPq) provided financial support via the payment of the fees at the University of Durham, personal maintenance and transportation for the duration of the Ph.D. course.

The Universidade de Brasília provided financial support, as well as access to numerous research laboratory facilities and the logistic support during field work.

The mining companies FOSFÉRTIL S/A and Companhia Vale do Rio Doce kindly granted permission for the examination and sampling of their drill-core collections, as well as geological documentation from the Tapira and Salitre complexes. FOSFÉRTIL S/A also provided logistic support during the field work in Tapira.

Prior to the start of the Ph.D. course at Durham, preliminary research visits to the University of Durham and to the Technical University of Munich were sponsored by The British Council/CNPq and by the Deutscher Akademischer Austauschdienst (DAAD), respectively.

The University of Cambridge and the Technical University of Munich, for granting access to their electron microprobe and stable isotope facilities, respectively.

The Graduate Society, for all the assistance and accommodation provided to me and my family over these last four years.

Dr. C.H. Emeleus, Dr. D.G. Pearson and Dr. B. Turner offered invaluable suggestions and advice on several aspects of the project. R. Hardy, for the help with the XRF and XRD analyses at the University of Durham. Ron went beyond his professional duties many times in the search for the best XRF set-up for the analyses of carbonatites. Dr. C. J. Ottley for the help and guidance with ICP-MS analyses at the University of Durham. My knowledge of ICP analysis benefited greatly from his expert advice.

The staff in the Geology Department at Durham University, Carol, Claire, Dave Asbery, Dave Stevenson, Alan, George, Karen, Julie, many thanks for looking after me so well and for helping to sort out every single thing I needed, many times at very short notice.

Dr. S. J. Reed (Cambridge) and Dr. J.C. Gaspar and Dr. N.F. Botelho (Brasilia) are gratefully acknowledged for their help with microprobe analyses, and for their patience with the unusual equipment set-ups that were required for some of the analysed minerals.

Dr. G. R. Boaventura for the help with ferrous iron, carbon and sulphur analyses, at the University of Brasília, and for the innumerable hours of philosophic discussions and much laughter.

Dr. M. M. Pimentel and S. Gioia are thanked for their help with the Sr and Nd isotopic analyses at the Universidade de Brasília.

Dr. D. Blamart (Munich) and Dr. R.V. Santos (Brasília) are thanked for the help with carbon and oxygen stable-isotope analyses.

Prof. O. H. Leonardos, for helping to open the eyes of this once-basement-geologist to the world of alkaline rocks and carbonatites.

I benefited enormously from the help of many good friends during the duration of this project, not only in matters related to this thesis, but also in many other aspects of my life. In Durham: Mike, Ana, Roberto, Ercan, Nurdanne, Vicky, Kate, Sue, Sarah Acland, Sarah Woodland, Toby, Caroline, Matt, Irene, Brian, Luis, João, Rui, São, Marcos and Pascal. In Brasília: Geraldo, Othon, Márcio, Roberto, Gaspar, Nilson, Simone, Graça, Hirson, Fuck and Hardy. In Araxá: Hildor, Lúcia, Chico. In Cambridge: Jo and Andy. Many thanks to all of you.

Special thanks to Dr. Ercan Aldanmaz, for all the inspiring geochemistry discussions, and for the vital help in putting the final print of this thesis together, when it looked like time was going to be just too short.

Dr. Michael Richardson and Ana Maria, for being such great friends, and for making us feel part of the family since our first arrival in Durham and throughout all these years. Mike, many thanks also for all the hard and speedy work in proof-reading all my texts.

Seu Gilberto, Dona Julce, Dr. Mauro, Dona Evânia and Carlitos for their constant help and encouragement, and for sorting out everything that would otherwise have required my presence in Brazil. I would never have done it without you.

Carlitos, Cecília and Xixam, for being such good e-messengers.

Finally to TT, Déi and Dani, for their love and support throughout, and for having given so much of it and asked for so little in return, particularly during the last six months of this project. This thesis belongs to you as much as me.

CONTENTS

CHAPTER I - INTRODUCTION AND GEOLOGICAL SETTING

CHAPTER II - PETROGRAPHY

CHAPTER III – MINERAL CHEMISTRY

CHAPTER IV – GEOCHEMISTRY

CHAPTER V – PETROGENESIS

CHAPTER I - INTRODUCTION AND GEOLOGICAL SETTING

I.1 - INTRODUCTION

The Tapira complex is located in the western portion of the State of Minas Gerais, SE Brazil (Figure I.1), immediately to the north of Tapira village and approximately 30 km south-southeast of the city of Araxá. It is the southernmost of a series of Late-Cretaceous, carbonatite-bearing alkaline plutonic complexes belonging to the Alto Paranaíba Igneous Province (APIP, Gibson *et al.,* 1995b). The complex intrudes phyllites, schists and quartzites of the Late-Proterozoic Brasília mobile belt. The aim of this thesis is to: i) investigate the geochemical and petrological characteristics of the Tapira complex; ii) compare them with similar carbonatite complexes in the APIP and elsewhere; and iii) contribute to the understanding of the origin and evolution of carbonatites and associated igneous rocks.

Figure I.1- Map showing the location of the studied area, in western Minas Gerais State, Brazil.

1.2 - GEOTECTONIC FRAMEWORK

Figure I.2 presents a simplified tectonic framework of Brazil, as devised by Almeida and Svisero (1991). Three main types of tectonic domains are present: a) cratonic areas; b) Proterozoic mobile belts and c) Phanerozoic cover. The two major exposed cratonic areas are the São Francisco and Amazonas cratons. Smaller cratonic regions comprise the São Luis craton in the north and the Luis Alves and Rio de la Plata cratons in the south. The existence of a large continental area during the Archaean (the Paraná block), now lying underneath the sedimentary and volcanic cover of the Paraná Basin, has been suggested by Haralyi and Hasui (1982), on the basis of gravimetric data. This is consistent with the results of teleseismic studies (VanDecar *et al.,* 1995), which suggested the existence of a deep high-velocity zone under the northern Paraná Basin. A hypothetical (unexposed) Paraná craton has also been presumed by several authors (e.g. Soares *et al.;* 1990, Brod *et al.,* 1991; Viana *et al.*, 1995; Pimentel *et al.,* 1996a) but, due to the thick Phanerozoic cover, there is no direct evidence as to the nature of this unit. Nevertheless, if the Phanerozoic cover in Figure I.2 is disregarded, the geotectonic scenario is clearly one of ancient cratonic areas surrounded by younger mobile belts.

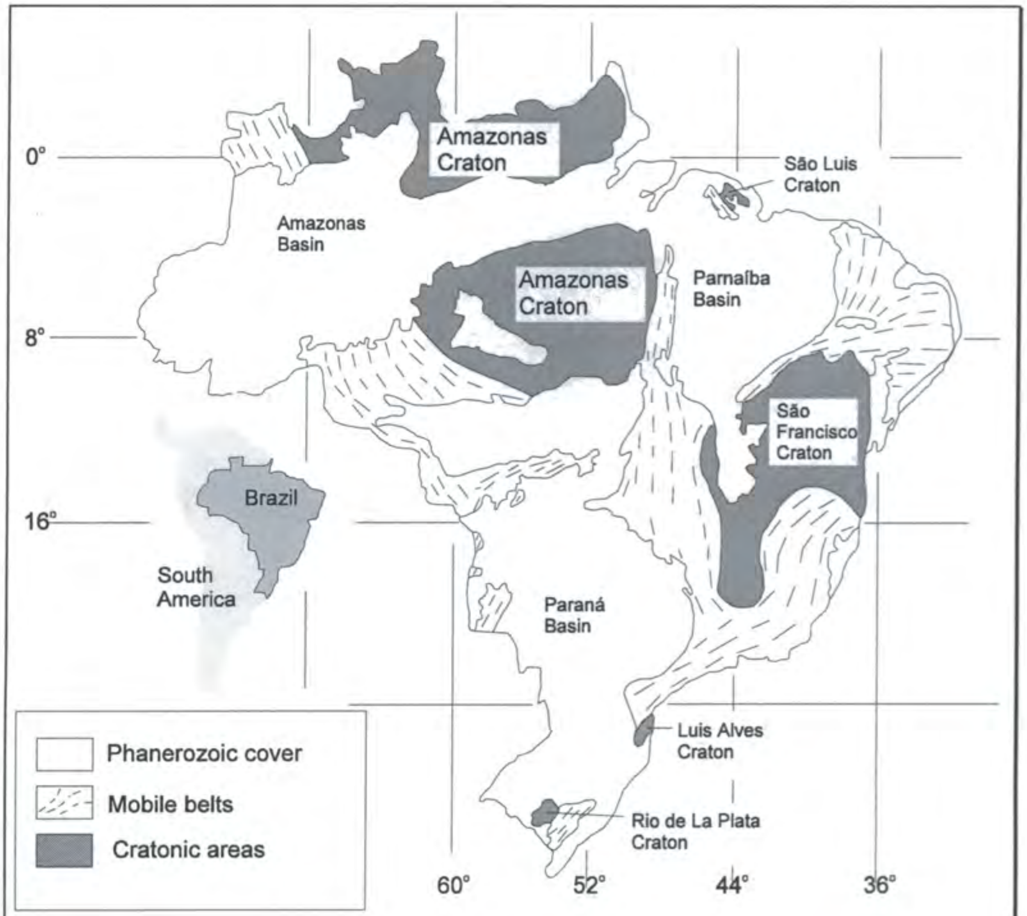

Figure I.2 - Simplified tectonic framework of Brazil (after Almeida and Svisero, 1991)

The geotectonic units that are relevant to the present research are: 1) the São Francisco Craton; 2) the mobile belts which surround that cratonic area; 3) the Paraná Basin; and 4) the Cretaceous alkaline provinces that occur along the margins of the latter (not shown in Figure I.2). The discussion in this chapter will therefore be focused on these units. Emphasis will be given to the Late-Proterozoic Brasília belt and to the Late-Cretaceous Alto Paranaíba Igneous Province (APIP), because these make up the immediate geological setting of the area. However, other major tectonic and magmatic provinces in central and Southern Brazil, and in Paraguay will be referred to for comparison. A brief description of the major tectonic units is given below. More extensive reviews can be found in the compilations by Schobbenhaus Filho *et al.* (1984), Dominguez and Misi (1993) and Pedrosa-Soares *et al.* (1994).

I.2.1 - THE SÃO FRANCISCO CRATON

The São Francisco Craton (Almeida, 1977) is surrounded by a number of mobile belts (Figure I.3) generated during the Brasiliano (Late Proterozoic) tectonic cycle, which culminated with the amalgamation of the South American Platform. These comprise the Brasília belt to the west, the Araçuaí belt to the east, the Alto Rio Grande belt to the south, and the Rio Preto, Riacho do Pontal and Sergipano belts to the north of the craton. The structures within the mobile belts indicate tectonic transport towards the craton, and the intensity of metamorphism and deformation increases away from the craton.

Although it is generally accepted that the São Francisco Craton has remained tectonically stable in relation to the Late-Proterozoic mobile belts, its margins may have been involved in the tectonic event of the Brasiliano Cycle to a variable extent (e.g. Haralyi and Hasui, 1982; Alkmim *et al.,* 1993). Furthermore, most of its area is concealed by an undeformed sedimentary cover of Proterozoic and Phanerozoic age (Schobbenhaus Filho *et al.,* 1984; Alkmim *et al.,* 1993). The exposure of the Archaean basement (granite-greenstone terrains), with ages ranging from 3,300 Ma to 2770 Ma (Pedrosa-Soares *et al.,* 1994, and references therein), is therefore restricted to two areas, located in the southern and in the northeastern portions of the craton (Figure I.3).

The exact limits of the craton have been a subject of debate and several authors have proposed different limits and configurations for it (e.g. Bernasconi, 1983; Schobbenhaus Filho *et al.,* 1984; Pires, 1986; Tompkins and Gonzaga, 1989; Trompette *et al.,* 1992a; Alkmim *et al.,* 1993). The works of Brod *et al.* (1991), Strieder and Nilson (1992) and Pedrosa-Soares *et al.* (1992) have demonstrated that significant portions of the mobile belts to the west (Brasília belt) and to the east (Araçuaí belt) of the craton consist of allochtonous thrust slices that may have suffered considerable horizontal transport towards the craton. Moreover, evidence from gravity (Almeida *et al.,* 1980; Lesquer *et al.,* 1981; Pires, 1986); xenolith (Leonardos *et al.,* 1993), seismic (VanDecar *et al.,* 1995) and geochemical/isotopic studies (Gibson *et al.,* 1995b) suggest some extent of sub-surface continuity of the São Francisco craton to the west, underneath the thrust slices of the Brasília belt. The limits of the craton may therefore be significantly wider than those originally envisaged by Almeida (1977). This is further emphasised in Figure I.3, where the thick solid line represents the presently accepted limits of the craton (Alkmim *et al.*, 1993).

Figure I.3 - The Brasiliano Sao Francisco Craton and the marginal mobile belts (after Alkmim et al., 1993). The arrows indicate the direction of tectonic transport.

Finally, the São Francisco craton is geographically divided in two by a NW-trending belt of low-grade metamorphic rocks (the Paramirin Province, Figure I.3). Since the work of Almeida (1977), this has been generally considered as an intra-continental rift, containing rocks deposited and metamorphosed during the Middle Proterozoic (and therefore incorporated into the cratonic area before the Brasiliano cycle). This interpretation is mainly based on geochronological data (e.g. Brito Neves *et al.*, 1979) and challenged by Trompette *et al.* (1992a,b) and Uhlein *et al.* (1998) who, on the basis of similarities with the stratigraphy and structural patterns of the Late-Proterozoic belts, suggest that the Paramirin belt was extensively deformed during the Brasiliano cycle and, therefore, cannot be considered part of the craton. They propose the division of the São Francisco Craton (*sensu* Almeida, 1977) in two separate cratonic areas, the São Francisco Craton proper, to the southwest, and the Salvador Craton (as an extension of the Congo Craton in Africa) to the northeast of the Paramirin Province. The clarification of this debate awaits more detailed geochronological investigations.

I.2.2 - THE BRASÍLIA BELT

Together with the Paraguay-Araguaia belt, the Brasília fold-and-thrust belt constitute the Tocantins Province (Figure I.4). The Brasília belt was formed during the Brasiliano cycle, by the tectonic inversion of sedimentary sequences deposited between 900 and 800 Ma (Fuck *et al.*, 1993) in a rifted basin at the western margin of the São Francisco Craton. The lithospheric extension during the rifting process reached the stage of ocean crust generation (Strieder and Nilson, 1992; Brod *et al.*, 1992). The subsequent thrusting of the volcanic and sedimentary sequences against the São Francisco Craton resulted in the formation of ophiolitic melanges (Strieder and Nilson, 1992). A similar scenario, involving the formation and subsequent tectonic inversion of a restricted (Red Sea-type) ocean basin is envisaged by Pedrosa-Soares *et al.* (1994) for the eastern margin of the São Francisco Craton (Araçuaí belt).

Fuck (1994) provided a summary of the current knowledge about the tectono-stratigraphic sub-division of the Brasília belt, recognising the following domains, from east to west: a) a cratonic zone, comprising restricted areas of exposed basement and extensive areas covered by the meta-sedimentary rocks of the Precambrian Paranoá and Bambuí Groups, as well as Phanerozoic sediments; b) an external zone, thrust over the cratonic zone, comprising the meta-sedimentary rocks of the Paranoá and Canastra Groups, and the Vazante and Ibiá Formations; c) an internal zone, comprising the Araxá Group (metamorphosed sediments and basic volcanics, ophiolitic mélange); d) a Brasiliano magmatic arc that evolved at 930-600 Ma and shows the chemical and isotopic signature of juvenile crust generated in an island arc environment (Pimentel and Fuck, 1992).

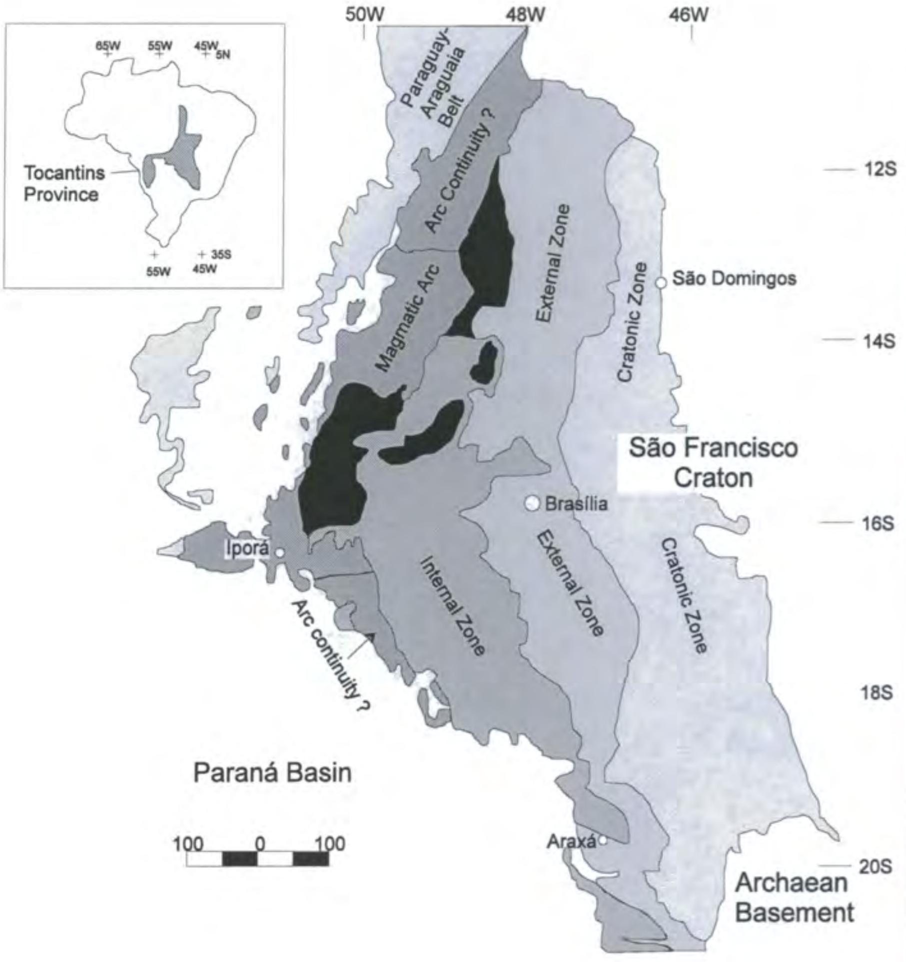

Figure I.4 - Tectono-stratigraphic domains of the Brasília belt (after Pimentel et al., 1996b). Areas in black represent fragments of the Goiás Massif (see text)

The understanding of the Brasília belt is further complicated by the existence of two sectors of contrasting structural orientation, situated respectively to the north and to the south of a major tectonic structure (the Pirineus lineament), located in Goiás State (Marini *et al.*, 1984). This inflection in the structural trends of the Brasília belt (Figure I.4) has been recently interpreted (Pimentel *et al.*, 1996b; Fonseca and Dardenne, 1996) as an indentation of the foreland to the west, against the eastward tectonic transport of the Brasília belt during the Late-Proterozoic collision between São Francisco and Amazonas cratons.

The northern section of the Brasília belt has a complex tectonic history, including the now well-established Goiás magmatic arc (Pimentel *et al.*, 1991; Pimentel and Fuck, 1992; Viana, 1995; Pimentel *et al.,* 1996b) and fragments of Archaean and Early-Proterozoic terrains (Goiás Massif). The latter have received contrasting interpretations (Fuck *et al.*, 1994; Fuck, 1994), but are lately considered as the original palaeogeographic limit between the São Francisco Craton and the Late-Proterozoic sedimentary basin (Pimentel *et al.,* 1996b).

The Araxá-Tapira region is located at the very south of the Brasília belt (Figure I.4). The geological setting of the southern Brasília belt is dominated by the Proterozoic meta-sedimentary rocks of the cratonic and external zones and by meta-sedimentary and meta-volcanic rocks of the internal zone of the Brasília belt. The geographic continuity of the magmatism of calc-alkaline affinity is hinted by Pimentel *et al.* (1996b) but has not as yet been positively demonstrated, which may be due to the extensive area covered by the Paraná Basin (Figure I.4).

More detailed models for the structural evolution of the northern and the extreme southern sectors can be found in Fonseca *et al.* (1995) and Valeriano *et al.* (1995), respectively.

I.2.3 THE PHANEROZOIC BASINS

After the final amalgamation of the South American Platform, at the transition from the Proterozoic to the Palaeozoic, the infilling of intra-cratonic basins (Figure I.2: Paraná, Amazonas, Parnaíba and - not shown - Sanfranciscana Basins) started in the Ordovician-Silurian (Schobbenhaus Filho *et al.*, 1984).

Relevant to the present study are the Paraná and Sanfranciscana Basins, occurring respectively to the south and to the north of an important structural high (the Alto Paranaíba Arch). The stratigraphic record of these basins is not complete in the study area. The units occurring in the Minas Gerais State and, in particular, in the Araxá-Tapira region, are described in section I.3.2 of this Chapter. For a complete account of the stratigraphic units of the Paraná Basin, the reader is referred to the works of Schobbenhaus Filho *et al.* (1984) and Zalán *et al.* (1990). The stratigraphy of the Sanfranciscana Basin is described in Seer *et al.* (1989) and Campos and Dardenne (1997a).

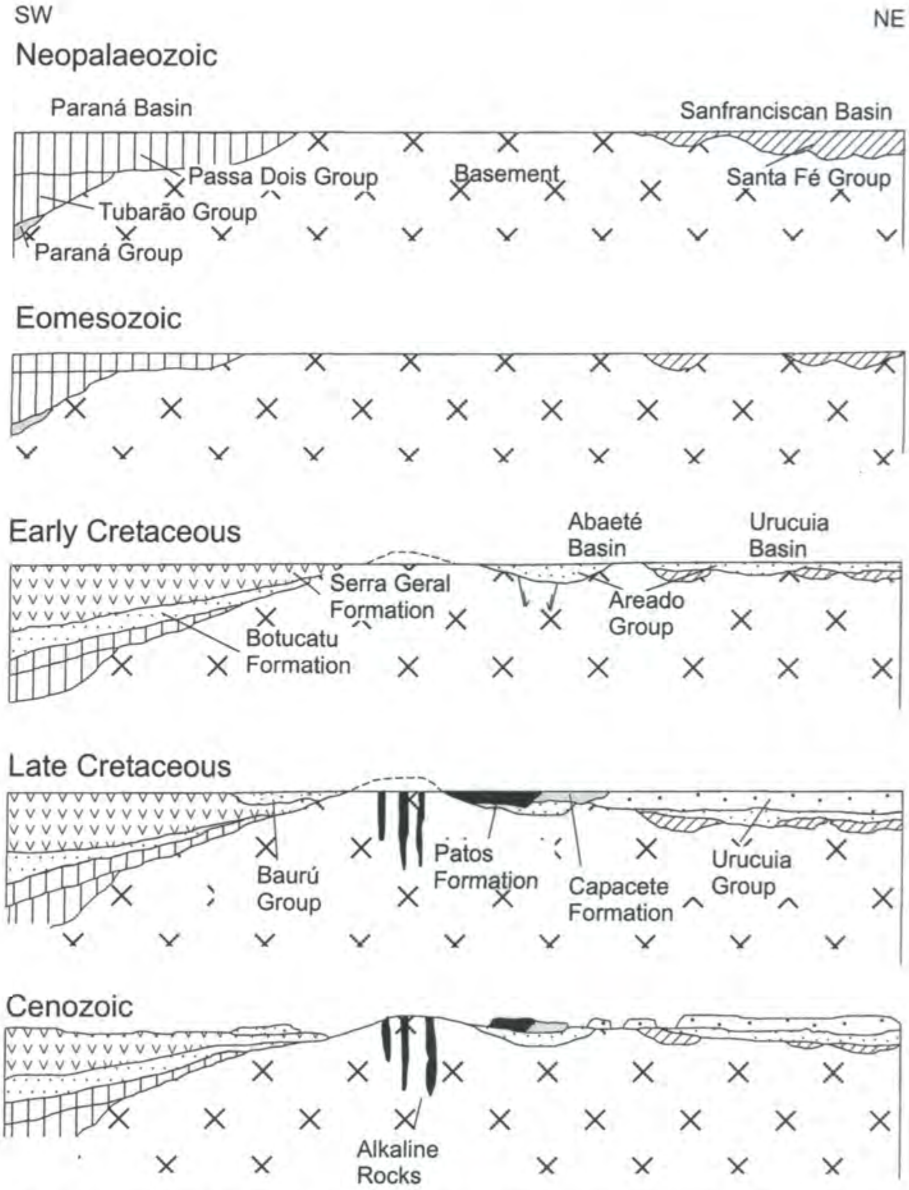

Figure I.5- Tectonic evolution of the Alto Paranaíba region, according to Campos and Dardenne (1997b)

A model for the tectono-stratigraphic evolution of the Paraná and Sanfranciscana Basins in the Alto Paranaíba region was devised by Campos and Dardenne (1997b). Figure I.5 illustrates how the independent sedimentation of the Paraná and Sanfranciscana Basin was greatly influenced by the uplift of the Alto Paranaíba Arch, which started in the Early Cretaceous but was particularly intense during the Late Cretaceous, coinciding with the emplacement of the APIP rocks. It should be noted that these two periods coincide with extensive magmatic activity in Southern Brazil (see below).

I.2.4 - THE CRETACEOUS-EOCENE MAGMATISM

Voluminous magmatism occurred in Central and Southern Brazil, and in Eastern Paraguay, from Early Cretaceous until Eocene times. This includes the extensive Early-Cretaceous continental flood basalts (CFB) that cover much of the Paraná Basin (also known as the Paraná CFB, of the Paraná-Etendeka CFB Province) and Early-Cretaceous to Eocene alkaline provinces that occur around the margins of the Paraná Basin (Figure I.6). In both cases, the magmatism has often been associated with the thermal and/or chemical influence of mantle-plumes impacting on the base of the underlying continental lithosphere (e.g. Herz, 1977; Toyoda *et al.*, 1994; Gibson *et al.,* 1995a,b, 1997a; VanDecar *et al.,* 1995; Thompson *et al.,* 1998). Contemporaneous CFB and alkaline rocks in western Africa have also been linked with plume impact (e.g. Milner *et al.*, 1995b; Milner and Le Roex, 1996; Lanyon and Le Roex, 1995; Le Roex and Lanyon, 1998)

The Cretaceous alkaline igneous provinces occurring at the margins of the Paraná Basin, in Brazil and Paraguay, have received increased attention during recent years, in a series of geochemical, isotopic and mineralogical studies (e.g. Morbidelli *et al.,* 1995b; Bizzi *et al.*, 1995; Gibson *et al.*, 1995a,b, 1997a; Comin-Chiaramonti and Gomes, 1996; Comin-Chiaramonti *et al.,* 1997; Carlson *et al.*, 1996; Thompson *et al.*, 1998). The location and age-grouping of these provinces is given in Figure I.6. The geographic distribution of their emplacement ages allows the grouping of these provinces into three main categories: a) the northern provinces (Poxoréu, Iporá, Alto Paranaíba) are Upper Cretaceous; b) the southern provinces, on both the west (Eastern Paraguay Province) and the east (Ponta Grossa Province) have a more widely variable age range; Early-Cretaceous magmatism (roughly contemporaneous to the Paraná CFB) seems to predominate but Late-Cretaceous alkaline rocks may also occur (e.g. in the Ponta Grossa province and further south, in the Lages and Piratini regions; c) the easternmost of the alkaline provinces (Serra do Mar) contains the youngest alkaline rocks, varying from Late Cretaceous to Eocene.

The Early-Cretaceous alkaline magmatism is thought to be associated with the impact of the Tristan mantle plume (Gibson *et al.*, 1997a), which is also considered to be responsible for the Paraná Etendeka CFB and for the contemporaneous alkaline magmatism in western Africa (Milner *et al.*, 1995b; Milner and Le Roex, 1996; Le Roex and Lanyon, 1998). The Late-Cretaceous and Eocene magmatism in the north and northeast margins of the Paraná Basin is thought to be related to the Trindade mantle-plume (Crough *et al.*, 1980; Gibson *et al.,* 1995b, 1997b; Thompson *et al.*, 1998). According to this model, the Poxoréu and Alto Paranaíba provinces are associated with the Late-Cretaceous impact of the starting head of the plume under central Brazil, whereas the Cretaceous-Eocene Serra do Mar province represents the leakage of hot mantle to the south as the thick, eastward-moving lithosphere of the São Francisco craton passed over the plume tail.

Gibson *et al.* (1995a) recognised a large-scale geographic zoning in Cretaceous mafic potassic magmas, whereby the mafic rocks in the northern provinces (including the Serra do Mar province, to the east) are high-Ti (>2.5 % TiO_2), whilst in the southern provinces the mafic rocks are typically low-Ti (< 2.5% TiO_2), regardless of age variation. They interpreted this and other differences in trace-element and isotopic signatures as the result of variations in the sub-continental lithospheric mantle (SCLM) sources. They also demonstrated the spatial association of "High-" and "Low-Ti" mafic alkaline rocks with the "High-" and "Low-Ti" geographical domains of the Paraná Continental Flood Basalts (CFB), and established a correlation of the two types of provinces with mobile belts and cratonic settings, respectively.

The Tapira alkaline-carbonatite complex, which is the main subject of this thesis is part of the Alto Paranaíba Igneous Province (Figure I.6). This province will be described in some detail in section I.3.3 of this chapter. For descriptions of the remaining provinces the reader is referred to the following literature. The location and field description of most individual localities of Brazilian and/or Paraguayan alkaline rocks and carbonatites can be found in the comprehensive compilation by Woolley (1987). More recent accounts are found in Gomes *et al.* (1990); Gibson *et al.* (1995b); Comin-Chiaramonti and Gomes (1996); Thompson *et al.* (1998)

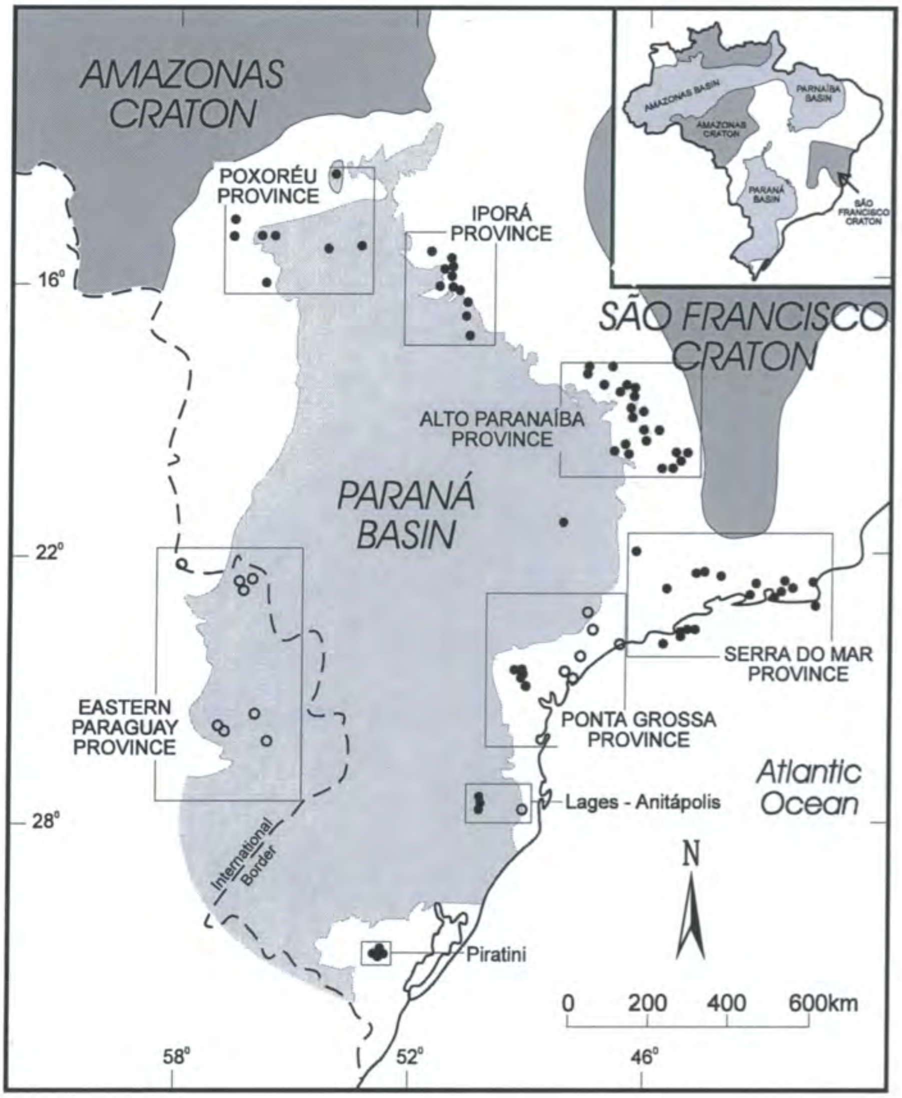

Figure I.6 - Location of the alkaline provinces of the margins of the Paraná Basin. Open circles represent Early Cretaceous rocks; solid circles are Late-Cretaceous rocks (except for the Serra do Mar Province - Cretaceous to Eocene). Adapted from Gibson et al. (1995b).

I.3 - REGIONAL GEOLOGY

The western part of the Minas Gerais State and, in particular, the Cretaceous alkaline rocks that occur in that area have long since been the subject of attention in the Brazilian geologic literature. The region of Araxá has been under scrutiny for its mineral resources since the eighteenth century. During the 1950's the importance of the alkaline intrusions, containing significant deposits of phosphate and niobium, became well established (Barbosa *et al.* 1970).

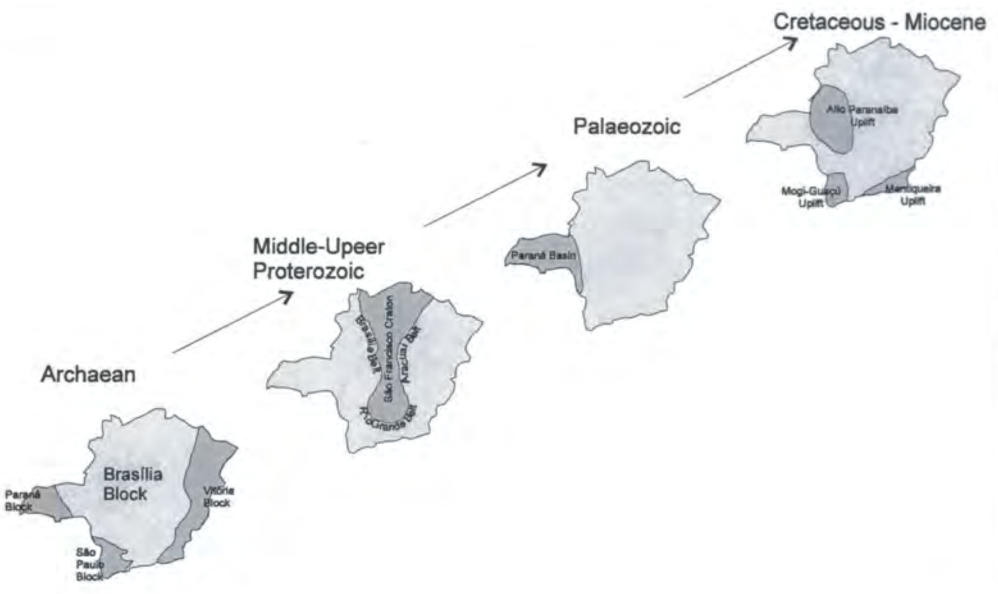

Figure I.7 - Main stages of geological evolution of the Minas Gerais State, according to Pedrosa-Soares et al. (1994)

Figure I.7 presents a simplified tectonic evolution of Minas Gerais state, as summarised by Pedrosa-Soares *et al.* (1994). Five major stages are recognised:

a) during the Archaean and Lower Proterozoic the region consisted of four large crustal blocks (Brasília, Vitória, São Paulo and Paraná)

b) during the Middle and Upper Proterozoic, a series of orogenic belts and platform sedimentary covers were established. The São Francisco Craton was then consolidated, surrounded by the Araçuaí, Alto Rio Grande and Brasília Late-Proterozoic fold belts

c) The beginning of the Palaeozoic marked the establishment of the Paraná Basin. The basin was then infilled with sediments and, later (Early-Cretaceous) with large volumes of flood basalt (Serra Geral Formation, or Paraná Basalts).

d) The uplift of the Alto Paranaíba, Mogi-Guaçú and Mantiqueira regions took place from the Cretaceous to the Miocene.

e) Establishment of continental basins and zones of tectonic reactivation, during the Neogene and Quaternary (not shown in Figure I.7).

The detailed geology of the Alto Paranaíba region is summarised in Figure I.8. An account of the aspects relevant to the present research is given in the sections below.

I.3.1 - LATE-PROTEROZOIC UNITS

The main lithologic units occurring in the vicinity of the Tapira complex belong to the internal and external zones of the Brasília belt (Fuck, 1994; Fuck *et al.*, 1994).

The internal zone is represented by the granite-gnaisses and the meta-sedimentary/meta-volcanic sequences of the Araxá Group. The former have geochemical affinity with syn-collisional granites and are extensively mylonitised, having been, in many instances, transformed in feldspathic micaceous mylonites (H. J. Seer, personal communication). This has traditionally misled previous investigators, who mapped many of these rocks as meta-sediments, but the work in progress by Seer suggests that significant portions of the Araxá schists may be of mylonitic origin. Similar, strongly mylonitised syn-kinematic granites have been reported by Brod *et al.* (1991) for the region of Coromandel, further to the north. Genuine meta-sedimentary rocks of the Araxá Group comprise quartz-mica-schists (occasionally containing one or more of the minerals garnet, staurolite and kyanite) and subordinated quartzites. Coarse- to fine-grained amphibolites, representing the Proterozoic ocean crust, also occur.

The external zone is represented in the area by the Canastra and Ibiá Groups. The Canastra Group is composed of locally carbonaceous schists, phyllites and quartzites, metamorphosed in the greenschist facies. In contrast with Araxá Group, the Canastra quartzites are volumetrically significant components of the meta-sedimentary succession, and exert an important control on the regional landscape, including the dome-shaped structure resulting of the intrusion of the Tapira complex (Figure I.9). The Ibiá Group consists of green-coloured carbonate-quartz-chlorite phyllites of greenschist metamorphic grade.

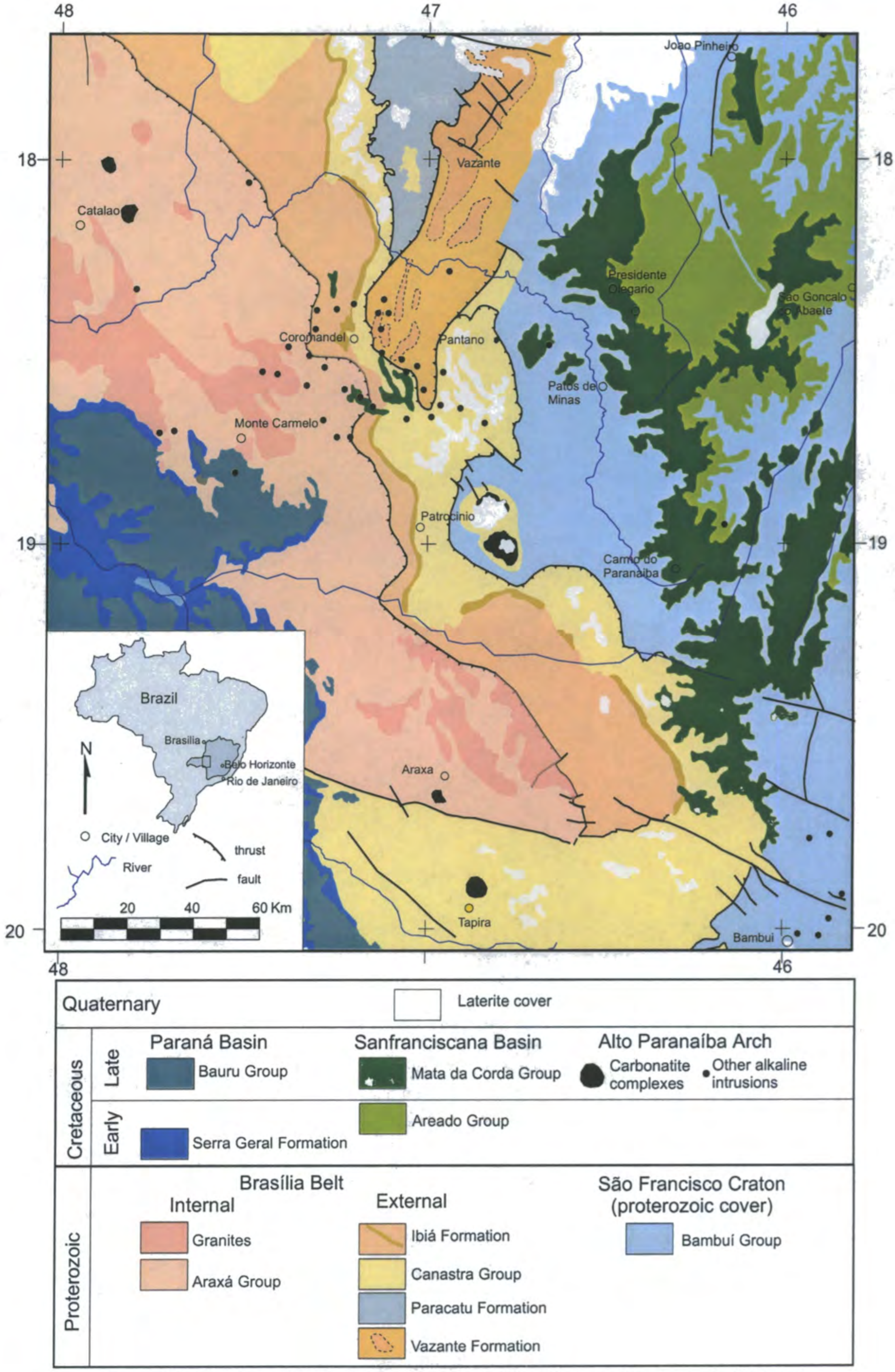

Figure I.8 - Geology of the Tapira Region (adapted fromPedrosa-Soares et. al., 1994 and Schobbenhaus et al., 1984).

The rocks of the internal zone of the Brasília belt are thrust over those of the external zone (Figure I.8) and these, in turn, are thrust over the rocks of the cratonic zone of the Brasília belt, consistent with the overall eastward tectonic transport (i.e. towards the São Francisco Craton) observed elsewhere.

I.3.2 - PALAEOZOIC TO CRETACEOUS UNITS

These rocks are associated to the infilling of the Paraná and Sanfranciscana Basin, respectively, to the NE and to the SW of the Alto Paranaíba Arch. The Phanerozoic units present in Minas Gerais State were summarised by Pedrosa-Soares *et al.* (1994) and are briefly described below.

Paraná Basin

Because the studied area is located at the very margin of the Paraná Basin, the stratigraphic record is rather incomplete, with only a few units represented.

The earliest sedimentary record of the Palaeozoic in Minas Gerais State is the Pouso Alegre Formation (Cambrian-Ordovician), composed of sandstones, arkoses, polymitic conglomerates, siltites, argilites and marls. These rocks show low-grade metamorphism and have been interpreted as either the base unit of the Paraná Basin or, alternatively, as molassic deposits associated with the end of the Brasiliano tectonic cycle (Pedrosa-Soares *et al.*, 1994).

The next depositional event in the area occurred during the Carboniferous-Permian, represented by the fluvial-glacial conglomerates, sandstones, siltstones and shales of the Aquidauana Formation (Tubarão Group).

During the Jurassic/Early Cretaceous the São Bento Group was deposited, comprising aeolian sandstones of the Botucatu Formation and the flood basalts (plus acidic volcanics) of the Serra Geral Formation. The basalts generally overlie, but are occasionally intercalated with, the aeolian sandstones. The Serra Geral Formation (Paraná CFB) correlates with the Etendeka Group of Northwestern Namibia (e.g. Milner *et al.*, 1995a), and the two units have often been collectively designated as the Paraná-Etendeka CFB province. This is a large igneous province, similar in volume/area to other world-wide CFB provinces (e.g. Karoo, Deccan, Columbia River, Siberia). High

Figure I.9 - Landsat (TM) image showing the dome structure surrounding the Tapira Complex (compare regional structure of the rocks of the Brasília Belt, to the north). The area of the phosphate mine is also clearly visible in the northern portion of the complex.

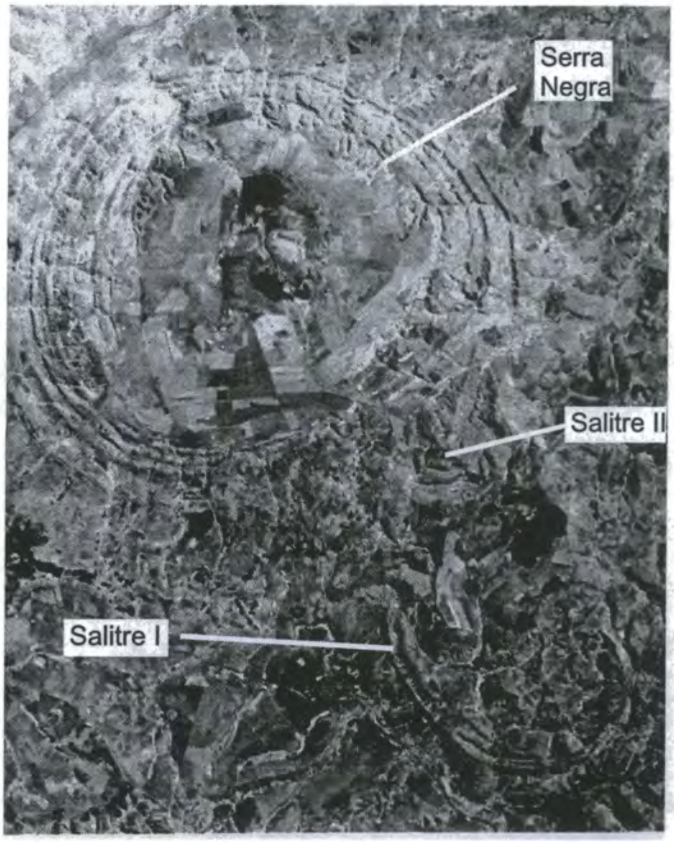

Figure I.10 - Landsat (TM) image showing the Serra Negra and Salitre carbonatite complexes. The dome structure is well defined around the Serra Negra complex, to the north, and less visible in Salitre, to the south.

precision ^{40}Ar-^{39}Ar dating by Turner *et al.* (1994) indicate that the main eruptive phase of the Paraná CFB occurred between 138 and 131 Ma.

The Bauru Group (a continental, terrigenous succession with subordinate carbonates) unconformably overlies the Serra Geral Formation. It was deposited in fan systems and lakes under a semi-arid regime. The basal unit of the Bauru Group (Uberaba Formation) is considered contemporaneous with the extensive Late-Cretaceous alkaline magmatism of the APIP (Pedrosa-Soares *et al.*, 1994).

By the end of the Late Cretaceous a period of relative stability was achieved in the region, until neotectonic reactivations of the Middle Miocene started shaping the present landscape in the area

Sanfranciscana Basin

The earliest sediments recorded from the Sanfranciscana Basin in Minas Gerais State are the Permian-Carboniferous glacial (tillites, diamictites, sandstones and shales) deposits of the Santa Fé Group, which can be correlated with the glaciation centred in the southeast portion of the Paraná Basin (Pedrosa-Soares *et al.*, 1994).

During the Cretaceous, the Sanfranciscana Basin became isolated from the Paraná Basin by the uplift of the Alto Paranaíba region. The Early Cretaceous is marked by the deposition of the Areado Group (conglomerates, siltstones, shales and sandstones) in a semi-arid environment. The shape of the depositional basin was controlled by NNE-trending faults (Seer *et al.*, 1989).

The Late Cretaceous witnessed the principal phase of uplift in the Alto Paranaíba, with accompanying extensive alkaline magmatism in the Sanfranciscana Basin. This is expressed by the alkaline-ultramafic volcanic rocks (flows, breccias, tuffs and small intrusions) of the basal unit of the Mata da Corda Group (Patos Formation). The volcanic rocks were spatially associated with, and are covered by sandstones and subordinate conglomerates (Capacete Formation) deposited in fan systems adjacent to the volcanic edifices (Seer *et al.*, 1989). During the Late Cretaceous the well-sorted sandstones, with subordinate conglomerates, siltstones and shales of the Urucuia Group were deposited in a fluvial environment, with some aeolian contribution. The Urucuia Group is considered to be partly synchronous with the Capacete Formation of the Mata da Corda Group (Campos and Dardenne, 1997a).

I.3.3 - LATE CRETACEOUS ALKALINE MAGMATISM

During the Late Cretaceous the western Minas Gerais and the adjacent portion of southern Goiás State were the site of emplacement of a large number of mafic to ultramafic, ultrapotassic alkaline rocks, collectively known as the Alto Paranaíba Igneous Province (APIP: Almeida, 1983; Gibson *et al.,* 1995b). This intense magmatic activity is represented by various types of intrusive (dykes, pipes, vents, diatremes, plutonic complexes) and extrusive (lavas and pyroclastics) bodies. The work by Gibson *et al.* (1995b) demonstrated that the magma types occurring in the APIP include kimberlites, madupitic olivine lamproites and kamafugites, in addition to large intrusive complexes composed of ultramafic plutonic rocks (mainly dunites and alkali-pyroxenites), phlogopite-picrite dykes (previously described as lamprophyres) and carbonatites. They have also shown that the province was emplaced in a narrow interval of time, between 80 and 90 Ma, despite a much wider span registered in the literature (e.g. Ulbrich and Gomes, 1981; Sonoki and Garda, 1988; Bizzi *et al.*, 1993, 1994). Rocks of kamafugitic affiliation are by far the most abundant in the province. Madupitic olivine lamproites are restricted to the NW portion of the APIP, including the occurrences at Bocaina, Córrego do Couro, Morro Alto, Mata do Lenço (Gibson *et al.*, 1995b). Pipes of diamondiferous (Gonzaga and Tompkins, 1991) kimberlites, containing xenoliths of garnet lherzolite (Leonardos *et al.*, 1993; Carvalho and Leonardos, 1995) occur at the locality of Três Ranchos (Goiás State), in the north of the province.

The ultrapotassic magmatism in the APIP took place mainly along the Alto Paranaíba Arch, a NW-SE trending structure which separates the Paraná and Sanfranciscana Basins. This structure is well marked by magnetic anomalies, interpreted by Bosum (1973) as the result of mafic dyke swarms emplaced along a N50°W direction. Some of the dipole anomalies observed in aeromagnetometry maps coincide with the intrusive alkaline bodies, whilst numerous others may represent unexposed intrusions. Two phases of uplift of the Alto Paranaíba Arch have been recognised (Campos and Dardenne, 1997b) and are present in the sedimentary record of the region

(Figure I.5). The first phase of uplift was less intense, and Early-Cretaceous in age (therefore contemporaneous with the formation of the Paraná flood basalts). The main phase of uplift occurred in the Late Cretaceous, and is associated with the alkaline magmatism of the Alto Paranaíba Igneous Province.

The alkaline magmatism is well represented in the stratigraphic record of the Sanfranciscana Basin, where extensive areas were covered by the Mata da Corda Group. The chemical and mineralogical similarities of these volcanic rocks to kamafugites is now firmly established (Seer and Moraes, 1988; Seer *et al.*, 1989; Sgarbi and Valença, 1993, 1994; Sgarbi and Gaspar, 1995; Gibson *et al.*, 1995a). K-Ar dating of phlogopite separates from the Patos de Minas-Carmo do Paranaíba region yielded an age of 83.6 ± 1.4 Ma. (Gibson *et al.*, 1995a).

Lavas and tuff horizons of the Mata da Corda Group commonly contain xenoliths of plutonic rocks such as dunite, pyroxenite, melilitite and syenite. This rock association is also common in the carbonatite complexes of APIP, and Seer and Moraes (1988) suggested that large amounts of these xenoliths in the volcanic breccias may indicate the presence of intrusive carbonatite-bearing complexes at depth. Furthermore, their petrographic description of the pyroxenite xenoliths (clinopyroxenites containing calcic augite, phlogopite, perovskite, apatite, melanite opaque minerals and occasionally Ba-rich feldspar) closely resembles the pyroxenites (bebedourites) of the Tapira complex, described in this thesis (see Chapter II). Combined with the occurrence of phlogopite-picrites dykes (Gibson *et al.*, 1995b), which are also abundant in Tapira and other carbonatite complexes of the APIP, and with the obvious provinciality/temporal association, this suggests a strong link between the kamafugitic rocks of the Mata da Corda and the APIP carbonatites. This point will be further investigated in detail in the subsequent Chapters of this thesis.

Carbonatite complexes occur in several of the alkaline igneous provinces surrounding the Paraná Basin and reviews of the Brazilian carbonatites can be found in Berbert (1984), Gomes *et al.* (1990) and Morbidelli *et al.* (1995b). In the APIP, a number of relatively large (up to 65 km^2), intrusive, carbonatite-bearing ultramafic complexes are found. These occurrences comprise the complexes of Catalão I and Catalão II in the southern Goiás State, and Serra Negra, Salitre I, Salitre II, Araxá and Tapira in western Minas Gerais State. The complexes intrude Late-Proterozoic metamorphic rocks of the internal and external domains of the Brasília Mobile belt, which are conspicuously deformed into dome structures (Figures I.9 and I.10).

The tropical weathering regime prevailing in the region, and the inward drainage patterns developed from the weathering-resistant quartzite margins of dome structures (e.g. Mariano and Marchetto, 1991; Danni *et al.*, 1991) resulted in the development of an extremely thick soil cover in most of the complexes. Surface outcrops are very rare and the best samples for geochemical studies are restricted to drill cores.

The Tapira complex is described in section I.3.4. A brief description of the other carbonatite-bearing complexes in the APIP is given below.

Catalão I (18°08'S; 47° 48'W) and Catalão II (18°02'S; 47°52'W)

The intrusions of Catalão I and II are the northernmost known carbonatite occurrences in the APIP.

Catalão I, situated approximately 20 km to the NE of the city of Catalão is the largest (27 km^2) and best known of the two complexes (e.g. Danni *et al.*, 1991; Gaspar and Araújo, 1995; Gaspar *et al.*, 1994; Araújo, 1996). This is a roughly circular-shaped (ca. 6.0 km in the N-S direction and 5.5 km in the E-W direction) multi-stage intrusion that domed the Late-Proterozoic schists and quartzites of the Araxá Group. The age of the Catalão I complex has been determined as 85 ± 6.9 Ma. (recalculation by Sonoki and Garda, 1988 of a K/Ar age by Hasui and Cordani, 1968). The rock-types occurring in the complex are mainly dunites, clinopyroxenites, carbonatites and metasomatic foscorites. Carbonatite occurs as a central massive sovite body, as well as widespread dykes and veins, whilst the ultramafic and metasomatic rocks dominate in the more external portions of the complex. Gibson *et al.* (1995b) reported the occurrence of phlogopite-picrite dykes up to 5 m thick from drill cores of Catalão I.

Brecciation and fenitisation of the county rock are conspicuous, resulting in the formation of orthoclase, aegirine and riebeckite in the fenitised quartzites. Danni *et al.* (1991) described the occurrence of aegirine-bearing nepheline syenites in the southern and western borders of the complex, but pointed out that these rocks appear to grade to the fenites. A metasomatic origin for these syenites have also been previously suggested by Carvalho (1974) and Carvalho and Bressan (1981). Feldspathoids are not present in the modal composition reported by Danni *et al.* (1991) for any of the other rock-types. The predominance of foscorites over the other rock-types testifies to the particularly intense hydrothermal processes that affected this complex. The occurrence of priderite, with compositions similar to those occurring in lamproites and kimberlites, has been reported in association with the late stage alteration of the ultramafic rocks by interaction with the carbonatite magma (Gaspar *et al.*, 1994).

Important deposits of phosphate, niobium, rare-earths, titanium and vermiculite are present in Catalão I (Carvalho and Bressan, 1981; Gierth and Baecker, 1986) and the complex is currently mined for apatite and pyrochlore.

The complex of Catalão II is intrusive in the meta-sedimentary rocks of the Araxá Group, forming a small (18 km^2) topographic high. The shape of the complex is irregular; elongated in the NE-SW direction and with sinuous east and west margins that reflect the existence of independent intrusions. Machado Junior (1992a) described the rock-types present in the Catalão II complex, as follows: a) pyroxenites are composed of augite, biotite, apatite, magnetite, zircon and accessory amphibole, K-feldspar, sphene and calcite. Felsic rock-types comprise quartz-and alkali feldspar-syenite, locally grading to more melanocratic varieties (up to 30% mafic minerals, mainly sodic pyroxenes, amphibole and mica); c) carbonatites include petrographic varieties of sovites, silicocarbonatites and beforsites; d) lamprophyre occurs as thin dykes with olivine phenocrysts set in a phlogopite-carbonate groundmass; d) foscorites are a product of metasomatic alteration of the ultramafic rocks.

Interestingly, the syenites described by Machado Junior (1992a) seem to be either silica-saturated (alkali feldspar syenites lacking both quartz and nepheline) or silica-oversaturated (quartz syenites). This contrasts with syenites from Tapira and Salitre, studied during the present research (see section I.3.4 below). His description of lamprophyres closely resemble the phlogopite-picrites that are common in other complexes. Machado Junior (1992b) obtained a Rb-Sr age of 83.4 ± 0.9 Ma for Catalão II.

Serra Negra (18°55'S; 46°50'W)

The Serra Negra complex, located to the east of the city of Patrocínio, is the largest of the carbonatite-bearing complexes of APIP. Amaral *et al.* (1967) obtained ages of 83.7 and 83.4 Ma in biotite from peridotite. The intrusion was forcibly emplaced in the quartzites of the Canastra Group, generating the best example of intrusion-related doming among the APIP complexes (Figure I.10).

According to Mariano and Marchetto (1991), the complex is composed of a central core of sovite (estimated to be ca. 4.5 km in diameter), often containing apatite in excess of 20% and up to 5 % dolomite, with accessory phlogopite, magnetite, humite, rutile, pyrochlore, baddeleyite, pyrrhothite and pyrite. This central carbonatite is surrounded by a zone of pyroxenite (bebedourite) essentially composed of salite, phlogopite, magnetite, perovskite, apatite, calcite and minor ilmenite. Dunites and peridotites occur near the northern and northwestern margin of the complex. The bebedourite series is layered, and modal variations are common, with zones of concentration of apatite or magnetite-perovskite. These are interpreted as facies variations of the bebedourites by Mariano and Marchetto (1991), although they also point out that these ore bodies vary from concordant to dyke-like. Similar features were found during the present research in the Tapira complex (see below) and are interpreted here as indicative of the remobilisation of crystal-mush aggregates, during the emplacement of partially-crystallised cumulate sequences.

Another striking feature of the Serra Negra dome is that the only contact effect observed is the silicification of the country rock. Mariano and Marchetto (1991) emphasise that, despite careful examination of the country rock, no fenites or even indications of alkali metasomatism are observed. Phlogopite-picrite dykes are reported by Gibson *et al.* (1995b), cutting the dunites of the northern margin of the complex.

Salitre I and II (19°03'S; 46°47'W)

The complexes of Salitre I and Salitre II occur immediately to the south of the Serra Negra complex, and these three bodies are considered to form a system of coalescing intrusions (Mariano and Marchetto, 1991). Salitre I has a distorted oval shape, with approximate dimensions of 7 km in the N-S direction and 5 km in the E-W direction. Salitre II is a small (2.5 km^2) plug located between the Salitre I and Serra Negra complexes. The topographic expression of the Salitre I and II complexes is somewhat less distinctive than that of Serra Negra. K/Ar dating of biotite in bebedourite yielded an age of 86.3 ± 5.7 Ma. (recalculated by Sonoki and Garda, 1988, from Hasui and Cordani, 1968). The Serra do Salitre (Salitre Mountains) is the type area for bebedourite, as defined by Tröger (1928, see also Chapter II in this thesis).

The petrographic types present in the complex have been described by Mariano and Marchetto (1991) and Morbidelli *et al.* (1995a). Salitre I is composed dominantly of pyroxenites (bebedourites) and feldspathic rocks (tinguaite, trachyte, fenite). A small plug of apatite-rich carbonatite occurs in the northern portion of the complex. As observed for Serra Negra, substantial modal variations are present in the ultramafic rocks, including olivine-, perovskite- and apatite-rich facies, in addition to the typical bebedourites. Other mineral phases present in the bebedourites are phlogopite, opaque minerals, melanite and sphene. The carbonatite is a sovite with variable amounts of apatite and opaque minerals, plus accessory dolomite and phlogopite. Morbidelli *et al.* (1995a) also report the presence of accessory olivine and zircon in the Salitre I carbonatite. Foscorites result from carbonatitic metasomatism of the ultramafic rocks. According to Mariano and Marchetto (1991) and Haggerty and Mariano (1983), a significant part of the feldspathic rocks occurring in the southern portion of Salitre I, previously interpreted as trachytes and phonolites, are in fact aegirine-nepheline-sanidine rheomorphic fenites. They distinguish the truly magmatic syenitic rocks from the fenites on the basis of the absence of magnetite and presence of sodic plagioclase, dalyite ($K_2ZrSi_6O_{15}$) and strontian loparite in the latter.

Salitre II is composed mainly of ultramafic rock-types (dunites, perovskitites, clinopyroxenites, locally crosscut by carbonatites dykes and veins.

Araxá - (19°38'S; 46°56'W)

The Araxá (also known as Barreiro) complex is a relatively small (diameter of 4.5 km) intrusion, situated approximately 6 km south of the City of Araxá, in Minas Gerais State. Available K-Ar age determinations (Sonoki and Garda, 1988) vary from 77 to 97 Ma.

The complex penetrates schists and quartzites of the Araxá Group which, in the same fashion as the other APIP complexes, are deformed into a dome structure. The complex has a particularly wide fenitisation aureole that reached up to 2.5 km from the contact, and resulted in the formation of arfvedsonite, calcite, alkali feldspar, sodic pyroxene and apatite in the quartzites, especially along fractures (Issa Filho *et al.*, 1984). As observed in Catalão I, the metasomatic rocks (foscorites, glimmerites) are volumetrically substantial in the Barreiro complex, but preserved remnants of the original ultramafic plutonic rocks are extremely scarce in the latter. One main carbonatite plug and a series of other small carbonatite intrusions occur in the carbonatite/foscorite core of the complex. A glimmerite zone occurs between this core and the fenitised country rock.

Unlike other carbonatite complexes in the APIP, in Araxá the predominant carbonatite type is dolomitic (beforsite), and typical sovites occur only in the NW portion of the complex (Silva, 1986). The complex has great economic importance (Grossi Sad and Torres, 1976; Silva, 1986), since it hosts the world's largest known niobium (bariopyrochlore) reserve. In addition to Nb, the Barreiro complex is also currently mined for phosphate and contains ore-grade reserves of uranium and rare-earths. Within APIP, the Araxá complex can be considered as an extreme example, with regard to the predominance of dolomitic carbonatites and to the intensity of the metasomatic alteration of the ultramafic rocks.

I.3.4 - GEOLOGY OF THE TAPIRA COMPLEX

The Tapira complex is the main subject of this research. It is the southernmost (19°53'S; 46°50'W) carbonatite-bearing complex in the APIP, located approximately 30 km southeast of the city of Araxá, Minas Gerais State. K-Ar dating of mica yielded ages of 85.6 and 87.2 Ma. (recalculation by Sonoki and Garda, 1988, of unpublished determinations by C. B. Gomes).

The complex is roughly elliptical, 35 km^2 in area, and consists dominantly of alkaline pyroxenite (bebedourite), with subordinate carbonatite, serpentinite (dunite), glimmerite, syenite, melilitic rock (uncompahgrite) and ultramafic potassic dykes. Economic concentrations of titanium, phosphate, niobium, rare-earths and vermiculite are associated with the weathering cover. The complex is currently being mined for phosphate (Figure I.9).

The country rocks are Proterozoic phyllites and quartzites of the Canastra Group, which have been deformed into a dome structure (Figures I.9, I.11, I.12), as well as fenitised and thermally affected, during the intrusion of the complex. The thermal and metasomatic effects, however, appear to be restricted to the quartzites in the immediate vicinity (few hundreds of metres) of the contact with the intrusion. In the country rocks closest to the contact, the interaction with metasomatic fluids resulted in the formation of sodic pyroxene and several generations of feldspars (Chapter II). The pyroxene disappears away from the contact but feldspathisation may persist (Figure I.13). This quartz-feldspathic fenite is easily altered under tropical weathering and rarely crops out, making it difficult to estimate the real extent of the fenite aureole. Locally the quartzite may develop columnar jointing due to the thermal effect of the intrusion (Figure I.14)

As is the rule with APIP carbonatite complexes, outcrops of Tapira alkaline rocks are rare. Some exposures are occasionally revealed by the progress of the mining activities and, in rare occurrences, poorly preserved rocks crop out in streams. Fresh samples are virtually restricted to drill core material.

A schematic representation of the rock distribution in the complex is presented in Figure I.15. Because most of the information was obtained from short segments (generally a few metres) of fresh rock at the bottom of drill cores, the observation of the spatial relationships between the different units is severely limited. Therefore, Figure I.15 is not intended as a geological map of the complex, but as a sketch to support the discussion of various aspects that will be developed in the remainder of this thesis. All the limits in the sketch are approximate, and the areas shown represent the predominance of a given rock type as deduced from the drill cores, rather than implying laterally or vertically continuous “stratigraphic” units.

Silicate Plutonic Series

In this thesis the coarse-grained silicate rocks (dunites, wehrlites, bebedourites and syenites) are referred to collectively as the Silicate Plutonic Series (SPS). The ultramafic rocks consist dominantly of bebedourite, subdivided into the B1 and B2 units (Figure I.15) on the basis of their spatial distribution and petrographic/compositional characteristics (see Chapter II). Because of their restricted occurrence dunites, wehrlites

Figure I. 11 - Sub-horizontal attitude of quartzites of the Canastra Group, away from the Tapira Complex.

Figure I.12 - Quartzites of the Canastra Group in the vicinity of the Tapira Complex. Note the sub-vertical character of the foliation, as a result of the deformation caused by the intrusion.

Figure I.13 - Fenitised quartzite of the Canastra Group. Note the lighter-coloured, subhedral porphyroblasts of feldspar weathering out.

Figure I.14 - Block of quartzite of the Canastra Group showing columnar jointing caused by the thermal effect of the intrusion.

and modal variations in the proportions of perovskite, magnetite and/or apatite are not distinguished from the associated B1 and B2 bebedourites in Figure I.15.

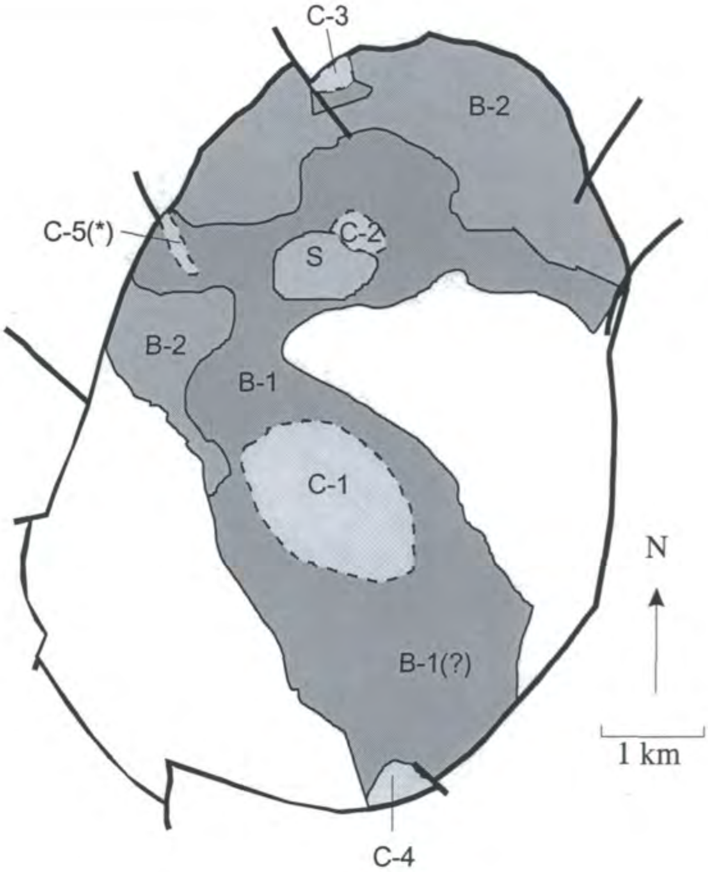

Figure I.15 - Geological sketch of the Tapira complex. Units represented are Bebedourites (B1, B2), Carbonatites (C1 to C5), Syenite and Syenite-carbonatite breccia (S). Drill core information in the southern portion of the complex is scarce. No drill-core information available in the white areas. (*) C5 rocks also occur as scattered dykes and veins throughout the complex.

Ultramafic rocks - Alkaline pyroxenites (bebedourites) comprise most of the ultramafic rocks. They vary from fine to coarse grained (locally pegmatitic), and consist mainly of diopsidic pyroxene with variable amounts of phlogopite, perovskite, apatite, magnetite, melanite and sphene. Strongly oriented fabric is relatively common (Figure I.16). As observed in other carbonatite complexes of the APIP, modal variations in the essential

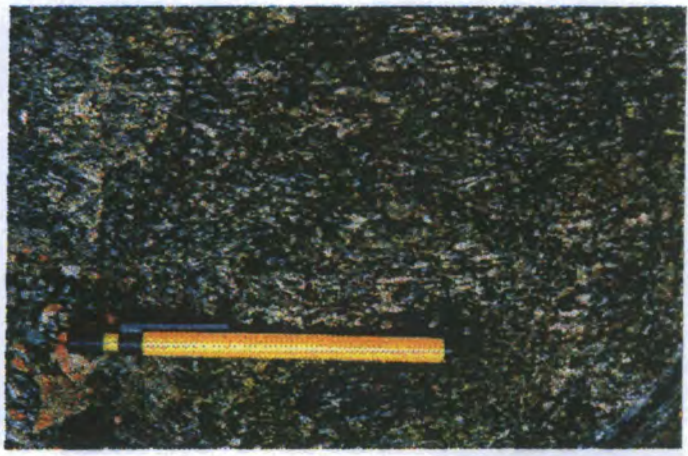

Figure I.16 *- Block of bebedourite in the Tapira mine area. The pencil shows the direction of the strongly oriented fabric, suggesting movement of a partially crystallised crystal mush.*

Figure I. 17 *- Magmatic layering in bebedourite. Outcrop in the Tapira mining area. Note the alternating phlogopite-rich and the relatively coarser grainsize of the phlogopite-rich rock. The recurrence of these phlogopite-rich layers indicates that the system was periodically enriched in volatiles. Their coarser grainsize is consistent with crystallisation in a more volatile-rich environment.*

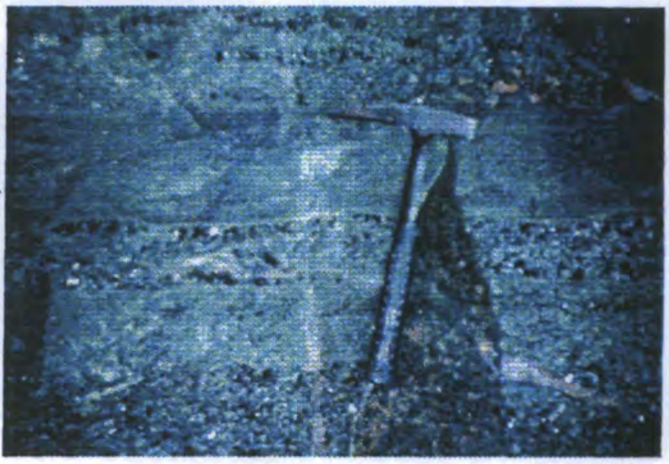

Figure I. 18 *- Segment of drill core showing a syenite-carbonatite breccia. The carbonatite intrudes the syenite, percolating along the fractures and causing the appearance of thin reaction rims (black) of phlogopite.*

Figure I. 19 *- Syenite intrusion, in the Tapira mine area. The rock is completely altered, but the contours of the intrusion (lighter patch in the bottom-centre of the mine wall) are still visible.*

mineral phases can produce facies rich in olivine (dunites, wehrlites), perovskite-magnetite or apatite. Whilst this is primarily the result of magmatic layering (Figure I.17), some of the apatite- or perovskite-magnetite-rich rocks may occur as discordant bodies cutting the igneous layering or even penetrating the country rock. Such features suggest the remobilisation of pockets of partially consolidated crystal-mush and, in conjunction with the scarcity of fenitisation effects, may indicate that the intrusion was partially consolidated during emplacement. Plutonic melilitic rocks (uncompahgrites) have been described from the northeastern border of the complex (Guimarães *et al.*, 1980). These are very coarse grained (crystals up to 3.5 cm) and consist mainly of melilite-group minerals (60%) with subordinate phlogopite, apatite, titanomagnetite, diopside, perovskite, and wollastonite.

The ultramafic rocks are intruded by syenites, carbonatites, and ultramafic dykes. Where intruded by carbonatites, the pyroxenites and dunites have been locally converted to metasomatic phlogopitites. These are the equivalent of the metasomatic foscorites and glimmerites described in the literature for other complexes of the APIP (see previous sections in this Chapter).

Syenites -These occur as fragments in carbonatite-syenite breccias (Figure 1.18), but also as independent intrusions (Figure I. 19) They are essentially composed of K-feldspar plus phlogopite and/or aegirinic pyroxene, with accessory zircon and sphene. The petrographic (Chapter II) and chemical (Chapter IV) characteristics of these rocks indicate an ultrapotassic affinity, consistent with the ultrapotassic character of other rock-types in Tapira and in the Alto Paranaíba Province.

Carbonatites

A number of carbonatite bodies intrude the SPS. rocks. The carbonatites were sub-divided into five units (C1 to C5), according to their location and petrographic or compositional characteristics (Figure I.15). The intrusions vary from massive carbonatite plugs through dykes to small veinlets. The silicate rocks intruded by carbonatite are often brecciated (Figure I.18, Figure I.20) and metasomatised to a variable extent.

The intrusion of carbonatites into ultramafic rocks often results in the development of a magnetite-phlogopite-dolomite fenite. The best examples of this "reaction rock" are found in drill cores from the contact of C1 carbonatite with the bebedourites and wehrlites of the B1 unit (Figure I.15).

Brecciation of SPS rocks by the intrusive carbonatite is also a common feature. In the northwest portion of the complex, C2 carbonatites intrude both the B1 bebedourites and the syenites. In the area marked "S" in Figure I.15, carbonatites percolate fractures in the syenitic rock to form monomitic breccias (Figure I.18), indicating intrusion by a magmatic stoping process. The detached angular fragments of syenite are usually surrounded by phlogopite-rich reaction rims. In the Tapira mine area, a more explosive style of carbonatite intrusion resulted in the local development of diatreme-facies polymitic breccias, containing angular blocks of several petrographic varieties of SPS rocks, in addition to less frequent xenolithic fragments of county rock. The blocks are variable in size and may exceptionally reach up to metric dimension. The matrix of these breccias may contain lapilli-sized fragments of the same rocks, but is mainly composed of fractured crystals in a carbonate-rich groundmass. The matrix varies locally to carbonatite (e.g. Figure I.20), suggesting that the breccias may have been periodically invaded by new carbonatitic material.

Three compositional types of carbonatite have been recognised in the complex:

(1) Sovites (C1, C3, C4) are typically medium to fine grained and essentially composed of calcite and phlogopite, with accessory amounts of clinopyroxene, amphibole, opaque minerals, apatite, pyrochlore, magnetite and pyrite. Veinlets of pyrite-phlogopite and dolomite-ankerite commonly cut the sovite.

(2) Dolomite sovites (C1, C2) occur as massive bodies and dykes cutting pyroxenites, earlier sovites and syenites. Rocks of the C2 unit show a close spatial association with syenites, in the northwest portion of the complex, but also occur as dykes and breccias elsewhere. The dominant rock-type is medium to fine grained, occasionally developing a porphyritic texture given by 2 to 3 mm calcite phenocrysts in a calcite-dolomite groundmass. Both the phenocrysts and the groundmass often display flow structure. Common accessory phases are phlogopite, pyrochlore and rare barite.

(3) Beforsites (C5) occur as scattered late-stage dykes and veinlets. These rocks are fine grained, commonly banded and sometimes show flow textures. Common accessories

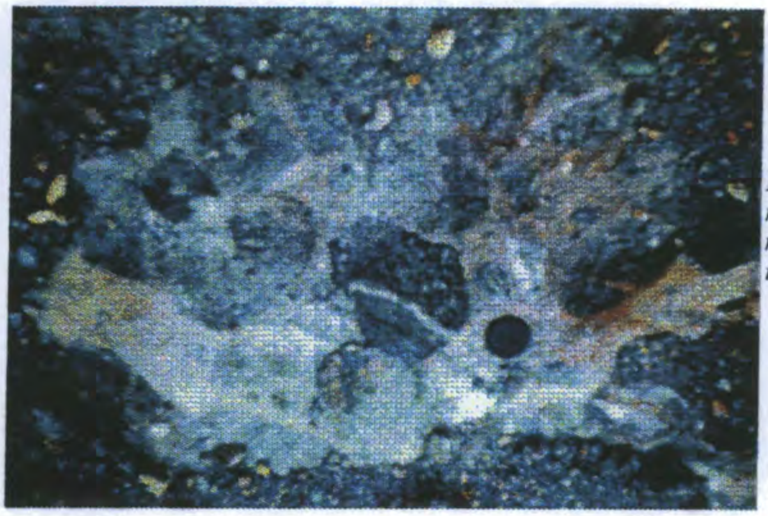

Figure I.20 - *Outcrop in the Tapira mine area. Polymitic breccia formed mainly angular fragments of SPS rocks in a carbonatite matrix.*

Figure I.21 - *Altered ultramafic dyke of the Tapira complex intruding schist of the Canastra Group. Note the centimetre-thick chilled margin of greenish-yellow colour, contrasting with the red-coloured internal portion of the dyke.*

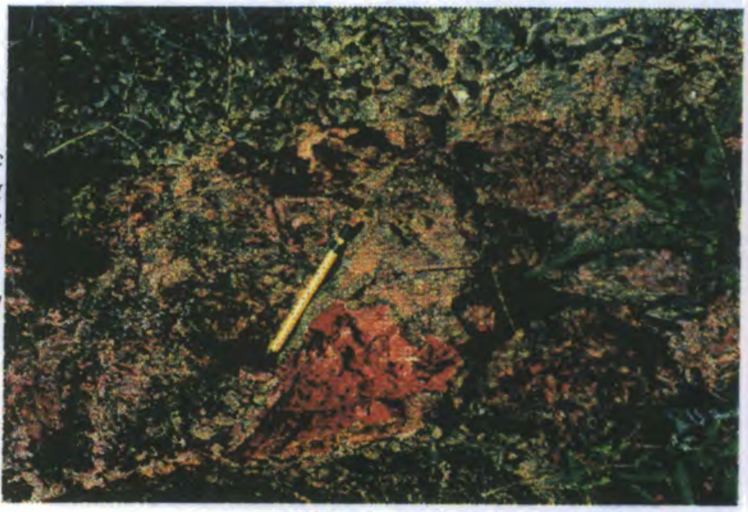

Figure I.22 - *Fresh phlogopite picrite dyke intruding granitic rock, near the city of Araxá. Note the chilled margins (darker colour) on both sides. This extremely well preserved dyke was sheltered from weathering by the more resistant country rock (photograph by H.J. Seer).*

comprise phlogopite, magnetite/ilmenite, apatite and pyrite. On the basis of drill core information, the C5 area in Figure I.15 may represent larger or more abundant dykes, but it should be stressed that C5 rocks occur in several other locations in the complex.

Ultramafic dykes

The plutonic rocks of the Tapira complex are crosscut by numerous thin ultramafic dykes. The dykes are usually a few centimetres or tens of centimetres thick, rarely reaching more than one metre. These rocks have been divided, on the basis of their chemical and mineralogical composition, into phlogopite-picrites and low-Cr dykes (see Chapters II and IV). Phlogopite-picrites consist of olivine phenocrysts set in a carbonate- and phlogopite-rich groundmass and often show evidence of flow-differentiation, with the olivine phenocrysts concentrated towards the centre of the dyke. Low-Cr dykes are very fine grained, with rare phenocrysts of phlogopite, clinopyroxene and/or apatite. Although both types of dykes are mostly restricted to the interior of the complex, they occasionally occur in the country rock, both in the vicinity and away from the complex. In this case the dykes are often completely altered (Figure 21) or, in extremely rare examples, fresh (Figure 22). Chilled margins (Figure 21, Figure 22) are a commonly observed feature in ultramafic dykes occurring outside the complex.

I.4 - SUMMARY

- Three main geotectonic domains can be recognised in central and southeastern Brazil: a) Archaean cratons; b) Proterozoic mobile belts; c) Phanerozoic sedimentary and volcanic cover. In the study area, these comprise, respectively, the São Francisco Craton, the Brasília mobile belt and the Paraná and Sanfranciscana Basins.
- Two major episodes of magmatic activity occurred during the Cretaceous. The Early Cretaceous magmatism comprise a) the Paraná continental flood basalts (CFB); and b) alkaline igneous provinces emplaced at the margins of the Paraná Basin. A second episode of intense magmatic activity, during the Late Cretaceous, produced the ultrapotassic rocks of the Alto Paranaíba Igneous Province (APIP), along with other alkaline igneous provinces, at the northern margins of the Paraná Basin.

- The APIP magmas were emplaced in metamorphic rocks of the Brasília belt, near the southwest margin of the São Francisco Craton. The alkaline rocks comprise kamafugites, lamproites, kimberlites and the carbonatite complexes of Araxá, Tapira, Serra Negra, Salitre (I and II) and Catalão (I and II).
- The Tapira complex is a composite intrusion, containing ultramafic plutonic rocks, with less abundant syenites, carbonatites and ultrapotassic ultramafic dykes.

CHAPTER II - PETROGRAPHY

II.1 - INTRODUCTION

This Chapter is concerned with the petrographic description of the studied silicate rocks and carbonatites, with emphasis on the rock suites from the Tapira complex. The information contained in it is primarily derived from samples collected by the author from drill cores and outcrops in the Tapira and Salitre complexes. However, in order to investigate possible correlations within the APIP, I was granted access to the personal collections of Prof. R. N. Thompson, Dr. S. A. Gibson, Prof. J. C. Gaspar, H. J. Seer, L. C. Moraes and I. G. Guimarães, for which I am deeply grateful. The complementary information obtained from the study of these additional samples was invaluable in the interpretation of some of the petrographic features described below.

As a first approach to the description of Tapira rock-types, the most obvious distinction is between rocks composed predominantly of silicate minerals (the Silicate Plutonic Series - SPS) and those composed essentially of carbonate (carbonatites). Fine-grained ultramafic dykes and rocks of apparently metasomatic origin are considered as separate units throughout this thesis, and described independently. As set out in Chapter I, the rocks of the Tapira complex may be arranged into different "lithostratigraphic" units on the basis of their location, composition and, less often, of the mutual relationships observed in drill cores. Accordingly, the SPS is subdivided into the B1 and B2 units and syenites; the carbonatites are subdivided into five groups (C1 to C5 units) and the dyke rocks are subdivided into phlogopite-picrites and low-Cr dykes.

II.2 - CRITERIA FOR ROCK CLASSIFICATION AND NOMENCLATURE

Because of their peculiar mineralogy, many of the Tapira rocks are difficult to fit into the commonly accepted criteria for the classification of magmatic rocks (e.g. Le Maitre *et al.,* 1989). One major reason for this is that many minerals which are not commonly considered in classification schemes (e.g. apatite, perovskite, phlogopite, magnetite, garnet) may be essential components of Tapira rocks. In particular, the ultramafic portion of the SPS and the dyke rocks pose severe difficulties to the application of established rock-classification systems.

The classification criteria used in this thesis will be discussed in the following paragraphs. It must be stressed that this Chapter is concerned with the petrographic classification alone. A chemical classification of Tapira rocks will be discussed in Chapter IV.

Classification of SPS rocks

The ultramafic portion of the SPS consists predominantly of cumulates (see below) with variable modal proportions of the essential minerals olivine, clinopyroxene, phlogopite, apatite, perovskite, chromite and magnetite. The classification of these rocks in a simplified framework (i.e. taking into account only the proportions of olivine and clinopyroxene) results in a progression from dunite through wehrlite to clinopyroxenite. However, in many samples the sum of modal apatite, perovskite and phlogopite exceeds that of olivine and clinopyroxene. In these cases, such classification is clearly inadequate to describe the composition, facies variations and the strongly alkaline character of Tapira rocks.

A slightly more accurate approximation would be achieved by adding the prefix alkali (e.g. alkali pyroxenite), as suggested by Le Maitre *et al.* (1989). However, their recommended criteria for the application of this prefix are: 1) the occurrence of modal feldspathoids and/or alkali pyroxene/amphibole; or 2) the presence of normative feldspathoids or acmite. With extremely rare exceptions, the ultramafic plutonic rocks of Tapira (and of other carbonatite complexes in the APIP) do not contain feldspathoids, and their clinopyroxene is diopsidic in composition, hence failing the first criterion. The use of normative composition to classify rocks in a sequence of cumulates with significant facies variations is, at best, adventurous. Therefore, the second criterion is rendered equally inapplicable. Moreover, the use of the name alkali-pyroxenite could induce confusion with jacupirangite, a particular variety of alkali-pyroxenite that is intimately associated with carbonatite complexes, but which differs from Tapira pyroxenites in that the latter usually do not contain nepheline. The same applies to the ijolitic series (melteigite, ijolite, urtite; distinguished on the basis of varying proportions of clinopyroxene and nepheline). These rocks, redefined by Le Maitre *et al.* (1989) as varieties of foidolite, are also commonly associated with carbonatite complexes. Again, the ijolite series is fundamentally distinct from Tapira rocks, as nepheline is an essential mineral in the former.

Tröger (1928, quoted in Tröger, 1935) defined "bebedourite" as a biotite- and perovskite- rich clinopyroxenite, typically containing 54% aegirinic diopside, 21% biotite, 14% perovskite, 10% opaque minerals and accessory apatite, K-feldspar and olivine. The type locality for this rock is the Bebedouro area, in the Salitre Mountains, Minas Gerais State (i.e. the Salitre Carbonatite Complex, in the Alto Paranaíba Igneous Province). This definition is a close enough match for most of the pyroxene-rich ultramafic plutonic rocks of Tapira. Furthermore, this rock-type is conspicuous in all carbonatite complexes of APIP, although in Catalão and Araxá significant amounts of bebedourite have been converted to phlogopite-rich metasomatic rocks ("glimmerites") by interaction with carbonatite magma or fluids. The term bebedourite has been frequently applied in the recent literature, in connection with carbonatite complexes of the Alto Paranaíba region (e.g. Gomes *et al.,* 1990; Lloyd and Bailey, 1991; Gibson *et al.,* 1995; Brigatti *et al.,* 1996). Finally, the use of this rock name is most successful in emphasising the differences between the ultramafic rocks associated with the APIP complexes and those associated with many carbonatite complexes elsewhere. Therefore, whilst appreciating that regional rock names should ideally be avoided when classifying igneous rocks, the designation bebedourite is preferred here as the best available match for the Tapira "pyroxenites" and their facies variations. The remainder of the plutonic rocks (dunites, wehrlites, and syenites) are named according to the guidelines of Le

Maitre *et al.* (1989).

Most of the ultramafic rocks in Tapira are described in the following sections as cumulates. Since the definition and nomenclature of cumulate rocks was proposed by Wager *et al.* (1960) it has been widely used in the literature. However, the applicability of the concept has also been challenged in a number of studies. The main problems with the use of the cumulate nomenclature are summarised by McBirney and Hunter (1995). During this research, the unavailability of long, continuous stratigraphic sections of the ultramafic rocks impeded the application of geochemical tests of the cumulate hypothesis (e.g. McBirney and Hunter, 1995; Meurer and Bordreau, 1998a) to the Tapira Complex. On the other hand, many of the ultramafic rocks of the SPS do not appear to be the product of crystallisation of a whole liquid in a closed system, and would therefore conform to the definition of cumulates, in a broad sense. This is supported by the following textural, compositional and chemical evidence:

- Substantial variation in the modal proportions of the essential constituents; this produces facies variations where the rocks are virtually monomineralic (e.g. rocks containing only apatite) or have a mineralogical composition that is inconsistent with any known natural liquid (e.g. rocks composed essentially by perovskite + apatite or by perovskite + magnetite.
- The presence of oikocrysts, where the intercumulus phases are compatible with the expected crystallisation sequence of silicate minerals (e.g. poikilitic pyroxene including olivine; poikilitic phlogopite including pyroxene or olivine + pyroxene).
- The occurrence, although rare, of dykes composed essentially of well-crystallised, equant grains of apatite (with very minor amounts of phlogopite), intruded in the quartzitic country rock. These are likely to represent the escape of a semi-consolidated, monomineralic mush of cumulus crystals, rather than an "apatite liquid". It should be stressed that, in contrast with other well known silicate magmatic system (e.g. layered intrusions of basaltic affinity), the crystallisation of apatite occurs at an very early stage in the evolution of the Tapira complex, as demonstrated later in this Chapter.
- The presence of modal banding, frequently observed in drill cores and in thin sections, as well as in more rare outcrops exposed in the mining area (see, for example, Figure I.17, in Chapter I).

- The regular recurrence of phlogopite-rich layers alternating with phlogopite-free layers (Figure I.17). This indicates that the system was periodically enriched in volatiles, probably as a result of the removal of anhydrous cumulus assemblages. The volatile-rich nature of the magma is further demonstrated by the occasional occurrence of interstitial carbonate in evolved bebedourites (see below) and the common presence of pegmatoids.
- With the exception of phlogopite, all the other modally significant phases in wehrlites and bebedourites have a density comparable to, or exceeding that of, forsteritic olivine (e.g. clinopyroxene, apatite, perovskite, melanite, titanomagnetite, chromite). Such high-density phases are unlikely to be kept in suspension, especially if the liquid from which they crystallise is assumed to have high contents of volatiles and, consequently, low viscosity.
- The whole-rock compositions of many of the ultramafic plutonic rocks, particularly the bebedourites and their facies variations, fall outside the geochemical trends of the fine-grained dyke rocks from Tapira (Chapter IV)

Nevertheless, some of the ultramafic rocks described in the following sections do occur as relatively fine-grained dykes (e.g. wehrlite dykes of the B2 unit, see below) or as homogeneous, medium to fine-grained rocks, with uniform modal compositions and lacking evidence of banding or typical cumulate textures (e.g. some evolved bebedourites). These particular rock-types could, of course, represent the *in situ* crystallisation of magmatic liquids, without prejudice to an overall interpretation of the ultramafic portion of the SPS as a sequence of cumulates, on a wider scale.

Classification of dyke-rocks

A suite of fine-grained ultramafic dykes occurs in Tapira, as well as in the other APIP carbonatite complexes. Such rocks have been traditionally described as lamprophyres, on the basis of the abundant olivine (and occasionally phlogopite) phenocrysts. On other occasions they have been mistaken for metasomatic glimmerites, because of the high modal percentages of phlogopite and carbonate. Gibson *et al.* (1995) stressed that these rocks do not fit the established nomenclature, and proposed the name phlogopite-picrite for them. Such rocks also fail to conform to the guidelines issued shortly after by Woolley *et al.* (1996) for the classification of lamprophyres, lamproites, kimberlites and rocks containing kalsilite, melilite and leucite. Therefore, the denomination proposed by Gibson *et al.* (1995) is adopted in this thesis; the name phlogopite-picrite is used for dyke rocks essentially composed of phenocrysts of olivine and subordinate phlogopite, set in a groundmass of phlogopite, opaque minerals, perovskite, apatite and carbonate.

During this research, the access to well preserved drill cores allowed the sampling of more evolved members of the phlogopite-picrite suite. These rocks are composed of phlogopite, apatite and, occasionally, clinopyroxene and garnet phenocrysts, set in a carbonate- and phlogopite-rich fine-grained groundmass. They show significant chemical differences (see Chapter IV) from the more primitive phlogopite-picrites, especially with regard to the compatible elements, such as Cr and Ni. Again, it is difficult to fit these rocks to any of the established nomenclature schemes. Apart from the high carbonate content, their mineralogy resembles that of the bebedourites, but this term will not be applied to the dykes, in order to avoid confusion with the cumulate rocks of the SPS. For the purposes of this thesis, they will be informally named low-Cr dykes.

Similarly to the bebedourites, this suite of ultramafic dykes appears to be conspicuous in the Alto Paranaíba Igneous Province. They occur associated with all carbonatite complexes and, less frequently, as isolated dykes elsewhere in the province, with no obvious geographic connection with carbonatites. Their petrogenetic significance in the context of the APIP carbonatite complexes will be discussed in detail later in this thesis.

Classification of carbonatites

Woolley and Kempe (1989) recommended that the name carbonatite be restricted to igneous rocks containing over 50% of carbonate minerals and that the petrographic varieties should be named on the basis of the type of carbonate present. According to this system, Tapira carbonatitic rocks can be mostly classified as coarse-grained calcite carbonatites (traditionally called sovites) and dolomite-bearing calcite carbonatites. Less frequently, dolomite may be the dominant or exclusive carbonate mineral of Tapira carbonatites, especially in late-stage dykes and veinlets. These rocks are commonly fine-grained and classify as dolomite carbonatites (also known as beforsites).

II.3 - SILICATE PLUTONIC SERIES (SPS)

The silicate plutonic rocks are subdivided into three main groups. The B1 and B2 units are composed dominantly of bebedourite, with subordinate wehrlite, and facies variations towards apatite- and/or perovskite- rich cumulates. The two units are distinguished on the basis of their: (i) location in the complex; (ii) mutual relationships within the drill cores and (iii) textural and compositional (Figure II.1) differences observed in thin section.

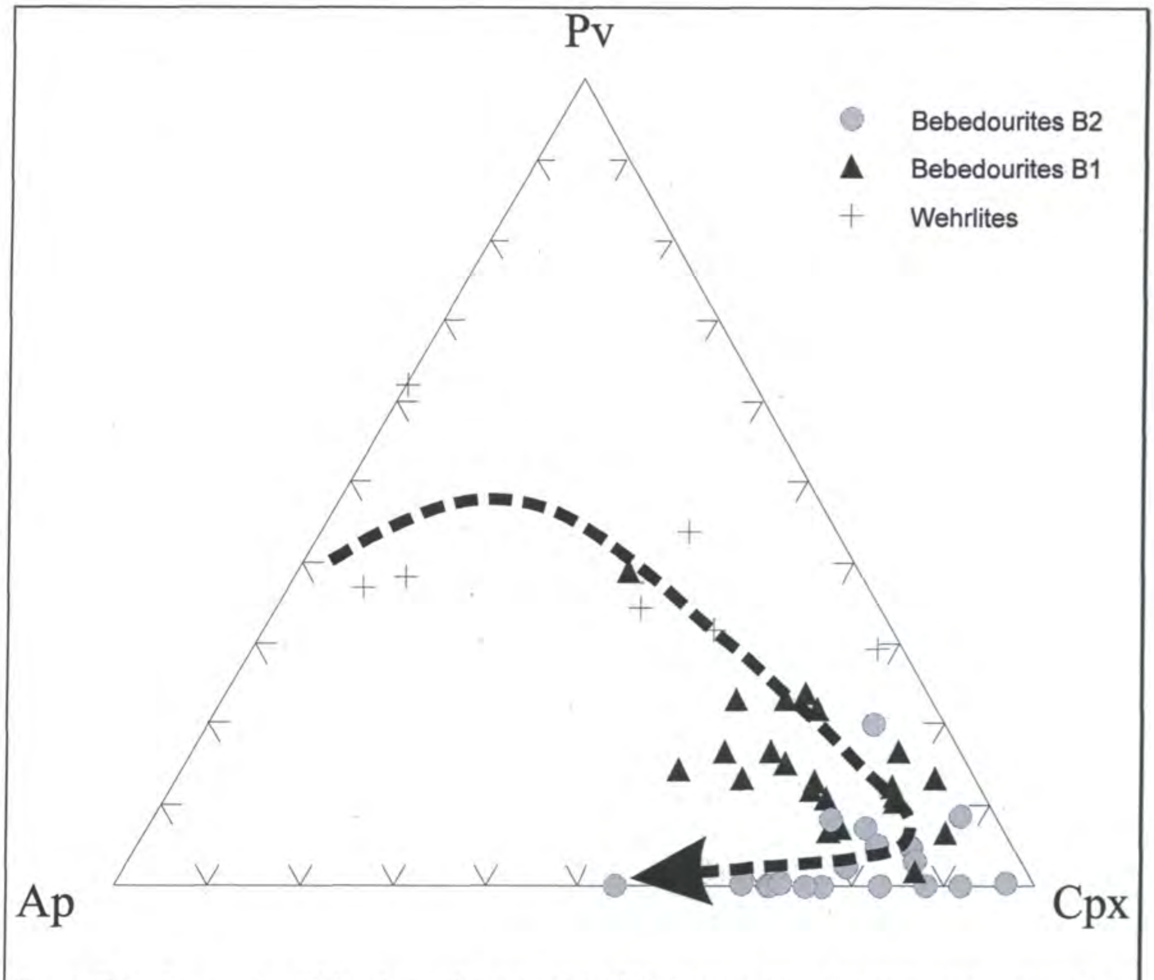

Figure II.1 - Composition of the ultramafic rocks of the SPS, in terms of modal percentages (Appendix 4) of apatite (Ap), perovskite (Pv) and clinopyroxene (Cpx) normalised to 100%. The dashed arrow represents the progressive changes in the order of crystallisation of these phases throughout the evolution of the complex (see text).

The B1 unit is geographically situated between the B2 unit, in the north, and the central carbonatites of the Tapira complex (see Figure I.15, in Chapter I). Wehrlites appear to be significant only in B1. In fact, no olivine-rich cumulates were observed in B2 at the level sampled. However, relatively fine-grained wehrlites occur as dykes intruded in B1 and may represent the olivine-rich counterpart to the B2 bebedourites. These wehrlite dykes are therefore assigned to B2, despite their occurrence outside the geographic domain of that unit. The third unit comprises syenites intrusive in the B1 bebedourites and wehrlites. All three units of the SPS are locally intruded by carbonatite.

II.3.1. B1 UNIT

Wehrlites and other olivine-bearing cumulates

A relatively small percentage of the samples collected from B1 contain olivine. Some of these are wehrlites, but variations towards olivine-bearing apatite- and/or perovskite-rich cumulates are also common. Although dunites are locally present, all the examples examined were too altered (serpentinised) to allow petrographic or chemical studies. Therefore, the following account will be concerned only with the wehrlites and their modal variations to perovskite- and apatite-rich cumulates.

Because preserved rocks can only be found in small sections at the bottom of the drillings, it is difficult to assess vertical variations in the complex. Some of the olivine-bearing rocks are located at greater depths (relative to the absolute altitude at the top of the drillings) than the bebedourites, suggesting that the former could represent deeper cumulate horizons in the complex. However, this is not necessarily the case for all olivine-bearing rocks in B1.

Most of the examined samples lack preferred mineral orientation but igneous layering is evident in some cases. This is particularly so in the apatite- and perovskite-rich rocks, which may display small-scale banding defined by centimetre-thick layers of olivine + apatite, alternating with slightly thinner bands of apatite + perovskite + opaques (Figure II.2). The textural relationships between the essential minerals in most rocks suggest crystallisation in the sequence:

olivine (+chromite?) ⇒ apatite ⇒ perovskite ⇒ clinopyroxene ⇒ phlogopite+opaques

Pyroxene (Figure II.3) and phlogopite (Figure II.4) are common intercumulus minerals. Apatite is a cumulus phase throughout the crystallisation sequence. Melanite, carbonate, tetraferriphlogopite (Figure II.5) and oxides may be present in late-stage veinlets or as a secondary replacement of the cumulate phases.

Olivine forms coarse-grained, subhedral to anhedral cumulate crystals. It may show variable degrees of serpentinisation and commonly contains abundant micro-inclusions of opaque minerals. Olivine crystals are locally coated by aggregates of small grains of perovskite and opaque minerals (Figure II.6) or by lamellae of phlogopite. Inclusions of primary phases in olivine are rare or absent, indicating its early-stage formation. Exceptions are the apatite- and perovskite-rich cumulates, where these two minerals are sometimes included in olivine. Some olivine crystals may be slightly deformed, indicating limited transport of the semi-consolidated rock.

The textural properties of pyroxene are dependent on the stage of evolution of the rock. In olivine-rich cumulates the pyroxene is typically an intercumulus phase, locally forming large oikocrysts (e.g. Figure II.3) that poikilitically include olivine, apatite and perovskite. However, as the amount of olivine decreases, clinopyroxene becomes a typical cumulus phase, accompanying perovskite and apatite.

The onset of apatite crystallisation occurs very early in Tapira ultramafic cumulates, possibly contemporaneously or slightly after olivine. Apatite persists as a typical cumulus phase until late in the crystallisation of the complex. It forms equant, often euhedral crystals or, alternatively, euhedral to rounded inclusions in all other mineral phases (but rarely in olivine).

In olivine-rich cumulates, perovskite is subhedral and poikilitic, suggesting a relatively late-stage crystallisation (certainly after the onset of olivine and apatite). As the amount of olivine decreases, perovskite becomes preferentially euhedral and contains only minor amounts of inclusions, indicating a cumulus origin. The existence of perovskite- and apatite-rich horizons within the wehrlites, where none of these minerals contains inclusions of silicate phases, testifies to the extreme silica-undersaturation of the liquids that generated the Tapira cumulates. It suggests that, at some stages during the crystallisation history of the complex, only very small amounts of silicate minerals were being formed (despite the liquid probably being within the

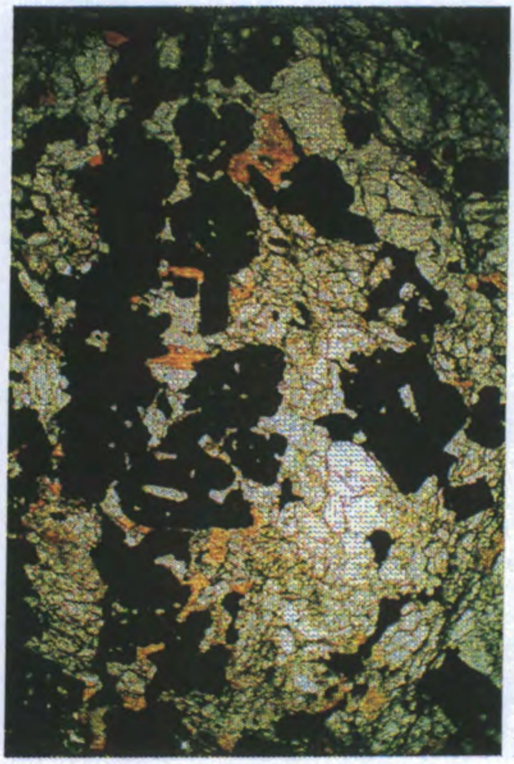
II.2


II.3

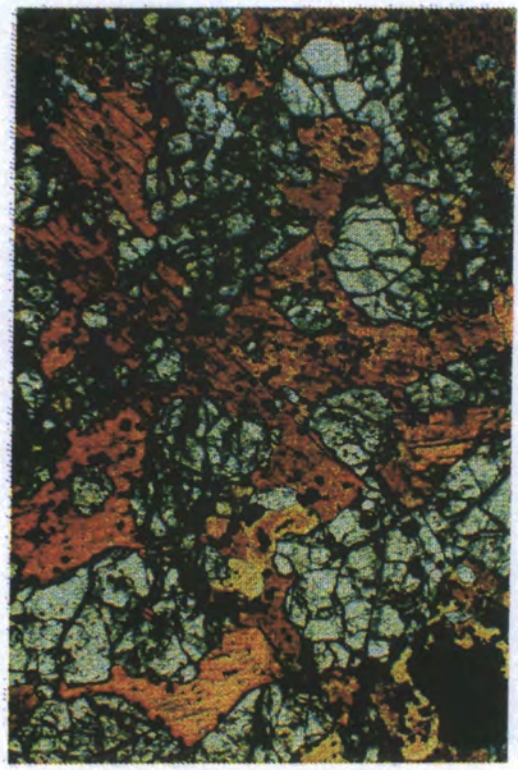
II.4

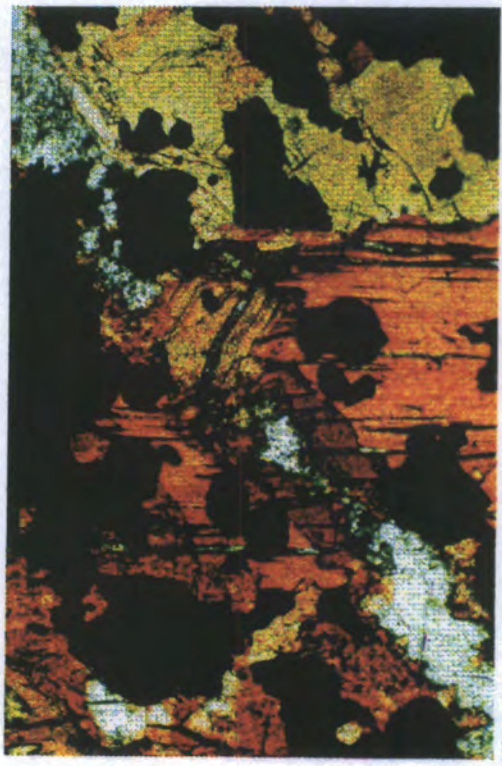
II.5

Figure II.2 *- Magmatic banding in perovskite-rich wehrlite. The euhedral perovskite is concentrated in thin layers, together with apatite and opaques, alternating with thicker bands where olivine (and subordinate clinopyroxene) dominates. Sample at015, plane-polarised light. Field of view = 12 x 7.2 mm.*

Figure II.3 *- Clinopyroxene oikocryst (large, light-coloured, optically continuous grain in the centre) in wehrlite. Sample at217, cross-polarised light. Field of view = 12 x 7.2 mm.*

Figure II.4 *- Intercumulus phlogopite, interstitial to rounded crystals of olivine and rare diopside, in wehrlite. Sample at025, plane-polarised light. Field of view = 6 x 3.7 mm.*

Figure II.5 *- Replacement of phlogopite by tetraferriphlogopite along the margins of a carbonate veinlet. Note the deep red colour and the inversion in the direction of highest absorption in the tetraferriphlogopite. Sample at101b, plane -polarised light. Field of view = 1.3 x 0.77 mm.*

temperature range of olivine and pyroxene crystallisation). This could result, for instance, from periodical fluctuations in the activity of the relevant components (e.g. SiO_2, TiO_2, P_2O_5). The removal of olivine and pyroxene would drive an already strongly undersaturated liquid towards even lower SiO_2 levels, with corresponding relative increase in TiO_2 and P_2O_5. Saturation of these components would promote extensive precipitation of perovskite and apatite, therefore driving the liquid back to relatively higher SiO_2 contents.

Phlogopite is a typical intercumulus phase (e.g. Figure II.4) in the wehrlites and other olivine-bearing rocks of the B1 unit. It forms interstitial poikilitic crystals, containing inclusions of all other phases in the rock. Phlogopite is commonly associated and contemporaneous with late-stage opaque minerals. Some phlogopite lamellae show evidence of deformation, suggesting that the rock has been affected by post-crystallisation movements. The optical characteristics of phlogopite in the olivine-bearing rocks (pleochroic from brown to orange, with $\alpha < \beta = \gamma$) suggest normal Al and Fe contents. However, in the vicinity of carbonate veinlets (e.g. Figure II.5), the margins of phlogopite crystals may develop reverse pleochroism ($\alpha > \beta = \gamma$) in shades of bright red and orange, indicative of replacement by tetraferriphlogopite (high Fe^{3+}, low Al). This variety of mica is clearly formed by metasomatic processes associated with the intrusion of carbonatites.

Two varieties of opaque minerals are present in the wehrlites. In the more olivine-rich samples they occur as small interstitial grains of chromite, usually associated with perovskite. In the more evolved cumulates the opaque minerals are titanomagnetite, and form at a later stage.

Bebedourites

This group comprises clinopyroxene-rich rocks containing essential perovskite, apatite, phlogopite and opaque minerals. Facies variations are recognised, defined by differences in the modal proportions of these minerals. Olivine and chromium-rich spinel are absent from bebedourites. Melanite (*s.l.*), carbonate and rare zirconolite may occur in accessory amounts. The spatial association of the bebedourites with the wehrlites in the B1 unit suggests that these two petrographic types are related to a single crystallisation trend, with the wehrlites (and possibly dunites) representing the lower levels of a layered sequence of ultramafic cumulates, and the B1 bebedourites representing the more differentiated rocks. However, it should be noted that the olivine rocks are volumetrically subordinate, and this sequence may be incomplete.

The texture of bebedourites from B1 is dominantly medium to coarse-grained. Pegmatite facies occur locally within this unit, with pyroxene and phlogopite crystals reaching up to several centimetres.

Preferred mineral orientation is common, resulting in the development of a foliation in some of these rocks. This structure is well marked by elongated prisms of diopside and apatite (Figure II.7), as well as by phlogopite laths. The possible origins of igneous foliation have been recently discussed by McBirney and Nicolas (1997) and by Meurer and Bordreau (1998b). In volcanic and sub-volcanic rocks, and in granitic intrusions, igneous foliation is produced mainly by magmatic flow. In cumulates, foliation can develop as a result of: a) shearing produced by viscous flow during crystallisation; b) primary alignment of inequant crystals (during accumulation); c) compaction of the cumulate pile. Meurer and Bordreau (1998b) observed vertical variations in the intensity of crystal alignment within a section of the Stillwater complex (Montana) and interpreted these as the result of compaction, rather than shearing. McBirney and Nicolas (1997) found that in the Skaergaard layered intrusion the development of layering and foliation due to shearing (dynamic processes) is predominant along the margins of the intrusion, whereas in the interior and on the Upper Border Series of Skaergaard non-dynamic processes dominate. In Tapira it is not possible to assess vertical changes in the fabric of the ultramafic rocks, due to the thick weathering cover. However, the intensity of foliation seems to increase laterally outwards in the B1 unit. Further, some of the characteristics described by McBirney and Nicolas (1997) for layered rocks that have undergone simple shear (e.g. sharp layering, with strong modal variations; well-developed foliation and lineation) are present in some Tapira rocks. This suggests that the partially consolidated margins of the intrusion may have been subjected to some degree of shearing during or shortly after emplacement.

Modal layering is often present in the B1 bebedourites. Figure II.8 shows the contact between a phlogopite-rich and a perovskite/melanite (*s.l.*)-rich layer. The relatively fine-grained aggregate of pyroxene, perovskite and melanite (*s.l.*), in the centre of the photograph) could possibly represent an autolith, eroded from elsewhere in the magma chamber and deposited at the interface between the two layers.

The order of crystallisation varies with evolution of the bebedourites. In the least evolved variants the crystallisation follows the sequence:

apatite ⇒ perovskite ⇒ clinopyroxene ⇒ phlogopite + opaques.

In the more evolved rocks this changes to:

clinopyroxene ⇒ perovskite ⇒ apatite ⇒ opaques + phlogopite.

Apatite forms small prismatic or rounded grains, occurring both as discrete crystals or as inclusions in all other minerals. Although apatite is present throughout the crystallisation history of the B1 unit, its modal percentage decreases steadily at first, and it becomes an interstitial phase to diopside. In the most evolved bebedourites, a renewed increase in modal apatite is observed.

Perovskite occurs as euhedral to subhedral crystals. Optically it is light brown in colour and usually displays a false anisotropy, induced by the conspicuous twinning. As observed for the wehrlites, perovskite may locally include euhedral apatite prisms (Figure II.9). However, in many of the bebedourites this feature is absent and the euhedral contours of perovskite suggest that it is an early-formed cumulus phase, as opposed to its relatively late appearance in the wehrlites.

Melanite (*s.l.*) may be present as rare discrete crystals or, more often, replacing the rims of perovskite crystals (Figure II.9). In the latter case the garnet has a deep brown-red colour, indicating high content of Ti. The discrete crystals are anhedral, less frequently subhedral, and have a lighter colour (orange/yellow), but may show both regular and irregular (patchy) zoning towards darker colours.

Clinopyroxene in B1 bebedourites is a pale-green diopside, showing very little or no pleochroism. It occurs as large prismatic crystals and locally contains abundant exsolution of opaque phases in structurally-controlled patterns. When zoning is optically visible it is irregular, with a tendency for the rims to show paler shades of


II.6

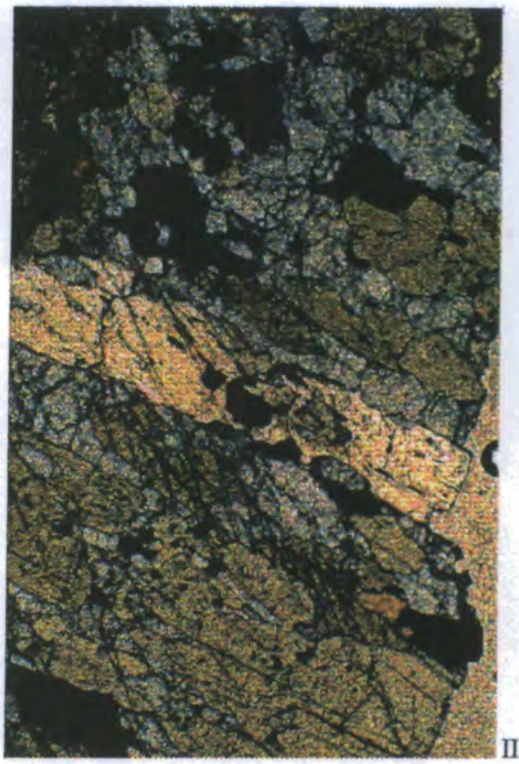
II.7

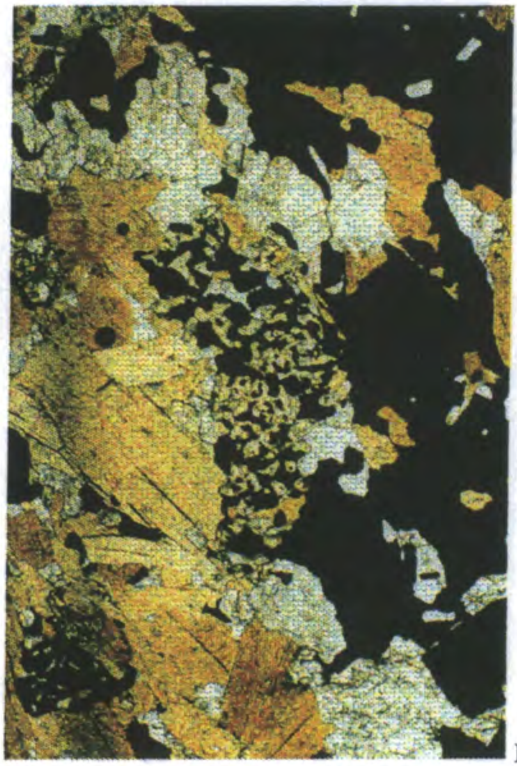
II.8

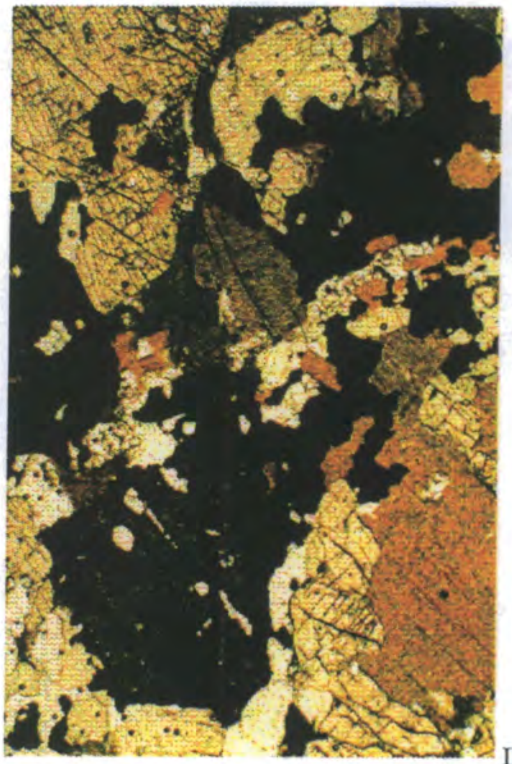
II.9

Figure II.6 *- Olivine surrounded by small crystals of perovskite (brown) and chromite (black). Note the interstitial character of the phlogopite. Sample at217, plane-polarised light. Field of view = 3 x 1.9 mm.*

Figure II.7 *- Strong preferred mineral orientation in bebedourite B1, given by the juxtaposition of clinopyroxene and apatite crystals. Note the prismatic inclusions of apatite in pyroxene. The fine -grained rock (top-left corner) is a wehrlite dyke of unit B2. Sample at126a, plane-polarised light. Field of view = 6 x 3.7 mm.*

Figure II.8 *- Autolith(?) of fine-grained aggregate (clinopyroxene+perovskite +melanite), deposited at the contact between coarse-grained perovskite+melanite-rich (right) and phlogopite-rich (left) layers of bebedourite. Sample at007, plane -polarised light. Field of view = 3 x 1.9 mm.*

Figure II.9 *- Perovskite (bottom) showing inclusions of apatite and replacement by melanite, in bebedourite of unit B1. Sample at003, plane-polarised light. Field of view = 6 x 3.7 mm.*

green than the cores. In some samples the large prismatic diopsides show preferred orientation. With the evolution of the bebedourites, diopside progresses from late-stage poikilitic crystals to early-stage cumulate phases. .

Phlogopite forms large anhedral crystals, with normal pleochroism; it includes or partially surrounds grains of diopside, apatite, perovskite, melanite (*s.l.*), suggesting that phlogopite is one of the latest phases to crystallise. Locally the lamellae may be deformed and show undulose extinction.

Opaques may crystallise at the same time as, or after, phlogopite. In the latter case they are typically interstitial and anhedral.

Zirconolite was identified in the pegmatite facies of B1. It occurs as rare, minute, euhedral or subhedral crystals of high refraction index and deep brown-red colour (Figure II.10). Together with perovskite, zirconolite is an indicator of strong silica-undersaturation. Its occurrence in the pegmatitic facies also signals the relative enrichment of zirconium in the residual liquid.

Melilite-bearing plutonic rocks

A coarse-grained pyroxene melilitolite (uncompahgrite) occurs near the northeast margin of the complex. This occurrence has been recognised by Guimarães *et al.* (1980), who determined the composition of the melilite as akermanitic. So far, this is the only known melilite-bearing rock from the Tapira complex. It is composed essentially of large (up to 3-4 cm) subhedral to anhedral crystals of melilite (Figure II.11), with subordinate amounts of euhedral perovskite, subhedral diopside and apatite, and interstitial phlogopite and opaques. Perovskite is partially replaced by melanite (*s.l.*). The melilite crystals are occasionally altered to a fine-grained mixture of calcite and wollastonite. The Tapira uncompahgrite is possibly a facies variation of the pegmatites of the B1 unit.

II.3.2. B2 UNIT

This unit occupies the northern margin of the Tapira complex. It is composed dominantly of bebedourites, usually containing higher amounts of clinopyroxene than those of B1. Olivine-bearing cumulates were not found in the studied drill cores. Nevertheless, a few dykes of wehrlite intruding the B1 bebedourites are included in this unit, on the basis of their mineralogical and petrographic similarities with other B2 rocks.

Wehrlite dykes

These rocks are medium to fine grained and composed essentially of olivine, clinopyroxene, melanite (*s.l.*), phlogopite, apatite and opaque minerals. A fundamental difference from the wehrlites in the B1 unit is that these dykes contain only minor amounts of perovskite, but have abundant primary garnet. The crystallisation order suggested by the textural relationships between the essential phases is:

apatite ⇒ olivine ⇒ clinopyroxene ⇒ garnet + phlogopite + opaques.

Olivine typically contains numerous euhedral inclusions of apatite (Figure II.12), consistent with the crystallisation of apatite at a very early stage in these rocks. This relationship contrasts with that observed in B1, where olivine precedes or is contemporaneous with apatite. Olivine crystals are variably altered to serpentine and oxidised material (Figure I.13)

Melanite (*s.l.*) occurs both as partial replacement of perovskite and as abundant primary crystals. These are euhedral and show optical zoning, with dark-brown cores and lighter brown rims. Figure II.13 illustrates a zoned garnet, where the rim is poikilitic and the core is virtually inclusion-free. This variety of garnet is interpreted as primary, formed from a liquid with higher silica content than the one that generated the wehrlites and bebedourites in B1. The paucity of perovskite in these rocks, despite the substantial availability of Ca and Ti (as shown by the occurrence of Ti-rich garnet), is in good agreement with a generally higher silica activity in the liquid.

Bebedourites

The bebedourites of the B2 unit are usually finer-grained and have higher pyroxene content than those of B1. Densely packed accumulations of diopside crystals with intercumulus phlogopite are common (Figure II.14). Apatite, perovskite, melanite (*s.l.*) and sphene are usually present in subordinate amounts.


II.10

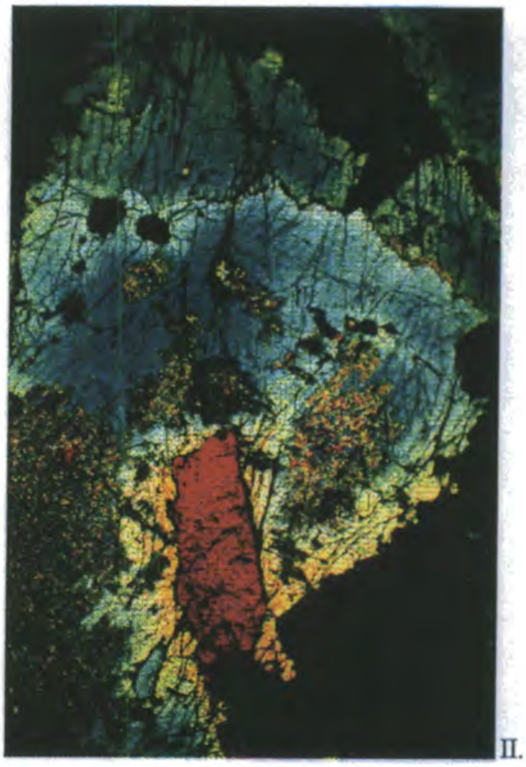
II.11

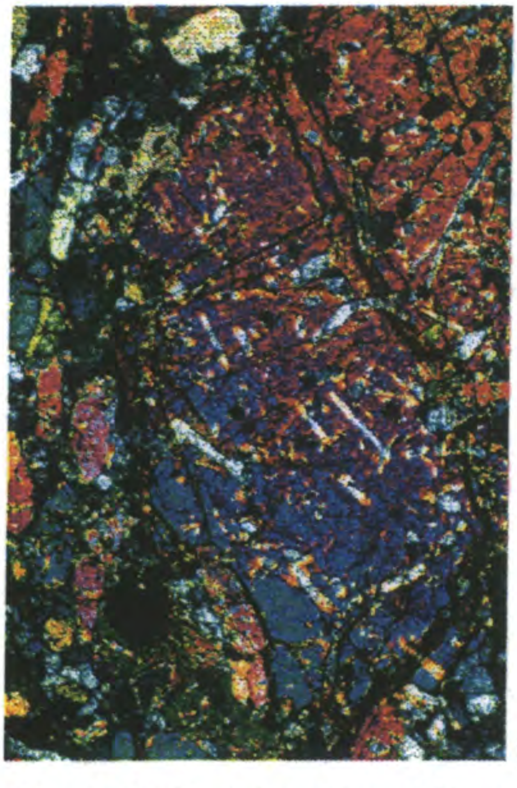
II.12

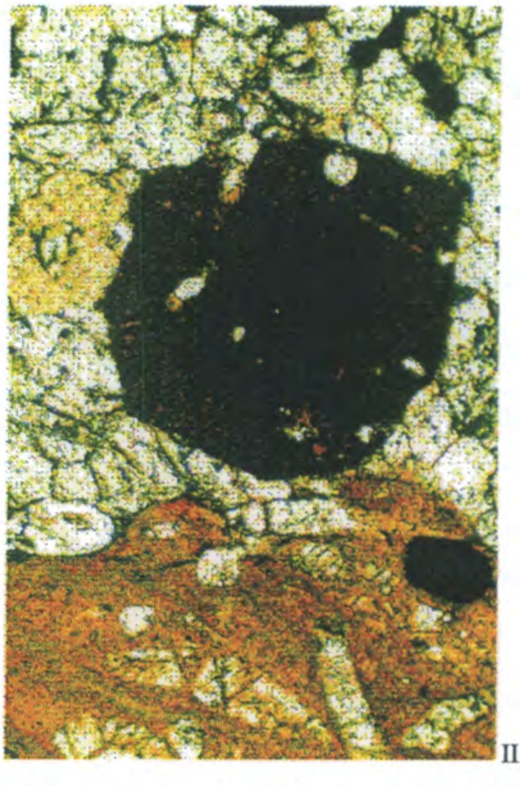
II.13

Figure II.10 *- Small zirconolite crystal in pegmatitic bebedourite. Sample at035, plane-polarised light. Field of view = 0.12 x 0.08 mm.*

Figure II.11 *-Melilite crystals in uncompahgrite, showing the typical uneven bluish birefringence. Note the included diopside (bright pink) and the altered patches composed of a fine-grained mixture of wollastonite and carbonate. Sample U-1, cross-polarised light. Field of view = 12 x 7.2 mm.*

Figure II.12 *-Large crystals of olivine in wehrlite dyke. The olivine shows abundant inclusions of prismatic apatite. Subhedral crystals of clinopyroxene (left) surround the olivine, defining a flow texture in the dyke. Sample at126b, cross-polarised light. Field of view = 3 x 1.9 mm.*

Figure II.13 *-Euhedral melanite in wehrlite dyke. Note the difference in colour and amount of inclusions between core and rim. The bottom side of the photograph is a serpentinised olivine, containing inclusions of prismatic apatite. Sample at126b, plane-polarised light. Field of view = 1.3 x 0.77 mm.*

The crystallisation sequence varies with the evolution of the bebedourites. At the very early stages the order appears to be:

apatite + perovskite ⇒ clinopyroxene ⇒ phlogopite ⇒ garnet ⇒ sphene.

This is later replaced by:

clinopyroxene ⇒ (± perovskite) ⇒ apatite ⇒ phlogopite ⇒ garnet ⇒ sphene ⇒ (± feldspar)

which is the dominant sequence in B2 bebedourites. Perovskite disappears and possible feldspar (see below) appears in the latest stages. Apatite may be a recurrent early phase in the most evolved bebedourites. As observed for B1, the bebedourites may show a strong mineral orientation, defined by juxtaposed prismatic crystals of diopside and apatite, as well as phlogopite lamellae (Figure II.15), but this feature is less common in B2.

Clinopyroxene is diopsidic in composition. The colour absorption is generally, but not always, stronger than in B1 diopsides. This results in deeper green colours that suggest a higher hedenbergite component. The grains vary from subhedral to euhedral, and may be either equant or prismatic. Zoning may be irregular (patchy) or concentric. In some samples the pyroxene is zoned towards paler rims (e.g. Figure II.14) whereas in others the opposite variation is observed (e.g. Figure II.15).

Perovskite is an early-crystallised phase in B2 rocks, but the mineral is invariably unstable, coated by one or more of opaques, melanite (*s.l.*) or sphene, in this order (Figure II.16). Interestingly, perovskite inclusions in pyroxene do not show any signs of replacement by silicates, suggesting that the earliest crystallised perovskite was in equilibrium with the liquid. The modal amount of perovskite decreases with the evolution of the bebedourites, and the mineral is often absent in the more evolved members of the sequence.

Phlogopite varies from interstitial lamellae (Figure II.14) to subhedral laths, in the more evolved rocks. The pleochroism is normal, although in somewhat stronger shades of orange or red than in B1. In rocks crosscut by carbonate veinlets, phlogopite lamellae are partially replaced by tetraferriphlogopite

Melanite (*s.l.*) occurs both replacing perovskite and as discrete primary crystals. The latter are euhedral to subhedral, zoned towards paler shades of brown.

Sphene occurs as a late-stage replacement of perovskite, often forming an external coating, after the perovskite had been partially converted to opaque minerals or garnet. Another variety of sphene occurs as euhedral to subhedral crystals, which are not spatially associated with perovskite and may have crystallised directly from the bebedourite liquid.

Carbonate veinlets crosscutting the B2 bebedourites are common. Some carbonate may migrate from the veinlets into the host pyroxenite, forming patches of interstitial carbonate. However, in some samples these patches do not show an obvious association with carbonate veinlets, in which case they may represent primary carbonate, formed from the crystallisation residue.

Some evolved bebedourites in the B2 unit, particularly those lacking perovskite, contain interstitial patches of fine-grained sericite with subordinate carbonates. These patches probably result from the alteration of accessory felsic minerals in the bebedourite, such as feldspars or feldspathoids. In most examples the original mineral cannot be accurately identified under the petrographic microscope, although alkali feldspar seems to be present in patches where alteration was incomplete (Figure II.17). Reconnaissance X-Ray Diffractometry (XRD) studies confirmed the presence of alkali feldspar in three of these rocks, one of which appears to contain the association orthoclase + nepheline (pseudoleucite?).

The interpretation of the felsic patches is not straightforward. They could either represent feldspars or feldspathoids crystallised from the residual magmatic liquid or, alternatively, derive from metasomatically introduced material. The occurrence of rare inclusions of feldspathic material within euhedral clinopyroxene supports the first alternative. Figure II.18 shows one such inclusion, composed of a finely-grained aggregate of feldspar with accessory mica. In contrast with the altered patches described above, the feldspar in this inclusion seems to be well preserved, having apparently been sheltered from post-magmatic processes by the host pyroxene. The globular shape of the inclusion is suggestive of the entrapment of a droplet of syenitic liquid in the crystallising pyroxene. This feature is interpreted here as a primary texture, and provides a possible link between the B2 bebedourites and the Tapira syenites by magmatic

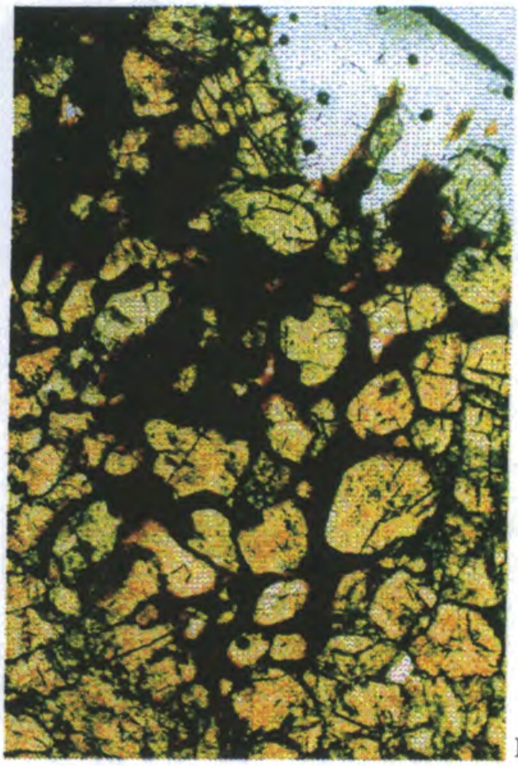
II.14


II.15

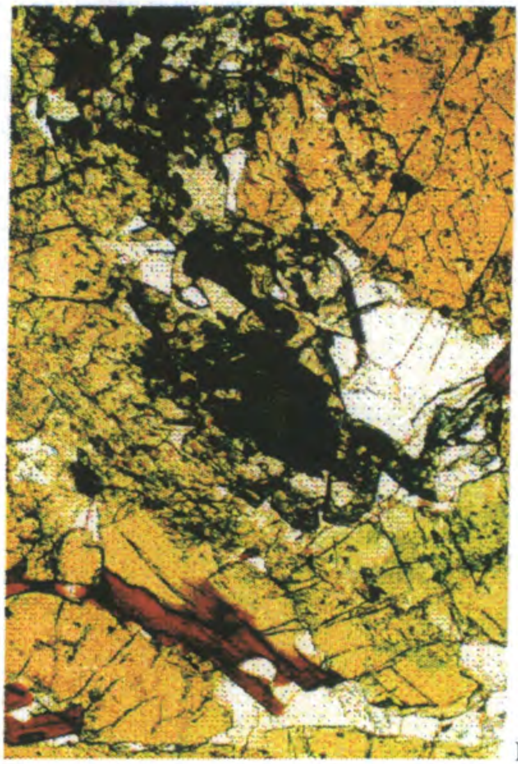
II.16


II.17

Figure II.14 *- Densely packed diopside crystals with intercumulus phlogopite. Bebedourite of the unit B2. In some pyroxene grains it is possible to observe zoning towards lighter-coloured rims, although the zoning pattern is mostly irregular. Sample at008, plane-polarised light. Field of view = 3 x 1.9 mm.*

Figure II.15 *- Strongly oriented fabric in coarse-grained bebedourite B2, given by the juxtaposition of prismatic diopside and apatite crystals. Sample at030, plane-polarised light. Field of view = 12 x 7.2 mm.*

Figure II.16 *- Unstable perovskite crystal (dark brown, in the centre), with replacement rims of opaque minerals and sphene. Phlogopite in this sample is partly secondary, replacing pyroxene (bottom). Sample at029, plane-polarised light. Field of view = 3 x 1.9 mm.*

Figure II.17 *- Interstitial patch of feldspar in bebedourite B2. The original feldspar is partially altered to a mixture of sericite and carbonate. Sample at032, cross-polarised light. Field of view = 6 x 3.7 mm.*

differentiation processes. The altered patches are likely to represent the same phenomenon, but have been obliterated by post-magmatic processes.

The relatively higher SiO_2 content of the liquid from which the B2 unit was formed is testified to by the following evidence: a) primary garnet in the wehrlite dykes; b) primary sphene and garnet in the bebedourites; c) primary (interstitial) feldspar in perovskite-free, evolved bebedourites; d) low modal content of perovskite throughout the B2 unit; and e) disequilibrium features of the existing perovskite, which is invariably replaced by Ti-rich silicate minerals. The existence of silicate-free perovskite inclusions in pyroxene suggests that silica increases in the liquid with magmatic differentiation, as normally expected. On the other hand, the occurrence of melanite (*s.l.*), rather than perovskite, in the - presumably - less differentiated wehrlites suggests that this increase was not smooth, but probably disturbed by oscillations in the silica activity of the system. Such oscillations could have been controlled by the preferential removal of silicate (olivine, clinopyroxene) or non-silicate (perovskite, apatite) phases. More complex alternatives would be the assimilation of the quartzitic country rock, resulting in uneven silica distribution in the liquid, or the involvement of these magmas in an episode of liquid immiscibility. These possibilities will be explored in detail in Chapter V.

Note on bebedourites from the Mata da Corda

Nearly all compositional and textural features observed in Tapira bebedourites, from both the B1 and B2 units, are present in clinopyroxenite xenoliths occurring within pyroclastic deposits of the Mata da Corda Group (Seer and Moraes, 1988; and thin sections from the localities of Chumbo and Lagoa Formosa examined during this research). In fact, the classification of those rocks as bebedourite would seem entirely appropriate. The petrographic similarities strongly suggest that the plutonic counterparts of the Mata da Corda kamafugites are bebedourites analogous to those occurring in the Tapira complex. This provides an important link between the carbonatites and the kamafugitic magmatism in APIP.

II.3.3. SYENITES

Tapira syenites occur as small intrusions in the B1 bebedourites. In turn, they are intruded and brecciated by dolomite-bearing calcite carbonatites of the C2 unit. The reaction of the syenites with the intrusive carbonatite results in the formation of abundant phlogopite at the margins of syenite fragments in breccias.

The syenites are composed essentially of K-feldspar, with aegirinic pyroxene and/or phlogopite/biotite as the principal mafic mineral. Altered patches suggest the presence of feldspathoids such as leucite and/or nepheline in some samples. One or more of the minerals sphene, zircon, carbonate, apatite and opaques may be present in accessory amounts. The texture is usually equigranular, medium- to fine-grained. Locally the syenites exhibit preferred mineral orientation, given mainly by tabular crystals of feldspar, but most of the studied samples lack oriented structures.

Feldspar occurs as subhedral, tabular crystals of orthoclase. Zoning is visible in some samples (Figure II.19). Optically recognisable perthites seem to be generally absent.

Pyroxene occurs as subhedral prismatic crystals with a deep green colour and strong pleochroism, indicative of aegirinic composition. Zoning is inconspicuous but may be present in some grains, marked by deeper green colour in the rims. Clinopyroxene occasionally includes small subhedral crystals of apatite. In most of the samples examined, the modal percentage of clinopyroxene is small and in many cases the only mafic mineral present is phlogopite/biotite. However, the concentration of glomeroporphyritic aggregates may locally result in over 30 modal % of clinopyroxene in a thin section. A second variety of clinopyroxene comprises fine-grained radial aggregates of acicular crystals (Figure II.20).

Phlogopite/biotite occurs in two varieties. The first one is the original mica from the syenite, and occurs as small subhedral isolated lamellae. The second variety is produced by the reaction of the syenite with interstitial carbonate or with intrusive carbonatite magma and may occur as: (i) anhedral lamellae, interstitial to feldspar grains; (ii) phlogopite margins in carbonate globules within the syenite; (iii) carbonate-phlogopite veinlets crosscutting the syenites; or (iv) phlogopite coating syenite fragments from carbonatite breccias.

Sphene occurs as small, euhedral, interstitial crystals, or as inclusions in feldspars. It is the main titanium-rich phase in Tapira syenites, since perovskite and melanite were not found in these rocks.


II.18

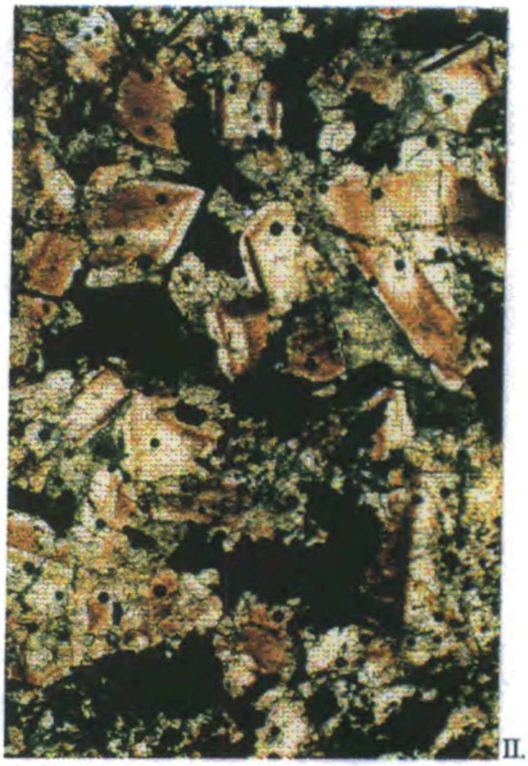
II.19

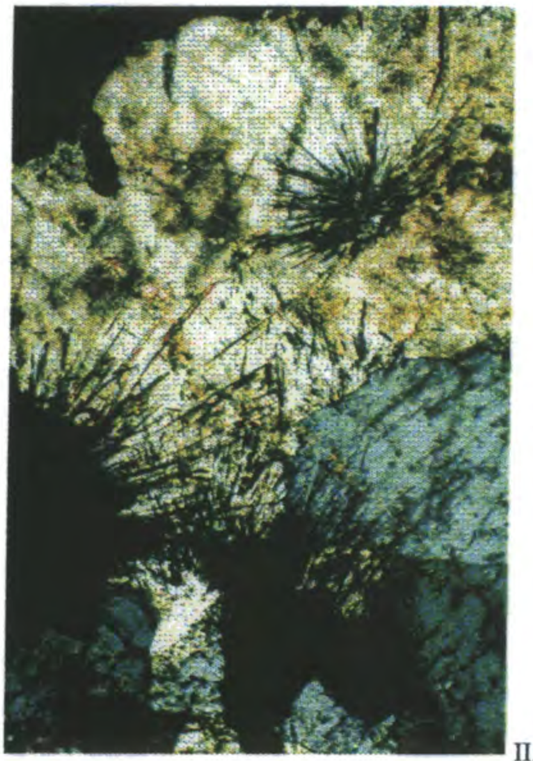
II.20

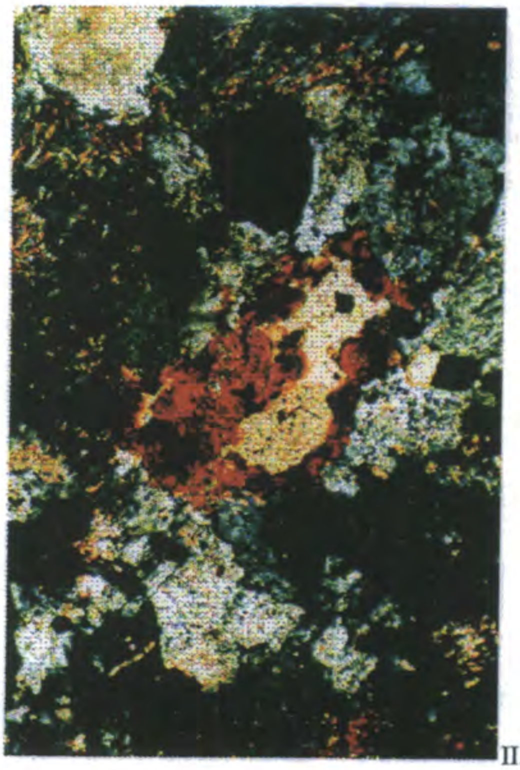
II.21

Figure II.18 *- Globular inclusion in diopside from bebedourite B2. The inclusion is a fine-grained aggregate of feldspar and mica. The feldspar within the inclusion is remarkably well preserved, in comparison with the interstitial feldspar in this sample (Figure II.17). The shape of the inclusion suggests a droplet of syenitic liquid trapped during the growth of the pyroxene. The pyroxene is concentrically zoned and partially includes apatite (top). Sample at032, plane-polarised light. Field of view = 0.66 x 0.4 mm.*

Figure II.19 *-Tabular euhedral orthoclase in syenite. Zoning is marked by the brown alteration. Aegirinic pyroxene (dark green, prismatic), opaques and interstitial carbonate (low relief) are also visible. Sample at012, plane-polarised light. Field of view = 3 x 1.9 mm.*

Figure II.20 *- Radial aggregates of acicular aegirine in syenite. Note also the absence of optically visible perthites in the feldspars. Sample at018, cross-polarised light. Field of view = 3 x 1.9 mm.*

Figure II.21 *- Globule of carbonate, apparently unrelated to carbonatite metasomatism, in syenite. The reaction of the carbonate in the globule with the host syenite results in the formation of a phlogopite rich margin. Sample at018, cross-polarised light. Field of view = 1.3 x 0.77 mm.*

Carbonate occurs in interstitial masses, which may be related to the crystallisation of CO_2-enriched residual liquid. Carbonate globules occurring locally within the syenites seem to support this hypothesis. In this case the reaction of the carbonate in the globule with the host syenite results in the formation of a phlogopite margin in the globule (Figure II.21). However, because the syenites are spatially associated with carbonatite intrusions, some of the interstitial carbonate is introduced by fluids derived from the carbonatites, making it difficult to estimate the relative proportion between these two varieties.

Zircon is a common accessory in Tapira syenites, occurring as anhedral, relatively large (up to 0.5 mm, Figure II.22) crystals. These do not produce pleochroic haloes when included in biotite, suggesting that Tapira zircons have relatively low contents of radioactive elements such as U and Th.

Altered patches, composed of a mixture of carbonate, sericite and clay minerals are present in some of the examined samples of syenite. Because the orthoclase in the same thin sections is virtually fresh, these patches are unlikely to be derived from the alteration of feldspar. They probably represent original feldspathoids, such as leucite and nepheline, which are more susceptible to alteration processes. The patches are often irregularly shaped (Figure II.23) but in some cases their contours resemble those of leucite crystals (Figure II.24) whereas others are rectangular, resembling nepheline or kalsilite (Figure II.25). A number of samples containing altered patches were subjected to a reconnaissance XRD investigation. In two of these samples a set of peaks consistent with the presence of leucite or analcime was found. Unfortunately, these minerals were not found in the thin sections investigated by electron microprobe, and a more detailed microprobe study is required to characterise their chemical composition.

In any case, the presence of leucite and analcime (as a likely product of the post-magmatic alteration of the former), suggested by the XRD data, is consistent with the ultrapotassic character of the alkaline rocks in the Alto Paranaíba Igneous Province (APIP). Leucite syenites have not been previously described in the province, but are known from the Serra do Mar Province, located to the southeast of the APIP. (Figure I.6).

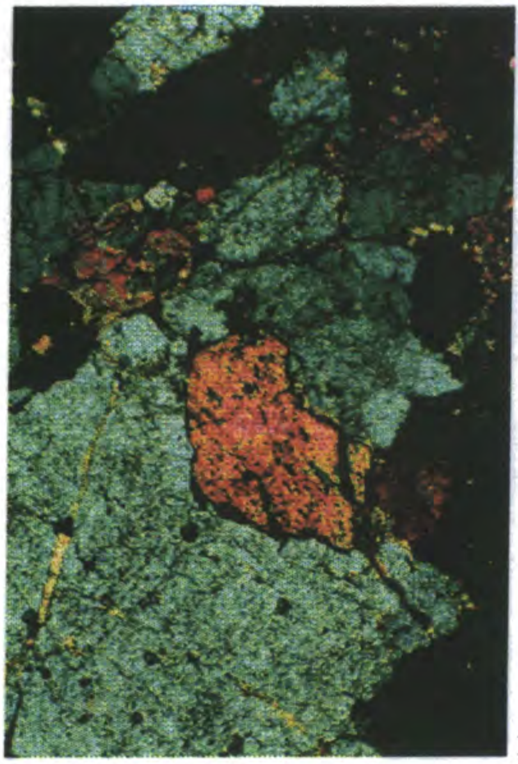

II.22

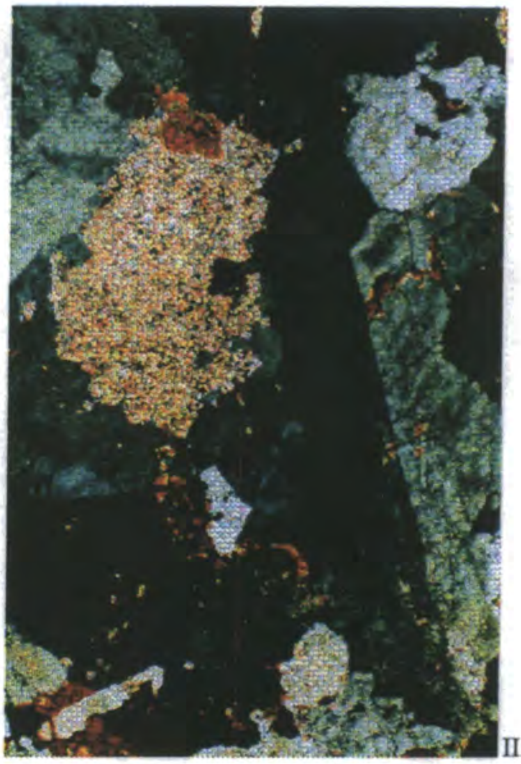

II.23

II.24

II.25

Figure II.22 *- Relatively large zircon crystal partially included in orthoclase from the Tapira syenite. Sample at302, cross-polarised light. Field of view = 2.24 x 1.47 mm.*

Figure II.23 *- Irregularly shaped patch composed of a fine-grained mixture of carbonate and sericite. Note the absence of alteration in the adjacent orthoclase. Sample at039, cross-polarised light. Field of view = 3 x 1.9 mm.*

Figure II.24 *- Altered hexagonal patch, included in unaltered feldspar. The shape of the altered area resembles that commonly observed in leucite crystals. Sample at018, plane-polarised light. Field of view = 3 x 1.9 mm.*

Figure II.25 *- Rectangular altered patches in syenite. The shape is strongly suggestive of nepheline or kalsilite. The patch near the centre of the picture suggests that the original mineral was zoned. Note that the feldspars (white) are alteration-free. Sample at115, plane-polarised light. Field of view = 3 x 1.9 mm.*

Note on fine-grained (microsyenite) dykes from Salitre

Fine-grained rocks of syenitic composition were not found in the studied drill cores or in outcrops from Tapira. However, these rocks are relatively well exposed in the Salitre complex, located further to the northwest in the APIP. A suite of felsic dykes from Salitre was examined petrographically and by XRD, and their chemical composition determined (Chapter IV), as a potential fine-grained equivalent of the Tapira syenites. As in Tapira rocks, the Salitre microsyenites are essentially composed of K-feldspar and aegirinic pyroxene. However, they also contain fine-grained perovskite and modally significant feldspathoids (Figures II.26 and II.27).

More importantly, the XRD study of one of these samples revealed the presence of peaks at D = 3.94, 3.119, 2.572, 2.479 and 2.43 Å, which indicate the presence of kalsilite (card number 11-579 in the JCPDS). In addition to kalsilite, the XRD results also suggest the presence of nepheline in these rocks. As nepheline and kalsilite are petrographically indistinguishable, the evaluation of their relative proportions, as well as a precise chemical characterisation awaits detailed microprobe studies of the Salitre rocks.

Kalsilite has been described in kamafugitic rocks from the APIP (Mata da Corda, Sgarbi and Valença, 1993) and from the contemporaneous Iporá Igneous Province, in the northern margin of the Paraná Basin (Junqueira-Brod, 1998), but has not been reported in connection with the carbonatite complexes. The occurrence of kalsilite in rocks from Salitre provides a crucial piece of evidence linking the carbonatite complexes with the kalsilite-bearing kamafugitic rocks of APIP. This is in good agreement with the remarkable petrographic similarities between the Tapira bebedourites and the clinopyroxenite xenoliths contained in the Mata da Corda kamafugites. Kalsilite has been reported from some of these xenoliths (Sgarbi *et al.*, 1998)

II.4 - CARBONATITES

The Tapira carbonatites were grouped into five different units (C1 to C5), according to their location in the complex (see Figure I.15, Chapter I) and to their mineralogical and petrographic properties. Apart from C5, which occurs as dykes crosscutting several rock- types in the complex, the stratigraphic relationships between these bodies are difficult to estimate from drill core data alone. Therefore, the sequential numbers were attributed to the units on the basis of limited indirect evidence, such as the spatial association with particular units of the SPS. The designations C1 to C5 also reflect the volumetric importance of each unit within the complex. Accordingly, C1 is the largest carbonatite body, composed essentially of calcite-carbonatites (sovites, subordinately dolomite-sovites) and intruding wehrlites and bebedourites of the B1 unit, in the centre of the complex. C2 consists of dolomite-bearing calcite-carbonatites (dolomite-sovites) spatially associated with syenites in the centre-north region. C3 and C4 are small bodies of sovite occurring, respectively, in the northern and southern border of the complex. C3 is spatially associated with bebedourites of the B2 unit, and seems to be located in the contact of B2 with a small area of B1 bebedourites (see Figure I.15). C4 is petrographically similar to C3 and crops out in an isolated area, where the contact with the country rock is not exposed. Finally, several late-stage dykes crosscutting the previous units were collectively placed in the C5 unit, regardless of their occurrence within the "C5" area of Figure I.15 or not.

It should be stressed that this ordering of the Tapira carbonatites is merely tentative, due to the lack of direct field evidence in most cases. In later sections of this thesis, evidence from rock and mineral chemistry will be examined seeking to confirm or refute this hypothetical "magmatic sequence" of the Tapira carbonatites. The petrographic aspects of each individual unit are described below.

II.4.1. C1 UNIT

This unit comprises granular, medium-grained calcite carbonatites and intrudes B1 wehrlites and bebedourites, brecciating and metasomatising these rocks, with the formation of phlogopite-rich fenites (see section II.6). The calcite carbonatites are frequently cut by dykes of late-stage dolomite carbonatites.

C1 carbonatites vary from homogeneous to locally banded. The essential minerals are calcite, phlogopite, magnetite and apatite, with subordinate amounts of dolomite, sulphides, baryte and pyrochlore. The texture is dominantly granular.

Carbonate minerals consist essentially of anhedral, equant (1-2 mm) grains of calcite. Post-magmatic processes resulted locally in low-temperature recrystallisation of the calcite. The recrystallised carbonate acquires a "cloudy" aspect, caused by the exsolution of several phases such as opaque minerals and Sr-, Ba- and REE-rich carbonates (Figure II.28, and Chapter III). This feature is particularly common in the C1 unit, probably as a function of the larger dimensions of this intrusion, which would favour the development of more extensive hydrothermal/carbothermal systems. The carbonate crystals may locally show preferred orientation, suggesting a certain degree of flow of the semi-consolidate carbonatite. Dolomite may occur as interstitial grains, or accompanying ankerite in the late-stage veinlets.

Phlogopite occurs as subhedral laths with very strong orange to deep-red reverse pleochroism, which is characteristic of tetraferriphlogopite (TFP). The crystals often show concentric oscillatory zoning and inclusions of carbonate, apatite and pyrochlore. No evidence of disequilibrium with the carbonatite liquid or reaction with adjacent minerals was found (Figure II.29). This variety of phlogopite is, therefore, interpreted as magmatic, crystallised directly from the carbonatitic liquid.

A different variety of phlogopite comprises xenocrysts derived from the ultramafic rocks of the SPS. These are particularly common in breccias formed in the vicinity of the contact with the SPS, but become rare towards the centre of the C1 intrusion. The phlogopite of this variety has normal pleochroism, in shades of yellow and orange, which is typical of ordinary phlogopite. The crystals invariably show evidence of disequilibrium with the carbonatite liquid, being replaced at the rims and along cleavages by TFP. The completion of the replacement process results in fine-grained aggregates of anhedral TFP. These are unlike the primary TFP described above, in that they do not exhibit euhedral shapes or regular zoning. However, the dispersal of these fine-grained aggregates may result in scattered TFP flakes, which are then indistinguishable from the primary mica.

The proportion of apatite is highly variable, as a function of the banded character of some of the C1 carbonatites. Apatite occurs as subhedral to more frequently rounded crystals. It may be concentrated in bands, together with TFP, or in irregular aggregates with TFP and pyrochlore. In some cases, the apatite-rich bands also contain xenocrystic phlogopite. The modal banding of C1 carbonatites suggests the influence of crystal accumulation processes in the formation of some of these rocks.

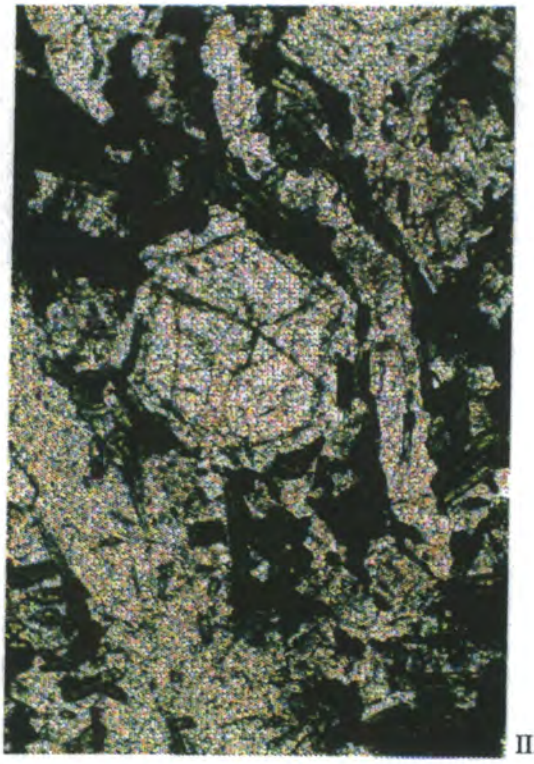

II.26

II.27

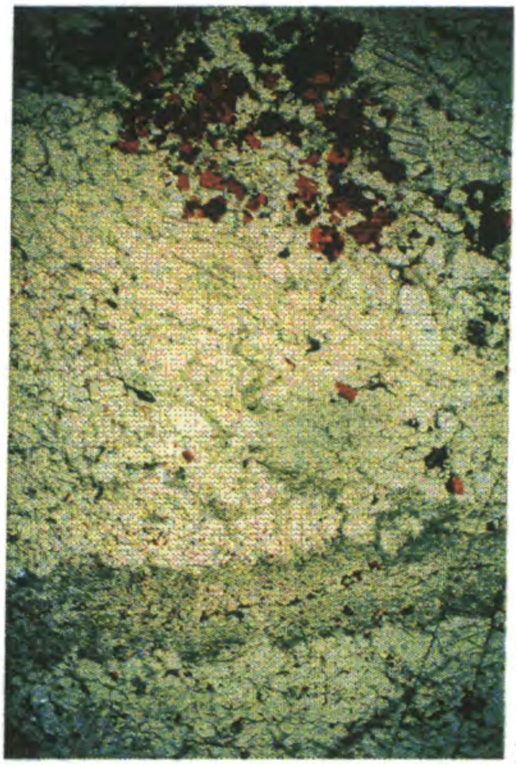

II.28

II.29

Figure II.26 *- Syenitic dyke from the Salitre Complex. Note the oriented prismatic feldspars and the hexagonal section of an euhedral feldspathoid (leucite?). Compare with Figure II.24. Sample sal-2, plane-polarised light. Field of view = 1.3 x 0.77 mm.*

Figure II.27 *- Syenitic dyke from the Salitre Complex. Note the orientation of feldspars and the rectangular section of feldspathoid (light grey, in the centre). This is uniaxial negative and could be either nepheline or kalsilite (see text). Compare with Figure II.25. Sample sal-2, cross-polarised light. Field of view =3 x 1.9 mm.*

Figure II.28 *- Carbonatite of the C1 unit. Note the orientation of the calcite grains, parallel to the phlogopite- and apatite-rich band at the top. Also note the development of "cloudy" calcite (see text) along a fracture at the bottom. Sample at055, plane-polarised light. Field of view = 12 x 7.2 mm.*

Figure II.29 *- Euhedral zoned phlogopite, in equilibrium with carbonatite. Note the strong pleochroism from yellow-orange to deep red-brown. Also note the extensive development of "cloudy" calcite, due to post-magmatic recrystallisation. Sample at136, plane-polarised light. Field of view = 2.15 x 1.3 mm.*

Pyrochlore is a conspicuous accessory in C1. It occurs as small euhedral to subhedral crystals, locally associated with apatite and TFP. Some crystals show a concentric zoning pattern (Figure II.30). Pyrochlore includes apatite and may include or be included in TFP.

Baryte occurs as scattered grains or as aggregates of granular or fibrous crystals, often altered to oxidised materials. The shape of the aggregates is irregular and sometimes baryte appears to be filling vugs in the carbonatite (Figure II.31). Fractures filled with baryte are common.

Opaque minerals occur as scattered grains of magnetite and late-stage subhedral sulphides (mainly pyrite, occasionally chalcopyrite).

II.4.2. C2 UNIT

The mode of emplacement of C2 carbonatite is variable. These rocks occur as: a) an independent intrusion (marked "C2", in Figure I.15); and b) as dykes and diatreme-facies breccias elsewhere in the complex. These two sub-types are described separately in the sections below. However, it should be emphasised that, since the two groups do not necessarily show spatial association, their inclusion in the same unit is merely tentative. These rocks share some compositional similarities (e.g. the presence of both calcite and dolomite as primary carbonates; occasional occurrence of zirconolite) and show a persistent association with syenites. However, a number of other features, such as contrasting textures and/or mode of emplacement (see below) could mean that carbonatites of more than one origin are present within the C2 unit.

"C2" intrusion

The rocks occurring in the C2 area of Figure I.15 are composed essentially of carbonate, with accessory opaque minerals and very small (in most cases negligible) amounts of phlogopite, amphibole, zirconolite, baryte and pyrochlore. These rocks are usually finer-grained than C1 (average grainsize 0.4 mm).

Carbonate minerals comprise calcite and dolomite. Both minerals may develop a cloudy appearance, caused by the exsolution of Sr- and Ba- rich phases in response to low-temperature recrystallisation. Deformation of carbonate crystals is recognised in some samples, leading to the development of mortar texture (Figure II.32), which

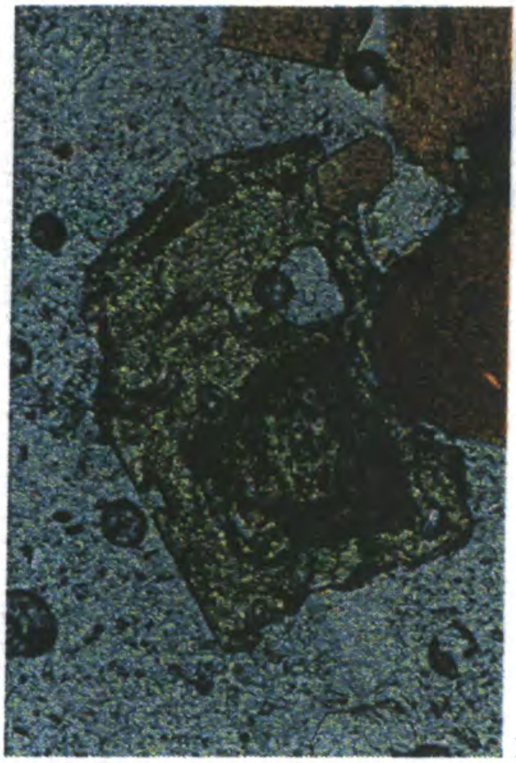

II.30

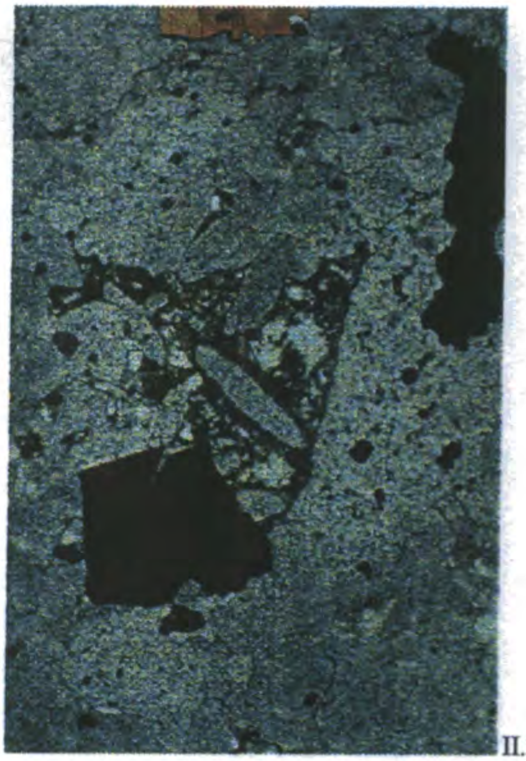

II.31

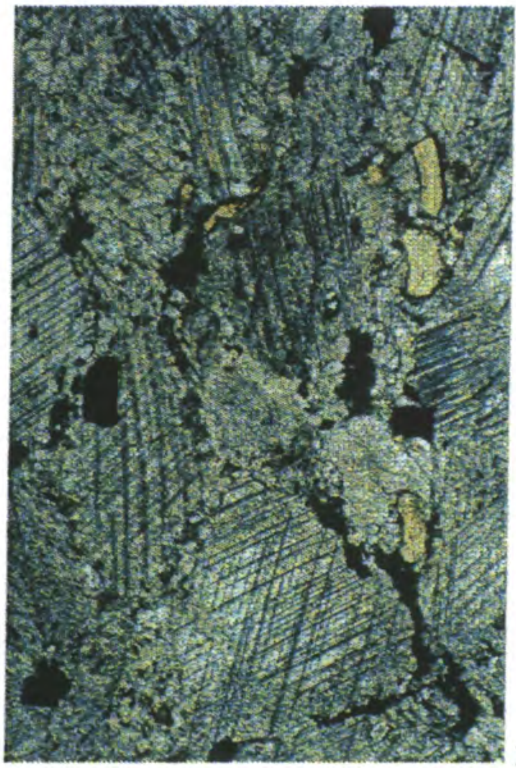

II.32

II.33

Figure II.30 *- Zoned pyrochlore in carbonatite of the unit C1. Note the subhedral contours, the inclusion of apatite (rounded, white) and the partial inclusion of carbonate and TFP at the margins of the crystal. Sample at136, plane-polarised light. Field of view = 0.66 x 0.4 mm.*

Figure II.31 *- Vug filled by partially altered baryte in carbonatite C1. Note the elongate calcite crystal within the baryte and the subhedral TFP. Sample at136, plane-polarised light. Field of view = 3 x 1.9 mm.*

Figure II. 32 *- Mortar texture in carbonatite of the unit C2, defined by aggregates of small crystals at the margins of the primary carbonates, due to deformation. Sample at050, plane-polarised light. Field of view = 3 x 1.9 mm.*

Figure II.33 *- Highly deformed carbonatite of the unit C2. Note the augen of carbonate in a finer-grained carbonate groundmass. This texture is interpreted as an evolution of that in Figure II.32, by increasing deformation. Sample at051, cross-polarised light. Field of view = 12 x 7.2 mm.*

ultimately evolves to a fine-grained fabric with isolated "augen" of the original carbonate (Figure II.33). This contrasts with the apparently permissive intrusion of carbonatite in the syenites (i.e., with the formation of magmatic stoping breccias, see Chapter I). It may be that the C2 intrusion of Figure I.15 consists of more than one batch of magma.

Phlogopite occurs only as tiny (0.1 mm) flakes, scattered in the carbonatite. These flakes may show either normal (ordinary phlogopite) or reverse pleochroism (TFP). The paucity and the reduced size of mica flakes in C2 make it difficult to ascertain the origin of this mineral. Direct precipitation from the carbonatite magma or disintegration of phlogopite xenocrysts seem equally probable. On the grounds of the similar optical properties and of similar composition (see Chapter III) the flakes of TFP are interpreted here as primary, whilst the flakes of ordinary phlogopite may be of xenocrystic origin.

Pyrochlore is rare and occurs as scattered, euhedral, small (up to 0.2 mm) zoned crystals. It is at least partly formed at a late stage, since it accompanies baryte in vugs.

Amphibole occurs in very few samples, forming radial aggregates of dark blue-green acicular crystals.

Opaque minerals consist mostly of small interstitial grains of subhedral magnetite, with subordinate amounts of relatively coarser-grained sulphides.

Zirconolite occurs as small, subhedral, deep red-brown crystals (Figure II.34). Zirconolite is the only zirconium mineral found in the Tapira carbonatites during this research. Furthermore, it seems to be restricted to carbonatites of C2 unit. It is interesting to note that the C2 carbonatites are spatially associated with the Tapira syenites, which are also enriched in zirconium (e.g. large zircon crystals, Figure II.22).

Dykes and breccias

C2 Carbonatites locally occur as fine-grained dykes, containing euhedral phenocrysts of apatite and tabular calcite, as well as deformed xenocrysts of phlogopite (Figure II.35) and, more rarely, diopside. The groundmass is composed of fine-grained calcite, dolomite, apatite, opaque minerals, phlogopite and chlorite. Zirconolite may be a rare accessory. Oriented calcite phenocrysts define a conspicuous flow texture. (Figure

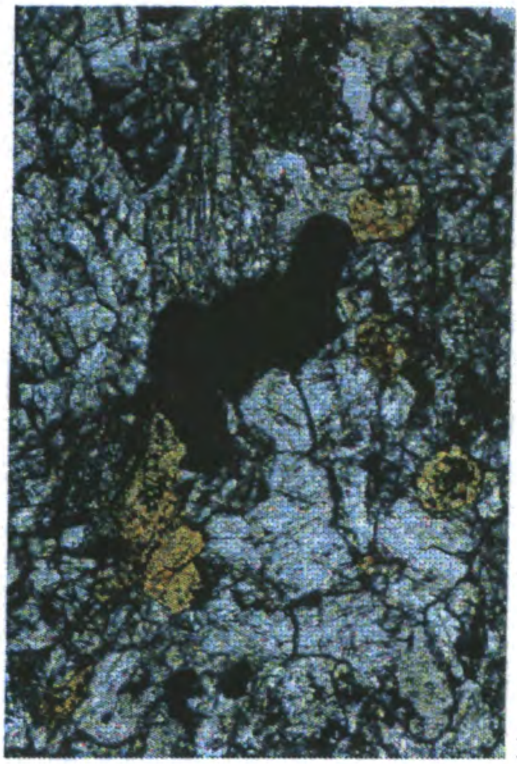

II.34

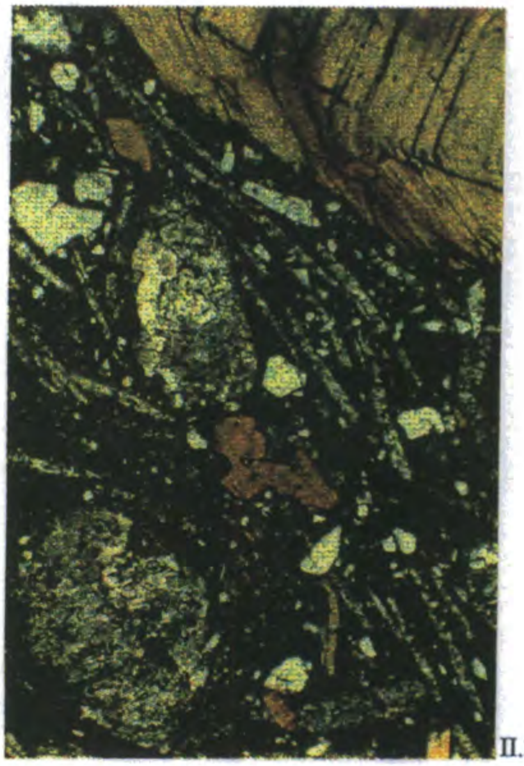

II.35

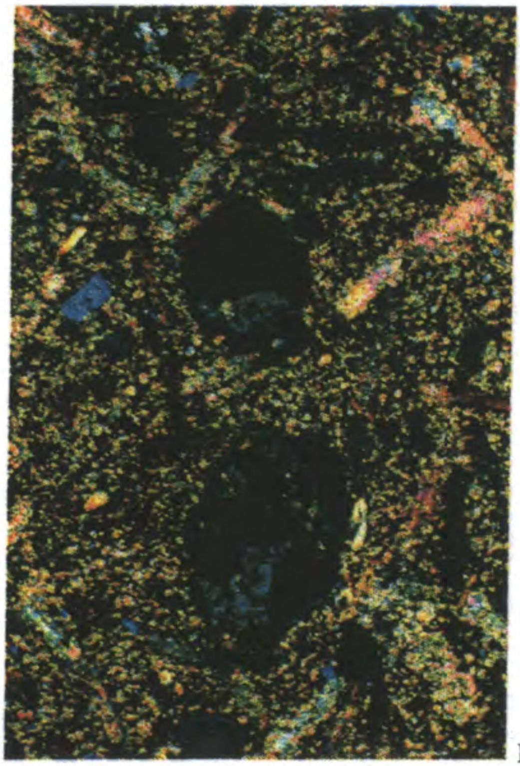

II.36

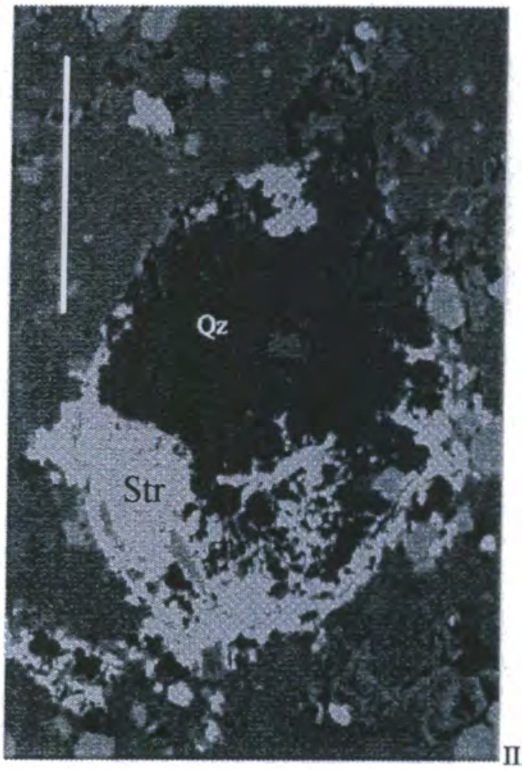

II.37

Figure II.34 *- Aggregate of zirconolite crystals in carbonatite C2 (deep brown-red, at the centre). Also note the small flakes of phlogopite. Sample at051, plane-polarised light. Field of view = 0.62 x 0.35 mm.*

Figure II.35 *-Deformed phlogopite xenocryst in dyke of carbonatite C2. Note the euhedral prismatic calcite, oriented in the direction of flow. Apatite microphenocrysts (locally euhedral) are also present. The two rounded, light-coloured patches are fine-grained feldspathic aggregates and suggest a link between this carbonatite unit and the syenites. Sample at219, plane-polarised light. Field of view = 3 x 1.9 mm.*

Figure II.36 *- View of feldspathic globules in cross-polarised light. Note the rounded shapes and the lack of alteration. Sample at219, cross-polarised light. Field of view = 3 x 1.9 mm.*

Figure II.37 *- Back-scattered electron (BSE) image showing a small grain of quartz (Qz, dark grey) being partially dissolved and replaced by strontianite (Str, bright light grey). The rounded shape of the quartz grain suggests that it may have derived from the meta-sedimentary country rocks. Scale bar = 50 µ.*

II.35). Globules composed of fine-grained feldspathic aggregates are common (Figures II.35, II.36), suggesting that C2 may have been contemporaneous with syenites, and that the two rock-types may be linked by a common origin (e.g. differentiation or liquid immiscibility). The C2 carbonatite dykes show evidence of some degree of crustal assimilation. Figure II.37 shows a partially assimilated rounded grain of quartz, presumably derived from the meta-sedimentary country rock.

A carbonatitic diatreme breccia has been temporarily exposed by the mining activities in Tapira (see Chapter I). This is composed of fragments with highly variable size (up to 1m), comprising several petrographic varieties of SPS rocks and, more rarely, fragments of country rock. The matrix is fragmental and extremely rich in xenocrysts (Figures II.38 and II.39), immersed in a carbonate-rich groundmass. The composition of the xenocrysts is highly variable, but they seem to derive mainly from the SPS rocks (e.g. clinopyroxene, olivine, apatite, phlogopite, opaques, perovskite).

Two varieties of clinopyroxene xenocrysts are present in the breccias and dykes of the C2 unit. The first consists of abundant xenocrysts of pale-green, weakly pleochroic diopside, similar to that in the bebedourites. The second comprises rare, deep green aegirinic pyroxene, similar to that of the syenites.

On the basis of the presence of both calcite and dolomite in the groundmass of the breccias and of the similarities between the xenocrysts present in the breccias and those present in the C2 dykes, the breccias are interpreted here as an explosive expression of the C2 magmatism.

Finally, the petrographic evidence points to an intimate association between C2 and syenites, suggesting that these two rock-types may be contemporaneous or have formed within a short period of time. This is supported by: (i) the presence of carbonate globules and interstitial carbonate patches in the syenites (lacking apparent association with carbonate veinlets); (ii) the spatial association between the two units in the complex; (iii) the small number of aegirinic xenocrysts in C2, compared with diopside; (iv) the presence of zirconolite as a common accessory mineral in C2, together with the abundance of zircon in the syenites; (v) the presence of feldspathic globules in C2 carbonatites.

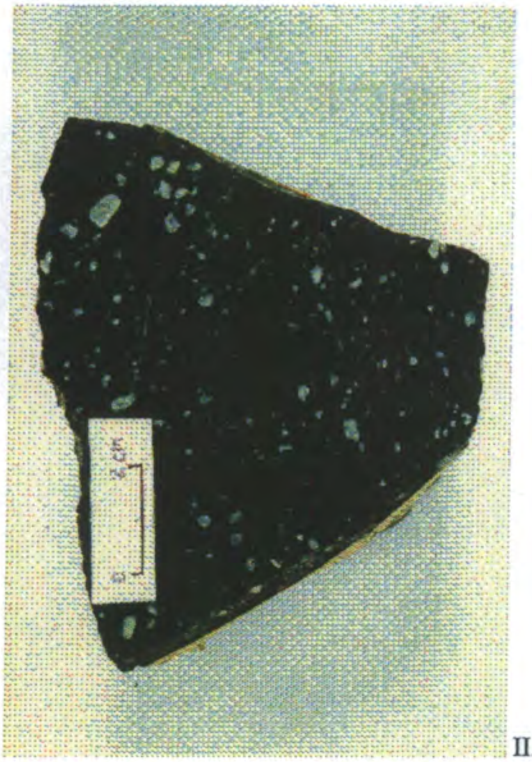

II.38

II.39

II.40

Figure II.38 *- Detail of the matrix of the carbonatitic breccia, containing numerous fragmented crystals of apatite and mafic minerals, derived from the SPS rocks. Sample tap-1b.*

Figure II.39 *- Matrix of the carbonatitic breccia. Note the fragmented crystals of apatite, olivine (partially serpentinised), pyroxene, phlogopite and opaque minerals. Compare the light-coloured diopside crystals derived from bebedourites with the dark green aegirine (near the centre) derived from syenites. Sample tap-1b, plane-polarised light. Field of view = 12 x 7.2 mm.*

Figure II.40 *- Xenocrystic phlogopite in carbonatite C3. The optical properties of the core are indicative of ordinary (high-Al) phlogopite, but the mineral is evidently in disequilibrium with the carbonatite, being partially dissolved and replaced by tetraferriphlogopite in the rims and cleavages. Compare this phlogopite with the primary tetraferriphlogopite crystals of carbonatite C1 (Figure II.29). Sample at060a, plane-polarised light. Field of view = 1.3 x 0.77 mm.*

II.4.3. C3 UNIT

This unit occurs in the northern extremity of the complex. It consists of medium- to coarse-grained (average grainsize = 2 mm) calcite-carbonatites, with isotropic structure and granular texture. The carbonatite is composed mainly of interlocking calcite crystals, and smaller (0.2-0.3 mm) rounded crystals of apatite. Opaques are common, and xenocrysts of clinopyroxene and phlogopite are conspicuous. Perovskite is an extremely rare accessory in C3.

Calcite occurs as an equigranular, closely packed arrangement of anhedral crystals that dominates the texture. The effects of post-magmatic alteration, observed in C1 and C2 (development of “cloudy” calcite) are remarkably restricted in C3. This is probably due to the smaller size of the C3 intrusion, with correspondingly downscaled hydrothermal or carbothermal systems.

Phlogopite is only present in C3 as xenocrysts. These comprise anhedral crystals of ordinary (normal pleochroism) phlogopite. They invariably display evidence of disequilibrium with the carbonatite liquid, such as embayed margins, irregular shapes and partially replacement by TFP, especially around the rims or along cleavages and fractures (Figure II.40).

Pyroxene is also xenocrystic, but has a more restricted distribution than phlogopite. The pyroxene xenocrysts are not as easily dissolved by the carbonatite liquid as those of phlogopite, but still show irregular, rounded or embayed margins. The xenocrystic origin is evident in Figure II.41. Note that the pyroxene in this picture shows an irregular shape and the inclusion of apatite (near the top-side of the crystal) terminates exactly at the limit of the xenocryst. Optically, the clinopyroxene xenocrysts in C3 are similar to the diopside in the bebedourites B-2, which is unsurprising, given the spatial association of the two units in the northern margin of the complex.

II.4.4. C4 UNIT

This unit is petrographically similar to C3, except for the apparent absence of diopside xenocrysts. Phlogopite xenocrysts show strong evidence of being dissolved into the carbonatite liquid, with fine-grained opaque minerals forming as a residue. In extreme cases, the phlogopite crystal is completely dissolved, leaving behind only a cloud of fine-grained opaque minerals and oxidised material (Figure II.42).


II.41

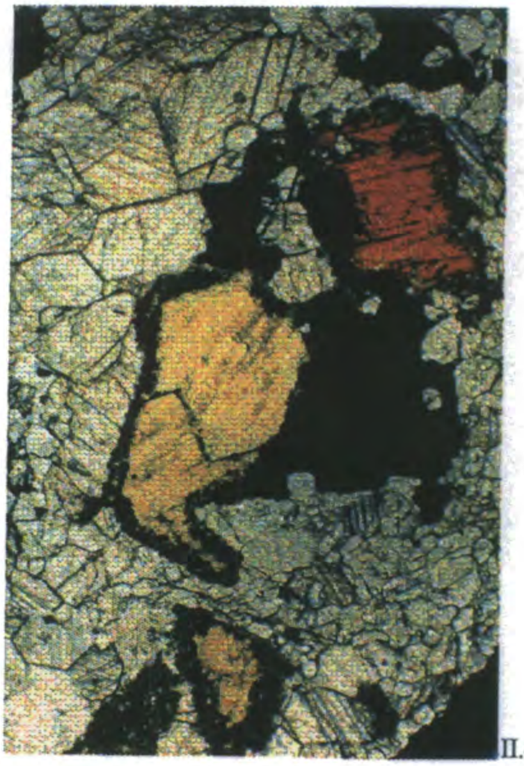
II.42

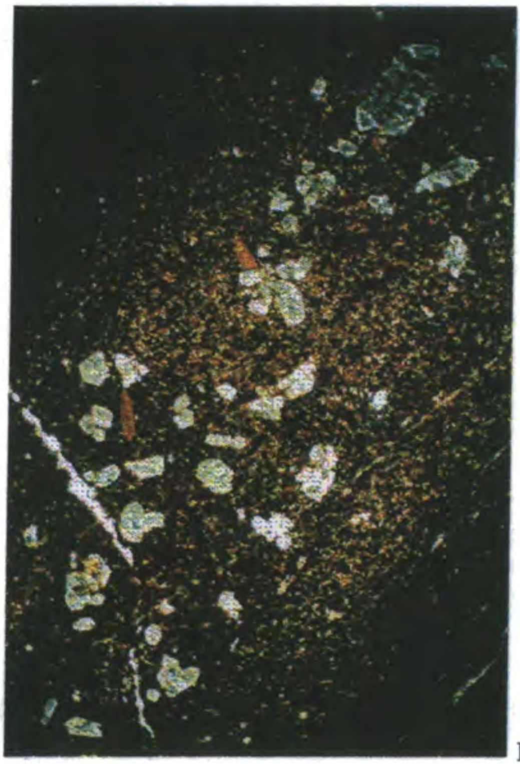
II.43

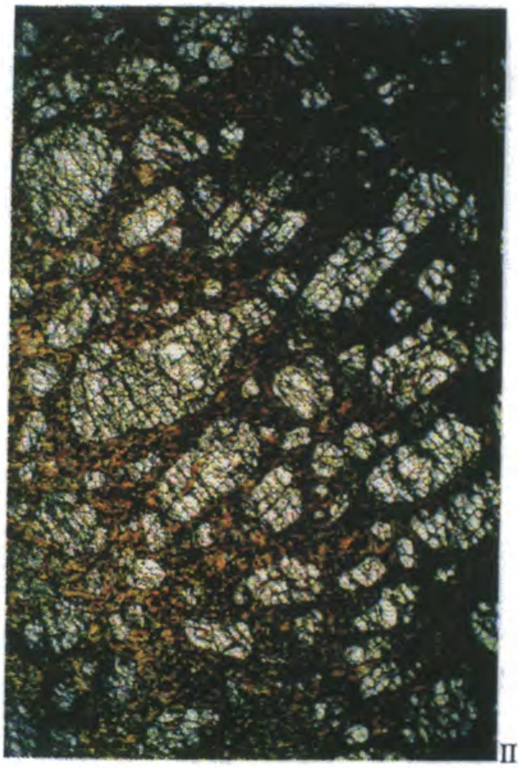
II.44

Figure II.41 *- Xenocrystic pyroxene in carbonatite of unit C3. Note that the apatite inclusions in the pyroxene do not have physical continuity outside the xenocryst. Sample at043, plane-polarised light. Field of view =6 x 3.7 mm.*

Figure II.42 *-Xenocrystic phlogopite in carbonatite of unit C4. The crystals are being dissolved by the carbonatite. Note the increasing intensity of dissolution, from top to bottom in the photograph. Sample at131, plane-polarised light. Field of view = 6 x 3.7 mm.*

Figure II.43 *-Accumulation of phenocrysts of serpentinised olivine in the centre of phlogopite-picrite dyke, by flow differentiation. Sample tp-90-4, plane-polarised light. Field of view = 12 x 7.2 mm.*

Figure II.44 *- Preserved olivine phenocrysts in the central portion of a phlogopite-picrite dyke. Note the high modal percentage of phenocrysts, produced by accumulation of olivine as a result of flow-differentiation. The crystals are aligned in the direction of flow. Sample at021, plane-polarised light. Field of view = 12 x 7.2 mm.*

II.4.5. C5 UNIT

A number of late-stage dykes and veins have been grouped under this unit. In Figure I.15 (Chapter I) an area is shown, in the northwestern portion of the complex, where these rocks are particularly common and which probably represents a larger dyke or system of dykes. However, the C5 rocks are not restricted to this region, but form thin dykes and veinlets throughout the complex. They are, therefore, considered as the latest carbonatite manifestation in Tapira.

Carbonatites of the C5 unit are usually fine-grained (0.2-0.3 mm) and equigranular, although coarser-grained facies may occur locally. They are composed of dolomite or mixtures of dolomite and calcite. Opaques and baryte are the common accessory minerals. Phlogopite (TFP) and apatite are very rare. Phlogopite xenocrysts do occur, showing the same disequilibrium features described above for other carbonatite units.

II.5 - ULTRAMAFIC DYKES

The plutonic rocks of the Tapira complex are crosscut by a large number of ultramafic dykes, subdivided here into phlogopite-picrites and low-Cr dykes. The thickness of these dykes is usually small (a few centimetres) but may exceptionally reach a few metres.

II.5.1. PHLOGOPITE-PICRITES

These rocks consist of phenocrysts of olivine (less frequently phlogopite, apatite clinopyroxene or perovskite) set in a fine-grained groundmass composed of phlogopite, carbonate, apatite, perovskite and opaque minerals. They commonly show evidence of flow-differentiation, defined by the accumulation of olivine phenocrysts towards the centre of the dykes (Figure II.43).

Olivine phenocrysts are subhedral to euhedral, varying from intensely serpentinised to perfectly fresh. The preferred orientation of phenocrysts in the direction of flow is common (Figure II.44). Olivine phenocrysts may be coated by aggregates of equant small crystals of perovskite and oxides (chromite). This texture is identical to that observed in the wehrlites (e.g. Figure II.6). Perovskite coating of olivine crystals has also been described from kimberlites (e.g. Reid *et al.,* 1975; Dawson and

Hawthorne, 1973). Locally the olivine phenocrysts are mantled by subhedral laths of phlogopite (Figure II.45). A similar texture has been described from lamproites (Mitchell and Bergman, 1991) and interpreted as the product of nucleation of magmatic phlogopite against olivine macrocrysts, rather than reaction between olivine and liquid. Mantling of olivine by phlogopite laths has also been reported by Gibson *et al.* (1994) from the kamafugitic diatreme of Serra do Bueno, in APIP. A second type of phlogopite mantling in olivine phenocrysts is illustrated in Figure II.46. In this case, anhedral masses of phlogopite form coronas around the olivine phenocrysts and are clearly the product of reaction (note, for instance, the ring of perovskite + opaques marking the contours of the original olivine crystal). The sample portrayed in Figure II.46 shows petrographic and chemical evidence of widespread post-magmatic alteration. This is possibly a phlogopite-picrite dyke caught in the hydro/carbothermal system of a late intrusion of carbonatite. This texture is therefore interpreted as a metasomatic feature, as opposed to the primary (magmatic) character of the texture in Figure II.45.

In addition to its occurrence with olivine, phlogopite is present as phenocrysts and is also an important constituent of the groundmass of phlogopite-picrites. The phenocrysts may be locally abundant and occur as subhedral laths, oriented or not (Figure II.47). They may be zoned towards tetraferriphlogopite, in samples where carbonate is modally abundant in the groundmass. The phlogopite laths show minor embayments, indicative of incipient dissolution of the phenocryst into the liquid (Figure II.47). Groundmass phlogopite occurs as subhedral to anhedral (interstitial) lamellae, which may be oriented or not.

Clinopyroxene is diopsidic in composition and occurs as rare phenocrysts, locally surrounded by phlogopite mantles.

Perovskite is an important constituent in the groundmass. It also forms rare subhedral phenocrysts, containing inclusions of apatite and fine-grained groundmass material.

Opaque minerals occur as small scattered grains in the groundmass (chromite + titanomagnetite) or slightly larger crystals (chromite) accompanying perovskite in rings formed around olivine phenocrysts.

Apatite occurs as small prismatic or equant crystals in the groundmass or, more rarely, as subhedral prismatic microphenocrysts (Figure II.48).


II.45


II.46


II.47

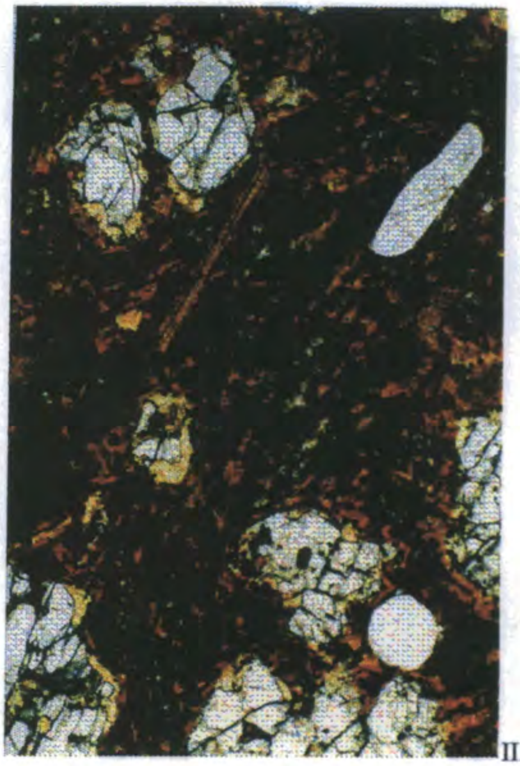
II.48

Figure II.45 *- Serpentinised olivine phenocryst, mantled by laths of phlogopite. The mantling is interpreted as a magmatic texture (compare with Figure II.46). Sample at022, plane-polarised light. Field of view = 3 x 1.9 mm.*

Figure II.46 *- Metasomatic replacement of olivine by masses of anhedral phlogopite. Note that the original limits of the olivine grains are marked by the mantles of perovskite + opaque minerals. Sample at120, plane-polarised light. Field of view = 3 x 1.9 mm.*

Figure II47 *- Subhedral to euhedral phenocrysts of phlogopite in phlogopite-picrite dyke. Note the rims composed of tetraferriphlogopite and showing irregular outlines, as result of a strongly poikilitic character, whilst the cores are virtually inclusion-free. Some crystals show embayed outlines indicating partial dissolution into the liquid. Sample 91SB2, plane-polarised light. Field of view = 3 x 1.9 mm.*

Figure II.48 *- Prismatic (top-right) and basal (bottom-right) sections of apatite microphenocrysts in phlogopite picrite dyke. Sample at022, plane-polarised light. Field of view = 3 x 1.9 mm.*

The formation of carbonate-rich zones in the groundmass of phlogopite-picrite dykes is locally observed. These may evolve to carbonate “pockets” (Figure II. 49) of irregular or globular shape, suggesting that immiscibility of carbonate-rich liquid from the phlogopite-picrite magma may have occurred as early as during the formation of olivine. Although immiscibility of silicate and carbonate liquids is by far more common at more evolved stages (e.g. carbonatite immiscibility from phonolitic magma) the process has been documented in ultramafic rocks such as kimberlites and ultramafic lamprophyres (e.g. Dawson and Hawthorne, 1973; Pearce and Leng, 1996).

II.5.2. LOW-CR DYKES

The low-Cr dykes typically contain phenocrysts of one or more of pyroxene, apatite, garnet and phlogopite, set in a groundmass of the same minerals plus opaques and carbonate.

Clinopyroxene phenocrysts (Figure II.50) are diopsidic in composition. They form subhedral prismatic crystals, locally surrounded by a rim of opaque minerals. In the groundmass, pyroxene occurs as subhedral to anhedral crystals, with a deeper green colour and locally develops acicular habit.

Phlogopite occurs as microphenocrysts or as euhedral to subhedral lamellae in the groundmass. The crystals commonly show preferred orientation, defining a flow texture in the low-Cr dykes. Both phenocrysts and groundmass phlogopite may be zoned towards deep reddish-brown rims. However, whilst the phenocrysts sometimes display evidence of reaction with the liquid, the flakes in the groundmass appear to be in equilibrium (Figure II.51). In many cases the colour absorption in the rims is so strong that the character of the pleochroism (i.e. normal or reverse) could not be determined. These rims may represent tetraferriphlogopite or, alternatively, titanian phlogopite. The zoning is interpreted as primary, rather than metasomatic replacement.

Apatite occurs as subhedral prismatic phenocrysts and microphenocrysts. It is often skeletal (Figure II.52), suggesting a relatively fast growth rate.

Garnet of melanite to andradite composition is common in the groundmass of low-Cr dykes. Melanite, rather than perovskite, is the main Ti mineral. Together with the absence of olivine and chromite, this is distinctive of the low-Cr dykes, when


II.49


II.50


II.51


II.52

Figure II.49 *- Irregularly-shaped pocket of carbonate (centre) in phlogopite-picrite dyke. The radial aggregates of acicular crystals within the pocket are of an unidentified mineral (wollastonite? amphibole?). Sample at014, plane-polarised light. Field of view = 6 x 3.7 mm.*

Figure II.50 *- Microphenocrysts of pyroxene (light green) and apatite (white) in low-Cr dyke. Sample at024, plane-polarised light. Field of view = 1.3 x 0.77 mm.*

Figure II.51 *- Euhedral lamellae of phlogopite in the groundmass of low-Cr dyke. The crystals are zoned towards deep reddish brown rims and appear to be in equilibrium. Also note the presence of acicular clinopyroxene (green). Sample at201, plane-polarised light. Field of view = 0.66 x 0.4 mm.*

Figure II.52 *- Skeletal microphenocryst of apatite in low-Cr dyke. Sample at201, plane-polarised light. Field of view = 0.66 x 0.4 mm.*

compared with the phlogopite-picrites. The garnet crystals are euhedral and zoned towards lighter-coloured rims.

With the magmatic evolution of the low-Cr dykes, the carbonate content progressively increases in the groundmass. This often leads to the formation of carbonate globules or ocelli (Figures II.53, II.54), suggesting that carbonate tends to form immiscible droplets within the low-Cr dykes. In some cases, the carbonate enrichment in the groundmass of low-Cr dykes is extreme and these rocks virtually grade to silico-carbonatites. The zoning of garnet seems to correlate well with this process. Figure II.55 shows garnet crystals from an extremely evolved (carbonate-rich) dyke. The cores of garnet crystals are dark-coloured and optically similar to the melanite occurring in less evolved dykes and in the B2 bebedourites. As the liquid evolves, the amount of Ti decreases abruptly and the garnet rims become close to andradite in composition. Whilst some of the darker cores may have irregular contours, indicating that they were partially dissolved by the liquid, the rims are perfectly euhedral and seem to be in equilibrium with the groundmass carbonate.

The sudden unavailability of Ti in the low-Cr dykes is difficult to explain only by progressive removal of melanite or another Ti-rich phase (e.g. to form bebedourite-like cumulates). It is possible that this abrupt change signals the onset of a more extensive event of liquid immiscibility.

II.6 - METASOMATIC ROCKS

II.6.1 - COUNTRY ROCKS

The intrusion of the Tapira complex resulted in deformation and metasomatism of the meta-sedimentary country rocks (quartzites and schists). The effects of metasomatism are more easily observed in the quartzites, because of their relatively simple initial composition and because these rocks crop out more often than the schists. The fenitisation aureole seems to be relatively restricted in Tapira although this is difficult to evaluate accurately, because of the poor exposure. The fenitised country rock can be found near the mining area and in rare outcrops around the margins of the complex.

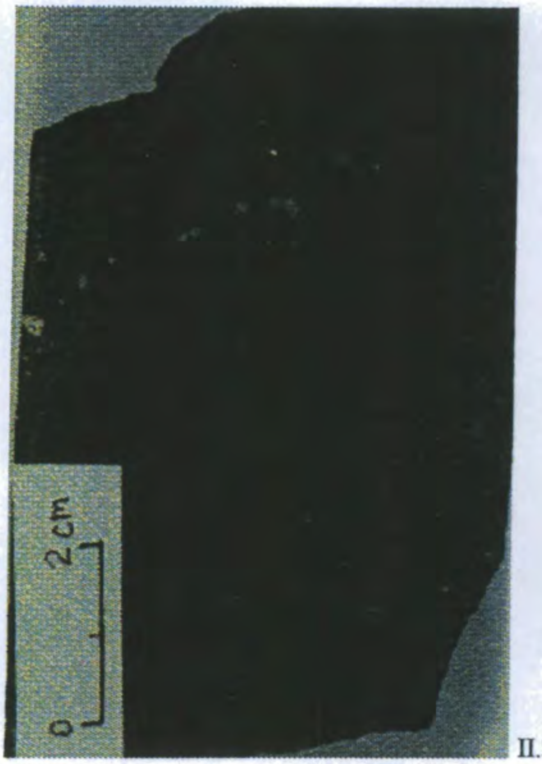

II.53

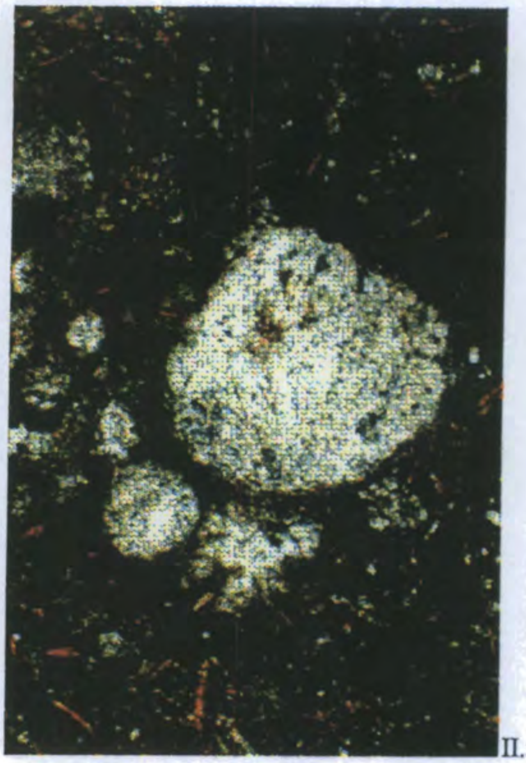

II.54

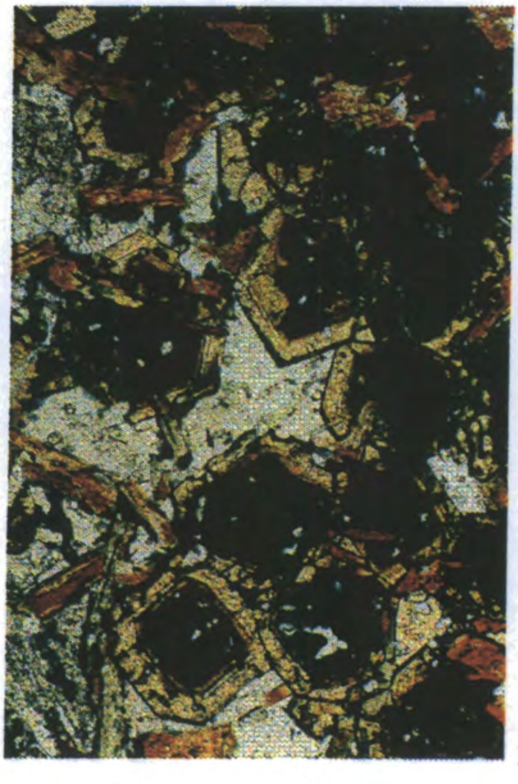

II.55

II.56

Figure II.53 *- Segment of drill core. Low-Cr dyke showing the formation of carbonate globules (white), suggesting the immiscibility of carbonate liquid from the dyke.*
Figure II.54 *- Rounded carbonate globules in fine-grained low-Cr dyke. Sample at207, plane-polarised light. Field of view = 2 x 1.3 mm.*
Figure II.55 *- Euhedral garnet crystals in the carbonate-rich groundmass of low-Cr dyke. The cores of crystals are melanitic in composition, whilst the light yellow rims are andradite. Note the crystal near the centre of the photograph, where the dark core shows evidence of partial dissolution. Sample at211, plane-polarised light. Field of view = 1.3 x 0.77 mm.*
Figure II.56 *- Fenitised quartzite. Note the dark lines marked by the formation of aegirine along the previously existing structures of the rock. Sample rja-t3.*

The first metasomatic effect observable in the quartzites is the formation of scattered porphyroblasts of alkali-feldspar. Closer to the contact with the complex, where metasomatism was more intense, the quartzites are converted to feldspar- and aegirine-rich fenites (Figure II.56). The structural fabric of the original rock may be preserved, or even enhanced, by the concentration of aegirine crystals along the pre-existing structure. Most of the quartz is transformed to alkali feldspar. The presence of substitution perthites in the feldspars (Figure II.57) suggests that multiple generations of alkali-feldspars were formed, perhaps during a prolonged metasomatic event or by several independent introductions of metasomatic fluids.

II.6.2 - SILICATE PLUTONIC ROCKS (SPS)

The effects of the intrusion of carbonatites in the Silicate Plutonic Series are clearly visible in drill-core samples. A phlogopite-rich reaction zone develops in the contact of syenite and carbonatite (Figure II.58). The thickness of this reaction zone is variable, but usually does not exceed a few centimetres.

In the ultramafic rocks of the SPS, the effects of carbonatite metasomatism are by far more intense. The dunites, wehrlites and bebedourites are converted into a phlogopite- carbonate- and magnetite-rich rock that has been classified as phlogopitite, glimmerite, foscorite, and silico-carbonatite by previous investigators of the APIP carbonatite complexes. This rock has also been occasionally confused with the magmatic phlogopite-rich rocks (phlogopite-picrites and low-Cr dykes). To avoid further misunderstanding, the metasomatic, phlogopite-rich products of the interaction of carbonatite liquids with the ultramafic portion of the SPS will be called simply "reaction rock" in this thesis.

The reaction rock (Figure II.59) is fine-grained, dark brown in colour and crosscut by abundant carbonate veinlets. Small-scale banding, with alternating phlogopite- and carbonate-rich zones is conspicuous. These alternating bands are always parallel to the contact (note the concentric pattern in Figure II.59, surrounding the preserved core of ultramafic rock). Similar textures have been described by Gaspar (1989), for ultramafic rocks subjected to carbonatite metasomatism in the Jacupiranga complex. The carbonate in the reaction rock is dolomite, and the mica has the strong red colour and reverse pleochroism typical of tetraferriphlogopite (Figure II.60).


II.57

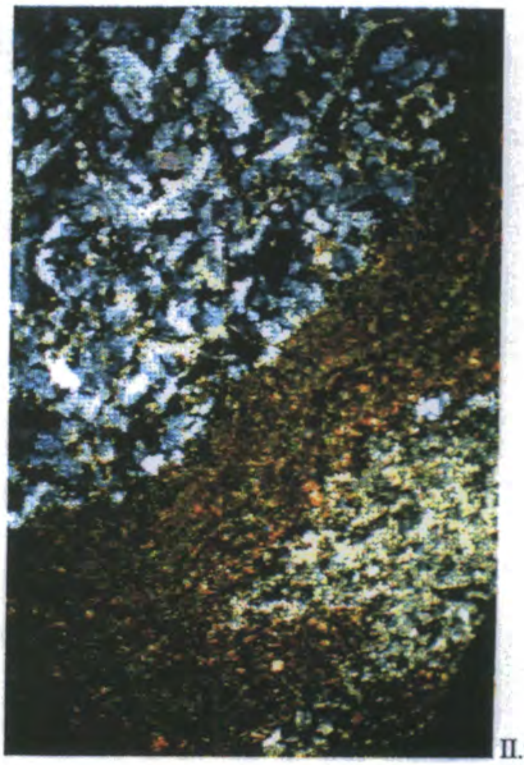
II.58

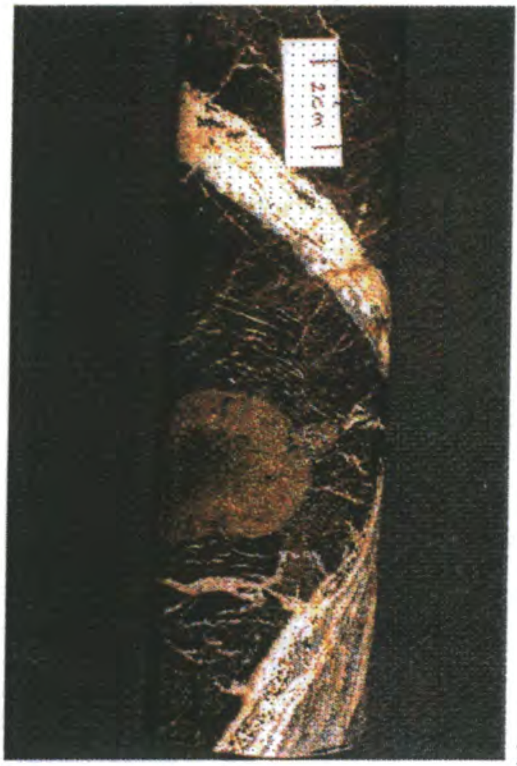
II.59


II.60

Figure II.57 *- Microscopic view of the fenite in Figure II.56. Note the small crystals of aegirinic pyroxene and the substitution perthites in the feldspar. Sample rja-t3, cross-polarised light. Field of view = 1.3 x 0.77 mm.*

Figure II.58 *- Phlogopite-rich reaction zone formed between syenite and intrusive carbonatite (bottom-right). Sample at305, cross-polarised light. Field of view = 12 x 7.2 mm.*

Figure II.59 *- Segment of drill core, showing the development of the reaction rock between carbonatite dykes and ultramafic rock of the SPS. Note the concentric banding, parallel to the contact with the preserved core of ultramafic rock.*

Figure II.60 *- Microscopic view of the reaction rock. Note the strong red colour of the mica, the carbonate bands parallel to the contact and the conversion of the pyroxenes to tetraferriphlogopite. Sample at019b, plane-polarised light. Field of view = 12 x 7.2 mm.*

The generation of tetraferriphlogopite by metasomatic processes has been demonstrated in previous sections of this Chapter. In fact, it appears that all tetraferriphlogopite in SPS rocks is accompanied by textural evidence of metasomatism. The same is not true of the primary tetraferriphlogopite in carbonatites C1 and of the zoned crystals in some of the phlogopite-picrites and low-Cr dykes. The chemical properties of Tapira micas will be investigated in a further section of this thesis, with a view to establishing possible differences between magmatic and metasomatic varieties.

II.7 - SUMMARY

- The petrographic characteristics of Tapira rocks are described in detail. The subdivision of the Silicate Plutonic Series (SPS) and of the Tapira carbonatites, established in Chapter I, is supported by detailed variations in mineralogy and texture of the Tapira rocks.
- Within the ultramafic portion of the SPS, two petrographically distinct groups (B1 ad B2) are recognised. In both groups, bebedourites (a variety of alkaline cllinopyroxenites containing essential perovskite, apatite and phlogopite) are largely predominant. Volumetrically subordinate olivine-rich rocks (mainly wehrlites) are also present. Facies variations towards perovskite- and/or apatite-rich rocks are common, particularly in B1.
- A progressive increase in SiO_2 activity is marked by the decrease of modal perovskite and the appearance of Ca-Ti silicates, such as melanite and sphene. This may occur in both B1 and B2 rocks but is a more prominent feature in the latter. Some evolved B2 bebedourites may contain interstitial feldspar and/or carbonate.
- Modal layering and strong mineral orientation, particularly in B1, suggest that most of the SPS is composed of cumulates, and that these may have been emplaced partially as a crystal mush. Some of B2 rocks, however, may represent the products of *in situ* crystallisation. Ultramafic pegmatites occur locally in B1. Their composition is mainly bebedouritic, but rare melilitolite (uncompahgrite) is also present.
- Tapira syenites are composed essentially of non-perthitic orthoclase, with subordinate aegirinic pyroxene and phlogopite, and accessory sphene, zircon and

carbonate. Some samples may possibly contain altered feldspathoids.

- Carbonatites are subdivided into five units (C1 to C5). Rocks of the C1 unit are coarse-grained calcite carbonatites, containing primary crystals of tetraferriphlogopite, apatite, magnetite and pyrochlore. Phlogopite xenocrysts and late-stage baryte and sulphides are also present.
- C2 carbonatite vary considerably in texture and composition. Rocks from the "C2" intrusion are composed essentially of calcite and subordinate dolomite, with accessory phlogopite and/or tetraferriphlogopite, pyrochlore, amphibole, opaques and zirconolite. The C2 dykes and the carbonatitic groundmass of diatreme-facies breccias contain primary crystals of tabular euhedral calcite, in addition to frequent xenocrystic material derived from the SPS and assimilated from the country rock. A possible association of C2 carbonatites with the syenites is suggested.
- C3 and C4 are petrographically similar, although not spatially associated. These are medium to coarse grained calcite carbonatites, with accessory apatite, opaques and rare perovskite (C3). Phlogopite and diopside xenocrysts, possibly entrained from the ultramafic SPS rocks, are locally abundant.
- C5 comprises dolomitc carbonatites, occurring as late-stage dykes and veins.
- Phlogopite-picrites are typically composed of olivine phenocrysts set in a fine-grained groundmass of phlogopite, carbonate, apatite and opaques. Carbonate "pockets" in the groundmass suggest a possible segregation of immiscible carbonate liquid.
- Low-Cr dykes lack olivine, but may contain phenocrysts of pyroxene, apatite, garnet and phlogopite, in a groundmass composed of the same phases plus carbonate and opaques. Carbonate ocelli and sudden changes in the optical properties of some minerals suggest that these rocks have been involved in liquid immiscibility processes.
- Metasomatic effects associated with the Tapira complex comprise the formation of aegirine- and feldspar-bearing fenites in the quartzite country rock, and various reactions between carbonatites and the silicate rocks of the SPS.

CHAPTER III – MINERAL CHEMISTRY

III.1 - INTRODUCTION

This chapter describes the chemical composition of some of the mineral phases in Tapira rocks. The mineralogy of carbonatites and associated silicate rocks is varied and complex, and the detailed study of all minerals identified in thin section goes far beyond the scope of this thesis. Instead, this study was concentrated on those minerals occurring as essential phases in a range of Tapira rocks, from wehrlites to syenites and carbonatites, with a view to identifying and monitoring magmatic processes involved in the genesis of Tapira rocks. Among the major mineral constituents of both carbonatites and silicate rocks, apatite is the only phase not included in this study. Apatite, together with rare accessory phases, such as pyrochlore and zirconolite, is part of current research in progress. The following sections of this Chapter will discuss the mineral chemistry of olivine, clinopyroxene, mica, perovskite, opaque minerals, garnet, feldspar and carbonates from the Tapira complex.

III.2 - OLIVINE

Olivine is present in dunites and wehrlites of the silicate plutonic series (SPS), in phlogopite-picrite dykes and as xenocrysts in carbonatitic breccias from the Tapira mine. This mineral is notably absent from the bebedourites and low-Cr dykes. At the relatively weathering-free level reached by the drilling works, bebedourites are by far the most abundant rock-type, whilst wehrlites are rare and dunites very rare. Only hydrothermally altered samples of dunite were found in the drill cores examined during this research, and these were not considered for whole-rock or mineral chemistry studies. Therefore, the following discussion will be based solely on the olivines from in wehrlites and phlogopite-picrites. The ranges and average composition of the studied olivines are presented in Table III.2.1. The complete set of analyses and calculated formulas are given in Appendix 2.

	Wehrlites		Phlogopite-picrites	
	Average	Range	Average	Range
SiO_2	40.10	39.57-40.55	39.97	38.98-40.72
TiO_2	0.02	0.00-0.09	0.03	0.00-0.12
Al_2O_3	0.01	0.00-0.07	0.01	0.00-0.21
FeO	12.46	11.58-13.87	11.54	9.48-16.55
MnO	0.82	0.53-1.02	0.16	0.07-0.34
MgO	46.03	44.94-47.08	46.98	42.93-48.78
CaO	0.46	0.13-0.70	0.16	0.02-0.50
NiO	0.09	0.00-0.22	0.31	0.03-0.52
Cr_2O_3	0.01	0.00-0.04	0.05	0.00-0.20

Table III.2.1 - Averages and compositional ranges of olivine (in wt % oxide) from Tapira wehrlites and phlogopite -picrites.

Olivine composition can be described in terms of the end-members forsterite (Mg_2SiO_4) fayalite (Fe_2SiO_4) and tephroite (Mn_2SiO_4). Ca substitution results in the monticellite (CaMgSiO4) - kirschsteinite (CaFeMgSiO4) series, although the pure kirschsteinite end-member does not occur naturally (Deer *et al.* 1992).

The range of olivine compositions in Tapira is relatively narrow, particularly in terms of major elements. The forsterite content of the studied grains varies from 84.2 to 86.9 mol % in the wehrlites, spanning a slightly wider interval (81.6 to 89.8 mol %) in phlogopite-picrites.

The observed forsterite contents in the least evolved phlogopite-picrite olivines are only marginally lower than the range of mantle olivines (89 - 92 mol %; Kostopoulos, 1991), suggesting that these rocks may correspond to primitive magmas. An attempt was made to correlate the composition of olivines from phlogopite-wehrlites with the bulk rock contents of FeO and MgO. Roeder and Emslie (1970) concluded that the partition coefficient Kd, defined as:

$$\boxed{Kd = \frac{(X_{FeO}^{Ol})\,(X_{MgO}^{Liq})}{(X_{FeO}^{Liq})\,(X_{MgO}^{Ol})}}$$

should equal 0.3 for olivine crystallised in equilibrium with basaltic liquid. Figure III.2.1 illustrates the variation of the calculated Kd for the studied phlogopite-picrite samples, assuming that their bulk compositions truly represent the magmatic liquids from which the olivines crystallised.

It can be observed from Figure III.2.1 that more than 80% of the calculated Kds are between 0.25 and 0.35, which suggests that the olivine crystallised in equilibrium with a liquid that is compositionally equivalent to the phlogopite-picrite dykes. The tailing towards higher Kd values in the histogram may be explained by the internal Fe-Mg variation of olivine crystals or, alternatively, by olivine accumulation in some dykes due to flow-differentiation (see Chapters I and II). Although the calculations suggest that the olivine phenocrysts are the product of equilibrium crystallisation, they must be viewed with caution, since the magmatic system in alkaline-carbonatite complexes is substantially different from that of basalts and variables such as oxygen fugacity and phenocryst removal or concentration through flow-differentiation may affect Kd.

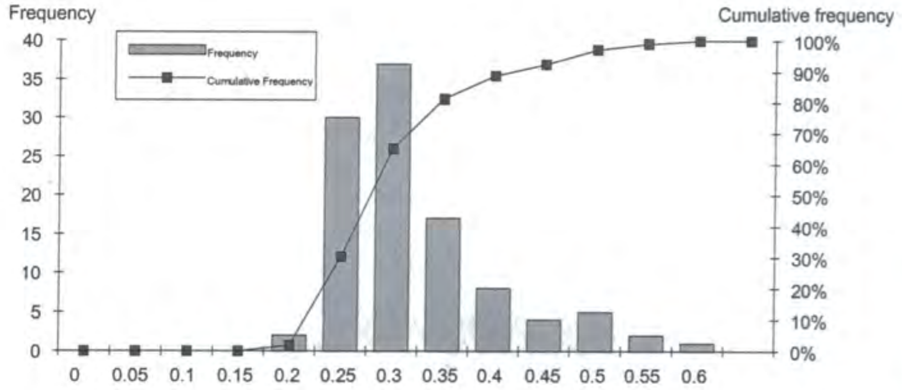

Figure III.2.1 - Histogram and cumulative frequency of calculated Kd Fe-Mg between olivine and the phlogopite-picrite host.

Obviously, wehrlite olivines cannot be interpreted in the same way, since the host rocks are cumulates and therefore do not represent magmatic liquids. However, the high forsterite content of these olivines still suggests that they crystallised in equilibrium with a primitive ultramafic liquid.

CaO, MnO and NiO are always present in noticeable amounts in Tapira olivines. The sum of the corresponding end-member mole fractions can reach up to 2.7 mol % in some individual grains.

MnO correlates negatively with the forsterite content in phlogopite-picrite olivines (Figure III.2.2). This is interpreted as the result of sympathetic behaviour of Fe and Mn. On the other hand, wehrlite olivines have distinctively higher MnO contents, but these are only poorly correlated with the percentage of the forsterite end-member, suggesting that manganese solubility in olivines from the two rock types is controlled by different processes. Also plotted in Figure III.2.2 are three analyses of olivine xenocrysts in carbonatite breccia. Despite the reduced number of analyses, a great variation in forsterite content is observed, suggesting that the xenocrysts originated from different sources (although probably all from within the SPS).

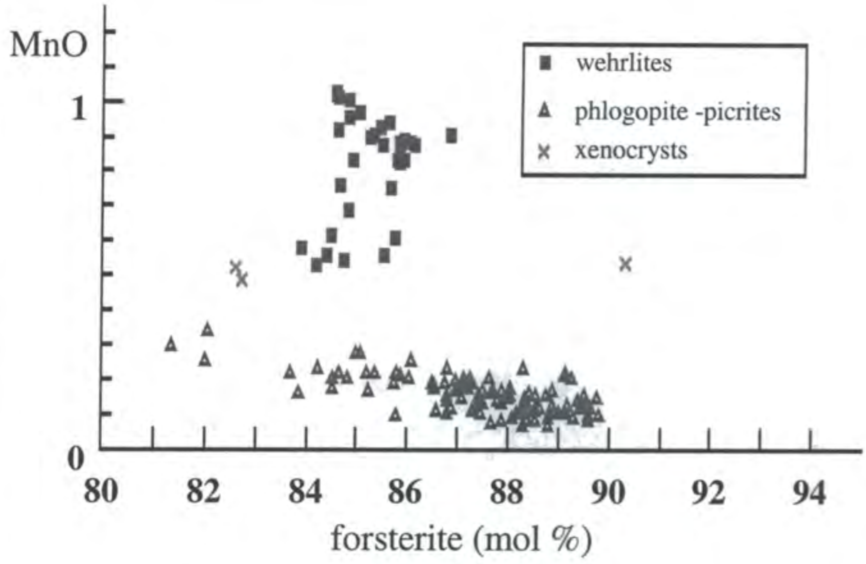

Figure III.2.2 - MnO wt. % variation with forsterite (mol %) in Tapira olivines.

The relatively high CaO content in Tapira olivines (Table III.2.1, Figure III.2.3) may be a result of the interaction of olivine with carbonatite or residual carbonatitic liquid. Experimental work by Brenan and Watson (1991) demonstrated that olivines in equilibrium with carbonatite liquids show an increase in the forsterite component and contained up to 0.5 wt. % CaO. Dalton and Wood (1993a) also reported up to 0.81 wt % CaO in olivine crystallised at 15 kb and 1150 °C, and established a positive correlation between the calcium content of olivine and that of the associated carbonatite liquid. This process is likely to have affected olivine in the phlogopite-picrite dykes, since the abundance of groundmass carbonate indicates that the residual liquid was carbonate-rich and may thus have reacted with olivine to produce the observed CaO-enrichment.

The exceptionally CaO-rich olivines of the wehrlites are, apparently, more difficult to reconcile with this model; there is very little or no interstitial carbonate in these rocks, that could indicate the existence of a carbonate-rich residual liquid. Such liquid could of course have been removed from the system or, alternatively, olivine may have originally crystallised from a relatively carbonate-rich liquid, and then removed from this system as cumulus crystals. In their compilation of analyses of igneous olivines, Simkin and Smith (1970) suggest a strong relation between pressure and the Ca content of olivine, with extrusive and shallow intrusive rocks containing olivine that has distinctively higher Ca than deep-seated plutonic rocks. This may suggest that the Tapira complex was emplaced at shallow depth.

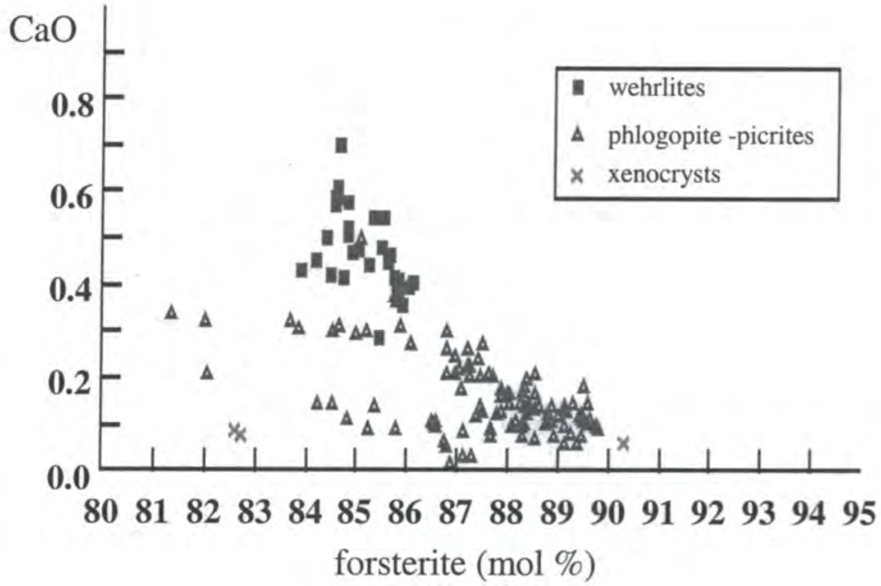

Figure III.2.3 - CaO wt % variation with mole % of forsterite in Tapira olivines

Up to 0.5 wt % NiO may be present in Tapira olivines. Nickel correlates positively with the forsterite content, and is higher in the phlogopite-picrites than in the wehrlites (Figure III.2.4). Such high NiO contents are considered a common feature of olivines crystallised from ultrapotassic magmas (e.g. Davis and Smith, 1993; Mitchell and Bergman, 1991; Mitchell, 1995). The high-Ni contents of the primitive magma may be linked with the substantially depolymerised character of the partial melts in the mantle, promoted by high potassium and volatile contents (Davis and Smith, 1993, and references therein). Highly depolymerised partial melts would tend to incorporate higher amounts of nickel than normal, due to a reduction in the olivine/melt Ni partition coefficient.

In the scenario proposed by Davis and Smith (1993) the crystallisation of phlogopite would substantially remove potassium and volatiles from the magma, increasing its polymerisation and consequently favouring the solubility of Ni in the crystallising olivine. The authors regard the effects of oxidation as a subject of controversy. However, if any, the effect of increasing oxygen fugacity would be to increase the solubility of Ni in olivine. Thus, the crystallisation of the phlogopite-picrites under higher fO_2 than the rocks of the SPS (see discussions later in this Chapter) is compatible with higher Ni contents of olivine in the former.

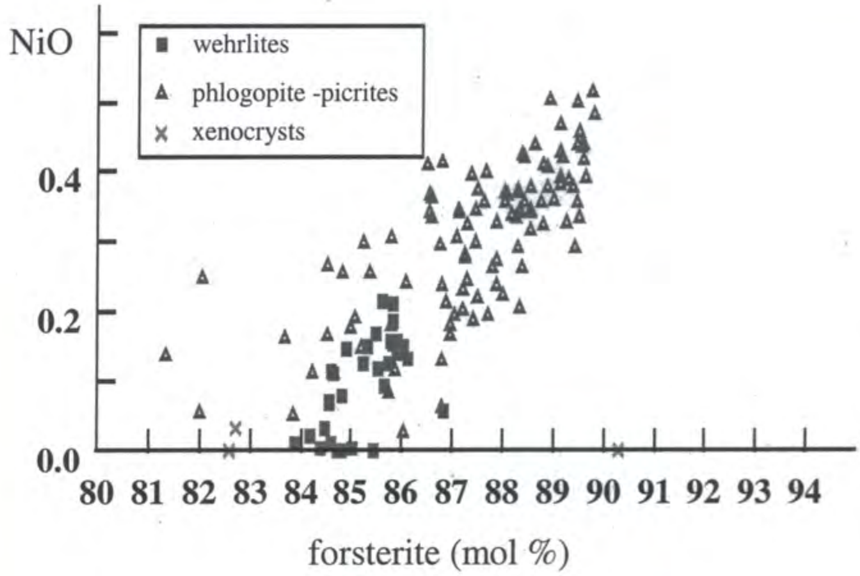

Figure III.2.4 - NiO wt. % variation with forsterite content of Tapira olivines.

On the basis of chemical composition alone, the olivines of phlogopite-picrites may be considered more primitive than those of wehrlites, which appears to preclude a direct link between them by a crystal fractionation process (i.e. wehrlites as the cumulate counterparts of the phlogopite-picrite liquids). The alternative explanations for this may be:

a) Olivine fractionated from the phlogopite-picrites accumulated to form dunites. These dunitic cumulates could be located either in a deeper level of the SPS or in a separate magma chamber, deeper in the crust.

b) Olivines in phlogopite-picrites and wehrlites represent different batches of magma, in a multi-stage process of differentiation and magma chamber replenishment.

c) The higher forsterite content of phlogopite-picrite olivines is a product of Fe-Mg exchange with the liquid (e.g. Brenan and Watson, 1991). Experimental work by Watson (1991) demonstrated that the diffusivity of iron in synthetic dunites (at 10 kb and 900-1300 °C) is far higher in the presence of carbonate melt (in that particular case Na_2CO_3) than in the presence of basaltic melt or H_2O-CO_2 fluids.

In any case, it is likely that the slowly-cooling plutonic rocks would have opportunity to re-equilibrate at low temperature, and olivine is probably more susceptible to compositional changes than pyroxene. Recent studies by McBirney (1998) demonstrated that trace-element contents of individual minerals in coarse-grained mafic rocks are not necessarily related to liquid composition.

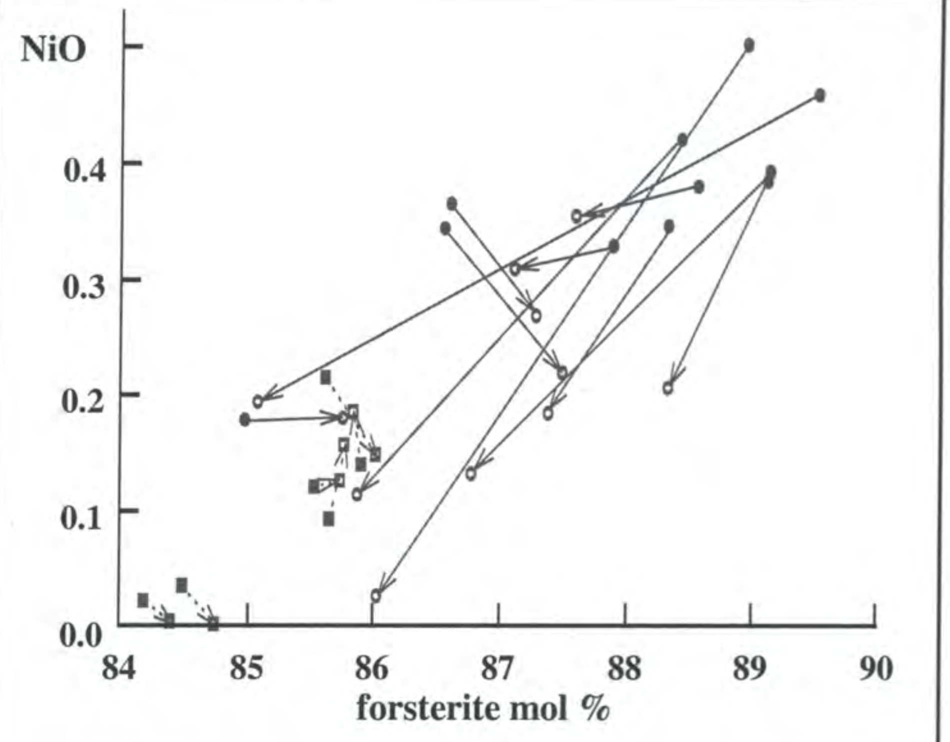

Figure III.2.5 Chemical variation of pairs of core-rim analyses in Tapira olivines. Cores are represented by solid symbols and rims by open symbols. Arrows (solid = phlogopite-picrites, dashed = wehrlites) point to rim composition. Circles = phlogopite-picrite olivines, squares = wehrlite olivines.

III.2.1. ZONING

Most olivine grains show some internal compositional variation, although this does not necessarily reflect magmatic processes. Normal, inverse, and irregular zoning are observed, sometimes in the same thin section, denoting a complex evolution for olivine in the Tapira Complex. The variation of NiO (wt. %) and mol % forsterite in pairs or rim-core analyses is illustrated in Figure III.2.5. Whilst NiO usually decreases from core to rim (except for two of the wehrlite olivine rim-core pairs in Figure III.2.5), the forsterite content may either decrease (normal zoning) or increase (inverse zoning). In most olivines from phlogopite-picrites, NiO correlates positively with the mole fraction of forsterite, which is the expected behaviour in igneous olivines. On the other hand, a small number of olivines in phlogopite-picrites, and most olivines from wehrlites, show a negative correlation between NiO and forsterite, which results from increasing forsterite content towards the rims.

Figure III.2.6 shows two microprobe traverses across olivine grains in a single thin section of phlogopite-picrite (sample at013). Column A represents olivine with normal zoning, whereby MgO, NiO decrease and FeO, CaO increase towards the rim. MnO is highest in the core, decreasing initially and later increasing towards the rim. Column B shows a profile across a relatively larger olivine grain (compare horizontal scales) that is inversely zoned with respect to FeO and MgO, highly variable in MnO and NiO, and normally zoned in terms of CaO. This type of olivine seems to have undergone a more complex evolution, probably involving extensive resorption and/or diffusion processes and may have a xenocrystic origin.

Dalton and Wood (1993b) concluded that the partitioning of Fe and Mg between carbonate and olivine under mantle conditions is a function of the Ca content in carbonate; the higher the concentration of Ca in carbonate the more magnesian the olivine. If their conclusions are applicable at lower crustal pressures, where the Tapira complex is thought to have formed, a similar process could be responsible for the increase in forsterite content of olivine grains, by re-equilibration with the calcite-rich groundmass in the phlogopite-picrite dykes.

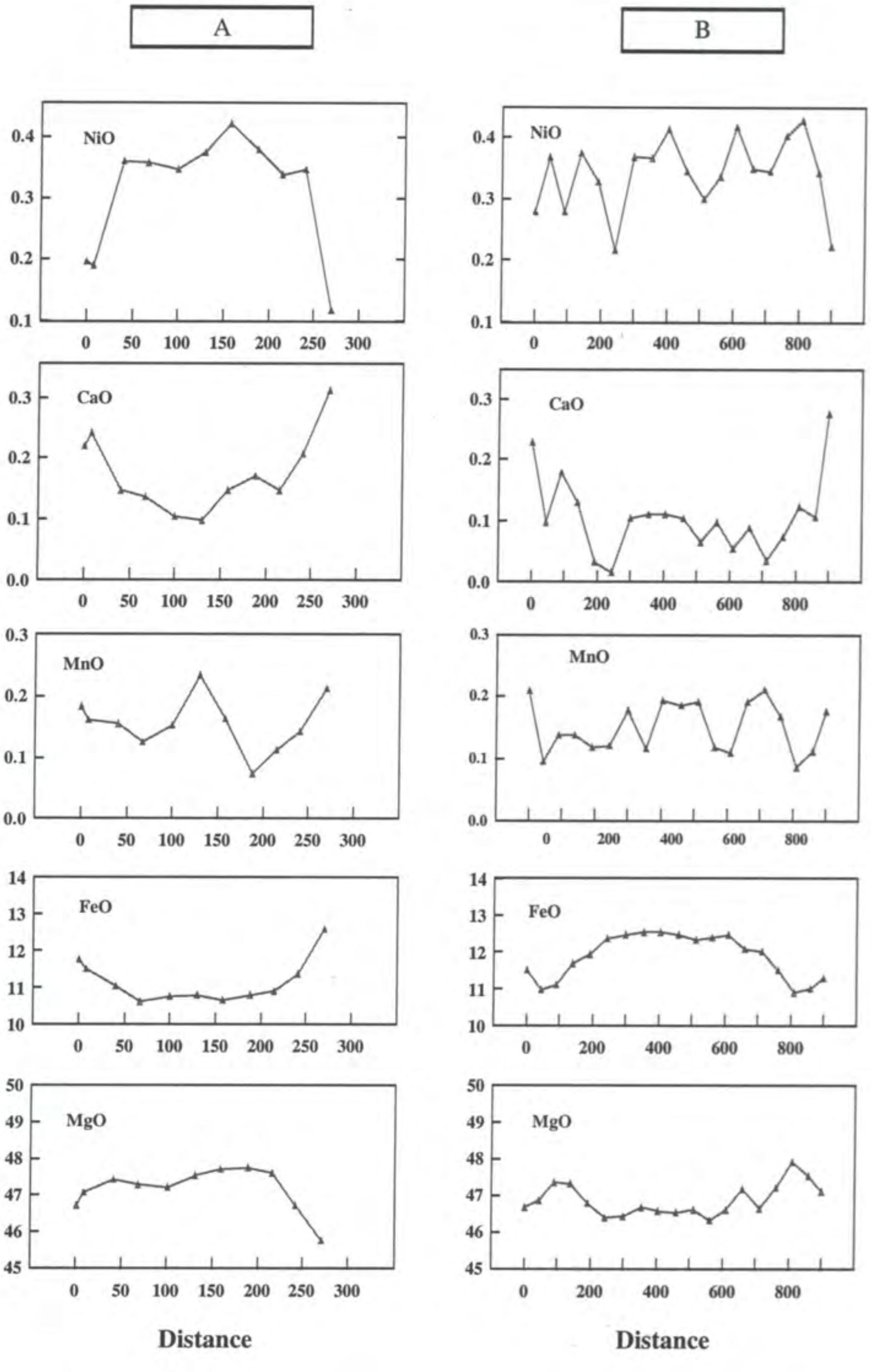

Figure III.2.6 - Microprobe profile in olivine grains from phlogopite-picrite sample at 013. Horizontal scales are in microns. Oxides in wt. %. See text for discussion.

Alternatively, Roeder and Emslie (1970) demonstrated that the Fe/Mg ratio of olivine in basaltic liquids is affected by oxygen fugacity. Higher oxygen fugacity will increase the ferric/ferrous iron ratio of the magma, leaving less ferrous iron available and, consequently, crystallising a more magnesian olivine. Unfortunately, the magmatic system in Tapira is substantially different from a basaltic magma and a direct application of their results to Tapira rocks is not warranted. However, several lines of evidence suggest that the crystallisation history of the Tapira complex was marked by dramatic variations in fO_2 and that at some stages substantial amounts of Fe^{3+} were available in the liquid (see for example section III.4 - Phlogopite). Oxygen fugacity may, therefore, have played an important role in the observed olivine zoning patterns.

Dalton and Lane (1996) pointed out that microprobe analyses of CaO near the borders of olivine grains adjacent to Ca-rich phases may be affected by secondary X-ray fluorescence, over distances of up to 70 microns, resulting in artificially high CaO results. However, the width of the calcium-rich rims of Tapira olivines (up to 200 microns) is difficult to explain by this effect alone, indicating that interaction with the carbonate-rich residual liquid is likely to have taken place.

The compositional ranges observed in Tapira olivines are similar to those reported for ultramafic plutonic rocks from other APIP complexes, such as Salitre I and Salitre II (Mariano and Mitchell, 1991) and Catalão (Araújo, 1996). Some of the observed features, such as relatively high CaO and MnO have been considered (Gaspar *et al.* 1998) as typical of carbonatite olivines.

III.2.2 - SUMMARY

- The composition of Tapira olivines suggests that they crystallised from primitive ultramafic liquids and in the phlogopite-picrites the olivines seem to be compositionally in equilibrium with the host dykes.
- Olivines from wehrlites and phlogopite-picrites show substantial differences in composition. Olivine in the slowly-cooling wehrlites is likely to have had enough time to re-equilibrate at low temperatures. Alternatively, the wehrlites may have formed from a liquid that was somewhat more evolved than the phlogopite-picrites.
- The high NiO content of Tapira olivines is similar to that observed in olivines from other types of ultrapotassic rocks.

III.3 - CLINOPYROXENE

Clinopyroxene has widespread occurrence in the Tapira silicate plutonic series (SPS). It is an essential constituent of bebedourites but is also present in wehrlites and, less often, in syenites. Pyroxene xenocrysts were recognised in sovites of the C3 intrusion (northern margin of the complex) and in carbonatite breccias from the Tapira mine, but this mineral was not found in any of the other carbonatite bodies (C1, C2, C4 and beforsitic C5 dykes). Among the dyke rocks, pyroxene is rare in the phlogopite-picrites and common in the low-Cr dykes. Finally, it may be present as a metasomatic phase in the fenites surrounding the complex.

The classification of pyroxenes adopted in this work is after Morimoto *et al.* (1988). The complete set of microprobe analyses and structural formulae can be found in Appendix 2. The formulae were calculated on the basis of 4 cations and 6 oxygen and the Fe^{3+}/Fe^{2+} ratios were estimated by charge balance. Where relevant, octahedral and tetrahedral positions will be indicated in the text by the superscripts $^{(VI)}$ and $^{(IV)}$, respectively

III.3.1 - COMPOSITIONAL VARIATION OF PYROXENES

The general formula of pyroxenes is $M2M1T_2O_6$ where M2 and M1 designate cations in distorted and regular octahedral co-ordination, respectively, whilst T identifies tetrahedrically co-ordinated cations. A number of cation substitutions are possible in the pyroxene formula, the main occupancy priorities are as follows (Morimoto *et al.,* 1988):

Tetrahedral site (T)	$Si^{4+} > Al^{3+} > Fe^{3+}$
Octahedral site (M1)	$Al^{3+} > Fe^{3+} > Ti^{4+} > Cr^{3+} > V^{3+} > Ti^{3+} > Zr^{4+} > Sc^{3+} > Zn^{2+} > Mg^{2+} > Fe^{2+} > Mn^{2+}$
Octahedral site (M2)	$Mg^{2+} > Fe^{2+} > Mn^{2+} > Li^{+} > Ca^{2+} > Na^{+}$

The two most common types of pyroxene solid solution series occurring in alkaline-carbonatite complexes are the series diopside ($CaMgSi_2O_6$)-hedenbergite ($CaFeSi_2O_6$), and (diopside, hedenbergite)-aegirine ($NaFe^{3+}Si_2O_6$). The former is characterised by the standard Fe-Mg substitution, at relatively constant Ca, whereas the latter is defined by Fe^{3+} and Na enrichment.

Tetrahedral deficiency occurs when the sum of Si and $^{(IV)}Al$ is less than 2 (on the basis of 4 cations and 6 oxygen) and must be compensated for by the allocation of adequate amounts of alternative cations to tetrahedral positions. $^{(IV)}Fe^{3+}$ (Morimoto *et al.,* 1988) and $^{(IV)}Ti^{4+}$ (Cundari and Salviulo, 1989; Carborin and Princivalle, 1996) have been suggested as possible alternatives.

The presence of titanium in pyroxenes is controlled by substitutions such as $^{(VI)}Ti^{(IV)}Al_2$-$MgSi_2$, or $^{(IV)}Ti^{4+}$-Si. Based on a study of natural diopsides from New South Wales leucitites, Cundari and Salviulo (1989) noted that Ti and Al solubility in pyroxene increases, but the $^{(IV)}Ti^{4+}/^{(IV)}Al$ ratio decreases with progressive differentiation. They suggest that Ti enters the tetrahedral site preferentially at higher temperatures whereas octahedral Ti is the preferred form at lower temperatures. They also conclude that increasing fO_2 favours the partition of Ti to pyroxene instead of Fe-Ti oxides. TiO_2-enrichment in evolved (sodic) pyroxenes has been described in ultrapotassic rocks (Sgarbi and Valença, 1994), nepheline-syenites (Nielsen, 1979), fenites and hydrothermal veins (Ranlov and Dymek, 1991). Gaspar (1989) reported up to 14 wt. % TiO_2 in pyroxene from fenites in the Jacupiranga carbonatite complex. Finally, a peculiar variety of aegirine containing up to 7 wt. % ZrO_2 has been described by Jones and Pecket (1980) in nepheline syenites from Motzfeldt (South Greenland).

During the early stages of differentiation of alkaline magmas, diopsidic pyroxene evolves along a path of progressive enrichment in the hedenbergite end-member. At a later stage, this is often followed by Fe^{3+}- and Na-enrichment, which drives the pyroxene composition away from diopside-hedenbergite series and towards the aegirine end member. The moment at which aegirine enrichment becomes significant varies substantially between different localities and types of alkaline magmatism (e.g. Platt, 1996b; Mitchell and Vladykin, 1996). In some cases the onset of aegirine enrichment does not occur until the pyroxene reaches a composition of nearly pure hedenbergite (e.g. Ilimaussaq, Larsen, 1976). At the other extreme, pyroxenes from the ultrapotassic complex of Little Murun, Russia (Mitchell and Vladykin, 1996) form a complete series of solid solutions from diopside to aegirine, at constantly low (< 15 mol %) hedenbergite.

The diopside-hedenbergite section of the trend is generally regarded as a product of magmatic evolution but the interpretation of aegirine enrichment is somewhat controversial. Morbidelli *et al.* (1995b) found that Fe- and Na- enrichment in pyroxene correlates with fractionation in Brazilian alkaline and alkaline-carbonatite districts, although they emphasise the lack of aegirine-rich pyroxene in areas where the most evolved rocks are of sodic composition or have agpaitic index < 1.1 (Tunas and Juquiá complexes, respectively). On the other hand, Gaspar (1989) interpreted the Na and Fe enrichment in Jacupiranga as a result of post-magmatic processes. The same interpretation is favoured by Araújo (1996) for the complex of Catalão.

According to Barker (1996) carbonatite clinopyroxenes typically vary from $CaMgSi_2O_6$ to $NaFeSi_2O_6$ but, similarly to phlogopite and olivine, they often show textural evidence of disequilibrium with the carbonatite liquids, suggesting a xenocrystic origin.

III.3.2 - TAPIRA CLINOPYROXENES

Most pyroxenes in Tapira have some amount of tetrahedral deficiency (i.e. Si + $^{(IV)}$Al < 2). Figure III.3.1 shows that there is a poor correlation between Si and $^{(IV)}$Al, especially below Si ≈ 1.95 p.f.u., when the trend clearly departs from the 1:1 substitution line. As Al is very low (always less than 0.1 p.f.u.), the addition of some other cation is required, in order to fill the tetrahedral site to the stoichiometric value of 2. Ti^{4+} + $^{(IV)}$Al correlate reasonably well with Si, varying along the 1:1 substitution line. Fe^{3+} + $^{(IV)}$Al also show some degree of negative correlation with Si, although most of the trend does not fit the substitution line. It must be stressed, however, that the Δ Fe^{3+} parameter plotted in Figure III.3.1 is calculated as Fe^{3+} - Na, assuming an ideal compensation of octahedral Fe^{3+} by Na in the aegirine molecule. The values are also subjected to uncertainties in the estimation of the Fe^{3+}/Fe^{2+} ratio. In any case, the good negative correlation between $^{(IV)}$Al+Ti and Si suggests that the substitution of $^{(IV)}Ti^{4+}$ for Si, as proposed by Cundari and Salviulo (1989), plays a significant role. According to

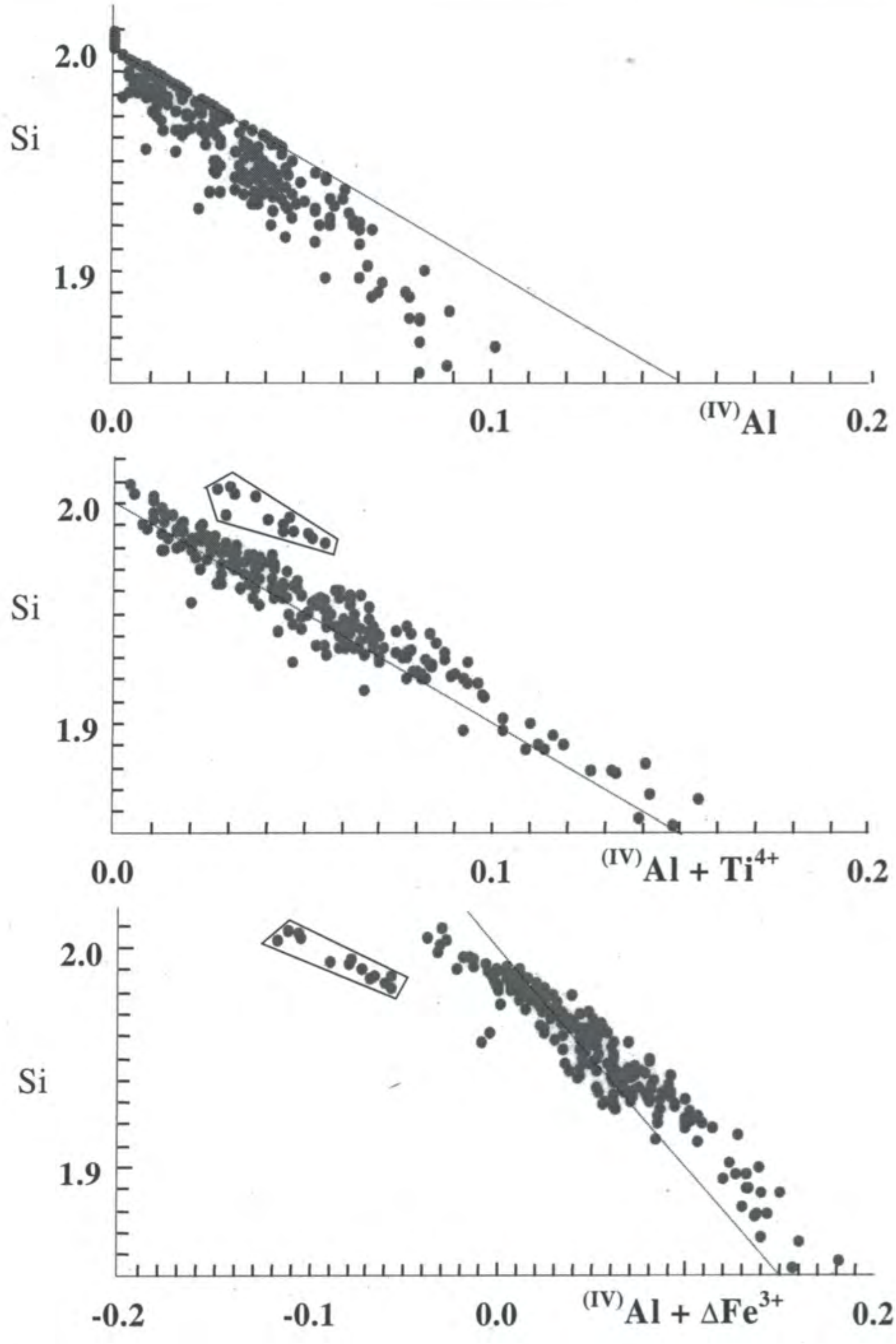

Figure III.3.1 - Si, $^{(IV)}$Al, Ti and ΔFe^{3+} (= Fe^{3+} - Na) variation in Tapira pyroxenes, in atoms per formula unit (p.f.u.). Note that $^{(IV)}$Al is poorly correlated with Si. The sum of $^{(IV)}$Al and Si is not enough to fill the tetrahedral deficiency in most cases. The sum of $^{(IV)}$Al and Ti shows the best correlation with Si. Dashed lines represent 1:1 substitutions. Solid-line polygon encloses analyses of fenite pyroxenes.

Carborin and Princivalle (1996), $^{(IV)}Ti^{4+}$ is a typical feature of pyroxenes from potassic alkaline rocks.

Some analyses form a separate group, detached from the main trend in Figure III.3.1. These comprise metasomatic pyroxene in fenites, and they are characterised by virtually no tetrahedral deficiency. In fact, some of these analyses show Si in excess of 2 p.f.u.

	Wehrlite (B1)	Bebedourite (B1)	Bebedourite (B2)	Carbonatite (C3)	Low-Cr Dyke	Syenite	Fenite
SiO_2	54.50	52.42	53.66	51.08	51.32	51.19	53.91
TiO_2	0.43	1.04	0.40	0.85	0.85	0.20	0.95
Al_2O_3	0.46	0.85	0.59	1.03	1.30	0.55	0.82
FeO	0.93	1.59	4.01	2.92	5.88	7.29	4.12
Fe_2O_3	1.47	2.62	2.64	3.38	5.65	13.69	13.47
Cr_2O_3	0.07	0.06	0.15	0.09	0.14	0.08	0.13
MnO	0.10	0.12	0.27	0.17	0.32	0.54	0.40
NiO	bd	bd	0.08	0.04	0.04	bd	bd
MgO	17.10	15.93	14.45	14.19	11.45	5.60	7.62
CaO	25.24	24.64	23.84	23.67	22.32	14.56	12.64
Na_2O	0.37	0.42	0.84	0.66	1.49	5.37	6.69
K_2O	bd	bd	bd	0.02	bd	bd	bd
Total	100.67	99.69	100.92	98.11	100.75	99.06	100.73
Tetrahedral cations							
Si	1.970	1.931	1.967	1.928	1.920	1.983	2.006
Al	0.020	0.037	0.026	0.046	0.057	0.017	
Sum T	1.990	1.968	1.993	1.974	1.977	2.000	2.006
Octahedral cations							
Al						0.008	0.036
Ti	0.012	0.029	0.011	0.024	0.024	0.006	0.027
Fe^{3+}	0.040	0.073	0.073	0.096	0.159	0.399	0.377
Fe^{2+}	0.028	0.049	0.123	0.092	0.184	0.236	0.128
Mg	0.922	0.874	0.790	0.798	0.638	0.323	0.423
Mn	0.003	0.004	0.008	0.005	0.010	0.018	0.012
Cr	0.002	0.002	0.004	0.003	0.004	0.003	0.004
Ni			0.002	0.001	0.001		
Ca	0.978	0.972	0.936	0.957	0.895	0.604	0.504
Na	0.026	0.030	0.059	0.048	0.108	0.404	0.483
K				0.001			
Sum M	2.011	2.033	2.006	2.025	2.023	2.001	1.994

Table III.3.1 - Representative analyses of clinopyroxenes from Tapira. (bd = below detection). Formulas calculated on the basis of 6 oxygens. Fe_2O_3 *calculated by charge balance.*

Representative analyses of pyroxene in each rock type are given in Table III.3.1. Figures III.3.2 to III.3.4 provide the framework for the classification of clinopyroxenes according to Morimoto *et al.* (1988).

Figure III.3.2 shows the general group to which the pyroxene belongs (i.e. Ca-Mg-Fe "quadrilateral" pyroxene, Ca-Na pyroxene, Na-pyroxene or "other"). The parameters "Q" and "J" used in Figure III.3.2 are defined as $Q = Ca + Mg + Fe^{2+}$ and $J = 2Na$ (Morimoto *et al.*, 1988). SPS pyroxenes are not discriminated by rock-type in the Figure, but cluster in two separate groups. Those from ultramafic rocks plot in the Ca-Mg-Fe ("Quad") pyroxene field and must be more accurately classified with the use of the diagram in Figure III.3.3. Pyroxenes from syenites and fenites plot in the Ca-Na pyroxene field, and are further classified in Figure III.3.4. Pyroxenes from phlogopite-picrites are similar in composition to those of the ultramafic rocks of the SPS, but analyses of pyroxene from low-Cr dykes span a wider variation range, gradating towards the Ca-Na pyroxene field. Analyses of fenite pyroxenes plot above the Q+J = 2 line, which is a relatively uncommon feature in pyroxenes (Morimoto *et al.*, 1988). Note that there is a substantial composition gap between the clusters of analyses in the Ca-Mg-Fe

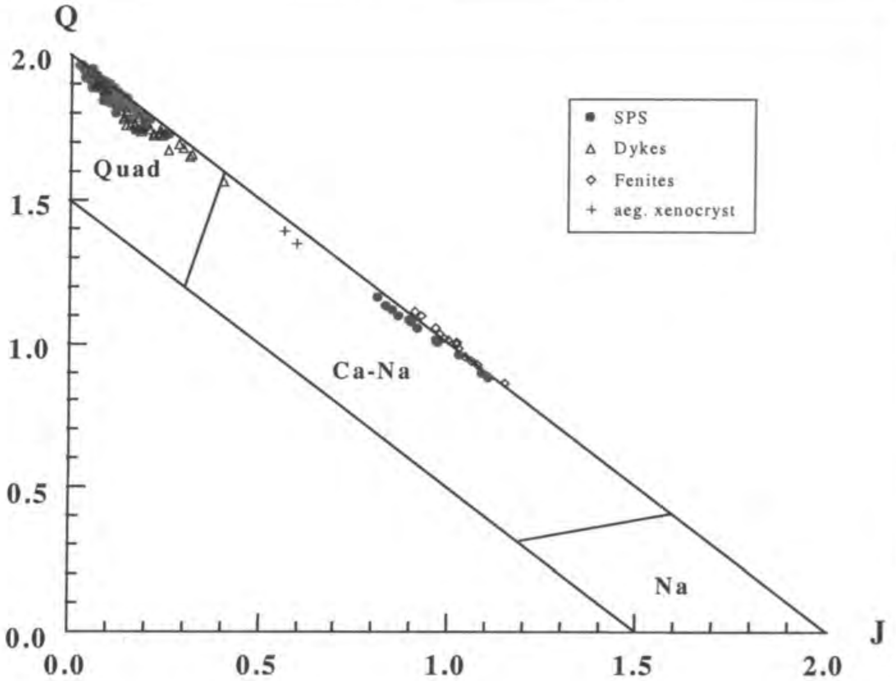

Figure III.3.2 - Q-J diagram for the classification of pyroxenes (after Morimoto *et al.*, 1988).

(quad) and Ca-Na fields, the only exception being the few analyses of a xenocrystic aegirine-augite, which plot half-way between the two groups.

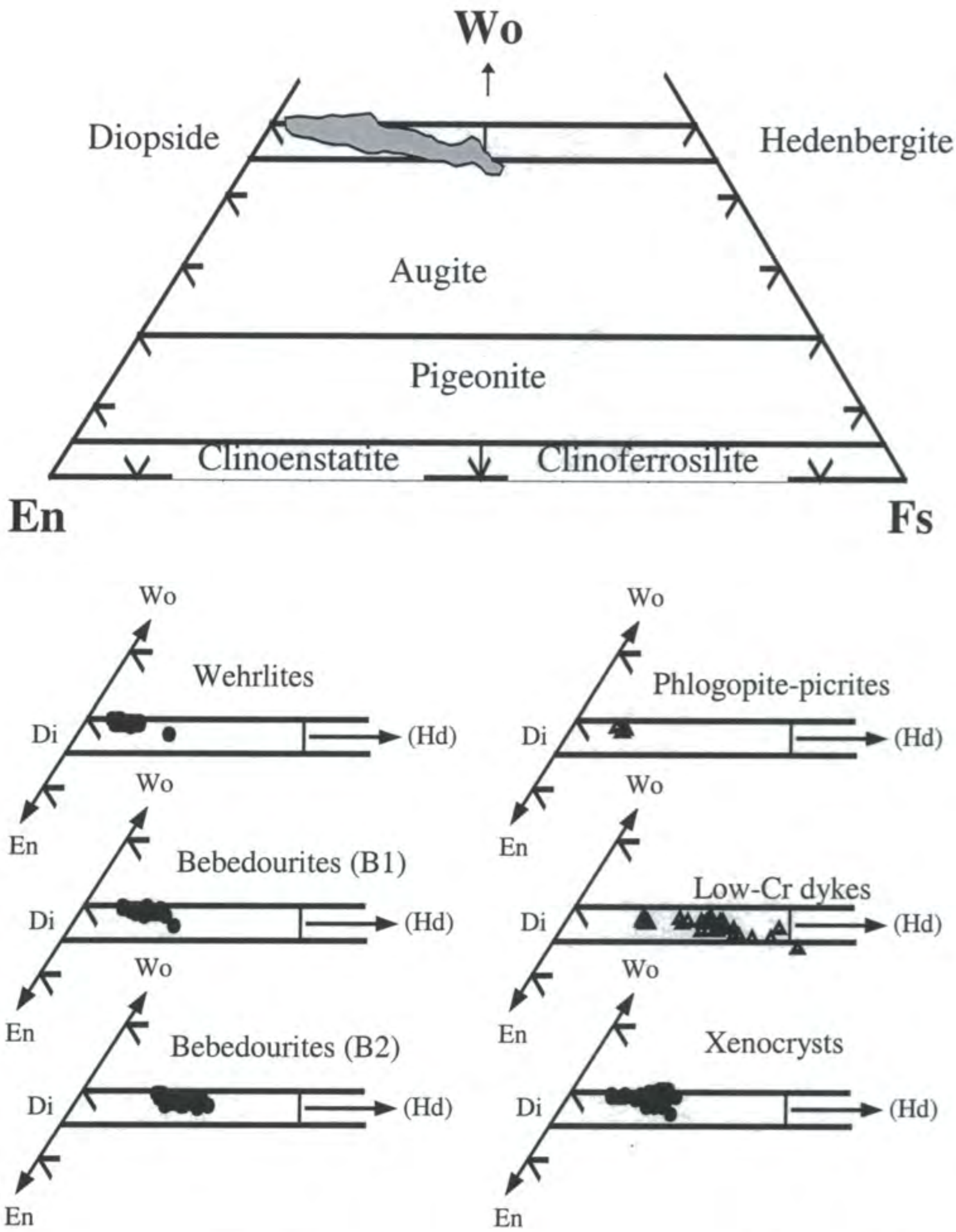

Figure III.3.3 - Classification of Tapira pyroxenes in the pyroxene "quadrilateral" (after Morimoto et al., 1988). Only the "quad" pyroxenes from Figure III.3.2 are shown. Note the progressive evolution from diopside towards hedenbergite enrichment in the SPS ultramafic rocks (from wehrlites to bebedourites) and the more evolved character of pyroxene in the low-Cr dykes. Shaded field in the top diagram includes all Ca-Fe-Mg pyroxenes from the complex.

Figure III.3.3 shows the classification of pyroxene in terms of the wollastonite, enstatite and ferrosilite end members. The least evolved pyroxenes in SPS occur in wehrlites and plot close to the ideal diopside end-member composition. Pyroxenes from B1 and B2 bebedourites show progressively higher contents of the hedenbergite end-member. Although mostly restricted to the diopside field, the pyroxenes from low-Cr dykes show the highest hedenbergite component amongst the Ca-Fe-Mg pyroxenes in Tapira. Xenocrystic pyroxenes in C3 carbonatites are closest in composition to those of bebedourites (B2)

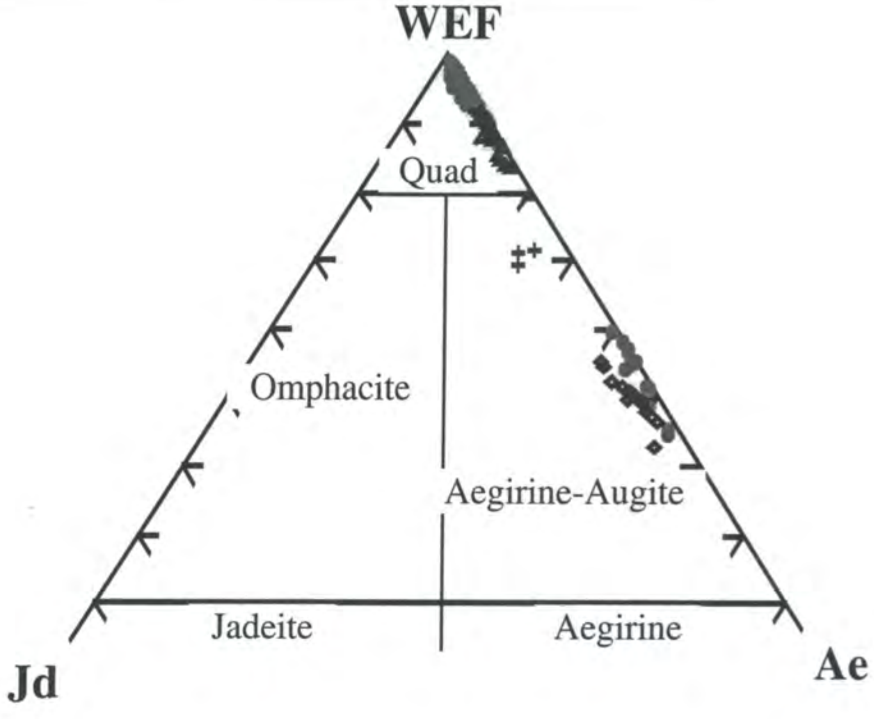

Figure III.3.4 - Classification of Na-Ca pyroxenes from Tapira (after Morimoto et al., 1988). For classification of the "Quad" pyroxenes see Figure III.3.3. Symbols as in Figure III.3.2.

Figure III.3.4 shows the classification of Ca-Na pyroxenes. All Ca-Na pyroxenes from Figure III.3.2 plot in the field of aegirine-augite, reaching a maximum of 53 mol % of the aegirine molecule. This variety of pyroxene is typical of the Tapira syenites and fenites. In the majority of Tapira pyroxenes the jadeite component is virtually non-existent, reflecting the very low Al contents.

Silicate plutonic series (SPS)

Although individual grains show little zoning, a progressive chemical variation is observed in pyroxene within the SPS. Average pyroxene compositions by rock type are shown in Figure III.3.5. Note that, although the main rock groups of SPS are ordered in a progressive differentiation sequence, the vertical scales of the diagrams are arbitrary. For instance, the syenites should ideally be separated from the B1 bebedourites by a distance much greater than that between B1 and B2, if a proportional scale was to be used. The evolution of the ultramafic rocks is reflected in clinopyroxene composition by decreasing SiO_2, MgO, CaO, and increasing FeO, MnO, Na_2O. Average TiO_2 and Al_2O_3 compositions (not included in Figure III.3.5) are slightly lower in the syenites than in wehrlites and bebedourites, but do not show significant variation within the ultramafic rocks. Other oxides such as Cr_2O_3 and NiO are very low and do not appear to vary significantly with differentiation. Cr_2O_3 is always lower than 0.2 wt. %, whilst NiO rarely exceeds 0.1 wt. % and is often below the microprobe detection limit.

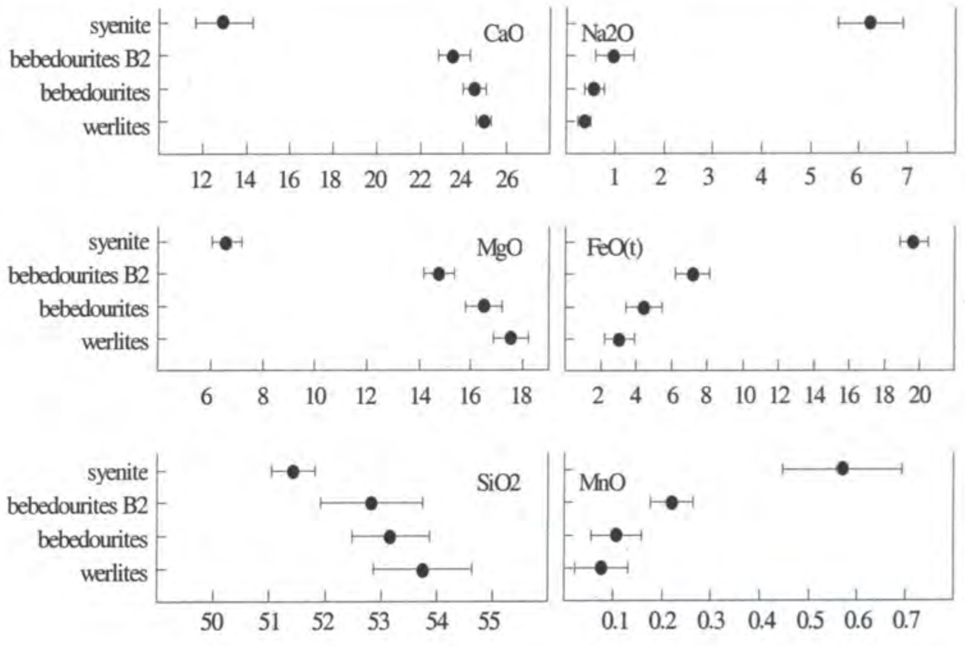

Figure III.3.5 - Average (solid circles) composition, by rock type, of SPS pyroxenes. The error bars represent ± one standard deviation. All displayed elements show a progressive variation that is consistent with magmatic differentiation, although the extreme composition of syenite pyroxenes suggests that part of the fractionation sequence is missing. Horizontal scales are wt.% oxide. FeO(t) = total iron calculated as FeO. Vertical scales are arbitrary.

Despite the arbitrary nature of the vertical scales in Figure III.3.5, a compositional gap between the pyroxenes from ultramafic rocks and syenites is evident for all elements except SiO_2. This feature results from the lack of intermediate differentiates between the two groups. In fact, neither feldspar-bearing mafic rocks nor mesocratic syenites were found during the present research. It must be stressed, however, that most of the sampling in Tapira was restricted to within the few metres reached by drilling beneath the weathered cover. Samples above this level are too weathered for chemical studies, and the portions below are obviously unreachable. Thus, intermediate rocks may be present but not be readily accessible.

Alternatively, if the Tapira complex is the product of a series of multiple injections of magma and/or crystal mush (as indicated by the field and drill-core evidence, see Chapter I), rather than a layered sequence of cumulates, it is most likely that the missing terms in the sequence were emplaced at different depths. Some of the pyroxene xenocrysts in carbonatite breccias have optical and chemical properties that are intermediate between those of the bebedourites and syenites, strongly supporting the concept that the intermediate rocks did form but the intrusions did not reach the same levels as other SPS rocks.

Figure III.3.6 illustrates the variation of SPS pyroxenes in terms of Ti and Al. Although the concentration of both elements is very low in Tapira clinopyroxenes, there seems to be a sympathetic variation between them in the SPS. The Al/Ti ratio of most pyroxenes varies between 1:1 and 3:1, apparently increasing with differentiation. Thus, pyroxenes of wehrlites and B1 bebedourites are mostly contained in the envelope defined by the Al/Ti ratios of 1:1 and 2:1, whereas B2 bebedourites and syenites seem to fit better with a 2:1 or slightly higher ratio.

According to Cundari and Salviulo (1989), the Ti solution in pyroxenes plotting above the 2:1 line in Figure III.3.6 (in this case most of wehrlites and B1 bebedourites) does not involve the $CaTiAl_2O_6$ component and, consequently, is likely to result from Si-Ti tetrahedral substitution. They argue that this type of substitution is favoured at higher temperature, Al being the preferred tetrahedral substitute at lower temperature. This is in good agreement with the lower Al/Ti ratio observed in pyroxenes of the least evolved Tapira rocks. The aegirine-augite xenocryst from the carbonatite breccia (which otherwise has a composition intermediate between bebedouritic and syenitic pyroxenes) plots along a much higher Al/Ti ratio (10:1) in Figure III.3.6. As this xenocryst is compositionally less evolved than syenitic pyroxenes, in terms of major element constituents, it seems unlikely that the high Al/Ti ratio should result from differentiation. Instead, its higher Al content (at roughly the same Ti as the syenitic pyroxene) may be related to crystallisation under higher pressure.

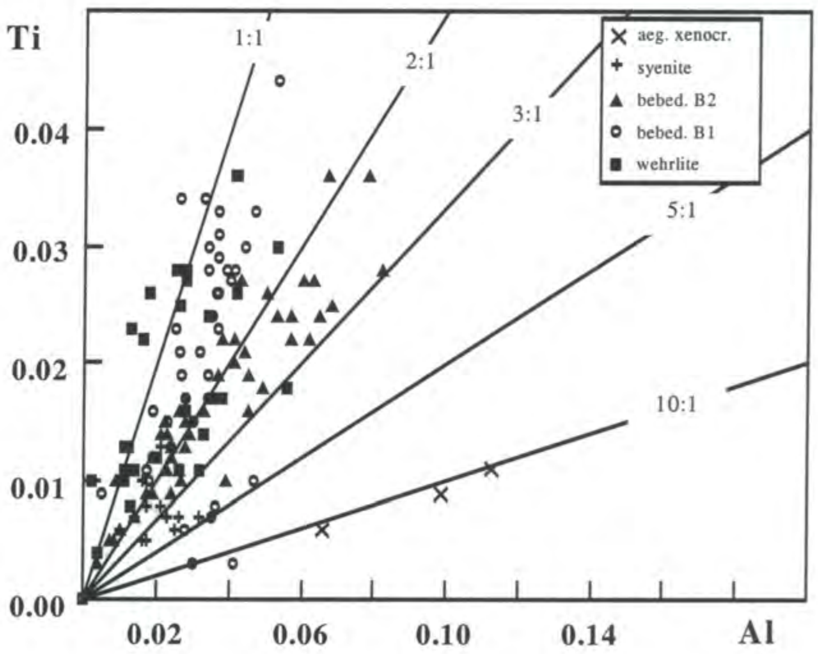

Figure III.3.6 - Ti and Al (p.f.u.) variation of SPS pyroxenes. Most analyses plot in the envelope defined by Al:Ti ratios of 1:1 and 3:1. Analyses of a aegirine-augite xenocryst in carbonatite breccia are plotted for comparison. These have Ti similar to the syenites, but much higher Al (Al:Ti = 10:1), suggesting that they were formed at higher pressure.

Dykes

Figure III.3.7 illustrates the composition of pyroxene in the dykes, compared with those in the plutonic rocks of the SPS. Pyroxenes in phlogopite-picrites and low-Cr dykes are chemically similar to those in wehrlites and bebedourites, respectively. Moreover, in the low-Cr dykes they reach significantly higher hedenbergite and aegirine contents than their bebedouritic equivalents. This suggests that wehrlites and bebedourites are possible cumulate counterparts of the dykes. Furthermore, the presence of more evolved pyroxene in the low-Cr dykes suggest that these rocks may be products of fractionation of the phlogopite-picrites.

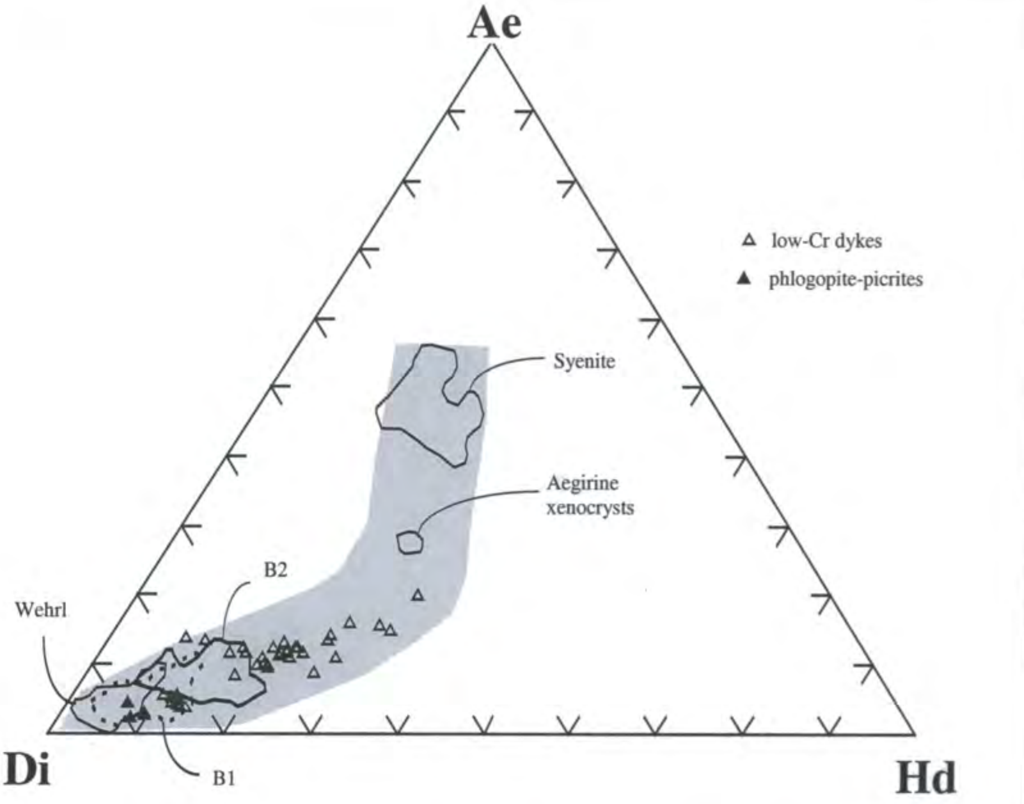

Figure III.3.7 Composition of pyroxene in Tapira dykes in terms of Diopside (Di), Hedenbergite (Hd) and Aegirine (Ae) components. Fields of SPS pyroxenes and aegirine xenocrysts are indicated for comparison. The shaded area depicts the probable evolutionary trend of Tapira pyroxenes.

The combined variation of clinopyroxene in the SPS and in the dykes suggests an evolutionary trend as depicted by the shaded area in Figure III.3.7. This starts with nearly pure diopside and progresses towards hedenbergite, with moderate aegirine enrichment. During this stage, the Hd/Ae ratio remains roughly constant at 2:1. At approximately $Di_{55}Hd_{30}Ae_{15}$, the trend is suddenly diverted towards aegirine enrichment, at nearly constant Di/Hd (≈ 3:2).

Carbonatites

Carbonatites of the C3 intrusion (northern margin of the complex) and carbonatitic breccias occurring in the mining area may contain xenocrysts of clinopyroxene. These are normally rounded or show textural evidence of disequilibrium (see Chapter II), indicating their xenocrystic character. In carbonatitic breccias, the occurrence of pyroxenes of contrasting composition, within the same thin section, supports this interpretation. The composition of carbonatite pyroxenes is compared with those in other rocks in Figure III.3.8

Pyroxenes included in C3 carbonatites are chemically unevolved and similar in composition to those of the ultramafic rocks of the SPS, which is difficult to reconcile with the generally accepted notion that carbonatites are some of the latest manifestations of the alkaline magmatism. In particular, they are similar to pyroxenes from B2 bebedourites, with which C3 carbonatites are spatially associated. This geographical association and the chemical data strongly suggest that carbonatite pyroxenes in Tapira were originally crystallised from an ultramafic silicate liquid, and only later incorporated into the carbonatite magma through assimilation of B2 bebedourites (or equivalent semi-consolidated cumulates).

Furthermore, as shown by Figure III.3.8, the xenocrysts in carbonatitic breccias cluster in two widely separate groups. One group comprises rare, evolved, dark-green pyroxene similar to those in the syenites, whilst the other group is more abundant, unevolved, light-green, similar to clinopyroxene in the wehrlites. The latter probably consist of crystals assimilated from SPS wehrlites during emplacement of the breccias. The former were discussed in previous sections and probably originate from relatively less-differentiated syenites that did not reach the same crustal level of the complex.

Clinopyroxene was not found in any of the other carbonatite occurrences (C1, C2, C4 and beforsitic C5 dykes).

Fenites

Pyroxenes in fenites form a distinctive compositional group and are compared with the magmatic pyroxenes in Figure III.3.8. Similarly to syenite pyroxenes, they are aegirine-augites (Figure III.3.4), but can be distinguished from the former by their higher Si, Ti and Al (Table III.3.1), lower Hd/Di ratio (Figure III.3.8) and textural properties (Chapter II).

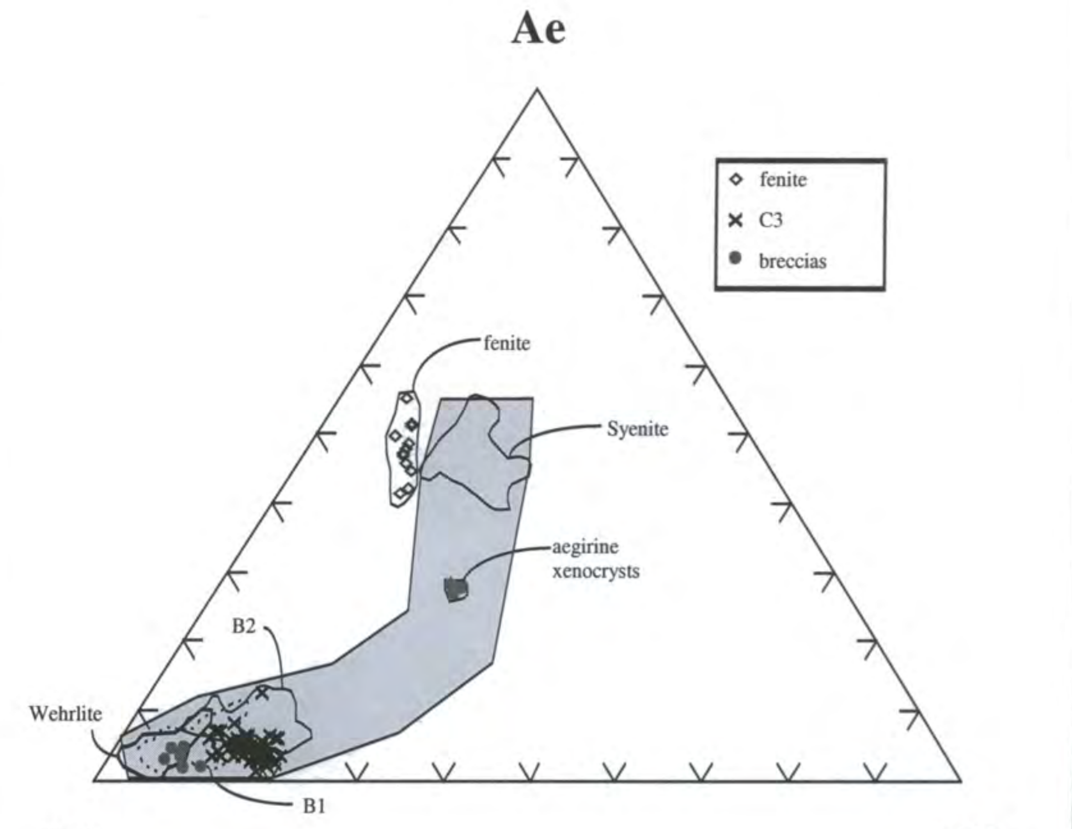

Figure III.3.8 - Composition of pyroxene from fenites and xenocrysts from carbonatitic rock, compared with the main SPS rock types. Shaded area is the probable pyroxene trend for Tapira magmas.

III.3.3 - COMPARISON WITH OTHER ROCK-TYPES

Mitchell and Bergman (1991) and Mitchell (1995b) reviewed the composition of clinopyroxenes in different types of alkaline rocks. The main characteristics of each type can be summarised as follows:

- Pyroxene in orangeites is rarely zoned and shows little variation between different localities. It usually has $^{(IV)}$Al-deficiency, leading to $^{(IV)}Fe^{3+}$ substitution, and follows an evolution trend from Fe-Al-Cr-poor diopside towards late-stage Ti-aegirine. Most orangeite pyroxenes do not show appreciable enrichment in the hedenbergite molecule with evolution.

- Lamproite pyroxenes are typically Al- and Na-poor diopside. They are similar to those in orangeites, but do not show the late-stage Ti-enrichment observed in the former.
- Pyroxenes from minettes and ultramafic lamprophyres are Al-rich, with the latter being also enriched in Ti.
- Pyroxenes from melilitites are typically diopsides with high TiO_2 (1-5 wt %), high Al_2O_3 (1-10 wt %) and very low Na_2O (< 1 wt %). They vary within the solid solution series diopside - $CaTiAl_2O_6$ - $CaAl(Al,Si)_2O_6$ (Mitchell, 1996b).
- Kamafugitic pyroxenes are considerably richer in TiO_2 and Al_2O_3 than those of orangeites and lamproites. However, the APIP kamafugites (Mata da Corda) differ from kamafugites elsewhere, in that their pyroxenes are remarkably Al-poor. According to Sgarbi and Valença (1994), these vary from diopside to Al-poor (always < 0.5 wt.% Al_2O_3), Ti-rich (2.7 - 8.43 wt.% TiO_2) aegirine-augite.

Pyroxenes of plutonic alkaline complexes have also been the subject of recent studies and reviews:

- According to Platt (1996b), in agpaitic nepheline-syenites the clinopyroxene initially evolves from diopside towards hedenbergite, becoming enriched in the aegirine molecule during the later stages. The onset of aegirine enrichment from a diopside-aegirine trend depends on the combined effects of temperature, oxygen fugacity and liquid composition, whilst silica activity does not seem to play a significant role.
- Pyroxenes from plutonic rocks of the ijolite series, commonly associated with carbonatite, follow evolutionary trends similar to those of the nepheline syenite complexes, albeit with less extreme hedenbergite enrichment (Platt, 1996a).
- In ultrapotassic plutonic complexes, pyroxene does not show the same strong hedenbergite-enrichment that is observed in their sodic equivalents. An extreme example is described by Mitchell and Vladykin (1996) in the Little Murun complex (Russia), where pyroxene evolves directly from diopside to aegirine, the complete solid solution having formed at very low (< 15 mol %) hedenbergite. However, they consider Little Murun as an unique example, since other potassic complexes in the region show moderate hedenbergite enrichment.

Clinopyroxene compositions from the APIP complexes are still scarce, except for the Catalão complex, which was studied in detail by Araújo (1996). The range of major-element variation in pyroxenes from Catalão is essentially the same as in Tapira, but aegirine-augite is interpreted as a product of non-magmatic processes. Similarly to Tapira, pyroxenes from Catalão are Ti- and Al-poor, the maximum figures reported by Araújo (1996) being 1.54 wt % TiO_2 and 1.18 Al_2O_3. Mariano and Mitchell (1991) describe diopside from pyroxenites of the Salitre I and II complexes, with end-member proportions similar to to those from Tapira and Morbidelli *et al.* (1995a) reported low Al_2O_3 (< 1 wt.%) and TiO_2 (< 3 wt.%) in pyroxenes from the Salitre I and Salitre II complexes. Unfortunately neither provide complete analyses of Salitre pyroxenes.

High-Zr aegirines, such as those described by Jones and Pecket (1980) were not found in Tapira. Those authors suggest that the factors controlling the formation of high-Zr aegirine are high peralkalinity, low CaO, low fO_2 (below the QFM buffer) and the absence of other Zr-bearing phases. In Tapira such conditions are not fulfilled, since the magmas are Ca-rich and the aegirine-bearing syenites contain accessory zircon.

Figure III.3.9 compares Tapira pyroxenes with those from various alkaline complexes, in terms of the diopside-hedenbergite-aegirine end-members. Tapira pyroxenes do not show the extreme hedenbergite enrichment of some sodic complexes, such as Ilimaussaq, but also do not fit with the Hd-poor of the ultrapotassic complex of Little Murun. The moderate Hd enrichment in Tapira pyroxenes approximates the trends in those of Uganda, Itapirapuã (Brazil) and the ultrapotassic complex of Sakun (Aldan Shield), although the former two reach higher levels of aegirine enrichment. The Tapira trend is compatible with the overall variation of pyroxenes from Brazilian alkaline rocks, envisaged by Gomes *et al.* (1996b) (not shown in Figure III.3.9).

Figure III.3.10 compares Ti and Al contents of Tapira pyroxenes with those in different types of alkaline rocks. The abundance of both elements in Tapira pyroxenes is very low, similar to those of orangeites and lamproites. Both Al and Ti are substantially lower than in pyroxenes of kamafugites (other than APIP). The Al/Ti ratio is slightly lower than in kamafugite pyroxenes and significantly lower than in pyroxenes of the Roman Province-type rocks and potassic alkaline rocks from Paraguay. The Al content of Tapira pyroxenes is comparable with those from APIP kamafugites (Mata da Corda Formation), but they do not reach the same high levels of Ti-enrichment as the latter.

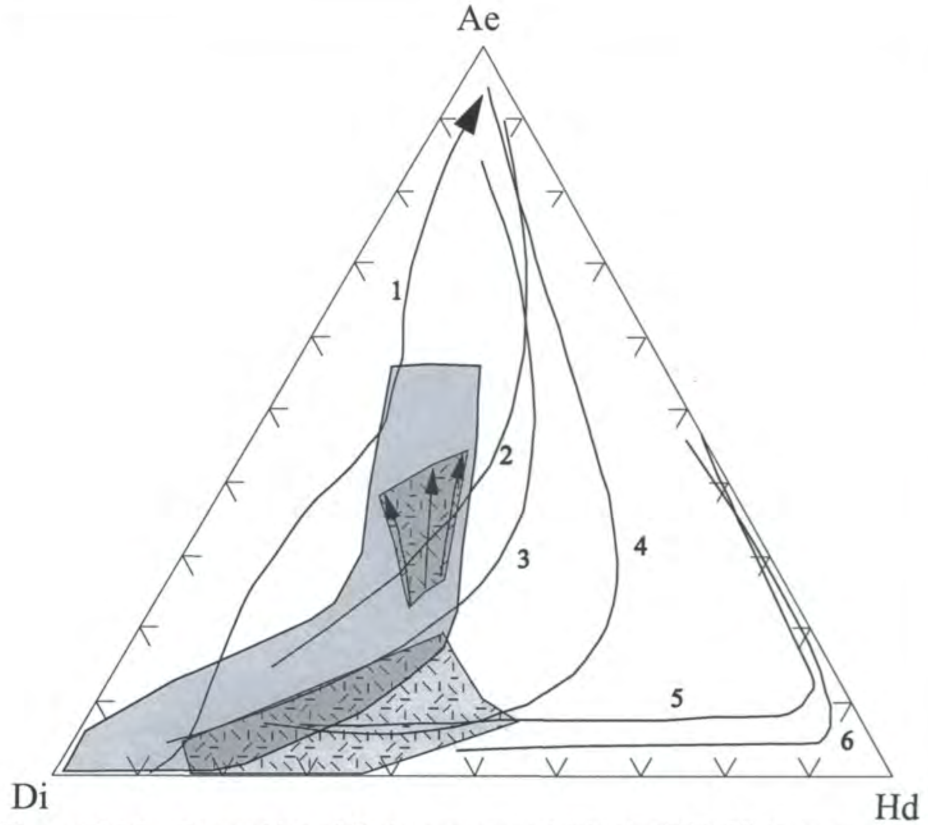

Figure III.3.9 - Composition of Tapira pyroxenes (plain shaded field) in terms of the Aegirine-Diopside-Hedenbergite end-members. Trends for various alkaline complexes (after Mitchell and Vladykin, 1996) are also shown: Little Murun (1); Itapirapuã (2); Uganda (3); South Qoroq (4); Nandewar (5); Ilimaussaq (6); Sakun (ornamented shaded fields).

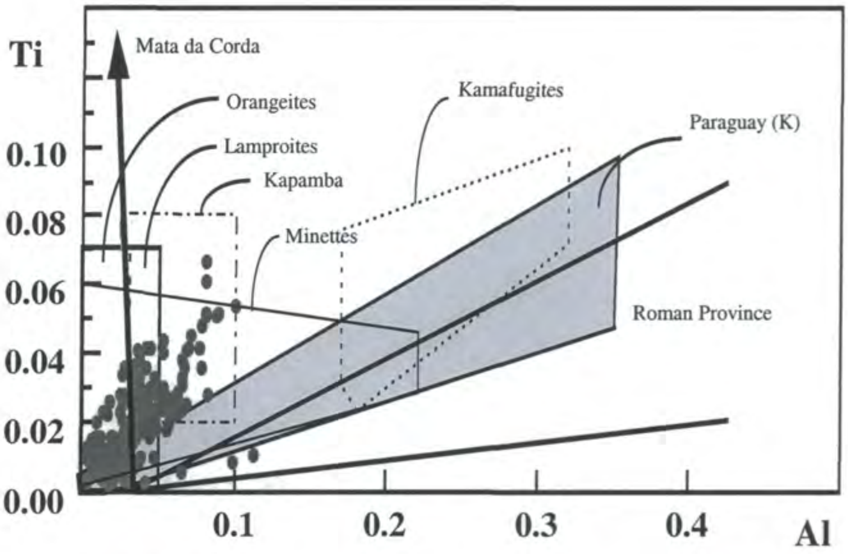

Figure III.3.10 - Al and Ti composition of Tapira pyroxenes compared with pyroxene in various types of alkaline rocks. Fields for orangeite, lamproite, Kapamba, kamafugite and Roman Province pyroxenes are from Mitchell and Bergman (1991). The arrow indicates the variation of the Mata da Corda kamafugite pyroxenes, based on four analyses published by Sgarbi and Valença (1994). The shaded field represent pyroxene from potassic alkaline rocks of the Asuncion-Sapucai graben, Paraguay (Cundari and Comin-Chiaramonti, 1996)

III.3.4 - SUMMARY

- Clinopyroxenes from the Tapira complex show a trend of compositional variation consistent with magmatic differentiation. In ultramafic rocks and dykes they evolve continuously from nearly pure diopside towards moderate enrichment in hedenbergite and aegirine. At a later stage of magmatic evolution, the aegirine component progressively increases at the relatively constant diopside/hedenbergite ratio of 3:2.
- Pyroxenes in carbonatites are interpreted as xenocrystic, on the basis of field, petrographic and chemical evidence. Two varieties of xenocrysts were identified, one derived from wehrlites and bebedourites of the silicate plutonic rock series, and the other probably derived from relatively unevolved syenites that presumably did not reach the same crustal level of the Tapira complex.
- Aegirine-augites of metasomatic origin occurring in fenites are chemically and petrographically distinct from those in syenites.
- The presented chemical data support the field and petrographic evidence for a multi-stage evolution of the Tapira complex, rather than a single layered sequence of cumulates.
- Tapira pyroxenes show strong similarities to those from other carbonatite-bearing complexes and kamafugitic rocks of the Alto Paranaíba Igneous Province. They are also compatible with the overall chemical trends of pyroxenes in other Brazilian alkaline districts, but chemically different from those in the western border of the Paraná Basin (Paraguay).
- The composition of the studied pyroxenes is similar to those in orangeites and lamproites, and significantly distinct from those in kamafugites and Roman Province-type rocks. It should be stressed, however, that pyroxenes of Alto Paranaíba kamafugites do not match the compositional range of world-wide kamafugites either.

III.4 - MICA

Mica is present in all of the Tapira rock-types and is therefore a crucial mineral in the investigation of the petrologic evolution of the complex. The following sections will discuss the compositional variation of micas in Tapira and compare them with other world-wide occurrences of carbonatites and alkaline rocks.

The nomenclature of trioctahedral micas used in the remainder of the text is after Bailey (1984), with the addition of tetraferriphlogopite (taken as the magnesian equivalent of ferri-annite). When relevant, the structural position to which the various cations are assigned will be indicated by the superscripts $^{(IV)}$ and $^{(VI)}$ for tetrahedral and octahedral cations, respectively. The ideal end-member compositions (for total cations = 16) referred to hereafter are given in Table III.4.1.

Mineral	Ideal end-member
Phlogopite	$K_2Mg_6(Si_6Al_2O_{20})(OH,F)_4$
Biotite	$K_2(Mg_{1.2\text{-}3.6}Fe^{2+}_{4.8\text{-}2.4})(Si_6Al_2O_{20})(OH,F)_4$
Annite	$K_2Fe^{2+}_6(Si_6Al_2O_{20})(OH,F)_4$
Ferri-annite	$K_2Fe^{2+}_6(Si_6Fe^{3+}_2O_{20})(OH,F)_4$
Tetraferriphlogopite	$K_2Mg_6(Si_6Fe^{3+}_2O_{20})(OH,F)_4$
Eastonite	$K_2Mg_4Al_2(Si_4Al_4O_{20})(OH,F)_4$
Siderophyllite	$K_2Fe^{2+}_4Al_2(Si_4Al_4O_{20})(OH,F)_4$

Table III.4.1 - Names and ideal end-member compositions of trioctahedral micas (after Bailey, 1984).

III.4.1 - CHEMICAL VARIATION IN TRIOCTAHEDRAL MICAS

Although most naturally occurring biotites have octahedral aluminium, and thus form a solid solution between the series phlogopite-annite and the series siderophyillite-eastonite (Deer *et al.*, 1992), this feature is rare in Tapira. In fact, most of the studied micas lack $^{(VI)}$Al completely and many have insufficient Al even to fill the tetrahedral positions. Therefore, the following discussion will concentrate on the more relevant, low-Al compositions, ranging between phlogopite-annite and phlogopite-tetraferriphlogopite (Table III.4.1).

A number of cation substitutions is known to occur in trioctahedral micas (Bailey, 1984). The most common cations in the octahedral site are Mg^{2+}, Al^{3+}, Fe^{2+} and Fe^{3+}. Less frequently Ti^{4+}, Mn^{2+}, Li^{+} and Cr^{3+} (among others) can also occupy octahedral positions. Tetrahedral cations are primarily Al^{3+} and Si^{4+}, although Fe^{3+} can substitute for Al^{3+} - a somewhat common feature in alkaline rocks and carbonatites - and some authors have argued for the presence of tetrahedral Ti^{4+} (e.g. Farmer and Boetcher, 1981). The interlayer site is occupied mostly by K^{+} and Na^{+}, with Ca^{2+} and Ba^{2+} as possible substitutes.

Octahedral substitutions

Substitution of Fe^{2+} for Mg^{2+} in the octahedral site defines the phlogopite-annite series, and is probably the most common substitution in trioctahedral micas. Fe^{2+} usually increases with magmatic evolution. In their investigation of phlogopite within ultrapotassic rocks from several localities, Edgar and Arima (1983) demonstrated that, although phlogopite is systematically more magnesian than the coexisting liquid, there is a sympathetic variation between the Mg/(Mg+Fe) ratio in the bulk rock and in phlogopite.

In carbonatite liquids, however, this relationship is not so straightforward. McCormick and Le Bas (1996) suggested that the Fe/Mg ratio of phlogopites crystallised from the Busumbu and Sukulu carbonatites (Uganda) is controlled by the co-precipitation of magnetite. They observed an initial decrease in the Fe/Mg ratio in zoned phlogopite, as Fe is consumed during the crystallisation of magnetite. When magnetite ceases to crystallise the Fe/Mg ratio of phlogopite increases progressively, leading towards biotite. They also found Al to decrease in mica, as a result of the progressively lower availability of this element in the magma, except in the late-stage micas when Al was added to the magma via country-rock assimilation. Furthermore, Gaspar and Wyllie (1987) detected MgO increase with relative age of carbonatite intrusions in the Jacupiranga complex (south-eastern Brazil).

Titanium is an important element in alkaline magmas, and phlogopite from rocks such as leucitites, melilitites and lamproites can be distinctively Ti-rich (Mitchell and

Bergman, 1991; Mitchell, 1995a). The solubility of Ti in phlogopite may be affected by paragenetic and/or physicochemical constraints. According to Edgar and Arima (1983), in the absence of Ti-bearing oxides phlogopite is the preferential site for TiO_2 in ultrapotassic rocks, if compared with other phases possibly crystallising at the same time (such as clinopyroxene and olivine). However, if Ti-magnetite or perovskite form concomitantly with phlogopite, titanium will partition preferentially to the former two minerals, and the TiO_2 content in phlogopite may approximate that of the clinopyroxene. Arima and Edgar (1981) suggested that the solubility of titanium in phlogopite is little related to the bulk rock composition, but strongly depends on the physical conditions prevailing during crystallisation. According to their review of experimental data, increasing temperature, increasing fO_2 and decreasing pressure all increase Ti solubility in phlogopite.

Finally, Mn can substitute for Fe^{2+} in the octahedral site. Lalonde *et al.* (1996) described Mn enrichment with Fe/(Fe+Mg) in mica from the Mont Saint-Hilaire intrusion (Canada), suggesting that the increase of Mn correlates positively with the amount of tetrahedral Fe^{3+}.

Tetrahedral substitutions

Among the possible tetrahedral substitutions, $Fe^{3+} \Leftrightarrow Al$ is by far the most important in alkaline rocks and carbonatites. This substitution defines the phlogopite-tetraferriphlogopite and annite - ferri-annite series, and is commonly indicated by:

a) strong negative correlation between Fe and Al

b) deficiency in the sum of the common tetrahedral cations (i.e. $Si + {}^{(IV)}Al < 8$)

c) excess of octahedral charges, caused by overestimated Fe^{2+} from microprobe analysis.

The presence of ${}^{(IV)}Fe^{3+}$ is related to the reverse pleochroism which is typical of tetraferriphlogopite. Even small amounts of ferric iron seem to induce this phenomenon. Farmer and Boetcher (1981) described reversely-pleochroic mica with Fe_2O_3 as low as 0.66 wt. % (0.07 ${}^{(IV)}Fe^{3+}$ p.f.u.), whilst Araújo (1996) detected a sharp change in the ${}^{(IV)}Fe^{3+}/{}^{(IV)}Al$ ratio, coincident with pleochroism reversal, at 0.5 ${}^{(IV)}Fe^{3+}$ p.f.u. Additional sound evidence for the presence of tetrahedral Fe^{3+} in tetraferriphlogopite is provided by Mössbauer spectroscopy studies (Dyar, 1987; Lalonde *et al.*, 1996; Araújo, 1996).

$^{(IV)}$Al-deficiency is typical of micas from lamproites and orangeites and has been interpreted as a direct consequence of the peralkalinity of the magma (Mitchell and Bergman, 1991; Mitchell , 1995b). Low Al concentration in the liquid and/or high oxygen fugacity have also been recognised as major inducing factors for the formation of tetraferriphlogopite (e.g. Arima and Edgar, 1981; Heathcote and McCormick, 1989; Brigatti *et al.*, 1996). Conditions such as these are fairly common in carbonatites, which is in good agreement with the frequent occurrence of tetraferriphlogopite in these rocks. Nonetheless, Dyar (1987) pointed out that there is Mössbauer spectroscopy evidence for tetrahedral iron in both Al-poor and Al-rich micas and Lalonde *et al.* (1996) reported micas with $^{(IV)}Fe^{3+}$ formed in an Al-rich environment.

An alternative hypothesis has been proposed to account for tetrahedral deficiency, involving $^{(IV)}Ti^{4+}$ instead of $^{(IV)}Fe^{3+}$. Farmer and Boetcher (1981) suggested that Ti^{4+} comes before Fe^{3+} in the order of preference to occupy tetrahedral positions, with Fe^{3+} entering the tetrahedral site only if there is still deficiency left.

Tetraferriphlogopite has often been linked with post-magmatic processes (Araújo, 1996; Zaitsev and Polezhaeva, 1994; McCormick and Heathcote, 1987; Mitchell, 1995a). In many cases the secondary character is indicated by petrographic evidence, such as mantling of pre-existing phlogopite crystals by tetraferriphlogopite, sharp compositional changes and various disequilibrium textures. Less frequently, the opposite pattern is observed. Farmer and Boetcher (1981) described phlogopite with reversely-pleochroic cores and normal-pleochroic rims in kimberlites and associated peridotite xenoliths. They point out, however, that the cores are richer in Al_2O_3 and poorer in $FeO_{(T)}$ than in other optically similar phlogopites, suggesting that the reverse pleochroism is not necessarily related to the $Fe^{3+} \Leftrightarrow Al$ substitution.

Interlayer site substitution

Amongst the common substitutions in the 12-fold co-ordinated interlayer site, Ba enrichment has been often described in carbonatites and alkaline rocks. Ba-rich eastonite (up to 5% Ba) occurring as overgrowths on previously-formed phlogopite in carbonatites from Arkansas has been interpreted as a product of the latest stages of groundmass crystallisation (McCormick and Heathcote, 1987). Gaspar and Wyllie (1982, 1987) found up to 10.3% BaO in phlogopites from the Jacupiranga carbonatites.

They report zoning in both directions (increasing and decreasing BaO towards the rim), but point out that high-Ba rims are more common than high-Ba cores. Even higher Ba contents (13 to 16% wt. % BaO) were reported by Seifert and Kampf (1994) for phlogopite in a nephelinite from Bohemia and are also interpreted as a result of late-stage Ba enrichment.

III.4.2 - PHLOGOPITES FROM THE TAPIRA COMPLEX

During this research, an extensive investigation of compositional variation in phlogopites from different rock types was carried out. The results of microprobe analyses and the corresponding calculated formulas are reported in Appendix 2. Two main phlogopite types occur in the studied rocks. In the silicate plutonic rocks series (SPS) the most common micas belong to the phlogopite-annite series, whilst carbonatites and metasomatic phlogopitites (= reaction rock, see Chapter II) may contain micas with an important tetraferriphlogopite - ferri-annite component, together with resorbed or partially replaced crystals of phlogopite-annite.

The role of tetraferriphlogopite and ferri-annite can only be properly assessed if the Fe^{3+}/Fe^{2+} ratio is known. In the case of microprobe analyses, however, ferrous and ferric iron cannot be distinguished, and this ratio has to be estimated. Procedures for iron recalculation invariably rely on a series of assumptions regarding the type of tetrahedral substitutions prevailing in each case. Dymek (1983) and Droop (1987) proposed recalculation methods for the estimation of the Fe^{3+}/Fe^{2+} ratio. However, Dymek's iterative normalisation procedure was devised for the recalculation of $^{(VI)}Al$-bearing biotites, which are substantially different from the phlogopites in this study. Droop's method is not applicable to minerals with cation vacancies and, as suggested by Mitchell (1995b) may result in overestimated Fe^{3+}. Recent Mössbauer spectroscopy studies (Araújo, 1996) have shown that Fe^{3+} is the main substituting cation in the tetrahedral position in tetraferriphlogopites from Catalão (a carbonatite complex in APIP). Furthermore, crystal-chemistry studies (Brigatti *et al.*, 1996) suggested that $^{(IV)}Fe^{3+} \Leftrightarrow {}^{(IV)}Al$ is the main tetrahedral substitution in Tapira. During this research the analyses were recalculated using the method suggested by Araújo (1996), as described below.

Microprobe results were first recalculated on the basis of 22 oxygen, and an appropriate amount of Fe was recast as $^{(IV)}Fe^{3+}$ in order to complete the tetrahedral site occupancy according to the equation:

$$^{(IV)}Fe^{3+} = 8 - Si - {}^{(IV)}Al$$

After adjusting FeO and Fe_2O_3 to the calculated ratio, the analyses were recalculated on the basis of 24 oxygen (H_2O calculated by stoichiometry). In some cases the first estimate of Fe_2O_3 by this procedure still leaves a small tetrahedral deficiency after re-normalisation on the basis of 24 oxygen. The method was then successively repeated until completion of the tetrahedral site. The good charge balances achieved indicate that this procedure provides an adequate estimate of Fe^{3+}/Fe^{2+} ratios in the studied micas.

The main chemical characteristics of phlogopite in each rock group are described below. Figure III.4.1 illustrates the compositional variation of mica by rock group, in terms of the relevant end-members. Most analyses cluster near the phlogopite end-member, with little solid solution towards more Al-rich compositions. It must be stressed, however, that this does not represent a true eastonite-siderophyllite component, because all of the aluminium is $^{(IV)}Al$. The slight deviation from the phlogopite-annite line towards the Al corner is probably the combined result of Al ⇔ Si variation in the tetrahedral site and normalisation of the variables to 100 % in the triangular diagram.

Starting from magnesian phlogopite, the following main compositional trends are depicted: a) variation along the phlogopite-annite join, marked by micas from the SPS and from some carbonatites; b) a trend towards ferri-annite, defined by the core-rim evolution of phlogopite in some of the phlogopite-picrites and low-Cr dykes; c) a trend towards tetraferriphlogopite, defined by micas from carbonatites, some phlogopite-picrites and the rims of micas from the reaction rock. Cores of the reaction rock micas are not individualised, but roughly coincide with the field for wehrlites.

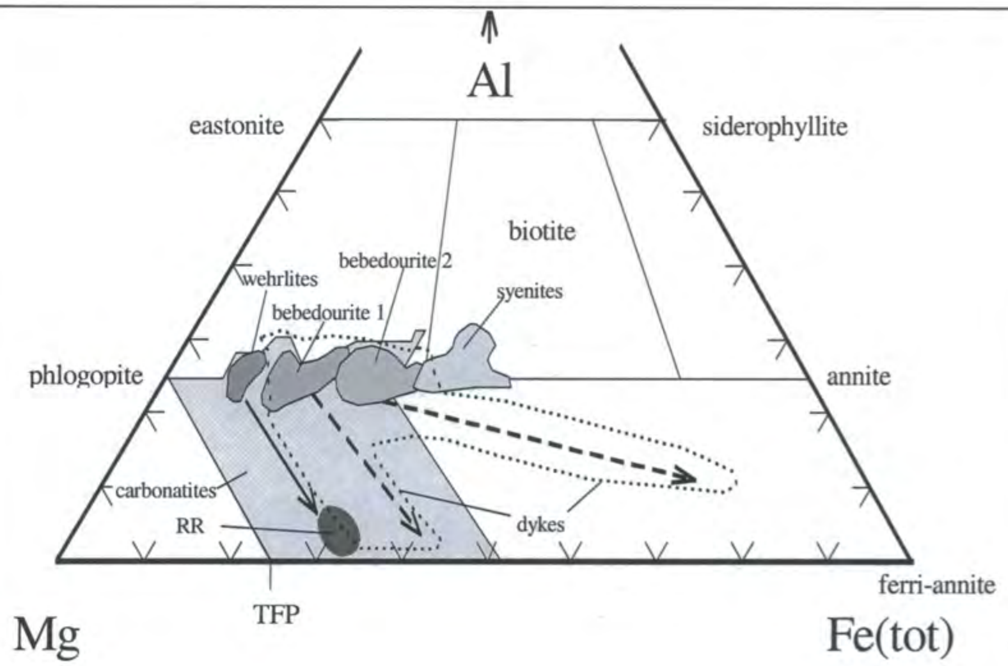

Figure III.4.1 - Compositional variation of mica in all studied rocks. Solid arrow indicates the compositional shift from the cores (wehrlite-like) to rims in the reaction rock (RR). Note the progression from phlogopite towards biotite with differentiation in the SPS, and the overlap of the carbonatite field with the fields of ultramafic rocks, but not with the syenites (see text). TFP = tetraferriphlogopite.

Silicate plutonic rocks series (SPS)

Phlogopite composition in the SPS varies along a continuous trend of increasing Fe^{2+} and decreasing Mg^{2+} with magmatic evolution (Figure III.4.2). Although some of the groups slightly overlap each other compositionally, there is a clear progression from magnesian phlogopite (Fe^{2+}/ Fe^{2+}+Mg as low as 0.07) in the wehrlites towards biotite (Fe^{2+}/ Fe^{2+}+Mg up to 0.49) in the more evolved syenites. This is consistent with the expected decrease of magnesium in the magma, with differentiation. The slight deviation from the ideal phlogopite-annite line in Figure III.4.2 may be accounted for by higher amounts of Ti (up to 3.69 wt % TiO_2) and Mn (up to 1.27 wt % MnO) in the more evolved rocks.

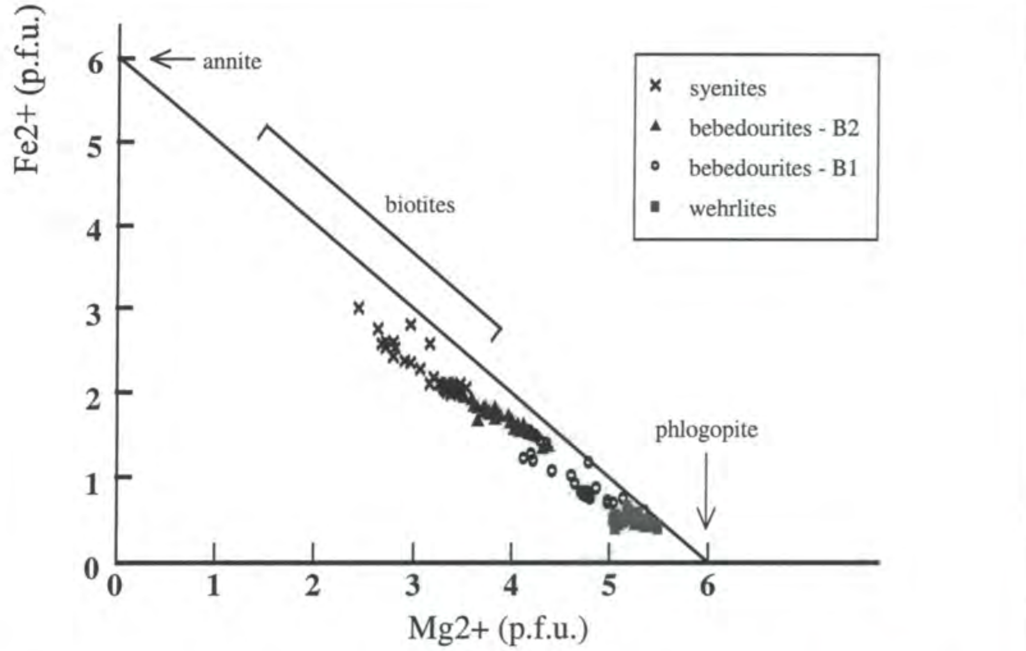

Figure III.4.2 - Fe^{2+} and Mg^{2+} variation in phlogopites of the plutonic silicate rocks. Note the continuous variation from Mg-rich (phlogopite) to Fe-rich (biotite) with differentiation.

Because the progression along the phlogopite-annite series seems to be directly related to the differentiation of the SPS, the ratio $Fe^{2+}/(Fe^{2+} + Mg)$ was used to gauge other chemical changes that could possibly be associated with the magmatic evolution of phlogopite. The tetrahedral cations Si, Al and Fe^{3+} do not vary substantially with $Fe^{2+}/(Fe^{2+}+Mg)$ from wehrlites to syenites. In fact, the differences between rock types are always smaller than the magnitude of the internal variation in each group. The lack of significant relative variation in the tetrahedral cations suggests that substitutions like phlogopite-tetraferriphlogopite are of little or no importance in the SPS.

Ti increases in phlogopite with the $Fe^{2+}/(Fe^{2+}+Mg)$ ratio, both between and within the rock groups, although the individual trends overlap considerably (Figure III.4.3). The lowest Ti was observed in a wehrlite (0.078 p.f.u.) and the highest in a syenite (0.433 p.f.u.). The pace of Ti variation with Fe/(Fe+ Mg) decreases considerably between the wehrlites and the bebedourites. (Figure III.4.3). This might be related to a change in the availability of Ti in the liquid (e.g. by extensive fractionation of Ti-bearing phases such as perovskite and/or Ti-magnetite during the previous stage) or, alternatively, a change in the prevailing physical conditions (e.g. Arima and Edgar, 1981; Edgar and Arima, 1983). Note that the trend for syenite mica in Figure III.4.3 is a progression of the trend for B2 bebedourites

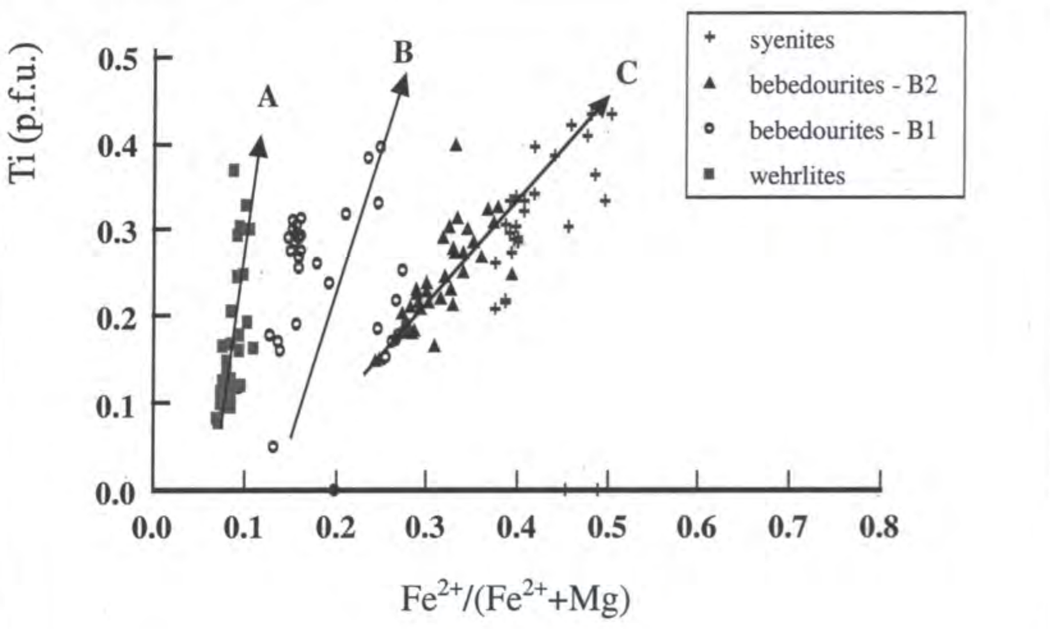

Figure III.4.3 - Ti variation with the $Fe^{2+}/(Fe^{2+} + Mg)$ ratio. Note the different slopes for the trends of wehrlites (A), two types of bebedourites and syenites (B and C), which suggest that Ti substitution is more strongly correlated with Fe/Mg in the more differentiated types.

Figure III.4.4 shows a strong negative correlation of Ti with octahedral site occupation (OSO) and a less well-defined negative correlation with Si + $^{(VI)}$Al in phlogopite from SPS.

The trend is compared with the Ti-substitution schemes:

$$2^{(VI)}Mg \Leftrightarrow {}^{(VI)}Ti + \square \text{ (Forbes and Flower, 1974)} \qquad (1)$$

and

$$^{(VI)}Mg + 2^{(IV)}Si \Leftrightarrow {}^{(VI)}Ti + 2^{(IV)}Al. \text{ (Robert, 1976)} \qquad (2)$$

but does not coincide with either of the mechanisms proposed for Ti substitution. This suggests that a combination of the two schemes might be involved. Similar features were observed by Brigatti *et al.* (1996), in a crystal-chemistry study of Tapira phlogopites. They are also present in phlogopite from lamproites (Mitchell and Bergman, 1991) and in micas crystallised during experimental studies of ultrapotassic

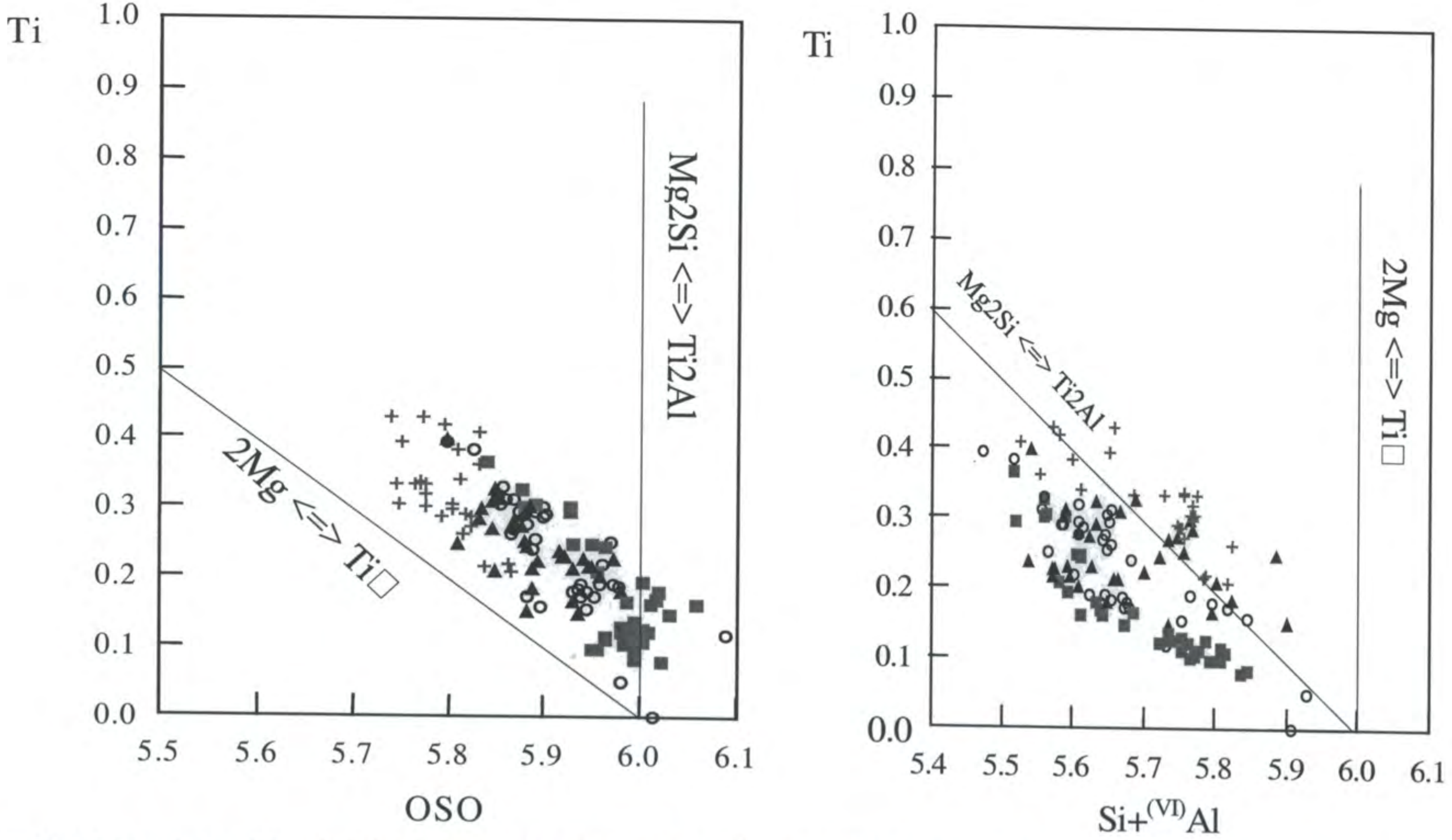

Figure III.4.4 - Ti variation with octahedral site occupancy (OSO) and with Si + $^{(VI)}$Al for SPS phlogopites. The data do not fit any of the substitution schemes, although the negative correlations suggest that the mechanism of Ti substitution may be a mixture of the two reactions. Symbols as in figure III.4.3 rocks (Arima and Edgar, 1981). The better-defined negative correlation of Ti with OSO suggests that the vacancy substitution scheme is somewhat dominant.

The TiO_2 increase from wehrlites to syenites is difficult to reconcile with the tendency of Ti-solubility to increase with increasing temperatures. Instead, one or more of the other constraining factors (decreasing pressure, increasing fO_2) suggested by Arima and Edgar (1981) must be prevailing over the temperature effect. Oxygen fugacity is expected to increase with differentiation and could lead to the observed Ti-enrichment in syenite phlogopites. Furthermore, textural evidence (Chapter II) indicates the emplacement of SPS at least partially as a crystal mush, suggesting that different rocks may have been formed at variable depths. On the other hand, the zoning pattern of phlogopite in some rocks shows a slight decrease in TiO_2 towards the rims, which could be attributed to the effect of decreasing temperature during crystallisation. In summary, temperature appears to be the most important constraining factor of Ti solubility in phlogopite on a local scale, whereas a combination of decreasing pressure and increasing fO_2 seems to control the differences between rock groups in SPS. This is consistent with a multi-stage evolution for the complex.

Mn correlates positively with the Fe^{2+} /(Fe^{2+}+Mg) ratio in the SPS, increasing steadily through the fractionation sequence, from less than 0.01 p.f.u. in the wehrlites to 0.08 atoms p.f.u. in the syenites. This indicates that Mn follows the progressive increase of Fe^{2+} along the phlogopite-annite series.

Potassium in the interlayer site increases from 1.75 p.f.u. in the wehrlites to 1.98 p.f.u. in syenites. Na decreases slightly with differentiation but the variability within groups exceeds the differences between different rock-types. Ba (up to 0.05 p.f.u.) and Ca (up to 0.03 p.f.u.) are generally low and do not show systematic variation. Ba is remarkably low (less than 0.01 p.f.u.) in some syenites, but this feature is not part of a Ba-decreasing trend in the preceding stages.

Figure III.4.5 shows a series of microprobe profiles across individual phlogopite grains from various rocks types. The first four columns show the evolution of primary (magmatic) mica. Wehrlite and bebedourite show similar behaviour, whereby the rims are slightly enriched in MgO and SiO_2, with a corresponding depletion in TiO_2 and Al_2O_3.

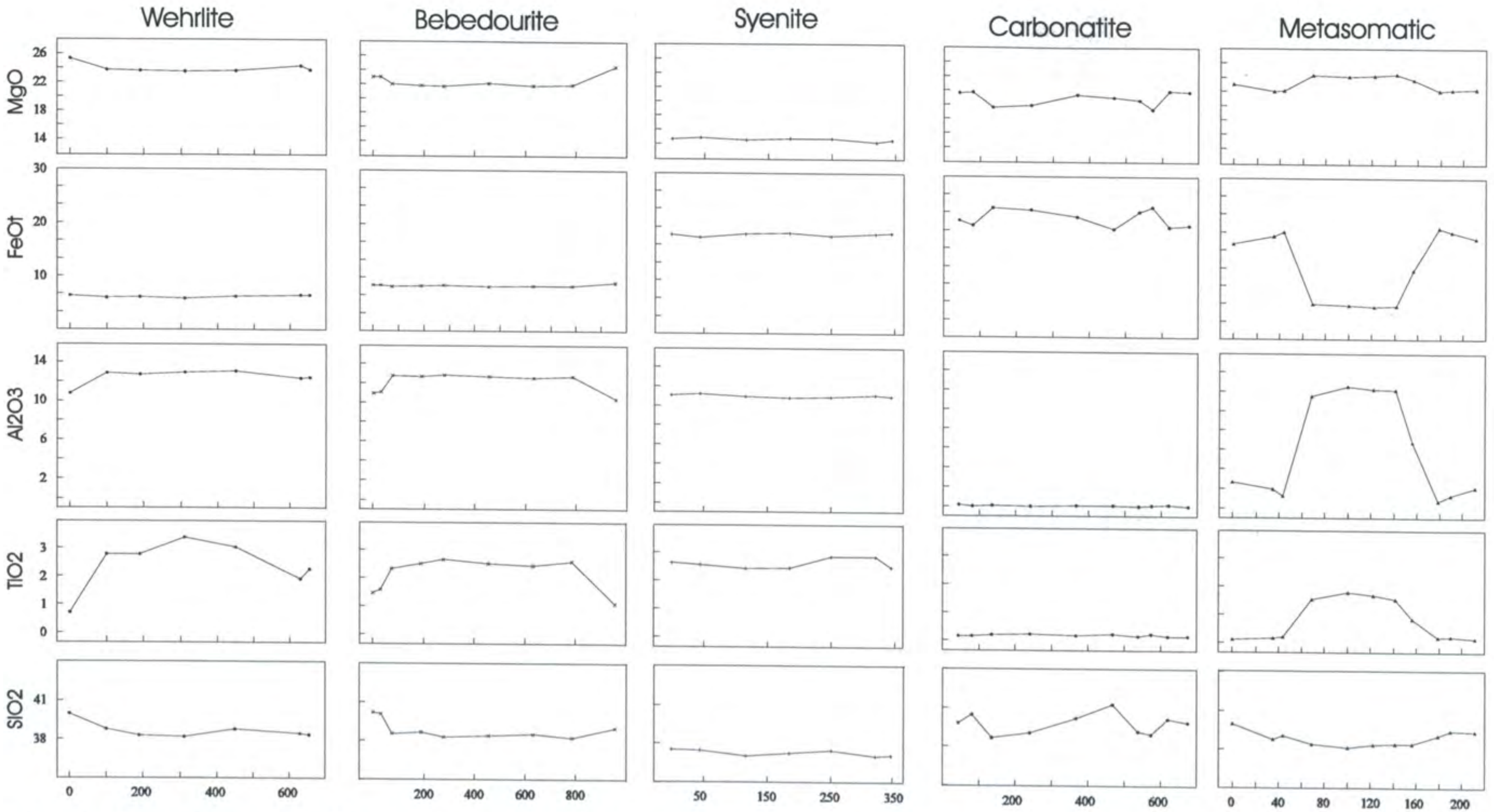

Figure 5 - Microprobe profiles in phlogopite of various Tapira rock-types. Vertical scales are identical for each element, to allow comparison. Note the abrupt variation in FeOt, Al2O3 and TiO2 in the rims of metasomatic mica, as opposed to the relatively flat patterns of primary phlogopites. SiO2 and FeOt are negatively correlated in the carbonatite. FeOt=total iron as FeO. Horizontal scales are in microns.

The coupled variation suggests that the substitution mechanism $^{(VI)}Mg + 2^{(IV)}Si \Leftrightarrow {}^{(VI)}Ti + 2^{(IV)}Al$ (Robert, 1976) is in place. Note that there is no iron increase associated with aluminium depletion. Syenite micas do not show any significant zoning but have higher FeO and lower MgO than micas in the ultramafic rocks. The zoning of phlogopite from carbonatite and metasomatic mica from the reaction rock (Figure III.4.5) will be discussed in the following sections.

Reaction rock

At the contact between carbonatite intrusions and ultramafic rocks of the SPS the interaction of carbonatite liquid with dunite, wehrlite or bebedourite results in the banded reaction rock, described in Chapter II. This is formed by alternate bands of carbonate and phlogopite + magnetite and grades into the original ultramafic rock away from the contact. Similar features have been described by Gaspar (1989) in the Jacupiranga complex and are common in other carbonatite complexes of the APIP (Issa Filho *et al.*, 1984; Araújo, 1996; Araújo and Gaspar, 1993).

The effects of metasomatism on phlogopite are recorded in the form of replacement rims of reversely-pleochroic tetraferriphlogopite (see Figures II.5 and II.40, in Chapter II), whilst the original composition of the magmatic phlogopite is often preserved in cores with normal pleochroism. The chemical differences between the preserved cores and the tetraferriphlogopite rims are sharp and coincide with the inversion of pleochroism. A chemical profile of mica from the reaction rock is presented in the right-hand-side column of Figure III.4.5.

The variation pattern of metasomatic micas is easily distinguished from those resulting from the magmatic evolution of the SPS (also shown in Figure III.4.5). Of the oxides represented in the profile, only SiO_2 shows a gradational progression from core to rim. In contrast, MgO, Al_2O_3 and TiO_2 decrease and FeOt increases abruptly. The magnitude of the chemical changes is also remarkable, especially if compared with the smoother and much less pronounced zoning of magmatic micas. Another outstanding feature is the increase in FeOt, coupled with Al_2O_3 depletion of similar magnitude. This feature strongly suggests Fe^{3+} substitution for Al in the tetrahedral site, and is clearly not present in the magmatic micas. Finally, MgO is low in the rims of metasomatic mica, whilst in micas from wehrlites and bebedourites magnesium tends to increase towards the rim. BaO is always below detection limit, unlike some late-stage micas in alkaline rocks and carbonatites (e.g. Seifert and Kampf, 1994; McCormick and Heathcote, 1987)

The chemical and petrographic evidence indicates that cores and rims of these micas crystallised under dramatically different chemical and/or physicochemical conditions. Moreover, the cores of micas in the reaction rock are compositionally similar to the magmatic phlogopite in the adjacent ultramafic rocks (compare, for instance, with wehrlite and syenite in Figure III.4.5). This is consistent with a metasomatic origin for the rims, rather than magmatic evolution.

Carbonatites

The relevant set of substitutions in carbonatite phlogopites is significantly different from those observed in the silicate plutonic rocks. Here the tetraferriphlogopite and ferri-annite end-members are important components of the micas (see Figure III.4.1). Accordingly, the $Fe^{3+} \Leftrightarrow Al$ substitution in the tetrahedral site would be expected to be a common feature in phlogopite from Tapira carbonatites (e.g. Brigatti *et al.*, 1996).

In Chapter II, three textural types of phlogopite were described in Tapira carbonatites. These are summarised below:

Type 1 - Large crystals of relatively Al-rich (up to 12.63% Al_2O_3) phlogopite, often showing evidence of resorption by the carbonatite magma and/or replacement by rims and irregular patches of reversely-pleochroic tetraferriphlogopite. This variety occurs in the central body of carbonatite (C1), and also in the C3 and C4, located at the margins of the complex. The textural evidence suggest that the phlogopite cores are xenocrystic, and that the tetraferriphlogopite is a reaction product between the assimilated phlogopite and the carbonatite liquid.

Type 2 - Large, euhedral tetraferriphlogopite crystals, showing concentric (often oscillatory) zoning patterns and no evidence of disequilibrium. A typical chemical profile is presented in Figure III.4.5. The oscillatory zoning generally involves variation of SiO_2, FeO and MgO and is reflected in different shades of red in the reversely-pleochroic grains. Aluminium and titanium are extremely low and do not vary. An interesting feature is the antipathetic variation of SiO_2 and FeO, suggesting mutual substitution. Besides not showing evidence of disequilibrium, these micas often include common carbonatite minerals, such as pyrochlore, apatite and carbonate. This variety of phlogopite is therefore interpreted as magmatic, crystallised directly from the carbonatite liquid during a quiescent period, when minor chemical or physicochemical changes in the system became imprinted in the mica (e.g. Heathcote and McCormick, 1989).

Type 3 - Minute, interstitial mica flakes. In C1 and C4 these are mainly tetraferriphlogopite, and are interpreted as crystallised directly from the carbonatite (by compositional analogy with type 2). In C2 some flakes are tetraferriphlogopite and some are intermediate members of the phlogopite-tetraferriphlogopite series. The extremely fine grain-size and paucity of mica flakes in C2 make the investigation of zoning patterns and disequilibrium textures difficult, effectively precluding a decision as to their magmatic or xenocrystic origin. Nevertheless, the simultaneous occurrence of both compositional types as isolated, scattered flakes in the same sample suggests that mica flakes in C2 actually represent a mixture of fine-grained phlogopite of different origins.

In summary, the only micas with clear textural evidence for magmatic crystallisation from a carbonatite magma are the euhedral, zoned crystals of tetraferriphlogopite in C1. However, small tetraferriphlogopite flakes in other carbonatites are interpreted here as magmatic on the grounds of similar composition. For intermediate members of the phlogopite-tetraferriphlogopite series, textural evidence is either inconclusive (e.g. some of the interstitial mica in C2) or indicates a xenocrystic origin (e.g. partially resorbed crystals in C1, C3 and C4).

Minor elements in all three types of carbonatite micas are low (up to 0.22 % BaO, < 0.1 % C_r2O_3) and do not allow discrimination between different types. High-Ba micas, such as those described by Gaspar and Wyllie (1982) for the Jacupiranga carbonatites, were not found during the present research.

The composition of carbonatite micas is compared with those of the SPS in Figure III.4.6. Micas from carbonatites and silicate rocks clearly follow different crystallisation paths. A sudden increase in FeO(t)/Al_2O_3 ratio (at FeO(t)/MgO ≈ 0.75), signals the crystallisation of tetraferriphlogopite in the carbonatites, whilst the plutonic silicate rocks follow the pattern of the phlogopite-annite series. The high-Al cores of micas from C1, C3 and C4 follow the phlogopite-annite trend and have composition similar to the micas of wehrlites and bebedourites in the lower range of FeO(t)/MgO.

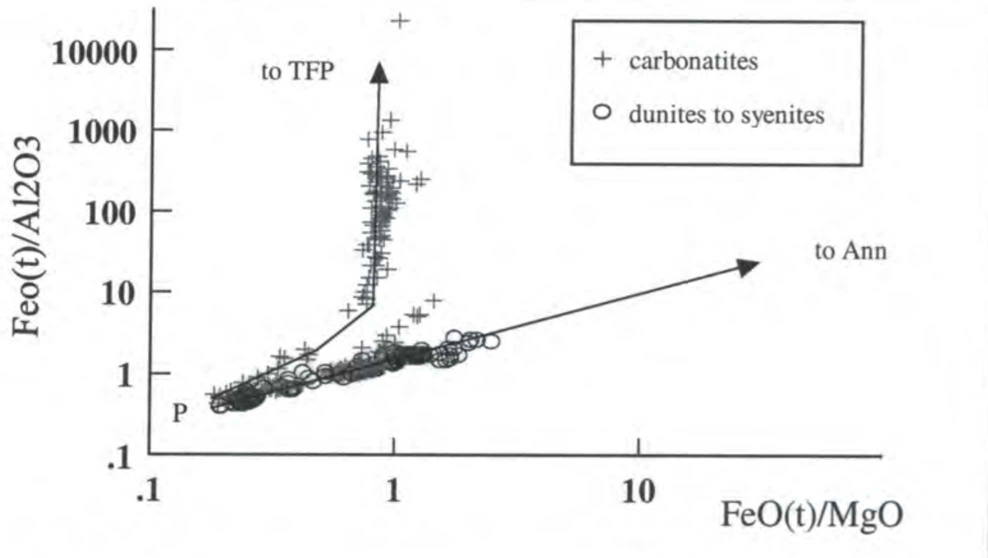

Figure III.4.6 - Iron variation with aluminium and magnesium in Tapira phlogopites. The carbonatite micas that plot along the phlogopite-annite line are interpreted as xenocryst cores (see text). The evolution of carbonatite micas towards tetraferriphlogopite is marked by the sharp increase in the $FeO(t)/Al_2O_3$ *ratio. Phlogopites from the SPS are plotted for comparison, and clearly do not show the same* $FeO(t)/Al_2O_3$ *enrichment. P = phlogopite, Ann = annite, TFP = tetraferriphlogopite. Note that the log scale is necessary to picture the wide range of Fe/Al variation.*

Since tetrahedral site deficiency is a characteristic of tetraferriphlogopite, tetrahedral substitutions are expected to play an important role in the crystallisation of these micas. The chemical behaviour of the major tetrahedral components in phlogopites from Tapira carbonatites is summarised in Figures III.4.7 to III.4.10. The studied micas cover the whole range of compositions in the phlogopite-tetraferriphlogopite series, but cluster preferentially near either one of the ideal end-members (Figure III.4.7). Phlogopites for which textural evidence of a magmatic origin is unequivocal (i.e. zoned euhedral phenocrysts from C1) invariably plot within a very short distance of the tetraferriphlogopite end-member. Many micas in this group either have very low $^{(IV)}Al$ or lack aluminium completely, in which case the tetrahedral site is filled exclusively with $^{(IV)}Fe^{3+}$ and Si.

The negative correlation between $^{(IV)}Fe^{3+}$ and Si in Figure III.4.8 and the antipathetic behaviour of these elements in Figure III.4.5 indicate reciprocal substitution, in agreement with the conclusions of Brigatti *et al.* (1996). The oscillatory nature of the zoning suggests that it is the result of subtle physical changes in the system and does not necessarily represent a magmatic evolutionary trend.

In contrast, the high-Al cores of mica xenocrysts in C1 and C3/C4 contain little $^{(IV)}Fe^{3+}$ (less than 0.6 p.f.u.) and most of the observed variation is between Si and $^{(IV)}Al$ (Figures III.4.8 and III.4.9). The analyses of this group cluster near the phlogopite end-member, like those of micas in the wehrlites and bebedourites. As seen previously, these higher-Al micas are in disequilibrium with the host carbonatite, and are interpreted here as xenocrystic phlogopite assimilated from the SPS.

The reversely-pleochroic rims and patches replacing phlogopite xenocrysts show a distinctive behaviour with respect to the tetrahedral cations. Only in this variety and in some interstitial flakes from C2, a strong negative correlation between $^{(IV)}Fe^{3+}$ and $^{(IV)}Al$ is present (Figure III.4.10). In fact, this group of analyses "bridges the gap" between the high-Al cores of xenocrysts and the high-Fe^{3+} primary carbonatitic mica, which otherwise seems to have evolved independently of the $^{(IV)}Fe^{3+} \Leftrightarrow {}^{(IV)}Al$ substitution.

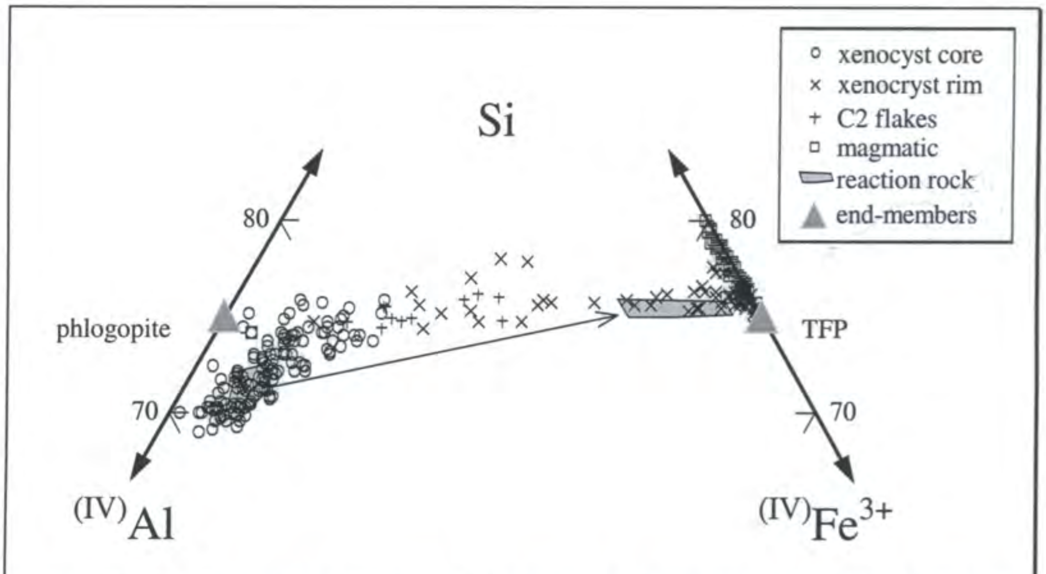

Figure III.4.7 - Compositional variation of carbonatite phlogopites, in terms of the three main cations in the tetrahedral site. Fields for cores and rims of micas in the reaction rock are plotted for comparison (arrow indicates core to rim). TFP = tetraferriphlogopite.

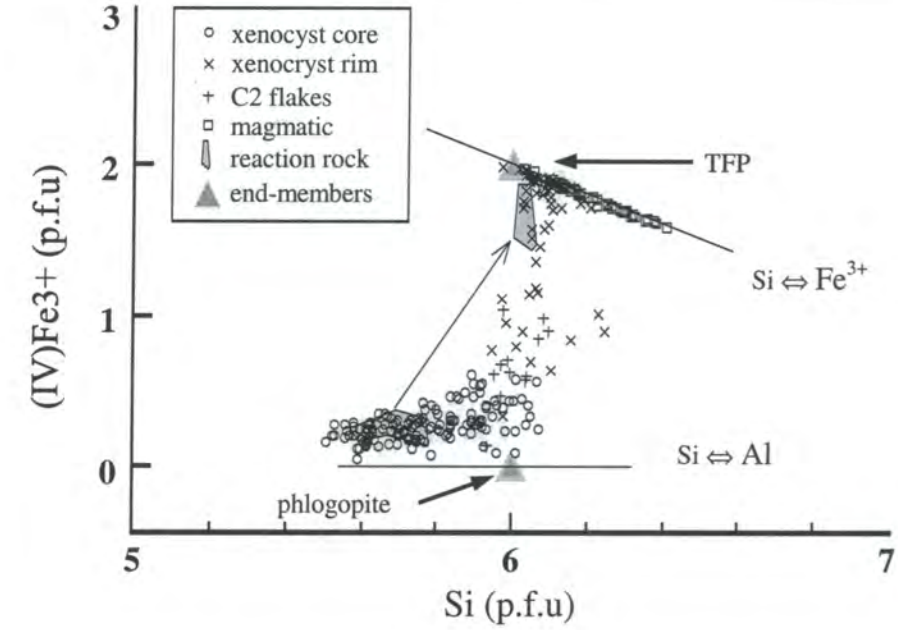

Figure III.4.8 - $^{(IV)}Fe^{3+}$ and Si variation in carbonatite phlogopites. Magmatic phlogopites from C1 have little or no $^{(IV)}Al$ and consequently plot along the substitution line Si ⇔ $^{(IV)}Fe^{3+}$. Cores of phlogopite xenocrysts are $^{(IV)}Fe^{3+}$ - poor, whilst the replacing rims are closer to tetraferriphlogopite. Fields for metasomatic phlogopites from the reaction rock are plotted for comparison (arrow indicates core-to-rim variation). TFP = tetraferriphlogopite.

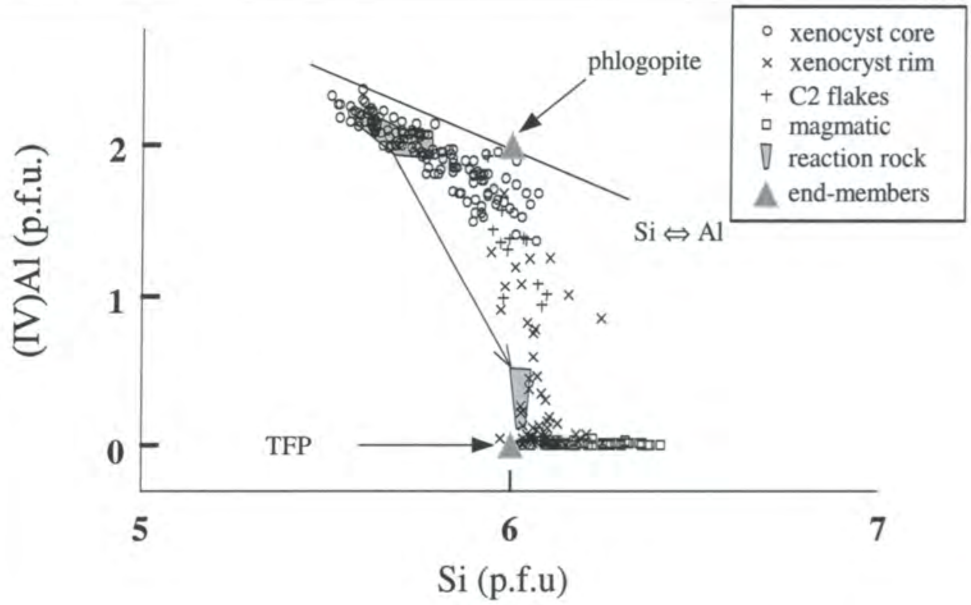

Figure III.4.9 - $^{(IV)}Al$ and Si variation in phlogopite from carbonatites. Magmatic micas are tetraferriphlogopite. Cores of $^{(IV)}Al$-rich xenocrysts plot along the Si ⇔ Al line. C2 flakes and rims of xenocrystic mica are intermediate in composition between magmatic and xenocrystic. Fields for metasomatic phlogopites from the reaction rock plotted for comparison (arrow indicates core-to-rim variation). TFP = tetraferriphlogopite.

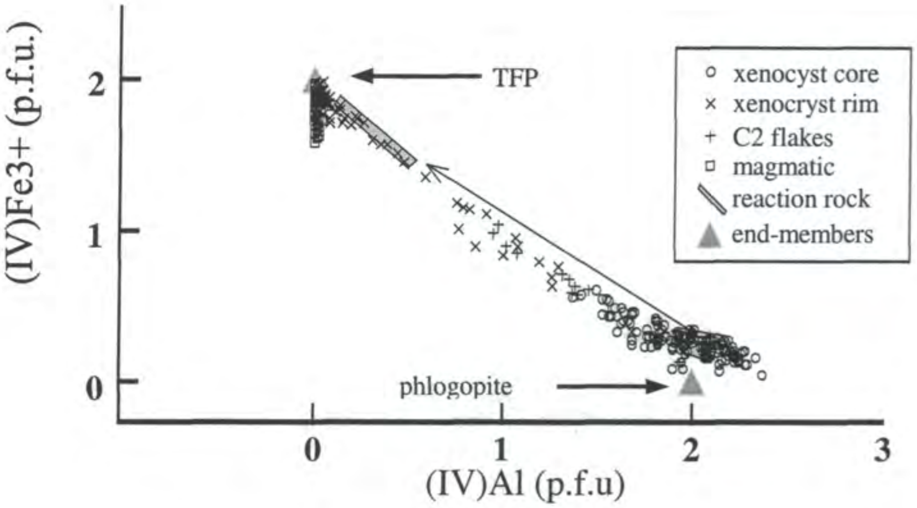

Figure III.4.10 - $^{(IV)}$Al and $^{(IV)}$Fe^{3+} variation in micas from carbonatites. Note the negative correlation between Al and Fe defined by the rims of xenocrysts and in the reaction rock, as well as some C2 mica flakes. TFP = tetraferriphlogopite.

Ultramafic dykes

Phlogopite is an essential constituent of phlogopite-picrites and low-Cr dykes. Groundmass mica is present in all dykes and some samples contain phlogopite phenocrysts and microphenocrysts. In general, the phlogopite-picrites contain less evolved, more magnesian phlogopite than the low-Cr dykes, but there is a significant overlap between the two groups.

Figure III.4.11 compares phlogopites from the dyke rocks with the carbonatites and SPS. The dykes cover most of the span of SPS micas and fit well along that trend, although some rim compositions tend to approximate the field of carbonatite micas. A possible reason for this behaviour is reaction between the earlier-formed phlogopites and carbonate-rich liquids, producing low-Al, high-Fe rims in micas of some samples. This is consistent with the abundant groundmass carbonate in some of the dykes. Alternatively, some of the dykes may have been affected by metasomatic fluids associated with late-stage carbonatites, in which case the low-Al rims are of metasomatic origin.

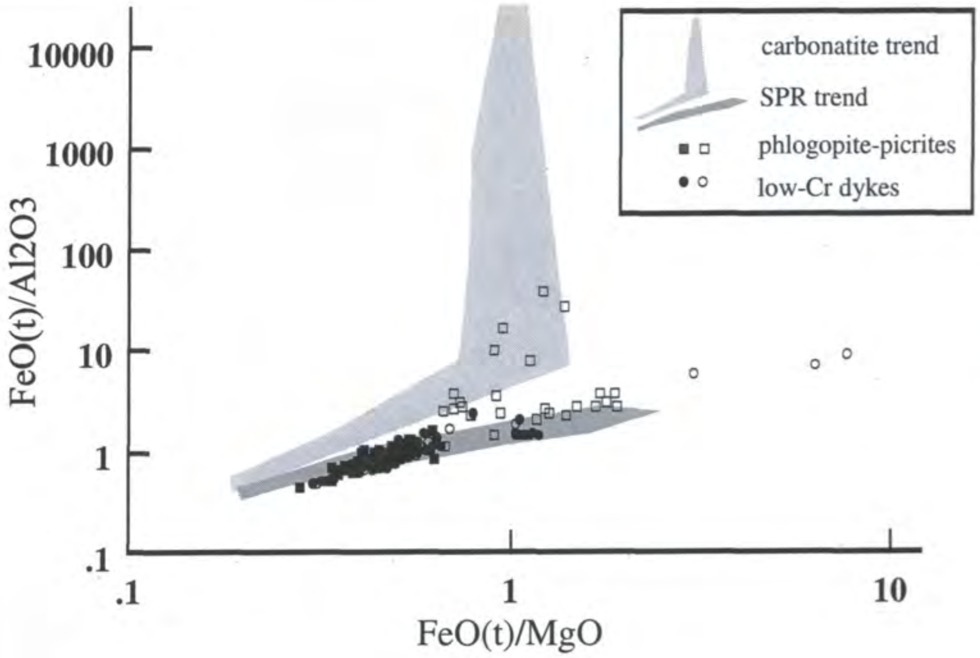

Figure III.4.11 - Iron variation relatively to magnesium and aluminium in micas from phlogopite-picrites and low-Cr dykes. Fields for SPS and carbonatite micas (including all groups) are shown for comparison. Most analyses follow the trend of the SPS, but some phlogopite rims deviate towards the trend of carbonatites. Filled symbols = cores; open symbols = rims.

Micas from the two types of dykes have the highest Ba content amongst Tapira micas (up to 2.95% BaO in phlogopite-picrites and up to 1.71% BaO in low-Cr dykes), with Ba usually decreasing from core to rim. Cr_2O_3 is generally low, but may exceptionally reach 1.2 %. Some micas in the low-Cr dykes seem to be enriched in chromium (up to 1% Cr_2O_3). In any case, Cr_2O_3 decreases from core to rim.

The compositional variation in zoned phlogopites from different dykes is illustrated in Figure III.4.12, in terms of titanium variation with FeO/(FeO+MgO) and with Al_2O_3. In the phlogopite-picrites (solid lines in Figure III.4.12) titanium increases initially with the FeO/(FeO+MgO) ratio of mica, before decreasing towards Ti-depleted rims. The early enrichment in TiO_2 may or may not be coupled with an increase in Al_2O_3, and the magnitude of Ti-depletion in the rims appears to be attenuated with increasing TiO_2.

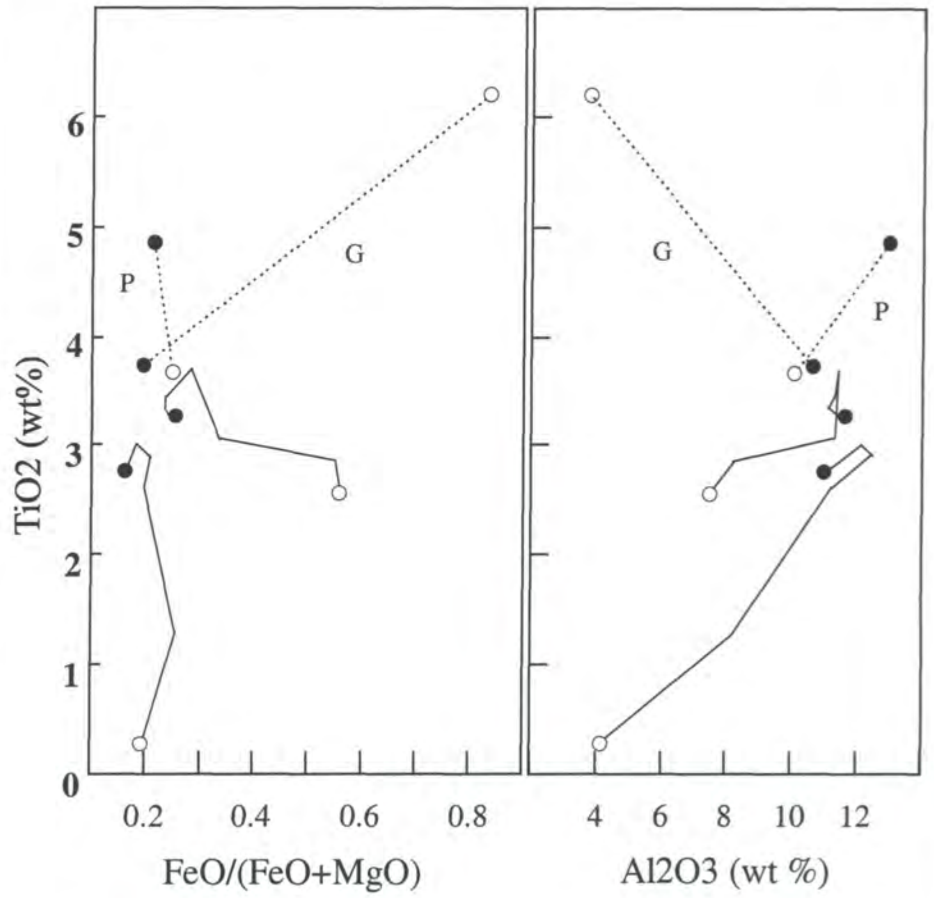

Figure III.4.12 - Chemical zoning of phlogopite in the phlogopite-picrites (solid lines) and low-Cr dykes (dashed lines). In the phlogopite-picrites, the lines represent chemical profiles across individual grains, from core (solid circles) to rim (open circles). In the low-Cr dyke the lines connect pairs of core-rim analyses of phenocryst (P) and groundmass(G) phlogopite.

Micas from low-Cr dykes (dashed lines in Figure III.4.12) have higher TiO_2 than micas from phlogopite-picrites. This is analogous to the evolution of the SPS, where Ti increases in micas of the more differentiated rock types. Phenocrysts and groundmass phlogopite show contrasting behaviour, with the former having higher-TiO_2 cores, whereas in the latter TiO_2 increases from core to rim. The trend of the phenocrysts in the low-Cr dykes is similar to the broad core-rim variation in the phlogopite-picrites. In the low-Cr dykes, the similarity between the rim of phenocryst and the core of groundmass phlogopite suggests a continued crystallisation trend where TiO_2 decreases at first, perhaps during crystallisation of a Ti-rich phase (perovskite or Ti-magnetite), and increases again towards the later stages. In all three examples the rims are always depleted in Al_2O_3 relatively to the cores. In both rock types the Al-depletion towards the rims may be the result of decreasing aluminium availability in the residual liquid.

It was seen in a previous section of this Chapter that micas from different rock types in the SPS show different Ti behaviour with FeO/(FeO+MgO). Figure III.4.13 compares those trends with the composition of micas in dykes and carbonatites. The dashed arrows in the diagram represent the core-rim variation of phlogopites in the dykes, except for the two highest TiO_2 pairs, where the arrows connect phenocrysts to groundmass phlogopite. The evolution trends of cores and rims (or groundmass) parallel, respectively, the trends of wehrlites + bebedourites(B1) and bebedourites (B2) + syenite. At least in the case of the low-Cr dykes, the results may suggest that micas started crystallising at a greater depth and the rims were formed at higher levels, during or after emplacement of the dykes, where lower pressure would favour the solution of Ti in the mica (e.g. Arima and Edgar, 1981). This shallower site would, presumably, coincide with the level of emplacement of B2/syenites, whose micas have FeOt/(FeOt+MgO) and TiO_2 similar to the rims of phlogopite in the dykes.

Also noteworthy in Figure III.4.13 is the comparatively high TiO_2 content of the cores of mica xenocrysts in carbonatites (light-shaded field). In fact, they cover a large span of SPS mica compositions (except, maybe, the syenites). This suggests that the carbonatite magmas assimilated mica crystals from different ultramafic rocks (i.e. wehrlites and the two groups of bebedourites).

The extreme enrichment of TiO_2 in the groundmass phlogopite of low-Cr dykes contrasts with Ti depletion in the rims of phlogopite-picrite micas. However, the cores of the latter register an initial increase in TiO_2 and the Ti-depletion of the rims appears to be attenuated, with increasing titanium content of the mica (Figure III.4.12). The micas crystallised from the carbonatite magma, on the other hand, show extremely low TiO_2 contents. An alternative reason for the behaviour of Ti and Al in primary (magmatic) micas from Tapira may be changes in the activity of these elements in the magma. If the whole composition span of Tapira rocks is considered, Al_2O_3 and TiO_2 show substantial variation (e.g. carbonatites extremely depleted in both Al_2O_3 and TiO_2) The rapid variations observed in some phlogopites from dykes may indicate abrupt chemical changes in the system (e.g. associated with liquid immiscibility).

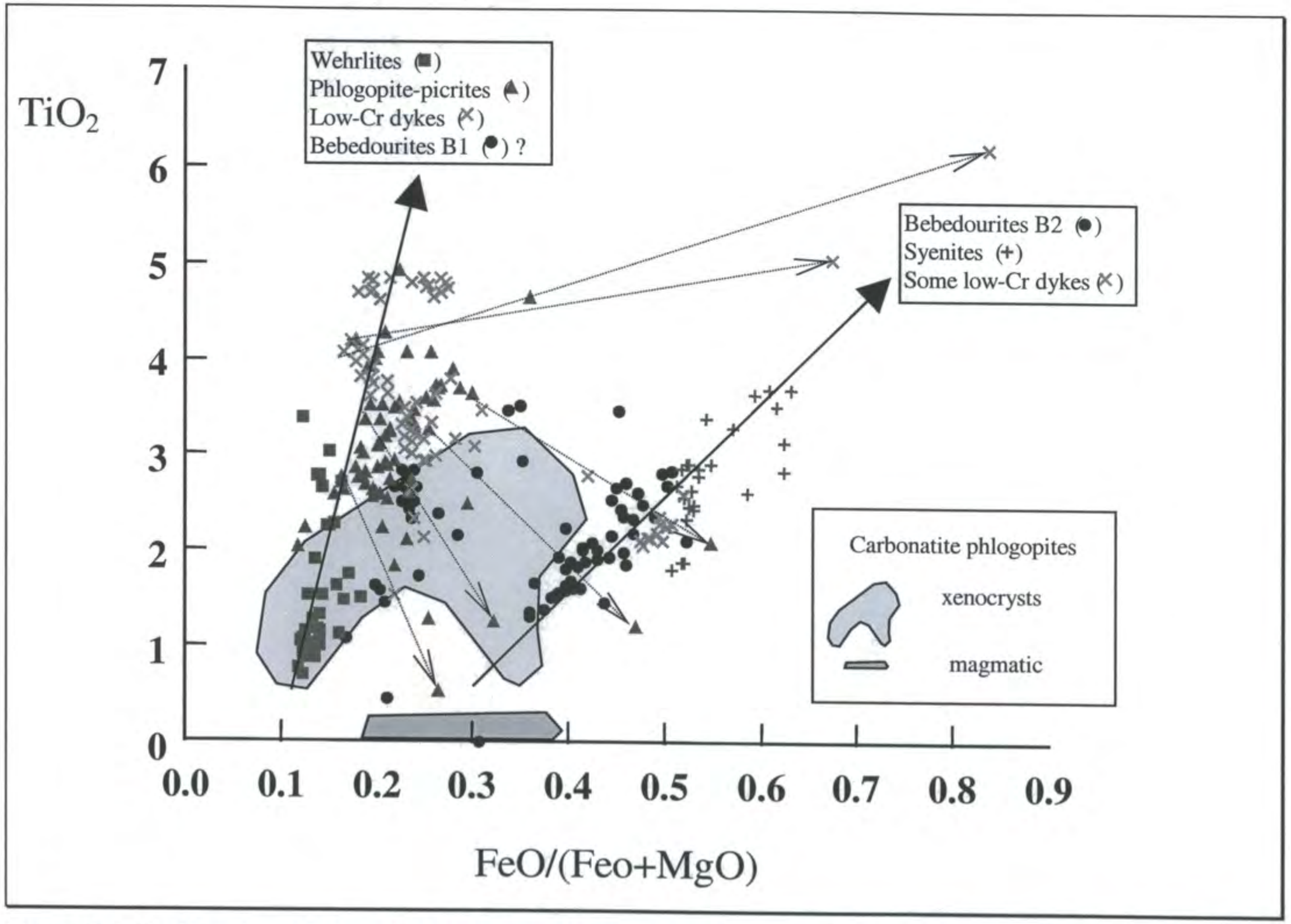

Figure III.4.13 - Variation of TiO_2 with FeO/(FeO+MgO) for micas of the SPS, phlogopite-picrites, and low-Cr dykes. Selected analyses of phlogopite rims in both types of dyke are plotted, and linked to the respective cores by the dashed arrows (arrow direction is core to rim). Compositional fields for xenocrystic and magmatic phlogopites from carbonatite are also shown.

III.4.3 - ORIGIN OF TETRAFERRIPHLOGOPITE

Tetraferriphlogopite is a common variety of mica in the APIP carbonatite complexes. Besides its occurrence in Tapira (Brigatti *et al.*, 1996 and this work), it has also been described from the intrusions of Araxá (Cruciani *et al.*, 1995), Salitre (Lloyd and Bailey, 1991) and Catalão (Araújo and Gaspar, 1993; Araújo, 1996).

Lloyd and Bailey (1991) described tetraferriphlogopite from the Salitre complex, associated with carbonate-silicate cryptocrystalline material in bebedourites. They interpreted the mica as a late-stage product, but consider the evidence to be inconclusive as to whether it crystallised from the residual liquid or resulted from introduction of material after crystallisation. Morbidelli *et al.* (1995a) reported the presence of tetraferriphlogopite in carbonatites and fenites from Salitre. Gaspar and Araújo (1995) and Araújo (1996) interpreted the tetraferriphlogopite of Catalão as the result of metasomatic interaction of the early-formed ultramafic rocks with carbonatite magma, in a process that led to the transformation of dunites and pyroxenites into phlogopitites. Issa Filho *et al.* (1984) interpreted the glimmerites of the Araxá complex as being of metasomatic origin, formed by phlogopitisation of ultramafic rocks. Although they do not provide phlogopite analyses (and the Araxá mica studied by Cruciani *et al.*, 1995 comes from a sovite), the textural features of the Araxá glimmerites resemble the reaction rock of Tapira.

Brigatti *et al.* (1996) studied the crystal chemistry of Tapira phlogopites. They suggested that the formation of tetraferriphlogopite (i.e. $^{(IV)}Fe^{3+}$ substitution accompanied by inversion of pleochroism and depletion in Al and Ti) is a magmatic process and increases with fractional crystallisation, in the sequence dunite ⇒ wehrlite ⇒ clinopyroxenite ⇒ bebedourite ⇒ garnet-magnetitite ⇒ perovskite-magnetitite ⇒ glimmerite ⇒ carbonatite. In fact they propose the division of Tapira rocks in two magmatic systems, one (alkaline-silicate system) including the first four rock types in that sequence and the other (silicate-carbonatite system) comprising the remaining three. However, their petrographic descriptions suggest that the studied rocks are mostly varieties of cumulate from the ultramafic magmas of the SPS. Perovskite- magnetite- and garnet-rich cumulates, for instance, are commonly associated with pyroxenites in Tapira and the very low TiO_2 content of Tapira carbonatites (see Chapter IV) suggests that the carbonatite liquid is unlikely to produce Ti-rich cumulates. Furthermore, the specimens described by Brigatti *et al.* (1996) do not include syenites or true carbonatites (maximum CO_2 content reported is 14.28%). Finally, they report the formation of hematite rims associated with tetraferriphlogopite, which could be the result of metasomatic processes.

The results of the present work - using a wider range of petrographic types - indicate that magmatic mica in the SPS evolves from phlogopite towards biotite, rather than tetraferriphlogopite, and that Ti contents of phlogopite increase with fractional crystallisation, albeit in a scenario of multi-stage magmatic evolution. It was also demonstrated in previous sections that magmatic crystallisation of tetraferriphlogopite is generally restricted to true (magmatic) carbonatites, the possible exceptions being groundmass mica in some carbonate-rich phlogopite-picrites. Whilst agreeing with the evolution proposed by Brigatti *et al.* (1996) for the ultramafic rocks (increasing Fe and Ti with decreasing Mg) and, indeed, extending this model to the most differentiated rocks (syenites), the results of the present research do not support their model of magmatic progression from phlogopite to tetraferriphlogopite in the SPS. Instead, the $^{(IV)}Fe^{3+} \Leftrightarrow {}^{(IV)}Al$ substitution reported by Brigatti *et al.* (1996) as magmatic, closely resembles the evolution of micas in the reaction rock and rims of xenocrysts, as well as that of metasomatic micas in Catalão (Araújo, 1996).

III.4.4 - OXYGEN FUGACITY

Figure III.4.14 provides an estimate of the oxidation state of the liquids from which phlogopite crystallised. Micas from the SPS plot in a trend sub-parallel to the nickel - nickel oxide buffer line, indicating that little variation in oxygen fugacity was involved in the differentiation of the plutonic silicate rocks. Primary tetraferriphlogopite from carbonatites, on the other hand, plot well above the line of the hematite-magnetite buffer, indicating the highly oxidised character of the carbonatite magmas in Tapira. The phlogopite xenocrysts in carbonatites are not plotted in the diagram but span the range of most of the SPS phlogopites, suggesting that the former were crystallised in less oxidising conditions than those prevailing in the carbonatite magma. Phlogopite flakes from C2 define a trend of increasing Fe^{3+} at high Mg, similar to the one proposed by Brigatti *et al* (1996, Figure 6) for the evolution of Tapira rocks. Finally phlogopite from phlogopite-picrites and low-Cr dykes plots along a number of trends of increasing Fe^{3+}

at variable Fe^{2+}/Mg, suggesting that variations in the oxygen fugacity may have occurred during the crystallisation of the dykes. Most phlogopites from dykes plot between the lines of hematite-magnetite and nickel-nickel oxide buffers.

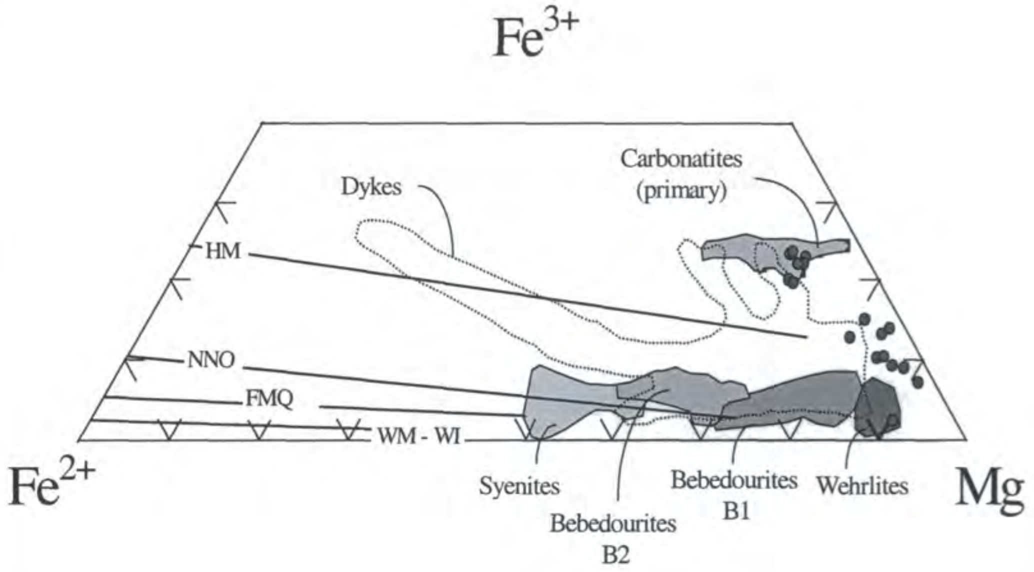

Figure III.4.14 - Composition of primary Tapira micas plotted in the diagram of Wones and Eugster (1965). Oxidation state of the system indicated by the oxygen buffers HM (hematite-magnetite), NNO (nickel-nickel oxide), FMQ (fayalite-magnetite-quartz), WM (wustite-mangetite), WI (wustite-iron). Solid circles indicate phlogopite flakes from carbonatite C2.

III.4.5 - COMPARISON WITH MICA FROM OTHER CARBONATITES AND ALKALINE ROCKS.

Mica composition and evolution in alkaline rocks is strongly dependent on the geochemical affinity of the magma. Mitchell (1995a) summarised the following points regarding compositional variation of phlogopite in potassic alkaline rocks:

- micas rich in both Ti and Ba are characteristic of leucitites and melilitites.
- micas from Group I kimberlites always have low TiO_2 (< 4%) and can evolve along two different trends, one of increasing Al_2O_3 and BaO, and the other of decreasing

Al_2O_3 (towards low-Ti tetraferriphlogopite). The latter is commonly interpreted as secondary in origin.

- Group II kimberlites (orangeites) also show two separate trends, one involving Fe ⇔ Al substitution (phlogopite-tetraferriphlogopite) and the other between the phlogopite-annite end-members.
- phlogopites from lamproites typically have high Ti, and evolve towards Ti and Fe enrichment with (Ti-tetraferriphlogopite) or without (Ti-biotite) Al depletion.
- micas from minettes and lamprophyres show a more variable behaviour, but in minette they are usually Al-rich.

Phlogopite evolution in carbonatites has been described as increasing Mg and Si and decreasing Al, Ti and Fe, coupled with incorporation of Fe^{3+} in tetrahedral sites during the later stages (Heathcote and McCormick, 1989). On the other hand, a similar trend seems to derive from metasomatic processes. McCormick and Heathcote (1987) interpreted tetraferriphlogopite in carbonatites from Arkansas as formed during dolomitisation of previous sovite, with ingress of Si, Mg, Fe^{3+} and removal of Al, Fe^{2+} and Ti from the system.

Figure III.4.15 compares phlogopites from Tapira with other examples of carbonatites and alkaline rocks, in terms of TiO_2 and Al_2O_3 compositions. As a general rule, phlogopite from the SPS, cores of xenocrysts in carbonatites and cores of mica crystals from dykes have Al_2O_3 ranging from 9 to 13 % and limited TiO_2 (up to ≈5%). This coincides roughly with the field for MARID micas and with the low-TiO_2 half of the field for kamafugite phlogopites, but is distinguished from minettes (Roman Province), alkaline rocks from Paraguay and the Brazilian carbonatites complexes of Jacupiranga and Juquiá by the lower Al_2O_3 and more restricted TiO_2. Primary carbonatite micas from Tapira cluster near the origin of the diagram, and cannot be distinguished in the adopted scale. A coupled depletion of TiO_2 and Al_2O_3, leading towards tetraferriphlogopite is typical of metasomatic and late stage micas. This variation is similar to that observed in orangeites, and distinguished from lamproitic tetraferriphlogopites, which are Ti-rich. The field of APIP carbonatite complexes includes analyses of phlogopite from silicate rocks and carbonatites of Salitre and Catalão, roughly coinciding with the compositional range of variation of Tapira micas.

Figure III.4.15 also provides an insight into the relative differences between micas from the APIP and those from other alkaline provinces emplaced around the margins of the Paraná Basin. The field for the Jacupiranga complex includes analyses of phlogopites from ijolitic rocks and carbonatites, with the latter being restricted to the very-low-TiO_2/high-Al_2O_3 end of the diagram. The compositional range occupied by the carbonatite phlogopites is marked by a sudden inflection of the Jacupiranga field towards higher Al_2O_3, suggesting that the latest stages of magmatism in that complex are characterised by high-Al mica. Indeed, Gaspar and Wyllie (1987) stated that micas from the Jacupiranga carbonatites almost always show $^{(VI)}Al$ as high as, or higher than, Fe^{2+}. A similar pattern is shown by the alkaline rocks from Paraguay. Although the field in Figure III.4.14 does not include carbonatite micas, an inflection towards high Al_2O_3 still appears at low TiO_2. Gomes *et al.* (1996b) draw attention to the fact that eastonite-siderophyllite is an important component of micas in the Paraguay alkaline rocks.

The field for Juquiá comprises only phlogopites from silicate rocks, and shows Al_2O_3 comparable to Jacupiranga and Paraguay, for the more restricted TiO_2 range covered. Therefore, the fields of mica from Jacupiranga, Juquiá and Paraguay are roughly coincident, and characterised by high-Al_2O_3 and variable (very low to very high) TiO_2. The lowest TiO_2 portions of the Jacupiranga and Paraguay fields are marked by a sudden increase in Al_2O_3. The TiO_2 / Al_2O_3 ratio is similar to that of minettes and Roman Province. On the other hand, carbonatite complexes of the APIP are characterised by lower Al_2O_3 (similar to that of kamafugite and MARID micas), and a more restricted TiO_2 range. Additionally, carbonatite micas are depleted in Al_2O_3, causing the fields to inflect towards tetraferriphlogopite (thus in the opposite direction to Jacupiranga + Juquiá + Paraguay).

The high-TiO_2 portion of the kamafugite field in Figure III.4.15 consists entirely of micas from APIP kamafugites (Mata da Corda Group, not individualised). If a genetic relationship exists between these rocks and the carbonatite complexes, the Mata da Corda micas may represent the high-Ti equivalent of Tapira/Salitre/Catalão, defining a wider APIP field, still at lower Al_2O_3 than Paraguay/Jacupiranga/Juquiá.

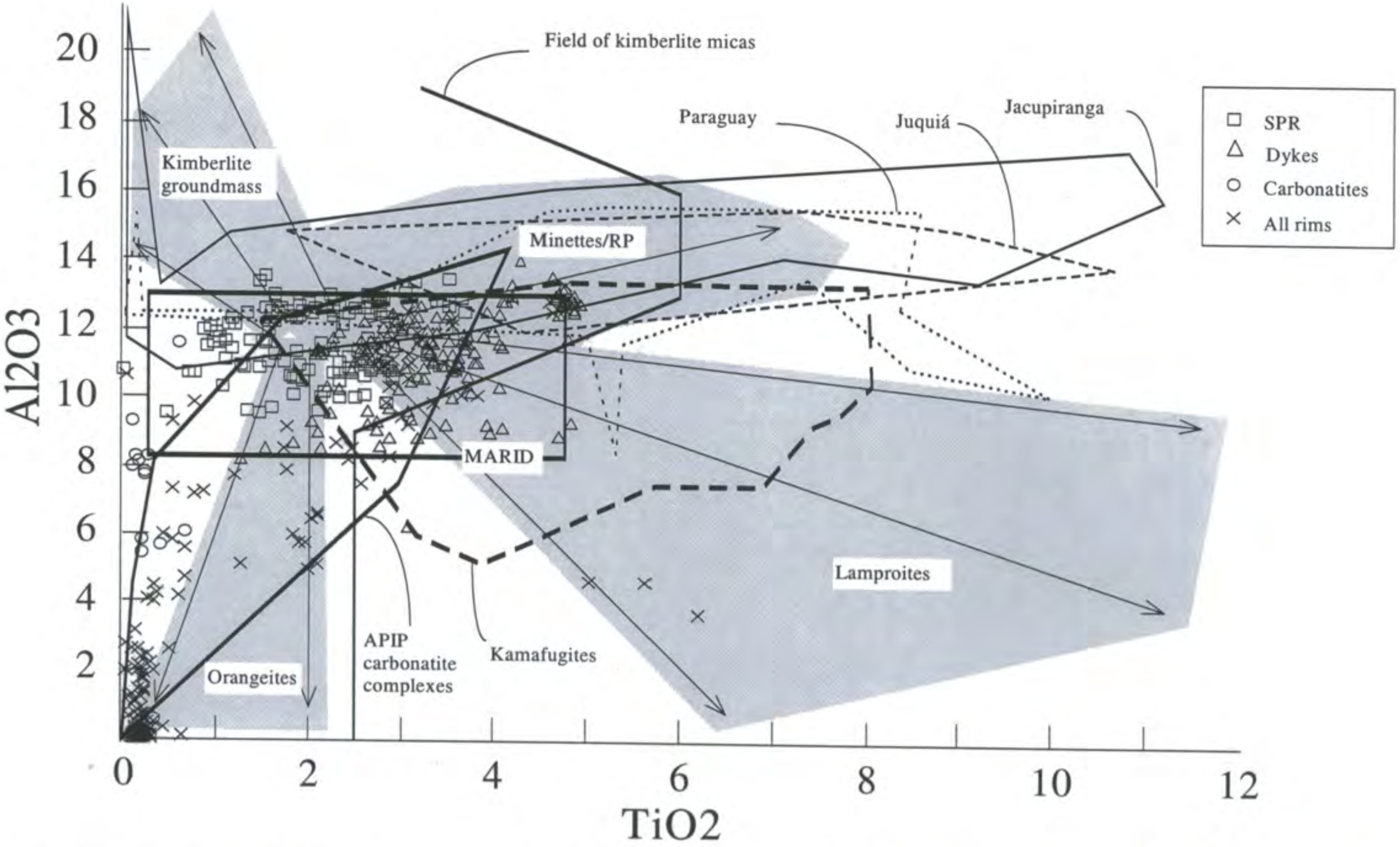

Figure III.4.15 - Al_2O_3 vs. TiO_2 for Tapira micas, compared to other alkaline rocks and carbonatite complexes. Fields for MARID, minette/RP (Roman Province) and kimberlite micas are from Mitchell and Bergman (1991). Trends for kimberlites, lamproites, minettes and orangeites after Mitchell (1995b). Field of kamafugite includes the brazilian occurrences of Mata da Corda (Sgarbi and Valença, 1994; Leonardos et al., 1991; Mitchell and Bergmann, 1991) and Amorinopolis (Danni and Gaspar, 1992), as well as kamafugites from Africa (Edgar, 1979), Italy (Conticelli and Peccerillo, 1992) and Arizona (Laughlin et al., 1989). APIP carbonatite complexes comprise data for Salitre (Lloyd and Bailey, 1991) and Catalão (Araújo, 1996). Fields of alkaline rocks from Paraguay (Comin-Chiaramonti et al., 1992, 1996) and for the Brazilian carbonatite complexes of Juquiá (Beccaluva et al., 1992) and Jacupiranga (Gaspar and Wyllie, 1987; Gaspar, 1989) are also represented.

Finally, it should be noted that the alkaline magmatism in the APIP is Upper-Cretaceous in age, and is interpreted as the result of the impact of the Trindade mantle plume in the lithosphere under southeast Brazil (Gibson *et al.*, 1995b), whereas Jacupiranga and Juquiá are Early Cretaceous and therefore contemporaneous with the Paraná flood-basalt magmatism (which in turn has been associated with the Tristan da Cunha mantle plume). Therefore, mica compositions may be reflecting two different tectono-magmatic situations. It must be stressed that the alkaline rocks from Paraguay cover a wider range of ages (240 to 39 Ma - Gomes *et al.*, 1996a), and the field plotted in Figure III.4.15 is not age-selective.

III.4.6 - SUMMARY

The results of the study of Tapira phlogopites can be summarised as follows:

- Primary phlogopites in carbonatites and silicate rocks seem to evolve independently and follow divergent trends.
- In the silicate plutonic rocks, mica evolves from high-Mg phlogopite in the least differentiated wehrlites to biotite in the more evolved syenites. This variation follows a continuous trend of Fe ⇔ Mg substitution. Ti and Mn also increase with differentiation.
- Ti variation indicates a multi-stage evolution for the SPS. Decreasing pressure and/or increasing oxygen fugacity seem to be the main factors controlling Ti increase in mica from the wehrlites to syenites, whereas temperature is the more significant factor on a local scale.
- Metasomatic micas are characterised by replacement of the original phlogopite by rims and patches of tetraferriphlogopite. The inversion of pleochroism coincides with a sharp decrease in MgO, Al_2O_3 and TiO_2 and increase in FeOt. There is no gradational zoning towards tetraferriphlogopite. The chemical changes involved are distinct from those associated with magmatic differentiation.
- A distinct chemical behaviour is displayed by magmatic tetraferriphlogopite in carbonatites, consisting basically of $^{(IV)}Fe^{3+} \Leftrightarrow Si$ substitution. These micas are virtually Al-free, and form euhedral crystals with oscillatory zoning.

- Textural and compositional evidence indicates that Al-rich phlogopite is not likely to have crystallised directly from the carbonatite magma. The presence of this type of mica in Tapira carbonatites is probably the result of assimilation of phlogopite from the silicate plutonic rock series, either during emplacement of the carbonatites or during the ascent of the carbonatite magma through pockets of partially crystallised ultramafic rock in the magma chamber.
- Alternatively, this variety of mica could have crystallised in equilibrium with a hybrid silicate-carbonate liquid at depth and have been removed from the system during an immiscibility event. Such liquid would have to be ultramafic, as there are no xenocrysts in the carbonatites with composition similar to the syenitic micas.
- If the high-Al micas in carbonatites had crystallised directly from the carbonate liquid (or evolved towards tetraferriphlogopite as a result of magmatic differentiation), a wider range in Fe^{3+} and Al would be expected in the cores of phlogopites from different carbonatite samples. This was not observed in the studied carbonatites, where mica seems to "jump" in composition from Al-phlogopite to tetraferriphlogopite.
- Micas in phlogopite-picrites and low-Cr dykes generally follow the compositional trend of the SPS. Phlogopite-picrites have the more primitive, and low-Cr dykes have the more evolved mica. With respect to mica composition, the dykes may be interpreted as the equivalents of the silicate plutonic rocks. Late-stage sharp chemical changes in phlogopite from the dykes may be signalling the onset of major chemical disturbances in the system, such as liquid immiscibility.
- Micas from Tapira are compositionally similar to those from the consanguineous complexes of Salitre and Catalão, and distinct from micas in the Jacupiranga and Juquiá alkaline-carbonatite complexes. Micas in the dykes and SPS have TiO_2 and Al_2O_3 contents similar to MARID micas and kamafugites, although the field for the latter extends to higher TiO_2.
- If the Mata da Corda kamafugites are considered, the APIP phlogopites define a field that is roughly parallel to that of Jacupiranga + Juquiá + alkaline rocks from Paraguay, but at significantly lower Al_2O_3. In the low-TiO_2 range (defined by the carbonatite micas) the two trends become divergent, inflecting towards low and high Al_2O_3, respectively.

III.5 - PEROVSKITE

Perovskite is an essential constituent of the wehrlites and bebedourites in the silicate plutonic rock series (SPS). It also occurs in the phlogopite-picrite dykes and, rarely, in carbonatites. The presence of perovskite in Tapira has economic significance, because the weathering of perovskite-rich SPS rocks ultimately produces ore-grade concentration of anatase, within the thick soil cover of the complex. The process of perovskite alteration has been studied by Banfield and Veblen (1992) but, despite its economic implications, this is beyond the scope of the present work. Therefore, the following discussion will refer to perovskite solely as part of the original mineral assemblage of the igneous rocks.

Perovskite is the main primary Ti mineral in the Tapira complex and an important host for the rare earth elements in the ultramafic cumulate rocks, having a major effect on the distribution of Ti and the REE during magma evolution.

In wehrlites and bebedourites perovskite occurs as a cumulus phase, accompanying olivine and clinopyroxene. In the phlogopite-picrite dykes it may be present as rare phenocrysts, discrete crystals in the groundmass or rings of discrete grains coating olivine phenocrysts. Perovskite was not found in the syenites, where sphene may occur instead. The perovskite-sphene equilibrium is constrained by temperature and silica activity of the magma, and Veksler and Teptelev (1990) demonstrated that the crystallisation of perovskite in alkaline magmas is inhibited by increasing Si and Al content of the liquid. Accordingly, the absence of perovskite in the syenites reflects the higher activities of Si and Al in the syenite system, compared with the ultramafic cumulates and dykes.

The structure of perovskite can be expressed by the ideal formula ABX_3, where A and B represent cations and X represents anions. In natural perovskites the anions are oxygen, and the formula may be then rewritten as ABO_3. The composition and proportions of the A and B cations, however, can be extremely variable. According to Mitchell (1996c), the A site can be occupied by over 20 elements and the site B by over 50 different elements, rendering perovskite a potentially very complex mineral. Nevertheless, the description of common, naturally-occurring perovskites can be simplified by considering the A site as occupied mostly by Na^+, K^+, Ca^{2+}, Sr^{2+}, REE^{3+}, Pb^{2+} and Ba^{2+}, and the B site by Ti^{4+}, Nb^{5+}, Fe^{3+}, Fe^{2+}, Ta^{5+}, Th^{4+} and Zr^{4+}. Cations in the A-site could therefore be mono- di- or trivalent and cations in the B site could be penta- tetra- or trivalent. More complex compositions can be generated by charge-compensating combined substitutions in the A (e.g. ${Na^+}_{0.5}$, ${Ce^{3+}}_{0.5} \Leftrightarrow Ca^{2+}$) or B (e.g. ${Fe^{3+}}_{0.5}$, ${Nb^{5+}}_{0.5} \Leftrightarrow Ti^{4+}$) sites (Mitchell, 1996c). This set of cations and substitutions is sufficient to explain the most relevant end-members (Table III.5.1) of natural perovskites, apart from silicate perovskites such as $(Ca,Mg,Fe)SiO_3$, which are only important in mantle assemblages (e.g. Deer *et al.*, 1992; Schubert and Tackley, 1995) and will not be discussed here. The microprobe analyses and calculated mineral formulae of Tapira perovskites can be found in Appendix 2.

Perovskite	$CaTiO_3$
Loparite	$(Na_{0.5}Ce_{0.5})TiO_3$
Lueshite	$NaNbO_3$
Latrappite	$Ca(Fe_{0.5}Nb_{0.5})O_3$
Macedonite	$PbTiO_3$
Tausonite	$SrTiO_3$
Synthetic	$KnbO_3$
Synthetic	$BaTiO_3$
Synthetic	$Ce_2Ti_2O_7$
Synthetic	$Ca_2Nb_2O_7$
Synthetic	$CaZrO_3$
Synthetic	$CaThO_3$

Table III.5.1 - End member composition of perovskites (after Mitchell, 1996c)

Figure III.5.1 shows the classification of Tapira perovskites in the system perovskite-loparite-tausonite-lueshite. All analyses plot within a limited composition range, varying from perovskite (*sensu strictu*) to Ce-perovskite, with up to 13.5 mol % of the loparite end-member. One analyses of a perovskite in a carbonatite (sample at043), shows a much higher loparite content (40 mol. %), although it is still classified as Ce-perovskite. Unfortunately, given the paucity of perovskite in the studied carbonatites, this is the only analysed perovskite grain from this rock type. The higher REE content of this perovskite is consistent with the generally accepted notion of REE-enrichment in this mineral with magma evolution. It is also noteworthy from Figure III.5.1 that all analysed perovskites have very low abundance of the tausonite and lueshite end-members.

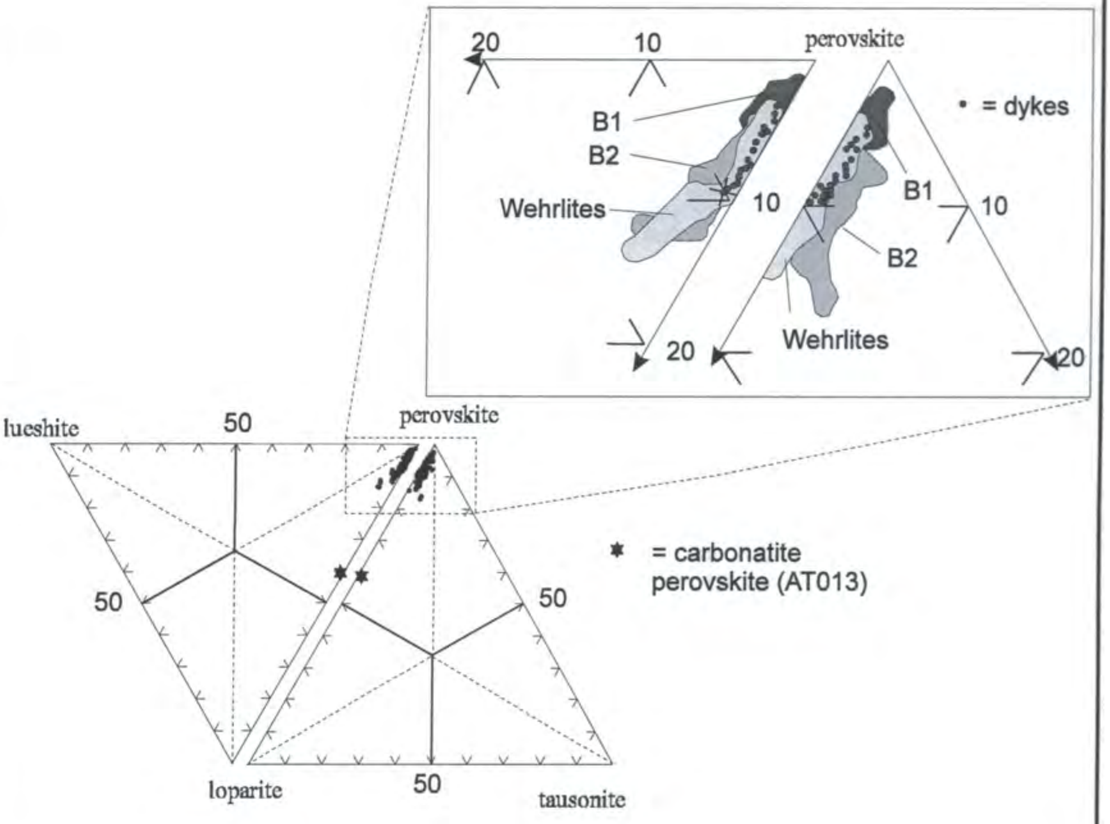

Figure III.5.1 - Classification of Tapira perovskites in the system perovskite-loparite-lueshite-tausonite. The analyses plot along the perovskite-loparite line, with very little contribution of the lueshite (Nb) and tausonite (Sr) end-members. The inset is a blow-up of the sector containing perovskites from the SPS.

The inset in Figure III.5.1 shows the composition of perovskites from different Tapira silicate rocks. Perovskites from the B2 bebedourites are more enriched in REE (loparite) than those from B1 bebedourites. They also show slightly higher Sr (tausonite) and Nb (lueshite) contents. Perovskites from wehrlites overlap the field for both types of bebedourite and partly coincide with perovskites from the phlogopite-picrite dykes. Some perovskites from wehrlites have slightly high Nb, similar to those of

B2 bebedourites but, in contrast with the latter, this is not accompanied by an increase in Sr. Perovskite from both wehrlites and phlogopite-picrites are typically poorer in the tausonite end-member than those in the bebedourites, although it should be stressed that the tausonite component is low in all Tapira perovskites.

III.5.1 - MAGMATIC EVOLUTION OF PEROVSKITE

The composition of perovskite can be related to the stage of evolution and to the type of magma from which it crystallised. As suggested by Veksler and Teptelev (1990), perovskite can be a relatively early-crystallising phase in silicate liquids. Its abundance in the ultramafic cumulates of SPS is consistent with this concept and indicates that it crystallised relatively early in the evolution of the complex. The normal evolution of perovskite in alkaline magmas is one of replacement of Ca by REE, Na, Sr, and replacement of Ti by Nb, i.e. early-formed Ca-Ti perovskite progresses towards lueshite and/or loparite with magmatic evolution (Mariano and Mitchell, 1991; Mitchell, 1996c).

Perovskite in ultramafic cumulate rocks is usually close to the $CaTiO_3$ composition. Mariano and Mitchell (1991) recognised some REE enrichment in perovskite from bebedourites of APIP carbonatite complexes, and related this to the interaction of early perovskite with late-stage hydrothermal fluids. They also pointed out that "*significant Sr and Na enrichment does not occur in these perovskites and they thus differ from perovskites in carbonatites*". In more evolved rocks, such as syenites, significant contents of the lueshite and tausonite end-members may be present (e.g. Mitchell and Vladykin, 1993). Further, perovskite in pegmatites associated with ultrapotassic syenite complexes and in some carbonatites may also show late-stage enrichment in Th (e.g. Mitchell, 1996c; Mitchell and Chakhmouradian, 1998).

This general pattern of perovskite chemical evolution is probably an oversimplified model, especially on a small scale. Campbell *et al.* (1997) demonstrated the presence of oscillatory and reverse (towards purer $CaTiO_3$) zoning patterns of individual Ca-Ti perovskites in ultramafic rocks from the Gardiner complex (East Greenland). They interpreted this as the result of chemical changes in the system, such as influx of new fluids or back-reaction of perovskite with the liquid. Nevertheless, they point out that perovskite-group minerals in the ultramafic rocks from Gardiner are Ca-Ti perovskite, whereas Nb-rich loparite (ca. 10% Nb_2O_5) occurs in syenite, thus confirming the tendency of REE and Nb-enrichment with magmatic evolution over a larger scale. Less often, unevolved Ca-Ti-perovskite has been reported in syenites (Magnet Cove, Flohr and Ross, 1990).

Perovskites from carbonatites usually evolve by progressive Na- and REE-enrichment (i.e. along the perovskite-loparite solid solution). The preliminary experimental results of Mitchell (1997) indicate that, because of the high solubility of Ti in carbonatite melts, perovskite is a relatively late-stage phase in carbonatite, contrasting with its early-stage crystallisation in silicate magmas. The first perovskite-group mineral in the haplocarbonatite system (at 650 °C and 1 atm) is Ca- and Ti-rich, but loparite can crystallise from the carbonatite liquid at lower temperatures. Under these experimental conditions, lueshite and tausonite are not stable phases in the synthetic haplocarbonatite system. This is consistent with observations in natural carbonatites, where the most commonly observed solid solution is between perovskite (*sensu strictu*) and loparite. Mitchell's results also show that in CO_2-bearing systems, Sr is strongly partitioned into the carbonate minerals rather than to perovskite, which is consistent with the very low tausonite content in the analysis of carbonatite perovskite (Figure III.5.1). In Tapira perovskite co-exists with carbonate in the phlogopite-picrites and in carbonatite. The partition coefficient for Sr between perovskite and carbonate was calculated for three phlogopite-picrite dykes and one carbonatite, according to the relation:

$$K_{Sr}^{(carbonate/perovskite)} = wt\ \%\ SrO^{(carbonate)} / wt\ \%\ SrO^{(perovskite)}$$

It should be noted that the calculations were based in the highest measured Sr content, because the carbonates tend to recrystallise during post-magmatic alteration, with the exsolution of Sr-rich phases (see Section III.9 of this Chapter). The results (Table III.5.2) confirm the strong partition of Sr to the carbonate. Note that this appears to increase with the carbonate content (expressed by wt % CO_2) in the sample.

The low levels of Nb in perovskite from Tapira carbonatite suggests that the system had relatively high levels of F and a relatively low Na/Ca ratio, therefore favouring the crystallisation of pyrochlore, rather than lueshite, as the main Nb phase (e.g. Jago and Gittins, 1993; Chakhmouradian and Mitchell, 1998).

	at022	at120a	at013	at043
CO_2 (wt. %) in whole-rock	5.96	8.22	9.05	25.06
SrO (wt. %) in carbonate	1.3	2.8	2.46	2.35
SrO (wt. %) in perovskite	1.07	0.97	0.83	0.54
$K_{Sr}^{(cc/pv)}$	1.21	2.88	2.96	4.35

Table III.5.2 - Partition coefficient for Sr between carbonate and perovskite ($K_{Sr}^{(cc/pv)}$) in some Tapira rocks.

The strong REE- and Na-enrichment (loparite component) in perovskite from Tapira carbonatite (nearly twice the highest REE content of perovskite in the silicate rocks) is consistent with a late-stage, independent crystallisation of this perovskite from the carbonatite magma, rather than with a xenocrystic origin. In sections III.3 and III.4, pyroxene and phlogopite from this same carbonatite sample were interpreted as xenocrysts. The fact that these two minerals are compositionally similar to their counterparts in the ultramafic rocks, whereas the perovskite has such an evolved composition, reinforces the concept that pyroxene and phlogopite in this carbonatite are xenocrysts. In fact, the high solubility of perovskite in carbonatite liquids (Mitchell, 1997) would probably favour the assimilation of any xenocrystic perovskite that entered the carbonatite liquid together with pyroxene and phlogopite.

III.5.2 - OXYGEN FUGACITY

The iron content of perovskite have been interpreted as an indication of oxygen fugacity (e.g. Dawson *et al.*, 1995). Accordingly, the low iron content in perovskites from the SPS wehrlites (up to 3.55 wt. % FeO) and bebedourites (up to 1.87 wt. % FeO) suggests that these rocks formed under relatively low oxygen fugacity. On the other hand, the analysis of perovskite from carbonatite yielded a much higher iron content (11.31 wt % FeO) and this perovskite is therefore interpreted as having formed under higher oxygen fugacity. This inference is consistent with: a) the occurrence of magmatic tetraferriphlogopite (section III.4) in the carbonatites and its absence in the SPS (except where associated with metasomatic replacement); b) the presence of melanite in the low-Cr dykes and SPS rocks (section III.7). The iron content of perovskites from the carbonate-rich phlogopite-picrite dykes (up to 3.03 wt. % FeO) is slightly higher than those in bebedourites, but similar to perovskites in wehrlite. Increasing oxygen fugacity in the dykes is suggested by the chemical evolution of phlogopite (section III.4), but this feature was not observed in the wehrlites. As suggested for the relatively high-CaO olivines from wehrlites (section III.2), it is possible that some of these perovskites crystallised from a liquid that was slightly more evolved and/or more carbonate-rich than the phlogopite-picrites.

III.5.3 - MINOR ELEMENTS

Rare earth elements (REE)

Several perovskite grains were analysed by electron microprobe, to determine the contents of the measurable rare-earth elements. The sum of the REE oxides varies from 0.73 to 8.12 wt % in perovskites from the SPS, 1.81 to 4.56 wt. % in perovskites from dyke rocks and reaches 17.82 wt. % in the perovskite from carbonatite. Perovskite was also manually separated from one wehrlite (sample at016) and analysed by ICP-MS. The results are presented in Figures III.5.2 and III.5.3, where yttrium (Y) from the microprobe analyses is used as a proxy for Ho.

Figure III.5.2 shows the nearly perfect correspondence of microprobe and ICP-MS data for the REE from La to Sm. The heavier elements Gd and Y (Ho in the ICP analysis) still show good agreement, but some deviation from the ICP values is observed. In fact, if the whole set of analytical data is considered, the scatter in Gd is considerably higher than in the lighter REE, suggesting that the discrepancy in Figure III.5.2 is related to a lower microprobe sensitivity due to the low Gd abundance. The difference between Y (microprobe) and Ho (ICP-MS) results may also be attributed to a combination of low microprobe sensitivity and, perhaps, to small differences in the geochemical behaviour of Y and Ho in the perovskite. The ICP-MS analyses defines a steep REE pattern in Figure III.5.2, with chondrite-normalised La/Lu ratio of 341, reflecting the strong preference of the light REE for perovskite.

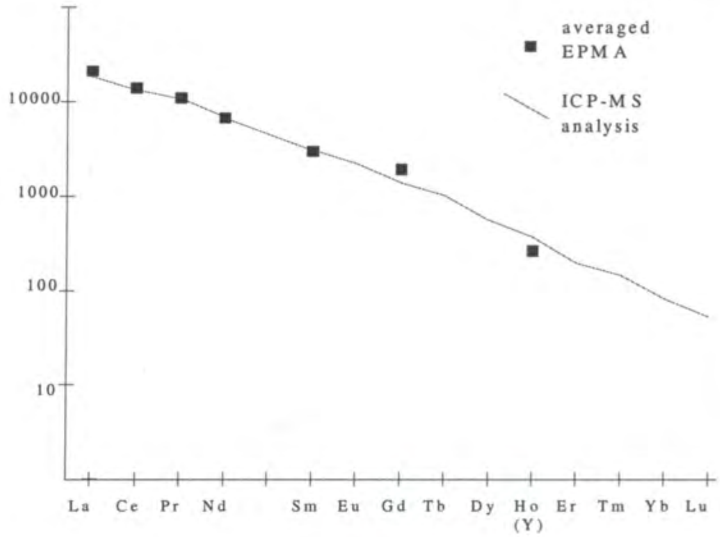

Figure III.5.2 - Comparison of chondrite-normalised REE data from ICP-MS and average microprobe analyses of perovskite in sample AT016. Microprobe yttrium data are plotted as a proxy for Ho.

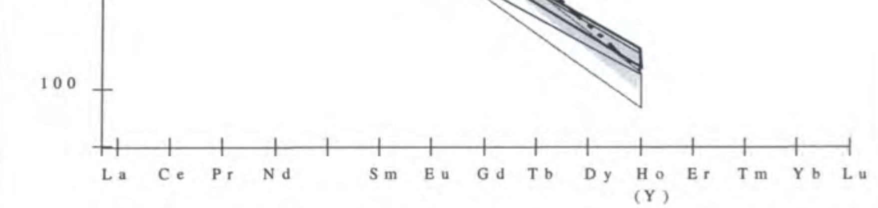

Figure III.5.3 - Chondrite-normalised REE patterns of perovskites in the SPS rocks and in carbonatite at043. The fields represent the compositional variation within each rock type, averaged by sample. Microprobe Yttrium data are plotted as a proxy for Holmium.

Figure III.5.3 shows the variation of REE in perovskite from different Tapira rock-types. The fields represent the range covered by the averaged analyses of different specimens within each unit. The REE abundance and the extent of LREE enrichment between perovskites from different silicate rocks are roughly similar, although the perovskites in B2 bebedourites can be distinguished from those in the B1 bebedourites by their higher LREE concentrations. This is in good agreement with the evidence from other minerals (e.g. phlogopite, clinopyroxene, see relevant sections in this Chapter), that bebedourites in the B2 unit are more evolved than those in B1. However, the presence of complex zoning patters (normal, reverse, oscillatory) in these perovskites suggests that their composition is not simply controlled by a smooth trend of progressive REE enrichment. The fact that the perovskites in wehrlites have REE contents intermediate between B1 and B2 bebedourites (rather than being less evolved than both) suggests that either the rocks crystallised from different liquids or the system underwent a complex evolution history, involving substantial fluctuation of the REE contents.

The perovskite from carbonatite shows significant REE enrichment and a steeper REE pattern, relatively to the silicate rocks. As shown by other elemental variations, this perovskite is clearly different from those crystallised in the SPS.

Zr and Th

Some perovskites from carbonatites and ultrapotassic syenites can be Zr- and/or Th-Rich. Lupini *et al.* (1992) reported up to 3.27 wt. % ZrO_2 and up to 1.7 wt. % ThO_2 in perovskite from the Polino carbonatite (Italy). However, this perovskite is Ca- and Ti-rich and, therefore, not evolved in the sense of Mitchell (1996c). Perovskite in carbonatite complexes of the Kola Peninsula may have up to 4.9 wt. % ThO_2 (Chakhmouradian and Mitchell, 1997). In the APIP, Mitchell (1996c) reported up to 6.19 wt. % ThO_2 in perovskite from a rheomorphic fenite associated with the Salitre complex. Limited Th and Zr data were obtained for perovskite in some of the Tapira dykes and SPS rocks. The results indicate low, albeit measurable, concentrations of Zr (up to 0.51 wt. % ZrO_2) and Th (up to 0.6 wt. %. ThO_2) in these perovskites. The Zr content successfully discriminates perovskites in wehrlites from those in bebedourites, whereby the former reach higher Zr contents (Figure III.5.4). Unfortunately, the perovskite from the Tapira carbonatite was not analysed for Zr or Th during this research, but the high analytical total obtained suggests that neither element is present at a significant level.

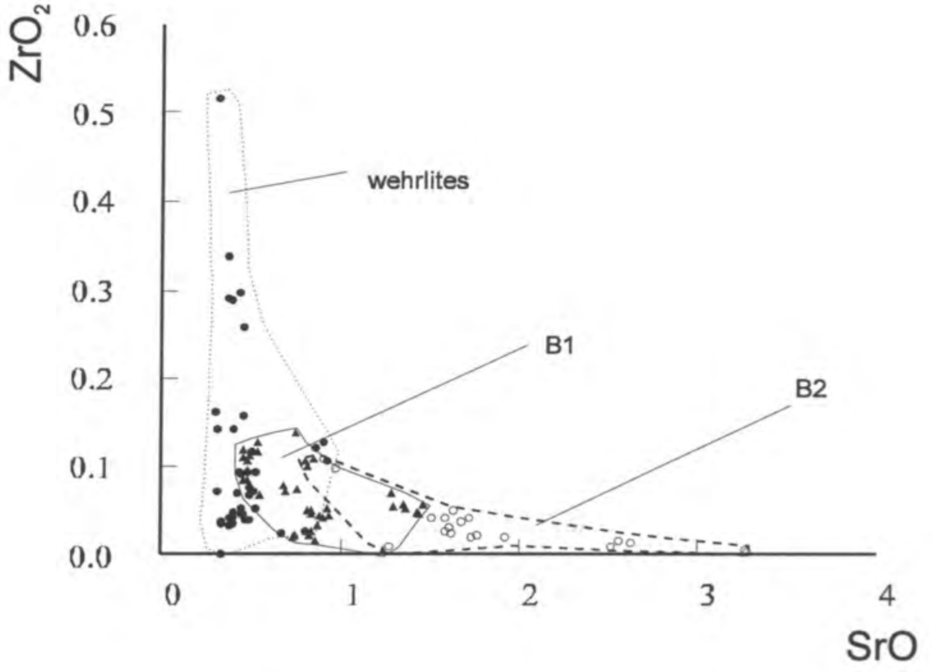

Figure III.5.4 - SrO and ZrO$_2$ (wt. %) variation of perovskites from the SPS.

III.5.4 - COMPARISON WITH OTHER ROCK TYPES

Figure III.5.5 shows the composition of Tapira perovskites in the system perovskite-loparite-tausonite, compared with perovskite in other types of alkaline rocks. It can be seen from the diagram that:

a) perovskites from carbonatite-bearing complexes are usually Sr-poor, evolving along the perovskite-loparite line of the diagram;

b) perovskites in orangeites and lamproites are Ca-Ti-rich, but show significant amounts of the tausonite (Sr) end-member;

c) perovskite-group minerals from syenites and fenites are Ca-Ti-poor and may form continuous solid solution between the tausonite-rich and loparite-rich end-members.

Tapira perovskites follow a trend from perovskite to loparite, similar to that observed in Magnet Cove (Arkansas), Polino (Italy) and Gardiner (East Greenland). Perovskite-group minerals from some carbonatite complexes, such as Schryburt Lake (Ontario), Lueshe (Zaire), and carbonatites from the Kola Peninsula may contain substantial Nb, in addition to the low Sr contents (Platt, 1994; Mitchell, 1996c; Chackhmouradian and Mitchell, 1998). These minerals evolve towards the lueshite end member (not shown in Figure III.5.5), a feature that has not been recognised in Tapira perovskites.

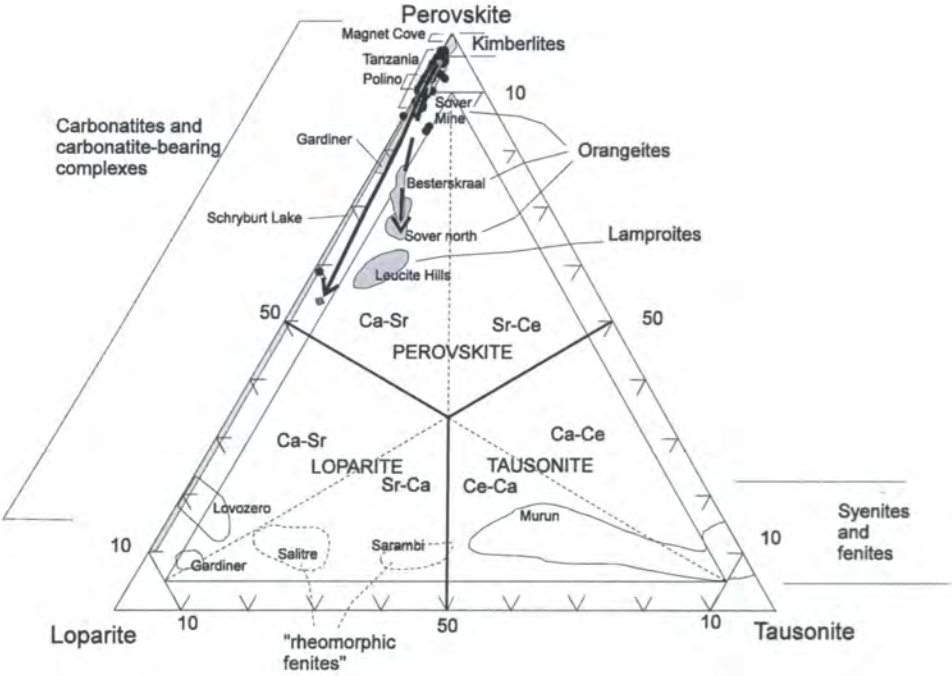

Figure III.5.5 - Composition of Tapira perovskites in the system Perovskite - Loparite - Tausonite (mol %). Tapira perovskites classify as perovskite (sensu strictu) and Ce-perovskite. The dashed arrow shows the evolution trend of perovskite in the Sover orangeites. Solid arrow shows the evolution trend of Tapira perovskites. Also shown are the compositional ranges of perovskites from Tanzanian nephelinites (Paslick et al., 1996), Schryburt Lake (Platt, 1994), Gardiner (Campbell et al., 1997), Magnet Cove (Flohr and Ross, 1989), Polino (Lupini et al., 1992). Other fields are from Mitchell (1996c).

Finally, the overall composition of the Tapira perovskites is similar to the ranges reported by Sgarbi and Valença (1994) and Sgarbi and Gaspar (1995) for perovskites from the Mata da Corda kamafugites (Alto Paranaíba Igneous Province). These are close to the perovskite end-ember, with limited solid solution towards loparite (i.e. average REE content of 3 wt. %; Sgarbi and Gaspar, 1995).

III.5.5 - SUMMARY

- Perovskite-group minerals from the silicate plutonic rocks and from phlogopite-picrites dykes have composition close to the perovskite end-member, with some solid solution towards loparite. One analysis of perovskite from carbonatite shows the strongest enrichment in the loparite molecule.
- Perovskite is an important REE carrier in Tapira rocks. The REE patterns are steep, with strong enrichment in the light REE. The fractionation of perovskite during the formation of the wehrlites and bebedourites should influence the distribution of REE in the liquid.
- The proportions of the Sr and Nb end-members (tausonite and lueshite) are low in all Tapira perovskites. In carbonate-bearing rocks, Sr is preferentially partitioned to calcite. The low Nb content of carbonatite perovskite suggests a high activity of fluorine and a low Na/Ca in the carbonatite magma, which would favour the crystallisation of pyrochlore as the main Nb mineral.
- Perovskites from B2 bebedourites are more evolved than those from B1. Perovskites from wehrlites are broadly similar in composition to those of the phlogopite-picrites, but may show slightly higher Nb contents. The composition range of wehrlite perovskites overlaps that of perovskites in B1 and B2 bebedourites.
- Tapira perovskites are similar in composition to those of other carbonatites and carbonatite-bearing complexes (Magnet Cove, Polino, Gardiner), and to perovskites from the Mata da Corda kamafugites. They are distinguished from perovskites in syenitic rocks by their much lower Sr contents. They also differ from perovskite-group minerals occurring in some carbonatites (e.g. Schryburt Lake, Ontario; Lueshe, Zaire; carbonatites from the Kola Peninsula), which are Nb-rich.

III.6 - OPAQUE MINERALS

The oxide minerals present in Tapira rocks comprise spinels (chromite, magnetite) and ilmenite. Magnetite is by far the most abundant species, occurring in both carbonatites and silicate rocks. Chromite is restricted to phlogopite-picrites and, occasionally, wehrlites. Ilmenite is rare, occurrings in few samples of carbonatites and silicate rocks. The composition ranges of Tapira oxide minerals are given in Table III.6.1. The complete set of microprobe analyses and the correspondent mineral formulae can be found in Appendix 2. Ferric/ferrous ratios were estimated from microprobe results according to the method of Droop (1987).

	Chromite	Magnetite	Ilmenite
TiO_2	5.40 - 11.96	0.35 - 19.00	32.57 - 54.28
Al_2O_3	3.18 - 8.09	0.00 - 2.74	0.00 - 0.03
Cr_2O_3	20.12 - 43.60	0.00 - 5.57	0.00 - 1.65
FeO_T	28.28 - 50.60	63.55 - 93.59	39.11 - 50.43
MnO	0.27 - 0.60	0.00 - 2.76	0.07 - 4.19
MgO	8.97 - 11.64	0.10 - 9.95	0.00 - 10.62
ZnO	0.00 - 0.12	0.00 - 0.048	0.00 - 0.18

Table III.6.1 - Compositional range (oxides wt. %) of Tapira magnetites, chromites and ilmenites. FeO_T *= total iron as FeO*

III.6.1 - SPINELS

The spinels from dyke rocks (phlogopite-picrites and low-Cr dykes) show compositional characteristics that are distinct from those in the associated coarse-grained plutonic rocks (SPS and carbonatites). For clarity, spinel analyses from these two groups are represented separately in Figures III.6.1 and III.6.2.

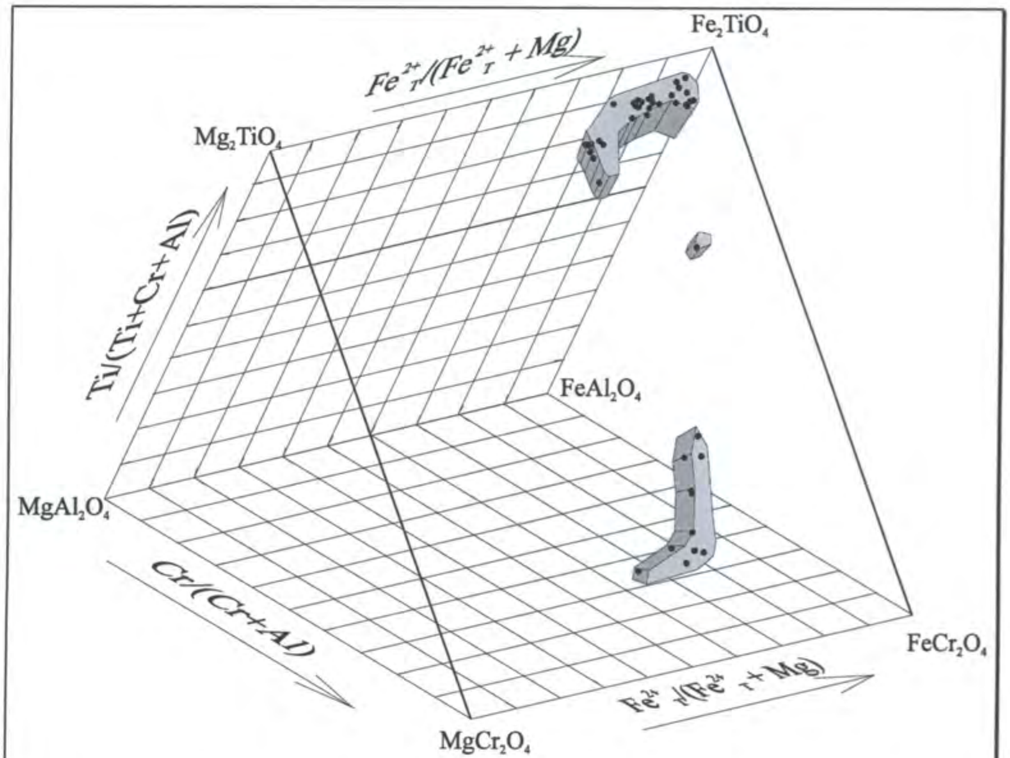

Figure III.6.1 - Representation of the composition of spinels from dyke rocks (phlogopite-picrites and low-Cr dykes) in the spinel prism. Fe^{2+}_T *= total iron calculated as* Fe^{2+}

Figure III.6.1 shows the composition of chromites from phlogopite-picrite dykes and magnetites from both phlogopite-picrites and low-Cr dykes. In this diagram, chromite analyses cluster near the bottom face of the prism and magnetites plot near the ulvöspinel (Fe_2TiO_4) apex. One isolated analysis plots between these two clusters, suggesting that a wider range of solid solution may exist between them. The trend of chromite evolution starts with an increase in the Fe/(Fe + Mg) ratio and later inflects towards relative Ti enrichment and Al and Cr depletion, at roughly constant Fe/(Fe+Mg). Magnetites follow a trend of early increase in the Ti/(Ti+Cr+Al) ratio with little change in Fe/(Fe+Mg), quickly inflecting towards progressive Fe/(Fe+Mg) increase. It is noteworthy that the least evolved magnetites have a Fe/(Fe+Mg) ratio similar to that of the most evolved chromites.

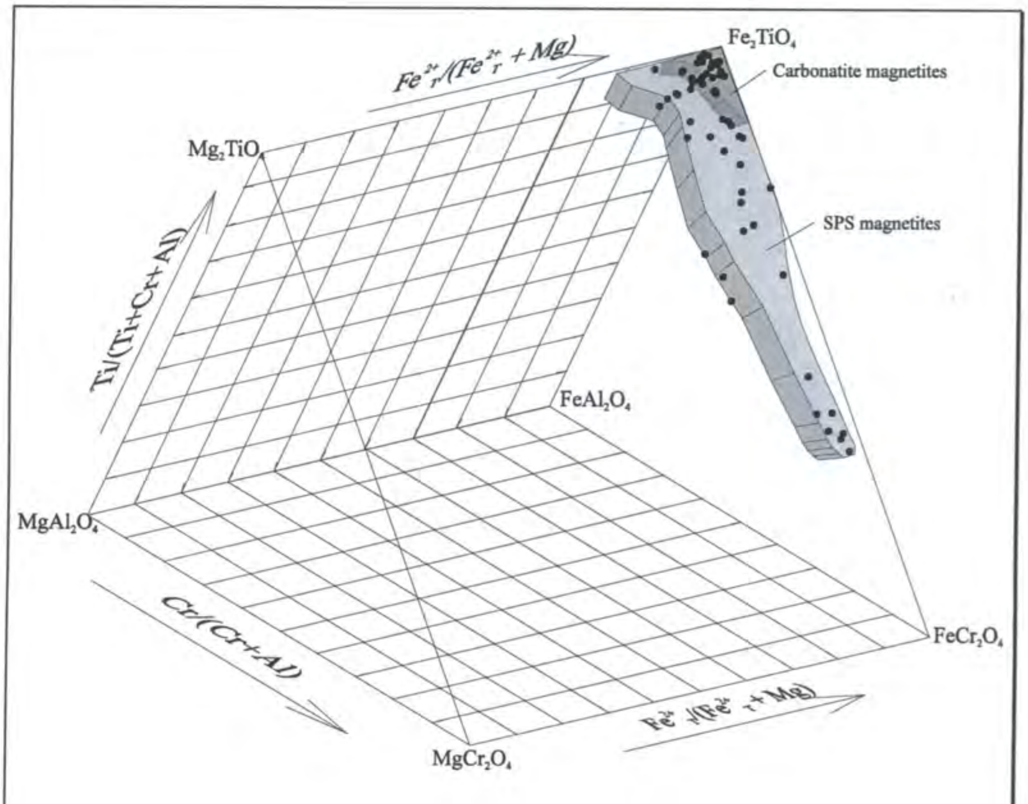

Figure III.6.2 - Composition of magnetites from the SPS and carbonatites, in the spinel prism. Fe^{2+}_T *= total iron calculated as* Fe^{2+}

Figure III.6.2 represents the composition of magnetites from the SPS and carbonatites. These spinels are characterised by a higher Fe/(Fe+Mg) than those from the dyke rocks. Magnetites from the SPS span a relatively wide compositional range. However, it must be emphasised that both Cr and Al contents are low in these magnetites and the apparent variation in the Cr/(Cr+Al) ratio could be partly induced by analytical scatter at low concentrations. Despite the considerable extent of compositional overlap in SPS magnetites, a consistent variation has been recognised in the sequence wehrlites ⇒ bebedourites (B1) ⇒ bebedourites (B2). This is marked by progressive depletion in TiO_2 and MgO, coupled with an increase in total iron (FeO_T) and in the estimated Fe_2O_3, but not in the estimated FeO contents. Manganese does not vary systematically between different SPS rock groups. Carbonatite magnetites plot in a very restricted field close to the ulvöspinel apex in Figure III.6.2. This reflects an extreme depletion in both Cr and Al, rather than an increase in Ti, when compared with the magnetites from the SPS.

The presence of Cr-Al-rich spinels in phlogopite-picrites is in good agreement with the less evolved character of these rocks, when compared with the low-Cr dykes. The same is true of the occasional presence of chromite in some, but not all wehrlites (EDS qualitative analyses only), when compared with the chromite-free bebedourites and carbonatites. In Tapira magnetites the chromium content is moderately low. One analysis of magnetite from a phlogopite-picrite yielded 5.57 wt. % Cr_2O_3 but all the remainder have less than 2.11 wt. % Cr_2O_3.

The increase in the Fe/(Fe+Mg) ratio with differentiation in the Tapira spinels is consistent with observations from other examples of alkaline rocks and carbonatites. Gaspar and Wyllie (1983b) pointed out that magnetites from the Jacupiranga complex show an increase in FeO/(FeO+MgO) ratios with decreasing age of the host carbonatite. Iron enrichment with magmatic evolution is also observed in spinels from lamproites (Mitchell and Bergman, 1991) and orangeites (Mitchell, 1995b).

Minor element contents of Tapira magnetites are also consistent with magmatic evolution of the host rock. Thus, magnetites from phlogopite-picrites have the highest TiO_2 (up to 16.8 wt. %), Al_2O_3 (up to 2.74 wt. %), MnO (up to 2.76 wt. %) and MgO (up to 9.95 wt. %), whilst magnetites in the SPS and carbonatites become progressively poorer in all minor elements, leading to compositions close to the ideal magnetite molecule.

Figure III.6.3 further illustrates the compositional differences of the various groups of Tapira spinels. Both Al_2O_3 and MgO are highest in spinels from the dyke rocks. The spinels from the coarse-grained SPS rocks and carbonatites are Al-poor, but the MgO variation suggests that spinels in wehrlites and bebedourites are less evolved than those in carbonatites. Magnetites from the metasomatic reaction rock (see Chapter II) are plotted in Figure III.6.3 for comparison. These are nearly pure magnetite, occupying a small field near the origin of the diagram. The presence of abundant exsolved lamellae of ilmenite in these magnetites suggests that they are the product of low-temperature recrystallisation of primary titanomagnetites from the original ultramafic rock.

In the system $FeO-Fe_2O_3-TiO_2$ (Figure III.6.4), Tapira magnetites plot near the join of the magnetite-(titanomagnetite)-ulvospinel solid solution. Despite the partial overlap of the two compositional fields, most analyses from dykes and coarse-grained rocks plot in separate regions of the diagram. Magnetites from the SPS and carbonatites can be distinguished from those in the phlogopite-picrites by their lower TiO_2 and higher estimated Fe_2O_3 contents. The presence of fine-grained exsolution lamellae of titaniferous phases (ilmenite, titanomagnetite) in SPS magnetites suggests that they have been re-equilibrated at lower temperatures, hence their apparently more oxidised character and the lower TiO_2 contents of the host grains, when compared with magnetites from the dyke rocks.

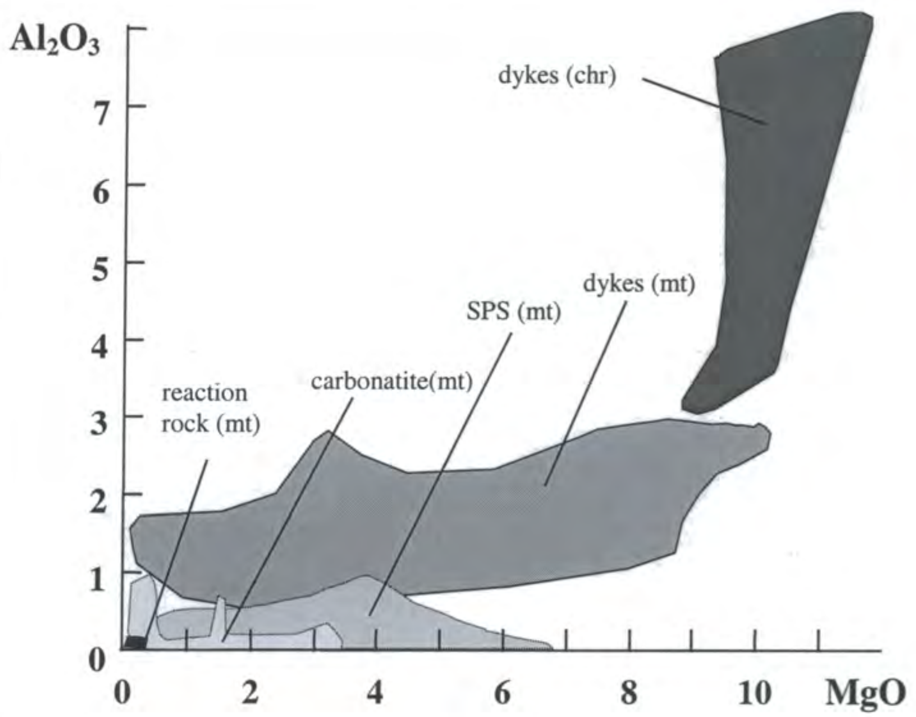

Figure III.6.3 - Al_2O_3 and MgO variation (wt. %) of Tapira spinels with the differentiation of the host rock. chr = chromite; mt = magnetite.

A potential limitation of the diagram in Figure III.6.4 is that it disregards the abundance of minor elements such as MgO, which may be important in this particular type of magnetites. For instance, Gaspar and Wyllie (1983b) reported up to 10 wt. % MgO in magnetites from the Jacupiranga carbonatites and Dawson *et al.* (1996) found magnetites from the Kerimasi carbonatites to contain up to 13 wt. % MgO. Magnetites from Tapira carbonatites are not particularly Mg-rich (up to 3.33 wt. % MgO), but those in the associated silicate rocks can reach up to 9.95 wt. % MgO. The inset in Figure III.6.4 shows the trend of Tapira magnetites when MgO is added to the ternary variable

FeO. The linearity of the trend is substantially improved, due to the removal of the scatter produced by variable amounts of Mg ⇔ Fe^{2+} substitution.

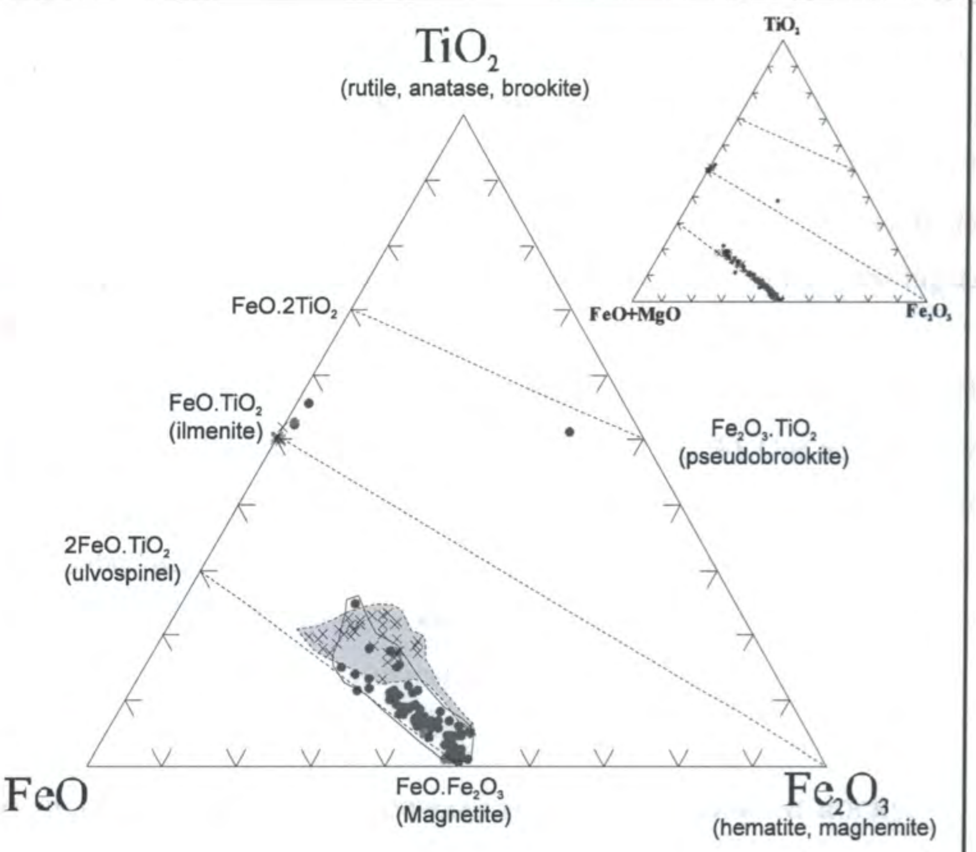

Figure III.6.4 - Composition of Tapira Fe-Ti oxides in the system TiO_2-FeO-Fe_2O_3 (mol. proportions). Circles = phlogopite-picrites + low-Cr dykes, "X" = SPS + carbonatites + reaction rock. The shaded field encompasses magnetites from the dyke rocks and solid line includes all other magnetites. The inset is a plot of the same analyses with MgO added to the FeO variable.

III.6.2 - ILMENITE

Whilst magnetite is a conspicuous mineral in Tapira rocks, ilmenite is relatively rare, and only a few analyses were obtained during the current research. Figure II.6.4 shows that Tapira ilmenites are typically Fe_2O_3-poor, plotting adjacent to the FeO-TiO_2 side of the diagram. The isolated analysis plotting near the TiO_2-Fe_2O_3 side is an exsolved lamella in magnetite from a wehrlite.

The composition of ilmenite can be further described in terms of the end-

The chemical characteristics of Tapira ilmenites (Figure III.6.6) are well within the compositional ranges commonly observed for carbonatite ilmenites and are similar to those of the Catalão carbonatite complex (APIP). The limited data suggests that they are slightly richer in Mg than those from orangeites and slightly richer in Mn than those from kimberlites (except Premier kimberlites), but any further interpretation must await for a more detailed microprobe investigation of Tapira ilmenites.

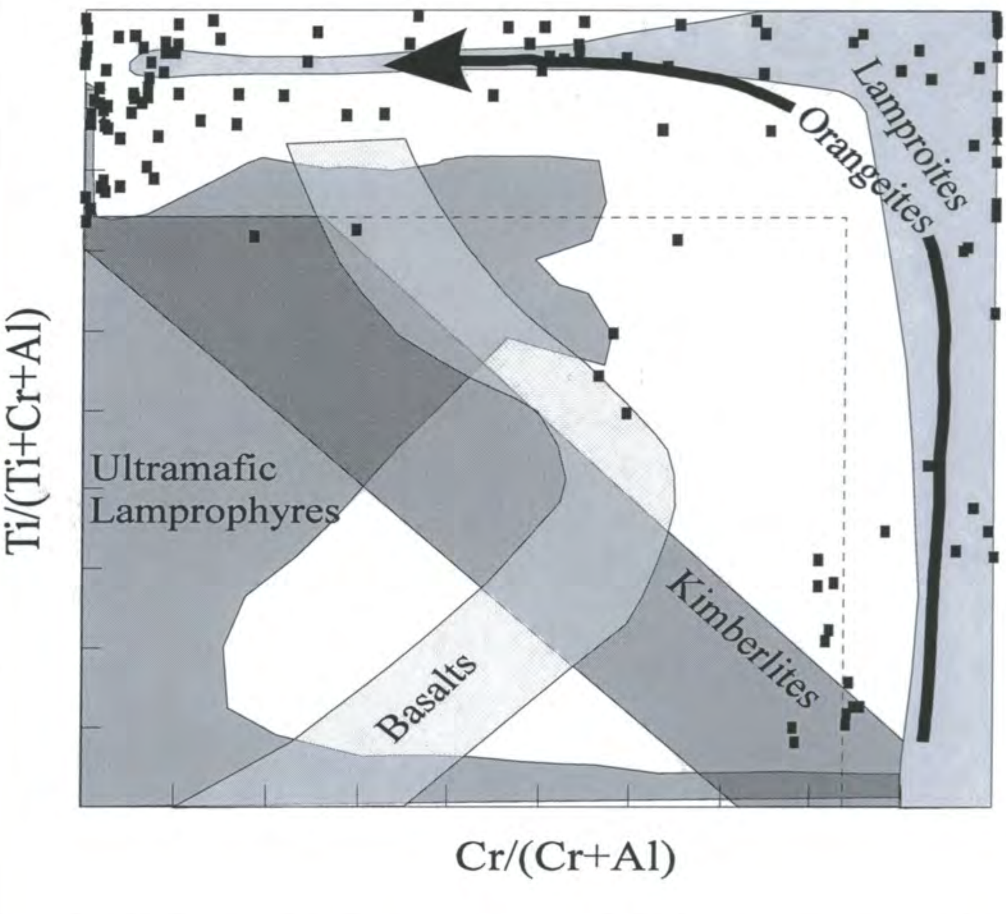

Figure III.6.5 - Composition of Tapira spinels in terms of Cr/(Cr+Al) and Ti/(Ti+Cr+Al), compared with spinels from other types of alkaline rocks. Compositional fields are after Mitchell (1995b).

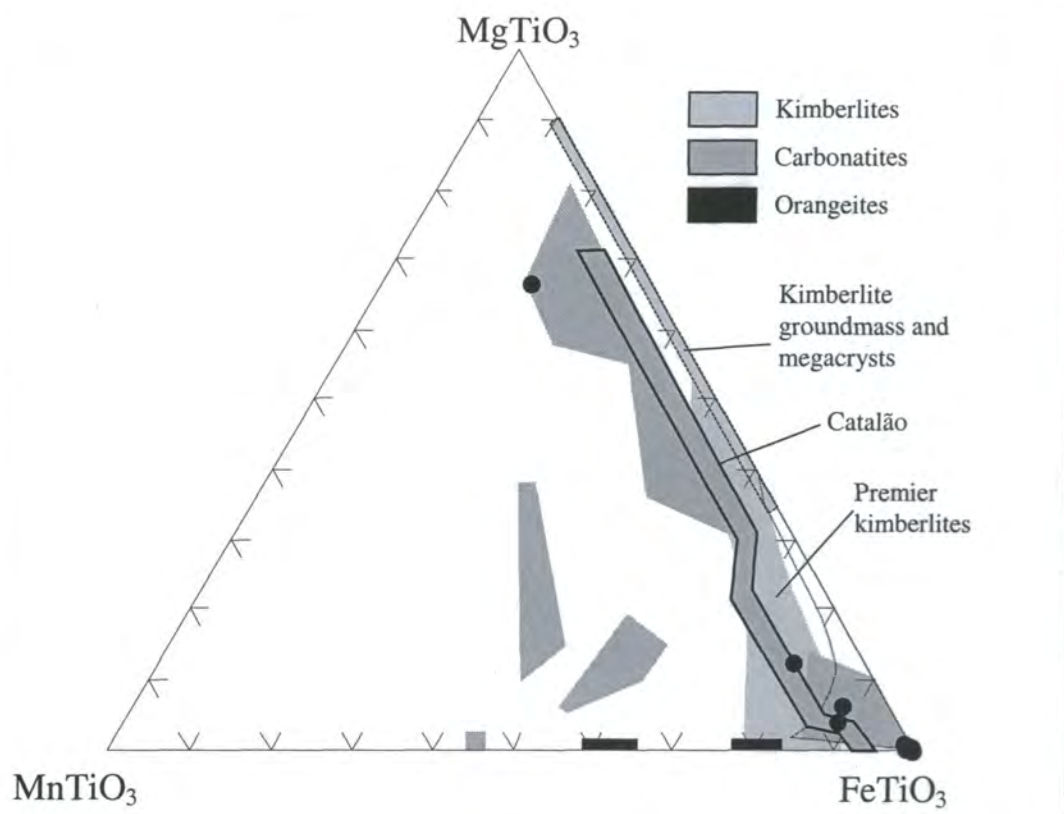

Figure III.6.6 - Composition of Tapira ilmenites (solid circles) compared to those in other types of alkaline rocks, in terms of the main end-members ilmenite, pyrophanite and geikielite. Data for Catalão ilmenites (solid-outlined, dark-shaded) is from Araújo (1996). Other fields as in Mitchell (1995b) and references therein.

III.6.4 - SUMMARY

- Cr-Fe-Ti oxide minerals occurring in the Tapira complex comprise chromite, magnetite and ilmenite.
- The chemical composition of spinels is consistent with the differentiation stage of the host rock. Cr-Al-rich spinels are restricted to the least differentiated rocks (phlogopite-picrites and wehrlites).
- Magnetite has a widespread occurrence, and may be TiO_2- and MgO-rich. Variation in magnetite chemistry is compatible with magmatic differentiation processes, and consistent with patterns observed in other carbonatite complexes.
- Magnetites from coarse-grained plutonic rocks were re-equilibrated at low temperature.

- The composition of Tapira spinels is similar to those in lamproites and orangeites
- Tapira ilmenites are within the compositional range of ilmenites from other carbonatite complexes.

III.7 - GARNET

Yellow to dark-brown titanian garnet occurs in Tapira rocks, either as rims on perovskite crystals from the silicate plutonic rock series (SPS), or as discrete euhedral crystals in the dyke rocks.

The structural formula of garnet can be expressed as $X_3Y_2Z_3O_{12}$, where X, Y and Z represent, respectively, dodecahedral, octahedral and tetrahedral cations. The ideal end-member compositions of common garnets are as follows (Table III.7.1):

Pyralspite garnets	
Pyrope	$Mg_3Al_2Si_3O_{12}$
Almandine	$Fe^{2+}{}_3Al_2Si_3O_{12}$
Spessartine	$Mn_3Al_2Si_3O_{12}$
Ugrandite garnets	
Grossular	$Ca_3Al_2Si_3O_{12}$
Andradite	$Ca_3(Fe^{3+},Ti)_2Si_3O_{12}$
Uvarovite	$Ca_3Cr_2Si_3O_{12}$
Hydrogrossular	$Ca_3Al_2Si_2O_8(SiO_4)_{1-m}(OH)_{4m}$

Table III.7.1 - Ideal end-member compositions of garnet

Tapira garnets are Ca-rich (30.3 - 33.7 wt. % CaO), Al-poor (< 2.4 wt. % Al_2O_3) and Cr-poor (< 0.17 wt. % Cr_2O_3) and, therefore, classify as andradite-type. They also contain variable amounts of TiO_2, ranging from 0.5 to 19.2 wt. %. Microprobe data are given in Appendix 2. Deer *et al.* (1992) further subdivide Ti-rich andradites into melanite and schorlomite, depending on whether Fe^{3+} or Ti predominates in the octahedral site, with the limit between them at approximately 15 wt. % TiO_2. Alternatively, Henmi *et al.* (1995) proposed the existence of a new titanian garnet end-member, which they named morimotoite ($Ca_3Ti^{4+}Fe^{2+}Si_3O_{12}$). This is derived from andradite by the substitution of Ti^{4+} + Fe^{2+} for $2Fe^{3+}$. However, Fehr and Amthauer

(1996) and Rass (1997) argued that this mechanism is inconsistent with the existing Mössbauer and XPS evidence for the presence of both Fe^{2+} and Fe^{3+}, as well as Ti^{4+} and Ti^{3+}, in this type of garnet.

The valency state and preferential cation distribution of Ti and Fe in Ti-rich garnets (Ti-andradite, melanite, schorlomite) remain a subject for debate (e.g. Malitesta *et al.,* 1995; Rass, 1997). Several site-assignment alternatives have been suggested, invoking combinations of some or all the cations Fe^{2+}, Fe^{3+}, Ti^{4+} and Ti^{3+}, and involving the octahedral, tetrahedral and dodecahedral sites. Due to this controversy (see discussion below), the weight percentage of TiO_2 is adopted here as a preferred classification criterion for Tapira garnets (Figure III.7.1). Most analyses fall below 15 wt. % TiO_2 in Figure III.7.1 and are therefore classified as melanites. A lesser number of schorlomitic garnets also occur.

III.7.1 - CATION DISTRIBUTION

The crystal chemistry of Ti-rich garnets often deviates from the site occupancy that would be expected if they were merely derived from andradite by Fe $\Leftrightarrow$ Ti exchange (Huggins *et al.,* 1977a). Melanites and schorlomites typically exhibit a Si deficiency in the tetrahedral site (i.e. Si < 3 cations per formula unit), although the sum of all tetravalent cations (Si + Ti +Zr) usually exceeds the value of 3. The Si deficiency has been correlated with the low activity of SiO_2 in the system from which these garnets crystallised (Dingwell and Brearley, 1985). Furthermore, they are characterised by an excess in divalent cations (X) and a deficiency in trivalent cations (Y).

Due to these apparent inconsistencies, a straightforward application of the ideal formula $X^{2+}_3\ Y^{3+}_2\ Z^{4+}_3\ O_{12}$ is not possible. However, the total number of cations per formula unit is usually close enough to the stoichiometry (8 cations per 12 oxygen) to suggest that mutual substitutions, rather than site vacancy, are responsible for the observed discrepancies. The cation assignment to each one of the different sites in Ti-rich garnets will be discussed in the sections below.

Dodecahedral site occupancy

In Tapira garnets, most of the dodecahedral site is occupied by Ca (2.82 to 3.08 atoms p.f.u.), leaving little scope for substitution by other divalent cations. In a few cases Ca exceeds the stoichiometric value of 3 cations p.f.u., which leads to the completion of the dodecahedral site with calcium alone, and the assignment of the excess Ca to octahedral positions. When Ca falls short of the ideal value of 3 cations p.f.u., possible alternatives to fill the dodecahedral site are Mn, Mg and Fe^{2+} (in addition to all available Na). The assignment of divalent cations to the dodecahedral site, after Ca and Na had been allocated, was made in the conventional order Mn > Mg (Platt and Mitchell, 1979; Dingwell and Brearley, 1985). Although some authors have presented evidence for the existence of Fe^{2+} in the dodecahedral site of Ti-rich garnets (e.g. Kühberger *et al.,* 1989), this was not required here, because Mg always exceeds the

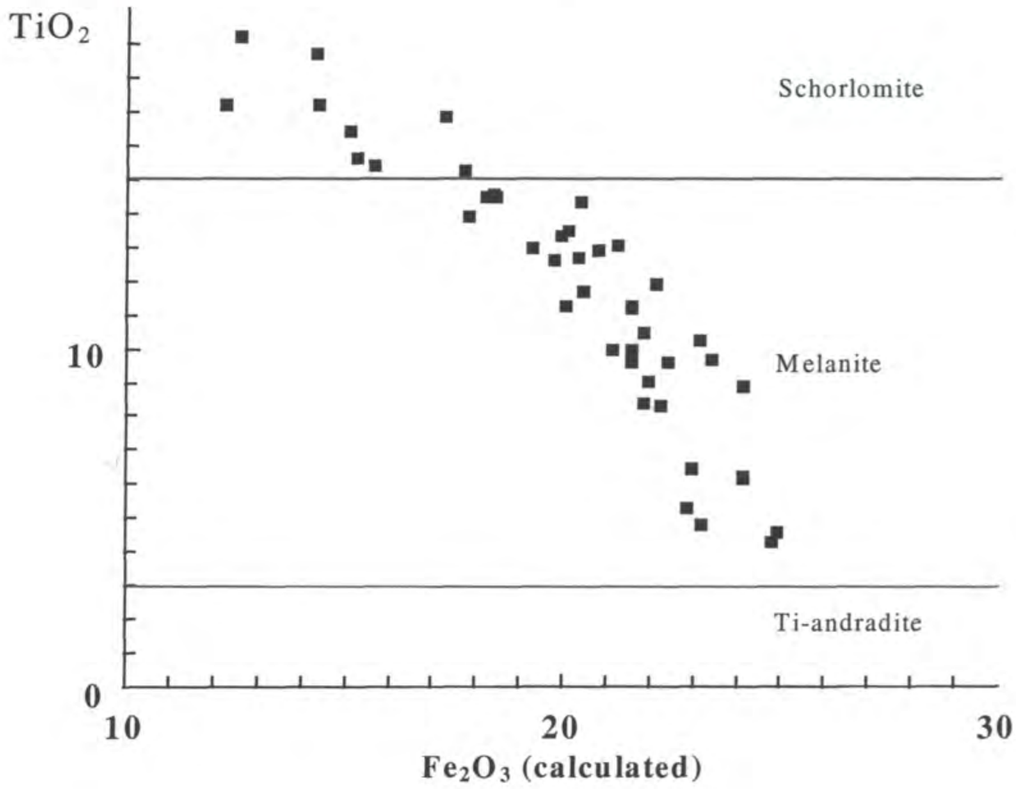

Figure III.7.1 - Classification of Tapira garnets based on the TiO_2 (wt. %) content.

amount necessary to complete the soichiometric site occupancy. Hence, the excess Mg and all Fe^{2+} were assigned to the octahedral site.

Tetrahedral site occupancy

Most Tapira garnets do not have enough Si to fill all the tetrahedral positions (ideally 3 cations p.f.u.). Commonly suggested alternatives to complete the tetrahedral site in melanite garnets are Al^{3+}, Fe^{3+} and Ti^{4+}, but the relative role of these cations and the substitution mechanisms remain a subject of debate. According to Huggins *et al.* (1977a) and Deer *et al.* (1992), the order of preference for tetrahedral occupancy, in addition to Si, must be $Al > Fe^{3+} > Ti$. Other authors argued that Al does not necessarily have the highest priority (e.g. $Fe^{3+} > Fe^{2+} >> Al = Ti$, Locock *et al.,* 1995). Despite existing evidence, from Mössbauer spectrometry, for the presence of tetrahedral Fe^{3+} and Fe^{2+} in Ti-garnets (Huggins *et al.,* 1977a; Dowty, 1971; Locock *et al.,* 1995), several authors argue the case for Ti as a preferred, if not exclusive, substitute for Si in tetrahedral positions (Howie and Woolley, 1968; Huggins *et al.,* 1977b; Dingwell and Brearley, 1985).

Figure III.7.2 shows the variation of the relevant cations with Si. Note that there is no correlation between Al and Si in Tapira garnets, while Fe^{3+} and Si show a positive correlation that effectively precludes mutual substitution. The excellent negative correlation between Si and Ti suggests that $Ti^{4+} \Leftrightarrow Si$ is the dominant substitution in the tetrahedral site. The poor fitting with the 1:1 substitution line in Figure III.7.2 is not unexpected, since Ti is present well in excess of the amount necessary to compensate for the Si deficiency and, consequently, some Ti must be in octahedral co-ordination. In fact, it is evident from the Figure that the maximum deviation from the 1:1 substitution line corresponds with the highest Ti contents.

Howie and Woolley (1968) observed similar features in their study of Ti-rich garnets from several localities and concluded, on the basis of the highly significant negative correlation, that Ti is the main substitute for Si in the tetrahedral site. As at Tapira, these garnets have Ti in excess of that necessary to compensate for Si deficiency.

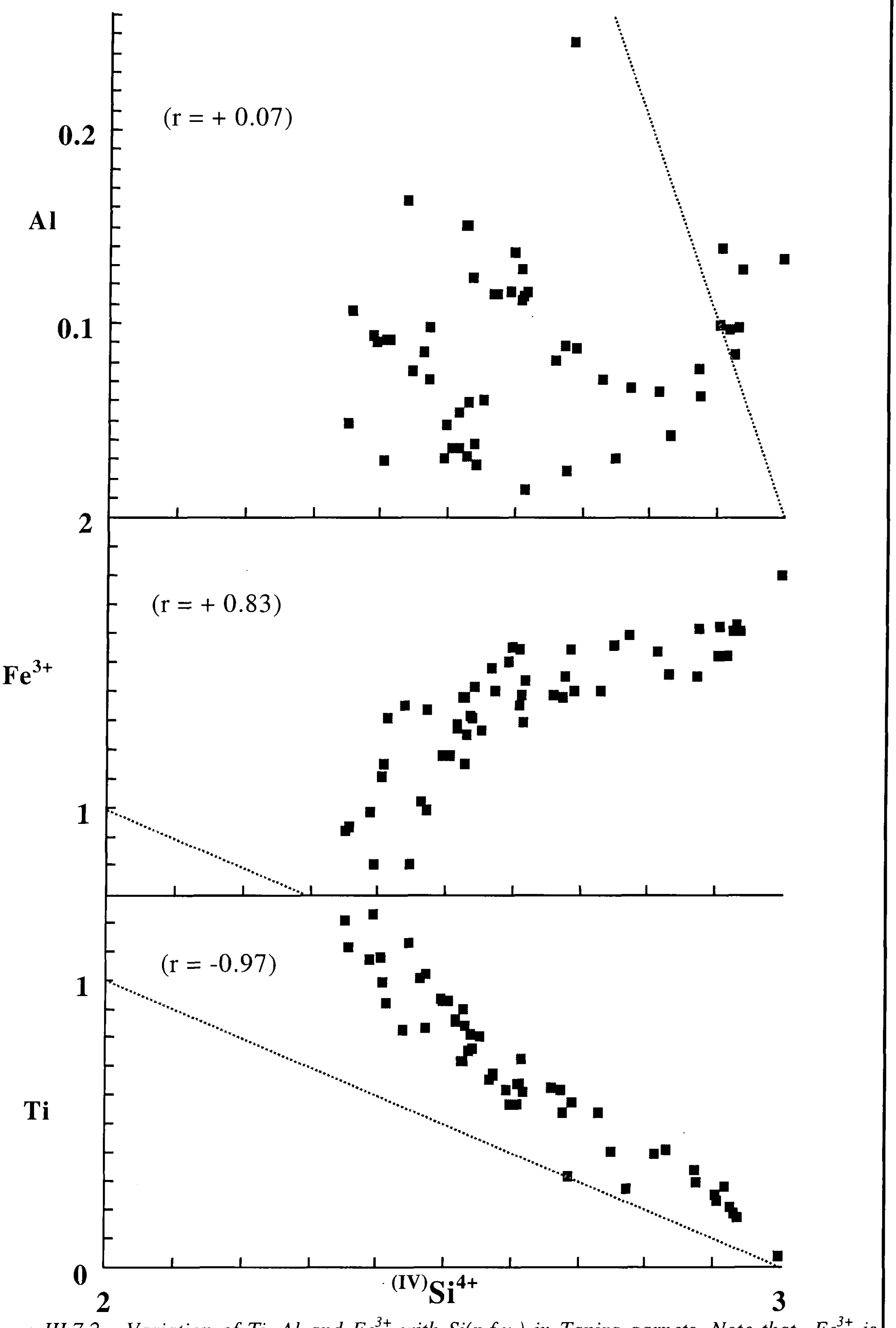

Figure III.7.2 - Variation of Ti, Al and Fe^{3+} with Si(p.f.u.) in Tapira garnets. Note that Fe^{3+} is positively correlated with Si and therefore is not likely to substitute for Si in the tetrahedral site. Al shows no significant correlation with Si, whereas Ti and Si have strong antipathetic correlation. r = correlation coefficient. Dashed lines indicate 1:1 substitution.

Given the mutual relations depicted in Figure III.7.2, Ti is considered the most likely substitute for Si in Tapira garnets. According to the recommendation of Howie and Woolley (1968) and Dingwell and Brearley (1985), Ti was assigned to tetrahedral positions until the completion of the stoichiometric requirements (i.e. $^{(IV)}Ti^{4+} = 3 - Si$). Since Ti + Si is always > 3 in Tapira garnets, all Fe^{3+} and Al, as well as the excess Ti were assigned to the octahedral site.

Substitution of $(O_4H_4)^{4-}$ for $(SiO_4)^{4-}$ (hydrogarnet substitution) has been suggested (Locock *et al.,* 1995; Amthauer and Rossman, 1998) as an alternative mechanism to account for Si deficiency in Ti-rich garnets and there is substantial evidence from infrared spectroscopy for the presence of H_2O in andradite garnets (Muntener and Hermann, 1994; Locock *et al.,* 1995; Amthauer and Rossman, 1998). Amthauer and Rossman (1998) pointed out that the hydrogarnet substitution is temperature-dependent, since they obtained up to 6 wt. % H_2O in garnets associated with low-temperature post-magmatic processes, but only 0.01 to 0.04 wt. % H_2O in high-temperature garnets from volcanic rocks.

The extent of hydrogarnet substitution cannot be directly assessed on the basis of microprobe data alone, although it might be indicated by low analytical totals. Microprobe analyses of Tapira garnets often yield low totals, but these are only weakly correlated with Si deficiency. Furthermore, the presence of Fe^{3+} equally leads to low analytical totals, if total iron is reported as FeO. When Fe_2O_3 is recalculated by stoichiometry and updated in the original analysis, the totals become very close to 100% and their correlation with the Si deficiency disappears completely. Hence, it is suggested that the hydrogarnet substitution is not substantial in Tapira garnets.

Finally, significant amounts of zirconium occur in Tapira garnets (up to 2.6 wt. % ZrO_2). Despite its tetravalent character and clear positive correlation with Ti, the presence of tetrahedral zirconium is considered unlikely, on the grounds of the large size of the ion Zr^{4+} (Dowty, 1971). Platt and Mitchell (1979) recommended the allocation of Zr to the octahedral position in Zr-rich garnets, although it is theoretically possible for Zr to enter the dodecahedral site as well.

Octahedral site occupancy

After completion of the dodecahedral and tetrahedral sites, Fe and Ti were the main remaining cations, with Zr, Mg, Al, Cr and, occasionally, Mn and Ca still available in subordinate amounts. Hence, the most important octahedral substitution is probably that of Ti for Fe^{3+}.

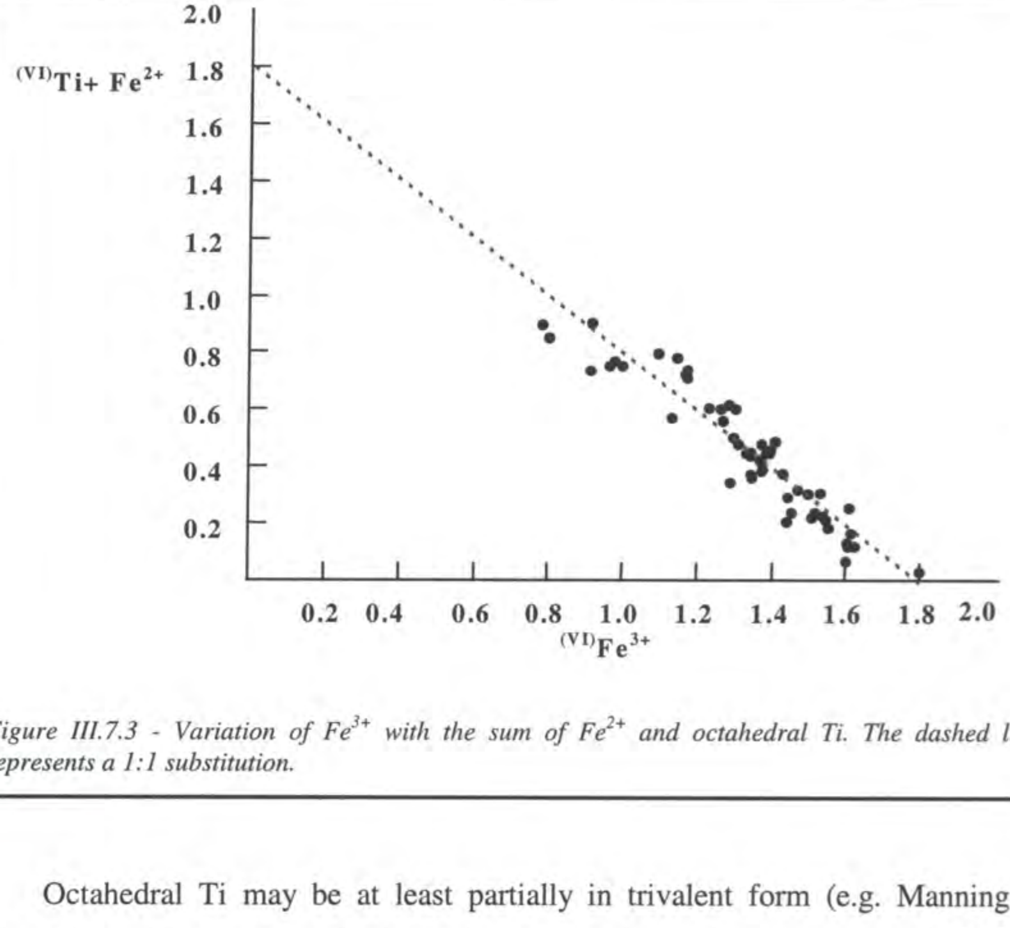

Figure III.7.3 - Variation of Fe^{3+} with the sum of Fe^{2+} and octahedral Ti. The dashed line represents a 1:1 substitution.

Octahedral Ti may be at least partially in trivalent form (e.g. Manning and Harris, 1970; Malitesta *et al.,* 1995), leading to the substitution vector $^{(VI)}Ti^{3+} \Leftrightarrow {}^{(VI)}Fe^{3+}$. There are no means of evaluating the Ti^{3+}/Ti^{4+} ratio from the electron microprobe data alone, but the best charge balances are obtained if all Ti is considered to be tetravalent and the amounts of Fe^{3+} and Fe^{2+} are estimated by stoichiometry (Droop, 1987). These calculations indicate that Fe^{2+} is present in Tapira garnets, although in subordinate amounts. In this case, a possible substitution scheme in the octahedral site would be $Fe^{2+}+Ti^{4+} \Leftrightarrow 2Fe^{3+}$. This seems to be a plausible model, given the strong negative correlation (Figure III.7.3) between the calculated Fe^{3+} and the combined amounts of Fe^{2+} and octahedral Ti (i.e. after deduction of tetrahedral Ti).

Note that the distribution fits well with the 1:1 substitution line, if an average occupancy of 0.2 cations p.f.u. is assumed for the other elements in octahedral co-ordination.

III.7.2 - ZONING

The chemical zoning of melanites and schorlomites is correlated with the optical and physical properties of the mineral (e.g. Howie and Woolley, 1968; Gomes, 1969; Dingwell and Brearley, 1985). In particular, the Ti content seems to have a strong effect on the colour, with higher Ti corresponding to the darker shades. Additionally, the increase in Ti is known to correlate positively with the refractive index, specific gravity and cell-size of andradite-melanite-schorlomite garnets (Howie and Woolley, 1968).

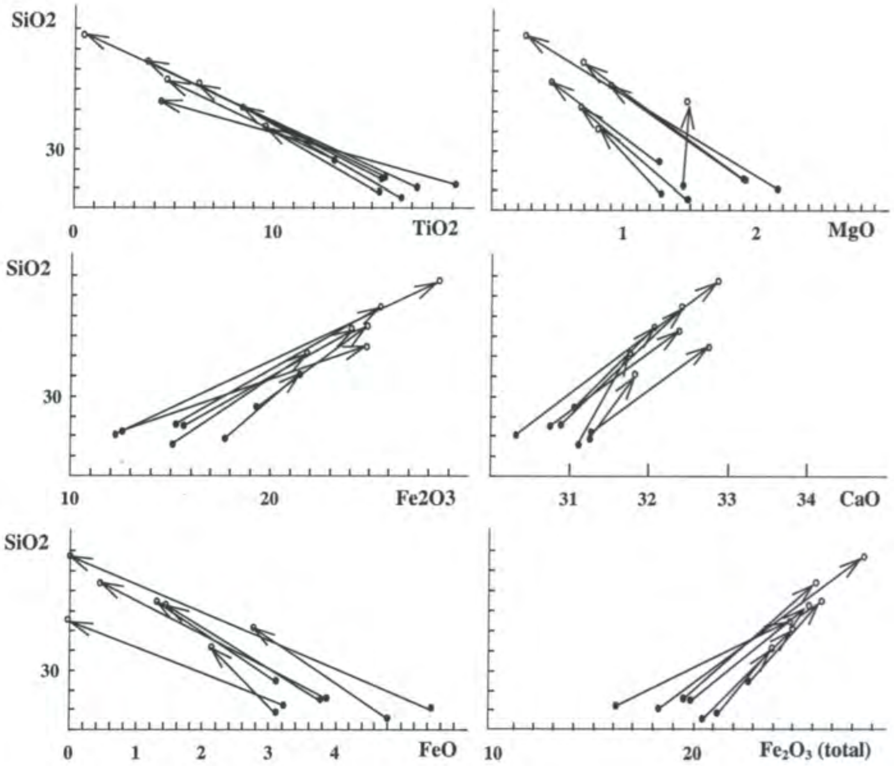

Figure III.7.4 - Chemical variation of selected oxides (wt. %) in zoned garnets from Tapira. Solid circles = cores, open circles = rims. Arrows indicate core-to-rim. Vertical scale for all diagrams is wt. % SiO_2

A number of rim-core points of Tapira garnets were analysed. The results are presented in Figure III.7.4. There is a consistent pattern of variation, with the cores enriched in Ti, Mg and Fe^{2+}, and the rims enriched in Si, Fe^{3+}, and Ca. This corresponds to a colour change from dark, deep brown cores to light yellow rims. Apparently homogeneous individual crystals show a similar correlation between colour and chemical composition. Decrease in Ti, coupled with increase in Si from core to rim, is a commonly recognised feature of melanite and schorlomite garnets elsewhere (Howie and Woolley, 1968; Gomes, 1969).

The sympathetic variation of Si with Fe and the antipathetic relation between Si and Ti from core to rim are in good agreement with the trends observed in Figure III.7.2 for the whole set of analyses.

III.7.3 – MINOR ELEMENTS

A number of minor and trace elements occur in measurable amounts in Tapira garnets. Na_2O is usually present, but rarely exceeds 0.6 wt. %, whilst P_2O_5 may reach up to 0.83 wt. %. NiO and Cr_2O_3 are low (up to 0.10 and 0.16 wt. % respectively). A limited number of WDS analyses were carried out to investigate some other trace elements. According to this preliminary data set, ZrO_2 may be as high as 2.63 wt. % and Nb_2O_5 may reach up to 0.3 wt. %. The sum of the oxides of La, Ce, Nd and Gd reaches up to 0.22 wt. % and there appears to be a relative enrichment towards the heavier REE. CuO and ZnO are usually below detection, exceptionally reaching 0.24 and 0.29 wt. %, respectively. In zoned grains, Nb, Zr, P and possibly the REE are enriched in the dark-coloured cores. A more thorough investigation of the trace element distribution in Tapira garnets, especially regarding Zr, Nb and the REE will be carried out in the future.

III.7.4 – OXYGEN FUGACITY

The presence of melanite and/or schorlomite has been interpreted as indicative of low oxygen fugacities (Huggins *et al.*, 1977b; Dawson, 1989; Dawson *et al.*, 1995). Kühberger *et al.* (1989) studied the Mössbauer spectra of Ti-garnets synthesised at different oxygen fugacities. They concluded that garnets formed at relatively low oxygen fugacity (controlled by the IQF = Iron+Quartz/Fayalite buffer) contained Fe^{2+} as well as Fe^{3+} and that both cations were distributed over the octahedral and tetrahedral sites. On the other hand, garnets formed at relatively high oxygen fugacity (NNO = Nickel/Nickel Oxide buffer) showed absorption peaks for Fe^{3+} only, with most of the Fe^{3+} (ca. 90%) present in octahedral, rather than tetrahedral sites.

If all titanium in Tapira garnets is assumed to be tetravalent, then the charge-balance recalculation of Fe into Fe^{2+} and Fe^{3+} results in a significant predominance of the trivalent species, although some Fe^{2+} is often present. The $Fe^{2+}/(Fe^{2+}+Fe^{3+})$ ratio ranges from 0 to 0.26 (exceptionally 0.33).

III.7.5 – ORIGIN OF TI-RICH GARNETS

Ti-rich garnets are typical of alkaline rocks (e.g. Keep and Russell, 1992; Dingwell and Brearley, 1985; Huggins *et al.,* 1977a), especially those with a high degree of silica undersaturation, and may occur as a primary or metasomatic phase (Flohr and Ross, 1990; Ulrych *et al.,* 1994). According to Mitchell (1996b) schorlomite and Ti-rich andradite are common products of sub-solidus reactions in melilitolite complexes. Platt and Mitchell (1979) considered Zr-rich titanian garnets as intimately associated with (and indicative of) magmatism of carbonatitic affinity.

Flohr and Ross (1989) described Ti-rich garnets of both magmatic and metasomatic origin in ijolite xenoliths from Magnet Cove, Arkansas. The passage from magmatic to metasomatic garnet is marked by progressive increase in Fe^{3+} and decrease in Ti. Some of these metasomatic garnets may have up to 3.5 wt % F.

Two textural varieties of garnet are present in Tapira rocks (Chapter II). One is interpreted as product of early-stage magmatic crystallisation, occurring as discrete crystals in low-Cr dykes and in wehrlites and bebedourites of the B2 unit. The other variety is clearly of late-stage origin and occurs as a coating on perovskite in wehrlites and bebedourites of both B1 and B2 units. The main chemical differences between primary and late-stage garnets from Tapira are the higher SiO_2, MgO and ZrO_2 of the former.

Ti-rich members of the andradite-schorlomite series have often been considered of magmatic origin, whilst Ti-poor andradites have, in many cases, been related to metamorphic or metasomatic settings (Deer *et al.,* 1992; Dingwell and Brearley, 1985).

This is in contrast with the observations from Tapira, where the late-stage garnet replaces perovskite, and is Ti-rich, while the primary zoned garnets may develop strong Ti depletion towards the rims.

The melanite coatings on perovskite from the B1 unit suggest that an increase in silica activity took place after most of the bebedourite had crystallised, resulting in the replacement of the primary perovskite by Ti-rich garnet. It seems unlikely that this reaction was associated with metasomatism, since other minerals in the wehrlites and bebedourites do not show signs of metasomatic alteration. This feature is better explained by the increase of silica activity in the residual (intercumulus) liquid. The lack of a recognisable trend of chemical evolution in this variety of garnet, within the SPS, is consistent with its late-stage origin.

The presence of melanite garnet (rather than perovskite) as the main Ti mineral crystallising in some low-Cr dykes and B2 plutonic rocks also suggests an increase in the activity of silica in the system, relatively to B1 and phlogopite-picrites. Furthermore, the zoning patterns of primary garnet indicate a relatively late episode of Ti and Zr depletion. This could be related to the crystallisation and removal of specific Ti or Zr minerals. For instance, zirconolite is present in pegmatitic bebedourites and in some carbonatites; but is relatively rare; zircon is a common accessory, in syenites. Which mineral phase could be associated to the sudden Ti depletion in the crystallising garnet is not clear. On the other hand, the zoning of melanite suggests a sharp, rather than gradational change in the composition of the magma with respect to Ti and Zr and may have been produced by liquid immiscibility processes.

III.7.6 – SUMMARY

- Both early- and late-stage Ti-rich garnets (melanites and schorlomites) occur in the Tapira complex. Primary magmatic garnets form euhedral, zoned, discrete crystals in low-Cr dykes and in plutonic rocks of the B2 unit. Late stage garnet occurs as coatings on perovskite, in wehrlites and bebedourites of the B1 and B2 units.
- Ti, rather than Al or Fe, seems to be the predominant substitute for Si in the tetrahedral site.
- A preliminary survey of trace elements by WDS microprobe analysis revealed the

presence of significant amounts of Zr (up to 2.63 wt. % ZrO_2). This is a common feature of Ti-garnets associated with carbonatite magmatism. Other elements present in measurable amounts are Na, P and the REE. This restricted data set suggests a relative enrichment in the heavier REE.

- The melanite-schorlomite rims on perovskite crystals are interpreted as the product of reaction of the early perovskite with a SiO_2-enriched residual liquid.

III.8 – ALKALI FELDSPARS

Alkali feldspar is an essential constituent of Tapira syenites and of the fenites surrounding the complex. Its occurrence in other Tapira rock-types is very restricted, but it may be present as a late phase in bebedourites of the B2 unit, as discrete grains and inclusions in apatite from low-Cr dykes and in feldspathic globules within C2 carbonatites (see Chapter II). Plagioclase feldspars were not found in any of the studied rock-types. The microprobe analyses carried out during this research included mainly feldspars from syenites and fenites, with the aim of recognising possible chemical differences between them. Table III.8.1 shows the compositional ranges of alkali feldspar in syenites and fenites, together with two analyses of feldspar from a low-Cr dyke. The latter, although extremely rare, are important from a petrogenetic point of view, since they probably represent the earliest feldspars crystallised in the complex. The complete set of mineral analyses and chemical formulae can be found in Appendix II.

Figure III.8.1 shows the classification of Tapira feldspars in the ternary system orthoclase - albite - anorthite. The analyses span a wide range of compositions along the Or-Ab line, always at very low An content. Feldspars from syenites have a much

	Syenites	Fenites	low-Cr dykes	
	(range)	(range)	inclusion in apatite	groundmass
SiO_2	60.98-64.62	63.93-67.94	64.79	62.65
Al_2O_3	17.31-18.99	18.13-19.42	17.05	16.55
Fe_2O_{3T}	0.04-1.76	0.11-0.80	0.71	2.83
MnO	0.00-0.08	0.00-0.06	0.02	0.00
MgO	0.00-0.15	0.00-0.09	0.10	0.84
BaO	0.40-2.53	0.03-0.68	0.07	0.00
CaO	0.00-0.07	0.00-0..01	0.67	0.23
Na_2O	0.06-0.79	0.48-9.05	0.10	0.05
K_2O	14.11-16.58	2.43-15.77	14.21	14.80
Total			97.72	97.95

Table III.8.1 - Composition of Tapira feldspars. Fe_2O_{3T} = Total iron expressed as Fe_2O_3.

narrower compositional range than those from fenites, clustering near the Or apex (always > 90 mol % of the Or component). Feldspars from fenites have a substantial and highly variable Ab component (5 to 85 mol %). The only feldspars where the An component is not negligible are those in the low-Cr dykes. However, Fe_2O_3T and MgO are also slightly high in these analyses (e.g. Table III.8.1), suggesting that these figures may result from some beam overlap with pyroxene in the fine-grained groundmass of the dykes. The high Ca content of the feldspar inclusion in apatite may result of overlap with the host.

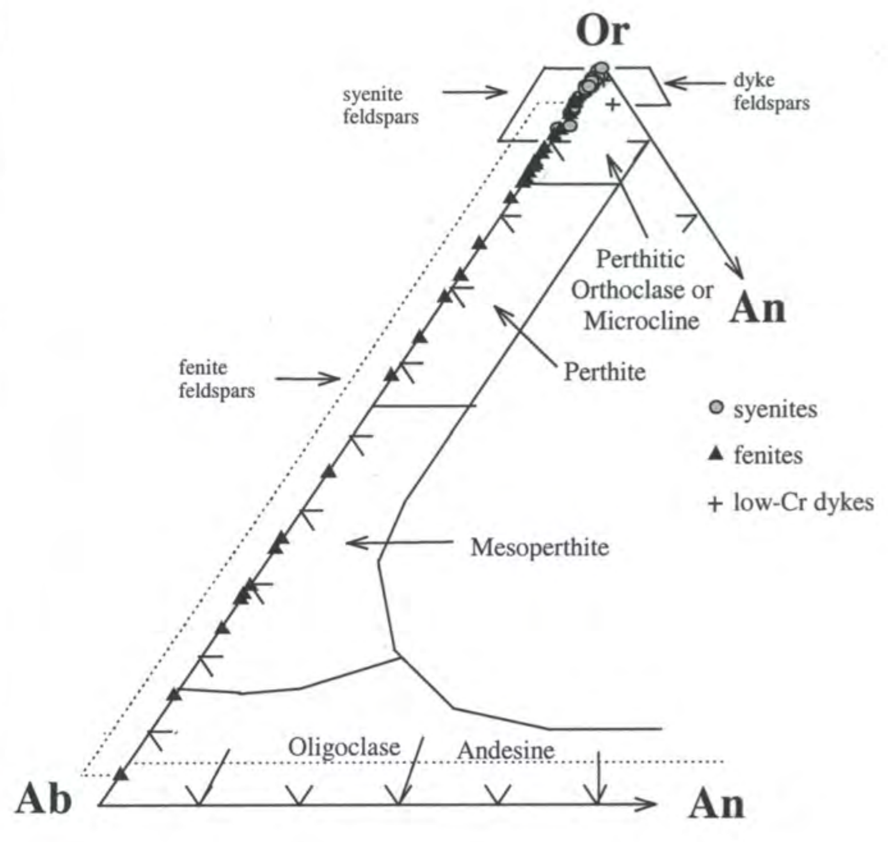

Figure III.8.1 - Classification of Tapira feldspars with respect to the end members albite (Ab), orthoclase (Or) and anorthite (An). After Deer et al. (1992).

Besides the relative proportion of the orthoclase and albite end-members, different feldspar generations can be distinguished on the basis of their Ba content (Figure III.8.2). Feldspars from syenites show much higher barium contents than those from fenites. Feldspars in low-Cr dykes can be distinguished from those in the syenites by their lower Ba.

The observed chemical differences between magmatic and metasomatic feldspars in the Tapira complex are important in investigating the origin of trachytic and syenitic rocks associated with carbonatite-bearing complexes in the APIP. Haggerty and Mariano (1983) interpreted feldspathic dyke rocks associated with the carbonatite complexes of Salitre I (APIP) and of Sarambi and Chiriguelo (Paraguay) as "rheomorphic fenites", containing sanidine with high iron contents (~ 0.7 wt. % Fe_2O_3) but low Na_2O (~ 1.2 wt %) and BaO (~ 0.6 wt. %). The study of some of these dykes (from the Salitre complex) during the current research (Chapters II and IV) suggests that they are magmatic rocks, rather than rheomorphic fenites. Carvalho (1974) described a rock of syenitic composition from Catalão and favoured a metasomatic origin for it, on the basis of field and petrographic observations. Unfortunately, analyses of feldspars in syenitic rocks are not available from the Catalão complex.

Orthoclase and/or albite of nearly pure composition are commonly observed in fenites associated with carbonatite magmatism (Le Bas, 1989). Accordingly, the restricted, near-end-member composition of alkali feldspars has often been taken as an indication of their metasomatic origin. Araújo (1996) pointed out that feldspars from phlogopitites in the Catalão complex are nearly pure orthoclase (Or 99.9-98.5 mol %) and interpreted them as product of fenitisation. Gaspar (1989) also described nearly pure orthoclase (> 90 mol % Or) as a metasomatic phase in the Jacupiranga complex, together with nearly pure albite.

On the other hand, Morbidelli *et al.* (1995) reported primary orthoclase of restricted composition from the Brazilian alkaline complexes of Juquiá, Poços de Caldas and Banhadão. Furthermore, Flohr and Ross (1990) studied Ba-rich feldspars in syenites from Magnet Cove, Arkansas, concluding that the earliest-formed feldspars in the syenites were Ba-rich, while late-stage and metasomatic feldspars were Ba-poor. In that case, the zoning patterns in magmatic feldspars indicate that the decrease in Ba is accompanied by an increase in the proportion of the Or molecule. The Ba-poor metasomatic feldspars from Magnet Cove may be microperthitic, with variable Na content.

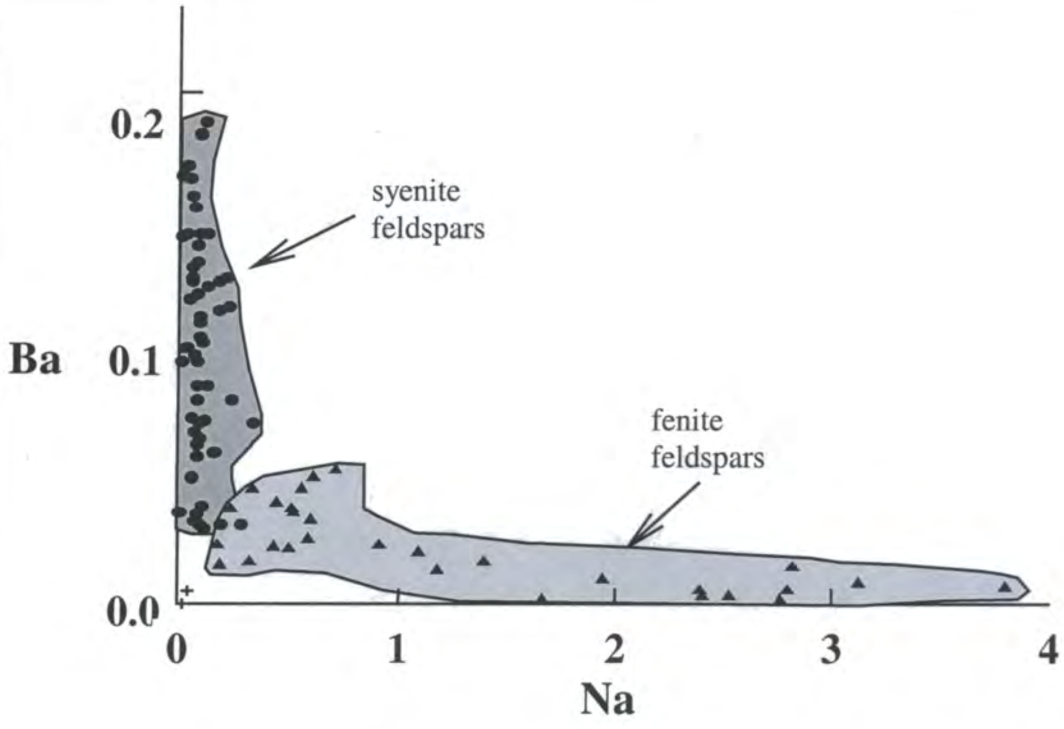

Figure III.8.2 - Variation of Ba against Na content (atoms per formula unit) of different feldspars generations from Tapira. Fields for syenite and fenite feldspars are indicated. Feldspars from low-Cr dykes (crosses) plot near the origin of the diagram.

In Tapira, the origin of the feldspathic rocks can be determined from field, petrographic and chemical evidence. For instance, syenites often occur as clearly igneous bodies, such as small intrusions emplaced well away from the contact of the complex with the country rock (Chapter I). The trace-element composition of these rocks (Chapter IV), as well as the chemical composition of minerals such as phlogopite and pyroxene (see the relevant sections in this Chapter) further emphasise their magmatic provenance. On the other hand, typical feldspathic fenites do occur near the margins of the Tapira complex and are clearly transitional into the quartzitic country rock. The chemical and petrographic properties of these rocks leave no doubt of their metasomatic origin, in contrast with the magmatic affiliation of the SPS syenites.

Interestingly, some of the chemical characteristics of metasomatic feldspars, previously described from other APIP and Paraguayan carbonatite complexes (see above) are in disagreement with the properties observed in Tapira. For instance, instead of clustering near the pure Ab and Or end-members, feldspars from Tapira fenites span a wide range of composition in the albite-orthoclase series. This most likely reflects the existence of several generations of metasomatic feldspars, formed over a prolonged period of hydrothermal activity. Such process would favour the partial substitution of previously formed feldspar grains by new, compositionally distinct feldspars. This is consistent with the common occurrence of substitution perthites in Tapira fenites (Chapter II). Magmatic feldspars, on the other hand, show restricted composition in terms of Na and K but have a distinctively wider range of minor element contents, such as Ba and Fe.

It should be stressed, however, that the chemical characteristics of igneous and metasomatic feldspars vary substantially between different carbonatite-bearing complexes, as discussed above. These variations are probably constrained by petrogenetic peculiarities of each complex, such as differences in the partition coefficients of trace-elements between feldspar and liquid or between immiscible liquids. Therefore, whilst clearly distinguishing between different feldspar generations in Tapira, these criteria are not necessarily applicable elsewhere.

III.8.1 - SUMMARY

- Feldspars have restricted occurrence in the Tapira complex, despite the relative textural diversity. Feldspars of magmatic origin are the major constituents of the syenites and also occur as rare discrete crystals and inclusion in apatite from the low-Cr dykes. Feldspars of metasomatic origin occur in the fenites surrounding the complex.
- Magmatic and metasomatic feldspars from Tapira can be distinguished on the basis of their chemical composition, as well as field and petrographic evidence.
- The wide variation of metasomatic feldspars along the Or-Ab series can be explained by prolonged hydrothermal activity, perhaps involving several stages of feldspar crystallisation.

III.9 - CARBONATES

A widely recognised characteristic of calcite and dolomite from carbonatites and related rocks is their high content of trace elements, especially Sr, Ba, and REE, when compared with carbonates of sedimentary or hydrothermal origin. Barker (1993) pointed out that textural evidence is often ambiguous and the trace-element content of the carbonates should be taken (usually in conjunction with isotope data) as the best indication of their magmatic origin.

III.9.1 CHEMICAL FEATURES OF CARBONATES FROM CARBONATITES

After the comprehensive work published by Quon & Heinrich (1966), who studied over 150 carbonate samples of carbonatites from several localities world-wide, carbonate minerals have only fairly recently received renewed attention (Wall *et al.*, 1993; Woolley & Buckley, 1993; Zaitsev & Polezhaeva, 1994; Dawson *et al.*, 1996; Zaitsev, 1996). The following chemical features are often reported:

Significant amounts of Sr are an undisputed characteristic of carbonatite calcites and dolomites. SrO is often present in excess of 1 wt. % and Wall *et al.* (1993) reported up to 13 wt. % SrO in carbonatite calcites from Rajasthan, India. Experimental evidence (Carlson, 1980) indicates that Sr content increases with temperature and the exsolution of Sr-rich phases from calcite during subsolidus re-equilibration has been observed in a number of localities (e.g. Wall *et al.*, 1993; Dawson *et al.*, 1996).

Magnesium is present in magmatic calcite in significant amounts (Quon & Heinrich, 1966), although this feature is shared with some carbonates of sedimentary or metamorphic origin. MgO contents of up to 3 wt. % are relatively common in carbonatite calcites (e.g. Ting *et al.*, 1994). Zaitsev & Polezhaeva (1994) have detected a decrease in Mg content of calcite from Kovdor (Kola Peninsula), in the neighbourhood of lamellae of exsolved dolomite. Ting *et al.* (1994) identified the presence of both clear (characterised by higher Mg and Fe) and "pitted" calcite inclusions in apatites from Sukulu, Uganda. They interpret the clear calcite inclusions partly as early-formed (before apatite) crystals and partly as melt inclusions, on the basis of heating experiments. The pitted, low-Mg calcite is interpreted as associated with post-magmatic processes. Gaspar (1989) also found exsolutions of dolomite in calcite from the Jacupiranga complex, but in that case they appear to be rare, at least on the scale of optical microscopy.

High manganese is considered a typical feature of calcites from carbonatites (Le Bas *et al.*, 1992; Dawson *et al.*, 1996), although low-Mn calcites have equally often been reported (Barber, 1974; Stoppa & Cundari, 1995), and Woolley *et al.* (1995) found the MnO contents of calcites from the Bingo carbonatite to be considerably variable. Zaitsev (1996) reported calcite containing MnO in excess of 5 wt. % in carbonatites from the Khibina Massif, recognising two different varieties. The first is associated with a late-stage carbonatite but has primary features, such as zoning and subhedral contours. The other variety has a clearly secondary origin, and can be distinguished from the primary Mn-calcite by its lower Sr content. It should be noted that calcites from the earliest carbonatite stages in Khibina are Mn-poor and Sr-rich. Both Mn and Fe contents in carbonatite calcites are likely to depend on the presence or not of associated dolomite, since Fe and Mn are preferentially partitioned to the latter (Dawson *et al.*, 1996; Gaspar, 1989). The presence of associated oxide phases such as magnetite will also affect the Fe and Mn distribution.

High barium (and strontium) contents have been suggested by Quon & Heinrich (1966) as the best chemical evidence of the magmatic origin of carbonates. However, whilst the high-Sr character is undisputed, barium enrichment is not observed so often. Dawson *et al.* (1996) found barium to be below the detection limit of the electron microprobe in all their samples of African carbonatites. Very low Ba contents are also reported for calcites and especially dolomites from many other carbonatites (e.g. Gaspar, 1989; Ting *et al.*, 1994). Furthermore, the progressive enrichment of Ba in the residual liquid with the magmatic evolution of carbonatites, and the frequent occurrence of barite in late-stage carbonatites (Woolley & Kempe, 1989; Le Bas, 1987, 1989) suggest that Ba is not removed from the melt on a large scale by crystallisation of carbonates. However, even an amount of 0.1 wt. % Ba in a carbonate from carbonatite would still be substantially higher than the contents of sedimentary carbonates (Quon & Heinrich, 1966)

III.9.2 - VARIATIONS IN CARBONATE WITH MAGMATIC EVOLUTION

A general consensus exists that Sr-rich calcite is the first carbonate to crystallise in most carbonatite complexes. In some extreme cases calcite may be absent, and carbonates of the magnesite-siderite series may occur in association with dolomite-ankerite (Woolley & Buckley, 1993). This requires the Mg:Ca ratio of the liquid to be higher than 1 (i.e. higher than in dolomite), which does not appear to be true for the majority of carbonatites.

During carbonatite fractionation, calcite is generally followed by dolomite and, at a later stage, ankerite. This results in a magmatic progression in the direction calciocarbonatite-magnesiocarbonatite-ferrocarbonatite. Although very common, this sequence is not universally observed. Le Bas (1989) draws attention to the influence of oxygen fugacity on the crystallisation order, stating that more oxidised magmas will favour the partition of Fe to magnetite (thus stabilising the Mg-carbonate), whilst low Fe^{3+}:Fe^{2+} ratios will result in formation of Fe-rich carbonate, and may lead to an inversion in the order of appearance of dolomite and ankerite.

According to this model, an evolving carbonatite liquid will initially produce calciocarbonatite (sovite), but the remainder of the differentiation sequence will depend on the oxygen fugacity. If it is low enough, magnesiocarbonatite may not form (differentiation ends at ferrocarbonatite). On the other hand, if it is excessively high, ferrocarbonatite could be suppressed from the fractionation sequence. In any case, the concentration of incompatible elements towards the latter stages often produces concentrations of REE, fluorine, barium, uranium and thorium in the final differentiation products.

The chemical composition of each carbonate species also varies during carbonatite evolution. Calcite becomes progressively depleted in trace elements with decreasing temperature, tending towards the ideal $CaCO_3$ end-member in the later stages. Dolomite is also progressively depleted in Sr (Zaitsev, 1996), but instead of becoming closer to the $MgCa(CO_3)_2$ end-member, dolomite tends to depart from it with differentiation of carbonatite, showing iron enrichment in the later stages. (e.g. Secher & Larsen, 1980; Woolley & Buckley, 1993)

III.9.3 - MINERAL CHEMISTRY OF TAPIRA CARBONATES

Calcite is by far the most abundant carbonate mineral in Tapira. It is the obvious essential component of the sovites and dolomite-sovites, as well as an important constituent of the groundmass and carbonate patches and ocelli found in phlogopite-picrites and low-Cr dykes. Dolomite and ankerite come next in abundance, and are present in dolomite-sovites, beforsites and some low-Cr dykes. Dolomite is also the main carbonate species in the banded metasomatic rock described in Chapters I and II ("reaction rock"). Ba-, Sr- and REE-carbonates are relatively rare, having been identified in this research only as exsolutions in calcite. The composition of calcite, dolomite, ankerite and strontianite from Tapira rocks was determined by electron microprobe. Their composition ranges are given in Table III.9.I and Figure III.9.1. The complete set of analyses can be found in Appendix 2. The main compositional characteristics of each type of carbonate are described in the following sections

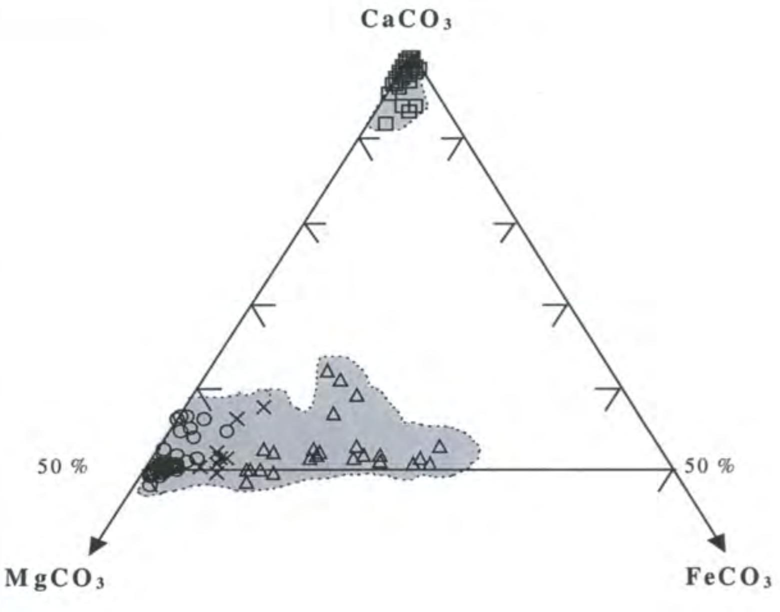

Figure III.9.1- Composition variation (mol %) of carbonates (except Ba and Sr carbonates) from the Tapira Complex. Squares = calcite, circles = dolomite, X = ferroan dolomite and triangles = ankerite. Note the excess $CaCO_3$ in some of the dolomite-ankerite series carbonates, and the calcite trend along the $CaCO_3$ -$MgCO_3$ side of the triangle.

Calcite

Calcite occurs in the studied rocks as two textural varieties with distinct chemical composition. Early calcite typically consists of crystals with a clear appearance, and contains significantly high amounts of SrO (up to 4.33 wt. %) and MgO (up to 1.3 wt. %). Cooling (or, alternatively, interaction with late-stage hydro/carbothermal fluids) causes the primary calcite to recrystallise and exsolve most of the minor components in the process, giving origin to a second (late-stage) generation of calcite. This has a distinctive "cloudy" appearance conferred by numerous micro-inclusions of exsolved minerals set in a close-to-ideal calcite host.

Strontianite and opaque minerals are the most common exsolution types, but qualitative EDS microprobe analysis also revealed the presence of Ba carbonates and REE-rich minerals. In most cases the small grain size of the exsolutions precludes quantitative microprobe analysis, especially because of the larger beam-size used to avoid damage to the carbonate (see Appendix 1). The substantial depletion of the recrystallised host calcite in trace elements is illustrated (for Sr and Ba) in Figure III.9.2.

	CaO	MgO	FeO	MnO	SrO	BaO
Calcite	53.42 (49.58-55.58)	0.41 (0-2.56)	0.23 (0-2.40)	0.16 (0-0.76)	1.67 (0-4.33)	0.30 (0-1.58)
Dolomite	29.76 (27.69-33.82)	19.69 (17.26-21.17)	1.42 (0.09-3.21)	0.43 (0.04-1.20)	1.10 (0.39-2.26	0.21 (0-1.71)
Fe-Dolomite	29.88 (28.69-32.65)	16.60 (14.14-18.18	4.55 3.59-5.5	0.93 (0.08-1.5)	0.35 (0.17-0.61)	0.2 (0-1.36)
Ankerite	29.39 (27.85-34.28)	12.53 (8.04-17.05)	11.43 (7.11-18.61)	0.80 (0.16-2.16)	0.21 (0-0.62)	0.05 (0-0.14)
Strontianite (*)	13.80 (8.13-18.43)	BD	0.05 (0-0.28)	BD	32.28 (26.98-45.98)	12.27 (7.74-18.64)

Table III.9.1 - Average and range (in brackets) of various carbonates from Tapira, analysed by electron microprobe. . Data are in wt. % oxide and include analysis for all rock types. BD = below detection limit. (*)=semi-quantitative analyses.

Similar exsolutions of trace-element-rich minerals in carbonatite calcites have been observed by Dawson *et al.* (1996) for the carbonatites of Panda Hill (Tanzania) and

Tundulu Hill (Malawi). Those authors describe two separate generations of calcite. As in Tapira, the first generation consists of clear, Sr-rich crystals, whereas a later generation comprises "cloudy", low-Sr calcite containing exsolved strontianite.

Care must be exercised to avoid confusion between the rather sudden depletion caused by subsolidus exsolution and the more gradual changes in the trace-element abundance expected to derive from magmatic evolution. As Figure III.9.2 shows, even calcites where exsolved minerals are apparently absent (therefore interpreted as primary calcite) show a gradual progression towards a purer $CaCO_3$. This is interpreted as a magmatic feature, in contrast with the abrupt "jump" of calcite to a depleted composition due to subsolidus re-equilibration.

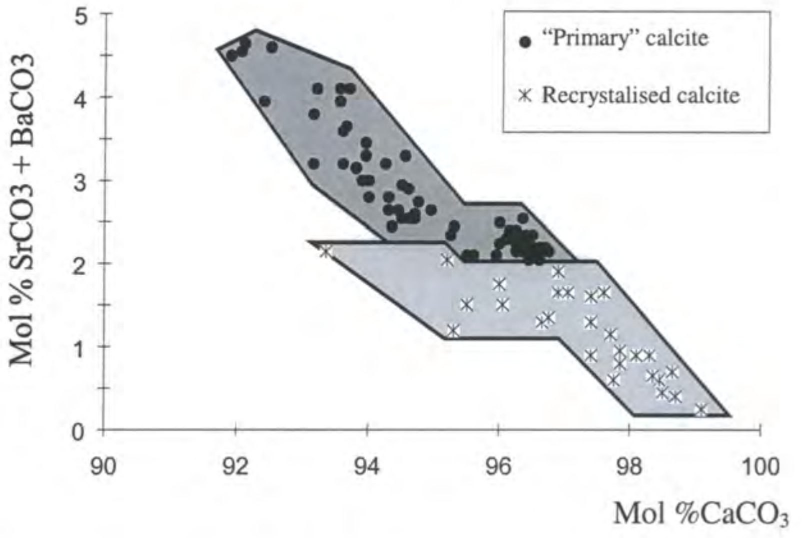

Figure III.9.2 - Compositional variation of clear (primary) and "cloudy" (recrystallised) calcite from Tapira carbonatites.

The following discussion of the magmatic evolution of Tapira calcites will be based solely on the chemical characteristics of early (clear) calcites, as this is the variety that crystallised directly from the carbonatite liquid.

The studied calcites contain relatively moderate amounts of magnesium (up to 2.5 wt. % MgO), and high contents of strontium (up to 4.33 wt.% SrO). Iron is not particularly high in most samples, despite the 2.4 wt.% FeO maximum in Table III.9.1.

Manganese is generally low (below 0.8 wt.% MnO). From Figure III.9.1 it is clear that Tapira calcites do not follow a strong Fe-enrichment trend. Instead, most analyses plot along the calcite-magnesite side of the triangle, except for some calcites from late-stage carbonatites.

Compositional differences between early and late-stage crystals (e.g. phenocrysts and groundmass) are not readily recognisable in most Tapira rocks, due to their overall coarse-grained equigranular texture. In some carbonatite dykes, however, the presence of tabular, euhedral calcite phenocrysts set in a fine-grained groundmass of calcite and dolomite allows the study of such compositional variations. Microprobe results for phenocrysts and groundmass carbonates in a dyke of dolomite-sovite from the C2 unit are presented in Figure III.9.3.

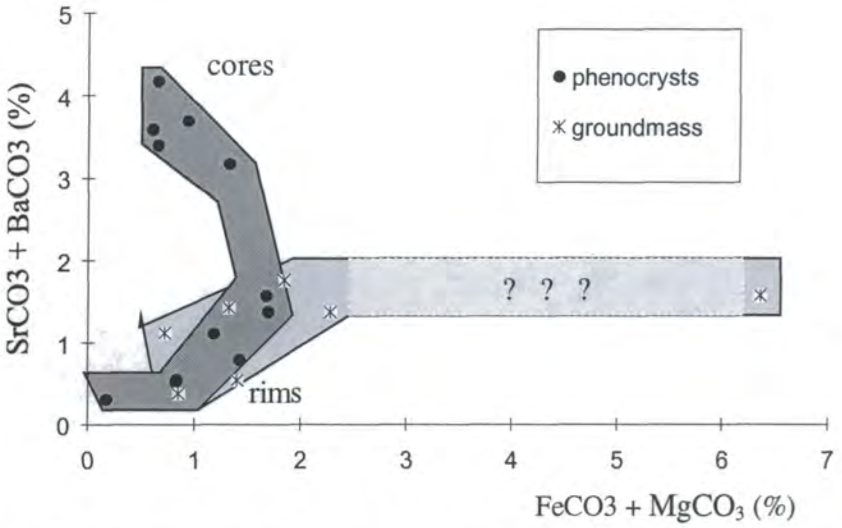

Figure III.9.3 - Variation trends of phenocrysts and groundmass calcite in a dolomite-sovite dyke. The phenocrysts show an initial increase in iron and magnesium but this trend is reversed at approximately half-way, leading to compositions progressively depleted in all trace-elements. The isolated, high-magnesium analysis of groundmass calcite may be the result of overlap of the electron beam with the adjacent groundmass dolomite.

The evolution trend of phenocrysts shown in the diagram is a composition of analyses of various individual phenocrysts, rather than a chemical profile on a single grain, but pairs of core-rim analyses are in good agreement with this general trend. The earliest calcites are rich in Ba and Sr, but not necessarily in Fe and Mg. In fact, there appears to be an initial increase in Mg and Fe, whilst Sr and Ba progressively decrease.

At a later stage, presumably coinciding with the onset of dolomite crystallisation, the calcite phenocrysts show a trend of progressive depletion in all minor elements, eventually leading towards the crystallisation of a carbonate very close to an "ideal" $CaCO_3$. It should be noted that the second leg of the trend overlaps the composition range of the groundmass calcite.

The suggestion that the observed inflection in the calcite phenocryst trend coincides with the onset of dolomite crystallisation is supported by: (a) the actual presence of dolomite, in the groundmass; and (b) the widely accepted concept that Fe partitions preferentially to dolomite instead of calcite (e.g. Gaspar, 1989; Zaitsev & Polezhaeva, 1994; Dawson *et al.*, 1996).

There is also a marked variation in calcite composition between the individual carbonatite units (C1 to C5) in the Tapira complex. If samples are considered individually, the evolution trends are masked by composition overlaps but, if the average calcite composition for each group is considered, some regular variations can be observed (Figure III.9.4). The average composition of calcite seems to bear a direct relation with sample location in the complex (and possibly with intrusion age).

Although carbonatites C3 and C4 are not spatially related, their calcites are very similar in composition. These two carbonatite bodies also share some similarities in whole-rock geochemistry (Chapter IV) and in the mode of occurrence (small intrusions at the margins of the complex). Because of these similarities calcites from the two units are plotted together in Figure III.9.4. The vertical scale of the diagram is arbitrary.

On average, calcites from the central body of carbonatite (C1) have the highest MgO, BaO and SrO contents. These elements decrease in abundance through C2 to C4 and are lowest in C5. FeO and MnO also decrease from C1 to C4. Carbonatites from the C5 unit, comprising small late-stage dykes and veinlets, do not follow this trend. The reason for this may be enrichment of the residual liquid in Fe and Mn. Ankerite or Fe-dolomite are often associated with alongside calcite in C5 rocks, suggesting late-stage enrichment in Fe and Mn, which is a well-known feature of carbonatite complexes.

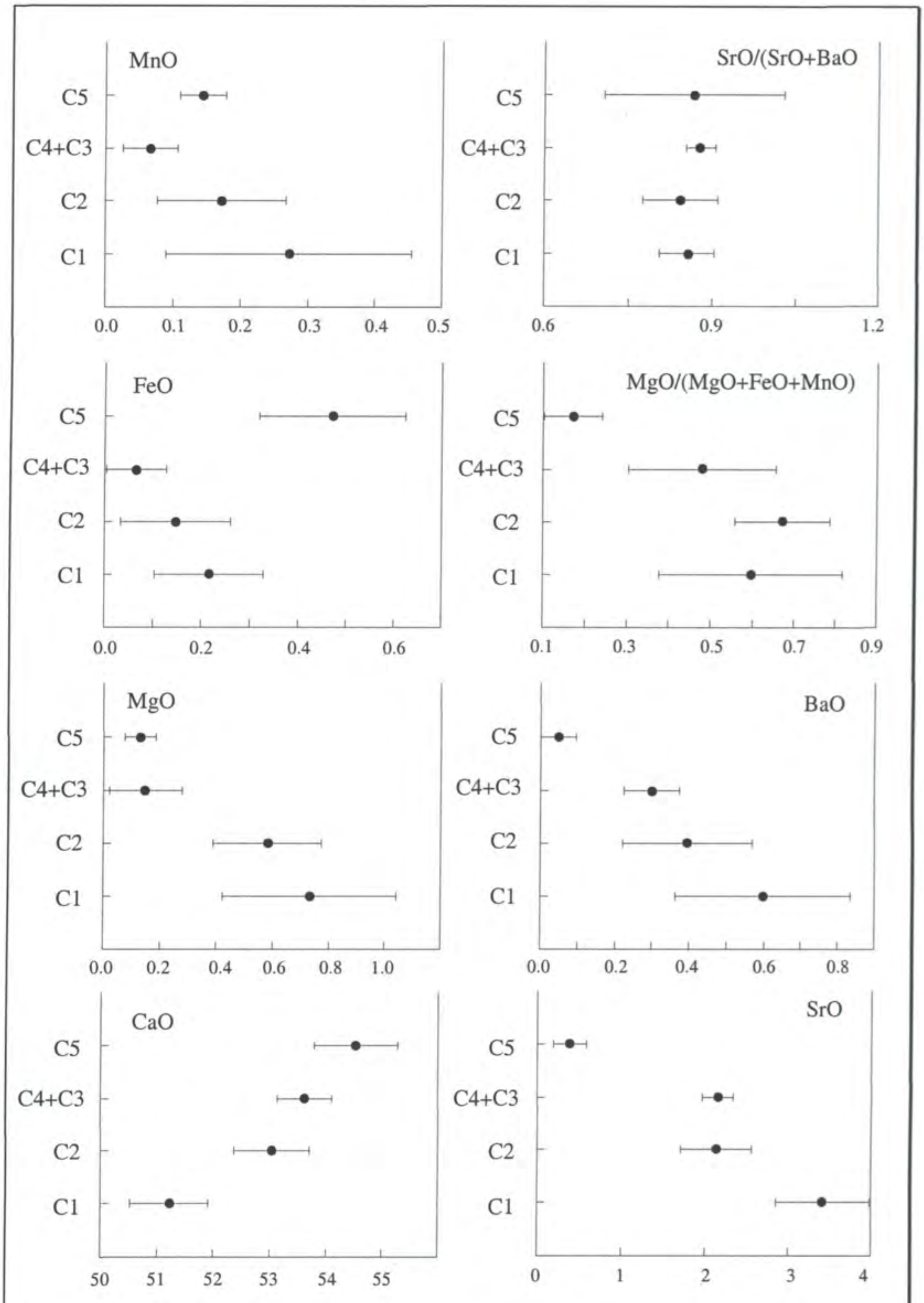

Figure III.9.4 - Chemical variation of calcites from different carbonatite bodies in Tapira. The vertical scale is arbitrary and intended to represent the relative progression of the groups in age (C1= oldest). Error bars are average ± 1 standard deviation

Although MgO, FeO and MnO all decrease in calcite from C1 to C4, the ratio MgO/(MgO+FeO+MnO) increases initially from C1 to C2. This is in keeping with the initial enrichment observed in the phenocrysts (Figure III.9.3). After the onset of dolomite crystallisation (in C2), this ratio decreases steadily to the end.

Assuming that high-temperature calcite is more likely to accept substitution of other divalent ions for Ca^{2+}, it seems that the carbonatites of the central C1 body were formed at the highest temperatures, whilst the external C3 and C4 carbonatite dykes crystallised at lower temperature. Alternatively, the observed trends may indicate that the various generations of carbonatites crystallised from different liquids, progressively depleted in the relevant components. Sr and Ba do not show significant variation relative to each other in calcites from different intrusions, as shown by nearly constant SrO/(SrO+BaO) ratio in Figure III.9.4.

Calcite also occurs in the groundmass and carbonate patches in phlogopite-picrite and low-Cr dykes. A progressive variation in calcite composition is observed, with the calcite from phlogopite-picrites showing higher Sr and Ba contents than that from low-Cr dykes. Compared with carbonatites, calcites from the ultramafic dykes are intermediate between C2 and C3+C4. Calcite in some low-Cr dykes shows marked enrichment in iron, and may be associated with ankerite rather than dolomite.

Dolomite and ankerite

Carbonates of the dolomite-ankerite series are relatively rare in C1 carbonatites, but become an increasingly important constituent in the C2 dolomite-sovites and associated dykes, in C5 late-stage dykes and veinlets, and in the groundmass and carbonate pockets (ocelli) in low-Cr dykes. Dolomite is also an essential constituent of the metasomatic products developed at the contact between ultramafic silicate rocks and the C1 intrusion ("reaction rock", see chapters I and II). As observed for calcite, dolomite may occur as "cloudy" crystals , peppered with micro-inclusions, although this phenomenon is less common in dolomite.

The composition of dolomites and ankerites from Tapira is represented in Figure III.9.1. The limit between dolomite and ankerite adopted here is that suggested by Deer *et al.* (1992), i.e. carbonates with Mg/Fe ratio ≤ 4:1 are classified as ankerite. The earliest formed magmatic dolomites are those in C1 and C2, and typically have considerable amounts of strontium (up to 1.8 wt. % SrO), combined with low contents of Fe and Mn. Dolomites of later stages become progressively Fe-rich (Fe-dolomite), and eventually give way to the formation of ankerite. The enrichment of Fe and Mn, relatively to Mg, in late-stage carbonates has been observed in other carbonatite complexes (e.g. Secher & Larsen, 1980; Woolley & Buckley, 1993). In Tapira this coincides with a sharp decrease in the Sr content (Figure III.9.5).

The metasomatic dolomites of the reaction rock are a remarkable exception. Despite being clearly of secondary origin, they show surprisingly high Sr content, coupled with high Mg/(Mg+Fe+Mn). Their Sr concentrations are even higher than the earliest magmatic dolomites of C1 and C2. A striking difference, however, resides in the fact that the metasomatic dolomites are also Ba-rich (up to 1.7 %), whilst the primary dolomite usually has much lower Ba. The only other dolomites from Tapira with BaO higher than 0.2 wt. % occur in late-stage veins and small dykes. This Ba enrichment is consistent with a late-stage origin for dolomite, as observed by Gaspar (1989).

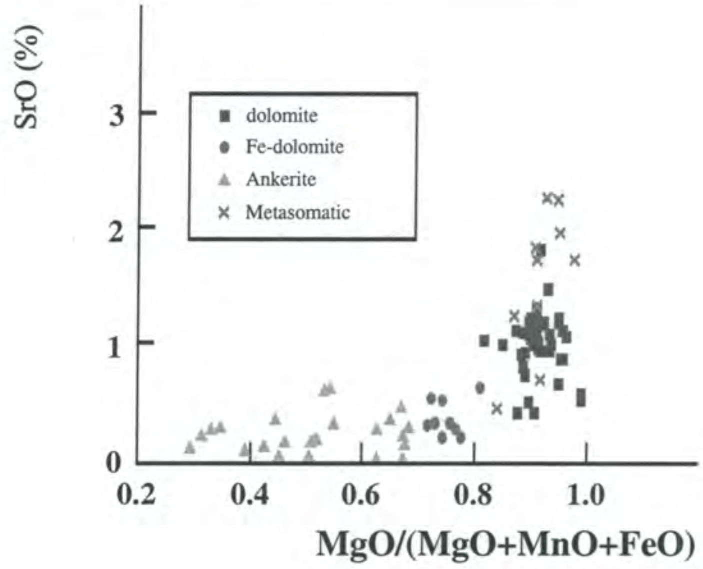

Figure III.9.5 - Sr variation of dolomites of all rock type from Tapira. Note that the more evolved dolomites and ankerites are enriched in Fe and Mn and have the lowest Sr.

On the other hand, this metasomatic dolomite does not show the typical iron enrichment of other late-stage dolomites in the complex. The presence of abundant magnetite in the reaction rock suggests a relatively high oxygen fugacity, which would tend to stabilise an iron-poor carbonate.

The low-Cr dykes seem to have the most evolved magmatic carbonates of the dolomite-ankerite series. These occur in the groundmass and in small carbonate-rich pockets. The dolomite is clearly enriched in iron, varying from Fe-dolomite to more frequent ankerite. Sr (Figure III.9.5) and Ba contents are usually very low.

In Figure III.9.1 it was seen that some dolomites and ankerites deviate from the ideal composition towards $CaCO_3$ enrichment. According to Deer *et al.* (1992), high-temperature dolomite can have up to 5 mol % of excess $CaCO_3$. In Tapira, however, this does not seem to be restricted to early-crystallising phases.

Exsolved phases in carbonate minerals

Sr-, Ba- and REE- rich phases were identified by qualitative EDS microprobe analysis and occur as inclusions in calcite and, less often, in dolomite. These result from the subsolidus re-equilibration of primary carbonates, with exsolution of trace-element-rich phases (e.g. Figure III.9.3).

Semi-quantitative analyses are given for strontianite in Appendix 2. Strontianite from Tapira is rich in barium (up to 18.6 wt. % BaO) as well as in calcium (up to 18.4 wt. % CaO). The complete solid solution in the system $BaCO_3$ - $SrCO_3$ has been synthesised in experiments (e.g. Chang, 1971) and Ba substitution for Sr is common in natural strontianites (Deer *et al.*, 1992). The high Ba contents of the exsolved strontianite suggest that Ba, as well as Sr, is enriched in the early-formed calcites. This agrees with the variation observed in Figures III.9.3 and III.9.4.

III.9.4 - CARBONATE THERMOMETRY

The increase, with temperature, in the solubility of magnesium (Goldsmith & Newton, 1969; Bickle & Powell, 1977; Powell *et al.*, 1984; Anovitz & Essene, 1987) and strontium (Chang, 1965, 1971; Carlson, 1980) in calcite, and the corresponding phase equilibria, have been used to devise various geothermometers. It should be stressed that the application of geothermometers based on microprobe analysis of carbonates may be difficulted by the need to use of a defocused electron beam that may, potentially, overlap exsolved phases or inclusions. Also, carbonates are highly susceptible to subsolidus transformations and metasomatic alteration, which are extremely common processes in carbonatite complexes. Furthermore, if dolomite is exsolved from calcite during cooling, this will affect the temperatures calculated from the calcite-dolomite geothermometer (Zaitsev & Polezhaeva (1994).

Zaitsev & Polezhaeva (1994) obtained calcite-dolomite temperatures up to 700 °C for the Kovdor carbonatites, by recalculating the exsolved dolomite back into calcite composition. Results attained by their approach are up to 270 °C higher than previous estimates. This method, however, requires a detailed study of the textures, geometry and relative abundance of the exsolved phases that is beyond the scope of the present study.

A series of attempts was made to apply carbonate thermometry to the Tapira complex. The results are presented in Table III.9.2 and Figure III.9.6, but the above-mentioned restrictions emphasise the need of caution in their interpretation. Calcite-dolomite temperatures obtained using the thermometer of Anovitz & Essene (1987) are presented in Table III.9.2. Due to the possibility of continuous subsolidus re-equilibration, calcite-dolomite pairs were chosen where the Mg content of calcite was highest. Most temperatures range from 400 to 500 °C. Two samples (at051 and at056) yielded temperatures below 300 °C but, apart from them, there is not a large variation within the complex.

		CaCO3	MgCO3	FeCO3	T °C
C1	at042	0.955	0.041	0.003	494
	at044	0.967	0.029	0.002	433
	at052	0.970	0.026	0.002	413
	at136	0.962	0.030	0.006	443
C2	at045	0.968	0.027	0.004	420
	at046	0.971	0.025	0.003	403
	at049	0.966	0.029	0.004	434
	at051	0.977	0.016	0.006	323
	at056	0.986	0.012	0.001	248
	at212	0.933	0.035	0.030	500
Low-Cr dykes	at205	0.940	0.025	0.033	457

Table III.9.2 - Temperatures calculated for calcite coexisting with dolomite for Tapira rocks, according to Anovitz & Essene (1987).

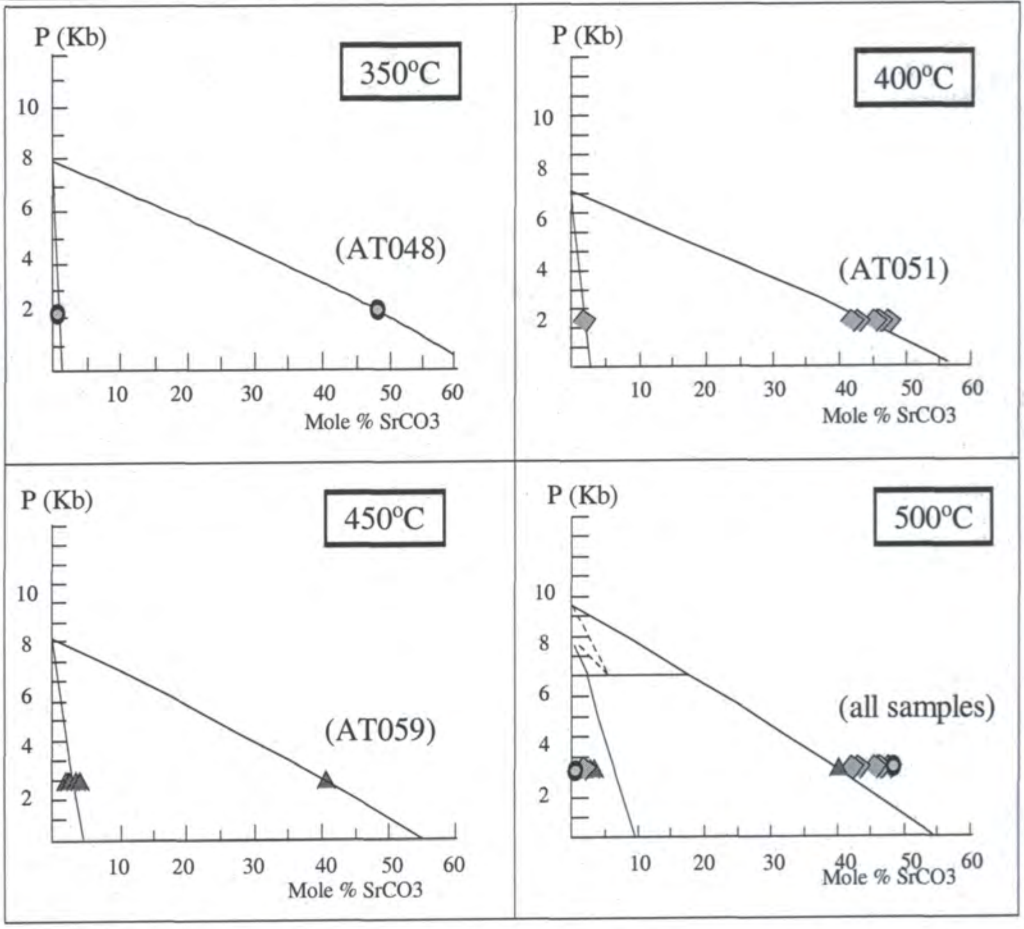

Figure III.9.6 - Isothermal sections in the system $CaCO_3$ -$SrCO_3$ (Carlson, 1980), showing coexisting calcites and strontianites from Tapira. Samples AT048 and AT059 are from C1 and AT051 is from C2.

Figure III.9.6 is a series of isothermal sections through the system $CaCO_3$ - $SrCO_3$ from Carlson (1980). Pairs of carbonate analyses from different samples show best fits between 350 and 450°C, suggesting, that subsolidus re-equilibration happened at variable temperatures for different rocks. Note that no fit is obtained at 500°C (bottom right), placing an upper limit for the exsolutions of strontianite from calcite. Also noteworthy is the small range of pressures for the best fits of individual carbonate pairs, between 2 and 3 kb.

Due to the potential effect of continuous subsolidus transformations, the results can provide only a minimum estimate of temperatures for carbonatite formation in the complex. It is interesting, however, that in all cases they should indicate the highest temperatures for the C1 carbonatites. The only exception to this rule is a C2 dyke (at212, in Table III.9.2), that yielded a calcite-dolomite temperature of 500°C. This is a thin dyke with primary textures well preserved, and no visible evidence of subsolidus exsolutions

III.9.5 COMPARISON WITH OTHER CARBONATITES

Sr content in calcites from Tapira was found to be moderate, if compared with some extreme compositions such as those reported by Wall *et al.* (1993; up to 13 wt. % Sr in calcite), but it is generally higher than those reported for several other world-wide carbonatites.

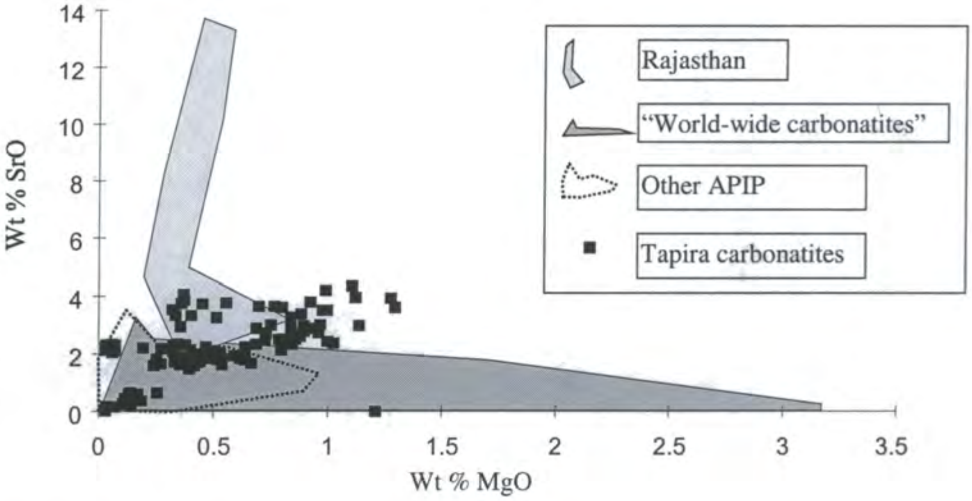

Figure III.9.7 - Calcite compositions from Tapira, compared to several world carbonatites and to the high-Sr dyke of Rajasthan. Source of data for Rajasthan is Wall et al. (1993). World-wide carbonatites include data from African (Ting et al., 1994; Dawson et al., 1996; Woolley et al., 1995), Italian (Stoppa & Lupini, 1993), Chinese (Le Bas et al., 1992), Russian (Zaitsev, 1996), Paraguayan (Castorina et al., 1996) and Brazilian (Gaspar, 1989; Torres, 1996; Araújo, 1996) carbonatites.

In Figure III.9.7 the Sr and Mg contents of calcites from Tapira carbonatites and dykes are compared with a number of world-wide carbonatites. The sources of data for this diagram do not include analyses for which there was indication of low-temperature exsolution. In many cases, a general positive correlation of Sr with Mg is observed, although the ratio of Sr to Mg seems to differ from one locality to another. The calcites from most carbonatites reported in the literature seem to have lower Sr/Mg than Tapira, which in turn has lower ratios than those of the Rajasthan carbonatite (Wall *et al.*, 1993). Calcites from the Khibina carbonatite of Kola Peninsula (not distinguished from world-wide carbonatites in Figure III.9.7) have a Sr/Mg ratio similar to Tapira.

Analyses of calcite from other carbonatites of the Alto Paranaíba Igneous Province (Araxá, Torres, 1996 and Catalão, Araújo, 1996) are also plotted in Figure III.9.7. These seem to have Sr/Mg ratios similar to those of Tapira calcites, but with lower abundance of both elements. This may be due more extensive subsolidus recrystallisation in Catalão and Araxá, since products of metasomatism are particularly abundant in these two complexes.

Other carbonatites occurring along the eastern and western border of the Paraná Basin seem to plot well inside the field of the world-wide carbonatites. This is certainly true for Jacupiranga (Gaspar, 1989), and possibly also for carbonatites in Paraguay (Castorina *et al.*, 1996) although data for the latter are based on analysis of sample leaches and may represent a mixture of different carbonate phases. It should be stressed that both Jacupiranga and the Paraguayan carbonatites are remote in location, as well as in age (Early-Cretaceous) from the APIP.

The span of magnesium variation is relatively restricted in Tapira calcites, in comparison with some other carbonatites (Figure III.9.7). This may reflect the effects of subsolidus recrystallisation, with exsolution of Mg-carbonate. Dolomite or Fe-dolomite are locally present as inclusions in recrystallised calcite, although they are not particularly abundant. Furthermore, it was seen from Figures III.9.3 and III.9.4 that even the earliest formed calcites are only moderately enriched in Mg. This suggests that the moderate Mg content is a primary feature in Tapira calcites.

III.9.6 - SUMMARY

- As suggested by Le Bas (1989), carbonatite evolving under relatively high oxygen fugacity will tend to follow the path calciocarbonatite - magnesiocarbonatite - ferrocarbonatite. This is consistent with the presence of dolomite as a significant constituent from carbonatite C2, the trend of calcite evolution along the calcite-magnesite side of Figure III.9.1, the presence of conspicuous magnetite and the common occurrence of tetraferriphlogopite in Tapira carbonatites (see section III.4).

- Tapira calcites show a consistent chemical progression towards purer $CaCO_3$ from C1 to C5. All trace-elements decrease in this direction, but Fe and Mn increase in C5 (late-stage dykes and veins). The ratio of magnesium to iron and manganese increases initially, until the onset of dolomite crystallisation, and decreases steadily thereafter. Dolomite, on the other hand, tends to depart from the ideal composition in the late stages, showing enrichment in iron and manganese.
- Establishing the age relations between the different groups of carbonatites in the complex is a difficult task, since most occurrences are only accessible through drilling. However, the observed chemical trends of Tapira carbonates are similar to those described by Gaspar (1989) for the well-exposed carbonatites of Jacupiranga. This suggests that C1 can be interpreted as the earliest and C5 as the latest carbonatite intrusions, at least on the basis of calcite chemistry.
- Carbonates in the phlogopite-picrite dykes are chemically less evolved than in the low-Cr dykes.
- Temperature estimates based on the $CaCO_3$-$MgCO_3$-$FeCO_3$ and $CaCO_3$-$SrCO_3$ systems vary substantially between samples. The highest temperatures obtained are approximately 500°C but this is probably reflecting the temperature of subsolidus re-equilibration. The results are best considered as minimum estimates of crystallisation temperature.
- Calcites from Tapira have distinctively higher Sr than many world-wide carbonatites. It is possible that other complexes in APIP also show this feature.

CHAPTER IV - GEOCHEMISTRY

IV.1 - INTRODUCTION

This Chapter is concerned with the description of the geochemical features of the various rock-types of the Tapira complex and their comparison with similar rocks elsewhere. A detailed geochemical study of major and trace elements was carried out on the various lithostratigraphic units described in the previous Chapters. The carbonatites and carbonate-rich mafic dykes (phlogopite-picrites and low-Cr dykes) were further studied, to determine carbon and oxygen stable isotopes in calcite and dolomite. Finally, a preliminary Sr and Nd isotope investigation was carried out on a small number of samples, in order to investigate the relationships between carbonatites and silicate rocks, and also to examine the possible effects of crustal contamination in the Tapira complex. The analytical techniques are described in Appendix 1, and the geochemical data are presented in Appendix 3.

IV.2 - WHOLE-ROCK GEOCHEMISTRY

As set out in the previous Chapters, many of the rocks in the Silicate Plutonic Series (SPS) of the Tapira complex represent accumulations of crystals, rather than just liquids, which poses difficulties for the interpretation of their chemical composition. On the other hand, the fine-grained dykes (phlogopite-picrites, low-Cr dykes and some carbonatites) are likely to represent, or at least approximate, the composition of some of the magmatic liquids associated with Tapira. Among these, the ultramafic dykes are of particular interest, since they can provide insights into the chemical aspects of primitive liquids involved in the petrogenesis of the complex. For this reason, the present Chapter will deal initially with the investigation of the dyke rocks, in an attempt to set out the scenario in which the chemical characteristics of the other rocks can be examined.

IV.2.1 - PHLOGOPITE-PICRITE DYKES

Although some isolated occurrences of phlogopite-picrites are found throughout the Alto Paranaíba Igneous Province (APIP), these rocks seem to be particularly associated with the carbonatite-bearing intrusions in the province (Gibson *et al.,* 1995b, and this work). They have not been investigated in detail to date and their study is likely to shed some light on the regional carbonatitic magmatism.

The field, petrographic and mineralogical evidence discussed in the previous Chapters suggests that phlogopite-picrites are likely to represent magmatic liquids. Since the mineralogy of these rocks also indicates that they are the least evolved dykes in Tapira, it seems logical to investigate whether they can be regarded as: a) parental magmas to other rocks in the complex; and b) primary magmas derived from the mantle.

Major-element oxides

Major-element analysis of the phlogopite-picrites (and also of low-Cr dykes and carbonatites) must take into account the abundance of some elements that are usually regarded as traces in other igneous rocks. In some samples, elements such as Ba and Sr can reach percentage levels. In such cases, BaO and SrO must be included in the major element analyses, in order to achieve acceptable analytical totals (see Appendix 1).

A second problem posed by these rocks is that Loss on Ignition (LOI) figures are mostly related to the presence of groundmass carbonate and/or carbonate globules (ocelli). In most examples of igneous rocks the LOI value is regarded as an indication of post-magmatic alteration and it may be desirable to recalculate the major-element oxides to a total of 100 %. However, this does not hold if the LOI is related to primary minerals as is the case of Tapira rocks. In the case of phlogopite-picrites and low-Cr dykes, the recalculation of the samples on a "dry" basis would induce unrealistic interpretation of the data. For this reason, and also to allow direct comparisons with the carbonatites, the database was recalculated to include CO_2 (or LOI, when CO_2 analysis was not available). Consequently, the figures for the major-element oxides are reported in this thesis on a "wet" basis.

Phlogopite-picrites display progressive variation in many of the major-element oxides, and are probably best considered as representing several stages of a differentiating series. The following general features can be regarded as typical of the phlogopite-picrite series. All samples are extremely silica-undersaturated (SiO_2 = 24.30 - 33.40 wt. %), carbonate-rich (CO_2 = 3.29 - 21.9 wt. %) and strongly potassic (K_2O = 2.68 - 5.87 wt. %). CaO (9.31 - 19.41 wt. %) and TiO2 (3.24 - 5.37 wt. %) are high and Al_2O_3 (1.63 - 4.69 wt. %) is low. The K_2O/Na_2O ratio varies from 2.14 to 14.86, on a wt. % basis. The high MgO (8.73 - 21.34 wt. %) testifies to the unevolved character of these rocks. The mg-number varies from 42 to 62, and correlates positively with strongly compatible trace elements, such as Cr and Ni. The chemical variation of major elements with magma evolution is described in detail in section IV.2.3.

Trace elements

The high Cr (134 - 1012 ppm) and Ni (82-932 ppm) contents are consistent with the ultramafic character of these rocks and suggest that the least evolved members of the phlogopite-picrite series can be considered as primary magmas. Scandium is moderately high, varying from 22 to 37 ppm. Phlogopite-picrites are strongly enriched in incompatible elements. In particular, Ba, Sr and the sum of the rare-earth elements (REE) often reach concentrations of a few tenths of a percent. The phlogopite-picrites show relatively high concentrations of the high-field-strength elements (HFSE): Nb

(160 - 360 ppm); Ta (10 - 22 ppm); Zr (470 - 1000 ppm) and Hf (10-23 ppm). The trace-element distribution is illustrated in the chondrite-normalised spider diagram of Figure IV.1. It can be seen that all samples behave coherently, forming a consistent pattern. The diagram peaks at La, with the most enriched samples showing La concentration over 1600 times the chondritic abundance. Negative anomalies at Rb, K and Sr, together with a less pronounced negative Ti anomaly, can also be observed. Few samples show an incipient phosphorus negative anomaly. The normalised ratios of "paired elements" (i.e. elements with similar geochemical behaviour) such as Zr/Hf$_{(N)}$, Y/Ho$_{(N)}$ and Nb/Ta$_{(N)}$ show little variation , in the ranges 1.16-1.52, 8.6-9.9 and 0.58-1.34, respectively.

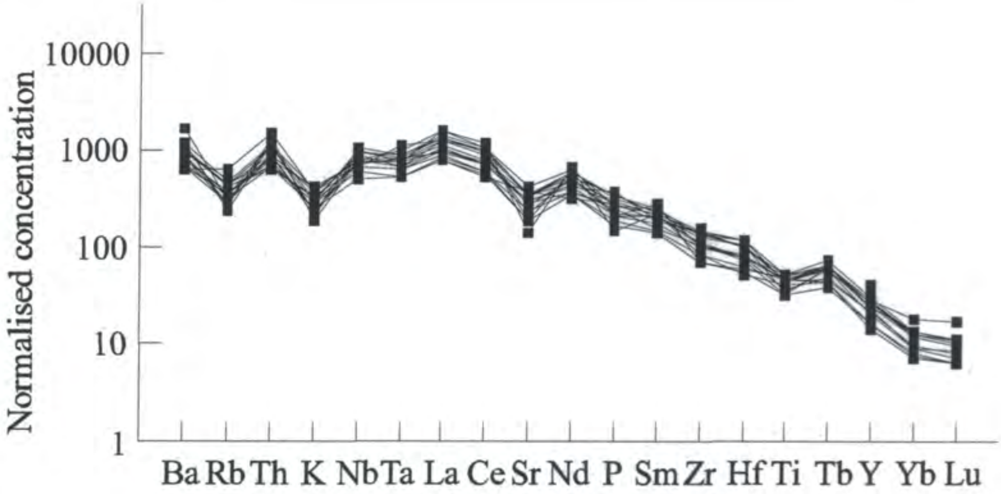

Figure IV.1 - Trace-element diagram showing the composition of phlogopite-picrites, normalised to chondrite (except Rb, K and P) according to Thompson et al. (1984).

The rare-earth element (REE) patterns of phlogopite-picrites are shown in the chondrite-normalised diagram of Figure IV.2. The pattern is smooth and steep, showing strong enrichment of the light rare-earth elements (LREE) relative to the heavy rare-earths (HREE). Chondrite-normalised La/Lu ratios (La/Lu$_{(N)}$) range from 69 to 210, but most values are concentrated between 90 and 160. La/Sm$_{(N)}$ ratios vary from 16.7 to 19.3.

Chemical classification of the phlogopite-picrites

Any attempt at a chemical classification of the phlogopite-picrites has to account for the peralkaline (molecular ratio of alkalis to aluminium ranging from 1.04 to 3.02) and ultrapotassic (K_2O/Na_2O varying from 2 to 15) character of these rocks, as well as their extreme silica-undersaturation. Classification diagrams involving the relative abundance of silica and alkalis, such as those of Cox *et al.* (1979) and Le Maitre *et al.* (1989) are difficult to apply, because of the excessively low silica content of the phlogopite-picrites. Mitchell (1996a) emphasised that the total alkalis vs. silica (TAS) diagram is "totally inadequate" for the classification of several types of alkaline rocks, such as kimberlites, lamproites, kamafugites, melilitites and nephelinites.

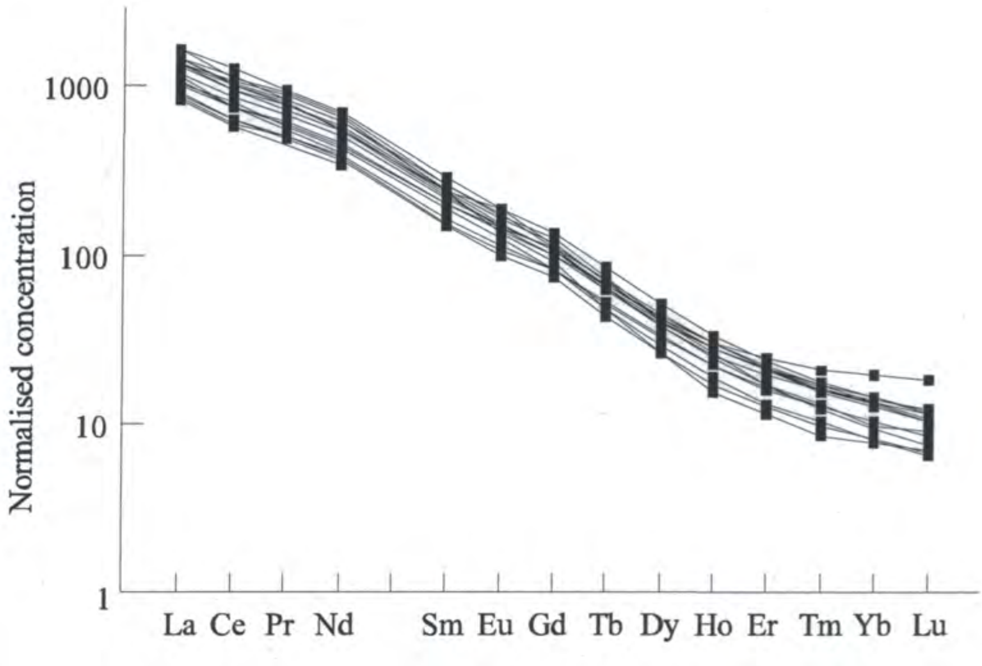

Figure IV.2 - Chondrite-normalised REE patterns of phlogopite-picrites. Normalisation factors are from Boynton (1984).

A chemical scheme for the classification of ultrapotassic rocks was devised by Foley *et al.* (1987). Before the system is applied, the whole-rock analyses must pass a chemical screen, in order to confirm the ultrapotassic character of the rock and to concentrate the classification on mafic varieties only. This chemical screen requires that the rock has MgO > 3 wt. %, K_2O > 3 wt. %, and K_2O/Na_2O > 2. All the studied samples of phlogopite-picrite have MgO higher than 8 wt. %, therefore satisfying the first condition. Figure IV.3 shows the variation of the K_2O/Na_2O ratio with the K_2O concentration. Of the studied samples, only one fails to satisfy the minimum K_2O limit, despite its relatively high K_2O/Na_2O ratio. This sample shows textural evidence of alteration, which could be responsible for changes in the original K_2O content.

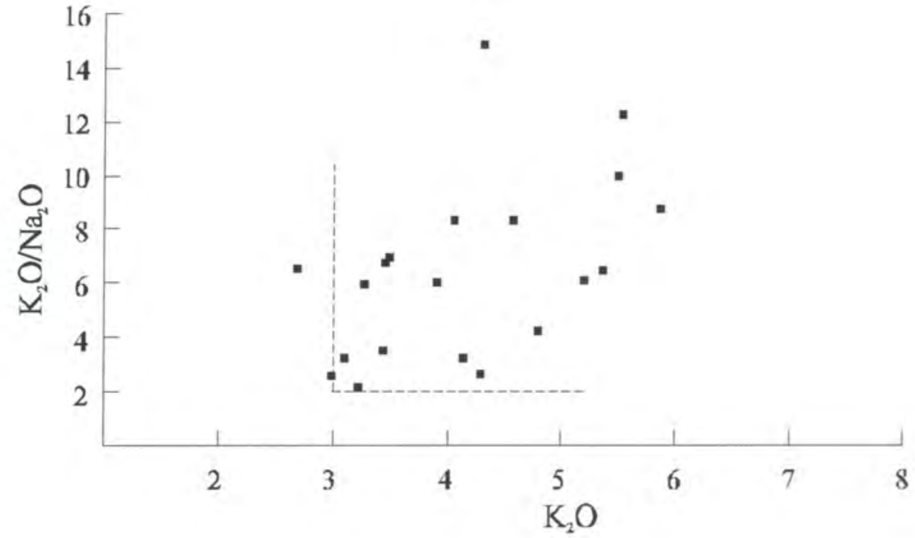

Figure IV.3 - K_2O and K_2O/Na_2O relationships of phlogopite-picrites. The dashed lines represent the minimum values for ultrapotassic rocks, according to Foley *et al.* *(1987)*

Figures IV.4 and IV.5 are plots of phlogopite-picrite analyses in a number of the classification diagrams proposed by Foley *et al.* (1987), utilising the major element compositions. The phlogopite-picrites invariably plot within or near the field of Group II ultrapotassic rocks (kamafugites).

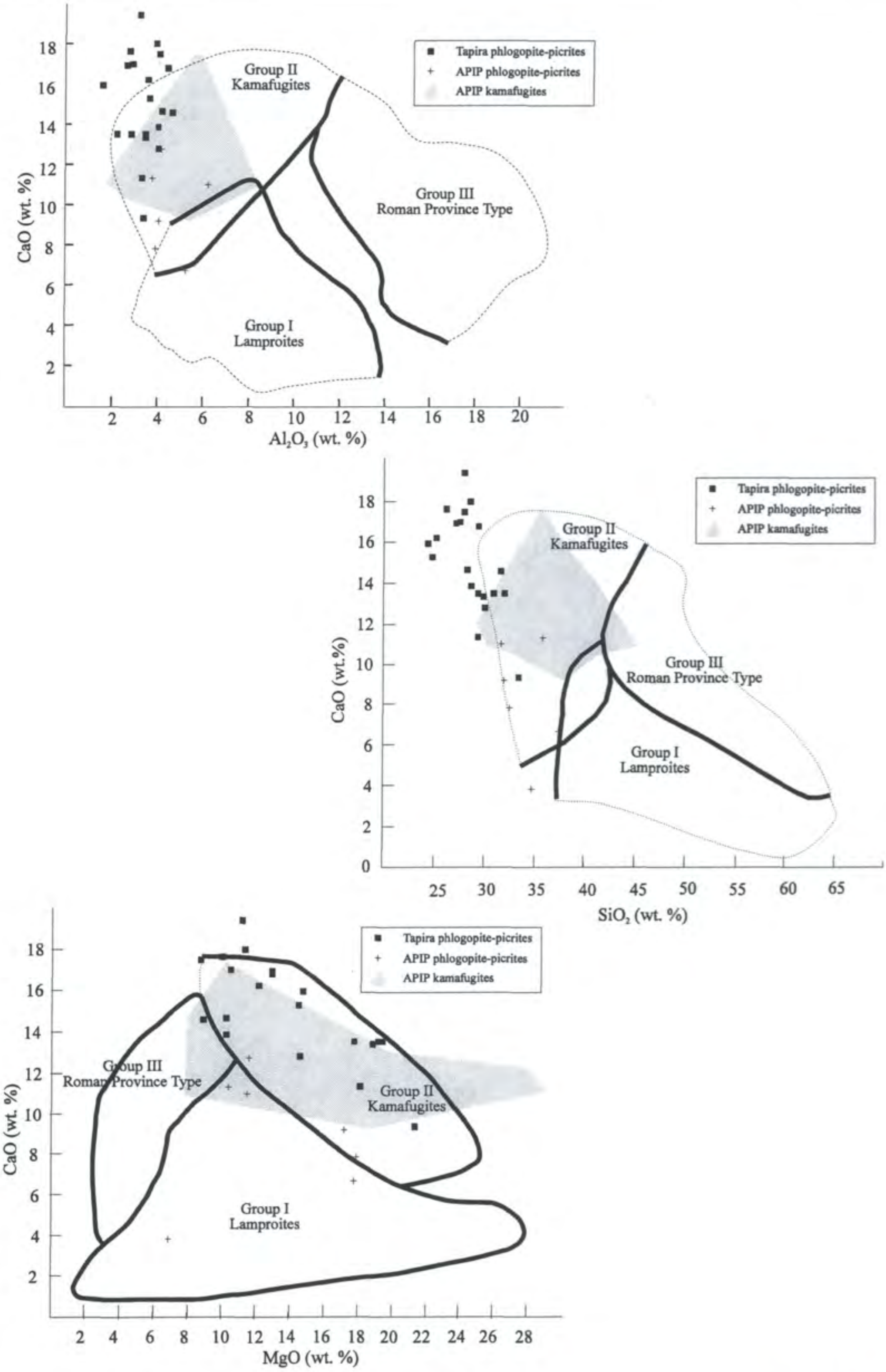

Figure IV.4 - CaO variation with Al_2O_3, SiO_2 and MgO, in classification diagrams of Foley et al. (1987), showing the composition of Tapira phlogopite-picrites. Data for other APIP phlogopite-picrites and kamafugites are from Gibson et al. (1995b) and this work. Dotted lines outline the composition limits of the sample set used by Foley et al. (1987).

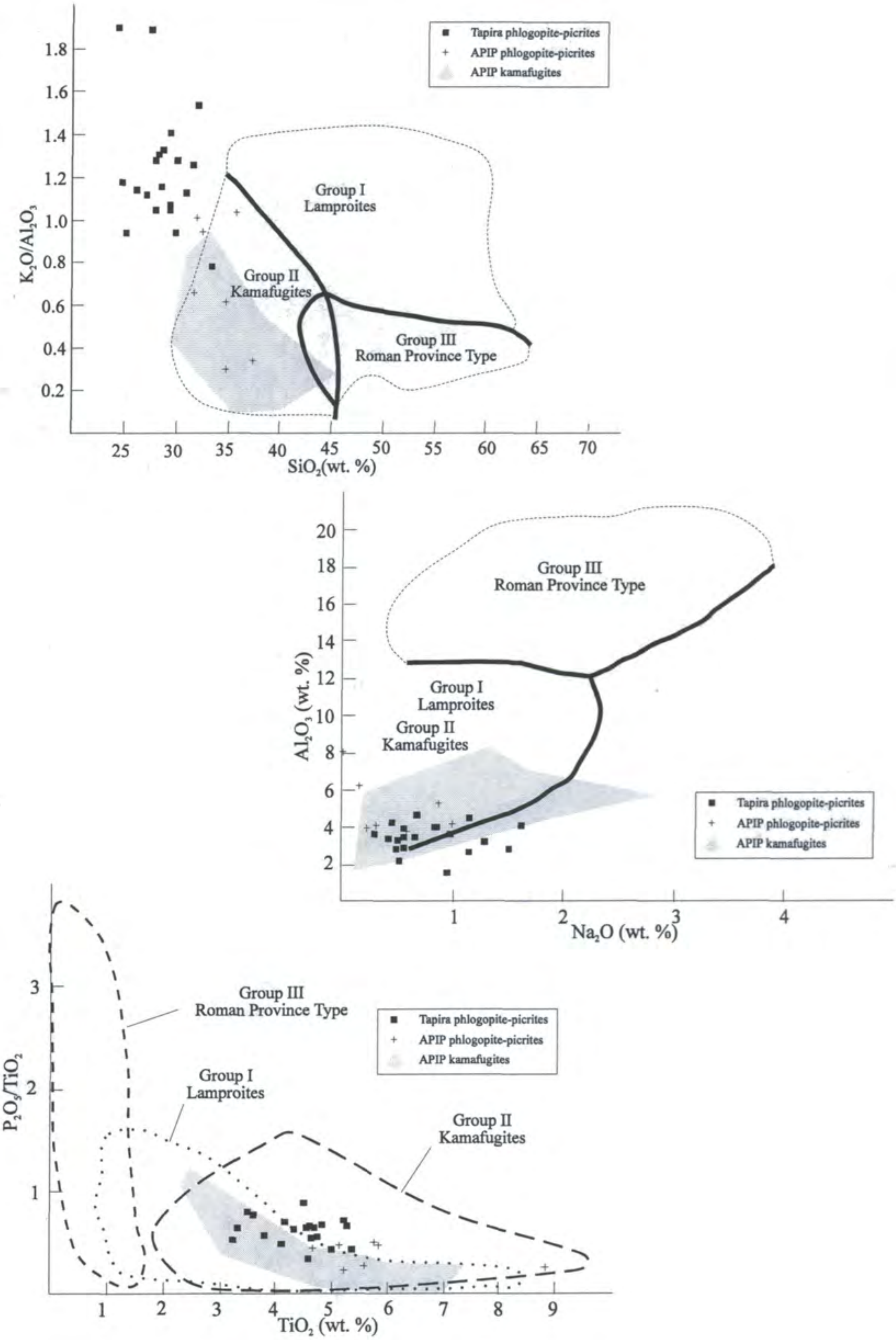

Figure IV.5 - Additional major-element classification diagrams for ultrapotassic rocks (after Foley et al., 1987). Sources of data as in Figure IV.4.

Although the mineralogy of these rocks does not warrant their classification as kamafugites in a petrographic sense (Chapter II), their geochemical affinity with the kamafugitic series is obvious, at least in terms of major elements. Data from Gibson *et al.* (1995b) for kamafugitic rocks of the APIP and for phlogopite-picrites associated with other carbonatite complexes in the province are also plotted in Figures IV.4 and IV.5, for comparison. Phlogopite-picrites from Tapira have slightly lower SiO_2 and Al_2O_3 than the APIP kamafugites and higher CaO than phlogopite-picrites from other APIP carbonatite complexes. The K_2O/Al_2O_3 ratio is higher in Tapira phlogopite-picrites than in both groups of APIP rocks.

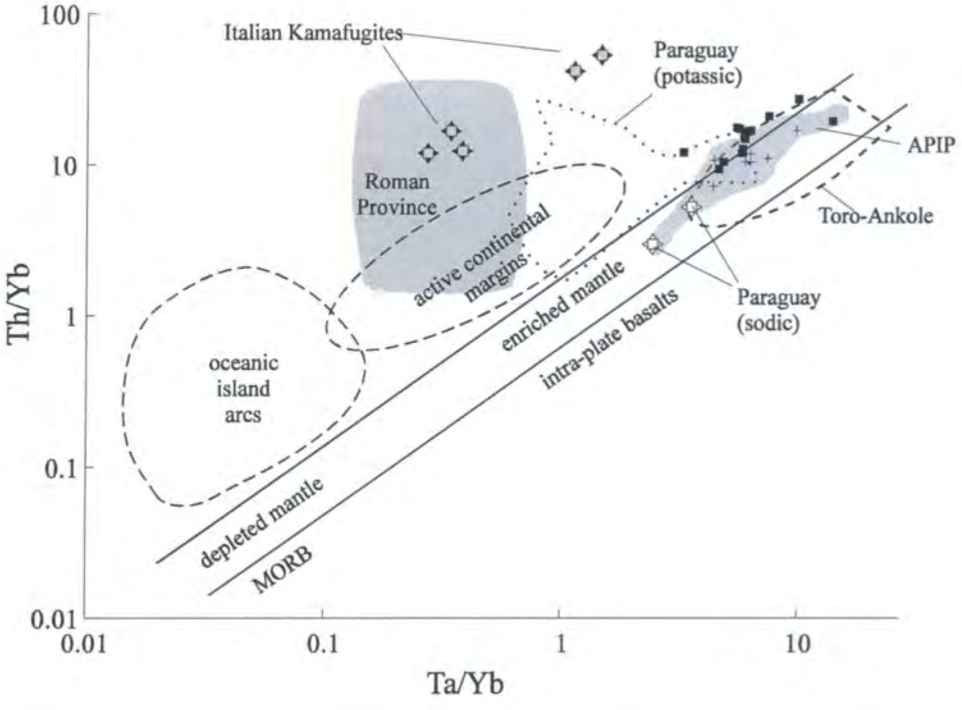

Figure IV.6 - Th/Yb vs. Ta/Yb diagram showing the composition of Tapira phlogopite-picrites (solid squares), compared with other rock types. Data for potassic and sodic rocks from Paraguay are from Comin-Chiaramonti et al. (1997), Italian kamafugites from Conticelli and Peccerillo (1992) and from Peccerillo et al. (1988), APIP rocks from Gibson et al. (1995b). Other fields are from Wilson (1989), and references therein.

The geochemical affinity of phlogopite-picrites with kamafugitic rocks is also observed in trace-element ratio diagrams, such as Th/Yb vs. Ta/Yb and Th/Zr vs. Nb/Zr (Figures IV.6 and IV.7).

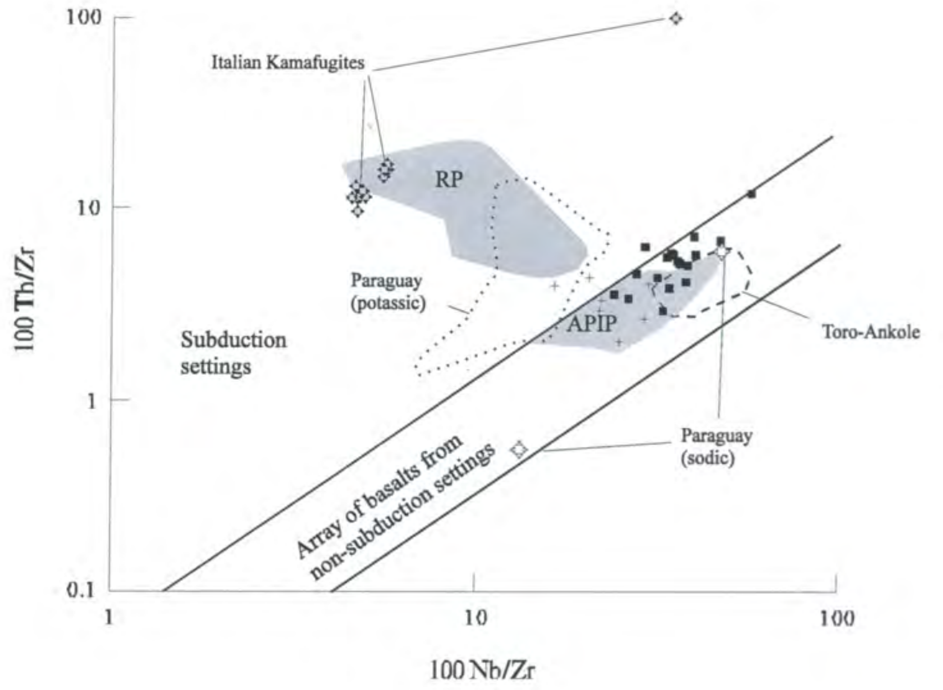

Figure IV.7 - Th/Zr vs. Nb/Zr diagram, showing the composition of phlogopite-picrites from Tapira (solid squares) and other APIP complexes (crosses), compared with other potassic rocks from other provinces. Data for APIP rocks are from Gibson et al. (1995b), Italian kamafugites are from Conticelli and Peccerillo (1992) and Peccerillo et al. (1988). Other fields are after Comin-Chiaramonti et al. (1997).

Both diagrams show that phlogopite-picrites and APIP kamafugites plot at the higher end of the array of rocks derived from non-subduction related mantle sources. The similarity of APIP rocks to the Toro-Ankole kamafugites is also evident. APIP rocks are distinct from other potassic rocks such as the Roman Province-type, Italian kamafugites and Eastern Paraguay, which have lower relative concentrations of niobium and tantalum. Sodic alkaline rocks from Paraguay, however, have composition analogous to APIP, a feature also noted by Comin-Chiaramonti *et al.* (1997), who assumed for these rocks a source similar to that postulated by Gibson *et al.* (1995b) for the Alto Paranaíba ultrapotassic magmas.

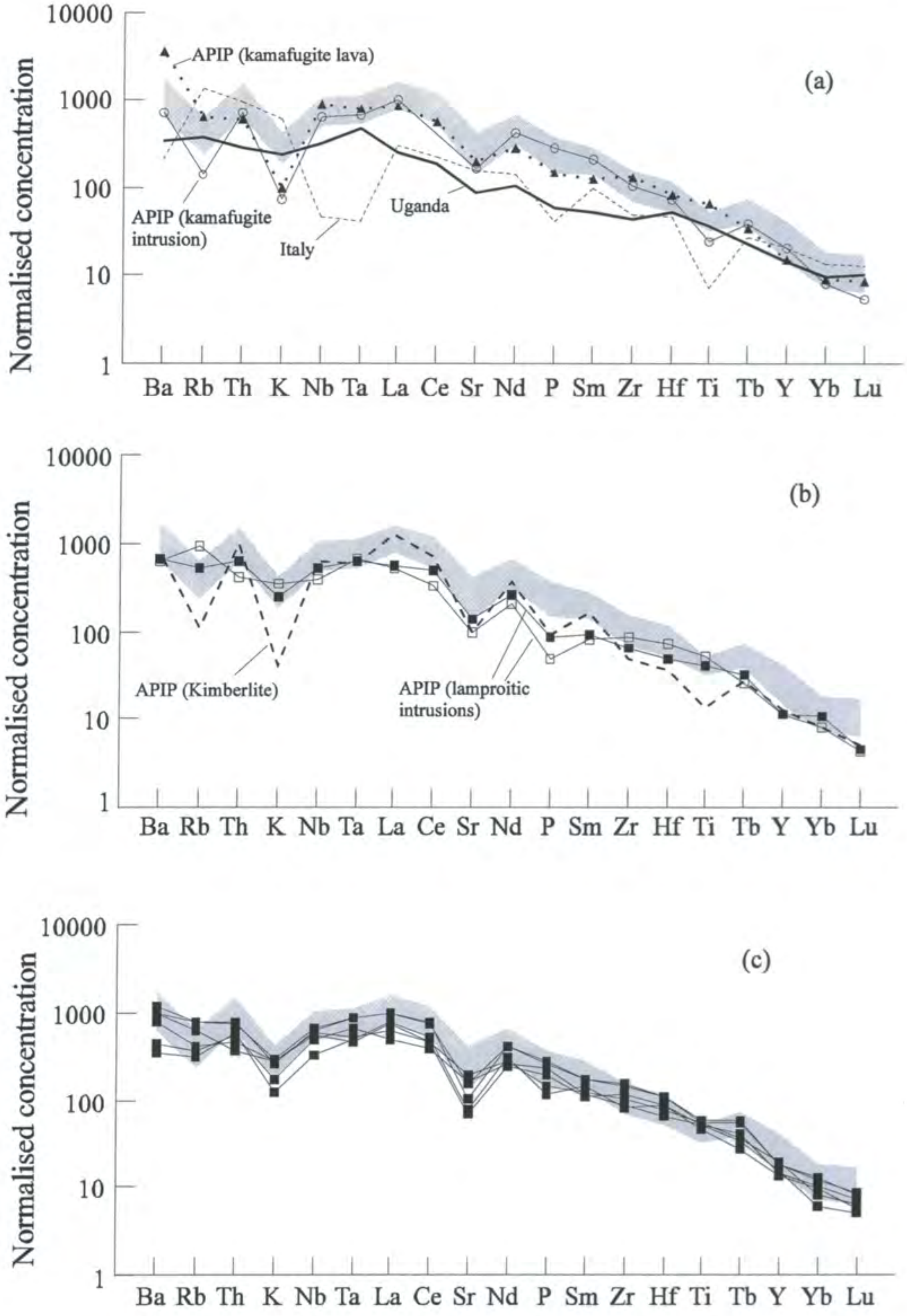

Figure IV.8 - Spider diagrams comparing the composition of Tapira phlogopite-picrites (shaded field) with: (a) kamafugites from APIP (Gibson et al., 1995b), Italy (Peccerillo et al, 1988) and Uganda (Thompson et al., 1984); (b) kimberlite and lamproitic rocks from APIP (Gibson et al., 1995b); (c) phlogopite-picrites associated with other APIP complexes (Gibson et al., 1995b). Concentrations normalised to chondrite (except Rb, K and P) according to Thompson et al. (1984).

Finally, Figure IV.8 compares the chondrite normalised distribution of trace elements in the Tapira phlogopite-picrites with that of other examples of alkaline rocks. The pattern for Tapira samples agrees well with those of the APIP kamafugites and shows a nearly perfect coincidence with phlogopite-picrites from other carbonatite complexes in the province. Both the Ugandan and Italian examples of kamafugites are less enriched in most elements than the APIP rocks. Additionally, the Italian kamafugites exhibit a characteristic negative anomaly in Nb and Ta, which is lacking in the Ugandan and APIP rocks. The negative anomalies of K and Rb are more pronounced in the sample of APIP kimberlite than in the phlogopite-picrites. APIP lamproitic rocks are distinguished from the phlogopite-picrites by their lower contents of LREE, and by the absence of negative Rb and K anomalies.

IV.2.2 - LOW-CR DYKES

This group comprises a series of fine-grained rocks that, although still ultramafic, are mineralogically more evolved than the phlogopite-picrites. Their chemical composition is also more variable than the former, and it is possible that rocks included in this unit had more than one origin or evolved along different paths.

Major-element oxides

The low-Cr dykes can be distinguished from the phlogopite-picrites by their lower MgO (2.99-12.48 wt. %), higher CaO (15.93 - 26.03 wt. %), P_2O_5 (2.04 - 6.02 wt. %) and, in some cases, higher CO_2 (1.07 - 22.27 wt. %). This reflects the absence of olivine and the increase in the proportion of clinopyroxene, apatite and groundmass carbonate. In the more extreme cases of carbonate enrichment, the low-Cr dykes can be considered as transitional to silico-carbonatites. Like the phlogopite-picrites, the low-Cr dykes are extremely silica-undersaturated (SiO_2 from 18.4 to 36.7 wt. %) and have low Al_2O_3 contents (2.04 - 7.41 wt. %). They are also strongly potassic (2.56 - 5.95 wt. % K_2O), with variable K_2O/Na_2O ratio (1.2 - 13.2).

Trace elements

The more evolved character of the low-Cr dykes, in comparison with the primitive phlogopite-picrites, leads to a more significant control of trace-element concentration by processes such as fractional crystallisation or liquid immiscibility

The most striking difference in trace-element content between phlogopite-picrites and low-Cr dykes is the extreme depletion in some compatible elements, such as Cr and Ni, in the latter. The concentrations of both elements are usually below 40 ppm, signalling the extensive previous fractionation of olivine and Cr-rich spinel. One of the analysed samples (at020) yielded 245 ppm Cr and 86 ppm Ni, which are closer to the values observed in some (evolved) members of the phlogopite-picrite series. Nevertheless, this sample is still included in the low-Cr dykes group, on the grounds of petrographic similarities, such as the higher amount of pyroxene and the absence of olivine phenocrysts.

It is noteworthy that not all compatible elements (using the term on a broad sense) are depleted in the low-Cr dykes. For instance, Sc may reach concentrations even higher (up to 68 ppm) than those observed in the phlogopite-picrites. Among a number of Tapira mineral separates analysed for trace elements by ICP-MS (see Appendix 2 for data), clinopyroxene yielded significant Sc concentrations (111 ppm), while other calcium-rich minerals, such as apatite, perovskite and calcite, contain negligible amounts of Sc. Therefore, the enrichment of this element in some of the low-Cr dykes most likely signals the contribution of clinopyroxene.

The low-Cr dykes are generally enriched in incompatible elements, with very high Sr (up to 11000 ppm in a high-carbonate sample, but generally between 2000 and 6000 ppm) and Ba (up to 5600 ppm). The abundances of Zr and Hf are variable in the low-Cr dykes, with some of the analysed samples reaching up to 4000 ppm Zr and up to 64 ppm Hf. Niobium reaches higher concentrations (230-520 ppm) than in the phlogopite-picrites, but Ta can be relatively depleted (1-22 ppm) in some samples. This disparate behaviour induces wide variations in chondrite-normalised Nb/Ta ratios, which will be discussed in greater detail, together with the possible petrogenetic implications, in Chapter V.

Figure IV.9 illustrates the trace-element relationships in the low-Cr dykes, along with a shaded field representing the composition range of phlogopite-picrites. The spider diagrams for most samples (representative analyses plotted in Figure IV.9a) show good approximation to the phlogopite-picrite series, apart from slightly higher concentrations of the REE, Zr and Hf. However, for a small group of samples (Figure IV.9b) the trace-element distribution departs significantly from this pattern. Although their major-element contents are similar to those of the first group, these rocks have much higher Zr and Hf concentrations, strong Th depletion, no Sr anomaly and a positive P anomaly. Note that this group also has lower LREE and higher HREE than the phlogopite-picrites and the remainder of the low-Cr dykes.

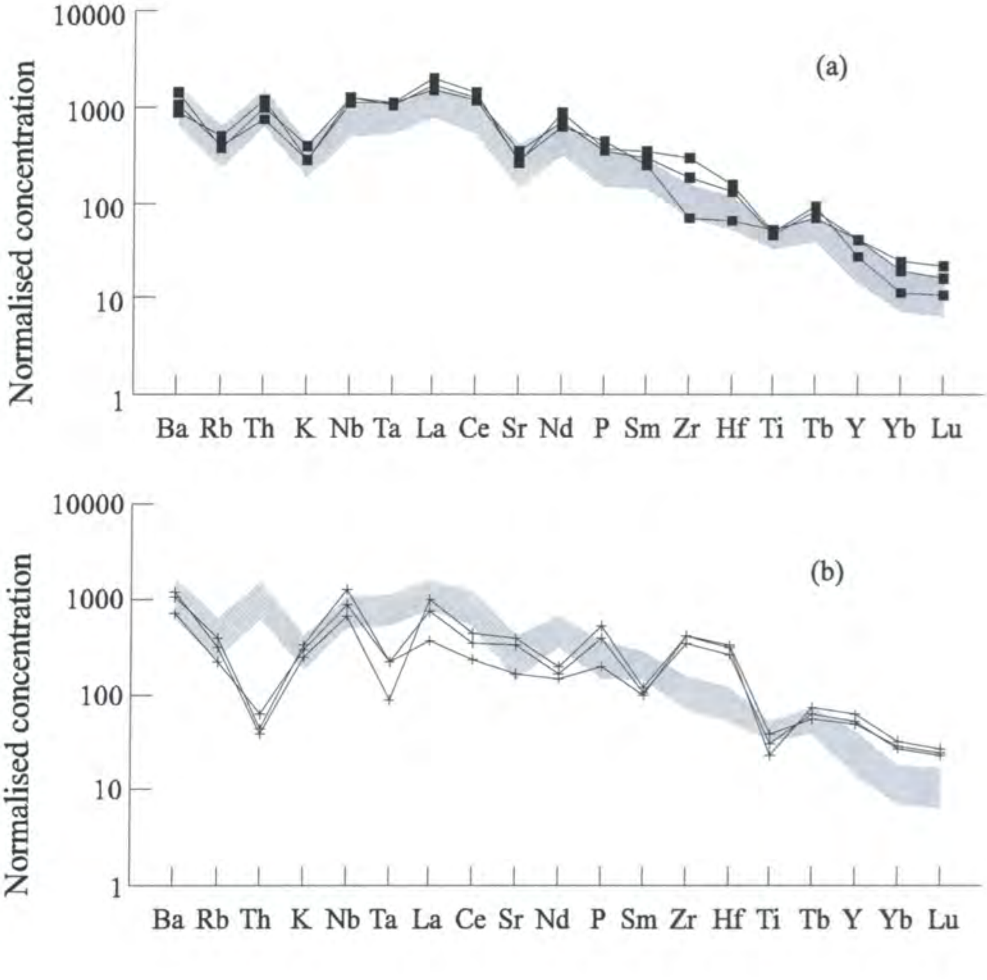

Figure IV.9 - Normalised trace-element diagrams for low-Cr dykes, compared with the range of phlogopite-picrites (shaded field). The low-Cr dykes can be divided in two groups, represented in (a) and (b), according to their trace-element relationships (see text). Concentrations normalised to chondrite (except Rb, K and P) according to Thompson et al. (1984).

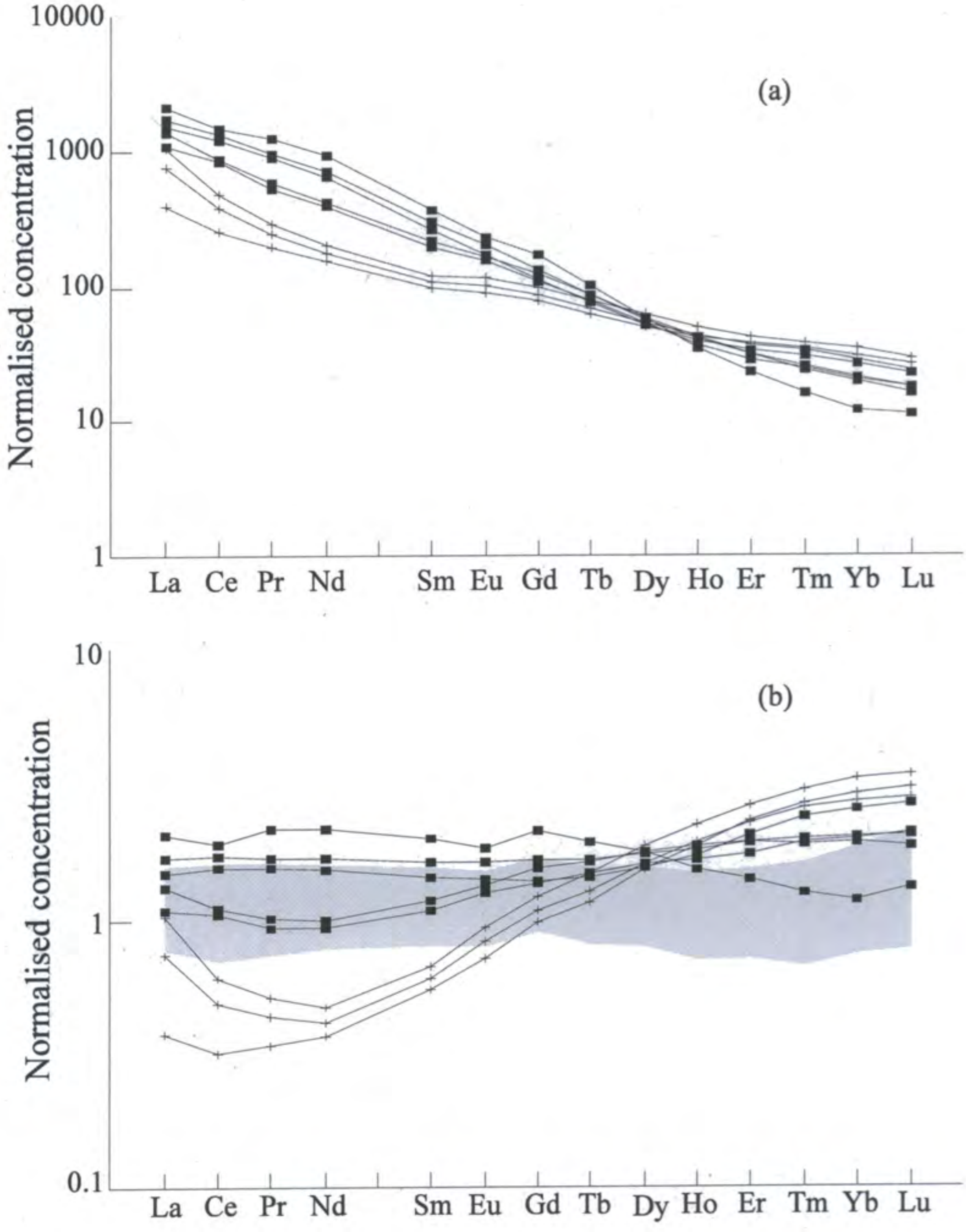

Figure IV.10 - REE patterns of low-Cr dykes normalised to: (a) chondritic values of Boynton (1984) and (b) primitive phlogopite-picrite (sample at021a). The shaded field in diagram (b) covers the range of Tapira phlogopite-picrites.

The REE patterns of low-Cr dykes are illustrated in greater detail in Figure IV.10. The first diagram shows chondrite-normalised REE patterns and the second diagram shows the values normalised to a primitive phlogopite-picrite sample (at021a), together with the range of phlogopite-picrite compositions (shaded field). The two groups of low-Cr dykes (from Figure IV.9) have contrasting behaviour, when compared with the phlogopite-picrites. The first group produces normalised REE patterns that are parallel to those of phlogopite-picrites, albeit at generally higher values for all REE. This can be considered as a natural progression of the phlogopite-picrites (note that the shaded field is skewed towards values higher than 1, representing the evolution within the phlogopite-picrite series). The low-Cr dykes with positive Zr-Hf and negative Th anomalies (Figure IV.9) are depleted in LREE and enriched in HREE, relative to the phlogopite-picrites. Figure IV.10 shows that the REE patterns of these rocks "cross over" those of the first group at Dy.

Figure IV.11 shows the REE patterns of Tapira minerals, normalised to the values of primitive phlogopite-picrite. The diagrams suggest that extensive removal of apatite or perovskite (or both) from a phlogopite-picrite liquid would result in an anticlockwise rotation of the REE patterns of the residual liquid, with decrease in the LREE/HREE ratios. Furthermore, apatite removal would also promote a relative depletion of the residual liquid in the rare-earth elements from Ce to Eu, whilst the extraction of perovskite would induce a stronger depletion in rare-earth elements from Gd to Er. The REE patterns of the residual liquids are less likely to be affected by calcite, which has REE abundances similar to the phlogopite-picrites, or by pyroxene and phlogopite, which have much lower REE contents.

At first sight, the comparison between Figures IV.10 and IV.11 would suggest that extensive fractionation of apatite can explain the anomalous behaviour of some of the low-Cr dykes. However, a positive anomaly of phosphorus and a negative anomaly of titanium in Figure IV.9b seems to argue in favour of perovskite fractionation. Furthermore, the removal of perovskite (or apatite) cannot account for all of the anomalous behaviour displayed by these rocks in spider diagrams (e.g. Th, Zr and Hf anomalies and the changes in Nb/Ta ratio). Alternative reasons for these anomalies will be explored in detail in Chapter V.

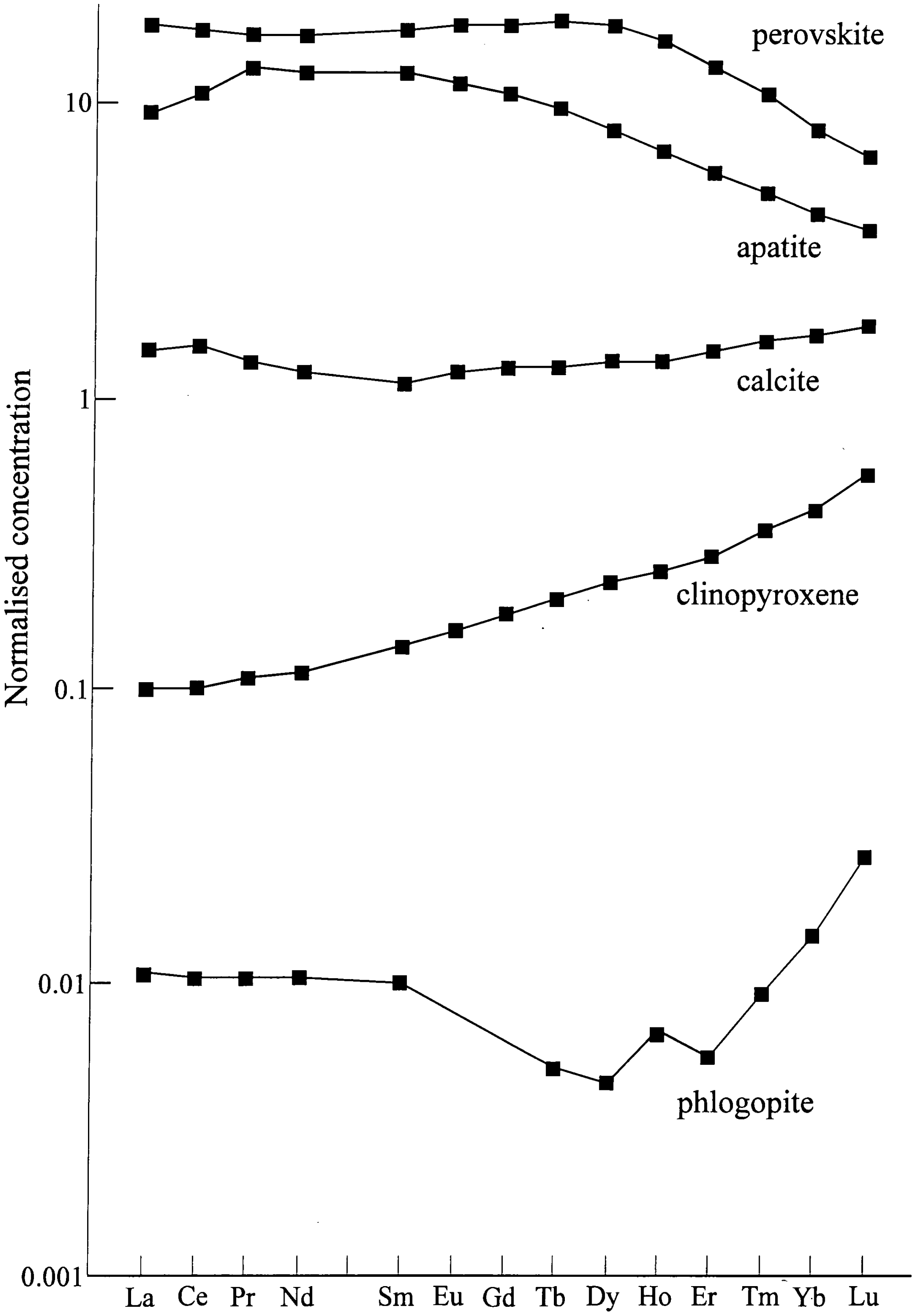

Figure IV.11 - REE patterns of minerals from the Tapira complex, normalised to primitive phlogopite-picrite composition. See Appendix 2 for analyses.

IV.2.3 - A "LIQUID LINE OF DESCENT" FOR THE MAFIC DYKES?

The mineralogical and chemical evidence suggests that the mafic dykes in Tapira form a series of differentiating liquids. However, several attempts at monitoring the evolution of these liquids on Harker diagrams, by plotting the whole-rock analyses against differentiation indices such as SiO_2 and MgO, or against trace elements such as Cr, Ni or Zr, failed to provide an adequate representation of the evolution of these rocks. For instance, Cr and Ni are good indicators of differentiation within the phlogopite-picrites, but are inadequate for the low-Cr dykes, which cluster at very low Cr and Ni values. Given the extremely low SiO_2 content of these rocks, the removal of olivine at an early stage would actually result in a decrease in SiO_2 content of the residual liquid, rendering silica clearly ineffective as a fractionation index. MgO (or magnesium number) fails to account for the increase in groundmass carbonate with evolution, which is an important feature of the Tapira dykes. Elements which are incompatible in most magmatic systems may behave compatibly with regard to minerals such as perovskite, apatite and carbonate) and, consequently, should not be used as a differentiation index.

A better result has been obtained by using the ratio CaO/(CaO+MgO) as a differentiation index for the mafic dykes (Figures IV.11 and IV.12). This ratio provides a satisfactory way of monitoring, for example, the fractionation of olivine and pyroxene, whilst also accounting for the increase in interstitial carbonate in the more evolved rocks. The diagrams are not entirely adequate for the representation of perovskite and apatite, which would ideally require the inclusion of TiO_2 and P_2O_5 in the calculation of the differentiation index. However, it is shown below that this problem can be satisfactorily avoided by the use of the whole-rock composition of apatite- and perovskite cumulates, as an approximation for solid fractions removed from the liquids.

Figure IV.12 shows the variation of selected major-element oxides as a function of the CaO/(CaO+MgO) ratio. The composition ranges of several relevant minerals and representative analysis of Tapira cumulates are plotted in the diagrams, for comparison, and the possible effects of solid-fraction removal are indicated by arrows. For most elements, the diagrams are consistent with a continuous evolution from phlogopite-picrites to low-Cr dykes by magmatic differentiation, and with the textural relationships and crystallisation orders established in Chapter II.

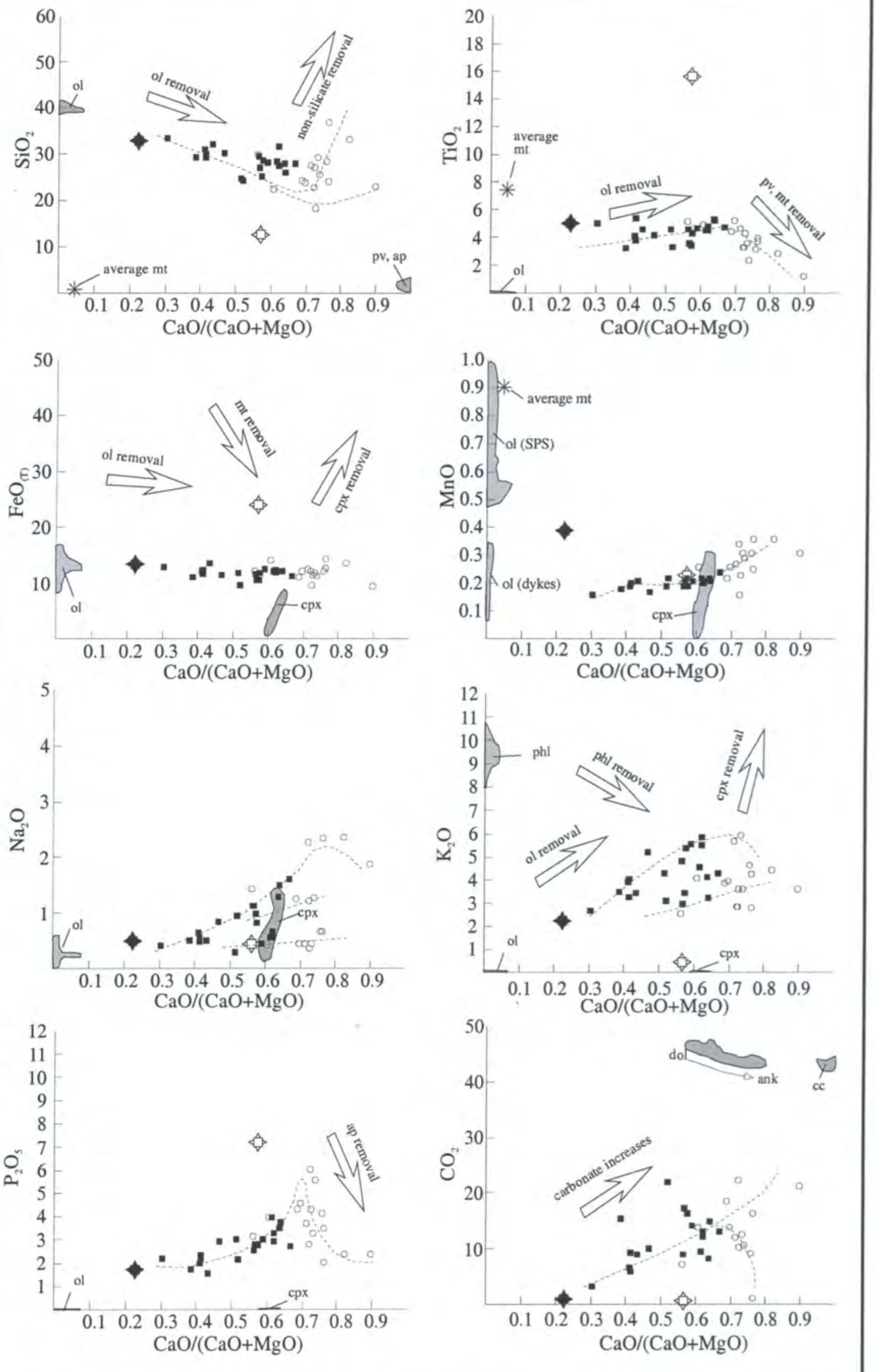

Figure IV.12 - Major-element oxides (wt. %) variation with magma evolution of phlogopite-picrites (solid squares) and low-Cr dykes (open circles). Compositions of relevant minerals and of olivine-rich (solid star) and apatite-perovskite-rich cumulate (open star) are indicated. Ol=olivine, mt=magnetite, pv=perovskite, ap=apatite, cpx=clinopyroxene, phl=phlogopite, dol=dolomite, ank=ankerite, cc=calcite. See text for explanation.

The fractionation of olivine exerts a strong control on the chemistry of the liquids at the early stages of crystallisation. Note that in most diagrams the trend of whole-rock analyses progresses away from the olivine-rich cumulate, suggesting that rocks such as dunites and wehrlites in the SPS may have been produced by fractionation from phlogopite-picrite liquids. Also noteworthy is the gentle decrease in SiO_2 at the early stages of evolution. The progressive silica depletion results from the fact that the SiO_2 content of the primitive phlogopite-picrites is lower than that of olivine. SiO_2 only increases in the residual liquid when significant amounts of non-silicate minerals are removed. This may be a recurrent process in the evolution of the complex, but seems to be particularly significant at the transition from phlogopite-picrites to low-Cr dykes. Note that the variation of TiO_2 and P_2O_5 can be explained by the formation of perovskite-apatite-rich cumulates.

The behaviour of the alkalis is less straightforward. The diagrams suggest the presence of more than one evolution trend, These could also be the result of subsolidus changes in the alkali contents of the rocks or, alternatively, they could indicate a multi-stage evolution of the dykes.

The progressive increase of CO_2 with the differentiation index is consistent with the increase in groundmass carbonate, observed in thin section. However, the trend of the low-Cr dykes seems to bifurcate, suggesting that perhaps an event of liquid immiscibility has occurred (see discussion in Chapter V). This is consistent with the existence of carbonate ocelli in the dyke rocks (Chapter II).

The variation of selected trace elements with magma evolution is presented in Figure IV.13. It is clear from the diagrams that compatible elements, such as Cr and Ni, show a negative correlation with the differentiation index. Sc shows a distinct behaviour, increasing slightly at first, when olivine removal controls the system, but decreasing sharply at the interface between phlogopite-picrites and low-Cr dykes, when the behaviour of Sc is controlled by the removal of clinopyroxene.

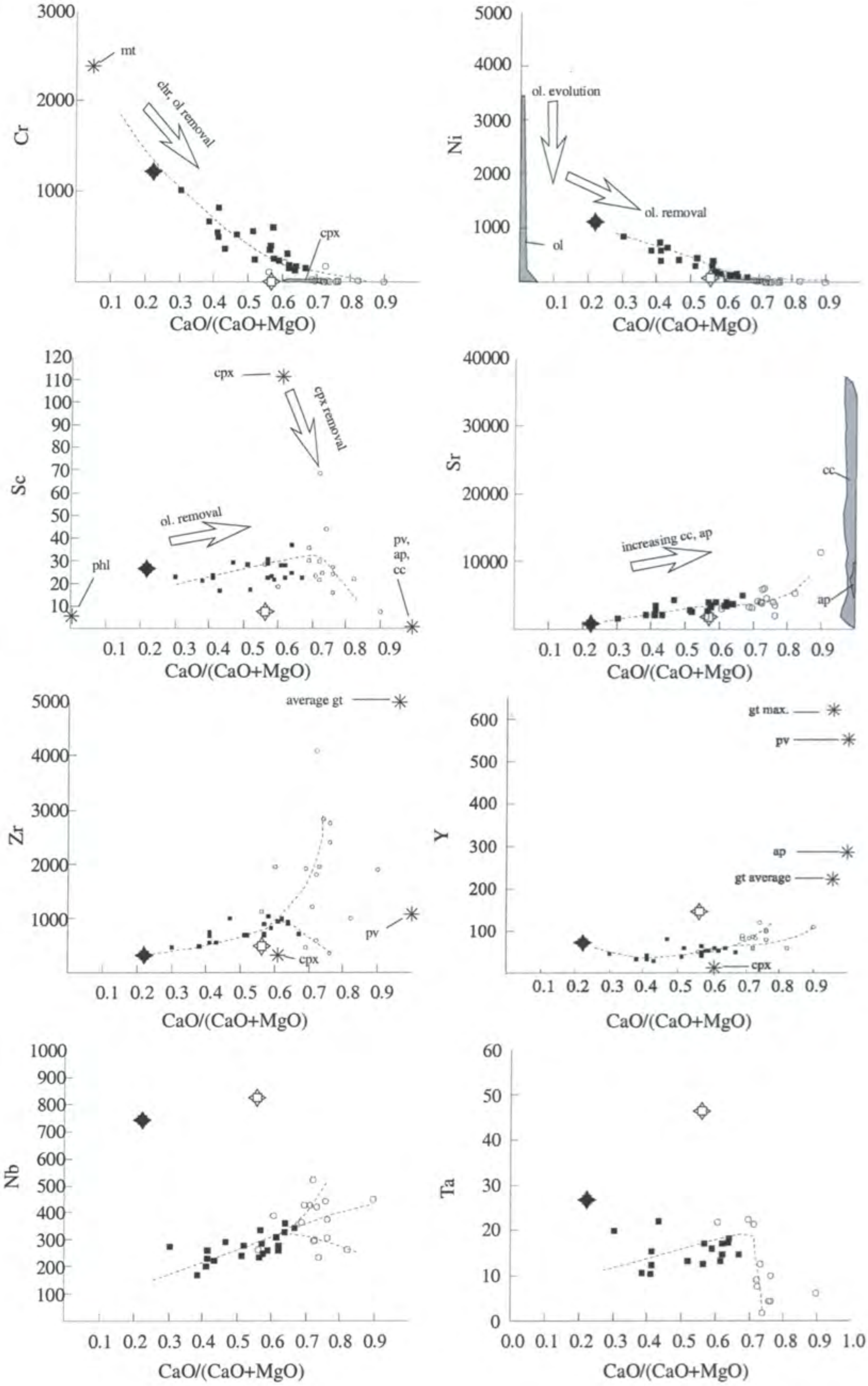

Figure IV.13 - Variation of trace elements (ppm) with magmatic evolution. Symbols and mineral abbreviations as in Figure IV.12, plus chr=chromite, gt=garnet.

Among the incompatible elements, Sr increases progressively with differentiation. This is consistent with carbonate- and apatite enrichment, since these two minerals are major Sr hosts in the Tapira complex (see Chapter III for discussion of carbonate, and Appendix 2 for ICP analysis of apatite). Zr (and Hf, not shown in Figure IV.13) increases steadily with differentiation in the phlogopite-picrites, but the low-Cr dykes define two separate trends, one of enrichment and the other of depletion in Zr, which correspond to the two groups depicted in Figure IV.9. Rocks of the high-Zr group contain abundant melanite garnet, which seems to be an important Zr carrier in Tapira mafic rocks (Chapter III).

Yttrium seems to decrease slightly at first and then increase progressively with differentiation. However, it should be noted that both examples of cumulate rocks (Figure IV.13) are enriched in Y, relative to the fine-grained dykes. This may be reflecting the accumulation of minerals such as perovskite and/or apatite in the coarse-grained rocks. The increase in Y during the latest stages of differentiation may be related to presence and accumulation of melanite garnet. However, as observed for other elements, more than one trend seem to be present in the more evolved dykes. It is possible that the controls of magmatic processes on Y (and, therefore, on the heavy REE) are more complex than can be depicted in the adopted diagrams.

The diagrams for Nb and Ta illustrate the disparate behaviour previously observed between these two elements in spider diagrams. Both elements increase progressively in the phlogopite-picrites with differentiation, but Ta decreases abruptly in the low-Cr dykes. This depletion does not seem to affect Nb to the same extent, thus resulting in a significant increase in the Nb/Ta ratio of the rock (see Chapter V).

Finally, Figure IV.14 illustrates the control of clinopyroxene fractionation. As discussed above, MgO is *not* a suitable differentiation index for Tapira dykes, but the plot of MgO against Sc/Cr is particularly effective in showing the relationships of the ultramafic dykes with the ultramafic plutonic rocks. Note that if phlogopite-picrites and low-Cr dykes are considered independently, the former are consistent with the extensive fractionation of olivine and Cr-rich spinel to form the wehrlites, whilst the Sc/Cr ratio of the latter seems to be dominantly controlled by the removal of clinopyroxene to form the bebedourites. Syenite analyses are also plotted in the diagram, for comparison.

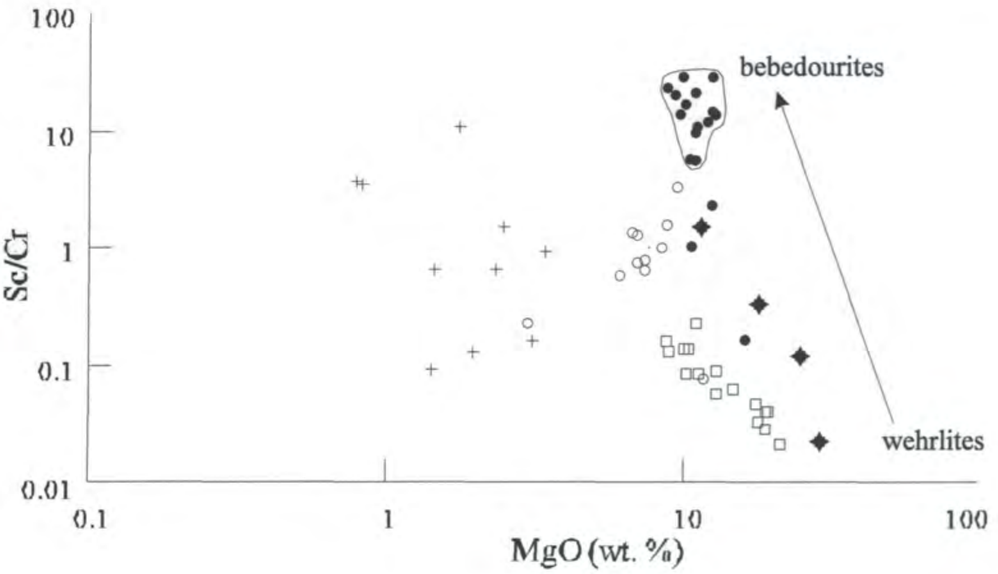

Figure IV.14 – Sc and Cr relationships between olivine-bearing cumulates (solid stars), bebedourites (solid circles), phlogopite-picrites (open squares) and low-Cr dykes (open circles). Note the increase in the Sc/Cr ratio with the evolution of the cumulates. Compositions of syenites (crosses) are plotted for comparison

IV.2.4 - SILICATE PLUTONIC SERIES (SPS)

The interpretation of the chemical properties of the SPS rocks is less straightforward than that of the dykes, due to the effect of extensive crystal accumulation (e.g. the olivine-rich and the perovskite-apatite-rich cumulates shown in Figures IV.12 and IV.13). As discussed previously, many of the ultramafic SPS rocks are unlikely to be representative of real magmatic liquids. Nevertheless, some general chemical features and differences between the various types of ultramafic rocks (e.g. wehrlites and bebedourites in the B1 and B2 units) are pointed out in the sections below.

Wehrlites and olivine-bearing cumulates

The chemical composition of the olivine-bearing rocks is highly variable, both in terms of major and trace elements, depending on which mineral phases accompany olivine in the rock. For example, TiO_2 may reach up to 15.6 wt. % in perovskite-rich rocks, and P_2O_5 may be as high as 10.5 wt. % in apatite rich rocks. These rocks have generally low SiO_2 (12 - 33 wt. %) and high, but variable, MgO (11 - 30 wt. %), $Fe_2O_{3(T)}$ (12 - 27 wt. %) and CaO (8-26 wt. %).

The olivine-rich rocks also usually contain significant amounts of Cr (up to 1200 ppm) and Ni (up to 1100 ppm), which distinguishes them from the generally Cr- and Ni-poor bebedourites. However, it should be stressed that exceptions to this rule do occur, and some of the wehrlites may be Cr- and Ni-poor, while rare bebedourites may contain high amounts of these elements.

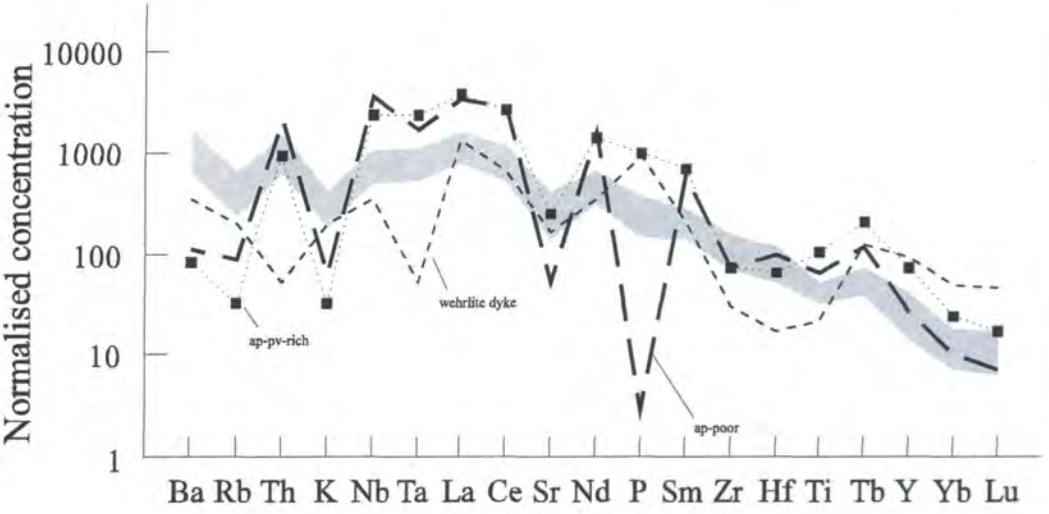

Figure IV.15 - Normalised trace-element diagram of olivine-bearing cumulates from SPS, compared with the range of phlogopite-picrites (shaded area). Concentrations normalised to chondrite (except Rb, K and P) according to Thompson et al. (1984).

The relationships of incompatible elements in olivine-bearing cumulates are summarised in the spider-diagram of Figure IV.15, and compared with the range of phlogopite-picrites. If the latter can be considered representative of unevolved magmatic liquids in Tapira, some inferences may be made regarding the behaviour of various trace elements. For instance, it is clear from Figure IV.15 that elements such as Ba, Rb, K, and, to a lesser extent, Sr and Zr, behave incompatibly with respect to the common mineral assemblages of SPS rocks (i.e. mostly olivine, clinopyroxene, perovskite and apatite). On the other hand, elements that are usually considered incompatible in other magmatic systems, such as Nb, Ta and the REE are clearly compatible with regard to the same mineral assemblage. The mineral chemistry data (Chapter III) suggest that the main host for Nb and Ta in these rocks is probably perovskite, whilst the REE are hosted by both apatite and perovskite. A medium-grained wehrlite dyke is plotted alongside the coarse-grained cumulates in Figure IV.15. In Chapter II these dykes were assigned to the B2 unit, on the grounds that they crosscut B1 bebedourites and show crucial mineralogical differences from the coarser-grained B1 wehrlites (e.g. the occurrence of melanite, instead of perovskite, as the main Ti phase). The lower concentrations of Th, LREE, Zr, Hf and Ti, and the much higher Nb/Ta ratio of the wehrlite dyke shown in Figure IV.15 support the inference that these dykes are fundamentally distinct from B1 wehrlites.

The REE patterns of the olivine-bearing SPS rocks are shown in Figure IV.16, normalised to chondrite and to the primitive phlogopite-picrite. The pattern for the B2 wehrlite dyke contrasts with that of the coarser-grained rocks, and approximates that of some of the low-Cr dykes in Figure IV.10(b).

Some of the REE behaviour can be explained through the control exerted by specific mineral phases accumulated in these rocks. For instance, the apatite-perovskite-rich cumulate is enriched in the middle REE, relative to the apatite-poor cumulate. It could also be argued that the enrichment in heavy REE in the wehrlite dyke is associated with accumulation of garnet. On the other, hand, some of the variations are difficult to explain as a mineralogical effect. For example, despite the very high phosphorus content (9.9 wt. % P_2O_5, note also the positive P anomaly in Figure IV.15) of the wehrlite dyke, this rock is relatively depleted in the light to middle REE.

Bebedourites

The absence of both olivine and Cr-rich spinel, and increased amounts of clinopyroxene, in comparison with the olivine-bearing rocks, is reflected in the chemical composition of most bebedourites by higher SiO_2, Na_2O and CaO, and lower $Fe_2O_{3(T)}$, MnO, and MgO. The very low Cr (usually below 20 ppm) and Ni (usually below 50 ppm) contents and the high Sc (up to 145 ppm), which are typical of both B1 and B2

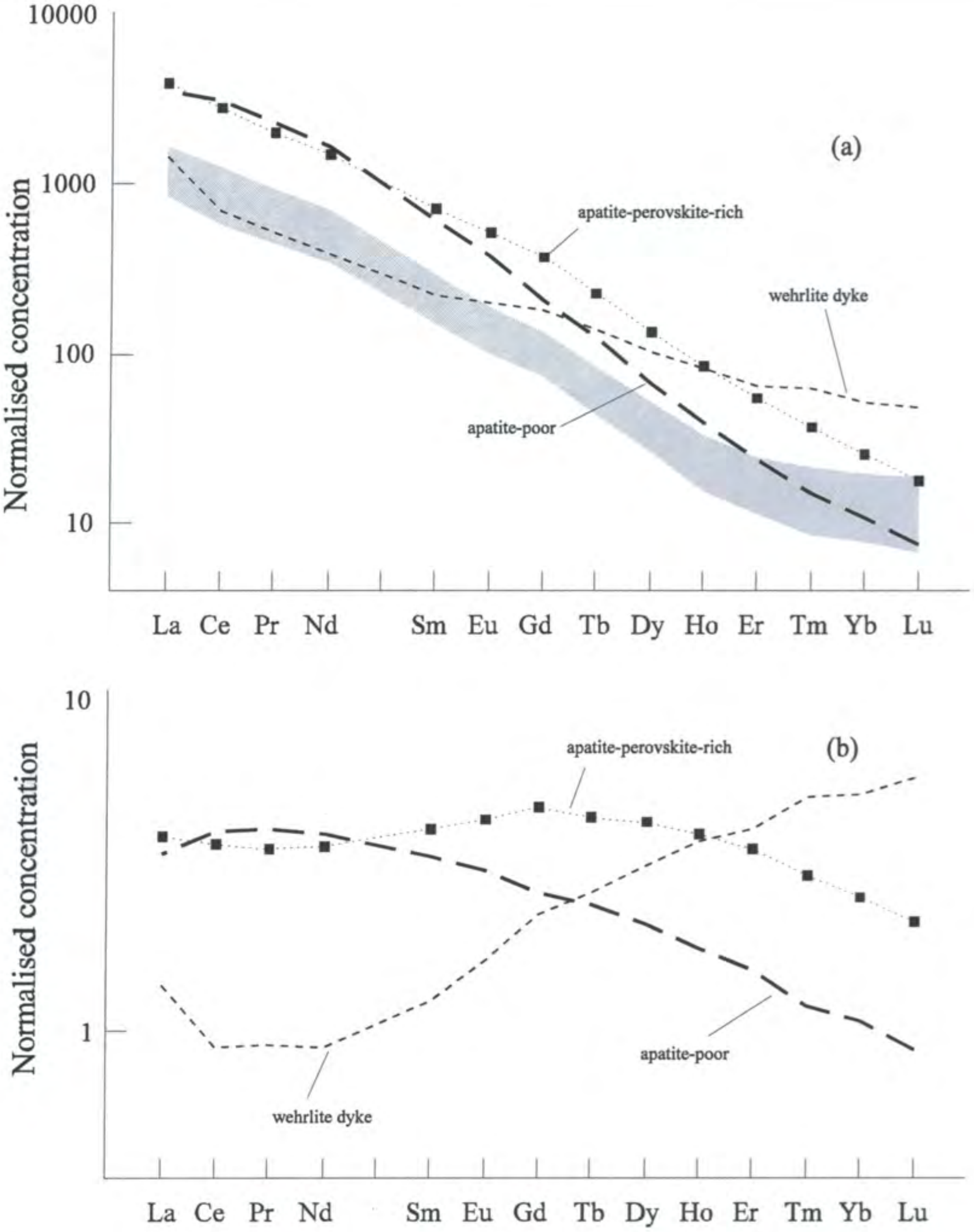

Figure IV.16 - Rare-earth patterns of olivine-bearing SPS rocks, normalised to: (a) chondrite (Boynton, 1984) and (b) primitive phlogopite-picrite. Shaded field in diagram (a) is the range of phlogopite-picrite compositions.

bebedourites, can also be explained by the same changes in mineralogy. In rare cases, substantial amounts of Cr (over 800 ppm in one sample) testify to the occasional recurrence of chromite crystallisation within the bebedourite sequence. Interestingly, the amount of Ni in the same sample falls just short of 140 ppm, since olivine is not present.

Although the chemical composition of the bebedourites is variable and, in many cases, there are extensive compositional overlaps between rocks of the B1 and B2 units, some broad chemical distinctions between the two units can be outlined. In terms of major elements, B1 bebedourites have higher TiO_2 and tend to have slightly higher MgO, whilst bebedourites from B2 have higher contents of SiO_2, MnO and to a lesser extent, CaO. Regarding the trace elements, B2 rocks have notably higher Zr, Th and lower Y than B1. Bebedourites of the B2 unit are also enriched in LREE in comparison with B1, for the same SiO_2 content. Spider diagrams for representative analyses of bebedourites from the two units are presented in Figures IV.17 and IV.18.

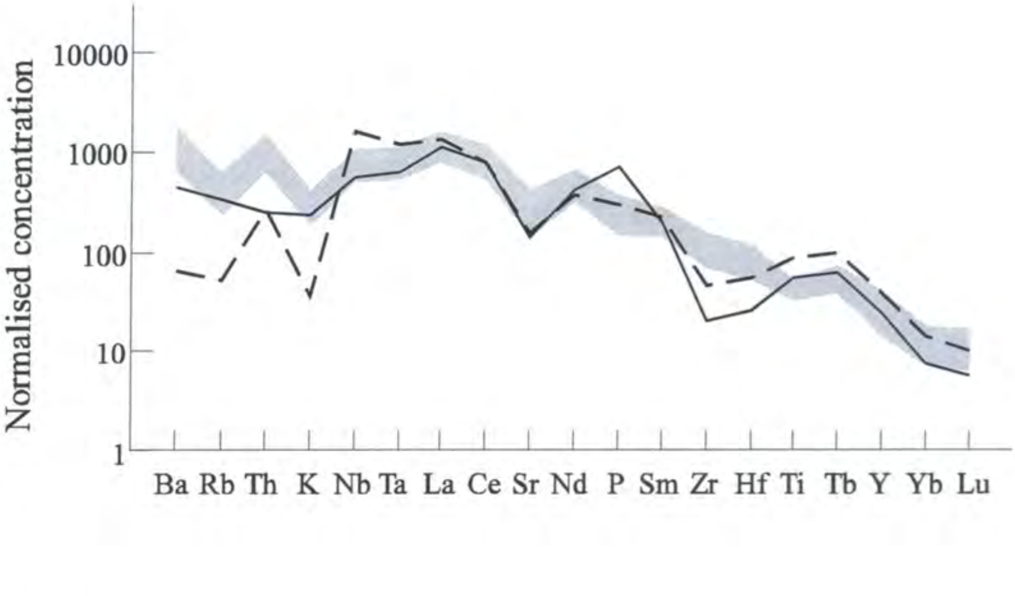

Figure IV.17 - Trace-element variation of selected analyses of B1 bebedourites compared with the range of phlogopite-picrites (shaded field). Concentrations normalised to chondrite (except Rb, K and P) according to Thompson et al. (1984).

Most B1 bebedourites are characterised by small or non-existent relative negative anomalies of Rb and K (Figure IV.17), although these features may be shown by a small number of samples (e.g. dashed line in Figure IV.17). Phosphorus and titanium highs are conspicuous in many spider diagrams of these rocks, associated with increased modal contents of perovskite and apatite. The corresponding slight negative P and Ti anomalies, locally observed in the phlogopite-picrites (shaded field in Figure IV.17) and the negative Ti anomaly commonly found in the low-Cr dykes (Figure IV.9) may, therefore, indicate the removal of these minerals to form the plutonic rocks.

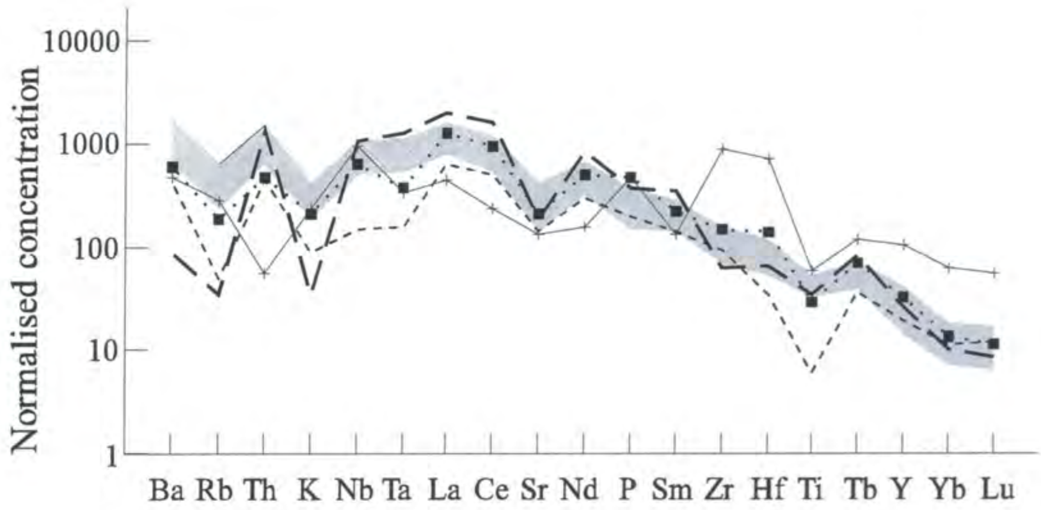

Figure IV.18 - Normalised trace-element diagram of representative analyses of group B2 bebedourites. Shaded field is the range of phlogopite-picrite compositions. Concentrations normalised to chondrite (except Rb, K and P) according to Thompson et al. (1984).

The spider diagrams for B2 bebedourites are more variable. Representative samples of commonly observed patterns are shown in Figure IV.18.

While the trace-element diagrams of some B2 bebedourites are not too dissimilar to those of the B1 unit (Figure IV.17), other samples produce more "spiky" patterns. Many of the B2 samples show a negative Ti anomaly, consistent with the extensive perovskite fractionation during earlier stages (B1). High modal percentages of apatite are represented by highs in P. The higher Zr and Hf contents of these rocks, when compared with B1, support the evidence from petrography and mineral chemistry for a more evolved character of B2. One sample with extreme Zr- and Hf- enrichment also shows a negative Th anomaly and strong relative enrichment in heavy REE, forming a pattern that is remarkably similar to some of the low-Cr dykes (Figure IV.9b). Another prominent feature in Figure IV.18 is the wide variation in the Nb/Ta ratios. This sudden change in the behaviour of Nb and Ta seems to be a conspicuous geochemical signature of relatively evolved mafic rocks from Tapira (i.e. some low-Cr dykes and B2 bebedourites) and will be discussed in Chapter V.

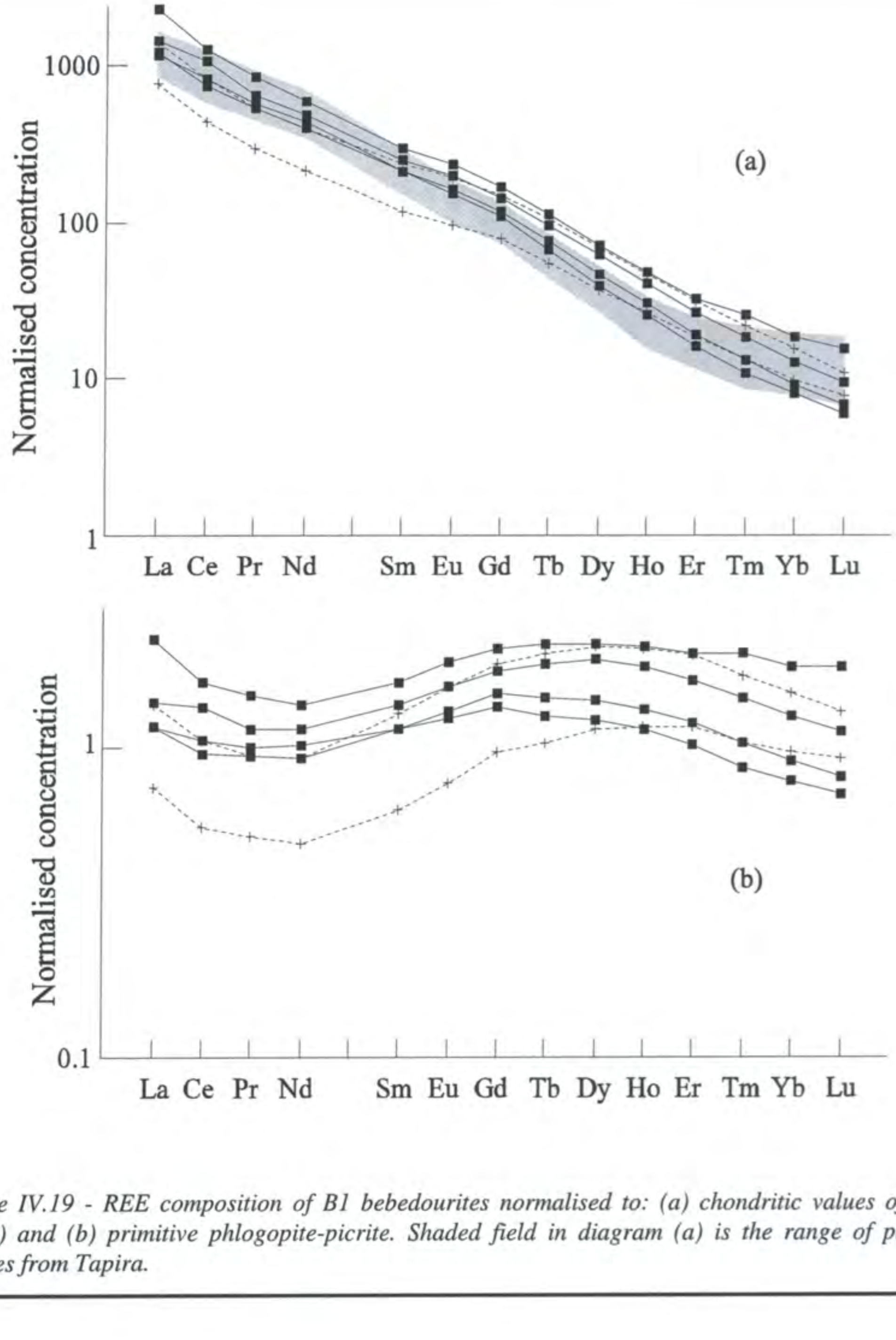

Figure IV.19 - REE composition of B1 bebedourites normalised to: (a) chondritic values of Boynton (1984) and (b) primitive phlogopite-picrite. Shaded field in diagram (a) is the range of phlogopite-picrites from Tapira.

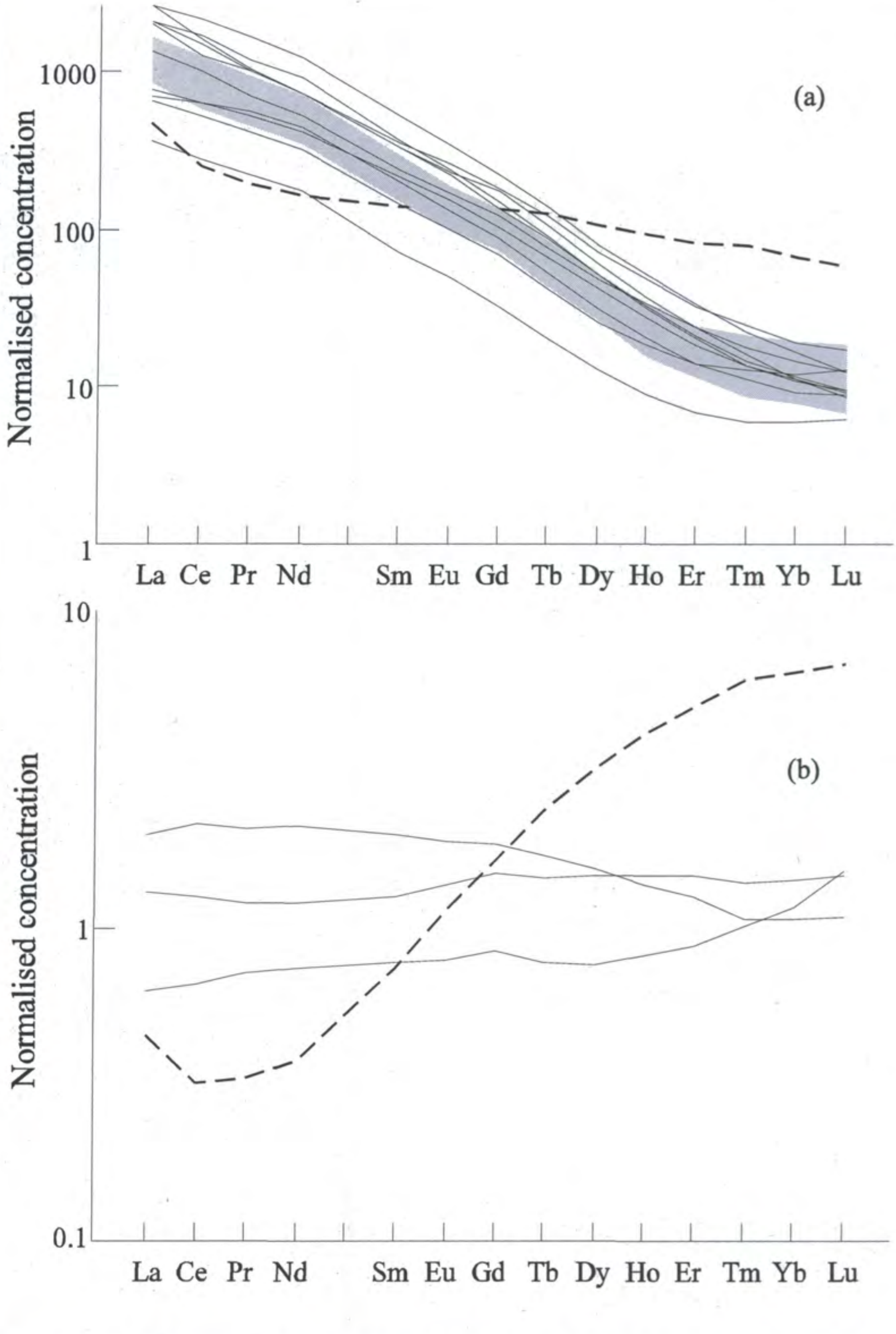

Figure IV.20 - REE patterns of B2 bebedourites, normalised to: (a) the chondritic values of Boynton (1984) and (b) primitive phlogopite-picrite. Dashed line is a high-Zr, low-Th bebedourite (see text).

The rare-earth element patterns for bebedourites of B1 and B2 units are presented in Figures IV.19 and IV.20, respectively. B1 bebedourites have La/Lu ratios similar to those of the phlogopite-picrites, but slightly different concentrations in the ranges from Ce to Sm and from Tb to Tm. As discussed previously, this may be controlled by the relative proportions of perovskite and apatite in the rock. Note that the "crossover" REE patterns observed in some low-Cr dykes and B2 rocks are not present in B1 bebedourites. The B2 bebedourites (Figure IV.20) also show La/Lu ratios similar to the phlogopite-picrites but span a much wider range of REE concentration. When normalised to the primitive phlogopite-picrite values, the majority of B2 bebedourites patterns are relatively flat or peak between Ce and Sm, suggesting some control by apatite, which is consistent with petrographic evidence. The dashed line in Figure IV.19 is the high-Zr, low-Th sample of B2 bebedourite discussed previously (see above, and Figure IV.18). The REE "crossover" pattern resembles that of the B2 wehrlite dyke and some of the low-Cr dykes.

Syenites

Tapira syenites vary from alkaline to peralkaline. The peralkalinity index (P.I.), calculated as the molecular ratio $(K_2O + Na_2O)/Al_2O_3$, varies from 0.81 to 1.12 but most samples are concentrated between 0.85 and 0.95. These values are significantly lower than those observed in Tapira mafic dykes (mostly between 1.0 and 3.0), underlining the fact that the syenites are not as Al-deficient as the mafic rocks. Syenitic dykes associated with the Salitre complex have P.I values that are slightly higher (from 1.0 to 1.3) than those of Tapira syenites.

The potassic to ultrapotassic character of Tapira syenites is clearly indicated by their K_2O/Na_2O ratios (on a wt. % basis), which vary from 5.8 to 34.6, but are usually higher than 20.

With regard to the major elements, Tapira syenites are characterised by SiO_2 varying from 53 to 55 wt. %, Al_2O_3 from 15.8 to 18.9 wt. %, very high K_2O (12.9 to 14 wt. %) and low Na_2O (0.38 to 0.65 wt. %). CaO contents vary greatly (from 1.62 to 9.16 wt. %), but correlate positively with CO_2, suggesting that a significant part of the calcium is hosted by variable amounts of interstitial and/or secondary carbonate, rather than by silicate minerals. P_2O_5 varies from 0.02 to 0.78 wt. %, Fe_2O_3(T) from 2.71 to 5.66 wt % and CO_2 from 1.55 to 4.67 wt. %. One sample of clinopyroxene-rich syenite often falls outside the ranges described above, showing higher TiO_2 Fe_2O_3 (T), MnO, CaO and Na_2O, and lower SiO_2, Al_2O_3 and K_2O than the remainder of the syenites.

As expected for evolved felsic rocks, all compatible elements are present in very low concentration. One remarkable exception is Sc, which may reach up to 30 ppm, but is only present in significant amounts in the clinopyroxene-bearing syenites, confirming the previous observations that Sc distribution is strongly controlled by the pyroxene.

The distribution of other trace elements is illustrated in Figure IV.21. The most prominent feature of the diagram is the positive anomaly of Zr and Hf, flanked by troughs at P and Ti. Also noteworthy is the relatively low REE abundance, when compared with those of the phlogopite-picrites, and the variable Nb/Ta ratios. Chondrite-normalised REE diagrams for representative samples of Tapira syenites are shown in Figure IV.22. It can be seen from the diagram that the syenites have lower REE contents than the phlogopite-picrites. The middle REE are particularly depleted, resulting in an concave-upward pattern. In some samples of Tapira syenites, particularly those spatially associated with the carbonatite-syenite breccias, the geochemical behaviour of the REE diverges from this general pattern.

The distribution of other trace elements is illustrated in Figure IV.21. The most prominent feature of the diagram is the positive anomaly of Zr and Hf, flanked by troughs at P and Ti. Also noteworthy is the relatively low REE abundance, when compared with those of the phlogopite-picrites, and the variable Nb/Ta ratios. Chondrite-normalised REE diagrams for representative samples of Tapira syenites are shown in Figure IV.22. It can be seen from the diagram that the syenites have lower REE contents than the phlogopite-picrites. The middle REE are particularly depleted, resulting in an concave-upward pattern. In some samples of Tapira syenites, particularly those spatially associated with the carbonatite-syenite breccias, the geochemical behaviour of the REE diverges from this general pattern.

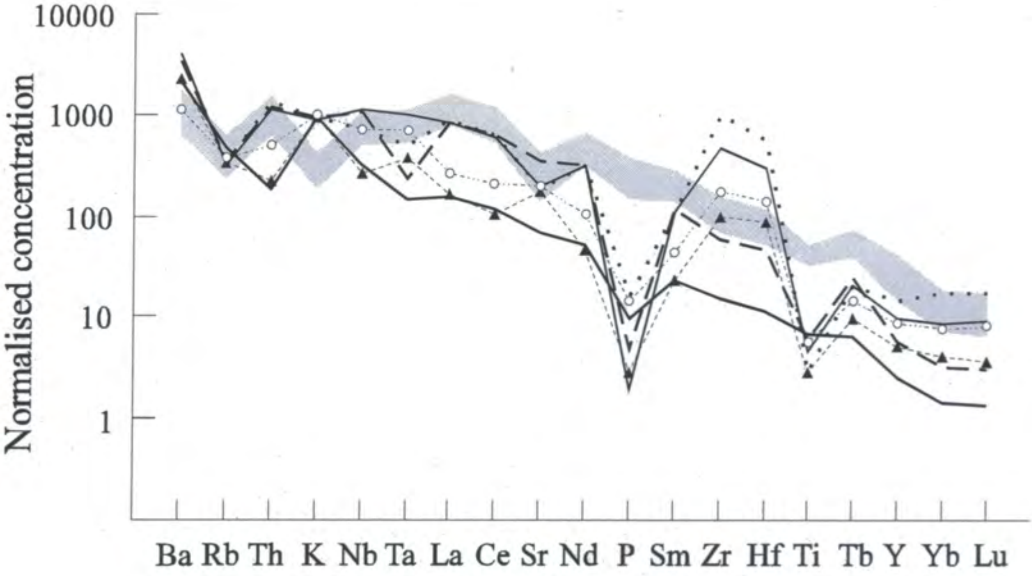

Figure IV.21 - Chondrite-normalised trace-element diagram for Tapira syenites. Concentrations normalised to chondrite (except Rb, K and P) according to Thompson et al. (1984). Shaded field is the range of phlogopite-picrites.

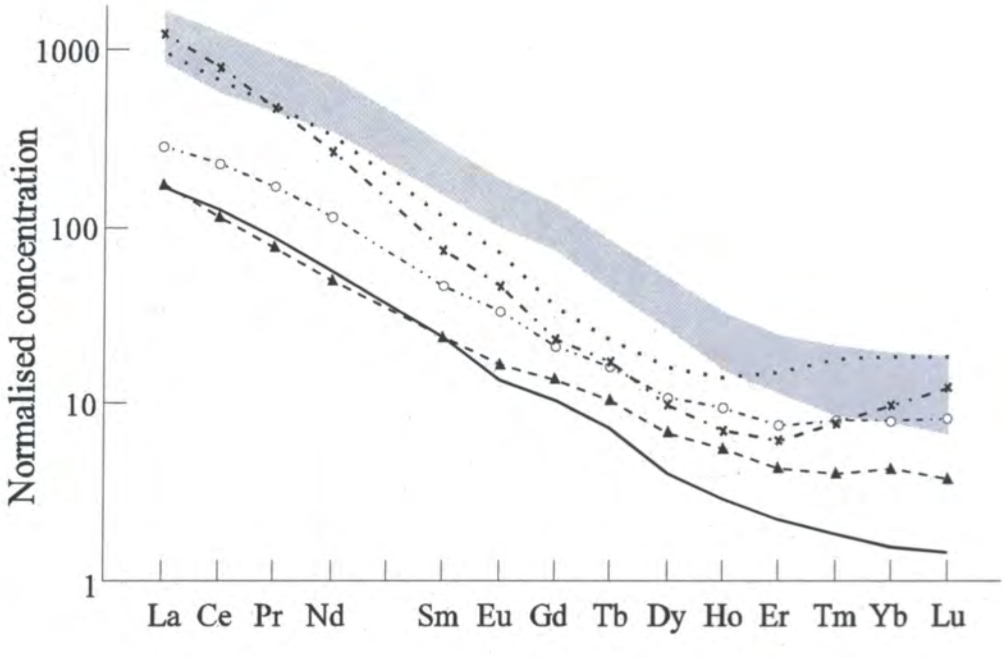

Figure IV.22 - REE patterns of Tapira Syenites, normalised to the chondritic values of Boynton (1984).

This feature is enhanced in a REE-diagram normalised to the phlogopite-picrite composition (Figure IV.23). The shaded field in the diagram represents the range of all syenite samples from Tapira and from Salitre analysed during this research. Most samples produce patterns that are roughly parallel to the limits of the field, and are not shown in the diagram. Some samples of syenitic fragments in breccias are displayed individually to illustrate their anomalous behaviour. Note that these samples have variable contents of heavy REE but, instead of forming sub-parallel trends, the patterns tend to converge into a single steep line, in the region of the light REE, at high concentrations. This phenomenon is interpreted here as suggestive of carbonatite metasomatism in the brecciated syenite, resulting in the elevation and homogenisation of the lighter REE contents. This interpretation is consistent with field and petrographic evidence and with the fact that Tapira carbonatites show extreme LREE/HREE fractionation (see section IV.2.5 below).

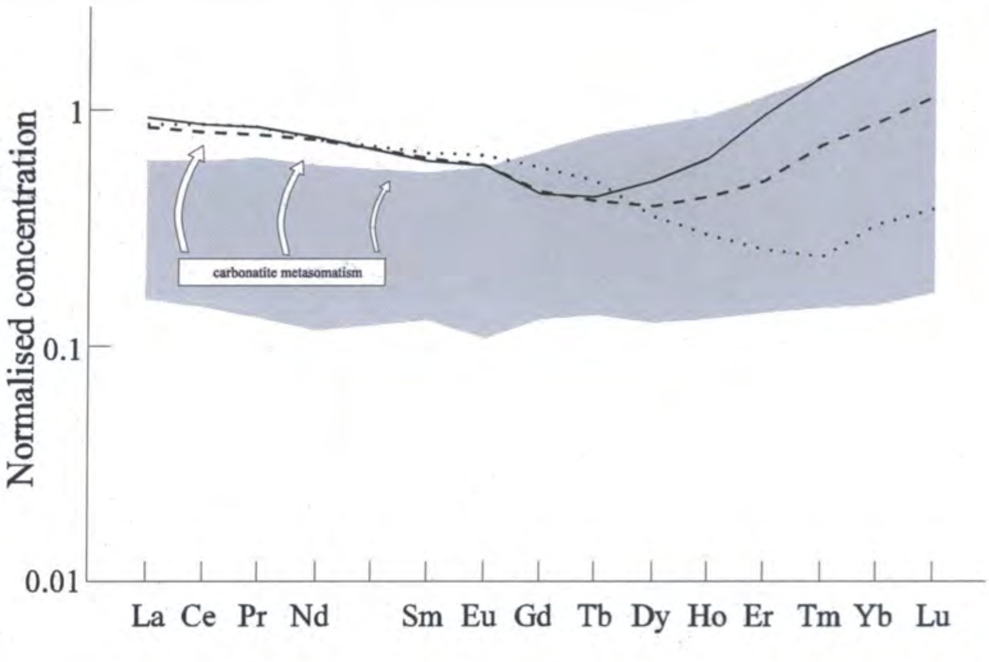

Figure IV.23 - REE concentrations of Tapira syenites (shaded field), normalised to primitive phlogopite-picrite values. Some samples of syenites in carbonatite-syenite breccias are plotted individually and possible shifts in the patterns of LREE, due to carbonatite metasomatism, are indicated by arrows.

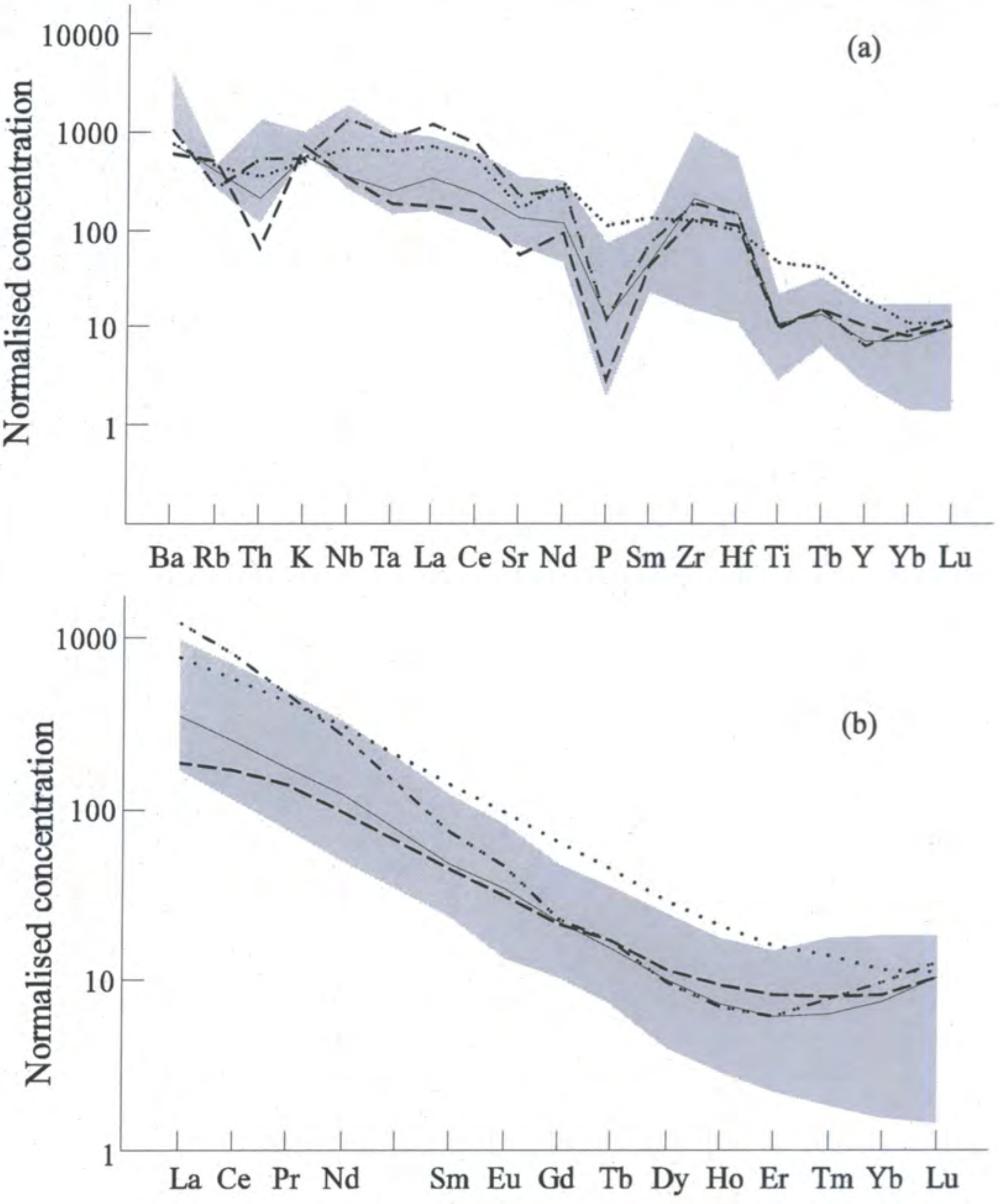

Figure IV.24 - (a) Trace element patterns of Salitre syenites, normalised to chondrite (except Rb, K and P,) according to Thompson et al. (1984); (b) Rare-earth patterns of Salitre syenites, normalised to chondritic values of Boynton (1984). Shaded field in both diagrams represents the range of Tapira syenites.

A number of syenitic dykes from the Salitre complex were analysed to provide a comparison with Tapira rocks. Some significant differences in major elements can be pointed out, with Salitre rocks having higher Na_2O (2.78 - 7.21 wt. %), slightly higher SiO_2 (41 - 60 wt. %) and lower K_2O (7.25 - 9.96 wt. %) than Tapira syenites. However, the trace-elements and REE distribution are similar in syenites from both complexes (Figure IV.24)

IV.2.5 - CARBONATITES

Mineralogically, the carbonatites in the Tapira complex are dominantly calcite-carbonatites, with subordinate amounts of dolomite-bearing calcite-carbonatites and restricted occurrences of dolomite-carbonatite. With the exception of some dykes and breccias associated with the C2 unit, all other carbonatites have less than 10 wt. % SiO_2, and the majority of samples have less than 5 wt. % SiO_2. The concentrations of TiO_2 and Al_2O_3 are usually below 1 wt. %. Alkalis are present in low concentrations, with Na_2O varying from 0 to 0.8 wt. % and K_2O reaching up to 2.6 wt. % (depending on the amount of phlogopite present in the sample). P_2O_5 may reach up to 7.7 wt. %. $Fe_2O_{3(T)}$ and MgO are usually below 10 wt. %, except for the breccias, where $Fe_2O_{3(T)}$ may reach up to 19 wt. %, and dolomite-carbonatites, which have MgO varying from 17 to 20 wt. %.

Woolley and Kempe (1989) suggested a chemical classification of carbonatites based on the relative proportions of CaO, MgO, FeO and MnO. According to this scheme, if the ratio $CaO/(CaO+MgO+FeO+Fe_2O_3+MnO)$ is greater than 0.8 the rock is classified as a calciocarbonatite. Rocks where the ratio is less than 0.8 may be called magnesiocarbonatite or ferrocarbonatite, depending on whether $MgO/(FeO+Fe_2O_3+MnO)$ is higher or lower than 1.

A plot of Tapira carbonatites in terms of the relevant elements is presented in Figure IV.25. Most of the analysed samples from C1 and C2 plot within the calciocarbonatite field. The carbonatite dykes and the groundmass of some breccias from C2 plot within the ferrocarbonatite field. Although extensive overlap exists between carbonatites of the different units. there seems to be a tendency for the $MgO/(Fe_2O_{3(T)} + MnO)$ ratio to decrease in the sequence C1 ⇒ C2 ⇒ C3.

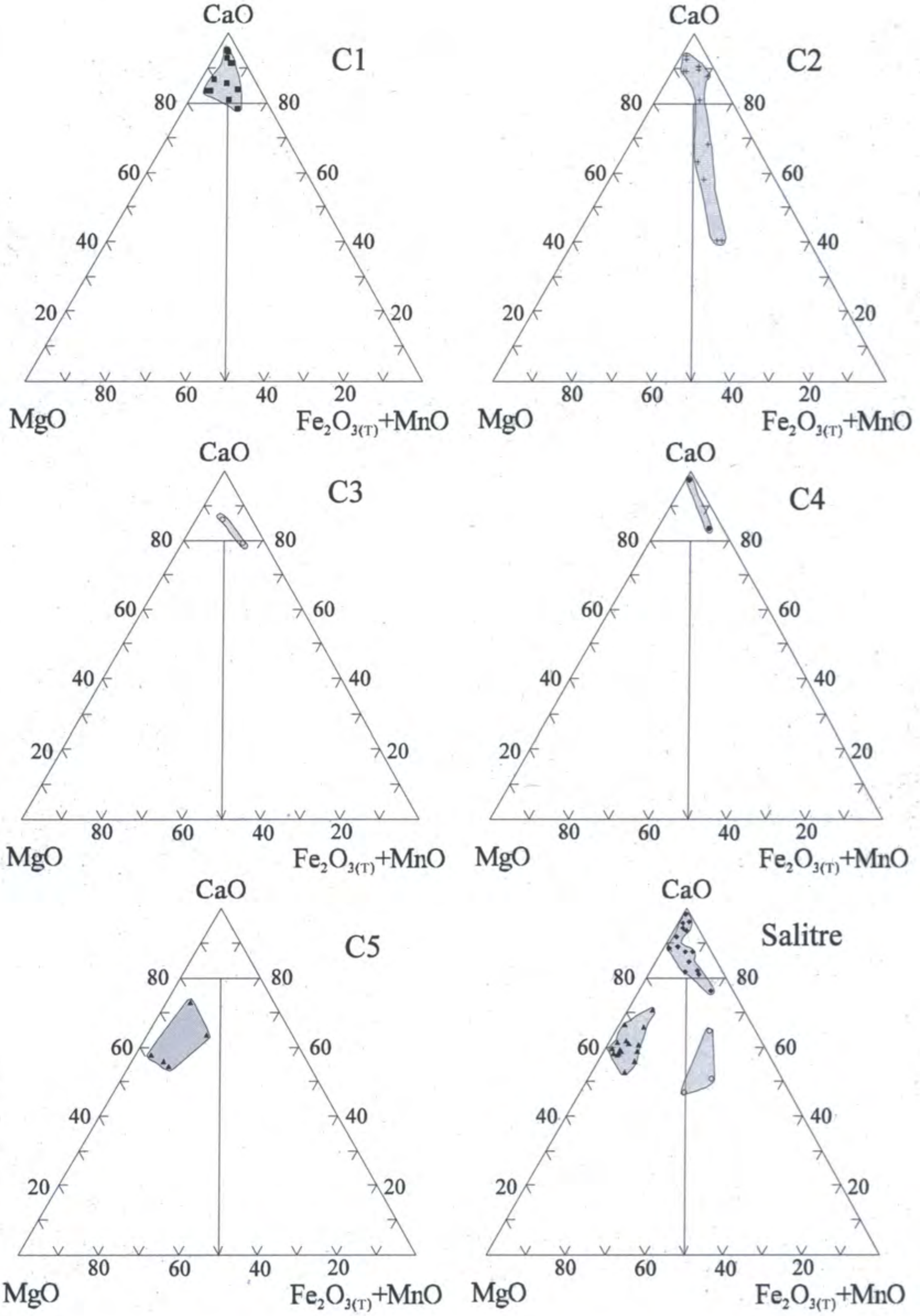

Figure IV.25 - Classification of Tapira (C1 to C5) and Salitre carbonatites, according to Woolley and Kempe (1989)

However, it must be stressed that the interpretation of the diagram is not straightforward, since the elements concerned are not hosted only by carbonates. For instance, a magnetite-rich carbonatite may plot in the ferrocarbonatite field, even if the only carbonate present is calcite. Similarly, phlogopite-rich carbonatites will tend towards the magnesiocarbonatite field, even if dolomite is not present.

Tapira carbonatites show extreme concentration and wide variation in the abundance of several trace elements. The amounts of compatible elements are usually very low and, on average, the lowest contents are found in rocks of C1 and C5. Most samples of Tapira carbonatites have Cr below 25 ppm, Ni below 15 ppm, V below 215 ppm and Sc below 20 ppm. Notable exceptions are the carbonatite dykes and high-level breccias of the C2 unit, where all compatible elements are present in higher amounts than in the coarser-grained carbonatites. These rocks may have up to 65 ppm Cr, 22 ppm Ni, 380 ppm V and 40 ppm Sc.

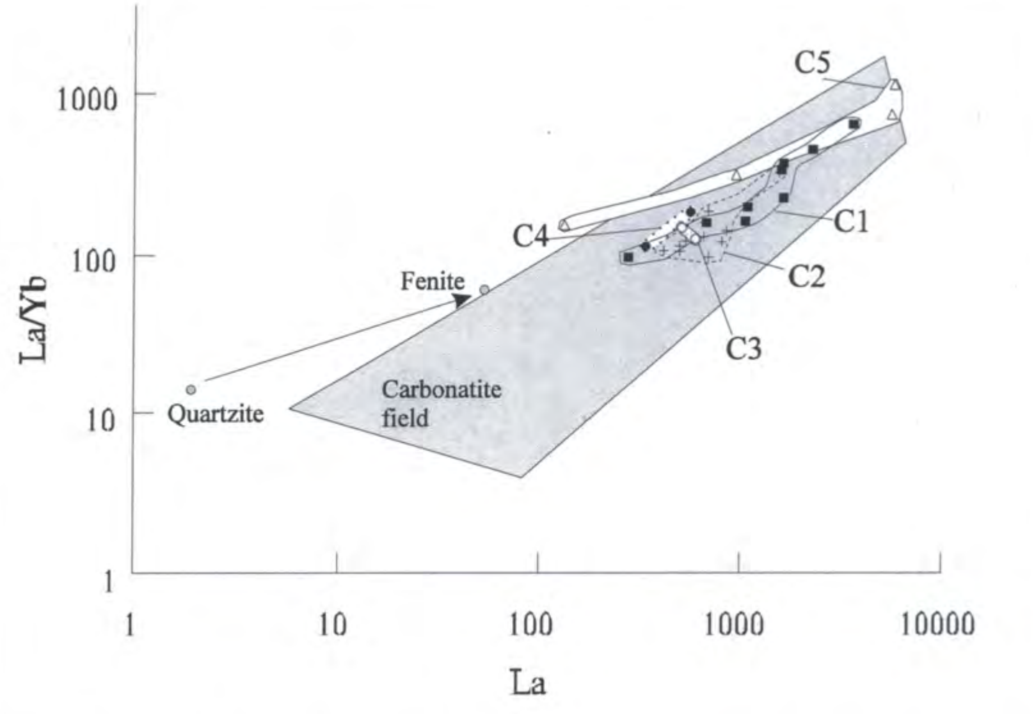

Figure IV.26 - La/Yb vs. La diagram, showing the composition of Tapira carbonatites, grouped into units C1 to C5. Carbonatite field is from Andersen (1987). Also plotted in the diagram are analyses of a country rock (quartzite) and a fenite associated with the Tapira complex.

The LREE/HREE fractionation in carbonatites is the strongest among Tapira rocks. La/Yb ratios vary in the range 95-635 for the C1 unit, 95-321 (but most samples below 180) for C2, 125-144 for C3, 111-185 for C4 and 150-1130 for the late-stage dolomite carbonatites of C5. The La/Yb ratio of Tapira carbonatites is plotted against La in Figure IV.26. All the samples plot in the upper half of the carbonatites field, demonstrating their strong LREE/HREE fractionation.

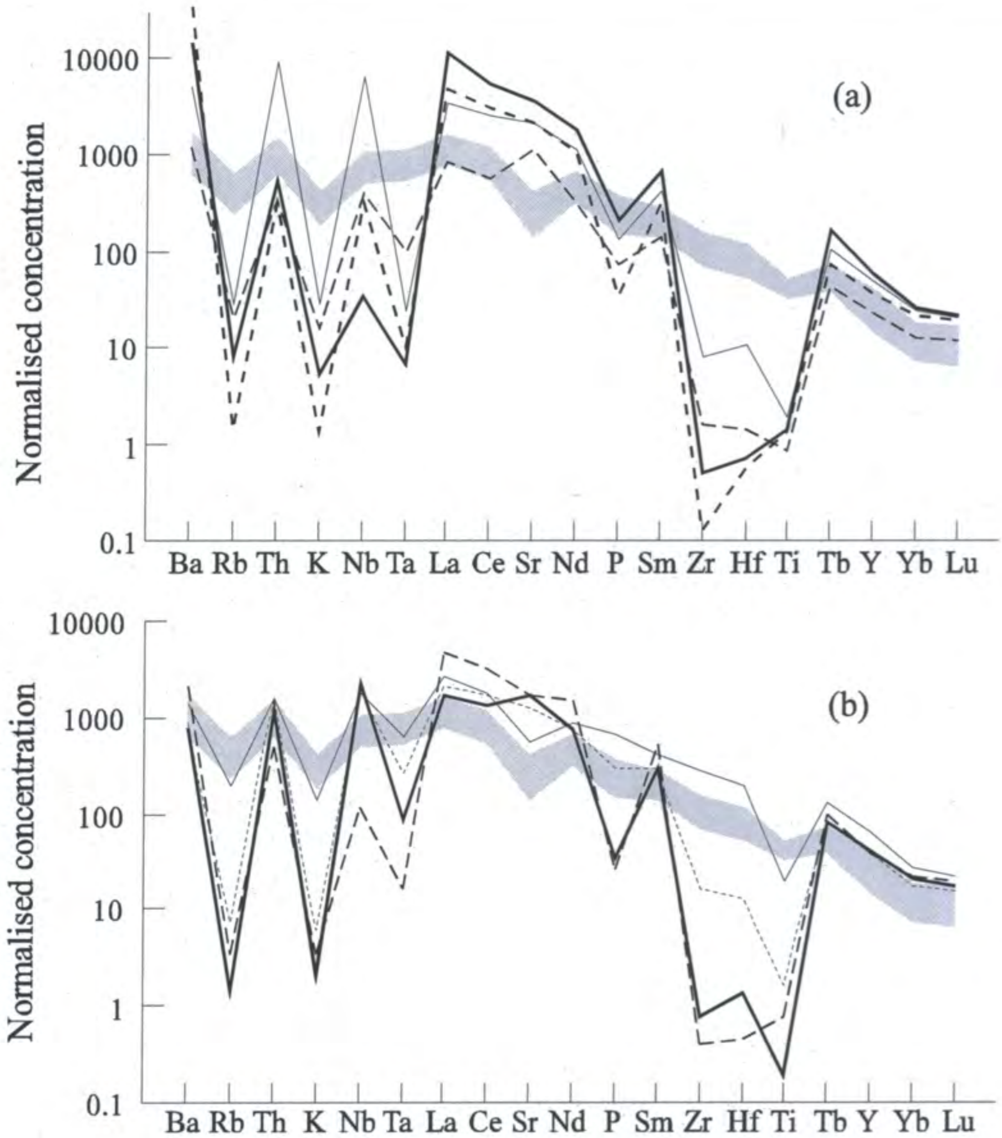

Figure IV.27 - Spider-diagrams for selected samples of carbonatites from C1 (a) and C2 (b), compared with the range of phlogopite-picrites (shaded field). Concentrations normalised to chondrite (except Rb, K and P) according to Thompson et al. (1984).

Spider-diagrams for carbonatites from the various units are presented in Figures IV.27 and IV.28. Tapira carbonatites are strongly enriched in Ba, Nb and REE, and depleted in Rb, K, Ta, Zr, Hf and Ti, with respect to the phlogopite-picrite field.

The most striking feature of C1 carbonatites is the "spiky" nature of the trace-element patterns, with alternate enrichment and depletion of several elements, including the geochemical pairs Nb-Ta and Zr-Hf. Niobium and tantalum are extremely fractionated from each other (compare with the Nb/Ta ratio of the phlogopite-picrites - shaded field), with Nb showing strong relative enrichment. Both Zr and Hf are depleted in all C1 samples. The Zr/Hf ratio is variable and apparently decreases with increasing degree of Zr depletion, suggesting that Hf is slightly more compatible than Zr in the carbonatite system.

C2 Carbonatites show similar features, but with less extreme REE enrichment and a lesser degree of fractionation between Nb and Ta. There is a consistent correlation between chemical composition and the location or mode of occurrence of the C2 carbonatites. The fine-grained dykes and the groundmass of the high-level breccias (Tapira mine, see Chapter I) show a lesser degree of Zr and Hf depletion, as well as the smallest Rb and K anomalies. Carbonatites that intrude and brecciate the main syenite body (see region marked "S" - Figure I.15, in Chapter I) show the greatest degree of Zr and Hf depletion, as well as the most prominent negative anomalies of Rb, K. Ta and P. The carbonatite intrusion in bebedourites, which forms the main C2 body in Figure I.15, shows patterns intermediate between the other two types.

These relationships suggest that the chondrite-normalised trace-element pattern of C2 carbonatites becomes progressively more irregular, and the characteristic depletion in Rb, K, Ta, Zr and Hf become more pronounced with magmatic evolution. Alternatively, as suggested in Chapter II, it is possible that the main C2 body is a composite intrusion of more than one batch of carbonatite magma. As observed for C1, the Zr/Hf ratio tends to decrease with the degree of Zr and Hf relative depletion, changing from > 1 in the least depleted rocks to < 1 in the most depleted.

Rocks from the C3 and C4 units have most of the features observed in the spiderdiagrams for previous carbonatite units, but the magnitude of the anomalies is

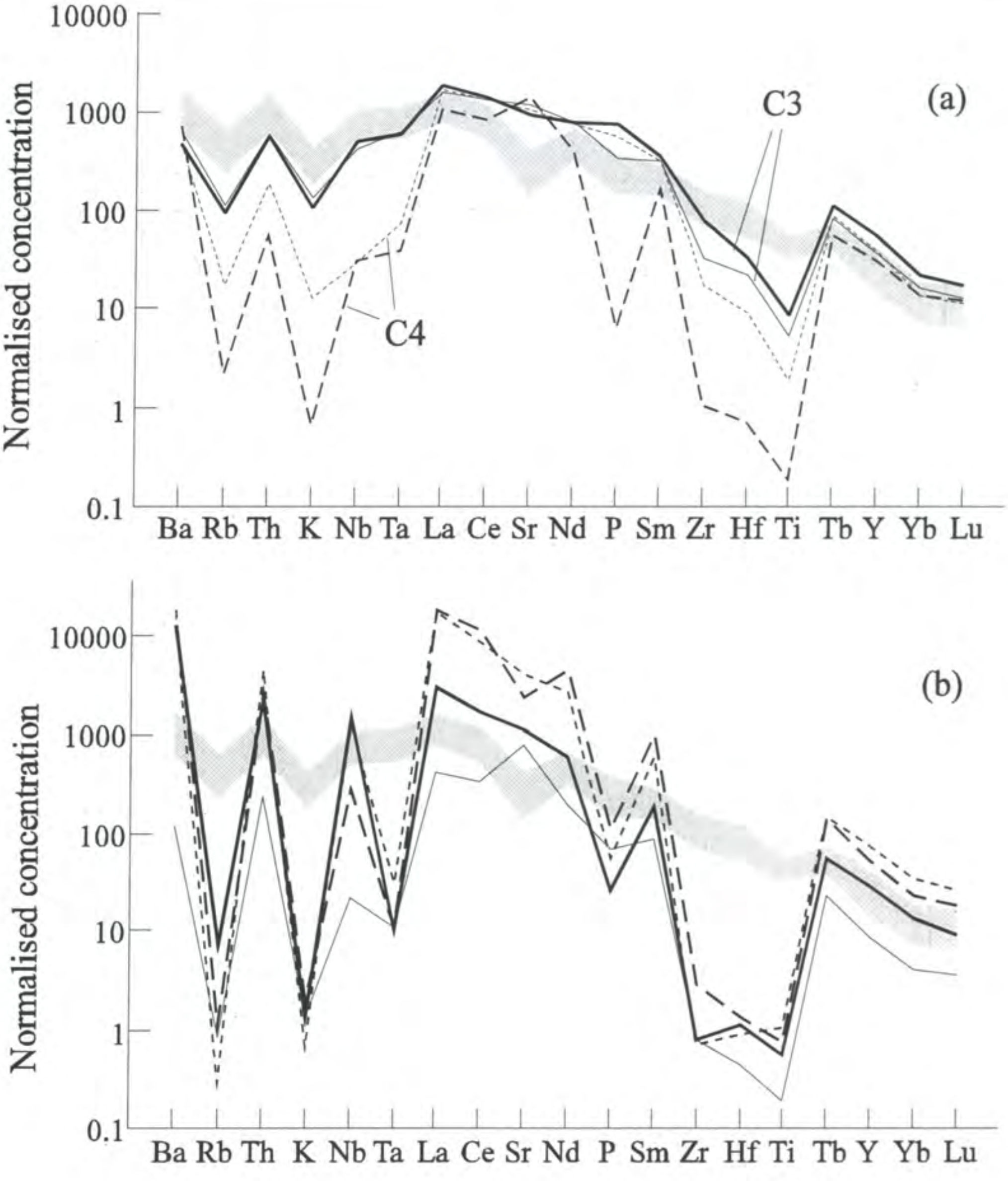

Figure IV.28 - Normalised trace-element diagrams for carbonatites from: (a) C3 and C4; (b) C5. Shaded field is the range of phlogopite-picrites. Concentrations normalised to chondrite (except Rb, K and P) according to Thompson et al. (1984).

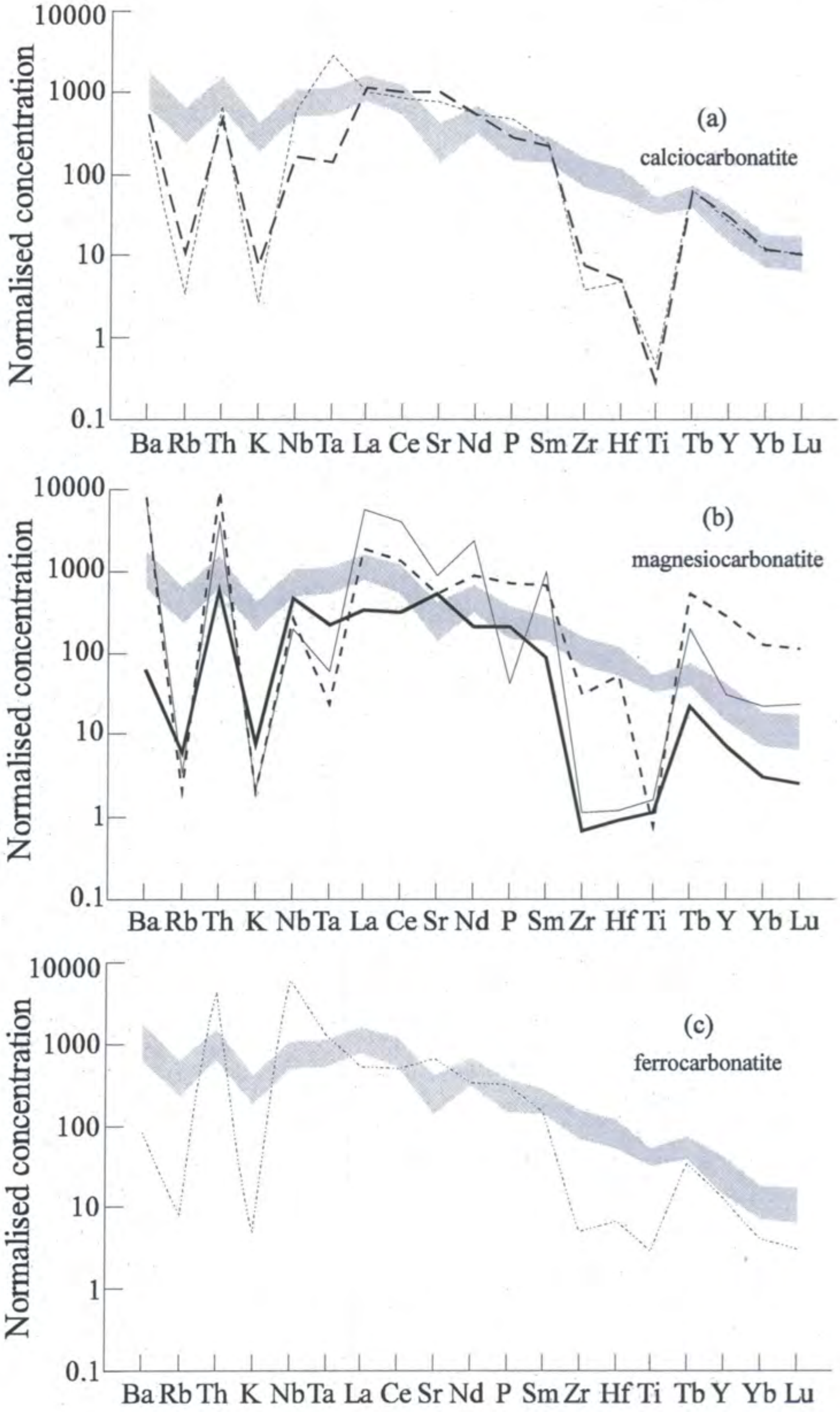

Figure IV.29 - Normalised trace-element diagrams for various types of Salitre carbonatites. Concentrations normalised to chondrite (except Rb, K and P) according to Thompson et al. (1984).

smaller. C3 carbonatites, in particular, shows the closest approximation to the pattern of phlogopite-picrites. A significant difference is observed in the behaviour of Nb and Ta between the carbonatites from C1+C2 units and those from C3+C4. While carbonatites from the former two units show a conspicuous negative Ta anomaly, the latter have Nb/Ta ratios that are similar to those of the phlogopite-picrites, although in C4 the absolute concentrations of both Nb an Ta are significantly lower. The Zr-Hf section of the spiderdiagram does not show the slope inversion observed in C1 and C2. Finally, it should be noted that the likeness observed in key chemical features between C3 and C4 is consistent with the similarities previously noted in the petrography and mineral chemistry of these rocks.

The chondrite-normalised trace-element patterns for the late-stage magnesiocarbonatites of the C5 unit most closely resemble those of the calciocarbonatites in C1, with very prominent negative anomalies of Ta, Zr and Hf, and variable but mostly high REE contents. As in C1 (and to a lesser extent in C2) the Nb/Ta ratio of C5 carbonatites is extremely high, which implies a strong fractionation between these two elements. Possible causes for this will be discussed in the next Chapter.

Finally, a number of carbonatites from the Salitre complex were analysed during the present research. The trace-element and REE patterns for selected Salitre samples are presented in Figure IV.29. The Salitre rocks show the same features that typify Tapira carbonatites, such as high REE contents and negative anomalies of Ta, Zr and Hf. All of these features seem to be more prominent in the magnesiocarbonatites than in the calciocarbonatites, suggesting that carbonatite evolution leads to a continuous enhancement of these typical geochemical signatures. It is noteworthy that the ferrocarbonatite sample shown in the Figure IV.29 is extremely enriched in Nb.

IV.3 - STABLE CARBON AND OXYGEN ISOTOPES

Carbon and oxygen stable isotope data have been reported for the APIP carbonatite complexes of Araxá, Catalão and Tapira, by Santos and Clayton (1995) and Toyoda *et al.* (1994). However, the main emphasis of these works was placed on regional-scale comparison between complexes, and they do not account for possible variations with carbonatite stratigraphy within individual complexes. Furthermore, previous studies do not include data for the Salitre complex, and the data available for Tapira comprise mainly samples with relatively high ^{18}O contents, which are likely to have been affected by pervasive post-magmatic recrystallisation (see discussion below).

A carbon and oxygen stable-isotope study of calcites and dolomites from Tapira and Salitre was carried out during this research, with a view to investigating the existence (or otherwise) of primary carbonates in both complexes, and to monitor processes such as the within-complex isotopic evolution and the effect of hydrothermal alteration in Tapira. A smaller number of carbonate-rich dykes (phlogopite-picrites and low-Cr dykes) were also analysed, to investigate possible genetic links of these rocks with the carbonatites, as suggested by petrographic and chemical evidence. The analytical procedures can be found in Appendix 1 and the results are tabulated in Appendix 3.

IV.3.1 - TAPIRA COMPLEX

Carbonatites

Figure IV.30 shows the isotopic composition of the Tapira carbonates, using the "delta per mil" notation, given by

$$\partial = \left(\frac{R\ sample}{R\ reference} - 1 \right) x \quad 10^3$$

where R represents the isotope ratio (i.e. ^{18}O/^{16}O for oxygen and ^{13}C/^{12}C for carbon). The reference values are the Standard Mean Ocean Water (SMOW), for δ^{18}O, and the Pee Dee Belemnite (PDB), for δ^{13}C.

Tapira carbonatites follow a trend of positive correlation between δ^{18}O and δ^{13}C. With respect to carbon, most samples plot within the expected range of variation for primary igneous carbonate. The oxygen isotopic composition is more variable, with approximately half the samples plotting within the field of primary carbonatites, while the remainder are relatively enriched in ^{18}O. Nevertheless, the values obtained for Tapira carbonatites during this research are generally lower than those of Santos and

Clayton (1995) and Toyoda *et al.* (1994).

Despite the noticeable correlation between $\delta^{18}O$ and $\delta^{13}C$, observed for the whole set of analyses, data in Figure IV.30 still show considerable scatter. However, if calcite and dolomite are considered separately, the latter shows excellent correlation between $\delta^{13}C$ and $\delta^{18}O$, plotting along a line with an approximate slope of 0.5 (except for the very lowest $\delta^{13}C$ contents). Most calcite analyses plot to the right of this line, and, although a positive correlation is still visible, calcite is clearly responsible for most of the scatter in the diagram. One anomalous sample shows much lower $\delta^{18}O$ than the remainder (Figure IV.30) for both calcite and dolomite.

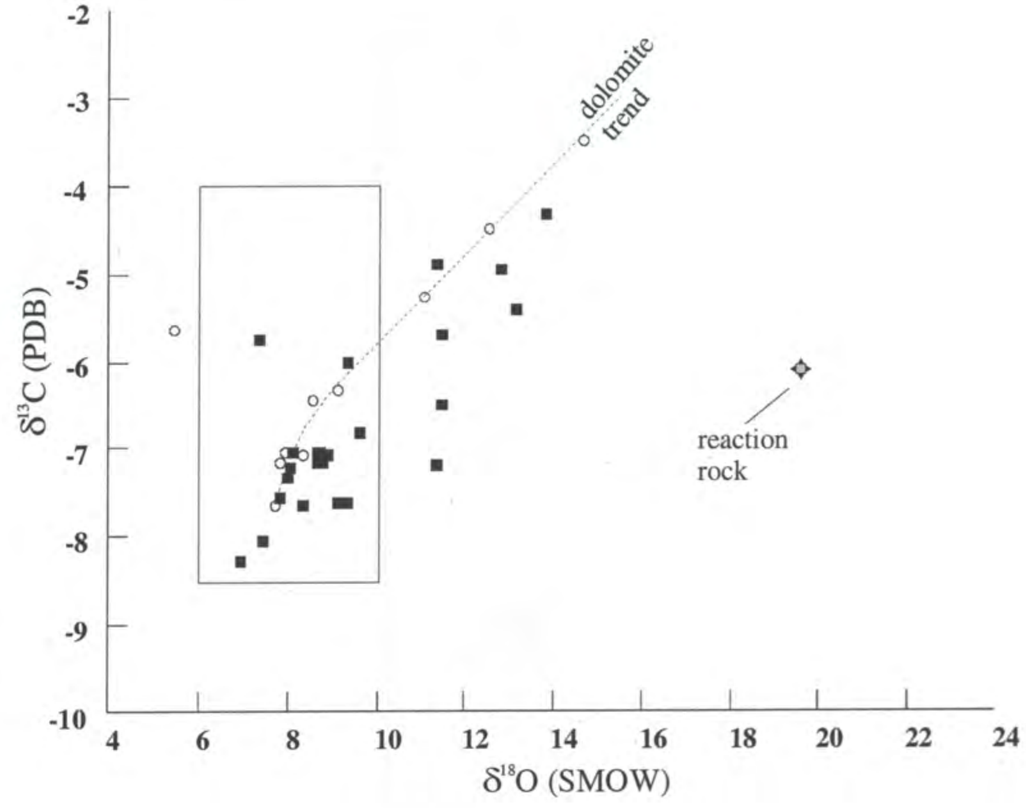

Figure IV.30 - Carbon and oxygen stable isotope composition of calcites (solid squares) and dolomites (open circles) from Tapira carbonatites. The solid-line box is the expected composition of mantle-derived (primary) igneous carbonatites (Taylor et al., 1967). The lower $\delta^{13}C$ limit of the box is set at –8.5, to include the composition of Oldoynio Lengai carbonatites (J. B. Dawson, personal communication, 1999) Dashed line shows the trend of Tapira dolomites. Dolomite from the reaction rock (star) is plotted for comparison.

Progressive enrichment in both ^{13}C and ^{18}O is expected for carbonates undergoing Rayleigh fractionation in the presence of a H_2O- and CO_2-bearing fluid (or magma), and is dependent on the H_2O/CO_2 ratio of the system (e.g. Pineau *et al.*, 1973). On the other hand, the disparate behaviour between calcite and dolomite, described above, suggests that post-magmatic processes may have disturbed the system. Figure IV.31 shows the isotopic composition of pairs of coexisting calcite and dolomite in all analysed samples. The data set includes carbonatites and mafic dykes, and the dolomite trend of the carbonatites (from Figure IV.30) is also plotted.

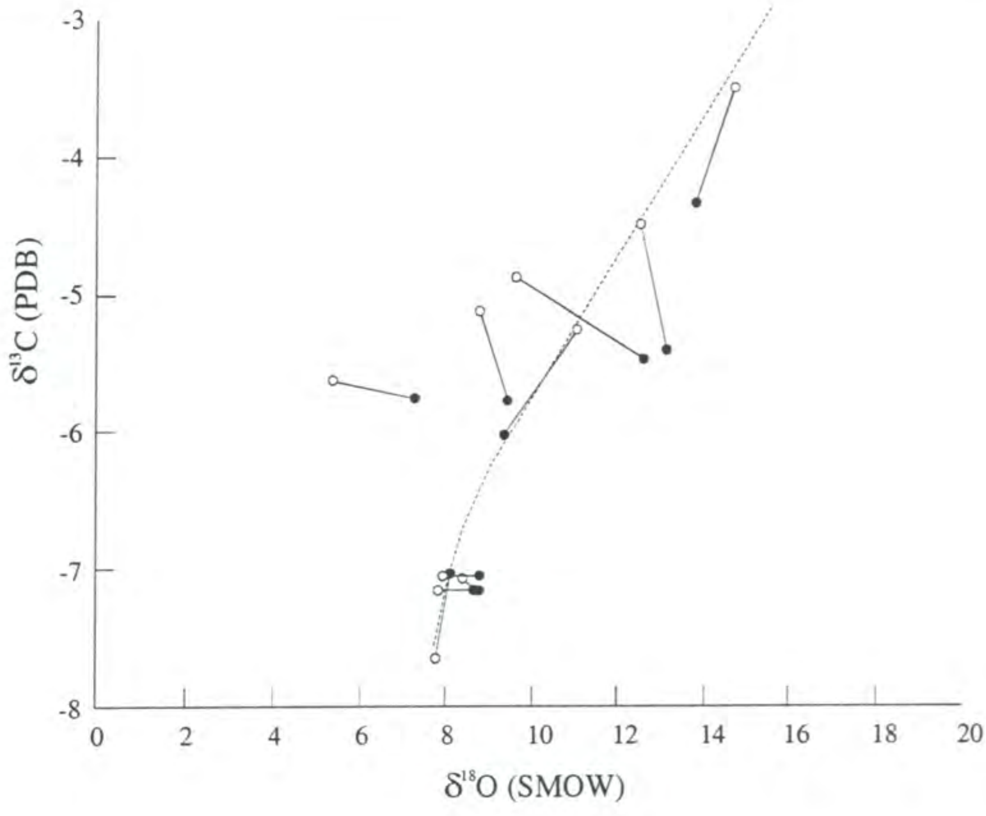

Figure IV.31 - Isotopic composition of pairs of coexisting calcite (solid circles) and dolomite (open circles), in Tapira carbonatites and mafic dykes.

In a system in equilibrium, some isotope fractionation can be expected between coexisting calcite and dolomite, with the latter being enriched in both $\delta^{13}C$ and $\delta^{18}O$ relative to calcite (Deines, 1989). The negative oxygen fractionation (i.e. $\delta^{18}O_{calcite} > \delta^{18}O_{dolomite}$) observed in many of the analysed pairs suggests, therefore, that the two minerals are in isotopic disequilibrium, lending further support to the inference of post-magmatic disturbances to the system. The two samples where isotope fractionation is in the expected direction (i.e. higher $\delta^{18}O$ *and* $\delta^{13}C$ in dolomite) are fine-grained carbonatite dykes. Also note that the dolomites from mafic dykes fall to the left of the dashed line (the carbonatite "dolomite trend").

Carbon fractionation between analysed pairs of calcite and dolomite is variable: most samples with low $\delta^{13}C$ do not show any significant variation in carbon isotopic composition between the two minerals. For the samples with higher values of $\delta^{13}C$, dolomite is enriched in ^{13}C relative to calcite.

In some Tapira carbonatites, the post-magmatic alteration produces strings of "cloudy" recrystallised carbonates which exsolve Sr- Ba- and REE-rich phases, as well as oxide minerals. Therefore, further insight can be gained on the influence of post-magmatic alteration by studying these carbonates. Ideally, this study should be carried out on individual grains (e.g. by ion microprobe fitted with a laser fluorination system), given the grainsize scale of the observed variations in mineral chemistry. During this research, an alternative, semi-quantitative approach was adopted, making use of the fact that the exsolved opaque minerals increase the magnetic susceptibility of the host carbonate grain, and thus enable the use of magnetic means (e.g. Frantz separator) to obtain concentrates of fresh and altered carbonates. As this is only intended to provide the general direction of the isotopic shift produced by post-magmatic alteration, it is not crucial that the concentrates are of extreme purity. The results are displayed in Figure IV.32. The isotopic composition of most samples is shifted towards higher $\delta^{18}O$, in some cases by a substantial amount, with only one sample where a small shift in the opposite direction was observed.

Although there is some variation in the behaviour of carbonate pairs, with some cases of $\delta^{13}C$ enrichment in the altered carbonate, the overall changes in oxygen are of far greater intensity, suggesting that one might expect greater shifts in $\delta^{18}O$ than in $\delta^{13}C$, during post-magmatic alteration. This may be related to a high H_2O/CO_2 ratio of the fluids involved. At first sight the patterns observed in Figure IV.32 would suggest that both calcite and dolomite are equally susceptible to changes in isotopic composition when subjected to late-stage alteration. However, it should be noted that the samples represented were deliberately chosen for clearly displaying a second (recrystallised) generation of carbonate in thin section.

Given the relationships observed in Figure IV.30, it seems more likely that the isotopic composition of calcites was more readily disturbed than that of dolomites. This may be especially true where signs of recrystallisation are not obvious from the thin section. When the rock was obviously subjected to alteration (e.g. samples in Figure IV.32, also note the high $\delta^{18}O$ of the dolomite from the reaction rock, in Figure IV.30), both calcite and dolomite appear to have been affected. Negative isotope fractionation of oxygen between dolomite and calcite (Figure IV.31) has been interpreted as an indication that calcite was isotopically changed whilst dolomite retained the original isotope composition (Deines, 1989). This model seems to hold for Tapira carbonates.

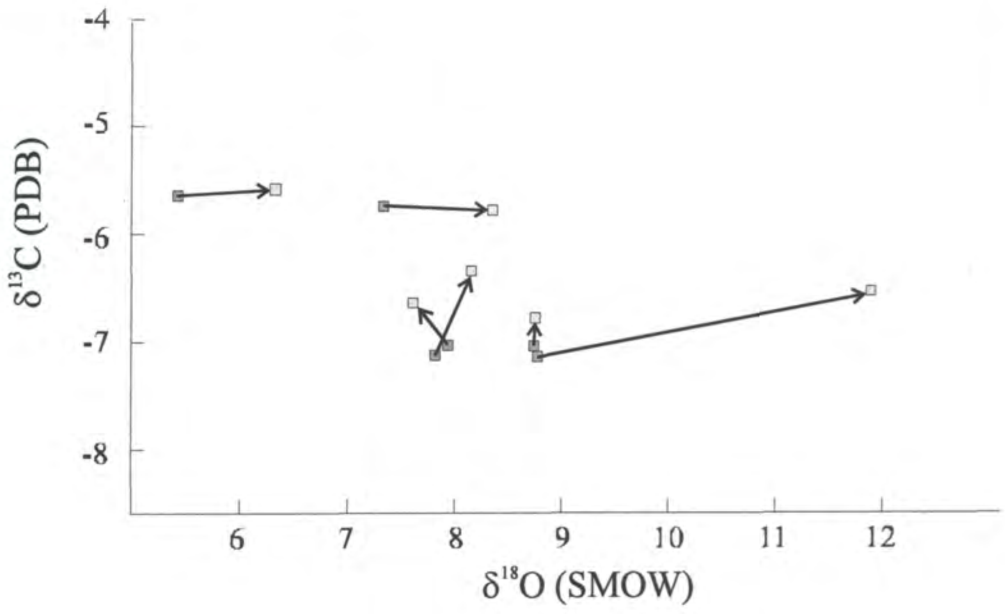

Figure IV.32 - Isotopic variation between concentrates of "clear" (fresh) and "cloudy" (altered) carbonate. The lines join concentrates of the same sample, arrows point towards the altered carbonate.

When considered individually, the different carbonatite units from Tapira show restricted isotopic ranges, which are distinctive for each unit (Figure IV.33). An immediate distinction can be made in the diagram, between those samples from the larger-volume, coarser-grained, carbonatite intrusions, which are concentrated in the lower part of the overall trend, and the finer-grained carbonatite dykes, which have generally higher values of both $\delta^{13}C$ and $\delta^{18}O$. It is also evident that the units C2, C3, C4 and C5 are more or less aligned with the trend of Tapira dolomites, and that compositions from C1 carbonates are shifted from this trend, towards ^{18}O enrichment.

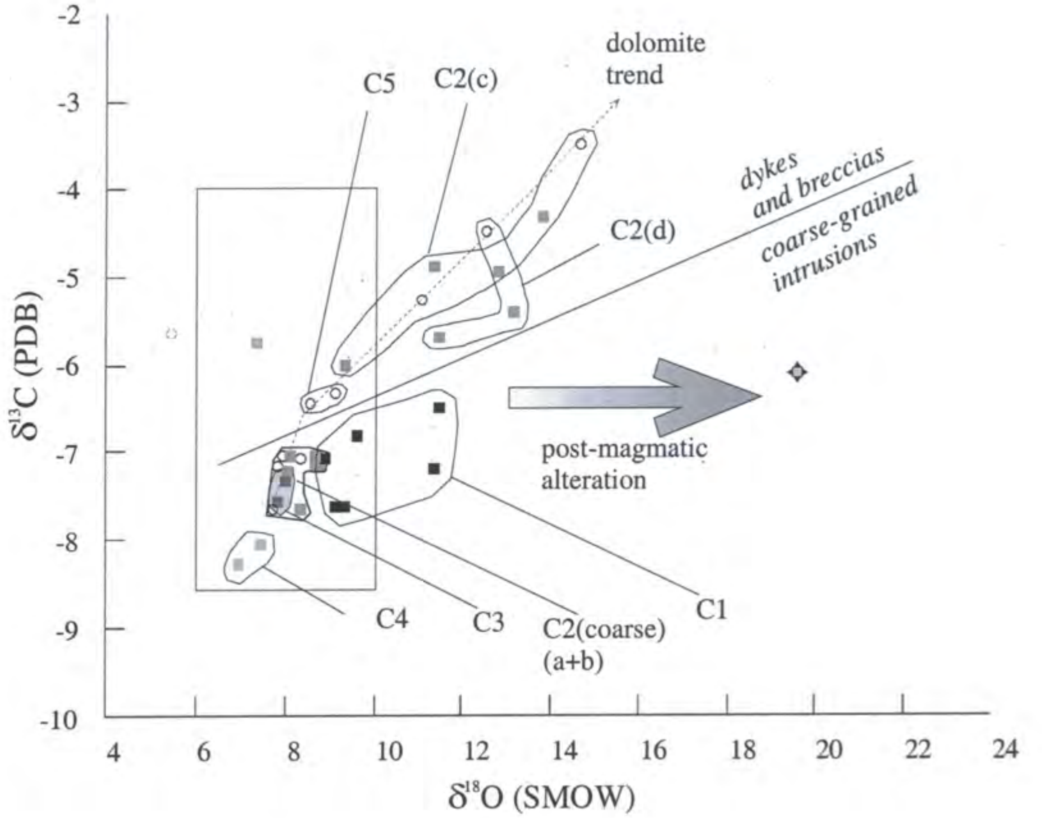

Figure IV.33 - Isotopic composition of Tapira carbonatites by unit (C1 to C5). C2 carbonatites are further subdivided in fields "a" to "d" (see text). Composition of dolomite in the reaction rock (star) and the general direction of isotopic changes due to post-magmatic alteration are also indicated.

The concept that the dolomite trend reflects isotope fractionation during magmatic evolution of the carbonatites (and not post-magmatic alteration) seems to be supported by the fact that individual units show restricted compositional ranges, suggesting that each unit represents a discrete step in the evolution history of carbonatite magmatism in Tapira. It should be noted that the C1 unit is the largest, central body of carbonatites in Tapira, and the ^{18}O-enrichment of these rocks, relative to the smaller intrusions, may be the result of more vigorous hydro/carbothermal systems associated with this particular intrusion.

C2 rocks are a remarkable exception to the generally restricted range of isotopic variation within individual carbonatite units, since C2 carbonatites alone span the widest compositional range in Figure IV.33. However, it should be noted that this unit encompasses rocks with widely variable modes of occurrence, collectively placed in C2 on the basis of chemical and mineralogical similarities (Chapters I, II, III) These comprise: a) coarse-grained bodies intrusive in B1 bebedourites, b) coarse-grained carbonatites that intrude and brecciate syenites, c)fine-grained carbonatite dykes found in various locations in the complex and d) high-level (explosive) breccias in the Tapira mine area. If these sub-units are individualised, a relationship between isotopic composition and mode of occurrence becomes evident. Accordingly, a number of trends (a to d) are depicted in Figure IV.33. Sub-units (a) and (b) plot within the box of primary carbonatites. Although carbonates in the syenite-carbonatite breccias seem to have a slightly lower $\delta^{18}O$, the two fields are virtually indistinguishable in the scale adopted. Carbonates from both sub-units (c) and (d) are enriched in ^{13}C and ^{18}O relative to the coarser grained intrusions, and may represent more evolved isotopic composition. Note that the calcite (but not the dolomite) in the groundmass of the high-level breccias is slightly enriched in $\delta^{18}O$. This is not unexpected, since these rocks would be particularly susceptible to post-magmatic alteration.

Mafic dykes

The isotopic composition of calcites and dolomites of a number of phlogopite-picrites and low-Cr dykes are presented in Figure IV.34, together with the field for all Tapira carbonatites.

The majority of the carbonates in the mafic dykes plot within the field of Tapira carbonatites, and approximately one half of the samples plots within the range of mantle-derived compositions. Calcite analyses show a considerable scatter, which is consistent with the behaviour previously noted for the carbonatites, and the calcite-dolomite isotopic disequilibrium is also present in carbonate pairs from the mafic dykes. The trend of dolomite evolution in Tapira carbonatites is also plotted in the diagram. However, the dolomites from the mafic dykes do not plot along this line, but have slightly lower ^{18}O than those in the carbonatites. Given the small number of dolomite analyses from mafic dykes, it is impossible to constrain their evolution path. However, if it is assumed that they followed a fractionation trend similar to the carbonatite dolomites, the transposition of the "dolomite-trend" (from Figure IV.30) should fit the analyses from the mafic dykes. This is illustrated by trend labelled (2) in Figure IV.34. While one should be aware that this is a largely unconstrained assumption, it is possible that the area between trends (1) and (2) represents better the range of primary isotopic composition of Tapira carbonates.

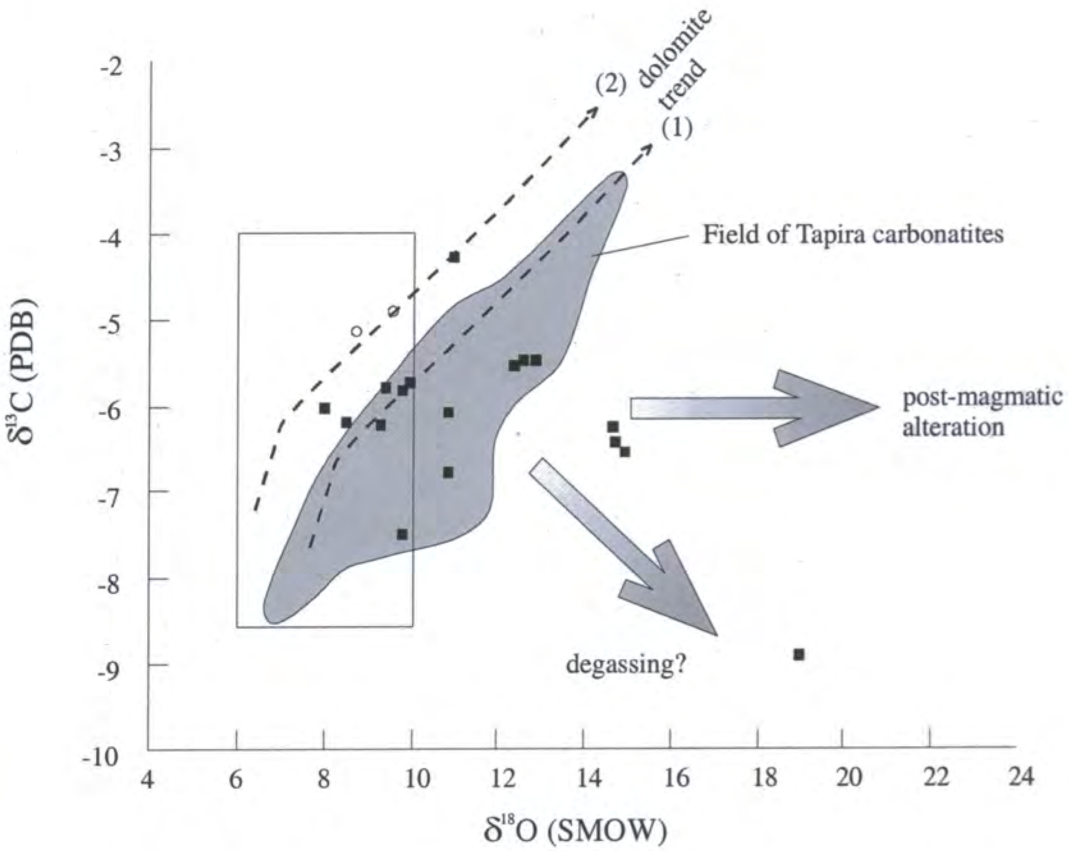

Figure IV.34 - Carbon and oxygen isotope composition of groundmass carbonate in phlogopite-picrites and low-Cr dykes from the Tapira complex. Squares = calcite, circles = dolomite.

The effect of late-stage disturbances in the isotopic system of mafic dykes seems to be more complex than that observed in the carbonatites. A similar shift towards ^{18}O enrichment can be argued, but some samples appear to define a negative slope in the diagram, where ^{18}O enrichment is accompanied by ^{13}C depletion. It is possible that more than one process was involved in disturbing the carbon and oxygen isotopic system of the dykes. Some authors (e.g. Zheng, 1990; Demeny and Harangi, 1996) have suggested that degassing of a fluid containing CO_2 may produce trends similar to that observed in Tapira mafic dykes. The presence of post-magmatic alteration does not invalidate, of course, the inference that the original carbonate in the groundmass of the mafic dykes was primitive and similar in composition to that of the carbonatites, as shown by the dolomites and by the least ^{18}O-enriched calcites in Figure IV.34.

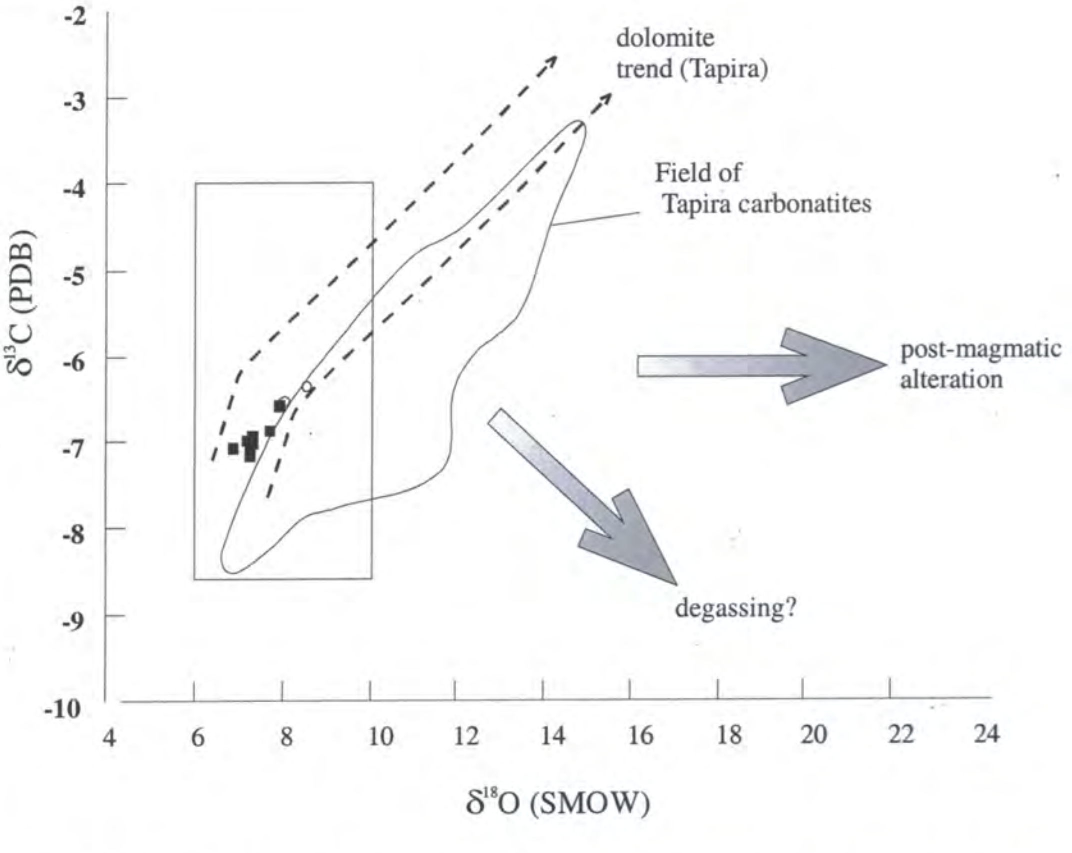

Figure IV.35 - Carbon and oxygen stable isotope composition of calcites (solid squares) and dolomites (open circles) of carbonatites from the Salitre complex. Trend of Tapira dolomites and possible paths of post-magmatic alteration are also shown.

IV.3.2 - SALITRE COMPLEX

Only carbonatites from Salitre were analysed for carbon and oxygen isotopes. In contrast with Tapira, a long drill core section of Salitre carbonatite was available for sampling during this research. This enabled the collection of exceptionally fresh samples, from much deeper into the core of the carbonatite intrusion (and, consequently, less prone to have been exposed to the peripheral hydro/carbothermal alteration systems). Calcite analyses were carried out in samples of calciocarbonatites and one ferrocarbonatite; dolomite analyses were from magnesiocarbonatites. The results are shown in Figure IV.35.

As expected from the absence of obvious signs of postmagmatic alteration, both calcite *and* dolomite plot in a trend of positive correlation between $\delta^{13}C$ and $\delta^{18}O$. More significantly, all samples analysed are contained in the "dolomite-trend" of Tapira rocks, lending further support to the interpretation (see above) that, in Tapira, the dolomites retained their original isotope composition while calcites were isotopically modified by post-magmatic processes. Finally, it should be noted that all analysed calcites and dolomites from Salitre plot well within the range of primary carbonatites, regardless of the compositional rock-type (calcio- ferro- or magnesio-carbonatite).

IV.3.3 - COMPARISON WITH OTHER CARBONATITE COMPLEXES

The volume of carbon and oxygen stable isotope data now available for carbonatites world-wide is large, and the isotopic evolution trends of different complexes are quite variable (e.g. Deines and Gold, 1973), depending on each individual history of fractionation, contamination and post-magmatic alteration. Therefore, any attempt to establish long-range correlations or to detect a common "isotopic signature" for different carbonatite complexes (unless the study is restricted to unevolved/unaltered samples) seems fruitless.

Rather than attempting intra-provincial correlations, Figure IV.36 compares the carbonatites from Tapira and Salitre with examples of three carbonatites that underwent very distinct isotopic histories. Jacupiranga, in southeastern Brazil, is considered an example of carbonatite whose carbon and oxygen isotopes were not extensively modified by assimilation of crustal material (Nelson *et al.*, 1988) or late-stage fenitisation (Santos, 1994; Santos and Clayton, 1995), and as such, plots in a restricted field, inside the range of mantle-derived isotopes. The Chiriguelo carbonatite, in northeastern Paraguay, shows a wide variation in $\delta^{18}O$, which is interpreted by Censi *et al.* (1989) as the result of the influx of meteoric waters at very low temperature conditions, after hydrothermal re-equilibration of the carbonatite. The Mato Preto

Carbonatite, in southeastern Brazil, shows a steep trend, with wide variations in $\delta^{13}C$, which result from contamination with the limestone country rock (Santos *et al.*, 1990; Santos and Clayton, 1995).

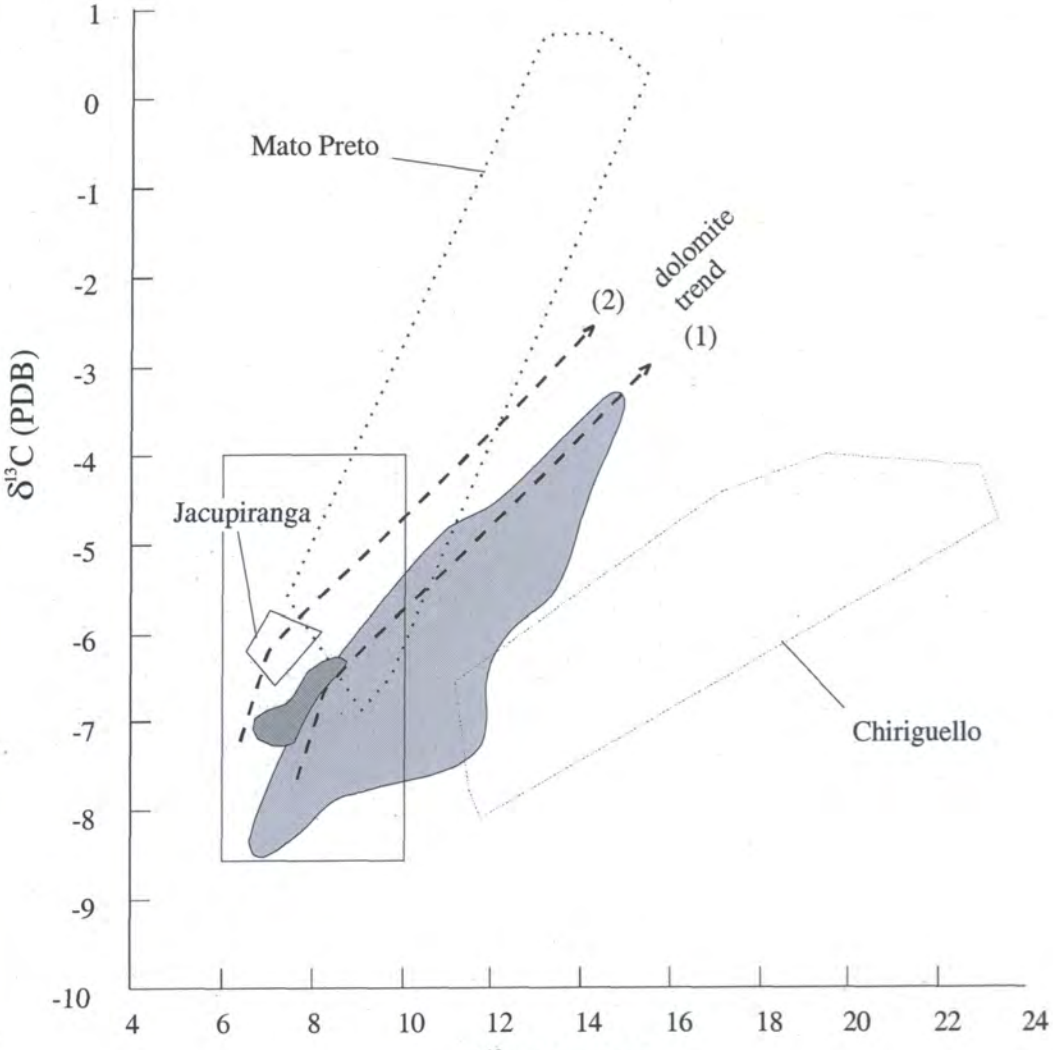

Figure IV.36 - Comparison of the carbon and oxygen isotope data of Tapira (light-shaded field) and Salitre (dark-shaded field) with the carbonatite complexes of Chiriguelo (Censi et al., 1989) Jacupiranga and Mato Preto (Santos, 1994; Santos and Clayton, 1995).

Tapira samples do not show either the strong $\delta^{18}O$ enrichment of Chiriguelo or the strong $\delta^{13}C$ enrichment of Mato Preto. The least isotopically evolved samples from Tapira and all analysed samples from Salitre plot within the primary carbonatite box, resembling those of Jacupiranga. Also note that both Salitre and Jacupiranga plot within or very near the lower end of the Tapira "dolomite trend".

IV.4 - SR AND ND ISOTOPES

Selected samples of wehrlite, bebedourite, mafic dykes, syenite and carbonatite were analysed for Sr and Nd isotopes, with a view to investigating the relationships between carbonatites and silicate rocks in the Tapira complex and to identify possible effects of crustal contamination, as well as to compare Tapira rocks with other ultrapotassic rocks in the APIP.

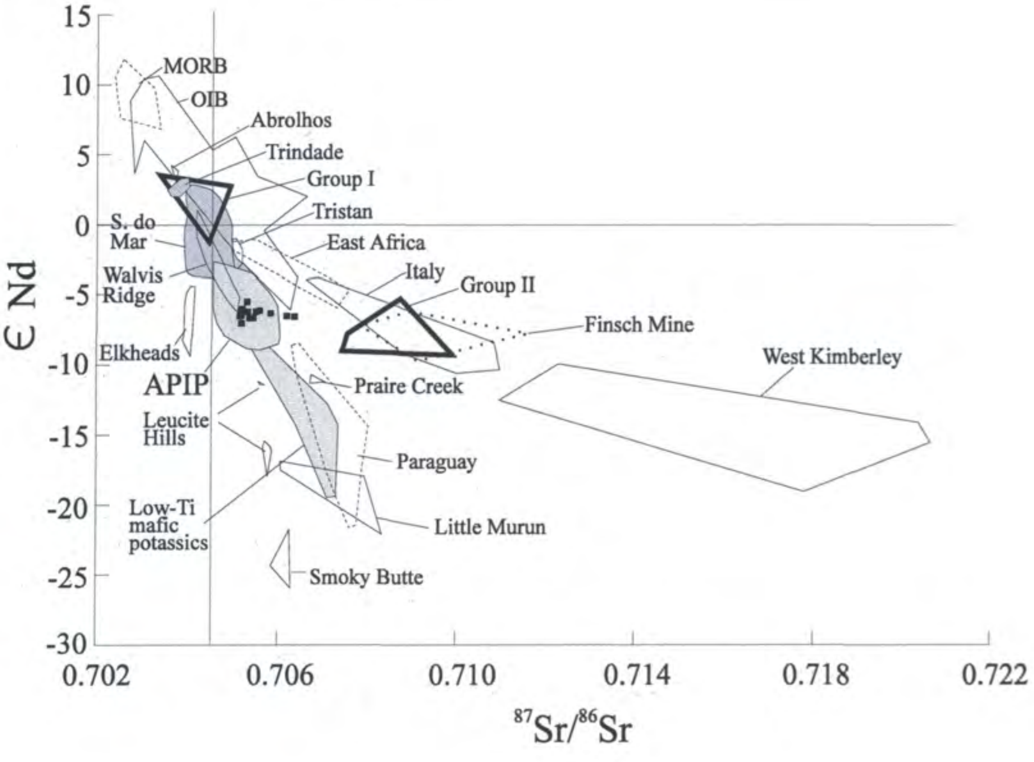

Figure IV.37 - Sr and Nd isotopic composition of Tapira rocks (solid squares), compared with other ultrapotassic provinces. Data sources are: Serra do Mar, Thompson et. al. (1998); Little Murun, Mitchell et al. (1994); East Paraguay carbonatites, Castorina et al. (1996). All other fields after Gibson et al. (1995b), and references therein.

The results are illustrated in Figure IV.37, in terms of ∈ Nd and initial $^{87}Sr/^{86}Sr$ ratios. Most Tapira rocks plot within the field of the Alto Paranaíba Igneous Province, suggesting that they are derived of a source similar to the other ultrapotassic rocks of the APIP. A small group of samples, however, shows a shift towards higher $^{87}Sr/^{86}Sr$, which may indicate the effect of crustal contamination.

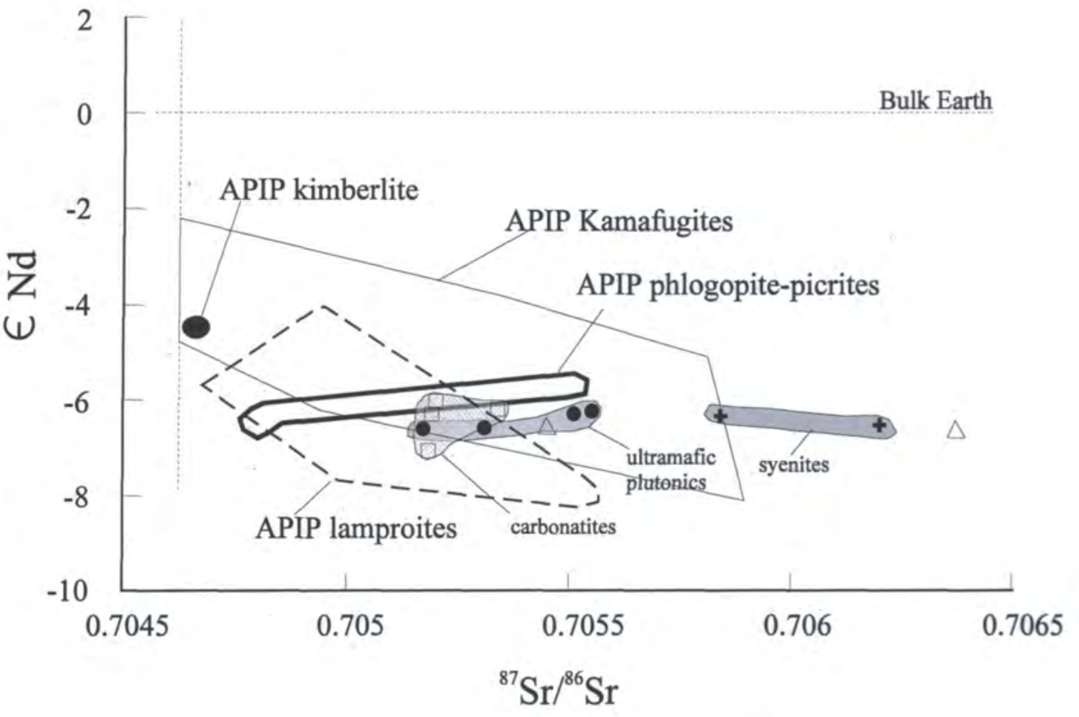

Figure IV.38 - Detail of Sr-Nd diagram, showing the composition of Tapira carbonatites (open squares), ultramafic plutonic rocks (wehrlites and bebedourites, solid circles), syenites (crosses) and mafic dykes (open triangles). Also shown are the compositions of APIP kimberlites, and fields for APIP kamafugites and phlogopite-picrites (Data from Gibson et al., 1995b).

Figure IV.38 shows the same diagram on a more detailed scale, to allow the representation of Tapira rock-types individually. The variation in ∈ Nd is very small for the whole set of analyses, which are concentrated at ∈ Nd values intermediate between those of other APIP phlogopite-picrites and APIP kamafugites. On the other hand, some significant variations can be observed in $^{87}Sr/^{86}Sr$ ultramafic rocks of the SPS have Sr isotopes similar to those of the carbonatites, although they plot along a trend of $^{87}Sr/^{86}Sr$-enrichment. The two analysed syenites show substantially higher $^{87}Sr/^{86}Sr$ ratios, plotting outside the overall field of APIP rocks. One of the analysed ultramafic dykes has a Sr-isotopic ratio like that of the carbonatites and ultramafic plutonics, but the other dyke plots near the syenites and has the highest calculated $^{87}Sr/^{86}Sr$. Because the variation in Nd isotopes is negligible, and consistent with the remainder of APIP magmatism, the data suggests that some degree of crustal contamination was responsible for the wider range observed in $^{87}Sr/^{86}Sr$. The effects of crustal assimilation and possible constraints on the petrogenesis of the Tapira complex will be will be discussed in more detail in Chapter V.

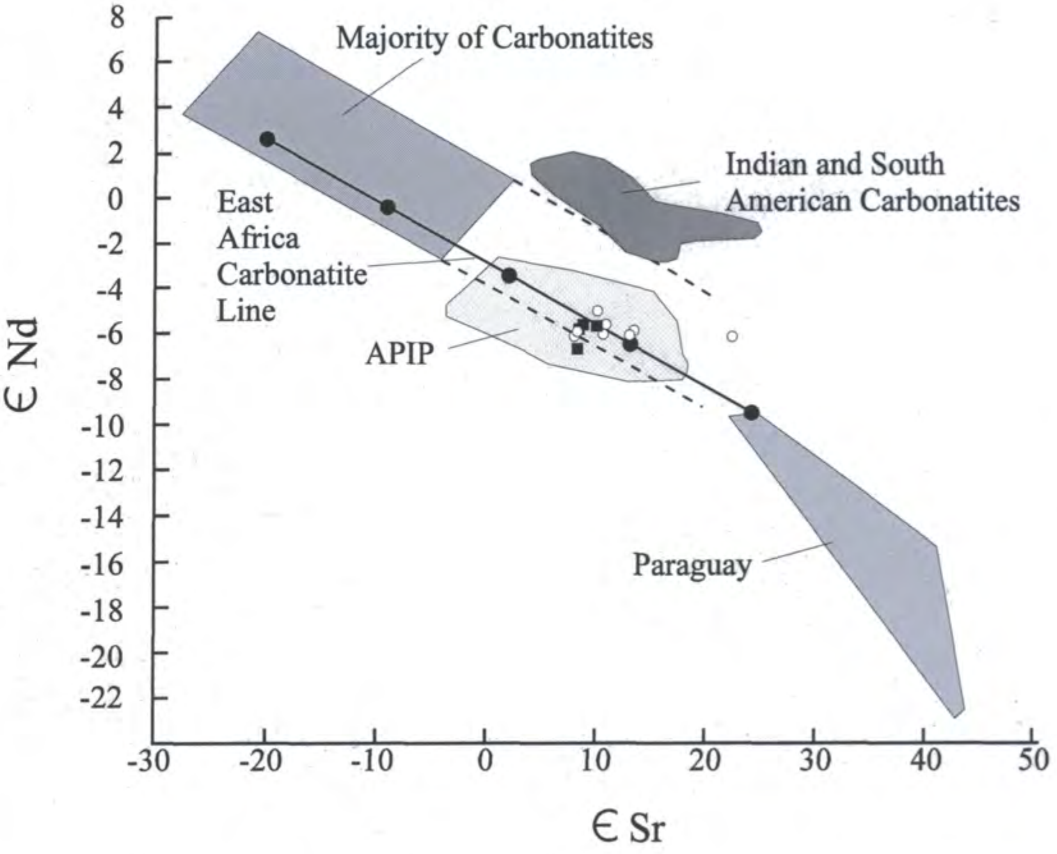

Figure IV.39 - Composition of Tapira carbonatites (solid squares), compared with the majority of world carbonatites and South America + India carbonatites (Harmer and Gittins, 1998). Also shown are the East Africa Carbonatite Linę (Bell and Blenkinsop, 1987) and the fields for APIP rocks (Gibson et al., 1995b) and carbonatites from Eastern Paraguay (Castorina et al., 1996).

Harmer and Gittins (1998) have recently presented a comprehensive compilation of Sr and Nd isotopic data for carbonatites world-wide, and concluded that 77% of their database plots within the limits of a parallelogram with the long sides parallel to the East African Carbonatite Line of Bell and Blenkinsop (1987), the main exceptions being carbonatites from India and South America. Figure IV. 39 shows the composition of

Tapira carbonatites compared with the results of Harmer and Gittins (1998). The samples analysed during this research fall outside the field of the majority of world-wide carbonatites, but do not agree with the postulated South America and India compositions. Instead, Tapira carbonatites (as well as other APIP rocks and carbonatites from Paraguay) plot close to the East Africa Carbonatite Line, on the continuation of the parallelogram of Harmer and Gittins (1998).

IV.5 - SUMMARY

- Phlogopite picrites from the Tapira complex are carbonated, silica-undersaturated ultrapotassic rocks and show strong chemical affinity with rocks of the kamafugitic series. Their major- and trace-element composition is similar to kamafugitic rocks from the Alto Paranaíba Igneous Province (APIP), and virtually identical to phlogopite-picrites occurring elsewhere in the province.
- The low-Cr dykes are slightly more evolved examples of ultramafic dykes in the Tapira complex. Some of the low-Cr dykes have trace-element signatures similar to the phlogopite picrites, but others show “anomalous” characteristics, such as negative anomaly at Th, high chondrite-normalised Nb/Ta ratios and positive anomalies at Zr and Hf. The chondrite-normalised REE patterns of this latter group are less steep, and “cross over” those of the phlogopite-picrites.
- Some of the wehrlites and bebedourites from the B2 unit show the same “anomalous” geochemical signatures as the group of low-Cr dykes described above, and may be related to those rocks.
- Tapira syenites are depleted in LREE, relative to the primitive phlogopite-picrites, and show strong enrichment in Zr and Hf.
- Most Tapira carbonatites show extreme LREE/HREE fractionation, and are strongly depleted in Zr, Hf, Rb and K, relative to the primitive phlogopite-picrites. These rocks also typically show a very high chondrite-normalised Nb/Ta ratio. However, carbonatites from the C3 (and, perhaps C4) unit typically lack most of these features.
- Syenites and carbonatites from the Salitre complex show geochemical characteristics similar to those observed in the Tapira counterparts.

- Calcites and dolomites from Tapira carbonatites and carbonate-rich ultramafic dykes have carbon and oxygen stable-isotope compositions compatible with a mantle origin. However, they also show evidence of CO_2 degassing and late-stage hydrothermal alteration. Calcites seem to have been more affected by hydrothermal alteration than dolomites.
- Tapira carbonatites and silicate rocks show a restricted range of Sr- and Nd- isotopic ratios, mostly within the range of other APIP rocks.

CHAPTER V - PETROGENESIS

V.1 - INTRODUCTION

The main objective of this Chapter is to explore the implications of the data presented in this thesis for the origin of Tapira magmas and to provide a model for their evolution. An assessment of the evidence and petrogenetic models presented by previous workers in the Alto Paranaíba Igneous Province (APIP), and their consequences for the petrogenesis of the Tapira complex, will be made initially. This is followed by the interpretation of the new data obtained during this research, and their consolidation in a petrogenetic model for Tapira.

V.2 - THE MANTLE SOURCES OF THE ALTO PARANAÍBA MAGMATISM

The Cretaceous magmatism in the Alto Paranaíba Igneous Province (APIP) has been the subject of recent chemical and isotopic studies, which have attempted to identify the geochemical characteristics of the mantle sources of these rocks (e.g. Toyoda *et al.* 1994; Bizzi *et al.,* 1995; Gibson *et al.,* 1995b; McDonald *et al.,* 1995; Carlson *et al,.*1996). With the exception of Toyoda *et al.* (1994) a general consensus seems to emerge from these studies that the vast majority of APIP magmas originated from the sub-continental lithospheric mantle (SCLM), and that this mantle source was previously enriched in incompatible trace-elements. The predominance of rocks with mineralogical and/or geochemical affinities with those of the kamafugitic series, in both plutonic and volcanic settings of APIP, is also now widely recognised (e.g. Sgarbi and Valença, 1993; Sgarbi and Gaspar, 1995; Sgarbi *et al.,* 1998; Gibson *et al.,* 1994, 1995b; Tompkins *et al.,* 1998; Araújo *et al.,* 1998). Finally, it is also generally accepted that the large-volume kamafugitic magmas were generated at shallower depths than the coeval small-volume kimberlites.

However, the proposed models differ with respect to: a) the causes and tectonic controls of the magmatic activity; b) depth of melting of some of the magmas concerned; c) origin and nature of the processes which led to the enrichment of the mantle source. Some of the divergence in petrogenetic models proposed for the APIP may be attributed to inconsistency in the application of nomenclature schemes For instance, rocks from the locality of Limeira have been variably classified as kimberlites (Bizzi *et al.,* 1995), kamafugites (Gibson *et al.,* 1995b) and lamproites (Carlson *et al.,* 1996). Furthermore, Carlson *et al.* (1996) describe the Alto Paranaíba magmatism as a "mixture of sodic and ultrapotassic mafic volcanic rocks" (with the kamafugites as the sodic end-member) but this concept finds little support in most of the other recent studies of APIP, which regard the potassic to ultrapotassic rocks as vastly predominant in the province.

Further complication is introduced by the adoption of different geochronologic frameworks for the Cretaceous alkaline magmatism surrounding the Paraná Basin. For instance, Gibson *et al.* (1995a,b; 1997a) distinguish two separate episodes, in the Early and Late Cretaceous, that they associated with the impacts of the Tristan da Cunha and Trindade mantle plumes under the South American plate. In this scenario, the APIP magmatism is considered to be related to the second (Trindade) event. On the other hand, the study of Bizzi *et al.* (1995) encompasses a much wider time interval (120-75 Ma) for the Alto Paranaíba magmas. This apparent disagreement may partially result from the inherent scatter of old radiometric dates. A combination of the discussion in Gibson *et al.* (1995b) and in Thompson *et al.* (1998) about the relative accuracy of the published age determinations and the criteria for screening out potentially unreliable ages produces two peaks of activity, at the Early and Late Cretaceous. The continuity of the latter, from the Late-Cretaceous to the Eocene, is represented by the Serra do Mar Igneous Province, to the southeast of APIP, therefore suggesting a progression of the magmatic activity from west to east (Thompson *et al.,* 1998).

Some of the petrogenetic models suggested for the APIP are summarised and briefly discussed in the paragraphs below.

Gibson *et al.* (1995b) proposed that the Late-Cretaceous impact of a mantle plume beneath the relatively thick lithosphere of SE Brazil, at around 85 Ma, is the cause of the widespread mafic to ultramafic, potassic to ultrapotassic magmatism in the Alto Paranaíba region. According to this model, the mantle plume acted mainly as a source of heat, which penetrates the overlying lithospheric mantle through conduction and/or advection by asthenosphere-derived melts. The result of this thermal perturbation is the melting of readily-fusible portions of the sub-continental lithospheric mantle (SCLM) which would, in turn, produce the voluminous ultrapotassic magmatism of the APIP. Evidence from major- and trace-element geochemistry, and from Sr-Nd isotopic ratios, points to an origin of APIP ultrapotassic magmas within the SCLM. Plate-tectonic reconstructions (e.g. Morgan, 1983; O'Connor and Duncan, 1990) place the starting head of the Trindade mantle plume under the Alto Paranaíba region in the Late Cretaceous, thus lending further support for the association between the arrival of this mantle plume and the APIP magmatism. In this scenario, the Brasília mobile belt, where the ultrapotassic magmas were emplaced, would have acted as a "thinspot" relative to the thicker lithosphere of the adjacent São Francisco craton, thus favouring a greater degree of asthenospheric upwelling and, consequently, the production of APIP magmas from the overlying SCLM.

The reconciliation of the high degree of LREE/HREE fractionation with the high absolute abundances of REE requires that the mantle source had been enriched in incompatible elements prior to partial melting. This enrichment is attributed by Gibson *et al.* (1995b) to the percolation of K- and Ca- rich small-fraction melts from the asthenosphere, possibly involving a combination of silicate-and carbonate- rich melts.

Finally, detailed variations in the chemical properties of kamafugites, lamproites and kimberlites from APIP led Gibson *et al.* (1995b) to suggest heterogeneities in the source regions of these rocks. Thus, the high CaO and Sc of the kamafugites are interpreted as indicative of a clinopyroxene-rich (wehrlite, or peridotite veined by clinopyroxene-rich material) mantle source for these magmas. The favoured mechanism for the production of the postulated source mineralogy is the conversion of mantle harzburgite or lherzolite to wehrlite by reaction with dolomitic carbonatite melt (e.g. Dalton and Wood, 1993a; Moore and Wood, 1998). This is believed to take place at relatively low pressures in the mantle (< 25 kb), suggesting a relatively shallow origin for the kamafugite magmas. On the other hand, the presence of high-pressure assemblages in xenoliths (Carvalho and Leonardos, 1995) and the high MgO/CaO ratio of the Três Ranchos kimberlite suggests a much deeper (> 150 km), clinopyroxene-depleted source. Some of the geochemical characteristics of the APIP lamproitic rocks (e.g. CaO, Al_2O_3, Sc concentrations) are intermediate between those of the kamafugites and those of the Três Ranchos kimberlite, suggesting that the source for the lamproitic magmas is somewhat depleted in clinopyroxene with respect to the kamafugites. Gibson *et al.* (1995b) also interpreted the relatively low SiO_2 and high CaO contents of these rocks, when compared with typical lamproites, as indicative of slightly CO_2-rich conditions in the source. They further suggested that the higher K and Ti of these rocks, relative to APIP kamafugites and kimberlites, as a result of incorporation of phlogopite into the melt, favouring a locally less-oxidised environment for the mantle source of APIP lamproites.

Bizzi *et al.* (1995) proposed an origin from lithospheric (EMI-like) mantle for melts formed at relatively shallower depths (i.e. kamafugites and carbonatites), and a mixture of upwelling asthenospheric (HIMU-like) melts and a volumetrically dominant EMI component for the rocks derived from greater depths (kimberlites). They interpreted the kamafugitic and other "rift-related alkalic rocks" as the crystallisation products of relatively evolved magmas suggesting, on the basis of the observed low magnesium number (49 to 53), that such liquids have suffered previous fractionation of olivine and, possibly, chromite. On the other hand, such differences may also be attributed to variable degrees of partial melting (Gibson *et al.*, 1995b) or mineralogical variations in the source (Carlson *et al.*, 1996). The mg-number values obtained by Gibson *et al.* (1995b) in kamafugitic lavas are significantly higher (up to 74) than those of Bizzi *et al.* (1995), suggesting a less evolved character for these magmas.

The extreme LREE enrichment of the APIP magmas, accompanied by lesser variation in the HREE, is interpreted by Bizzi *et al.* (1995) as indicative of the presence of residual garnet in the mantle source of APIP magmas. These authors suggest that an increase in the depth of melting in the province, from east to west, resulted in the genesis of kamafugites in the eastern portions of APIP and kimberlites in the west. This seems to be supported by evidence from platinum-group-element geochemistry (Bizzi *et al.,* 1995; McDonald *et al.,* 1995). Furthermore, the mechanism proposed for the generation of melts at several different depths invokes the control of rift-related structures, consistent with the fact that the shape of the Sanfranciscana Basin, which contains the Mata da Corda kamafugites, is tectonically controlled (Seer *et al.,* 1989). The geotectonic scenario proposed by Bizzi *et al.* (1995) has important economic implications, especially for the exploration of diamond and carbonatite-related deposits (e.g. Nb, P, Ti). However, it is difficult to reconcile with the following:

a) the possible subsurface continuity of the São Francisco craton westwards, under the thin-skinned thrust cover of the Brasília belt (see discussion in Chapter I). This would imply a progressively thicker lithosphere from west to east, across the geographic domain of the Brasília belt.

b) the evidence presented in this thesis and in Gibson *et al.* (1995b) indicates that the magmatism of kamafugitic affinity is not limited to the area covered by Mata da Corda Group, in the eastern region of APIP. Furthermore, the carbonatite complexes, which are equally thought to have been generated at relatively shallow depths in the mantle, are all emplaced to the west of the main outcrop area of the Mata da Corda Group. In this sense, it should be noted that the carbonatite complexes of Catalão I and II are even located to the west of the Três Ranchos kimberlite.

c) the tectonic constraints proposed by Bizzi *et al.* (1995) rely heavily on their interpretation that the magmatism in the APIP is controlled by extension and rifting. Mafic potassic, volatile-rich magmas are generally thought to represent the initial stages of melting, upon heating and/or extension of the sub-continental lithospheric mantle (McKenzie, 1989; Thompson *et al.*, 1990; Gibson *et al.*, 1995b). With continuing extension and rifting, the magmatic activity may progress towards less alkaline varieties and, ultimately, result in the production of continental flood basalts (CFB) from the upwelling asthenosphere. In the case of the APIP, the mafic potassic, strongly alkaline and undersaturated magmas are vastly predominant and a typical rift-related succession of Late-Cretaceous age, including decompression melts from the asthenosphere, has yet to be described.

d) some of the rift-related rocks described by Bizzi *et al.* (1995) are as old as 120 Ma and, therefore, may be associated with the Early-Cretaceous magmatic event (e.g. Paraná CFB and some of the alkaline provinces situated at the margin of the Paraná Basin further to the south - see Chapter I), rather than with the Late-Cretaceous APIP magmatism.

Bizzi *et al.* (1995) pointed out that the APIP magmas carry a Dupal signature, both in terms of Sr and Pb isotopic ratios whose origin is attributed to the Late-Proterozoic tectono-thermal event associated with the development of the Brasília belt. On the basis of the isotopic similarities with South Atlantic hot spots (e.g. the Tristan-Walvis Ridge system), they suggest that the asthenospheric sources of the OIB were contaminated with the delaminated Brazilian lithosphere.

Carlson *et al.* (1996) also favoured a lithospheric source for the APIP magmas, based on Os-isotope evidence. They point out that the low $^{187}Os/^{188}Os$ ratios indicate a basalt-depleted peridotitic source for the APIP kimberlites, whilst lamproites were derived from a peridotite slightly to moderately depleted in a basalt component. The higher $^{187}Os/^{188}Os$ and higher Re/Os of the kamafugites favour a source composed of lithologies such as pyroxenite, websterite and/or eclogite. They concluded that some of the highest-MgO (kimberlites) magmas emplaced in the Brasília belt retain evidence of an Archaean/Early Proterozoic Re-depletion event. This is consistent with independent evidence from gravimetric (Pires, 1986) and seismic (VanDecar *et al.,* 1995) data, as well as xenolith studies (Leonardos *et al.,* 1993; Carvalho and Leonardos, 1995) for the sub-surface continuity of the São Francisco Craton under the thrust slices of the Brasília belt. However, Carlson *et al.* (1996) emphasise that this older Os signature does not extend as far west as the Três Ranchos kimberlite, suggesting that the source of the Três Ranchos kimberlite is composed of an Archaean lithosphere that suffered Re-enrichment by metasomatism during the Late Proterozoic. The sources of lamproites and kamafugites would have been accreted to the lithosphere during the formation of the Brasília belt, in the Late Proterozoic.

With regard to the isotopic similarities between the EMI component of the Brazilian SCLM and the OIB erupted from South Atlantic hot-spots, such as Tristan da Cunha, Carlson *et al.* (1996) adopt an approach similar to that of Bizzi *et al.* (1995), suggesting that delamination of the Brazilian lithosphere, and its incorporation into the convecting mantle, is responsible for the isotopic characteristics of the OIB. They also point out that the EMI signature of the Brazilian SCLM originated during the collisional event that formed the Brasília belt, suggesting that the denser lithosphere of the mobile belt was preferentially involved in the delamination process.

In an earlier isotopic study of various Brazilian carbonatites Toyoda *et al.* (1994) also recognised a Dupal-type signature. They divided the studied rocks into a southern group, comprising Anitápolis and Jacupiranga carbonatites, associated in time and space with the Early-Cretaceous position of the Tristan da Cunha mantle plume, and a northern group (Araxá, Tapira and Catalão) coinciding in space and time with the Late-Cretaceous starting point of the Trindade mantle plume track. However, Toyoda *et al.* (1994) conclude that carbonatites from both groups have similar Pb and Sr signatures, and that their isotopic ratios reflect the influence of the Tristan plume. Their favoured petrogenetic model postulates that the mantle source for northern group (i.e. APIP) carbonatites is asthenospheric material from the Tristan plume, which became trapped under the crust and was reactivated in the Late Cretaceous by the Trindade hot-spot. In their teleseismic study of the region, VanDecar *et al.* (1995) proposed a similar geotectonic framework, interpreting a seismic low-velocity zone under the northern Paraná Basin as the fossil remnants of the Tristan plume.

Sasada *et al.* (1997) presented noble-gas isotopic data for Brazilian (Jacupiranga and Tapira) and Canadian carbonatites. They conclude in support of a primordial noble-gas signature for these rocks, and found no evidence of subduction-related components. They suggest that the mantle source of the studied carbonatites differs substantially from MORB, being relatively undegassed in comparison with the latter.

Further constraints on wide-scale provinciality, and the role of the asthenospheric versus lithospheric mantle source in the Cretaceous magmatism surrounding the Paraná Basin were established by Gibson *et al.* (1995a). These authors recognised "Low-Ti" and "High-Ti" melt source regions (located, respectively around the southern and northern Paraná Basin) for the mafic potassic igneous rocks from SE Brazil and Paraguay. They highlighted the strong correlation of these domains with both: a) the distribution of the low- and high-Ti Paraná CFB (cf. Peate *et al.,* 1992) and b) the tectonic framework of the area (i.e. association of the low-Ti type with cratonic areas and the high-Ti type with mobile belts). Gibson *et al.* (1995a) interpret this provinciality as ultimately reflecting differences in the underlying SCLM, with the lower time-integrated $^{143}Nd/^{144}Nd$ and the higher Nd model ages of the low-Ti potassic rocks suggesting a mantle source that had undergone metasomatic enrichment in the Early Proterozoic.

It could be argued that the work by Toyoda *et al.* (1994) was concerned with carbonatites only, and that evidence from the study of silicate alkaline magmas does not necessarily apply, unless the two rock-types share a common origin. In the case of the Tapira and Salitre complexes, the data presented in this thesis strongly suggest that the origin of the carbonatites is inextricably linked with the ultrapotassic magmatism in the province (see discussion below). If this is the case, then the widespread, low- and high-Ti provinciality of the magmatism surrounding the Paraná Basin argues against the single asthenospheric origin for "southern" and "northern" carbonatites envisaged by Toyoda *et al.* (1994). The same constraints seem to apply to other carbonatites emplaced around the margins of the Paraná Basin. Note, for example, that carbonatites from Eastern Paraguay have Nd isotopic signatures similar to the low-Ti mafic potassics of Gibson *et al.* (1995a). However they do not, apparently, apply to the Jacupiranga carbonatites.

To date, it seems difficult to reconcile the tectonic/petrogenetic concepts of Toyoda *et al.* (1994) and Sasada *et al.* (1997) with those of Bizzi *et al.* (1995) and Carlson *et al.* (1996). For instance, Toyoda *et al.* (1994), suggest that the Dupal signature of the APIP carbonatites is derived from an asthenospheric mantle plume, while the latter two works postulate that the Dupal signature of the South Atlantic mantle plumes is derived from the delamination of an EMI-type Brazilian continental lithosphere.

In any case, the chronological relationship between the impact of the Tristan and Trindade plumes and the magmatism in Southern Brazil provides an attractive tectonic framework for the investigation of the Cretaceous magmatism in southern Brazil. However, it does not imply that some or most of the magmas must be generated within the ascending plume and, consequently, show a compulsory "plume" signature. In fact, for ultrapotassic provinces world-wide the geochemical and isotopic signatures of the local lithosphere seem to dominate over those of the convecting mantle (Mitchell, 1996a). This is also demonstrated on a smaller scale, by the low- and high-Ti provinciality of mafic potassic rocks in southern Brazil (Gibson *et al.,* 1995a). It is noteworthy that APIP magmas lack the negative Nb-Ta anomalies (suggestive of a subduction component or, alternatively, of residual titanates in the source of the magmas) that are found in some occurrences of ultrapotassic to potassic rocks, such as those of the Aldan Shield (Bogatikov *et al.* , 1994), Highwood Mountains, Montana (O'Brien *et al.,* 1995) Central Italy (Stoppa and Cundari, 1995) and Paraguay (Comin-Chiaramonti *et al.,* 1996)

V.3 - PETROGENESIS OF THE TAPIRA COMPLEX

Various aspects concerning the origin and evolution of the Tapira rocks will be discussed in the remainder of this Chapter. An initial assessment of the evidence for magmatic liquids (or otherwise) in the studied samples is followed by the investigation of the possible sources of the primitive magmas associated with Tapira and by a discussion of the evolution of these liquids at crustal levels.

V.3.1 - WHICH ROCKS WERE LIQUIDS?

Any attempts towards a petrogenetic model for the formation of the Tapira complex must include an assessment of which of the studied rock-types are (i) likely to represent or approximate to liquids; and (ii) products of post-melting processes, such as crystal accumulation or liquid immiscibility. In particular, the coarse grained plutonic rocks may either be the product of *in situ* crystallisation, in which case their bulk-rock chemistry would tend to reflect that of the original magma, or they may be formed by accumulation of one or more mineral phases, in which case the chemical composition will depart significantly from that of the liquid. In the case of ultramafic rock-types, the common occurrence of substantial variation in the modal composition of the rock means that textures and structures produced by crystal accumulation (such as igneous layering and changes in cumulus-intercumulus relationships of various phases) are more easily recognisable. However, both syenites and carbonatites can also be generated by accumulation processes, i.e. by flotation of feldspar and carbonate crystals, respectively, to the upper regions of a magma chamber. In coarse-grained varieties of these rocks, the recognition of accumulation processes may be difficult by petrographic means alone, and one must rely to a greater extent on the chemical evidence.

Volcanic rocks or fine-grained dykes may provide a better estimate of the composition of the original magmatic liquids. If that is the case, an assessment of the possible effects of magma evolution is still required, to distinguish samples that may represent the primitive magmas from those which suffered modifications through fractionation, assimilation or liquid immiscibility. The following sections provide a discussion of the evidence on relevant rock-types studied during this research.

Fine-grained dykes

In sub-volcanic igneous complexes the obvious approach of geochemical studies is to investigate the chemical composition of the associated volcanic rocks, particularly of the glassy varieties, in order to obtain the closest approximation of the evolving magmas. Although the Tapira complex seems to have been ultimately intruded at a high-level (see discussion below) it is strongly weathered and deeply eroded, and no remnants of associated volcanic rocks are preserved in the immediate vicinity of the complex.

An alternative approach, in the absence of glassy volcanics, is to investigate the fine-grained dykes associated with the intrusion. A number of fine-grained ultramafic potassic dykes (phlogopite-picrites and low-Cr dykes) and fine-grained carbonatite dykes from Tapira, as well as microsyenitic dykes from Salitre were studied during this research. Although some of the phlogopite- and carbonate- rocks have been previously mistaken for fenitisation products, the following petrographic and field evidence clearly indicate their magmatic origin: a) porphyritic textures, with euhedral phenocrysts; b) flow textures; c) flow-differentiation structures (in the phlogopite-picrites) and d) discordant tabular (dyke) shapes of the intrusions.

The common presence of phenocrysts suggests that the fine-grained dykes may have been affected by crystal fractionation processes, to an unknown extent. This is particularly well illustrated by the accumulation of phenocrysts by flow differentiation, in the central portion of some phlogopite-picrite dykes. However, because the phenocrysts in phlogopite-picrites consist largely of olivine, their influence on whole-rock chemistry should not affect extensively the trace-element contents (other than Ni). This is illustrated (Chapter IV) by the very consistent REE- and trace-element patterns displayed by all analysed phlogopite-picrites.

The chemical (e.g. high MgO, Cr and Ni contents, undifferentiated REE patterns, mantle-derived carbon and oxygen isotopes of the groundmass carbonate) and petrographic evidence suggest that the least evolved magmas in Tapira (phlogopite-picrites) are primitive liquids. Tapira rocks are also compositionally similar to phlogopite-picrites associated with other APIP carbonatite complexes, and have strong geochemical affinities with the kamafugitic magmatism in the province. It has been argued (Bizzi *et al.* 1995; see discussion above) that APIP kamafugites do not represent primitive magmas but are relatively evolved. From the evidence presented in this thesis, the Tapira phlogopite-picrites are clearly capable of fractionating olivine and chromite, and should therefore be considered primitive.

Other varieties of fine-grained dykes (i.e. the low-Cr dykes, some carbonatites from Tapira, and the microsyenites from Salitre) are likely to represent evolved liquids or near-liquid compositions. In this sense, it is obvious from the petrography and major-element chemistry that the low-Cr dykes are incapable of producing olivine- and/or chromite-rich cumulates. In fact, the extremely low concentrations of Cr and Ni in these rocks suggest that they evolved from a more primitive liquid (e.g. a phlogopite-picrite) by extensive precipitation of these same mineral phases. The composition of the low-Cr dykes is appropriate for the fractionation of clinopyroxene, apatite and some perovskite, which makes them an attractive alternative of parental liquids to bebedourite-like plutonic rocks. The low Cr and Ni, high Sc and CaO, and the occurrence of the same minerals as phenocrysts in the low-Cr dykes is consistent with this interpretation. The evidence suggests that the low-Cr dykes can be considered the fine-grained equivalents of the bebedourites.

However, many of the geochemical properties of the low-Cr dykes, described in Chapter IV (e.g. crossover REE patterns and dramatic changes in Th, Nb, Ta, Zr and Hf), especially in the more evolved specimens, are difficult to explain by fractionation of a particular phase or combination of phases. These variations may indicate the involvement of liquid immiscibility processes in the origin of these rocks, in addition to crystal fractionation, as discussed in a later section of this Chapter.

Fine-grained syenites have not been found in Tapira, during this research. However, a set of microsyenite dykes from Salitre was studied, in order to gain some insight into the composition of the evolved, felsic silicate liquids associated with APIP carbonatite complexes. The euhedral, sometimes optically zoned phenocrysts of pyroxene, feldspar and feldspathoid (kalsilite?, nepheline?) set in a very fine-grained groundmass, often showing flow textures, testify to the magmatic character of these rocks. Also, the whole-rock chemical compositions define a trend consistent with magmatic differentiation of felsic liquids, and their trace-element signatures suggest the involvement of liquid immiscibility processes in their genesis (see below)

The fine-grained carbonatite dykes of the C2 unit may also represent magmatic liquids. This is suggested by textural evidence, such as the occurrence of microporphyritic textures, flow texture and euhedral carbonate microphenocrysts. Furthermore, the zoning patterns of calcite microphenocrysts (Chapter III) and the fractionation patterns of carbon and oxygen isotopes (see below) are compatible with magmatic evolution processes, supporting the interpretation above.

Taken together, the ultramafic to felsic range of dyke rocks provide the best (yet incomplete) available approximation of the range of alkaline magmas involved in the generation of the complex.

Coarse-grained ultramafic rocks

The rocks comprising the ultramafic section of the SPS are unlikely to represent magmatic liquid compositions. Field and petrographic evidence has been presented (Chapters I, II), pointing to a cumulate origin for most of the studied samples The whole-rock chemical composition of these rocks can also be satisfactorily explained in terms of accumulation of variable amounts of olivine, clinopyroxene, chromite, apatite and perovskite. The chemical evolution of several of the essential minerals (e.g. clinopyroxene, phlogopite, opaque minerals, perovskite - Chapter III) is consistent with magmatic evolution and forms a substantial body of evidence for the generation of these rocks by progressive fractional crystallisation from an undersaturated, alkaline, potassic, ultramafic parent magma. Similar rock suites have been ascribed a cumulate origin in carbonatite-bearing complexes from the APIP (Mariano and Marchetto, 1991). In Tapira, the field evidence, as well as some of the chemical and mineralogical variations observed in the ultramafic plutonic rocks point to a multi-stage evolution for the complex rather than a single differentiating intrusion.

Coarse-grained syenites

Figure V.1 shows the composition of coarse-grained syenitic rocks from Tapira and fine-grained syenitic dykes from Salitre in the total alkalis vs. silica (TAS) diagram. The fields for the classification of volcanic rocks are included in the diagram for reference only. These fields may, perhaps, be relevant for the fine-grained dykes, but the rock-names obviously do not apply to the plutonic rocks from Tapira. The majority of Tapira samples have very high alkali contents and, apart from one pyroxene-rich sample, cluster tightly between 14 and 15 wt. % K_2O+Na_2O (calculated on a dry basis, for this diagram). Together with the very high K_2O/Na_2O ratios (Chapter IV) and the limited range of SiO_2 values, this may suggest that the chemical composition of Tapira syenites reflects the accumulation of K-feldspar crystals.

Such an interpretation is consistent with the behaviour of these rocks in the quartz (Q) - nepheline (Ne) - kalsilite (Ks) system of Figure V.2. In contrast with the trend expected for evolved, felsic to holofelsic, coarse grained syenites, the Tapira rocks plot well away from the thermal nepheline-syenite minimum, and within the leucite field. The following reasons can be considered to explain this behaviour.

a) The studied syenites were prevented from evolving until the nepheline-syenite minimum was reached (i.e. syenite magmas were "frozen" before complete evolution). This could conceivably be achieved if the syenite magma lost a substantial amount of volatiles, through a process such as degassing or separation of an immiscible carbonatite liquid, with sodium partitioning more strongly than potassium to the segregated fluid or melt.

b) Tapira syenites consist mainly of K-feldspar crystals accumulated by flotation towards the upper portions of the magma chamber. This is consistent with the very high contents of K and Ba observed in Tapira syenites, when compared with the microsyenite dykes from Salitre.

c) The experimental data in the Qz-Ne-Ks system does not accurately represent the phase relations of ultrapotassic syenites. Mitchell (1996c) suggested that the bulk composition of the parental magmas to some of these rocks lies well outside the quartz-nepheline-kalsilite system, and that perhaps the kalsilite-forsterite-quartz-H_2O system of Luth (1967) is more relevant to their crystallisation.

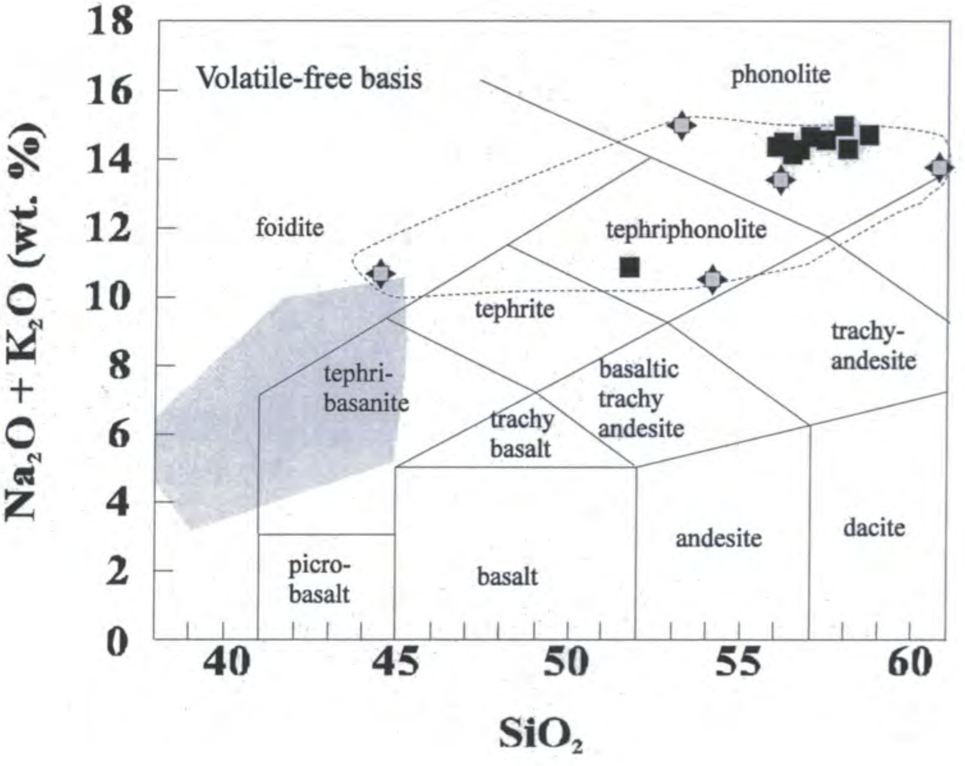

Figure V.1 Composition of Tapira coarse-grained syenites (squares) and microsyenite dykes from Salitre (stars) in the total alkalis vs. silica diagram (Le Maitre et. al., 1989) . The shaded area represents the composition of kamafugitic rocks (after Mitchell, 1996a)

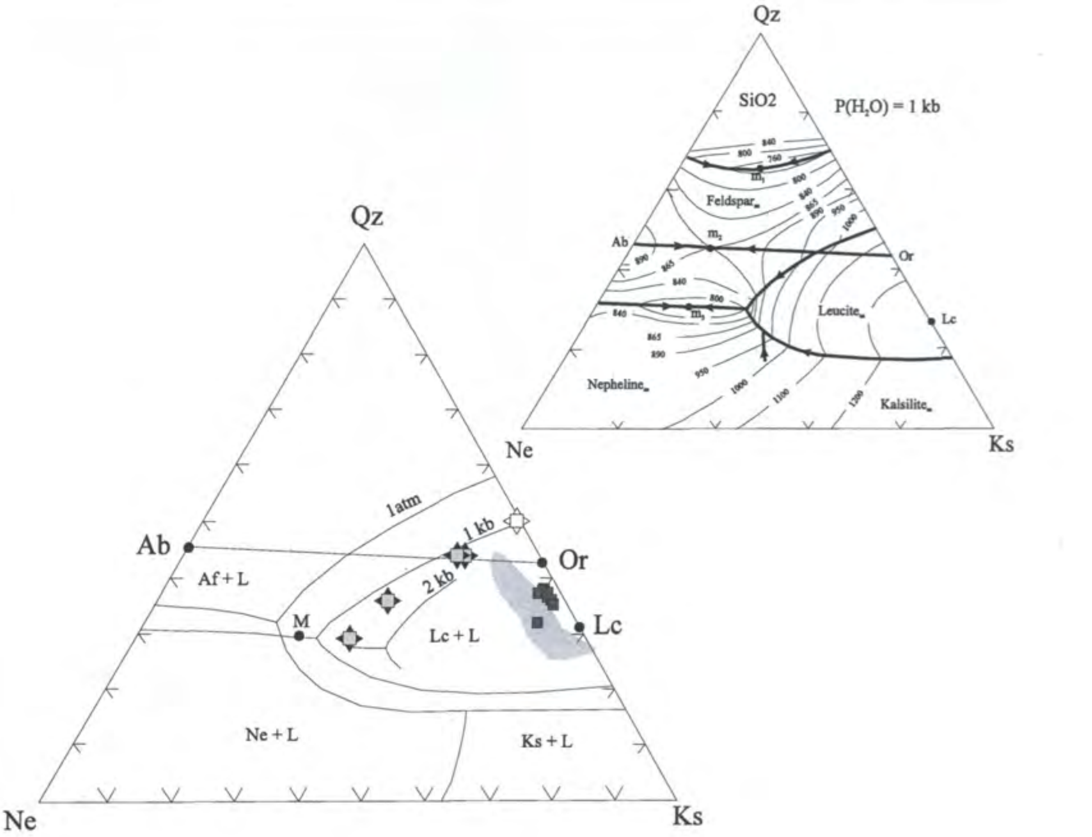

Figure V.2 - Composition of Tapira (squares) and Salitre (stars) syenitic rocks in the quartz - nepheline - kalsilite system, with the phase relations at 1 atm, 1kb and 2 kb The top right diagram represents the liquidus phase relations at $P(H_2O)$ = 1 kb. Qz = quartz, Ne = nepheline, Ks = kalsilite, Or = orthoclase, Ab = albite, Lc = leucite, L = liquid, M= ternary minimum. The shaded field represents the composition of syenites from the Baikal-West Aldan ultrapotassic province. Diagrams are from Mitchell (1996c) and Platt (1996).

A comparison of Tapira syenites with the fine-grained dykes from Salitre provides interesting constraints on this problem. Note that, in contrast with Tapira rocks, the analyses of the Salitre dykes plot along a well-defined trend towards the syenite ternary minimum (Figure V.2). This crystallisation path shows excellent agreement with experimental data; it is parallel to (and intermediate between) the trends of leucite + K-feldspar crystallisation at 1 and 2 kb. This suggests that the syenites differentiated at low pressure, and is consistent with several independent lines of evidence for a high-level emplacement of the Tapira and Salitre complexes. (see relevant sections in this Chapter). The open star in Figure V.2 is a syenite clast from the

São Gotardo locality, in APIP (Gibson *et al.,* 1995b) and illustrates the high-K end of the fractionation trend of microsyenite dykes. It should be noted that, although the K_2O/Na_2O ratios of the Salitre dykes are much lower (1 to 2.7) than those of Tapira coarse-grained syenites (5.8 to 34.6), they still approach the syenite minimum from the potassic side, consistent with the overall potassic to ultrapotassic character of APIP magmas. The São Gotardo sample has a K_2O/Na_2O ratio of 31.

The fact that the Salitre fine-grained rocks were able to evolve along the expected crystallisation path, starting from highly potassic compositions, strongly suggests that phase relations in the Qz-Ne-Ks system provide an adequate framework for the description of the studied rocks. However, the question remains of whether, in Tapira, the syenites were "frozen" at an unevolved stage or represent accumulation of feldspar crystals. The scarcity of sodic fenites, when compared with the widespread products of potassic metasomatism observed in Tapira and in other APIP carbonatites complexes (Araxá, Catalão) seems to favour the second hypothesis. Some of the fenites surrounding the Tapira complex do contain sodic minerals (aegirine, albite), but there is no apparent spatial relationships between these fenites and the syenites. Note that the ultrapotassic syenites from the Synnyr and Little Murun complexes (Baikal-West Aldan ultrapotassic province, Mitchell, 1996c) behave similarly to Tapira samples in Figure V.2, failing not only to plot near the thermal minimum but even to define a trend towards it. Some of these rocks are described by Mitchell (1996c) as flotation cumulates, and this seems to be the most likely origin of Tapira coarse-grained syenites.

Another interesting feature of the Tapira syenites is that their feldspars appear to be perthite-free, as far as optical recognition is possible. The extremely high contents of the orthoclase (Or) end-member in all microprobe analyses of these feldspars suggests that cryptoperthites are also absent. Regardless of whether they are cumulates or "frozen" unevolved magma, if the dependence of phase relations (Figure V.2, top-right diagram) on pressure and temperature can be applied, one would expect hypersolvus crystallisation of the feldspars in Tapira syenites, with the subsequent generation of perthites upon cooling. According to Mitchell (1996a), some undersaturated potassic plutonic rocks, such as malignites (*sensu* Mitchell and Platt, 1979, *not* synonymous with mela-foyaite) *"contain a potassium feldspar whose composition falls outside the limits of the alkali feldspar solvus; thus, perthites cannot be formed in these rocks"*. This is, in turn, interpreted as defining a *"genetically distinct series of one-feldspar potassic syenites"* (Mitchell, 1996c), in sharp contrast with the typical perthitic nature of feldspar in the more sodic syenites (e.g. foyaites).

In addition to evidence presented earlier in this thesis (e.g. XRD lines for kalsilite in Salitre microsyenites, high Ba content in feldspars from Tapira, similarities in pyroxene chemistry between Tapira and ultrapotassic plutonic complexes), the occurrence of non-perthitic orthoclase as the sole feldspar type lends further support to an ultrapotassic affiliation of Tapira syenites. Note that this is in disagreement with the interpretation of Haggerty and Mariano (1983) and Mariano and Marchetto (1991) that these rocks are "rheomorphic fenites" and also with the traditionally accepted notion (e.g. Le Bas, 1985) that pure orthoclase or pure albite are typical of syenitic fenites associated with carbonatite intrusions. Unfortunately, the Salitre dykes were not investigated by microprobe during this research, but the comparison of feldspar composition in both complexes seems a good prospect for future investigation.

Coarse-grained carbonatites

Whether the coarse-grained carbonatites from Tapira represent liquids or accumulation of calcite crystals is a difficult question. In some cases, particularly where the sample is virtually monomineralic (i.e. composed essentially of calcite) a cumulate origin can be readily accepted. Experimental evidence summarised by Lee and Wyllie (1998a,b) shows that a carbonated silicate magma cannot cross the silicate-carbonate liquidus field boundary through differentiation (see Figure V.10). Therefore, rocks that are nearly-pure calciocarbonatites probably represent accumulation of calcite crystals, instead of the products of *in situ* crystallisation of the carbonatite (or silicocarbonatite) magma. In Tapira the chemical evidence suggests that the parental magmas of the complex were, ultimately, carbonate-rich silicate liquids (see discussion later in this Chapter). Accordingly, the coarse-grained, calcite-rich and silicate-poor carbonatites are interpreted here as flotation cumulates. However, some samples containing substantial amounts of silicate minerals could represent the final stages of fractionation from a silicate parental magma or, alternatively, the relatively unevolved product of liquid immiscibility.

V.3.2 - MANTLE ORIGIN OF THE TAPIRA MAGMAS

Several lines of evidence, from this research and from previous works on Tapira point to a mantle origin for the magmas that originated the complex.

The relatively restricted Sr and Nd signatures of APIP rocks, together with the isotopic similarities between Tapira rocks and the remainder of the APIP (Chapter IV) suggest a broadly similar mantle source for the whole of the Late-Cretaceous ultrapotassic rocks in the Alto Paranaíba region, including the carbonatite-bearing complexes. This source has lower $\in$ Nd values (-2 to -8) and higher initial $^{87}Sr/^{86}Sr$ ratios (0.7045 to 0.706) than the bulk-Earth, indicating that it constitutes an enriched SCLM. Nd model ages (Gibson *et al.,* 1995b; Bizzi *et al.,* 1995) and Os isotopic data (Carlson *et al.,* 1996) suggest that the tectono-thermal event responsible for the enrichment occurred during the Late Proterozoic. Therefore, the source enrichment took place long before the arrival of both the Tristan (Early Cretaceous) and Trindade (Late Cretaceous) mantle plumes, lending further support to a lithospheric mantle source of the APIP magmas.

The carbon and oxygen signature of calcites and dolomites from Tapira and Salitre are consistent with an ultimate origin from the mantle for the carbonatites and for the carbonated mafic dykes. In this respect, it should be noted that, whilst oxygen isotopes are widely susceptible to post-magmatic changes, carbon seems to be less affected by these processes. Note that the carbon stable isotope composition of the Salitre carbonatites and of those less fractionated samples from Tapira show $\delta^{13}C$ values of around -7. This is slightly lower than those observed for the Jacupiranga carbonatites (See Figure IV.36, Chapter IV), and consistent with the values expected for materials originated from the SCLM (Javoy *et al.,* 1986).

Mitchell (1996b) considered the Tapira complex to be similar to ultramafic complexes associated with the melilitite clan, such as Iron Hill (Colorado), Gardiner (East Greenland) and the melilitolite-bearing complexes of the Kola-Kandalaksha and Maimecha-Kotui regions of Russia. According to Mitchell, ultramafic plutonic complexes of the melilitite clan consist dominantly of rocks of the ijolite suite, commonly accompanied by carbonatites, but are distinguished from melilitolite-bearing complexes of the nephelinite clan by the paucity of nepheline-syenites. Despite the occurrence of rare melilitolite in Tapira, the present study revealed no ijolitic rocks (as well as no nepheline syenites). The same is true for the Catalão complex where members of the ijolitic suite were not found (Araújo, 1996). This suggests that the APIP carbonatite-bearing complexes do not share some important features of the complexes attributed by Mitchell (1996b) to the melilitite clan.

As demonstrated in Chapter IV, the bulk-rock chemistry in the phlogopite-picrites from Tapira and other carbonatite complexes most closely resemble the chemical features of the APIP kamafugites (e.g. Mata da Corda volcanics). In particular, the likeness in trace-elements and REE suggests that the phlogopite-picrites and the kamafugites share a common source, and underwent similar post-melting processes. This link between the kamafugitic rocks and the carbonatite complexes is further emphasised by the common presence of xenoliths of pyroxenite (bebedourites) and ultrapotassic syenites within the Mata da Corda pyroclastics, indicating the presence of magma chambers similar to the Tapira complex at depth, in the Mata da Corda region. This is consistent with the suggestion by Lloyd and Bailey (1991), that kamafugites may be the parental magmas for APIP bebedourites.

The association of carbonatites with potassic rocks of kamafugitic affinity is well known from the Late Pleistocene Umbria-Latium ultra-alkaline district (ULUD), Central Italy (Stoppa and Cundari, 1995). However, it should be noted that the origin and tectonic environment of these rocks is distinct from those of the APIP complexes. For instance, Stoppa and Lavecchia (1992) and Lavecchia and Stoppa (1996) suggested an asthenospheric source (and no relation to a subducted slab) for the Italian kamafugite-carbonatite association. Also, some of the key features in mineral chemistry and whole-rock geochemistry of the Italian kamafugites and carbonatites are distinct from those of the APIP (Chapters III and IV), and resemble the mafic-potassic/carbonatite associations of Eastern Paraguay.

A ongoing debate in the carbonatite literature is concerned with the relationships between the carbonatites and silicate rocks, in carbonatite complexes. The intimate spatial association suggests that the two rock suites are genetically related. However, this is not universally agreed, and Harmer and Gittins (1998) recently reviewed evidence for an independent origin for spatially-associated carbonatites and silicate rocks. The evidence obtained during this research favours a cogenetic relationship for all Tapira rocks. Some relevant point are summarised below.

a) The consistent evolution trends observed in the composition of various mineral phases suggests that different units of silicate rocks are linked by a differentiation process.

b) The narrow range and the similarities in Sr and, particularly in Nd isotopic ratios between Tapira carbonatites and silicate rocks suggests that both rock suites originated from a similar source, rather than representing independent magmas. Some rocks, however, show a wider variation in Sr isotopic ratios, which can be interpreted as the product of crust assimilation processes (see below).

c) The presence of similar, mantle-derived carbon- and oxygen-isotope signatures in both the carbonatites and the carbonate-rich phlogopite-picrites and low-Cr dykes, suggest that the groundmass carbonate of the dykes is of primary origin, and not introduced during late-stage carbonatite metasomatism. Isotope fractionation trends compatible with magmatic evolution can be found in Tapira rocks, although it should be stressed that the effects of late-stage hydrothermal/carbothermal alteration and/or degassing may be substantial in many samples.

d) The apparent continuity of whole-rock geochemical trends from the phlogopite-picrites to the low-Cr dykes, is consistent with the fractionation of expected mineral phases or existing combinations (i.e. cumulates).

V.4 - THE EMPLACEMENT OF TAPIRA MAGMAS

Subsequent to melting in the mantle source, the Tapira magmas seem to have undergone significant evolution at higher levels in the crust. The relevant evidence for this is discussed in the sections below.

V.4.1 - SINGLE EMPLACEMENT VERSUS MULTIPLE INTRUSIONS

The extensive doming of the quartzitic country rock, and the commonly observed evidence for intrusion-related strain and flow, in the coarse-grained rocks of

Tapira suggests a forcible intrusion of the complex, perhaps in part as a crystal mush. The same characteristics seem to be a common feature of the APIP carbonatite complexes. In Salitre, Lloyd and Bailey (1991) described phlogopite crystals deformed by intrusion-related stress and alignment of clinopyroxene crystals produced by the flow of a crystal-mush during the intrusion.

Although many of the rock-types in the Tapira complex can be considered in one form or other as the product of crystal accumulation, the overall structure and the stratigraphic relationships visible from drill cores argue against a simple, relatively calm fractionation in a single magma chamber. Multiple intrusions are a common feature of carbonatite-bearing plutonic complexes (e.g. Le Bas, 1987; Barker, 1989). In the Jacupiranga complex, Gaspar and Wyllie (1987) described five independent phases of carbonatite intrusion, interpreted as the products of a series of batches of carbonatite magma from a magma chamber differentiating at depth.

The following evidence suggests a multiphase evolution of the Tapira complex, involving multiple intrusions of both silicate rocks and carbonatites, probably derived from one or more differentiating magma chambers at depth

a) Dykes of wehrlites from the B2 unit are intrusive in B1 bebedourites.

b) Absence of a coherent spatial relationship between petrographic types that are, presumably, consecutive stages of differentiation (e.g. feldspar-bearing bebedourites of the B2 unit and pyroxene-rich syenites)

c) Incomplete differentiation sequences (unless their observation is hindered by the poor exposure), with missing dunites and mela-syenites.

d) Compositional "gap" in the chemistry of key minerals (such as pyroxene) and apparently "misplaced" position of perovskites from wehrlites in the overall trend of perovskites from Tapira

e) Intrusive character of the carbonatites in the SPS, brecciating and metasomatising the ultramafic rocks (e.g. reaction rock) and the syenites (e.g. magmatic stoping breccias, with development of metasomatic rims in fragments of syenite)

f) Crosscuting relationships between petrographically and chemically distinct generations of carbonatite.

g) Possible existence of carbonatites produced by different processes (i.e.

liquid immiscibility and fractionation, see below)

h) Presence of primitive ultramafic dykes intruded in more evolved rock-types, including the carbonatites.

V.4.2 - LEVEL OF EMPLACEMENT

Although the mineralogical composition of Tapira rocks is extremely varied and contains many phases of petrological interest, it offers extremely poor constraints to the calculation of temperatures and pressures of crystallisation. The peculiar mineral assemblages and the influence of the fractionation of particular phases, such as perovskite, affect the distribution of key elements to a poorly understood or experimentally constrained extent. Therefore, common geothermometers and geobarometers (e.g. Douce, 1993; Ghiorso and Sack, 1991; Lindsley, 1983; Nimis, 1995; Righter and Carmichael , 1996), which are used to constrain the intensive variables of silicate magmatic systems, cannot be reliably applied to carbonatite or carbonatite-silicate magmas.

One possible alternative approach is the use of the oxygen isotope thermometry. of coexisting minerals. During this research the only mineral phases analysed for stable isotopes were calcites and dolomites. However, these have been proved to be in isotopic disequilibrium (Chapter IV), and are, therefore, unsuitable for oxygen-isotope thermometric calculations. A potentially more reliable mineral pair for oxygen thermometry would be, for example, pyroxene-magnetite, and this seems a good prospect for future investigation. Sgarbi *et al.* (1998) have carried out oxygen-isotope geothermometry on kamafugitic volcanic rocks and pyroxenite xenoliths of the Mata da Corda Group, and estimated a crystallisation temperature of 1140 °C for the mafitites, 920-820 °C for leucitites and kalsilitites and 750-690 °C for the coarse-grained pyroxene xenoliths. The lower temperatures of the latter are consistent with some isotopic resetting during slow cooling. The petrographic similarities with bebedourites from Tapira suggests that the Mata da Corda xenoliths can be considered representative of underlying Tapira-like magma chambers. If this is true, the temperatures in the range 750-690 °C may be considered as a reference (minimum) value for the final equilibration of Tapira bebedourites and, perhaps, the 1140 °C temperature would approximate those of the liquids parental to the Tapira complex. It must be noted, of course, that this is a largely unconstrained assumption. For the Tapira carbonatites, the coexisting calcite-strontianite equilibrium (Chapter III) provides a minimum temperature of 450 °C, which also reflects the widespread post-crystallisation processes, rather than true magmatic temperatures. However, and perhaps more importantly, the calcite-strontianite equilibrium suggests the emplacement of the Tapira carbonatites at low pressures (2 to 3 kb). i.e., sub-volcanic conditions. Various alternative and independent lines of evidence support a high-level site for the final emplacement of the Tapira and Salitre complexes, as summarised in the following sections.

Field and petrographic evidence

In Tapira and, to a much greater extent, in Catalão and Araxá, the abundance of hydro/carbothermal alteration products, such as extensive phlogopitisation of the ultramafic rocks suggests a sub-volcanic level of intrusion, at least for the late-stage carbonatites. Further evidence comes from the diatreme-facies breccias in the phosphate mining area of Tapira. These rocks testify to the existence of explosive magma-country rock interactions during the intrusion of the complex, probably nurtured by the ability of the magmas to exsolve volatile components at low pressures.

However, the (presumably) related volcanic rocks, such as lavas and pyroclastics are notably lacking in the immediate vicinity of the APIP carbonatite complexes. In the eastern portion of the APIP (e.g. Mata da Corda region), substantial volcanic and pyroclastic deposits are preserved, and make up one of the world-largest exposure of kamafugitic sequences, but in the western portion of the APIP only the subvolcanic roots of such magmatism are preserved. In fact, the extreme susceptibility of the rocks from carbonatite complexes to the prevailing tropical weathering regime, suggests that these rocks are only available for sampling because they have been largely preserved within dome structures made up of the less weathering-prone rocks of the Brasília belt (schists and quartzites).

Chemical evidence

While the Tapira syenites may be interpreted as cumulate rocks, the chemical composition of fine-grained syenites from Salitre suggests that they evolved at low pressure (1 to 2 kb, see Figure V.2). This is consistent with the calcite-strontianite equilibrium in Tapira carbonatites at 2 to 3 kb (see above, and Chapter III)

Evidence from fission track analyses

Using fission-track analysis in apatites from the complexes of Tapira and Catalão, and a geothermal gradient of 27 °C/km for Tapira (as opposed to 15 °C/km for samples from the São Francisco craton), Amaral *et al.* (1997) concluded that the region was subjected to a relatively slow cooling from 95 to 85 °C in the period between 90 and 60 Ma, followed by a much faster cooling from 85 °C to 27 °C from 60 Ma to the present. This translates into estimated erosion rates of 12 m/Ma between 90 and 60 Ma ago, and 36 m/Ma in the last 60 Ma. Although it should be noted that such estimates are dependent upon apatite reaching a temperature low enough for the fission-track damage to be preserved, a simple back-calculation based on the erosion rates estimated by Amaral *et al.* (1997) suggests an emplacement depth of about 2.5 km for the Tapira complex.

Evidence from stable isotopes

Santos and Clayton (1995) presented carbon and oxygen isotope data for carbonatite complexes of APIP (Araxá, Catalão, Tapira), and other Brazilian (Jacupiranga, Mato Preto) carbonatites. On the basis of the restricted ranges observed in carbon isotopes, coupled with the wide variation in oxygen, Santos and Clayton (1995) suggested that the APIP complexes represent high-level intrusions (compared with Jacupiranga), where the effect of low-temperature hydrothermal alteration controls the distribution of oxygen isotopes. They have demonstrated that the H_2O/CO_2 ratio of the fluid interacting with the carbonatite, as well as the fluid/rock ratio, greatly affect the isotopic composition of carbonates.

In Tapira, the oxygen-isotope composition of calcites seems to have been more extensively affected than that of dolomites (Chapter IV). Figure V.3 shows a plot of the calcites analysed during this research, compared with three of the isotope exchange models calculated by Santos and Clayton (1995), for low-temperature hydro/carbothermal alteration. The models show the behaviour of calcite composition upon interaction with fluids of different CO_2/H_2O ratios, at variable temperature and fluid/rock ratios. The origin for all models (i.e., the starting composition of calcite) is $\delta^{13}C$ = -6 ‰ and $\delta^{18}O$ = 6 ‰.

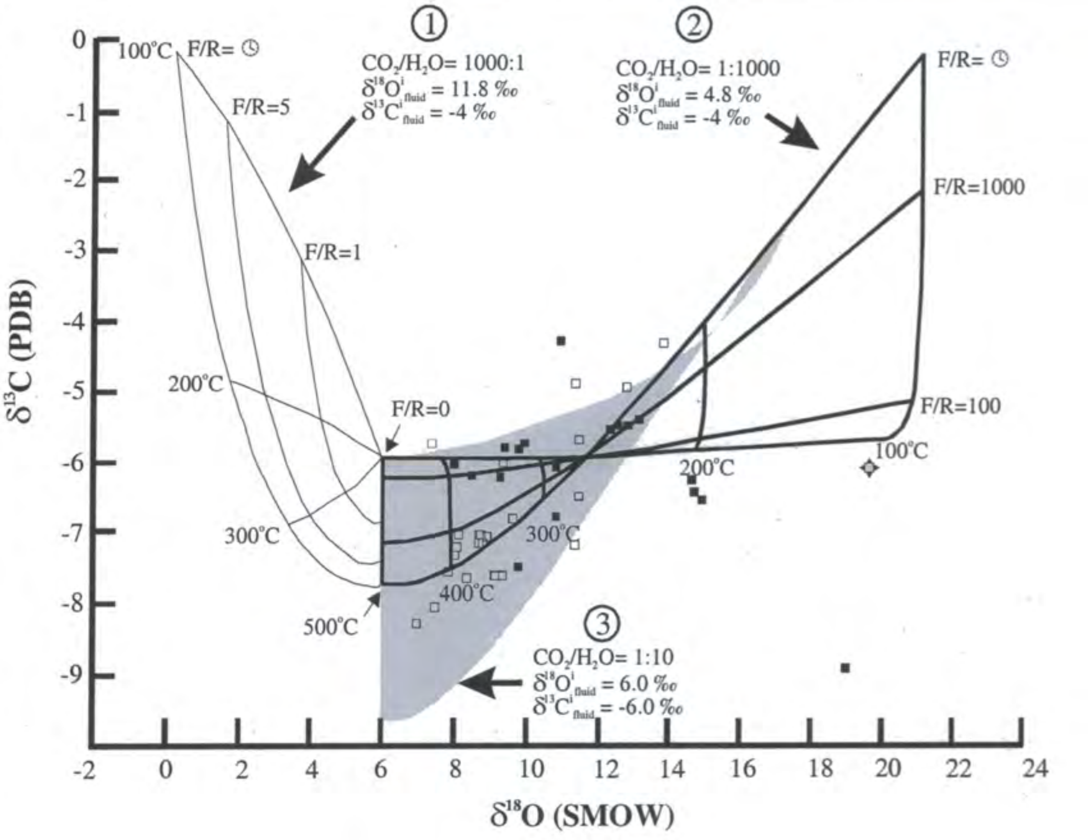

Figure V.3 - Isotopic composition of calcites from Tapira carbonatites (open squares) and mafic dykes (solid squares), compared with isotope-exchange models of Santos and Clayton (1995). The theoretical models are labelled 1 to 3, and represent different CO_2/H_2O ratios and distinct isotopic compositions of the fluid. The composition of dolomite formed by fenitisation of ultramafic rocks by carbonatite ("reaction rock") is plotted for comparison (star).

As observed by Santos and Clayton (1995) for the APIP complexes in general, most of the isotopic variation can be explained by models labelled "2" and "3" in Figure V.3, suggesting that the carbonatites interacted with H_2O-rich (CO_2/H_2O ratios of 1/1000 and 1/10, respectively), low-temperature fluids. For the Tapira complex, model "3" seems to account for most of the variation in the analysed calcites. Note that the composition assumed for the fluid in this case ($\delta^{18}O$=6‰, $\delta^{13}C$= 6‰) is that of a typical magmatic carbonate, and the same as the starting calcite. The analysis of dolomite from the reaction rock is also plotted in the diagram. If the model can be applied to this dolomite, its composition seems to have been generated at a very low CO_2/H_2O ratio and very low temperature. However, none of the isotope exchange models in Figure V.3 can explain the trend of negative correlation of $\delta^{13}C$ with $\delta^{18}O$, observed in some of the Tapira mafic dykes.

Javoy *et al.* (1978) measured the carbon isotope fractionation between CO_2 and carbon dissolved in basalt, concluding that ^{13}C is relatively enriched in the CO_2 vapour by a factor of 4-4.5 ‰ (1120-1280 °C; 7 to 8 kb). Experimental studies on the fractionation of carbon isotopes during carbonate-silicate liquid immiscibility (Mattey *et al.,* 1990) observed fractionation between CO_2 and both the carbonate and the silicate liquid. Their results indicate that ^{13}C becomes relatively enriched in the vapour, by a factor of ~ 2 ‰ with respect to the carbonate melt (1300 °C - 1400 °C; 20 to 30 kb) and 2.4 ‰ with respect to the silicate melt (1200 °C - 1400 °C; 5 to 30 kb), but that litlle variation occurs between the two melts. Based on these results and on differences in the experimental techniques, Mattey *et al.* (1990) argue that the carbon-isotope fractionation factors obtained by Javoy *et al.* (1978) may be too high. In any case, the experimental evidence suggests that the degassing of a CO_2 vapour phase from either liquid will promote a relative $\delta^{13}C$ depletion in the liquid.

The co-variation of $\delta^{13}C$ and $\delta^{18}O$ has been modelled by Zheng (1990), for different temperatures and carbon concentrations in the degassing fluid. For XCO_2 up to 0.3, calcite precipitating from a H_2CO_3-dominated fluid shows a positive correlation between $\delta^{13}C$ and $\delta^{18}O$, but at $XCO_2 = 0.4$, the evolution curve of calcite composition has a negative slope (Figure V.4), similar to the trend of calcites from some mafic dykes. This suggests that some of the isotopic variation observed in Tapira calcites may be due to degassing of a CO_2-rich fluid. Note that extreme $\delta^{13}C$ depletion is attained at very low temperature, but if the temperatures during the degassing are relatively high, it may become impossible to distinguish the effects of this process from those of low-temperature hydrothermal alteration (compare the model of Santos and Clayton, 1995 - shaded area in Figure V.4).

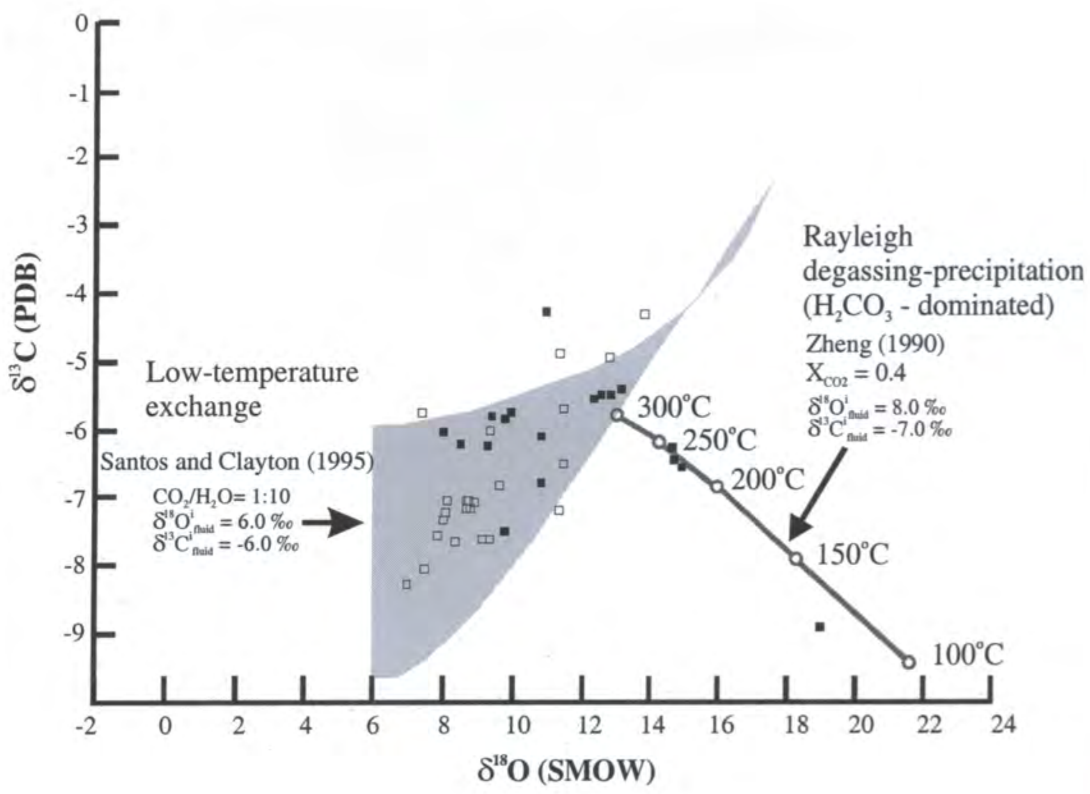

Figure V.4 - Isotopic composition of calcites from Tapira carbonatites and mafic dykes (symbols as in Figure V.3), compared to the degassing model of Zheng (1990) for XCO_2 = 0.4 and H_2CO_3 as the dominant carbon species in the fluid (solid line, with circles for calcite composition at different temperatures). Shaded area is model 3, from Figure V.3.

The dolomites from Tapira form a consistent trend and show little scatter, plotting along a line of positive correlation between $\delta^{13}C$ and $\delta^{18}O$, which may be related to isotope fractionation during magmatic evolution. The analytical results are plotted in Figure V.5, together with the Rayleigh fractionation model paths of Pineau *et al.* (1973). These curves show the variation in $\delta^{18}O$ and $\delta^{13}C$ of a carbonate crystallising from a magma at 700 °C, for variable CO_2 /H_2O ratios.

The dolomites from fined-grained (C2) carbonatite dykes show remarkable agreement with the fractionation path for a CO_2/H_2O ratio of 1/1 in the fluid or magma. The dolomite that plots furthest away from this trend, at comparatively low $\delta^{18}O$ and high $\delta^{13}C$ is from a coarse-grained carbonatite. This rock may have suffered low-temperature isotope exchange with a CO_2-rich (fenitising?) fluid such as that of model 1 in Figure V.3. Dolomites from other coarse-grained carbonatites form a relatively tight cluster at low $\delta^{18}O$ and $\delta^{13}C$. They seem to define a trend with a higher slope than the dolomites from the dykes, suggesting a higher relative concentration of CO_2 in the liquid. However, this is difficult to evaluate because of the limited range of both carbon and oxygen isotopic compositions of these rocks. Similarly, the small number of dolomite analyses from mafic dykes precludes any interpretations, other than that $\delta^{13}C$ and $\delta^{18}O$ seem to be positively correlated.

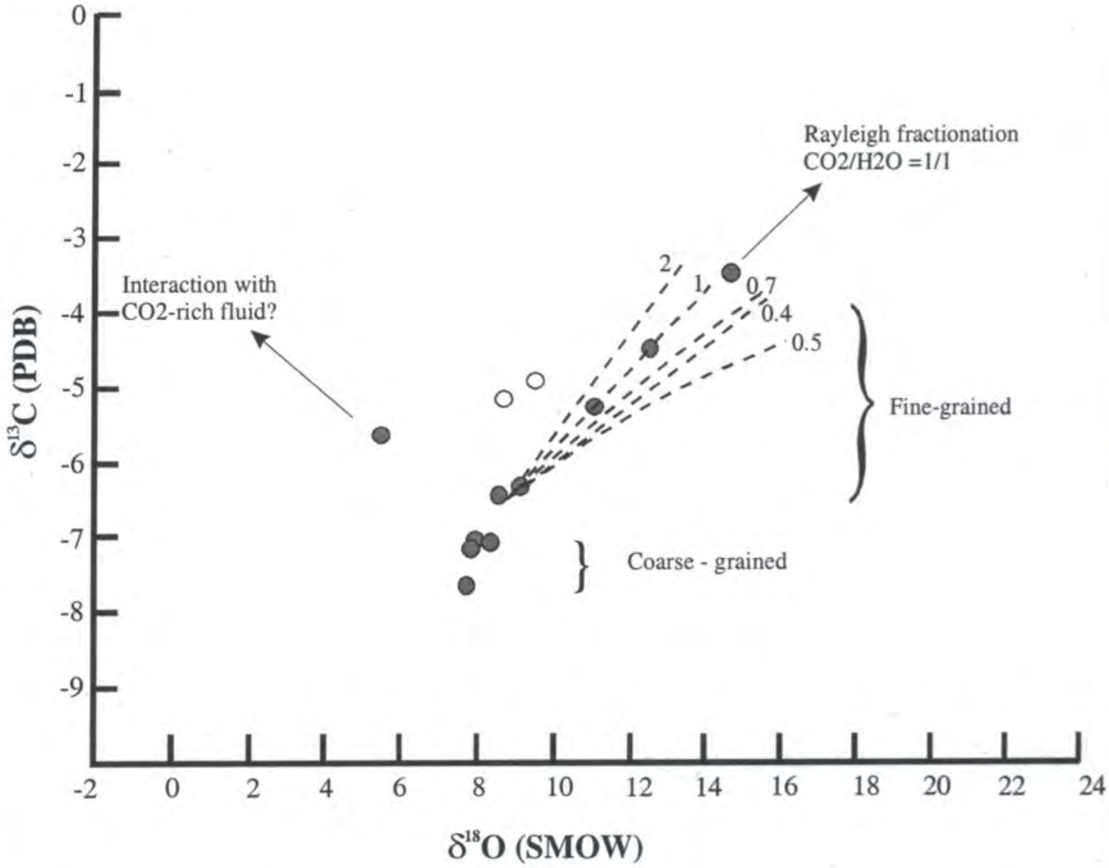

Figure V.5 - Composition of Tapira dolomites, compared with the fractionation models of Pineau et al. (1973) for a closed system, at 700 °C and different CO_2 / H_2O ratios. Solid circles = carbonatite dolomites; open circles = dolomites from mafic dykes.

Similar relationships were observed by Reid and Cooper (1992) in the Dicker Willem carbonatite complex, in southern Namibia. These authors identified a "phenocryst array", where calcite and dolomite phenocrysts show a positive correlation between $\delta^{13}C$ and $\delta^{18}O$, plotting along a line with a 0.65 slope, whilst the recrystallised groundmass carbonates scatter towards higher $\delta^{18}O$ values. More importantly, they observed a coupled $\delta^{18}O$ enrichment and $\delta^{13}C$ depletion in late-stage dykes, which they interpret as the product of progressive degassing of a CO_2-H_2O fluid.

The data presented in this thesis extend the published oxygen isotope compositions of Tapira carbonates into the range of primitive $\delta^{18}O$, and demonstrate that magmatic (as well as hydrothermal) processes may be responsible for the observed variations. They also show (discussion above, and Chapter IV) that some of the variations associated with late-stage carbo/hydrothermal alteration depend on a range of factors, such as: the size of individual intrusions; the mode of occurrence of the carbonatite (dyke, breccia, plutonic, etc.); the mineral species of carbonate analysed and, possibly, the relative age of the intrusion.

These conclusions do not contradict those of Santos and Clayton (1995), regarding the emplacement of the APIP complexes at shallow depths, since the products of hydrothermal alteration, as well as the hydrothermal oxygen signatures, appear to be far more abundant in the APIP complexes than in Jacupiranga (e.g. Nelson *et al.,* 1988; Morikiyo *et al.,* 1990; Santos, 1994; Santos and Clayton, 1995; Toyoda *et al,* (1994). In fact, a sub-volcanic setting for the Tapira complex is further emphasised by the evidence for CO_2 degassing from the mafic dykes.

V.5 - EVOLUTION OF TAPIRA MAGMAS

V.5.1 -CRUSTAL ASSIMILATION

The geochemical and isotopic similarities observed within the complex, and between Tapira rocks and the remainder of APIP magmatism, would argue in favour of a limited (if any) effect of crustal assimilation in the composition of the studied rocks. However, some evidence for crustal assimilation was found during this research, and this is discussed in the sections below. In any case, it should be emphasised that the extreme enrichments in Sr, Nd and most incompatible trace elements, and the strong LREE/HREE fractionation observed in Tapira rocks mean that the amount of crustal contamination necessary to substantially modify their original geochemical and isotopic signature would be very high. The highly silica-undersaturated character of all rock types in the Tapira complex suggests that large-scale assimilation of crustal rocks is unlikely to have happened.

Petrographic evidence

Petrographic evidence of crustal contamination can be found in rare samples. The most obvious example is the presence of crustal xenoliths in the diatreme-facies carbonatite breccias associated with the C2 unit. Less conspicuous evidence comprises the occurrence of rounded, partially digested quartz grains in some of the C2 dykes (see Chapter II).

Some of the observed mineral disequilibria, such as the sphene and/or melanite rims coating in perovskite crystals, could be attributed to assimilation of crustal material. This type of replacement is typically observed in B2 bebedourites, suggesting a relative increase in silica activity in the system from which these rocks crystallised. Together with the geographic position of B2, adjacent to the country-rock in the northern margin of the complex, this could indicate assimilation of silica-rich country (quartzite). However, the Sr-isotope composition of B2 rocks, in particular, does not seem to register any significant $^{87}Sr/^{86}Sr$ enrichment (see below), and the increase in SiO_2 activity could as easily be assigned to normal magmatic processes.

Isotopic evidence

Most of the samples studied during this research plot within the range of Sr- and Nd-isotopic ratios of the APIP. With rare exceptions, there is good agreement between the carbonatites and the silicate rocks, suggesting that the two rock suites originated from a similar source. In particular, the isotopic composition of the B2 bebedourites is virtually identical to that of the carbonatites. The high absolute REE contents of the Tapira rocks, even in the most primitive ultramafic types, suggest that the Nd-isotopic signature is related to their mantle source, and that the system is unlikely to be greatly disturbed by crustal assimilation processes. In contrast, the analysed samples may show substantial variations in Sr contents and rocks with the lowest Sr contents may be useful in pinpointing relatively small amounts of crustal contamination. The following discussion will, therefore, concentrate on the evidence from Sr isotope systematics.

Figure V.6 shows the initial $^{87}Sr/^{86}Sr$ ratios of various Tapira rocks, plotted against their Sr content. A general increase in $^{87}Sr/^{86}Sr$ can be observed with decreasing Sr content, suggesting that, if assimilation of crustal material occurred, the system has been buffered for Sr isotopes in the more Sr-rich samples. Some detailed variations in this general pattern provide important petrogenetic clues and will be discussed individually in the following paragraphs.

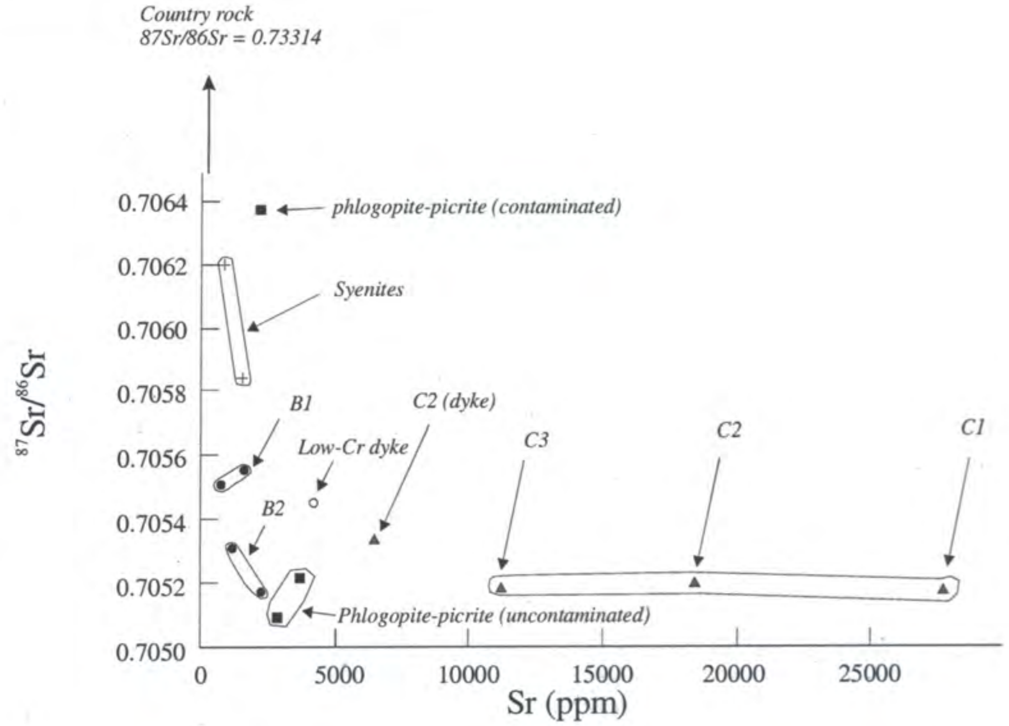

Figure V.6 - Initial Sr isotpe ratio plotted against the Sr content of Tapira rocks. Solid square = phlogopite-picrites, open circles = low-Cr dykes, solid circles = ultramafic plutonic rocks, triangles = carbonatites, crosses = syenites. The composition of Tapira country rock (quartzite) is also indicated.

Although samples from the B2 unit have relatively low Sr contents, they do not show enrichment in radiogenic Sr. If anything, the samples from the B1 unit (which do not show evidence for late-stage SiO_2-enrichment to the same extent as B2) have the most radiogenic Sr-isotopic ratios among the ultramafic plutonic rocks. Therefore, the observed increase in SiO_2 in the late stage mineral assemblages of B2 must be related to magma chamber processes (i.e. residual enrichment during fractionation or, alternatively, the separation of carbonate-rich material by liquid immiscibility or fractionation processes). The fact that B2 and the carbonatites have nearly identical Sr- and Nd-isotopic ratios may suggest a strong link between these two units.

Coarse-grained carbonatites from units C1, C2 and C3 show variable Sr contents, but virtually no variation in initial $^{87}Sr/^{86}Sr$ ratios (Figure V.6). This is expected, since the high absolute abundance of mantle-derived Sr in the carbonatites means that any effect of crustal contamination on Sr isotopes would be extremely diluted and, most probably, undetectable. The isotopic composition of these carbonatites may therefore, be taken as representing the isotopic characteristics of their parental melt source, regardless of whether crustal contamination took place or not. Interestingly, the analysed fine-grained carbonatite dyke from C2 has a slightly higher Sr isotope ratio, when compared with the larger, coarse-grained intrusions.

The syenites show higher $^{87}Sr/^{86}Sr$ than both the ultramafic plutonic rocks (B1 and B2) and carbonatites (C1, C2, C3). In their Sr- and Nd-isotopic study of several African carbonatites, Harmer and Gittins (1998) recognised a systematic variation in these rocks, whereby the isotopic signature of the carbonatites seems to be closer to the most primitive magmas (e.g. melilitites and olivine-nephelinites), while the evolved liquids (nephelinites and phonolites) have a more enriched signature. They argue that the isotopic differences observed are inconsistent with an origin of the carbonatites by liquid immiscibility at a late, crustal stage in their evolution, since the two immiscible liquids must necessarily be in isotopic equilibrium at the moment of separation.

At first sight, the Sr-isotope contrast between Tapira syenites and carbonatites would seem to support Harmer and Gittins (1998) hypothesis, thus ruling out an origin by liquid immiscibility between syenites and carbonatites. However, a corresponding Nd-isotope shift would be expected, if Tapira syenites derived from a more enriched mantle source than that of the carbonatites. This was not found in the analysed samples; in fact the initial $^{143}Nd/^{144}Nd$ ratios of syenites and carbonatites from Tapira are virtually identical.

The alternative explanation, involving assimilation of crustal material and a more effective buffering of the Sr system in the carbonatites seems to explain better the Sr isotope relationships observed in Tapira. Furthermore, the syenites show strong trace-element evidence for the involvement of liquid immiscibility processes in some form, during their genesis (see below). Whether these rocks are the direct product of immiscibility or were formed by further differentiation of an immiscible liquid is debatable, and will be further explored later in this Chapter. For the moment it is sufficient to note that, as conceded by Harmer and Gittins (1998), their observations do not necessarily rule out immiscibility of carbonatite from a more primitive (i.e. ultramafic) silicate parent, and that if crustal assimilation comes into play after the immiscibility process, then the Sr and Nd composition may be buffered to a different extent in the silicate and carbonatite conjugate liquids.

The fine-grained dyke-rocks from Tapira show a complex behaviour, with respect to Sr. Two samples of phlogopite-picrite dykes (unpublished data from the work by Gibson *et al.,* 1995b) have $^{87}Sr/^{86}Sr$ initial ratios identical to those of the carbonatites and B2 bebedourites. One sample of low-Cr dyke and a C2 fine-grained carbonatite dyke have slightly higher $^{87}Sr/^{86}Sr$. and one phlogopite-picrite sample has the highest observed $^{87}Sr/^{86}Sr$ among the Tapira rocks. This sample is outside the overall range of primitive magmas in the province (compare Figures IV.37 and IV.38, in Chapter IV). As with the syenites, the enrichment in radiogenic Sr is *not* accompanied by a corresponding change in Nd isotopes. These detailed variations apparently contradict the observations and discussion made in the paragraphs above, since both the primitive and the high-Sr rocks would be expected to have low $^{87}Sr/^{86}Sr$. The one factor that is shared by all $^{87}Sr/^{86}Sr$ -enriched samples (apart from syenites) is that they come from thin, fine-grained dykes.

Kerr *et al.* (1995) proposed a mechanism of crustal Assimilation during Turbulent magma Ascent (ATA), in contrast with the common concept of Assimilation-Fractional Crystallisation (AFC), in their study of the Mull Tertiary lavas (NW Scotland). According to this model, MgO-rich, low-viscosity magmas ascending through the crust will move under a regime of turbulent flow, and can become rapidly contaminated with readily-fusible material from the wall rock. More viscous magmas will tend to flow under a laminar regime and, consequently, may not become contaminated with crustal components. The concept was successfully applied by Thompson *et al.* (1998) for the Serra do Mar alkaline province (southeast Brazil) to explain how some of the more magnesian magmas in the province became contaminated with crustal components while the more evolved compositions do not show the same features.

ATA provides an attractive model to explain the relationships observed in Figure V.6. The low viscosity of the carbonatite and mafic dykes with high- $^{87}Sr/^{86}Sr$ ratios is attested by their emplacement as thin dykes (only a few centimetres thick in all cases), high MgO content (in the case of phlogopite-picrite and low-Cr dyke) and carbonate-rich character. Assimilation through this process would certainly be aided by the high surface-to-volume ratio of the dykes, and the magnitude of the contamination-related isotopic shift would be further enhanced in those samples with lower Sr content.

V.5.2 -CRYSTAL FRACTIONATION AND THE GENESIS OF THE SILICATE PLUTONIC SERIES (SPS)

The ultramafic cumulate sequence

The variations observed in modal mineralogy and in the chemical composition of essential minerals suggest that the sequence

B1 wehrlites ⇒ B1 bebedourites ⇒ B2 wehrlites ⇒ B2 bebedourites

represents a general progression of successively more evolved cumulates. On the other hand, detailed variations in mineral chemistry often seem to follow unexpected trends, suggesting that the origin of the SPS by fractional crystallisation is occasionally "disturbed" by some other process. As discussed previously, the most likely scenario is that the Tapira complex represents the amalgamation of multiple intrusions, which could be derived from a larger, differentiating magma chamber at depth.

The cumulate sequence in the Tapira complex is largely dominated by bebedourite-type rocks. Wehrlites comprise only a minor part of the sequence, and dunites are even more rare. According to the evidence presented in this thesis, the bebedourites are likely to be the result of crystal fractionation from low-Cr dykes, while the differentiation of phlogopite-picrites should produce olivine- and chromite-rich cumulates. This has important implications for the petrogenesis of the Tapira complex.

For instance, the notable scarcitiy of olivine-rich cumulates may suggest that the phlogopite-picrite magma differentiatied mainly in an intermediate magma chamber at greater depth.

It could be argued that the olivine-rich rocks exist in the same magma chamber as the bebedourites, but simply have not been “exposed” at the level of sampling reached by the drillings. This could be the likely situation in a vertically-zoned body, but there is no firm evidence that the Tapira complex has such a structure. For instance, some (but not all) wehrlite samples come from greater depths in the complex, but no correlation between depth and modal variations in bebedourites have been observed during this study. Instead, as argued previously, the complex is composed of several independent intrusions. These observations suggest that the missing olivine-rich cumulates were largely formed in a deeper magma chamber.

The fractionation of the essential minerals in the SPS ultramafic rocks is likely to introduce complications in the interpretation of the chemical properties of the evolving magmas, producing effects that contrast with the commonly accepted notion of compatibility and incompatibility of trace elements (i.e. relative to the crystallisation of basaltic systems). In particular, perovskite and apatite may produce substantial changes in the REE concentrations of the residual liquid. Perovskite usually displays stronger enrichment in total and light REE and stronger LREE/HREE fractionation than apatite (e.g. Dawson *et al.,* 1994b; Campbell *et al.,* 1997). Jones and Wyllie (1984) concluded that a substantial part (up to 16%) of the total REE of kimberlites may be contained in perovskite. Campbell *et al.* (1997) modelled perovskite crystallisation from magmas of the Gardiner complex (East Greenland), concluding that fractionation of even a small amount (2.5%) of perovskite with moderate REE contents (approximately 3% REE_2O_3) would produce a decrease in chondrite-normalised La/Lu ratios of the magma from 235 to 165, and produce 40% relative depletion in the La concentration of the liquid. Gibson *et al.* (1995b) also related the variation in the La/Yb ratio of some of the evolved APIP lavas to the fractionation of perovskite, and suggested that apatite fractionation may account for the observed P troughs in some of the APIP magmas. Therefore, some of the variation observed in the REE patterns between phlogopite-picrites and low-Cr dykes in Tapira may be related to removal of apatite and/or perovskite (see Chapter IV).

The Tapira syenites

One striking feature of the SPS is its compositional bimodality. Among the plutonic silicate rocks in Tapira there are abundant ultramafic rocks (mostly bebedourites) and a less voluminous, but still important, group of felsic to holofelsic rocks (syenites). Rocks with compositions intermediate between these two extremes are absent, except for a few examples of feldspar-bearing bebedourites in B2 and rare pyroxene-rich syenites.

As with the missing dunites, the intermediate rock-types may be present in deeper-seated magma chambers. This is suggested by the occurrence of mela-syenite xenoliths, together with bebedourite and perovskite-peridotite nodules, within the pyroclastic deposits of the Mata da Corda (Bizzi *et al.,* 1995) and in conglomerates derived from the latter (Gibson *et al.,* 1995b). The fact that Tapira coarse grained syenites are likely to be cumulates of alkali-feldspar crystals may also explain the apparent absence of more melanocratic varieties. Alternatively, the hypothesis that some of the syenites have been produced by liquid immiscibility cannot be discarded at this stage. It is interesting to note that fine-grained dykes of intermediate composition are also rare.

V.5.3 - CARBONATITES GENERATED BY LIQUID IMMISCIBILITY

Field and petrographic evidence for carbonatite-silicate immiscibility has been presented by several authors (e.g. Dawson and Hawthorne, 1973); Dawson *et al.,* 1994a; Bogoch and Magaritz, 1983; Church and Jones, 1995). In Tapira, the presence of carbonate globules (ocelli) in the groundmass of phlogopite-picrites (Chapter II) suggests that immiscible carbonatite liquid may have formed at a very early stage in the differentiation sequence of a carbonated silicate magma. The following sections will discuss the constraints imposed by the evidence presented in this thesis on the possible role of liquid immiscibility during the evolution of the Tapira complex, and investigate the petrogenetic consequences of this process, in the light of experimental evidence from the literature.

Chemical fingerprints of liquid immiscibility

When carbonate-silicate liquid immiscibility occurs, many chemical elements may preferentially enter one of the conjugate liquids. Therefore, geochemical "fingerprints" may be generated in each side of the immiscible pair and these, in turn, may be useful to pinpoint the occurrence of liquid immiscibility during the evolution of a given rock suite. The relative preference of a particular element for the carbonate or silicate liquid can be quantified by the distribution coefficient ($K_D^{sil/carb}$) defined as the concentration of the element in the silicate liquid divided by the concentration of the element in the conjugate carbonatite liquid. Data on the partition of various elements between silicate-carbonatite immiscible pairs have been reported (e.g. Wendlandt and Harrison, 1979; Hamilton *et al.,* 1989; Jones *et al.,* 1995; Veksler *et al.,* 1998b), but the number of studies is still small, and some variables are still poorly. For instance, the results for a single element may vary significantly and the partition of some elements between silicate and carbonate liquid may be strongly dependent on temperature, pressure or composition of the system (i.e. mafic or felsic). In a recent study using a centrifuge autoclave, Veksler *et al.* (1998b) achieved excellent separation of the immiscible silicate and carbonate liquids, and thus were able to overcome some of the technical problems for experimental determination of partition coefficients between immiscible liquids.

The following general observations can be made from the studies mentioned above, and are of particular relevance for the investigation of the Tapira complex:

a) Th partitions preferentially into the silicate liquid (Jones *et al.,* 1995).

b) Sr and Ba partition preferentially into the carbonate liquid (Hamilton *et al.,* 1989; Jones *et al.,* 1995; Veksler *et al.,* 1998b)

b) Both Nb and Ta seem to partition into the silicate liquid (Hamilton *et al.,* 1989; Jones *et al.,* 1995; Veksler *et al.,* 1998b), but data for both elements under the same experimental conditions are scarce. Veksler *et al.* (1998b) has recently pointed out that Ta partitions into the silicate liquid to a much larger degree than Nb. Consequently, some degree of Nb-Ta decoupling can be expected if liquid immiscibility occurs in the genesis of carbonatite complexes. Hamilton *et al.* (1989) detected a consistent dependence of Ta behaviour on pressure, temperature and composition. According to their results the partition of Ta into the silicate liquid is enhanced by decreasing temperature, decreasing pressure and increasing polymerisation of the silicate liquid. Unfortunately, the study by Hamilton *et al.* (1989) did not include Nb. However, based on the Ta variation, there is a (largely unconstrained) possibility that the magnitude of Nb-Ta decoupling during immiscibility may depend on the same variables.

c) Zr and Hf partition very strongly into the silicate liquid. The study by Veksler *et al.* (1998b) has shown an average enrichment factor of 62 for Zr and 107 for Hf, in the silicate liquid, relative to the carbonatite. These results are consistent with those of Hamilton *et al.* (1989) for Hf, but not for Zr, but Hamilton *et al.* (1989) detected a large scatter in their Zr and Hf data. Veksler *et al.* (1998b) also suggest that some decoupling of the geochemical pair Zr-Hf may be expected during immiscibility, although this should be of a lesser magnitude than that of the pair Nb-Ta.

d) The rare-earth elements may show variable behaviour. Although the magnitude of REE partition coefficients between silicate and carbonatite immiscible liquids varies from one experimental work to the other, the results of Hamilton *et al.* (1989) and Veksler *et al.* (1998b) show that there is a consistent internal behaviour, within the REE group. Thus, the $K_D^{sil/carb}$ increases progressively from La to Lu, for a range of experimental conditions, but whether (or which) REE will effectively partition into the silicate or carbonate liquid seems to be strongly dependent on pressure, temperature and composition of the starting materials. In any case, it should be noted that the progressive differences in the partition coefficients are likely to produce LREE/HREE fractionation in the immiscible pair, with La/Lu ratios increasing in the carbonatite liquid and decreasing in the corresponding silicate conjugate. The low-pressure studies of Veksler *et al.* (1998b) suggest that, except for La, the remainder of the REE show preference for the silicate liquid.

The results of Hamilton *et al.* (1989), for a range of pressures, temperatures and different starting compositions, suggest that the partition of the REE into the silicate liquid is favoured by increasing temperature (at constant P = 3kb) and decreasing pressure (at constant T = 1150 °C). The effect of pressure is particularly interesting, since it suggests that all REE partition into the silicate liquid at < 2 kb, and all REE partition into the carbonate liquid at 6 kb. At 3 kb Hamilton *et al.* (1989) obtained $K_D^{sil/carb} < 1$ for the LREE and $K_D^{sil/carb} > 1$ for the HREE, with Gd closest to the unity (0.93). This would suggest, as stated by Hamilton *et al.* (1989), that only carbonatite generated by liquid immiscibility at relatively high pressures will become strongly enriched in REE, relatively to the silicate liquid. The $K_D^{sil/carb}$ for the LREE seems to be higher in more evolved (phonolitic) than in less evolved (nephelinitic) liquids, but the $K_D^{sil/carb}$ for the HREE does not vary a great deal with composition. This suggests that the LREE/HREE fractionation between the conjugate liquids (see above) would be enhanced in felsic systems.

According to the considerations above, a number of geochemical signatures may be expected to occur in silicate and carbonate immiscible liquids. These include anomalously high Nb/Ta and La/Lu ratios, and low relative abundances of Th, Zr, and Hf, in the carbonatite liquid. Several of these geochemical signatures can be detected in chondrite-normalised multi-element plots. More importantly, the silicate conjugate should have corresponding, and opposite, anomalies, making this a powerful method to test both immiscibility and consanguinity between carbonatites and associated silicate rocks.

All these immiscibility-related anomalies mentioned above are present in Tapira rocks, in some form or another. They occur in low-Cr dykes, B2 wehrlites and bebedourites, syenites and carbonatites, but are apparently absent in the most primitive phlogopite-picrites. Several examples of this have been presented in this thesis, and the reader is referred to Chapter IV for the detailed variations. The significance will be discussed later in this Chapter but, for now, it is enough to emphasise that the geochemical evidence for the involvement of liquid immiscibility in the genesis of Tapira rocks is compelling. Furthermore, a more restricted data set from Salitre suggests that this is the case for that complex also.

Evidence from experimental petrology

Carbonate-silicate liquid immiscibility is now a magmatic phenomenon well-established experimentally. Recent reviews and updates of the current experimental knowledge applied to both mantle and crustal conditions can be found in Lee and Wyllie (1996, 1997a,b 1998b), Brooker (1998), Moore and Wood (1998), Dalton and Presnall (1998a,b), Kjarsgaard (1998), Petibon *et al.* (1998). The framework provided by these experimental studies lends further support to the hypothesis of generation of Tapira rocks by liquid immiscibility, and places some additional constraints on the petrogenesis of the complex.

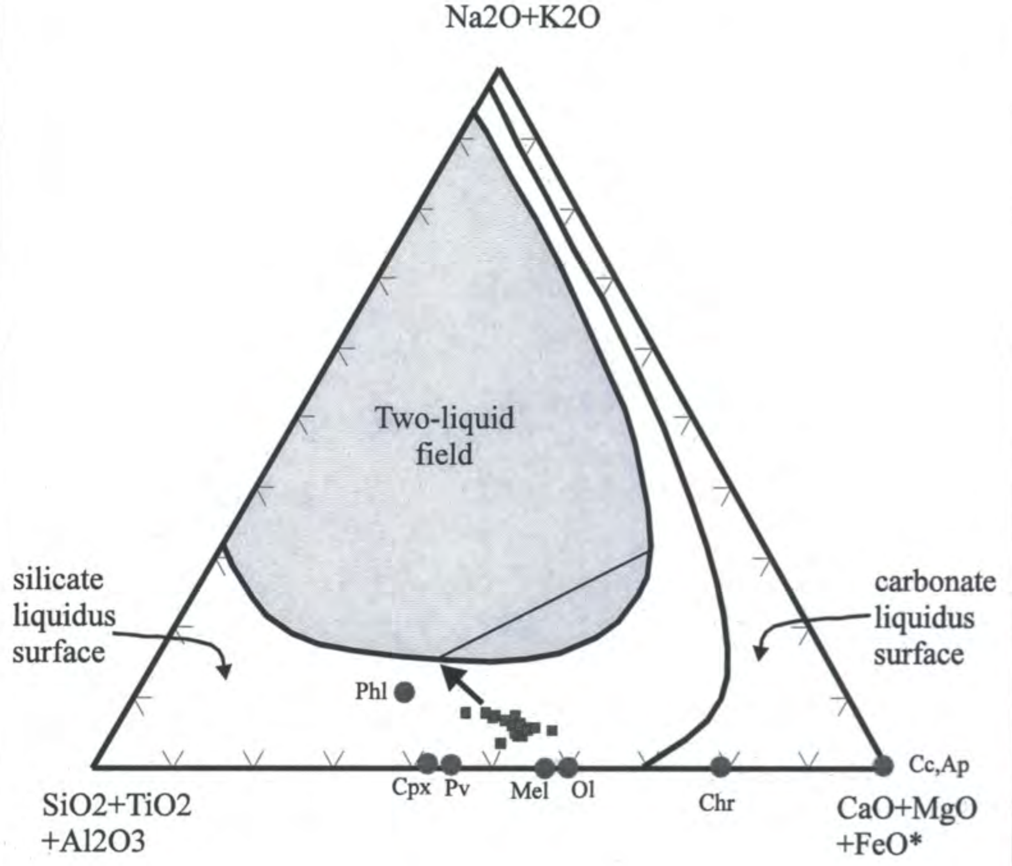

Figure V.7 - Representation of Tapira phlogopite-picrite compositions in the Hamilton projection (after Lee and Wyllie, 1997b). The composition of relevant mineral phases is also plotted: Ol = Olivine; Mel = melilite, Pv = perovskite, Cpx = clinopyroxene, Chr = chromite, Cc = calcite, Ap = apatite, Phl = phlogopite.

Figure V.7 shows the composition of Tapira phlogopite-picrites in the Hamilton projection, together with the silicate-carbonate miscibility gap, the silicate-carbonate liquidus boundary (after Lee and Wyllie, 1997b), and with a number of possible mineral phases. For the minerals analysed during this research the average composition is plotted. Additional mineral phases are ideal compositions. Note that the shape and size of the miscibility gap and of the silicate-carbonate liquidus boundary can vary significantly, depending on pressure, temperature, composition and CO_2 saturation (e.g. Lee and Wyllie, 1998b; Brooker, 1998; Kjarsgaard, 1998). However, their precise location in this and similar diagrams in the remainder of this Chapter is not critical for the purpose of illustrating the behaviour of Tapira rocks and exploring possible alternatives of liquid evolution

The predominance of olivine phenocrysts, and the progressive variations in MgO and Cr of the phlogopite-picrites suggest that olivine and chromite are the main mineral phases produced by fractionation from these rocks. The diagram illustrates that the removal of a mixture of olivine and chromite at first, possibly with some perovskite and pyroxene at a later stage, will drive the residual liquid towards the two-liquid miscibility gap and, consequently, towards the production of conjugate silicate and carbonate liquids. This is significant in the Tapira complex, because it indicates that liquid immiscibility may have occurred at a relatively early stage in the magmatic evolution, and is in good agreement with the presence of carbonate ocelli in some of the phlogopite-picrite dykes.

The composition of Tapira low-Cr dykes is illustrated separately, in the diagram of Figure V.8. Note that these rocks do not contain olivine phenocrysts and are depleted in chromium. Instead, the petrographic and geochemical evidence indicate that they will fractionate clinopyroxene, phlogopite and perovskite, with variable amounts of apatite. K- feldspar is present in small amounts in the groundmass and is also found as rare inclusions in apatite microphenocrysts from some low-Cr dykes. Together with the presence of interstitial K-feldspar in the most evolved bebedourites of the B2 unit, this suggests that, during the latest stages of differentiation, felsic potassic phases will crystallise from these rocks, in addition to clinopyroxene and phlogopite. In Tapira the felsic silicate minerals seem to be mainly feldspar, but kalsilite has been reported by Sgarbi *et al.* (1998) in (bebedourite-like) clinopyroxenite xenoliths from the Mata da Corda Group.

As a consequence of the removal of the mineral assemblage described above, the composition of the residual liquids will progress away from the $SiO_2 + TiO_2 + Al_2O_3$ apex and towards the CaO + MgO + FeO (and not towards alkali enrichment). This trend is apparently inconsistent with the expected major-element variation in the vast majority of igneous systems (i.e. decrease in MgO, coupled with increase in SiO_2 and alkalis), but it has been increasingly considered a plausible alternative in recent studies of carbonatites and associated rocks (Veksler *et al.,* 1998a; Kjarsgaard, 1998). In the low-Cr dykes this trend is accompanied by relative enrichment in groundmass carbonate.

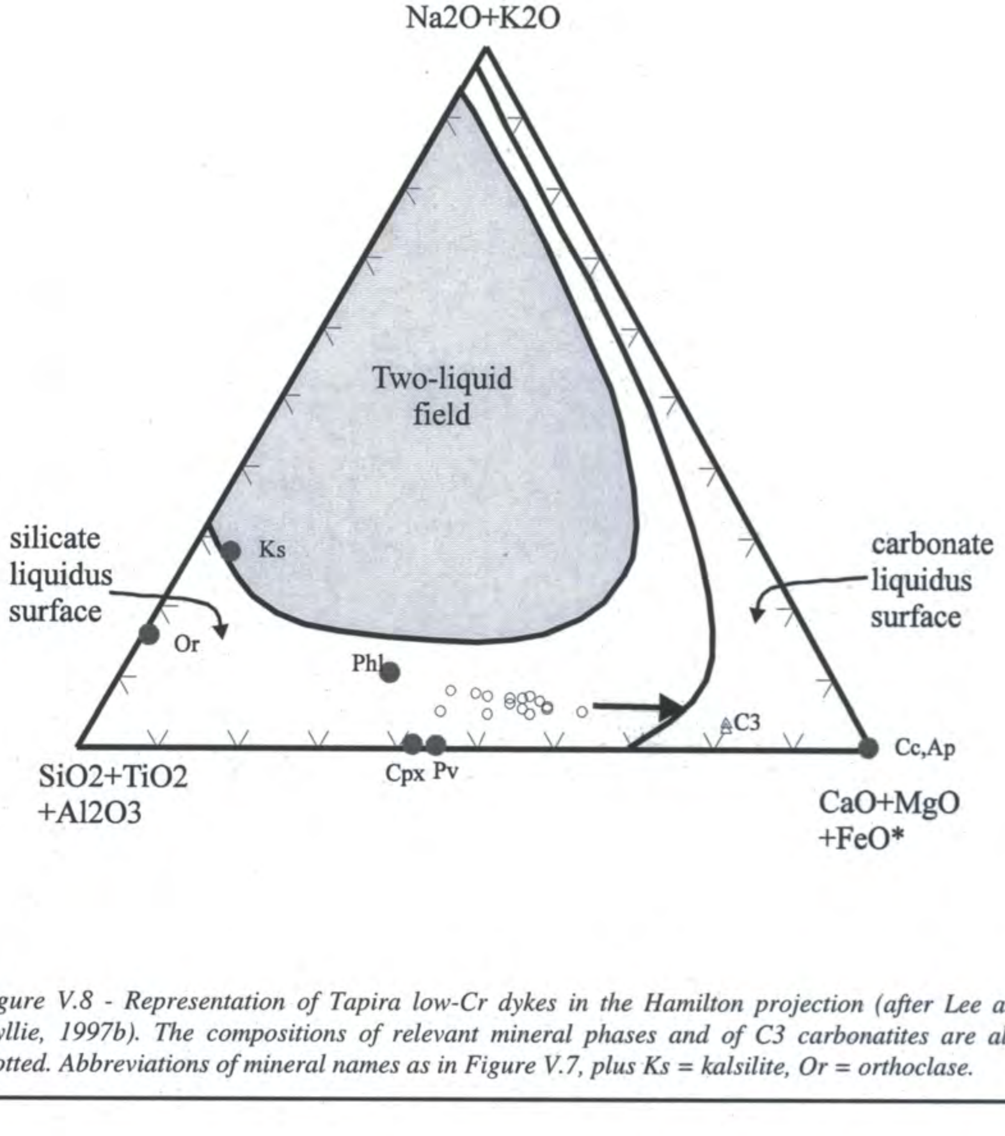

Figure V.8 - Representation of Tapira low-Cr dykes in the Hamilton projection (after Lee and Wyllie, 1997b). The compositions of relevant mineral phases and of C3 carbonatites are also plotted. Abbreviations of mineral names as in Figure V.7, plus Ks = kalsilite, Or = orthoclase.

It was shown in Chapter IV that the ratio CaO/(CaO+MgO) provides a satisfactory way of monitoring magmatic differentiation in the phlogopite-picrites and low-Cr dykes. Therefore, although the Hamilton projection of Figures V.7 and V.8 indicates the general sense of variation of the evolving liquid, it is not possible to use this diagram to accurately pinpoint detailed features.

Further insight can be gained by plotting the composition of phlogopite-picrites and low-Cr dykes in the pseudoquaternary system (SiO_2 + Al_2O_3 + TiO_2) - (MgO + FeO_T) - (Na_2O + K_2O) - CaO (Figures V.9 and V.10). The diagram of Figure V.9

highlights the wide variation in the MgO + $FeO_{(T)}$ in the mafic dykes and the apparent presence of more than one trend, with starting points at different MgO + FeO concentrations. This suggests that the samples analysed represent successive batches of progressively more differentiated liquids. Accordingly, three distinct paths for the residual liquids have been depicted in Figure V.9. Although it cannot be represented in this diagram, the arrows point in the direction of general CO_2 increase.

The differentiation trend of the most primitive dykes is indicated by the arrow labelled 1. In these liquids, the fractionation of olivine crystals (but not clinopyroxene or phlogopite) will produce an increase in alkalis and decrease in silica with concomitant enrichment in CO_2. The composition of the residual liquids will then be driven towards the Na_2O + K_2O apex (at the rear of the diagram), and the trend is likely to intercept the two-liquid volume surface, thus producing a silicate-carbonatite immiscible pair. The occurrence of immiscibility in this case would also be favoured by the relative increase in the CO_2 concentration, by virtue of the removal of silicate phases (e.g. Brooker, 1998). As discussed previously, carbonatites formed in this way would show geochemical fingerprints of the immiscibility process, such as Nb-Ta decoupling, high LREE/HREE fractionation and Zr+Hf depletion. These features are present in several samples of Tapira carbonatites, particularly those of the C1 and C2 units. Also, because the evolving liquid intercepts the miscibility gap at a relatively early stage, the carbonatites generated by this process would have relatively high MgO contents. Although some of the C1 and C2 carbonatites probably represent accumulations of calcite crystals (see discussion earlier in this Chapter, and also Figure V.10 below) their MgO content is generally higher than those from C3 and C4. This is consistent with the crystallisation of primary tetraferriphlogopite (Chapter III) in C1 carbonatites and with the presence of interstitial or groundmass dolomite in C2 carbonatites.

If the liquid is slightly more fractionated (Trend 2, shown on Figure V.9), the precipitation of olivine may be accompanied by clinopyroxene and phlogopite. In this case, the composition of the residual liquids will still move away from the SiO_2 + TiO_2 + Al_2O_3 apex and, as in Trend 1, a progressive relative increase in carbonate will occur, since only silicate phases are precipitating. The evolution path may or may not hit the two –liquid volume surface, depending on the type and relative proportion of the

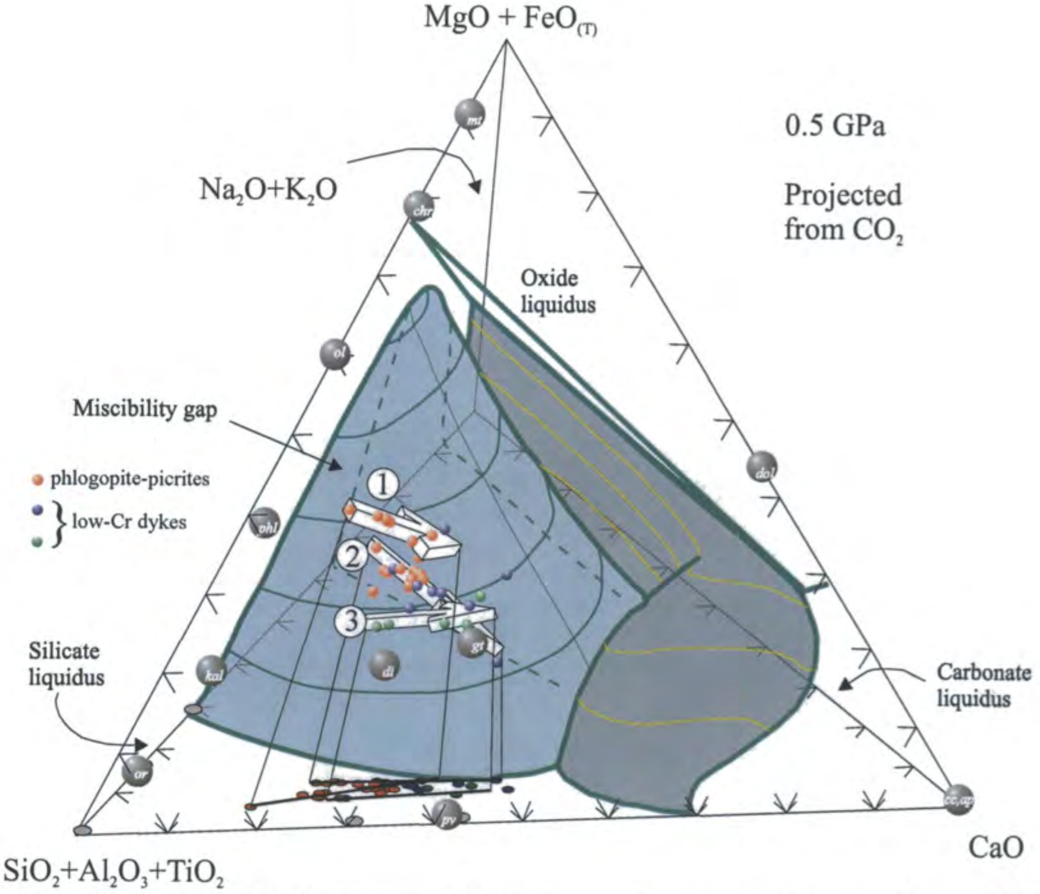

Figure V.9 - Composition of the Tapira mafic dykes in the pseudoquaternary diagram of Lee and Wyllie (1998b). The composition of relevant mineral phases is also plotted. Mineral abbreviations: mt = magnetite; chr = chromite; ol = olivine; phl = phlogopite; dol = dolomite; kal = kalsilite; or = orthoclase; di = diopside; gt = garnet; pv = pervskite; cc = calcite; ap = apatite. See text for explanation.

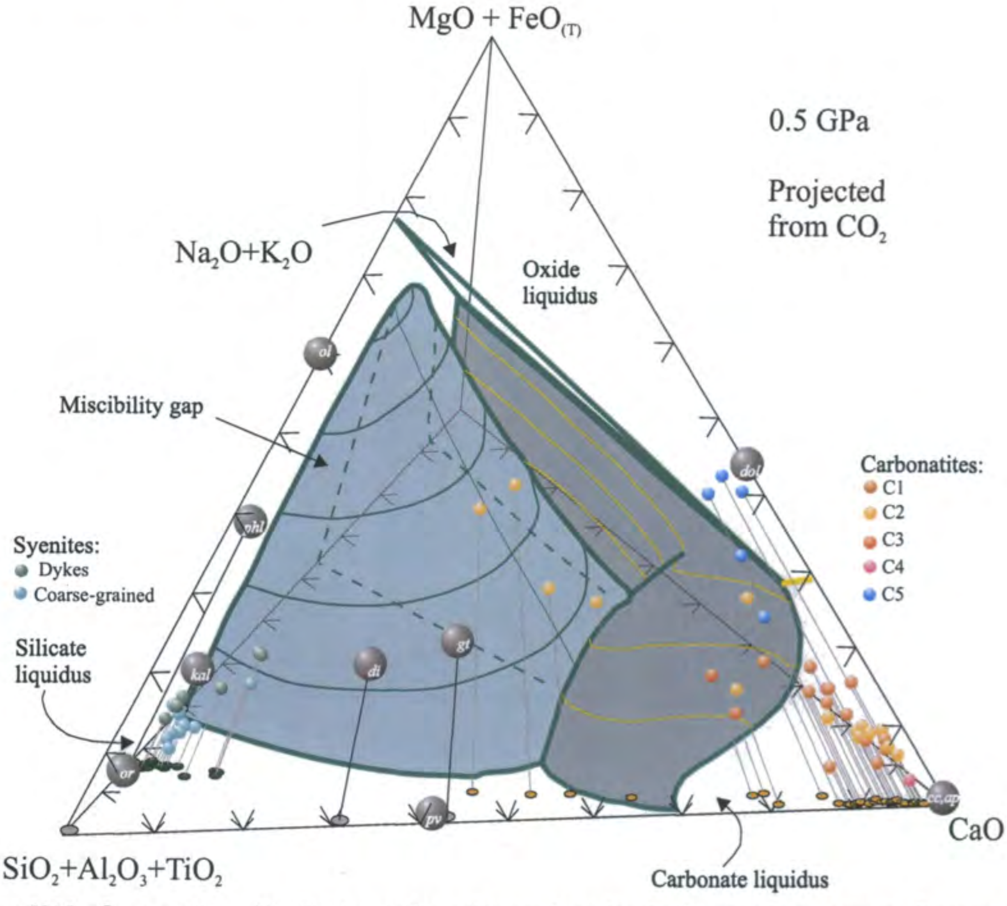

Figure V.10 - Composition of the Tapira carbonatites and syenites in the pseudoquaternary diagram of Lee and Wyllie (1998b). Mineral abbreviations as in Figure V.9. See text for explanation.

crystallising phases. For instance, extensive crystallisation of phlogopite will remove alkalis from the liquid, and may now drive the composition of the residual liquids towards the CaO apex, thus preventing the trend from intercepting the two-liquid field.

V.5.4 - CARBONATITES GENERATED BY FRACTIONATION

If Trend 2 in Figure V.9 does not intercept the two-liquid surface, carbonatites may form when the evolving liquid intercepts the carbonate-silicate liquidus field boundary. Note that carbonatites formed in this way would lack the geochemical signatures of immiscible liquids, discussed above.

According to Lee and Wyllie (1998a, b) the carbonate and oxide liquidus volumes in the (SiO_2 + Al_2O_3 + TiO_2) - (MgO + FeO_T) - (Na_2O + K_2O) - CaO pseudoquaternary system (Figure V.10) are “forbidden zones” for residual fractionation products from silicate parent liquids. Therefore, compositions plotting within these two volumes must either represent accumulation of carbonate crystals or cannot derive from a silicate parent through fractionation.

Tapira carbonatites from C1 to C5 units are plotted in the pseudoquaternary phase diagram of Figure V.10. Carbonatites from C3, some samples from C1 and fine-grained dykes from C2 plot near the silicate-carbonate liquidus field boundary, but all the remainder of Tapira carbonatites plot within the carbonate liquidus volume or oxide (periclase) liquidus volume. The two samples of C2 carbonatite that plot furthest from the CaO apex fall well within the silicate liquidus volume. These samples are from the groundmass of the diatreme-facies breccias, and their high silica content is, at least partially, related to the presence of fragmental material from both the silicate alkaline rocks and the silica-rich country rock.

Among Tapira carbonatites, only rocks from the C3 unit do *not* show strong depletion in Zr + Hf and strong decoupling between Nb and Ta. In fact, these carbonatites have a chondrite-normalised Nb/Ta ratio similar to the parental magmas of Tapira (see Figure V.11), suggesting that they were not formed by an immiscibility process. Furthermore, C3 carbonatites contain abundant phlogopite and clinopyroxene, but the composition and textural properties of these silicate phases suggest that they are entrained xenocrysts from the SPS rocks (see Chapters II and III). These characteristics, together with the position of C3 carbonatites in Figure V.10 and their spatial association with the B2 bebedourites, suggest that C3 are the final residue of the fractionating magma from which B2 crystallised. The abundance of entrained xenocrysts from B2 suggests that the carbonatites may have separated from the forming pile of B2 cumulates by a process such as filter pressing.

The interpretation of the C4 carbonatites is less straightforward, since these rocks have relatively low Nb/Ta ratio, but show some degree of relative Zr + Hf depletion. In the case of C4, the compositions plot well inside the carbonate liquidus volume in Figure V.10) indicating that, if they were originated by a fractionation process similar to the one described above, the samples studied must represent cumulates.

V.6 - A MODEL FOR THE FORMATION OF THE TAPIRA COMPLEX

In Chapter IV it was pointed out that some of the more evolved low-Cr dykes, as well as wehrlite dykes and some B2 bebedourites share a number of "anomalous" geochemical properties, when compared with the remainder of Tapira silicate rocks. These remarkable differences include: a) anticlockwise rotation of REE patterns, which "cross over" those of the primitive liquids; b) strong depletion in Th; c) strong enrichment in Zr + Hf and d) decoupling of Nb/Ta. In Figure V.9 these anomalous samples are aligned along trend labelled 3. It is clear that they represent a batch of liquids that are more evolved than trends 1 and 2, but the interpretation of their peculiar geochemistry is complicated. At first sight, the "crossover" REE patterns and the positive anomalies of Zr + Hf suggest that these liquids represent the silicate side of an immiscible silicate-carbonatite pair. On the other hand, Th would be expected to increase, and the Nb/Ta ratio would be expected to decrease in the silicate-rich immiscible liquid, but the Nb/Ta and Th variations observed in these rocks are the opposite, apparently contradicting the immiscibility hypothesis.

It is suggested here that these rocks are derived from an ultramafic silicate magma that was itself formed by a previous liquid immiscibility event. In this sense, if the parental composition for Trend 3 was the silicate-rich side of an immiscible pair, it would have acquired some of its anomalous characteristics from the first immiscibility event (e.g. from when trend 1 intercepted the two-liquid surface in Figure V.9), such as the relative enrichment in Zr + Hf, and the crossover REE patterns. However, for some reason, Nb and Ta did not undergo strong decoupling during this first immiscibility event. Hamilton *et al.* (1989) have demonstrated that the magnitude of Ta partitioning into the silicate liquid increases with decreasing pressure and temperature and with the increasing polymerisation state of the magma. It is possible that the Nb-Ta decoupling would be less pronounced in a primitive liquid, formed by immiscibility at greater depth. Alternatively, since both Nb and Ta show preference for the silicate liquid (although with different partition coefficients) the Nb-Ta decoupling is likely to be more pronounced in the carbonate-rich liquid than in the silicate-rich liquid.

Therefore, if an ultramafic magma, such as that in Trend 1, reaches the miscibility gap, the immiscible silicate liquid may show only a small Nb-Ta decoupling, whilst producing, for other elements, a full "immiscibility" signature (e.g. strong relative Zr + Hf enrichment and "crossover", LREE-depleted patterns in the silicate liquid). If this silicate half of the immiscible pair continues differentiating by fractionation of olivine (for example Trend 2 in Figure V.9, it may undergo a relative build-up of carbonate concentration in the fractionation residue, and might hit the miscibility gap a second time. This more evolved magma, undergoing liquid immiscibility at a lower temperature (and, possibly, shallower level in the crust) may now produce strong Nb-Ta decoupling but less pronounced REE fractionation between the silicate and carbonate liquids. If this happens, the carbonate-rich half of this second immiscible pair could, conceivably, exhibit contrasting signatures (i.e., strong relative Zr + Hf enrichment and crossover REE patterns inherited from the first immiscibility episode and high Nb/Ta ratio plus strong Th depletion, produced by the second).

These peculiar geochemical properties can be found in rocks of Trend 3, in Figure V.9. If these liquids now undergo further fractionation of silicate phases (at this stage possibly involving a substantial contribution from feldspar or feldspathoid) they may evolve towards ever increasing carbonate concentration, but will not be able to produce future immiscible liquids. Therefore, they will tend to follow the fractionation path leading to intersection of the silicate-carbonate liquidus boundary, eventually crystallising carbonatite. It must be stressed, however, that this carbonatite, although formed ultimately by fractionation, will show an "immiscibility signature", because this was already imprinted in the fractionating liquid 3.

It should be noted that if clinopyroxene, phlogopite, feldspar or feldspathoid come into the crystallisation sequence at an intermediate stage, they may conceivably cause the formation of fractionation-type carbonatite with an intermediate geochemical signature.

The composition of coarse-grained syenites from Tapira and fine-grained syenite dykes from Salitre is shown in Figure V.10. The coarse-grained syenites from Tapira plot in a very tight cluster while the fine-grained dykes span a wider compositional range, suggesting, as discussed previously, that the former are feldspar cumulates and the latter represent different stages of an evolving liquid. Note that Trend 3 in figure V.9 would be reasonably aligned with, and move away from, the compositional space occupied by syenites in Figure V.10).

This petrogenetic model seems to explain the unexpected signatures not only of Tapira magmas, but also of the related cumulates (e.g. anomalous signatures in some rocks of the B2 unit - Chapter IV). However, there are two *sine qua non* conditions for the model to be viable:

1 - The first, and probably the second immiscibility events have to occur at relatively high temperature, i.e. at a relatively undifferentiated stage. This is required so that the fractionation trend hits the miscibility gap for the first time in Figure V.9 at a high enough $MgO+FeO_{(T)}$ level, so that the carbonate-rich branch still contains significant amounts of silica, and the silicate-rich branch is still relatively unevolved.

2 - The carbonate-rich conjugate liquid originating from the second immiscibility event has to lose CO_2 (probably by degassing). If this is accompanied by loss of alkalis, the composition of the liquid may be shifted back to the silicate liquidus volume, so that a fractionation trend like 3 can be resumed. This is consistent with the presence of more than one trend in the mafic dykes, with respect to CO_2, Na_2O and K_2O, noted in Chapter IV. The mixed geochemical fingerprints of the samples in this trend requires that they followed a path similar to:

Trend 1 ⇒ immiscibility ⇒ Trend 2 (silicate-rich branch) ⇒ immiscibility ⇒
⇒ Trend 3 (carbonate-rich branch) ⇒ fractionation without immiscibility.

The sample at the starting point of Trend 3 has a very low CO_2 content (1.07 wt. %). Since the liquids of Trend 3 presumably formed the carbonate-rich branch of the immiscible pair in the second immiscibility event, the very low CO_2 content of this sample suggests that most of the original CO_2 was lost by degassing. It should be noted also that the samples with the more extreme coupled $\delta^{18}O$ enrichment - $\delta^{13}C$ depletion are generally the ones with lesser CO_2 contents.

A third condition for immiscibility to occur, in the case of Tapira compositions, is that substantial amounts of olivine must be fractionating. Once the magmas start fractionating clinopyroxene + phlogopite, or phlogopite + feldspar (or feldspathoid) the liquid is prevented from reaching the miscibility gap. Since this style of fractionation still can result in the build-up of CO_2 in the liquid, carbonatite may still form by fractionation.

A possible sequence of events is illustrated using the variations in chondrite-normalised Nb/Ta ratio, in Figure V.11. The ratio is plotted against a modified version of the differentiation index used in Chapter IV to monitor the evolution of the Tapira mafic dykes. Note that both the syenites and the B2 bebedourites plot in two distinct areas of the diagram; i.e. there is a high- and a low-Nb/Ta group of syenites, and a high- and low-Nb/Ta group of B2 bebedourites. It is suggested here that these distinct Nb/Ta signatures are related to different roles of liquid immiscibility in the generation of syenites and B2 bebedourites. Note also that the high Nb/Ta ratios in C1 and C2 carbonatites suggest that they are products of liquid immiscibility, whilst C3 and C4 have a fractionation-like Nb/Ta ratio.

Nb-Ta decoupling by liquid immiscibility may be more common than it was previously thought and may have been often overlooked. The data for syenites and carbonatites from the Salitre complex obtained during this research show many of the geochemical signatures described in the previous paragraphs for Tapira. The inset in Figure V.11 shows the same effects in a suite of melilitite - carbonatite - nephelinite dykes from the Turiy Peninsula , Russia (Ivanikov *et al.* 1998).

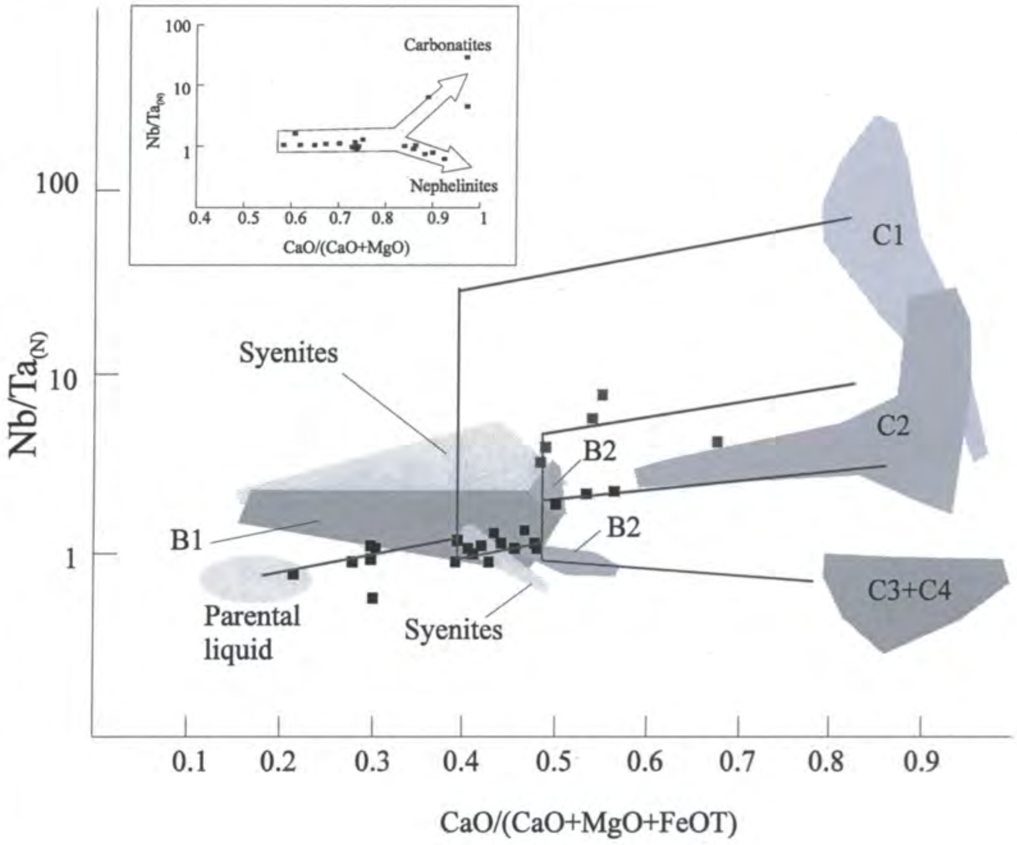

Figure V.11 - Chondrite-normalised Nb/Ta ratio of Tapira mafic dykes (solid squares) plotted against the CaO/(CaO+MgO+FeOT) ratio. Assuming a composition similar to the least differentiated phlogopite-picrite for the parental liquid, the solid lines indicate possible alternatives of evolution, in a mixed fractionation-immiscibility process. The inset shows the Nb/Ta decoupling in the data reported by Ivanikov et al (1998) for dykes of the Turiy Peninsula, Russia.

Implications for the interpretation of mineral chemistry

Some of the most intriguing variations observed in mineral chemistry during this research (Chapter III) seem to agree remarkably well with this petrogenetic model. These are summarised below:

a) It was observed in phlogopites from some of the more evolved low-Cr dykes that an SPS-like phlogopite core is coated by a carbonatite-like phlogopite rim (i.e. tetraferriphlogopite). This may be reflecting an immiscibility episode whereby the magma, although still containing appreciable amounts of mafic silicate minerals, becomes suddenly carbonate-rich. Because Al partitions strongly into the conjugate silicate-rich liquid ($K_D^{sil/carb}$ = 100, for the nephelinite system, and 200 for the phonolite system, calculated from the data of Hamilton *et al.*, 1989, at 1150 °C and 2 kb), phlogopites crystallising from this rock will evolve towards Al-deficient compositions (i.e. tetraferriphlogopite). This places severe constraints in the Ti-Al systematics of phlogopite, which has become a popular means of distinguishing different types of ultrapotassic rocks (e.g. Mitchell and Bergman, 1991; Mitchell, 1995).

b) Sudden changes in the composition of garnet, from melanite to andradite, in evolved low-Cr dykes from Trend 3, sometimes with partial resorption of the melanite core. Again, since Ti notably prefers the silicate liquid ($K_D^{sil/carb}$ = 5 for the nephelinite system and 4 for the phonolite system, calculated from the data of Hamilton *et al.*, 1989, at 1150 °C, 2 kb) the amount of Ti available for the crystallising garnet decreases abruptly, and a rim of andradite forms in the garnet.

c) Nb content in perovskite from some wehrlites is higher than in the bebedourites. This is in contrast with the expected increase of Nb in perovskite with magma differentiation, suggesting that some of the wehrlites crystallised from a batch of magma that was more "evolved" than that which formed some of the bebedourites.

d) Low NiO, coupled with high CaO and MnO contents in olivines from some wehrlites. These olivines seem to be more evolved than those from phlogopite-picrites, which contrasts with the expected variation, if the former are cumulates produced by olivine fractionation from the latter. In fact these anomalous olivines have some of the characteristics highlighted by Gaspar *et al.* (1998) to distinguish carbonatitic olivines from those crystallised from silicate rocks, in carbonatite complexes. This suggests that some of the wehrlites were fractionated from a carbonate-rich conjugate that previously originated by liquid immiscibility.

In summary, the data presented in this thesis and discussed in the model above indicate that both liquid immiscibility and fractionation processes were involved in the evolution of Tapira carbonatites and associated silicate rocks. However, neither of these mechanisms can individually account for the whole spectrum of chemical compositions and evolution trends of the various minerals and rock-types in the complex. Dawson (1998) has recently demonstrated that the apparently unexpected variations in mineral and rock chemistry, and the relationships between the different rock-types from the Oldoinyo Lengai volcano (Tanzania), cannot be explained by a single mechanism, but are the result of a complex interplay of processes such as fractionation, unmixing of silicate and carbonatite liquids and CO_2 degassing.

CHAPTER VI - CONCLUSIONS

The main conclusions of this research are summarised below:

- The Tapira Complex is a carbonatite/silicate-rock composite intrusion, emplaced into a Late Proterozoic mobile belt (Brasília belt), adjacent to the margin of a major cratonic area (São Francisco craton) in southeastern Brazil.
- This and other carbonatite-bearing complexes in the region are part of the Late-Cretaceous Alto Paranaíba Igneous Province (APIP), which is composed essentially of potassic to ultrapotassic rocks (kamafugites, lamproites, kimberlites)
- The complex is an amalgamation of several intrusions, containing mainly ultramafic rocks, such as wehrlite and bebedourite (a particular type of clinopyroxenite, with substantial modal proportions of apatite, perovskite and phlogopite), and subordinate amounts of carbonatite, syenite and rare melilitic rocks (uncompahgrite).

- Most of the silicate plutonic rocks can be considered cumulates. The ultramafic rocks are formed by fractionation of dense minerals from a (carbonated) alkaline, undersaturated, ultrapotassic magma. The coarse-grained syenites are flotation cumulates of K-feldspar crystals.
- At least two separate units of ultramafic rocks, named B1 and B2, are recognisable on the basis of their location in the complex, and of modal and chemical variations in the essential mineral phases. Unit B2 may consist of two separate intrusions, with distinct petrogenetic histories.
- The syenites are mineralogically and petrographically homogeneous, but trace-element systematics allows the recognition of petrogenetically distinct syenites in the Tapira complex.
- At least five episodes of carbonatite intrusions are recognisable, and were named C1 to C5. The carbonatites are mainly sovites, but dolomite sovites (C1, C2) also occur. Late stage carbonatitic activity comprises beforsites. Coarse-grained carbonatites in Tapira are mainly cumulates, but carbonatite dykes are likely to approximate the composition of some of the carbonate-rich magmas.
- The complex is crosscut by ultramafic fine-grained dykes. Two petrographic and chemical varieties are recognised: phlogopite-picrites are the most primitive rocks in the complex; low-Cr dykes represent more evolved liquids and typically lack olivine. Yet, they are still ultramafic in composition and are considered the fine-grained counterpart of the bebedourites. Both types of ultramafic dykes are carbonate-rich, and may contain carbonate ocelli, indicating that the immiscibility of carbonatite liquid occurred in these rocks.
- The chemical trends observed in the essential mineral phases of Tapira rocks are consistent with the magmatic evolution of the complex and support the subdivision of Tapira rocks into the units described above. Detailed variations in mineral composition can be successfully used to monitor different stages in the evolution of these magmas, and to pinpoint the onset of specific processes, such as liquid immiscibility.
- The geochemical characteristics of Tapira rocks are similar to those observed in the kamafugite suite in general, and in the APIP kamafugites, in particular.
- The petrographic similarities of bebedourites with clinopyroxenite xenoliths from

the Mata da Corda kamafugites suggests that the Tapira complex represents the deeply eroded remnants of a kamafugitic volcanic centre.

- Major- and trace-elements, and Sr- and Nd-isotope systematics indicate that the source of the Tapira magmas is similar to that of other ultrapotassic rocks in APIP. In detail, it is similar to that of the kamafugites. These magmas are believed to have originated in the sub-continental lithospheric mantle (SCLM), from a source that had been previously enriched in incompatible elements.
- The parental magmas of the Tapira complex underwent some differentiation in the crust, before their final emplacement. The phlogopite-picrite magma must have fractionated substantial olivine and chromite, but the products of this process are apparently not present in Tapira. Olivines in wehrlites from Tapira are more evolved than those in the phlogopite-picrites.
- Crystal fractionation from the low-Cr dykes may have produced the bebedourites. The majority of the bebedourites were emplaced as a crystal mush, but some may have formed *in situ*, and fractionated to produce carbonatite.
- The Tapira complex contains examples of carbonatites originated by liquid immiscibility and carbonatites formed by direct fractionation from a carbonated silicate magma. The latter are associated with bebedourites B2, and were most likely separated from the ultramafic fraction by filter pressing.
- Silicate-carbonate liquid immiscibility produces chemical signatures in both the carbonate-rich and the silicate-rich conjugate liquids. In the carbonatite, the immiscibility signature is translated by Th, Zr and Hf depletion, positive LREE/HREE fractionation and strong decoupling of Nb and Ta, with increase in the Nb/Ta ratio. The silicate liquid will show correspondent anomalies, in the opposite direction.
- Carbonatite generated as a fractionation residue will not show these signatures, especially if they are produced from a relatively primitive composition. However, if the fractionating liquid has been involved in a previous immiscibility event, the inherited geochemical signatures will be passed on to the carbonatite.
- In addition to the whole-rock geochemical signatures, abrupt variations in the mineralogy of the crystalline phases are associated with liquid immiscibility. This potentially places severe limitations for mineral-chemistry-based systematics of

alkaline rocks, such as kamafugites, kimberlites and lamproites, unless the effects of liquid immiscibility can be properly assessed in each case.

- Carbonatites generated by liquid immiscibility can accommodate economic concentrations of Nb, contradicting the forecast of Veksler *et al.* (1998).
- The two latter conclusions have important implications for the evaluation of the economic potential of alkaline rocks.
- All rock units identified in the Tapira complex can be genetically linked to each other, provided that the combined effects of liquid immiscibility, fractionation and CO_2 degassing are taken into consideration.

REFERENCES CITED

- Alkmim, F. F., Neves, B. B. B. and Alves, J. A. C. (1993). Arcabouço tectônico do craton do São Francisco. In J. M. L. Dominguez and A. Misi, Eds., O craton do São Francisco. Salvador, SBG BA-SE/SGM/CNPq, 45-62.

- Almeida, F. F. M. (1977). O craton do São Francisco. Revista Brasileira de Geociências, **7**: 349-364.

- Almeida, F. F. M. (1983). Relações tectônicas das rochas alcalinas mesozóicas da região meridional da Plataforma Sul-Americana. Revista Brasileira de Geociências, **13**: 139-158.

- Almeida, F. F. M., Hasui, Y., Davino, A. and Haralyi, N. L. E. (1980). Informações geofísicas sobre o oeste mineiro e seu significado geotectônico. Anais da Academia Brasileira de Ciências, **52**: 46-60.

- Almeida, F. F. M. and Svisero, D. P. (1991). Structural setting and tectonic control of Kimberlite and associated rocks of Brazil. In O. H. Leonardos, H. O. A. Meyer and J. C. Gaspar, Eds., 5th International Kimberlite Conference (Extended Abstracts). Araxá, Brazil, CPRM, Special Publication 3/91. 3-5.

- Amaral, G., Born, H., Hadler, J. C., Iunes, P. J., Kawashita, K., Machado, D. L., Oliveira, E. P., Paulo, S. R. and Tello, C. A. (1997). Fission track analysis of apatites from São Francisco craton and Mesozoic alcaline-carbonatite complexes from central and southeastern Brazil. Journal of South American Earth Sciences, **10**: 285-294.

- Amaral, G., Bushee, J., Cordani, U. G., Kawashita, K. and Reynolds, J. H. (1967). Potassium-argon ages of alkaline rocks from Southern Brazil. Geochimica et Cosmochimica Acta, **31**: 117-142.

- Amthauer, G. and Rossman, G. R. (1998). The hydrous component in andradite garnet. American Mineralogist, **83**: 835-840.

- Andersen, T. (1987). Mantle and crustal components in a carbonatite complex, and the evolution of carbonatite magma - REE and isotopic evidence from the Fen complex, Southeast Norway. Chemical Geology, **65**: 147-166.

- Anovitz, L. M. and Essene, E. J. (1987). Phase equilibria in the system $CaCO_3$-$MgCO_3$-$FeCO_3$. Journal of Petrology, **28**: 389-414.

- Araújo, A. L. N., Gaspar, J. C. and Bizzi, L. C. (1998). Petrography and mineralogy of kimberlites and kamafugites from the Alto Paranaíba Igneous Province, Mineras Gerais, Brazil: preliminary studies. 7th International Kimberlite Conference (Extended Abstracts). Cape Town 26-28.

- Araújo, D. P. (1996). Metassomatismo no complexo carbonatítico Catalão-I: implicações para a composição do magma carbonatítico e para o metassomatismo carbonatítico no manto superior. (Universidade de Brasília, M. Sc. Thesis), 415p.

- Araújo, D. P. and Gaspar, J. C. (1993). Fe^{+3} no sitio tetraédrico de flogopitas das rochas do complexo carbonatítico de Catalão I, Brasil. 4th Congresso Brasileiro de Geoquímica (Resumos Expandidos). Brasília, Sociedade Brasileira de Geoquímica, 62-63.

- Arima, M. and Edgar, A. D. (1981). Substitution mechanisms and solubility of titanium in phlogopites from rocks of probable mantle origin. Contributions to Mineralogy and Petrology, **77**: 288-295.

- Bailey, S. W. (1984). Classification and structures of the micas. In S. W. Bailey, Ed., Micas, Mineralogical Society of America, **13:** 1-12.

- Banfield, J. F. and Veblen, D. R. (1992). Conversion of perovskite to anatase and TiO_2 (B) - a TEM study and the use of fundamental building-blocks for understanding relationships among the TiO_2 minerals. American Mineralogist, **77**: 545-557.

- Barber, C. (1974). The geochemistry of carbonatites and related rocks from two carbonatite complexes, south Nyanza, Kenya. Lithos, **7**: 53-63.

- Barbosa, O., Braun, O. P. G., Dyer, R. C. and Cunha, C. A. B. (1970). Geologia da região do Triângulo Mineiro. Boletim DFPM/DNPM, **136**: 140p.

- Barker, D. S. (1989). Field relations of carbonatites. In K. Bell, Ed., Carbonatites: genesis and evolution. London, Unwin Hyman, 38-69.

- Barker, D. S. (1993). Diagnostic magmatic features in carbonatites: implications for the origins of dolomite- and ankerite-rich carbonatites. South African Journal of Geology, **96**: 131-138.

- Barker, D. S. (1996). Nephelinite-phonolite volcanism. In R. H. Mitchell, Ed., Undersaturated alkaline rocks: mineralogy, petrogenesis, and economic potential, Mineralogical Association of Canada Short Course, **24:** 23-44.

- Beccaluva, L., Barbieri, M., Born, H., Brotzu, P., Coltorti, M., Conte, A., Garbarino, C., Gomes, C. B., Macciotta, G., Morbidelli, L., Ruberti, E., Siena, F. and Traversa, G. (1992). Fractional crystallization and liquid immiscibility processses in the alkaline-carbonatite complex of Juquiá (São Paulo, Brazil). Journal of Petrology, **33**: 1371-1404.

- Bell, K. and Blenkinsop, J. (1987). Nd and Sr isotopic compositions of East African carbonatites - implications for mantle heterogeneity. Geology, **15**: 99-102.

- Belousova, E. A., Griffin, W. L. and Pearson, N. J. (1998). Trace element composition and cathodoluminescence properties of southern African kimberlitic zircons. Mineralogical Magazine, **62**: 355-366.

- Berbert, C. O. (1984). Carbonatites and associated Mineral Deposits in Brazil. Geological Survey of Japan Report n, **263**: 269-290.

- Bernasconi, A. (1983). The Archaean terranes of central-eastern Brazil: a review. Precambrian Research, **23**: 107-131.

- Bickle, M. J. and Powell, R. (1977). Calcite-dolomite geothermometry for iron-bearing carbonates. The Glockner area of the Tauern Window, Austria. Contributions to Mineralogy and Petrology, **59**: 281-292.

- Bizzi, L. A., De Wit, M. J., Smith, C. B., McDonald, I. and Armstrong, R. A. (1995). Heterogeneous enriched mantle materials and Dupal-type magmatism along the SW margin of the São Francisco Craton, Brazil. Journal of Geodynamics, **20**: 469-491.

- Bizzi, L. A., de Wit, M. J., Smith, C. B., Meyer, H. O. A. and Armstrong, R. (1993). Características isotópicas e origem dos kimberlitos e vulcânicas alcalinas relacionadas em Minas Gerais. 1st Simpósio Brasileiro de Geologia do Diamante (Anais). Cuiabá, Universidade Federal do Mato Grosso, Special Publication 2/93. 141-151.

- Bizzi, L. A., Smith, C. B., Meyer, H. O. A., Armstrong, R. and de Wit, M. J. (1994). Mesozoic kimberlites and related rocks in southwestern São Francisco craton, Brazil: a case for local mantle reservoirs and their interaction. In H. O. A. Meyer and O. H. Leonardos, Eds., 5th International Kimberlite Conference (Proceedings). Araxá, Brazil, CPRM, Special Publication 2/91. 156-171.

- Bogatikov, O. A., Kononova, V. A., Pervov, V. A. and Zhuravlev, D. Z. (1994). Petrogenesis of Mesozoic potassic magmatism of the central Aldan: a Sr-Nd isotopic and geodynamic model. International Geology Reviews, **36**: 629-644.
- Bogoch, R. and Magaritz, M. (1983). Immiscible silicate-carbonate liquids as evidenced from ocellar diabase dykes, Southeast Sinai. Contributions to Mineralogy and Petrology, **83**: 227-230.
- Bosum, W. (1973). O levantamento aeromagnético de Minas Gerais e Espírito Santo e sua sequência quanto à estrutura geológica. Revista Brasileira de Geociências, **3**: 149-159.
- Boynton, W. V. (1984). Geochemistry of the rare earth elements: meteorite studies. In P. Henderson, Ed., Rare earth element geochemistry, Elsevier, 63-114.
- Brenan, J. M. and Watson, E. B. (1991). Partitioning of trace-elements between carbonate melt and clinopyroxene and olivine at mantle P-T conditions. Geochimica et Cosmochimica Acta, **55**: 2203-2214.
- Brigatti, M. F., Medici, L., Saccani, E. and Vaccaro, C. (1996). Crystal-chemistry and petrologic significance of Fe^{3+}-Rich phlogopite from the Tapira carbonatite complex, Brazil. American Mineralogist, **81**: 913-927.
- Brito Neves, B. B., Kawashita, K., Cordani, U. and Delhal, J. (1979). A evolução geocronólogica da cordilheira do Espinhaço: dados novos e integração. Revista Brasileira de Geociências, **9**: 71-85.
- Brod, J. A., Leonardos, O. H., Meneses, P. R., Albuquerque, M. A. C., Almeida, R., Blanco, S. B., Cardoso, F. B. F., Romão, P. A., Tallarico, F. H. B. and Thomsen, F. P. R. (1992). Características geoquímicas da Sequência Vulcano-Sedimentar de Abadia dos Dourados, Grupo Araxá, Triângulo Mineiro, MG. Revista da Escola de Minas, **45**: 164-166.
- Brod, J. A., Leonardos, O. H., Meneses, P. R., Almeida, R., Araújo, R. N. J., Blanco, S. B., Cardoso, F. B. F., Carvalho, O. A., Junqueira, F. F., Riehl, W., Souza, J. C. F., Tallarico, F. H. B., Thomsen, F. P. R., Albuquerque, M. A. C., Berbert, M. L. C., Cerqueira, M. R. S., Chagas, M. A., Dias, R. R., Lima, C. V., Nakamura, E. T., Porto, S. G., Romão, P. A. and Santos, P. C. V. (1991). Tectono-estratigrafia da Faixa Brasília na Região do Alto Paranaíba. 3 Simpósio de Geologia do Centro-Oeste (Anais). Cuiabá, Brazil, SBG, 155-168.
- Brooker, R. A. (1998). The effect of CO2 saturation on immiscibility between silicate and carbonate liquids: an experimental study. Journal of Petrology, **39**: 1905-1916.
- Campbell, L. S., Henderson, P., Wall, F. and Nielsen, T. F. D. (1997). Rare earth chemistry of perovskite group minerals from the Gardiner Complex, East Greenland. Mineralogical Magazine, **61**: 197-212.
- Campos, J. E. G. and Dardenne, M. A. (1997a). Estratigrafia e sedimentação da bacia Sanfranciscana. Revista Brasileira de Geociências, **27**: 269-282.
- Campos, J. E. G. and Dardenne, M. A. (1997b). Origem e evolução tectônica da bacia Sanfranciscana. Revista Brasileira de Geociências, **27**: 283-294.
- Carborin, S. and Princivalle, F. (1996). A crystal-chemical study of pyroxenes with diopsidic structures in alkaline rocks from central-eastern Paraguay: some considerations on tetrahedrally coordinated Ti^{4+}. In P. Comin-Chiaramonti and C. B. Gomes, Eds., Alkaline magmatism in Central-Eastern Paraguay. Relationships with coeval magmatism in Brazil. São Paulo, Edusp/Fapesp, 157-180.

- Carlson, R. W., Esperança, S. and Svisero, D. P. (1996). Chemical and Os isotopic study of Cretaceous potassic rocks from Southern Brazil. Contributions to Mineralogy and Petrology, **125**: 393-405.

- Carlson, W. D. (1980). The calcite-argonite equilibrium: effects of Sr substitution and anion orientational disorder. American Mineralogist, **65**: 1252-1262.

- Carvalho, J. B. and Leonardos, O. H. (1995). Preliminary geothermobarometric studies on mantle xenoliths of kimberlites and associated rocks from the Alto Paranaíba, SE Brazil. 6th International Kimberlite Conference (Extended Abstracts). Novosibirsk, Russia 101-103.

- Carvalho, W. T. (1974). Aspectos geológicos e petrográficos do complexo ultramáfico-alcalino de Catalão I, GO. 28th Congresso Brasileiro de Geologia . Porto Alegre, Brazil, SBG, 5. 107-123.

- Carvalho, W. T. and Bressan, S. R. (1981). Depósitos minerais associados ao Complexo ultramáfico-alcalino de Catalão I - Goiás. In W. H. Schmaltz, Ed., Os principais depósitos minerais da Região Centro Oeste. Brasilia, DNPM, **6:** 139-183.

- Castorina, F., Censi, P., Barbieri, M., Comin-Chiaramonti, P., Cundari, A., Gomes, C. B. and Pardini, G. (1996). Carbonatites from Eastern Paraguay: a comparison with coeval carbonatites from Brazil and Angola. In P. Comin-Chiaramonti and C. B. Gomes, Eds., Alkaline magmatism in Central-Eastern Paraguay. Relationships with coeval magmatism in Brazil. São Paulo, Edusp/Fapesp, 231-248.

- Censi, P., Comin-Chiaramonti, P., Demarchi, G., Longinelli, A. and Orue, D. (1989). Geochemistry and C-O isotopes of the Chiriguelo carbonatite, northeastern Paraguay. Journal of South American Earth Sciences, **2**: 295-303.

- Chakhmouradian, A. R. and Mitchell, R. H. (1997). Compositional variation of perovskite-group minerals from the carbonatite complexes of the Kola Alkaline Province, Russia. Canadian Mineralogist, **35**: 1293-1310.

- Chakhmouradian, A. R. and Mitchell, R. H. (1998). Lueshite, pyrochlore and monazite-(Ce) from apatite-dolomite carbonatite, Lesnaya Varaka complex, Kola Peninsula, Russia. Mineralogical Magazine, **62**: 769-782.

- Chang, L. L. Y. (1965). Subsolidus phase relations in the systems $BaCO_3$ - $SrCO_3$, $SrCO_3$ - $CaCO_3$ and $BaCO_3$ - $CaCO_3$. Journal of Geology, **73**: 346-368.

- Chang, L. L. Y. (1971). Subsolidus phase relations in the aragonite-type carbonates: 1. the system $CaCO_3$-$SrCO_3$-$BaCO_3$. American Mineralogist, **56**: 1660-1673.

- Church, A. A. and Jones, A. P. (1995). Silicate-carbonate immiscibility at Oldoinyo Lengai. Journal of Petrology, **36**: 869-889.

- Comin-Chiaramonti, P., Censi, P., Cundari, A., De Min, A., Gomes, C. B., Marzoli, A. and Piccirillo, E. M. (1996). Petrochemistry of Early Cretaceous potassic rocks from the Asuncion-Sapucai graben, Central-Eastern Paraguay. In P. Comin-Chiaramonti and C. B. Gomes, Eds., Alkaline magmatism in Central-Eastern Paraguay. Relationships with coeval magmatism in Brazil - Appendix III. São Paulo, Edusp/Fapesp, 123-149.

- Comin-Chiaramonti, P., Cundari, A., Gomes, C. B., Piccirillo, E. M., Censi, P., Demin, A., Bellieni, G., Velazquez, V. F. and Orue, D. (1992). Potassic dyke swarm in the Sapucai graben, eastern Paraguay - petrographic, mineralogical and geochemical outlines. Lithos, **28**: 283-301.

- Comin-Chiaramonti, P., Cundari, A., Piccirillo, E. M., Gomes, C. B., Castorina, F., Censi, P., DeMin, A., Marzoli, A., Speziale, S. and Velazquez, V. F. (1997). Potassic and sodic igneous rocks from eastern Paraguay: Their origin from the lithospheric mantle and genetic relationships with the associated Paraná flood tholeiites. Journal of Petrology, **38**: 495-528.

- Comin-Chiaramonti, P. and Gomes, C. B. (1996). Alkaline magmatism in Central-Eastern Paraguay. Relationships with coeval magmatism in Brazil. São Paulo, Edusp/Fapesp. 458p.

- Conticelli, S. and Peccerillo, A. (1992). Petrology and geochemistry of potassic and ultrapotassic volcanism in central Italy - petrogenesis and inferences on the evolution of the mantle sources. Lithos, **28**: 221-240.

- Cox, K. G., Bell, J. D. and Pankhurst, R. J. (1979). The interpretation of igneous rocks. London, Allen, Unwin. 450pp.

- Crough, S. T., Morgan, W. J. and Hargraves, R. B. (1980). Kimberlites: their relation to mantle hotspots. Earth and Planetary Science Letters, **50**: 260-274.

- Cruciani, G., Zanazzi, P. F. and Quartieri, S. (1995). Tetrahedral ferric iron in phlogopite - Xanes and Mossbauer compared to single-crystal X-Ray data. European Journal of Mineralogy, **7**: 255-265.

- Cundari, A. and Comin-Chiaramonti, P. (1996). Mineral chemistry of alkaline rocks from the Asuncion-Sapucai graben (Central-Eastern Paraguay). In P. Comin-Chiaramonti and C. B. Gomes, Eds., Alkaline magmatism in Central-Eastern Paraguay. Relationships with coeval magmatism in Brazil. São Paulo, Edusp/Fapesp, 181-193.

- Cundari, A. and Salviulo, G. (1989). Ti solubility in diopsidic pyroxene from a suite of New South Wales leucitites (Australia). Lithos, **22**: 191-198.

- Dalton, J. A. and Lane, S. J. (1996). Electron microprobe analysis of Ca in olivine close to grain boundaries: the problem of secondary X-ray fluorescence. American Mineralogist, **81**: 194-201.

- Dalton, J. A. and Presnall, D. C. (1998a). Carbonatitic melts along the solidus of a model lherzoite in the system CaO-MgO-Al2O3-SiO2-CO2 from 3 to 7 GPa. Contributions to Mineralogy and Petrology, **131**: 123-135.

- Dalton, J. A. and Presnall, D. C. (1998b). The continuum of primary carbonatitic-kimberlitic melt compositions in equilibrium with lherzolite: data from the system CaO-MgO-Al2O3-SiO2-CO2 at 6 GPa. Journal of Petrology, **39**: 1953-1964.

- Dalton, J. A. and Wood, B. J. (1993a). The compositions of primary carbonate melts and their evolution through wallrock reaction in the mantle. Earth and Planetary Science Letters, **119**: 511-525.

- Dalton, J. A. and Wood, B. J. (1993b). The partitioning of Fe and Mg between olivine and carbonate and the stability of carbonate under mantle conditions. Contributions to Mineralogy and Petrology, **114**: 501-509.

- Danni, J. C. M., Baecker, M. L. and Ribeiro, C. C. (1991). The geology of the Catalão I carbonatite complex. In O. H. Leonardos, H. O. A. Meyer and J. C. Gaspar, Eds., 5th International Kimberlite Conference (Field Guide Book). Araxá, Brazil, CPRM, Special publication 3/91. 25-30.

- Danni, J. C. M. and Gaspar, J. C. (1992). Mineralogia e química do katungito de Amorinópolis, Goiás. 37th Congresso Brasileiro de Geologia . São Paulo, Brazil 85-86.

- Davis, L. L. and Smith, D. (1993). Ni-rich olivine in minettes from Two Buttes, Colorado - a connection between potassic melts from the mantle and low Ni partition coefficients. Geochimica et Cosmochimica Acta, **57**: 123-129.
- Dawson, J. B. (1989). Sodium carbonatite extrusions from Oldoinyo Lengai, Tanzania: implications for carbonatite complex genesis. In K. Bell, Ed., Carbonatites: genesis and evolution. London, Unwin Hyman, 255-277.
- Dawson, J. B. (1998). Peralkaline nephelinite-natrocarbonatite relationships at Oldoynio Lengai, Tanzania. Journal of Petrology, **39**: 2043-2060.
- Dawson, J. B. and Hawthorne, J. B. (1973). Magmatic sedimentation and carbonatitic differentiation in kimberlite sills at Benfontein, South Africa. Journal of the Geological Society of London, **129**: 61-85.
- Dawson, J. B., Pinkerton, H., Pyle, D. M. and Nyamweru, C. (1994a). June 1993 eruption of Oldoinyo Lengai, Tanzania - exceptionally viscous and large carbonatite lava flows and evidence for coexisting silicate and carbonate magmas. Geology, **22**: 799-802.
- Dawson, J. B., Smith, J. V. and Steele, I. M. (1994b). Trace-element distribution between coexisting perovskite,apatite and titanite from Oldoinyo Lengai, Tanzania. Chemical Geology, **117**.
- Dawson, J. B., Smith, J. V. and Steele, I. M. (1995). Petrology and mineral chemistry of plutonic igneous xenoliths from the carbonatite volcano, Oldoinyo Lengai, Tanzania. Journal of Petrology, **36**: 797-826.
- Dawson, J. B., Steele, I. M., Smith, J. V. and Rivers, M. L. (1996). Minor and trace element chemistry of carbonates, apatites and magnetites in some African carbonatites. Mineralogical Magazine, **60**: 415-425.
- Deer, W. A., Howie, R. A. and Zussman, J. (1992). An introduction to rock-forming minerals. Essex, Longman. 2nd ed 695p.
- Deines, P. (1989). Stable isotope variations in carbonatites. In K. Bell, Ed., Carbonatites: genesis and evolution. London, Unwin Hyman, 301-359.
- Deines, P. and Gold, D. P. (1973). The isotopic composition of carbonatite and kimberlite carbonates and their bearing on the isotopic composition of deep-seated carbon. Geochimica et Cosmochimica Acta, **37**: 1700-1733.
- Demeny, A. and Harangi, S. (1996). Stable isotope studies and processes of carbonate formation in Hungarian alkali basalts and lamprophyres: evolution of magmatic fluids and magma-sediment interactions. Lithos, **37**: 335-349.
- Dingwell, D. B. and Brearley, M. (1985). Mineral chemistry of igneous melanite garnets from analcite-bearing volcanic rocks, Alberta, Canada. Contributions to Mineralogy and Petrology, **90**: 29-35.
- Dominguez, J. M. L. and Misi, A. (1993). O craton do São Francisco. Salvador, SBG BA-SE/SGM/CNPq. 215p.
- Dowty, E. (1971). Crystal chemistry of titanian and zirconian garnet: I. review and spectral studies. American Mineralogist, **56**: 1983-2009.

- Droop, G. T. R. (1987). A general equation for estimating Fe^{3+} concentrations in ferromagnesian silicates and oxides from microprobe analyses, using stoichiometric criteria. Mineralogical Magazine, **51**: 431-435.

- Dyar, M. D. (1987). A review of Mossbauer data on trioctahedral micas: evidence for tetrahedral $Fe3^+$ and cation ordering. American Mineralogist, **72**: 102-112.

- Dymek, R. F. (1983). Titanium, aluminum and interlayer cation substitutions in biotite from high-grade gneisses, West Greenland. American Mineralogist, **68**: 880-899.

- Edgar, A. D. (1979). Mineral chemistry and petrogenesis of an ultrapotassic-ultramafic volcanic rock. Contributions to Mineralogy and Petrology, **71**: 171-175.

- Edgar, A. D. and Arima, M. (1983). Conditions of phlogopite crystallization In ultrapotassic volcanic rocks. Mineralogical Magazine, **47**: 11-19.

- Epstein, S., Graf, D. L. and Degens, E. T. (1964). Oxygene isotope studies on the origin of dolomites. In H. Craig, Miller and G. J. Wasserburg, Eds., Isotopic and Cosmic Chemistry. Amsterdam, North Holland Publishing Co, 169-180.

- Farmer, G. L. and Boetcher, A. L. (1981). Petrologic and crystal-chemical significance of some deep-seated phlogopites. American Mineralogist, **66**: 1154-1163.

- Fehr, K. T. and Amthauer, G. (1996). Comment on "Morimotoite, $Ca_3TiFe^{2+}Si_3O_{12}$, a new titanian garnet from Fuka, Okayama Prefecture, Japan" by Henmi et al. (1995). Mineralogical Magazine, **60**: 842-845.

- Flohr, M. J. K. and Ross, M. (1989). Alkaline igneous rocks of Magnet Cove, Arkansas: Metasomatized ijolite xenoliths from Diamond Jo quarry. American Mineralogist, **74**: 113-131.

- Flohr, M. J. K. and Ross, M. (1990). Alkaline igneous rocks of Magnet Cove, Arkansas: Mineralogy and geochemistry of syenites. Lithos, **26**: 67-98.

- Foley, S. F., Venturelli, G., Green, D. H. and Toscani, L. (1987). The ultrapotassic rocks - characteristics, classification, and constraints for petrogenetic models. Earth-Science Reviews, **24**: 81-134.

- Fonseca, M. A. and Dardenne, M. A. (1996). Arcabouço estrutural e evolução cinemática da Faixa Brasília em seu segmento setentrional. 39 Congresso Brasileiro de Geologia (Anais). Salvador, SBG/CPM, 98-101.

- Fonseca, M. A., Dardenne, M. A. and Uhlein, A. (1995). Faixa Brasília setor setentrional: estilos estruturais e arcabouço tectônico. Revista Brasileira de Geociências, **25**: 267-278.

- Forbes, W. C. and Flower, M. F. J. (1974). Phase relations of titan-phlogopite, $K_2Mg_4TiAl_2Si_6O_{20}(OH)_4$: a refractory phase in the upper mantle? Earth and Planetary Science Letters, **22**: 60-66.

- Fuck, R. A. (1994). A Faixa Brasília e a compartimentação tectônica na Província Tocantins. 4 Simpósio de Geologia do Centro-Oeste 184-187.

- Fuck, R. A., Jardim de Sá, E. F., Pimentel, M. M., Dardenne, M. A. and Pedrosa-Soares, A. C. (1993). As faixas de dobramento marginais do Craton do São Francisco: síntese dos conhecimentos. In J. M. L. Dominguez and A. Misi, Eds., O Craton do São Francisco. Salvador, SBG/SGM/CNPq, 161-185.

- Fuck, R. A., Pimentel, M. M. and Silva, L. J. H. D. (1994). Compartimentação tectônica da porção oriental da Província Tocantins. 38 Congresso Brasileiro de Geologia (Boletim de Resumos Expandidos). Camboriu, SBG, 1. 215-216.

- Gaspar, J. C. (1989). Geologie et mineralogie du complexe carbonatitique de Jacupiranga, Bresil. (Universite d'Orleans, Ph. D. Thesis), 343p.

- Gaspar, J. C., Araújo, A. L. N. and Melo, M. V. L. C. (1998). Olivine in carbonatitic and silicate rocks in carbonatite complexes. 7th International Kimberlite Conference (Extended Abstracts). Cape Town 239-241.

- Gaspar, J. C. and Araújo, D. P. (1995). Reaction products of carbonatite with ultramafic rocks in the Catalão I complex, Brazil: possible implications for mantle metasomatism. 6th International Kimberlite Conference (Extended Abstracts). Novosibirsk, Russia 181-183.

- Gaspar, J. C., Silva, A. J. G. C. and Araújo, D. P. (1994). Composition of priderite in phlogopitites from the Catalão I carbonatite complex, Brazil. Mineralogical Magazine, **58**: 409-415.

- Gaspar, J. C. and Wyllie, P. J. (1982). Barium phlogopite from the Jacupiranga carbonatite, Brazil. American Mineralogist, **67**: 997-1000.

- Gaspar, J. C. and Wyllie, P. J. (1983a). Ilmenite (High Mg, Mn, Nb) In the Carbonatites From the Jacupiranga Complex, Brazil. American Mineralogist, **68**: 960-971.

- Gaspar, J. C. and Wyllie, P. J. (1983b). Magnetite in the carbonatites from the Jacupiranga complex, Brazil. American Mineralogist, **68**: 195-213.

- Gaspar, J. C. and Wyllie, P. J. (1987). The phlogopites from the Jacupiranga carbonatite intrusions. Mineralogy and Petrology, **36**: 121-134.

- Ghiorso, M. S. and Sack, R. O. (1991). Fe-Ti oxide geothermometry: thermodynamic formulation and the estimation of intensive variables in silicic magmas. Contributions to Mineralogy and Petrology, **108**: 485-510.

- Gibson, S. A., Thompson, R. N., Dickin, A. P. and Leonardos, O. H. (1995a). High-Ti and low-Ti mafic potassic magmas: Key to plume-lithosphere interactions and continental flood-basalt genesis. Earth and Planetary Science Letters, **136**: 149-165.

- Gibson, S. A., Thompson, R. N., Dickin, A. P. and Mitchell, J. G. (1997a): Temporal variation in magma sources related to the impact of the Tristan mantle plume. In C. J. Hatton, Ed. PPM'97 International Symposium on plumes, plates & mineralisation (Abstracts). Pretoria, South Africa 37-38.

- Gibson, S. A., Thompson, R. N., Leonardos, O. H., Dickin, A. P. and Mitchell, J. G. (1995b). The Late Cretaceous impact of the Trindade mantle plume - evidence from large-volume, mafic, potassic magmatism in SE Brazil. Journal of Petrology, **36**: 189-229.

- Gibson, S. A., Thompson, R. N., Leonardos, O. H., Turner, S. E., Mitchell, J. G. and Dickin, A. P. (1994). The Serra do Bueno potassic diatreme - a possible hypabyssal equivalent of the ultramafic alkaline volcanics in the late Cretaceous Alto Paranaiba Igneous Province, SE Brazil. Mineralogical Magazine, **58**: 357-373.

- Gibson, S. A., Thompson, R. N., Weska, R. K., Dickin, A. P. and Leonardos, O. H. (1997b). Late Cretaceous rift-related upwelling and melting of the Trindade starting mantle plume head beneath western Brazil. Contributions to Mineralogy and Petrology, **126**: 303-314.

- Gierth, E. and Baecker, M. L. (1986). A mineralização de nióbio e as rochas alcalinas associadas no complexo Catalão I, Goiás. In C. Schobbenhaus, Ed., Principais depósitos minerais do Brasil. Brasília, Mme/Dnpm, **2:** 456-462.

- Goldsmith, J. R. and Newton, R. C. (1969). P-T-X relations in the system $CaCO_3$-$MgCO_3$ at high temperatures and pressures. American Journal of Science, **267-A**: 160-190.

- Gomes, C. B. (1969). Electron microprobe analysis of zoned melanites. American Mineralogist, **54**: 1654-1661.

- Gomes, C. B., Comin-Chiaramonti, P., Velázquez, V. F. and Orué, D. (1996a). Alkaline Magmatism in Paraguay: a review. In P. Comin-Chiaramonti and C. B. Gomes, Eds., Alkaline magmatism in Central-Eastern Paraguay. Relationships with coeval magmatism in Brazil. São Paulo, Edusp/Fapesp, 31-56.

- Gomes, C. B., Morbidelli, L., Ruberti, E. and Comin-Chiaramonti, P. (1996b). Comparative aspects between post-Palaeozoic alkaline rocks from the western and eastern margins of the Paraná Basin. In P. Comin-Chiaramonti and C. B. Gomes, Eds., Alkaline magmatism in Central-Eastern Paraguay. Relationships with coeval magmatism in Brazil. São Paulo, Edusp/Fapesp, 249-274.

- Gomes, C. B., Ruberti, E. and Morbidelli, L. (1990). Carbonatite complexes from Brazil: a review. Journal of South American Earth Sciences, **3**: 51-63.

- Gonzaga, G. M. and Tompkins, L. A. (1991). Geologia do diamante. , Principais depósitos minerais do Brasil. Brasília, DNPM/CPRM, **4a:** 42-58.

- Grossi Sad, J. H. and Torres, N. (1976). Geology and mineral resources of the Barreiro complex, Araxá, Minas Gerais. 1st International Symposium on Carbonatites . Poços de Caldas, Brazil 307-312.

- Guimarães, I. G., Amaral, M. A. M. and Garcia, L. R. A. (1980). Uncompahgrito de Tapira, MG. 31st Congresso Brasileiro de Geologia (Anais). Balneário de Camboriú, Santa Catarina, Brazil 4. 2050-2058.

- Haggerty, S. E. and Mariano, A. N. (1983). Strontian-loparite and strontio-chevkinite: two new minerals in reomorphic fenites from the Paraná Basin carbonatites, South America. Contributions to Mineralogy and Petrology, **84**: 365-381.

- Hamilton, D. L., Bedson, P. and Esson, J. (1989). The behaviour of trace elements in the evolution of carbonatites. In K. Bell, Ed., Carbonatites: genesis and evolution. London, Unwin Hyman, 405-427.

- Haralyi, N. L. E. and Hasui, Y. (1982). The gravimetric information and the archean-proterozoic structural framework of eastern Brazil. Revista Brasileira de Geociências, **12**: 160-166.

- Harmer, R. E. and Gittins, J. (1998). The case for primary, mantle-derived carbonatite magma. Journal of Petrology, **39**: 1895-1904.

- Hasui, Y. and Cordani, U. G. (1968). Idades Potássio-Argônio de rochas eruptivas mesozóicas do oeste mineiro e sul de Goiás. 22nd Congresso Brasileiro de Geologia 139-143.

- Heathcote, R. C. and McCormick, G. R. (1989). Major-cation substitution in phlogopite and evolution of carbonatite in the Potash Sulfur Springs complex, Garland County, Arkansas. American Mineralogist, **74**: 132-140.

- Henmi, C., Kusachi, I. and Henmi, K. (1995). Morimotoite, $Ca_3TiFe^{2+}Si_3O_{12}$, a new titanian garnet from Fuka, Okayama Prefecture, Japan. Mineralogical Magazine, **59**: 115-120.

- Herz, N. (1977). Timing of spreading in the South Atlantic: information from Brazilian alkalic rocks. Geological Society of America Bulletin, **88**: 101-112.

- Hinton, R. W. and Upton, B. G. J. (1991). The chemistry of zircon: variations within and between large crystals from syenite and alkali basalt xenoliths. Geochimica et Cosmochimica Acta, **55**: 3287-3302.

- Howie, R. A. and Woolley, A. R. (1968). The role of titanium and the effect of TiO_2 on the cell-size, refractive index, and specific gravity in the andradite-melanite-schorlomite series. Mineralogical Magazine, **36**: 775-790.

- Huggins, F. E., Virgo, D. and Huckenholz, H. G. (1977a). Titanium-containing silicate garnets. I. The distribution of Al, Fe^{2+}, and Ti^{4+} between octahedral and tetrahedral sites. American Mineralogist, **62**: 475-490.

- Huggins, F. E., Virgo, D. and Huckenholz, H. G. (1977b). Titanium-containing silicate garnets. II. The crystal chemistry of melanites and schorlomites. American Mineralogist, **62**: 646-665.

- Issa Filho, A., Lima, P. R. A. S. and Souza, O. M. (1984). Aspectos da geologia do complexo carbonatítico do Barreiro, Araxá, MG, Brasil. In CBMM, Ed., Complexos Carbonatiticos do Brasil: Geologia. São Paulo, CBMM, 20-44.

- Ivanikov, V. V., Rukhlov, A. S. and Bell, K. (1998). Magmatic evolution of the melilitite-carbonatite-nephelinite dyke series of the Turiy Peninsula (Kandalaksha Bay, White Sea, Russia). Journal of Petrology, **39**: 2043-2061.

- Jago, B. C. and Gittins, J. (1993). Pyrochlore crystallization in carbonatites: the role of fluorine. South African Journal of Geology, **96**: 149-159.

- Javoy, M., Pineau, F. and Delorme, H. (1986). Carbon and nitrogen isotopes in the mantle. Chemical Geology, **57**: 41-62.

- Javoy, M., Pineau, F. and Iiyama, I. (1978). Experimental determination of the isotopic fractionation between gaseous CO2 and Carbon dissolved in tholeiitic magma - a preliminary study. Contributions to Mineralogy and Petrology, **67**: 35-39.

- Jones, A. P. and Pecket, A. (1980). Zirconium-bearing aegerines from Motzfeldt, South Greenland. Contributions to Mineralogy and Petrology, **75**: 251-255.

- Jones, A. P. and Wyllie, P. J. (1984). Minor elements in perovskite from kimberlites and the distribution of rare-earth elements: and electron probe study. Earth and Planetary Science Letters, **69**: 128-140.

- Jones, J. H., Walker, D., Pickett, D. A., Murrell, M. T. and Beattie, P. (1995). Experimental Investigations Of the Partitioning Of Nb, Mo, Ba, Ce, Pb, Ra, Th, Pa, and U Between Immiscible Carbonate and Silicate Liquids. Geochimica et Cosmochimica Acta, **59**: 1307-1320.

- Junqueira-Brod, T. C. (1998). Cretaceous alkaline igneous rocks from the Aguas Emendadas region, Goias, Central Brazil. (University of Durham, M. Sc.), 161p.

- Keep, M. and Russell, J. K. (1992). Mesozoic alkaline rocks of the Averill plutonic complex. Canadian Journal of Earth Sciences, **29**: 2508-2520.

- Kerr, A. C., Kempton, P. D. and Thompson, R. N. (1995). Crustal assimilation during turbulent magma ascent (ATA); new isotopic evidence from the Mull Tertiary lava succession, N. W. Scotland. Contributions to Mineralogy and Petrology, **119**: 142-154.

- Kjarsgaard, B. A. (1998). Phase relations of a carbonated high-CaO nephelinite at 0.2 and 0.5 GPa. Journal of Petrology, **39**: 2034-2042.

- Kostopoulos, D. K. (1991). Melting of the shallow upper mantle: a new perspective. Journal of Petrology, **32**: 671-699.

- Kresten, P., Fels, P. and Berggren, G. (1975). Kimberlitic zircons - a possible aid in prospecting for kimberlites. Mineralium Deposita, **10**: 47-56.

- Kühberger, A., Fehr, T., Huckenholz, H. G. and Amthauer, G. (1989). Crystal chemistry of a natural schorlomite and Ti-andradites synthesized at different oxygen fugacities. Physics and Chemistry of Minerals, **16**: 734-740.

- Lalonde, A. E., Rancourt, D. G. and Chao, G. Y. (1996). Fe-bearing trioctahedral micas from Mont Saint-Hilaire, Quebec, Canada. Mineralogical Magazine, **60**: 447-460.

- Lanyon, R. and Le Roex, A. P. (1995). Petrology of the alkaline and ultramafic lamprophyres associated with the Okenyenya igneous complex, northwestern Namibia. S. Afr. Tydskr. Geol., **98**: 140-156.

- Larsen, L. M. (1976). Clinopyroxenes and coexisting mafic minerals from the alkaline Ilimaussaq intrusion, South Greenland. Journal of Petrology, **17**: 258-290.

- Laughlin, A. W., Charles, R. W. and Aldrich, M. J. (1989). Heteromorphism and crystallization paths of katungites, Navajo volcanic field, Arizona, USA. , Kimberlites and related rocks, Geological Society of Australia (Special Publication 14), 582-591.

- Lavecchia, G. and Stoppa, F. (1996). The tectonic significance of Italian magmatism - an alternative view to the popular interpretation. Terra Nova, **8**: 435-446.

- Le Bas, M. J. (1985). Nephelinites and Carbonatites. Journal of the Geological Society of London, **142**: p.704.

- Le Bas, M. J. (1987). Nephelinites and carbonatites. In J. G. Fitton and B. G. J. Upton, Eds., Alkaline Igneous Rocks. London, Geological Society of London (Special Publication 30), 53-83.

- Le Bas, M. J. (1989). Diversification of carbonatite. In K. Bell, Ed., Carbonatites: genesis and evolution. London, Unwin Hyman, 428-447.

- Le Bas, M. J., Keller, J., Kejie, T., Wall, F., Williams, C. T. and Peishan, Z. (1992). Carbonatite dykes at Bayan Obo, Inner-Mongolia, China. Mineralogy and Petrology, **46**: 195-228.

- Le Maitre, R. W., Bateman, P., Dudek, A., Keller, J., Lameyre, J., Le Bas, M. J., Sabine, P. A., Schmid, R., Sorensen, H., Streckeisen, A., Woolley, A. R. and Zanettin, B. (1989). A classification of Igneous rocks and glossary of terms: recommendations of the International Union of Geological Sciences Subcommission on the Systematics of Igneous Rocks. Oxford, UK, Blackwell Scientific Publications. 193p.

- Le Roex, A. P. and Lanyon, R. (1998). Isotope and trace element geochemistry of Cretaceous Damaraland lamprophyres and carbonatites, Northwestern Namibia: evidence for plume-lithosphere interactions. Journal of Petrology, **39**: 1177-1146.

- Lechler, P. J. and Desilets, M. O. (1987). A review of the use of Loss on Ignition as a measurement of total volatiles in whole-rock analysis. Chemical Geology, **63**: 341-344.

- Lee, W. J. and Wyllie, P. J. (1996). Liquid immiscibility in the join NaAlSi3O8-CaCO3 to 2.5 GPa and the origin of calciocarbonatite magmas. Journal of Petrology, **37**: 1125-1152.

- Lee, W. J. and Wyllie, P. J. (1997a). Liquid immiscibility between nephelinite and carbonatite from 1.0 to 2.5 GPa compared with mantle compositions. Contributions to Mineralogy and Petrology, **127**: 1-16.

- Lee, W. J. and Wyllie, P. J. (1997b). Liquid immiscibility in the join NaAlSiO4-NaAlSi3O8-CaCO3 at 1 GPa: Implications for crustal carbonatites. Journal of Petrology, **38**: 1113-1135.

- Lee, W. J. and Wyllie, P. J. (1998a). Petrogenesis of carbonatite magmas from mantle to crust, constrained by the system CaO - (MgO + FeO*) - (Na2O + K2O) - (SiO2 + Al2O3 + TiO2) - CO2. Journal of Petrology, **39**: 495-517.

- Lee, W. J. and Wyllie, P. J. (1998b). Processes of crustal carbonatite formation by liquid immiscibility and differentiation, elucidated by model systems. Journal of Petrology, **39**: 2005-2014.

- Leonardos, O. H., Carvalho, J. B., Tallarico, F. H. B., Gibson, S. A., Thompson, R. N., Meyer, H. O. A. and Dickin, A. P. (1993). O xenólito de granada lherzolito de Três Ranchos 4: uma rocha matriz do diamante na província magmática cretácea do Alto Paranaíba. 1st Simpósio de Geologia do Diamante (Anais). Cuiabá, Universidade Federal do Mato Grosso, Special Publication 2/93. 3-16.

- Leonardos, O. H., Ulbrich, M. N. and Gaspar, J. C. (1991). The Mata da Corda volcanic rocks. In O. H. Leonardos, H. O. A. Meyer and J. C. Gaspar, Eds., 5th International Kimberlite Conference (Field Guidebook). Araxá, Brazil, CPRM, Special Publication 3/91. 17-24.

- Lesquer, A., Almeida, F. F. M., Davino, A., Lachaud, J. C. and Mallard, P. (1981). Importance structurale des anomalies gravimetriques de la partie sud du craton fu Sao Francisco et de sa bordure occidentalle (Bresil). Tectonophysics, **76**: 273-293.

- Lindsley, D. H. (1983). Pyroxene thermometry. American Mineralogist, **68**: 477-493.

- Lloyd, F. E. and Bailey, D. K. (1991). Complex mineral textures in bebedourite: possible links with alkali clinopyroxenite xenoliths and kamafugitic volcanism. In O. H. Leonardos, H. O. A. Meyer and J. C. Gaspar, Eds., 5th International Kimberlite Conference (Extended Abstracts). Araxá, Brazil, CPRM, Special Publication 3/91. 263-269.

- Locock, A., Luth, R. W., Cavell, R. G., Smith, D. G. W. and Duke, M. J. M. (1995). Spectroscopy of the cation distribution in the schorlomite species of garnet. American Mineralogist, **80**: 27-38.

- Lupini, L., Williams, C. T. and Woolley, A. R. (1992). Zr-rich garnet and Zr-rich and Th-rich perovskite from the Polino carbonatite, Italy. Mineralogical Magazine, **56**: 581-586.

- Luth, W. C. (1967). Studies in the system KALSiO4 - Mg2SiO4 - SiO2 - H2O: I, inferred phase relations and petrologic applications. Journal of Petrology, **8**: 372-416.

- Machado Junior, D. L. (1992a). Geologia do complexo alcalino-carbonatítico de Catalão II (GO). 37th Congresso Brasileiro de Geologia (Boletim de Resumos Expandidos). São Paulo, Brazil 94-95.

- Machado Junior, D. L. (1992b). Idades Rb/Sr do complexo alcalino-carbonatítico de Catalão II (GO). 37th Congresso Brasileiro de Geologia (Boletim de Resumos Expandidos). São Paulo, Brazil 91-93.

- Malitesta, C., Losito, I., Scordari, F. and Schingaro, E. (1995). XPS investigation of titanium in Melanites from Monte Vulture (Italy). European Journal of Mineralogy, **7**: 847-858.

- Manning, P. G. and Harris, D. C. (1970). Optical-absorption and electron-microprobe studies of some high-Ti andradites. Canadian Mineralogist, **10**: 260-271.

- Mariano, A. N. and Marchetto, M. (1991). Serra Negra and Salitre - carbonatite alkaline igneous complex. In O. H. Leonardos, H. O. A. Meyer and J. C. Gaspar, Eds., 5th International Kimberlite Conference (Field Guide Book). Araxá, Brazil, CPRM, Special Publication 3/91. 75-79.

- Mariano, A. N. and Mitchell, R. H. (1991). Mineralogy and geochemistry of perovskite-rich pyroxenites. 5th International Kimberlite Conference . Araxá, Minas Gerais, Brazil 251-253.

- Marini, O. J., Fuck, R. A., Danni, J. C., Dardenne, M. A., Loguércio, S. O. and Ramalho, R. (1984). As faixas de dobramento Brasília, Uruaçu e Paraguai-Araguaia, e o Maciço Mediano de Goiás. In C. Schobbenhaus Filho, D. A. Campos, G. R. Derze *et al.* , Eds., Geologia do Brasil - Texto Explicativo do Mapa Geológico do Brasil e da Área Oceânica Adjacente Incluindo Depósitos Minerais, Escala 1:2.500.000, DNPM/MME, 251-303.

- Mattey, D. P., Taylor, W. R., Green, D. H. and Pillinger, C. T. (1990). Carbon isotopic fractionation between CO2 vapour, silicate and carbonate melts: an experimental study to 30 kbar. Contributions to Mineralogy and Petrology, **104**: 492-505.

- McBirney, A. R. (1998). The Skaergaard Layered Series. Part V. Included trace elements. Journal of Petrology, **39**: 255-276.

- McBirney, A. R. and Hunter, R. H. (1995). The cumulate paradigm reconsidered. Journal of Geology, **103**: 114-122.

- McBirney, A. R. and Nicolas, A. (1997). The Skaergaard Layered Series. Part II. Magmatic flow and dynamic layering. Journal of Petrology, **38**: 569-580.

- McCormick, G. R. and Heathcote, R. C. (1987). Mineral chemistry and petrogenesis of carbonatite intrusions, Perry and Conway Counties, Arkansas. American Mineralogist, **72**: 59-66.

- McCormick, G. R. and Le Bas, M. J. (1996). Phlogopite crystallization in carbonatitic magmas from Uganda. Canadian Mineralogist, **34**: 469-478.

- McDonald, I., Dewit, M. J., Smith, C. B., Bizzi, L. A. and Viljoen, K. S. (1995). The geochemistry of the platinum-group elements in Brazilian and Southern African kimberlites. Geochimica et Cosmochimica Acta, **59**: 2883-2903.

- McKenzie, D. (1989). Some remarks on the movement of small melt fractions in the mantle. Earth and Planetary Science Letters, **95**: 53-72.

- Meurer, W. P. and Boudreau, A. E. (1998a). Compaction of igneous cumulates part I: Geochemical consequences for cumulates and liquid fractionation trends. Journal of Geology, **106**: 281-292.

- Meurer, W. P. and Boudreau, A. E. (1998b). Compaction of igneous cumulates part II: Compaction and the development of igneous foliations. Journal of Geology, **106**: 293-304.

- Milner, S. C., Duncan, A. R., Whittingham, A. M. and Ewart, A. (1995a). Trans-Atlantic correlation of eruptive sequences and individual silicic volcanic units within the Paraná-Etendeka igneous province. Journal of Volcanology and Geothermal Research, **69**: 137-157.

- Milner, S. C. and Le Roex, A. P. (1996). Isotope characteristics of the Okenyenya igneous complex, northwestern Namibia: constraints on the composition of the early Tristan plume and the origin of the EM1 mantle component. Earth and Planetary Science Letters, **141**: 277-291.

- Milner, S. C., Le Roex, A. P. and O'Connor, J. M. (1995b). Age of Mesozoic igneous rocks in northwestern Namibia, and their relationship to continental breakup. Journal of the Geological Society of London, **152**: 97-104.

- Mitchell, R. H. (1979). The alleged kimberlite-carbonatite relationship: additional contrary mineralogical evidence. American Journal of Science, **279**: 570-589.

- Mitchell, R. H. (1995a). Compositional variation of micas in kimberlites, orangeites, lamproites and lamprophyres. 6th International Kimberlite Conference (Extended Abstracts). Novosibirsk, Russia 390-392.

- Mitchell, R. H. (1995b). Kimberlites, orangeites and related rocks. New York, Plenum Press. 410p.

- Mitchell, R. H. (1996a). Classification of undersaturated and related alkaline rocks. In R. H. Mitchell, Ed., Undersaturated alkaline rocks: mineralogy, petrogenesis, and economic potential, Mineralogical Association of Canada Short Course, **24:** 1-22.

- Mitchell, R. H. (1996b). The melilitite clan. In R. H. Mitchell, Ed., Undersaturated alkaline rocks: mineralogy, petrogenesis, and economic potential, Mineralogical Association of Canada Short Course, **24:** 123-151.

- Mitchell, R. H. (1996c). Perovskites: a revised classification scheme for an important rare earth element host in alkaline rocks. In A. P. Jones, F. Wall and C. T. Williams, Eds., Rare earth minerals: chemistry, origin and ore deposits. London, Chapman & Hall, **7:** 372.

- Mitchell, R. H. (1996d). Undersaturated potassic plutonic complexes. In R. H. Mitchell, Ed., Undersaturated alkaline rocks: mineralogy, petrogenesis, and economic potential, Mineralogical Association of Canada Short Course, **24:** 193-216.

- Mitchell, R. H. (1997). Preliminary studies of the solubility and stability of perovskite group compounds in the synthetic carbonatite system calcite-portlandite. Journal of African Earth Sciences, **25**: 147-158.

- Mitchell, R. H. and Bergman, S. C. (1991). Petrology of Lamproites. New York, Plenum Press. 447p.

- Mitchell, R. H. and Platt, R. G. (1979). Nepheline-bearing rocks from the Poohbah Lake complex, Ontario: malignites and malignites. Contributions to Mineralogy and Petrology, **69**: 255-264.

- Mitchell, R. H., Smith, C. B. and Vladykin, N. V. (1994). Isotopic composition of strontium and neodymium in potassic rocks of the Little-Murun Complex, Aldan Shield, Siberia. Lithos, **32**: 243-248.

- Mitchell, R. H. and Vladykin, N. V. (1993). Rare earth element-bearing tausonite and potassium barium titanates from the Little Murun potassic alkaline complex, Yakutia, Russia. Mineralogical Magazine, **57**: 651-664.

- Mitchell, R. H. and Vladykin, N. V. (1996). Compositional variation of pyroxene and mica from the Little Murun ultrapotassic complex, Aldan Shield, Russia. Mineralogical Magazine, **60**: 907-925.

- Mitchell, R. M. and Chakhmouradian, A. R. (1998). Th-rich loparite from the Khibina alkaline complex, Kola Peninsula: isomorphism and paragenesis. Mineralogical Magazine, **62**: 341-353.

- Moore, K. R. and Wood, B. J. (1998). The transition from carbonate to silicate melts in the CaO-MgO-SiO2-CO2 system. Journal of Petrology, **39**: 1943-1952.

- Morbidelli, L., Beccaluva, L., Brotzu, P., Conte, A. M., Garbarino, C., Gomes, C. B., Grossi-Sad, J. H., Riffel, B. F., Ruberti, E. and Traversa, G. (1995a). Aspectos mineralógicos e petrográficos de rochas ultramáficas e carbonatitos do complexo alcalino de Salitre, GO. 5th Congresso Brasileiro de Geoquímica . Niterói, Brazil, Sociedade Brasileira de Geoquímica, (CD-ROM edition).

- Morbidelli, L., Gomes, C. B., Beccaluva, L., Brotzu, P., Conte, A. M., Ruberti, E. and Traversa, G. (1995b). Mineralogical, petrological and geochemical aspects of alkaline and alkaline-carbonatite associations from Brazil. Earth-Science Reviews, **39**: 135-168.

- Morgan, W. J. (1983). Hot spot tracks and the early rifting of the Atlantic. Tectonophysics, **94**: 123-139.

- Morikiyo, T., Hirano, H. and Matsuhisa, Y. (1990). Carbon and oxygen isotopic composition of the carbonates from the Jacupiranga and Catalão I carbonatite complexes, Brazil. Bulletin of the Geological Survey of Japan, **41**: 619-626.

- Morimoto, N., Fabries, J., Ferguson, A. K., Ginzburg, I. V., Ross, M., Seifert, F. A., Zussmann, J., Aoki, K. and Gotardi, G. (1988). Nomenclature of pyroxenes. American Mineralogist, **73**: 1123-1133.

- Muntener, O. and Hermann, J. (1994). Titanian andradite in a metapyroxenite layer from the Malenco ultramafics (Italy) - implications for Ti-mobility and low oxygen fugacity. Contributions to Mineralogy and Petrology, **116**: 156-168.

- Nelson, D. R., Chivas, A. R., Chappell, B. W. and McCulloch, M. T. (1988). Geochemical and isotopic systematics in carbonatites and implications for the evolution of ocean-island sources. Geochimica et Cosmochimica Acta, **52**: 1-17.

- Nielsen, T. F. D. (1979). The occurrences and formation of Ti-aegirines in peralkaline syenites. An example from the Tertiary ultramafic Gardiner complex, East Greenland. Contributions to Mineralogy and Petrology, **69**: 235-244.

- Nimis, P. (1995). A clinopyroxene geobarometer for basaltic systems based on crystal-structure modelling. Contributions to Mineralogy and Petrology, **121**: 115-125.

- O'Brien, H. E., Irving, A. J., McCallum, S. and Thirlwall, M. F. (1995). Strontium, neodymium, and lead isotopic evidence for the interaction of post-subduction asthenospheric potassic mafic magmas of the Highwood Mountains, Montana, USA, with ancient Wyoming Craton lithospheric mantle. Geochimica et Cosmochimica Acta, **59**: 4539-4556.

- O'Connor, J. M. and Duncan, R. A. (1990). Evolution of the Walvis Ridge-Rio Grande Rise hot-spot system: Implications for African and South American plate motions over plumes. Journal of Geophysical Research, **95**: 17475-17502.

- Paslick, C. R., Halliday, A. N., Lange, R. A., James, D. and Dawson, J. B. (1996). Indirect crustal contamination: evidence from isotopic and chemical disequilibria in minerals from alkali basalts and nephelinites from northern Tanzania. Contributions to Mineralogy and Petrology, **125**: 277-292.

- Pearce, N. J. G. and Leng, M. J. (1996). The origin of carbonatites and related rocks from the Igaliko Dyke Swarm, Gardar Province, South Greenland: Field, geochemical and C-O-Sr-Nd isotope evidence. Lithos, **39**: 21-40.

- Peate, D. W., Hawkesworth, C. J. and Mantovani, M. S. M. (1992). Chemical stratigraphy of the Parana lavas (South America): classification of magma types and their spatial distribution. Bull. Volcanol., **55**: 119-139.

- Peccerillo, A., Poli, G. and Serri, G. (1988). Petrogenesis of orenditic and kamafugitic rocks from central Italy. Canadian Mineralogist, **26**: 45-65.

- Pedrosa-Soares, A. C., Dardenne, M. A., Hasui, Y., Castro, F. D. C. and Carvalho, M. V. A. (1994). Nota explicativa dos mapas geológico, metalogenético e de ocorrências minerais do estado de Minas Gerais. Escala 1:1.000.000. Belo Horizonte, COMIG - Companhia mineradora de Minas Gerais. 97p.

- Pedrosa-Soares, A. C., Noce, C. M., Vidal, P., Monteiro, R. L. B. P. and Leonardos, O. H. (1992). Toward a new tectonic model for the Late Proterozoic Araçuai (SE Brazil) West Congolian (SW Africa) belt. Journal of South American Earth Sciences, **6**: 33-47.

- Petibon, C. M., Kjarsgaard, B. A., Jenner, G. A. and Jackson, S. E. (1998). Phase relationships of a silicate-bearing natrocarbonatite from Oldoinyo Lengai at 20 and 100 MPa. Journal of Petrology, **39**: 2137-2152.

- Pimentel, M. M. and Fuck, R. A. (1992). Neoproterozoic crustal accretion in central Brazil. Geology, **20**: 375-379.

- Pimentel, M. M., Fuck, R. A. and De Alvarenga, C. J. S. (1996a). Post-Brasiliano (Pan-African) high-K granitic magmatism in Central Brazil: the role of Late Precambrian-Early Paleozoic extension. Precambrian Research, **80**: 217-238.

- Pimentel, M. M., Fuck, R. A. and Del'Rey-Silva, L. J. H. (1996b). Dados Rb-Sr e Sm-Nd da região de Jussara-Goiás-Mossamedes (GO), e o limite entre terrenos antigos do Maciço de Goiás e o Arco Magmático de Goiás. Revista Brasileira de Geociências, **26**: 61-70.

- Pimentel, M. M., Heaman, L. and Fuck, R. A. (1991). Zircon and sphene U-Pb geochronology of Upper Proterozoic volcanic-arc rock units from Southwestern Goiás, Central Brazil. Journal of South American Earth Sciences, **4**: 295-305.

- Pineau, F., Javoy, M. and Allegre, J. (1973). Etude systématique des isotopes de l'oxygène, du carbone et du strontium dans les carbonatites. Geochimica et Cosmochimica Acta, **37**: 2363-2377.

- Pires, F. R. M. (1986). The southern limits of the São Francisco craton. Anais da Academia Brasileira de Ciências, **58**: 139-145.

- Platt, R. G. (1994). Perovskite, loparite and Ba-Fe hollandite from the Schryburt Lake carbonatite complex, Northwestern Ontario, Canada. Mineralogical Magazine, **58**: 49-57.

- Platt, R. G. (1996a). The ijolite-series rocks. In R. H. Mitchell, Ed., Undersaturated alkaline rocks: mineralogy, petrogenesis and economic potential, Mineralogical Association of Canada Short Course, **24:** 101-121.

- Platt, R. G. (1996b). Nepheline syenite complexes - an overview. In R. H. Mitchell, Ed., Undersaturated alkaline rocks: mineralogy, petrogenesis and economic potential, Mineralogical Association of Canada Short Course, **24:** 63-99..

- Platt, R. G. and Mitchell, R. H. (1979). The Marathon dikes. I: Zirconium-rich titanian garnets and manganoan magnesian ulvospinel-magnetite spinels. American Mineralogist, **64**.

- Potts, P. J., Tindle, A. G. and Webb, P. C. (1992). Geochemical reference material compositions - Rocks, minerals, sediments, soils, carbonates, refractories and ores used in research and industry. Caithness, UK, Whittles Publishing/CRC Press. 313p.

- Powell, R., Condliffe, D. M. and Condliffe, E. (1984). Calcite-dolomite geothermometry in the system $CaCO_3$ - $MgCO_3$ - $FeCO_3$: an experimental study. Journal of Metamorphic Geology, **2**: 33-41.

- Quon, S. H. and Heinrich, E. W. (1966). Abundance and significance of some minor elements in carbonatitic calcites and dolomites. Mineralogical Society of India, IMA volume: 29-35.

- Ranlov, J. and Dymek, R. F. (1991). Compositional zoning in hydrothermal aegirine from fenites in the Proterozoic Gardar Province, South Greenland. European Journal of Mineralogy, **3**: 837-853.

- Rass, I. T. (1997). Morimotoite, a new titanian garnet? - discussion. Mineralogical Magazine, **61**: 728-730.

- Reed, S. B. J. (1996). Electron microprobe analysis and scanning electron microscopy in geology. Cambridge, Cambridge University Press. 201p.

- Reid, A. M., Donaldson, C. H., Dawson, J. B. and Brown, R. W. (1975). The Igwisi Hills extrusive "kimberlites". Physics and Chemistry of the Earth, **9**: 199-219.

- Reid, D. L. and Cooper, A. F. (1992). Oxygen and carbon isotope patterns in the Dicker-Willem carbonatite complex, southern Namibia. Chemical Geology, **94**: 293-305.

- Righter, K. and Carmichael, I. S. E. (1996). Phase-equilibria of phlogopite lamprophyres from western Mexico- biotite-liquid equilibria and P-T estimates for biotite-bearing igneous rocks. Contributions to Mineralogy and Petrology, **123**: No.1,1-21.

- Robert, J. L. (1976). Titanium solubility in synthetic phlogopite solid solutions. Chemical Geology, **17**: 213-227.

- Roeder, P. L. and Emslie, R. F. (1970). Olivine-liquid equilibrium. Contributions to Mineralogy and Petrology, **29**: 275-289.

- Santos, R. V. (1994). Oxygen and carbon isotopes in alkaline carbonatite complexes. (University of Chicago, Ph.D.), 187p.

- Santos, R. V. and Clayton, R. N. (1995). Variations of oxygen and carbon isotopes in carbonatites - a study of Brazilian alkaline complexes. Geochimica et Cosmochimica Acta, **59**: 1339-1352.

- Santos, R. V., Dardenne, M. A. and Matsui, E. (1990). Geoquímica de isótopos de carbono e oxigênio dos carbonatitos do Complexo Alcalino de Mato Preto, Paraná, Brasil. Revista Brasileira de Geociências: 153-158.

- Sasada, T., Hiyagon, H., Bell, K. and Ebihara, M. (1997). Mantle-derived noble gases in carbonatites. Geochimica et Cosmochimica Acta, **61**: 4219-4228.

- Schobbenhaus Filho, C., Campos, D. A., Derze, G. R. and Asmus, H. E. (1984). Geologia do Brasil - Texto explicativo do mapa geológico do Brasil e da área oceânica adjacente incluindo depósitos minerais, Escala 1:2.500.000, DNPM/MME. 114 p + Map.

- Schubert, G. and Tackley, P. J. (1995). Mantle dynamics: the strong control of the spinel-perovskite transition at a depth of 660 km. Journal of Geodynamics, **20**: 417-428.

- Secher, K. and Larsen, L. M. (1980). Geology and mineralogy of the Sarfartôq carbonatite complex, southern West Greenland. Lithos, **13**: 199-212.

- Seer, H. J. and Moraes, L. C. (1988). Estudo petrográfico das rochas ígneas alcalinas da região de Lagoa Formosa, MG. Revista Brasileira de Geociências, **18**: 134-140.

- Seer, H. J., Moraes, L. C. M. and Fogaça, A. C. C. (1989). Roteiro geológico para a região de Lagoa Formosa-Chumbo-Carmo do Paranaíba, MG. Belo Horizonte, SBG-MG. 58p.

- Seifert, W. and Kampf, H. (1994). Ba-enrichment in phlogopite of a nephelinite from Bohemia. European Journal of Mineralogy, **6**: 497-502.

- Sgarbi, P. B. A., Clayton, R. N., Mayeda, T. K. and Gaspar, J. C. (1998). Oxygen isotope thermometry of Brazilian potassic volcanic rocks of kamafugitic affinities. Chemical Geology, **146**: 115-126.

- Sgarbi, P. B. A. and Gaspar, J. C. (1995). Perovskites from the Mata da Corda kamafugites, MG, Brazil. 6th International Kimberlite Conference (Extended Abstracts). Novosibirsk, Russia 498-499.

- Sgarbi, P. B. A. and Valença, J. G. (1994). Mineral and rock chemistry of the Mata da Corda kamafugitic rocks (MG State, Brazil). International Symposium on the Physics and Chemistry of the Upper Mantle (Extended Abstracts). São Paulo, Brazil, CPRM/FAPESP, 27-29.

- Sgarbi, P. B. D. and Valença, J. G. (1993). Kalsilite in Brazilian kamafugitic rocks. Mineralogical Magazine, **57**: 165-171.

- Silva, A. B. (1986). Jazida de nióbio de Araxá, Minas Gerais. In C. Schobbenhaus, Ed., Principais depósitos minerais do Brasil. Brasília, MME/DNPM, **2:** 456-462.

- Simkin, T. and Smith, J. V. (1970). Minor-element distribution in olivine. Journal of Geology, **78**: 304-325.

- Soares, P. C., Fiori, A. P. and Carvalho, S. G. (1990). Tectônica colisional oblíqua entre o Bloco Paraná e a margem sul do Craton do São Francisco, no Maciço de Guaxupé. 36th Congresso Brasileiro de Geologia (Anais). Natal, RN, SBG, 6. 2723-2734.

- Sonoki, I. K. and Garda, G. M. (1988). Idades K-Ar de rochas alcalinas do Brasil Meridional e Paraguai Oriental: compilação e adaptação as novas constantes de decaimento. Boletim do IG USP Serie Cientifica, **19**: 63-85.

- Stoppa, F. and Cundari, A. (1995). A new Italian carbonatite occurrence at Cupaello (Rieti) and its genetic significance. Contributions to Mineralogy and Petrology, **122**: 275-288.

- Stoppa, F. and Lavecchia, G. (1992). Late Pleistocene ultra-alkaline magmatic activity in the Umbria-Latium region (Italy) - an overview. Journal of Volcanology and Geothermal Research, **52**: 277-293.

- Stoppa, F. and Lupini, L. (1993). Mineralogy and petrology of the Polino monticellite calciocarbonatite (central Italy). Mineralogy and Petrology, **49**: 213-231.

- Strieder, A. J. and Nilson, A. A. (1992). Melange ofiolítica nos metassedimentos Araxá de Abadiania (GO) e implicações tectônicas regionais. Revista Brasileira de Geociências, **22**: 204-215.

- Thompson, R. N., Gibson, S. A., Mitchell, J. G., Dickin, A. P., Leonardos, O. L., Brod, J. A. and Greenwood, J. C. (1998). Migrating Cretaceous-Eocene magmatism in the Serra do Mar alkaline province, SE Brazil: Melts from the deflected Trindade mantle plume? Journal of Petrology, **39**: 1493-1526.

- Thompson, R. N., Morrison, M. A., Hendry, G. L. and Parry, S. J. (1984). An assessment of the relative roles of crust and mantle in magma genesis: an elemental approach. Phil. Trans. R. Soc. London, **A310**: 549-590.

- Ting, W., Rankin, A. H. and Woolley, A. R. (1994). Petrogenetic significance of solid carbonate inclusions in apatite of the Sukulu carbonatite, Uganda. Lithos, **31**: 177-187.
- Tompkins, L. A. and Gonzaga, G. M. (1989). Diamonds in Brazil and a proposed model for the origin and distribution of diamonds in the Coromandel region, Minas Gerais, Brazil. Economic Geology, **84**: 591-602.
- Tompkins, L. A., Taylor, W. R., Ramsay, R. R. and Armstrong, R. (1998). The mineralogy and geochemistry of the kamafugitic Tres Barras Intrusion, Mata da Corda, Minas Gerais, Brazil. 7th International Kimberlite Conference (Extended Abstracts). Cape Town 920-922.
- Torres, M. G. (1996). Caracterização mineralógica do minério fosfático da mina da Arafértil S. A., no complexo carbonatítico do Barreiro, Araxá, MG. (Universidade de Brasília, M. Sc. Thesis), 149p.
- Toyoda, K., Horiuchi, H. and Tokonami, M. (1994). Dupal anomaly of Brazilian carbonatites - geochemical correlations with hotspots in the South-Atlantic and implications for the mantle source. Earth and Planetary Science Letters, **126**: 315-331.
- Tröger, E. (1928). Alkaligesteine aus der Serra do Salitre im westlichen Minas Geraes, Brasilien. Centralblatt für Mineralogie, Geologie und Paläontologie, **Abt A**: 202-204.
- Tröger, W. E. (1935). Speziell Petrographie der Eruptivegesteine - Ein nomenklatur-Kompendium. Berlin, Verlag der Deutschen Mineralogischen Gesellschaft. 360p.
- Trompette, R. R., Uhlein, A., Silva, M. E. and Karmann, I. (1992a). The Brasiliano São Francisco Craton revisited (central Brazil). Journal of South American Earth Sciences, **6**: 49-57.
- Trompette, R. R., Uhlein, A., Silva, M. E. and Karmann, I. (1992b). O craton brasiliano do São Francisco - Uma revisão. Revista Brasileira de Geociências, **22**: 481-486.
- Turner, S. T., Regelous, M., Kelley, S., Hawkesworth, C. and Mantovani, M. (1994). Magmatism and continental break-up in the South Atlantic: high precision ^{40}Ar-^{39}Ar geochronology. Earth and Planetary Science Letters, **121**: 333-348.
- Uhlein, A., Trompette, R. R. and Egydio-Silva, M. (1998). Proterozoic rifting and closure, SE border of the São Francisco Craton, Brazil. Journal of South American Earth Sciences, **11**: 191-203.
- Ulbrich, H. H. G. J. and Gomes, C. B. (1981). Alkaline rocks from continental Brazil. Earth-Science Reviews, **17**: 135-154.
- Ulrych, J., Povondra, P., Pivec, E., Rutsek, J. and Sitek, J. (1994). Compositional evolution of metasomatic garnet in melilitic rocks of the Osecna complex, Bohemia. Canadian Mineralogist, **32**: 637-647.
- Valeriano, C. M., Almeida, J. C. H., Amarante Simões, L. S., Duarte, B. P., Roig, H. L. and Heilbron, M. (1995). Evolução estrutural do domínio externo da Faixa Brasília no Sudoeste de Minas Gerais: registros de uma tectônica pre-Brasiliana. Revista Brasileira de Geociências, **25**: 221-234.
- VanDecar, J. C., James, D. E. and Assumpção, M. (1995). Seismic evidence for a fossil mantle plume beneath South America and implications for plate driving forces. Nature, **378**: 25-31.
- Veksler, I. M. and Teptelev, M. P. (1990). Conditions for the crystallisation and concentration of perovskite-type minerals in alkaline magmas. Lithos, **26**: 177-189.

- Veksler, I. V., Nielsen, T. F. D. and Sokolov, S. V. (1998a). Mineralogy of crystallised melt inclusions from Gardiner and Kovdor ultramafic alkaline complexes: implications for carbonatite genesis. Journal of Petrology, **39**: 2015-2032.

- Veksler, I. V., Petibon, C., Jenner, G. A., Dorfman, A. M. and Dingwell, D. B. (1998b). Trace element partitioning in immiscible silicate-carbonate liquid systems: an initial experimental study using a centrifuge autoclave. Journal of Petrology, **39**: 2095-2104.

- Viana, M. G. (1995). Geocronologia e geoquímica das rochas ortognáissicas e metavulcânicas da região de Mara Rosa, norte de Goiás. (Universidade de Brasilia, M. Sc.), 110p.

- Viana, M. G., Pimentel, M. M., Whitehouse, M. J., Fuck, R. A. and Machado, N. (1995). O arco magmático de Mara Rosa, Goiás: dados geoquímicos e suas implicações regionais. Revista Brasileira de Geociências, **25**: 111-123.

- Wager, L. R., Brown, G. M. and Wadsworth, W. J. (1960). Types of igneous cumulates. Journal of Petrology, **1**: 73-85.

- Wall, F., Le Bas, M. J. and Srivastava, R. K. (1993). Calcite and carbocernaite exsolution and cotectic textures in a Sr, REE-Rich carbonatite dyke from Rajasthan, India. Mineralogical Magazine, **57**: 495-513.

- Walters, L. J., Claypool, G. E. and Choquette, P. W. (1972). Reaction rates and dO18 variation for the carbonate-phosphoric acid preparation method. Geochimica et Cosmochimica Acta, **36**: 129-140.

- Watson, E. B. (1991). Diffusion in fluid-bearing and slightly-melted rocks: experimental and numerical approaches illustrated by iron transport in dunite. Contributions to Mineralogy and Petrology, **107**: 417-434.

- Wendlandt, R. F. and Harrison, W. J. (1979). Rare Earth partitioning between immiscible carbonate and silicate liquids and CO2 vapor: results and implications for the formation of Light Rare Earth-enriched rocks. Contributions to Mineralogy and Petrology, **69**: 409-419.

- Whipple, E. R. (1974). A study of Wilson's determination of ferrous iron in silicates. Chemical Geology, **14**: 223-238.

- Wilson, A. D. (1955). Determination of ferrous iron in rocks and minerals. Bulletin of the Geological Survey of Great Britain, **9**: 56-58.

- Wilson, M. (1989). Igneous Petrogenesis - A Global Tectonic Approach. London, Harper Collins. 466pp.

- Wones, D. R. and Eugster, H. P. (1965). Stability of biotite: experiment, theory, and application. American Mineralogist, **50**: 1228-1272.

- Woolley, A. R. (1987). Alkaline Rocks and Carbonatites of the World. Part 1: North and South America. London, British Museum (Natural History)/University of Texas Press. 216p.

- Woolley, A. R., Bergman, S. C., Edgar, A. D., Le Bas, M. J., Mitchell, R. H., Rock, N. M. S. and Smith, B. H. S. (1996). Classification of lamprophyres, lamproites, kimberlites, and the kalsilitic, melilitic, and leucitic rocks. Canadian Mineralogist, **34**: 175-186.

- Woolley, A. R. and Buckley, H. A. (1993). Magnesite-siderite series carbonates in the Nkombwa and Newania carbonatite complexes. South African Journal of Geology, **96**: 126-130.

- Woolley, A. R. and Kempe, D. R. C. (1989). Carbonatites: nomenclature, average chemical compositions, and element distribution. In K. Bell, Ed., Carbonatites: genesis and evolution. London, Unwin Hyman, 1-14.

- Woolley, A. R., Williams, C. T., Wall, F., Garcia, D. and Moute, J. (1995). The Bingo carbonatite-ijolite-nepheline syenite complex, Zaire: geology, petrography, mineralogy and petrochemistry. Journal of African Earth Sciences, **21**: 329-348.

- Zaitsev, A. and Polezhaeva, L. (1994). Dolomite-calcite textures in early carbonatites of the Kovdor ore deposit, Kola Peninsula, Russia: their genesis and application for calcite-dolomite geothermometry. Contributions to Mineralogy and Petrology, **115**: 339-344.

- Zaitsev, A. N. (1996). Rhombohedral carbonates from carbonatites of the Khibina massif, Kola Peninsula, Russia. Canadian Mineralogist, **34**: 453-468.

- Zalán, P. V., Wolff, S., Conceição, J. C. J., Marques, A., Astolfi, M. A. M., Vieira, I. S., Appi, V. T. and Zanotto, O. A. (1990). Bacia do Paraná. In G. P. Raja Gabaglia and E. J. Milani, Eds., Origem e Evolução de Bacias Brasileiras. Rio de Janeiro, PETROBRAS, 135-168.

- Zheng, Y. F. (1990). Carbon-oxygen isotopic covariation in hydrothermal calcite during degassing of CO2. Mineralium Deposita, **25**: 246-250.

APPENDIX 1 - ANALYTICAL TECHNIQUES AND DATA ASSESSMENT

A1.1 - SAMPLING STRATEGY AND PRELIMINARY SAMPLE PREPARATION

Due to the extensive tropical weathering regime prevailing in the study area, it is virtually impossible to obtain surface samples of alkaline rocks and carbonatites that are fresh enough for geochemical studies. To ensure the best possible quality, most samples used in this study were collected from drill cores, kindly made available by the mining companies Fosfértil - Fertilizantes Fosfatados S.A. and Companhia Vale do Rio Doce. In the Tapira Complex, the drilling usually persisted for only a few meters in the fresh rock below the mineralised weathering zone. Despite this limitation in depth, the set of drill cores available permitted a good lateral coverage, especially on and around the main ore reserves. For the Salitre complex, drilling usually reached greater (up to several tens of metres) depths in well-preserved rock, but lateral sampling was constrained by the fewer drill cores available. A more detailed sampling campaign was then conducted on the Tapira complex, and additional samples from Salitre were collected to allow comparison between the two complexes. A smaller number of suitable surface samples of the complexes and country rocks was collected from fresh blocks in the mining area of Tapira and from road cuts and streams over the region.

Thin sections for petrographic studies and microprobe analysis were made at the universities of Brasília and Durham. Samples for chemical analysis were selected on the basis of petrographic inspection and field information.

As carbonatite complexes are widely recognised as sites of strong hydrothermal and/or carbothermal activity, maximum care was taken to avoid altered surfaces or secondary veinlets. The hand-specimens were initially trimmed with a clipper saw, and any visibly altered portions discarded. Subsequently, the samples were reduced to coarse-grained (5-10 mm) fragments with a Fritsch Pulverisette jaw crusher, inspected again for alteration and finally ground to a fine-grained powder in a Fritsch Pulverisette agate ball mill. Between runs the jaw crusher blades were cleaned with a wire brush and absolute alcohol, and the agate pots and balls were thoroughly washed. Additional cleaning of the agate mill was achieved by periodical runs of quartz sand. The sample powders were stored in labelled self-sealing plastic bags for future analysis.

A1.2 - WHOLE ROCK ANALYSIS

A1.2.1- LOSS-ON-IGNITION (LOI)

Sample preparation

Sample powders were dried out in an oven at 105°C for 12 hours prior to analysis to drive out superficial moisture.

Analytical procedure

The weight (C) of porcelain crucibles was accurately determined. Approximately 3g of sample powder were added to each crucible and the accurate weight of crucible + sample $(C+S)_1$ recorded. The crucibles with sample powders were ignited in a Carbolite LMF furnace at 900 °C. After a minimum of 2 hours, they were removed from the furnace, allowed to cool, and the weight of crucible + ignited sample $(C+S)_2$ was determined. Loss-on-ignition was calculated by weight difference as

$$\boxed{LOI\,(\%) = \frac{(C+S)_1 - (C+S)_2}{(C+S)_1 - C} x100}$$

Data quality assessment

The use of Loss-on-Ignition (LOI) as an estimate of the total volatile content in geological samples has several limitations. The main sources of error in LOI results are: (a) weight gain on ignition (e.g. by Fe oxidation) and (b) post-ignition moisture absorption.

The gain on ignition by oxidation of ferrous iron was demonstrated by Lechler and Desilets (1987). Conversion of FeO to Fe_2O_3 during ignition will lead to a decrease in LOI figures by an amount that is proportional to the original concentration of FeO. Where independently determined FeO was available, a correction factor (CF) was calculated according to Lechler and Desilet's equation

$$\boxed{CF = (1.11x\,FeO) - FeO}$$

and the actual LOI determined as

$$\boxed{LOIc = LOI + CF}$$

LOI values are presented together with major-element analysis in Appendix 3. Where FeO data are lacking, the non-corrected LOI is reported.

Errors resulting from moisture absorption by the ignited powder can also be substantial, especially for carbonatites or other rocks containing large quantities of carbonate minerals. During this research the presence of the mineral portlandite

($Ca(OH)_2$) was detected by X-ray diffraction on ignited samples of carbonatite. The formation of portlandite presumably follows the sequence:

$$\underset{(calcite)}{CaCO_3} \xrightarrow{ignition} CaO + CO_2$$

and then

$$CaO + H_2O \xrightarrow{cooling} \underset{(portlandite)}{Ca(OH)_2}$$

An experiment was conducted to evaluate the effect of moisture absorption. A sample of SpecPure $CaCO_3$ was ignited, and repeated LOI determinations were made at progressively increasing time intervals. The results are summarised in the diagram of figure I.1 and indicate that, although dependent on a number of factors (such as grain size and environmental conditions), the transformation of CaO in portlandite can be a

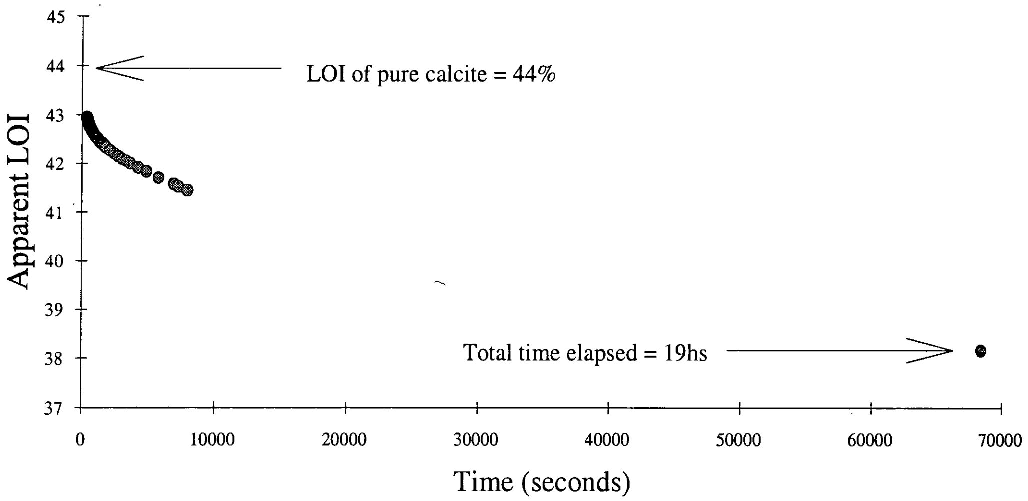

Figure AI.1 - LOI variation with time for pure $CaCO_3$, resulting from moisture absorption by the ignited sample.

very rapid process. During the experiment, the sample was allowed to cool for 3 minutes before measurements started, but even this short cooling period was enough to produce a substantial error in the analytical results (LOI at T=3 min was 43.34%, as opposed to the expected 44.0% for pure calcite). Although this type of error cannot be easily corrected for, it can be minimised by keeping the time between ignition and weighing to a minimum, and by allowing samples to cool down in a desiccator.

Further indirect evidence of moisture absorption is given by comparison of LOI results with independent CO_2 determinations conducted at the University of Brasília. For the studied carbonatites and carbonate-rich silicate rocks CO_2 results were consistently higher than LOI. Assuming that CO_2 is not likely to be the sole volatile present in the analysed rocks, it follows that LOI is a poor, low-accuracy, estimate of the amount of volatiles in carbonate-rich rocks, and should be interpreted merely as a minimum reference value.

A1.2.2. MAJOR ELEMENT ANALYSIS BY X-RAY FLUORESCENCE (XRF)

Sample preparation

An aliquot of 0.6g of ignited sample powder was added to 3.0g of Spectroflux 100B (lithium metaborate and lithium tetraborate), previously dried at 600°C in a Carbolite CSF 1100 furnace for 12 hours. The mixture was homogenised in a small Fritsch Pulverisette agate mill for 2 minutes, transferred to a platinum crucible and fused in a Carbolite CSF1200 furnace at 1050 °C. Great care was taken not to allow the fusion to stay in the furnace for longer than 20 minutes, in order to minimise volatile loss. The fusion was then poured into a graphite mould and pressed with an aluminium plunge to produce a glass disc. The discs were allowed to cool, labelled, and stored in plastic bags.

For carbonatites, however, this preparation method failed to produce adequately stable fusion discs, resulting in a high percentage of breakage during and after cooling. To overcome this problem, and also to obtain a matrix that was chemically closer to the range of standards available for calibration, the ignited carbonatite powders were mixed with SpecPure SiO_2 in a 1:1 ratio. This rock-SiO_2 mixture was then fused in the same way as described above. Data obtained by this method were subsequently recalculated to discard the added SiO_2. A number of pure SiO_2 fusion discs were used as control "blanks".

To minimise moisture absorption, all fusions were performed immediately after LOI, and the fusion discs were kept in a desiccator prior to analysis by XRF.

Analytical procedure

The fusion discs were analysed at the University of Durham with a Phillips PW1400 X-ray Fluorescence Spectrometer, fitted with a PW1500/10 automatic sample changer. A Rh tube was used as the source of X-rays. Calibration, correction factors for line overlaps and mass absorption coefficients were calculated using Phillips X40 software. The operating conditions were 80 kV and 35 mA for all the elements. For some samples, especially carbonatites rich in Ba, Sr and rare-earth elements (REE) the first attempts at determining major-element concentration failed to yield acceptable totals. The reasons for this are: (1) Heavy elements, such as Ba and the REE have a strong mass absorption effect and, if present in large amounts, can cause an overall suppression in the analytical signal, when compared with relatively poorer standards. This lower signal intensity causes the software to underestimate the actual major-element concentrations, and therefore produce low totals. (2) In carbonatites and some carbonate-rich silicate rocks, Ba, Sr, and sometimes REE are present in concentrations high enough to be considered major elements and, as such, should be added to the analytical totals. (3) High Ba in some samples was found to cause an overcorrection in the calculation of the matrix of mass-absorption coefficients.

The following modifications were then implemented to the analytical method: (a) incorporation of high-Ba, -Sr and -REE standards into the calibration set; (b) inclusion of BaO and SrO in the calculation of analysis totals; (c) change of parameters in the X-40 procedure that calculates the matrix of mass-absorption coefficients. The system requires that one of the analysed elements is removed from the calculations, so that all other coefficients are rated to it. In the routine method this element is usually Si. For this research Ba was chosen as the element to be removed from calculations, and an independent alpha factor was manually calculated for it.

New analysis of carbonatites with these modified settings produced totals within the acceptable limits of 99 to 101 %.

Calibration and data quality assessment.

The calibration was set up with the use of the international standards Mica-MG, BE-N, MRG-1, DNC-1, BIR-1, BHVO-1, NIM-P, SARM-40, W-2, NIM-N, OKA-1, DR-N, AGV-1, T-1, NIM-S, QLO-1, GSP-1, G-1, NIM-G and BCS-313, for which the corresponding sources and recommended values can be found in Potts *et al.* (1992). A kamafugite (XUXA) from the Alto Paranaíba Igneous Province, previously analysed by Gibson *et al.* (1995), was used as an additional monitor for analysis precision.

Analytical precision was monitored by several repetitions throughout the analytical run. The relative standard deviation (RSD %, reported in table I.1), is obtained by dividing the standard deviation by the average concentration of a given sample. This provides a better estimate of the analytical precision than the standard deviation alone, since RSD expresses the magnitude of the error as a percentage of the actual measurement.

	RSD (%)			
	AGV-1	BHVO-1	W-2	XUXA
SiO2	0.305	0.152	0.265	0.270
TiO2	0.479	0.793	0.764	0.759
Al2O3	0.482	1.063	0.927	2.277
Fe2O3	1.166	0.581	0.713	0.573
MnO	2.340	3.292	2.227	3.010
MgO	2.398	1.081	0.517	1.147
CaO	0.584	0.650	0.648	0.631
Na2O	2.101	2.660	2.190	3.506
K2O	0.449	0.704	0.850	0.517
P2O5	1.768	1.669	4.382	1.963

Table AI.1 - Reproducibility (precision) of major element analysis by XRF, expressed as relative standard deviation (RSD %) of replicate analysis on the same fusion disc throughout the analytical run.

Analytical accuracy was evaluated by least-squares regression between the recommended and observed values for international standards. The standard error of regression, reported in table I.2, is a measure of the error in estimating a dependent variable (analytical result) from an independent value (known concentration of standard) and its significance is related to the bulk part of the calibration line where the analysed sample is expected to be. Thus, a given standard error of regression is obviously more relevant for samples situated in the lower portions of the calibration line than for those with higher concentrations.

Oxide	Range (%)	standard error (%)
SiO_2	38.9 - 99.73	0.20
TiO_2	0.02 - 6.93	0.01
Al_2O_3	0.16 - 18.38	0.17
Fe_2O_3	0.02 - 18.18	0.08
MnO	0.005 - 1.03	0.005
MgO	0.01 - 25.33	0.11
CaO	0.02 - 40.32	0.09
Na_2O	0.01 - 4.45	0.03
K_2O	0.02 - 15.39	0.01
P_2O_5	0.00 - 1.84	0.01

Table AI. 2 - Accuracy of major element analysis by X-ray Fluorescence, expressed as the standard error in the regression of observed results on the recommended values for international standards.

A1.2.3 - TRACE-ELEMENT ANALYSIS BY X-RAY-FLUORESCENCE

Sample preparation

A mixture of sample powder and previously prepared 4% Mowiol solution was pressed in a SPECAC hydraulic press to 7 - 8 tons, to produce powder pellets. These were labelled, dried out in an oven at 105°C, and stored in plastic bags prior to XRF analysis. Press components were cleaned thoroughly between runs.

Analytical procedure

The pressed pellets were analysed for Cr, Sc, Zr, Ni, Co, V, Nb, La, Ce, Nd, Y, Rb, Sr, Ba and Th at the University of Durham, using a Phillips PW1400 X-ray Fluorescence Spectrometer, fitted with a PW1500/10 automatic sample changer. The X-ray source was provided by a Rh tube. The operating conditions were usually 80 kV and 35 mA. When necessary, analysis was carried out at a lower voltage (45 kV, 35 mA), to prevent excitation of elements such as Ba and the REE, and thus minimise their potential line interferences with other elements.

Calibration and data quality assessment.

A number of precautions must be taken when analysing carbonatites and strongly alkaline rocks by XRF. Line interference and mass absorption effects related to some trace-elements can be enhanced by their unusually high concentrations, and must be carefully investigated and corrected for. The standard correction procedures routinely applied to less extreme, sub-alkaline rocks were found to be insufficient to account for the observed variation in the carbonatites during this research. Instead, the calibration for trace elements was performed on an individual basis. This included: (a) performing scans over the peak and background regions to assess the presence and magnitude of line interferences, and (b) extending the calibration ranges, when required.

Whenever possible, the same set of calibration standards used for major elements was employed in trace-element analysis. However, the analysis of Ba, Sr, Ce, La and Nd in some of the studied rocks required the manufacturing of an additional set of synthetic standards, in order to extend the calibration ranges. These were prepared by addition of known amounts of each element (in SpecPure oxide or carbonate form) to selected international standard powders. These spiked powders underwent further mixing in a small Fritsch Pulverisette agate mill, for optimum homogeneity, and were finally pressed as pellets for XRF analysis. The composition of the spiked standards is reported in table I.3 and the recommended values for the other international standards used in calibration are those of Potts *et al.* (1992).

	La	Ce	Nd	Sr	Ba	Th
SARM40(H)	3778	7045	2536	89769		
SARM40(M)	1927	3598	1305	45684		
STM1(H)	3161	4933	940	9239	24599	1115
STM1(M)	1603	2514	494	4819	12156	554
NIM-S(H)				60236	82673	2932
NIM-S(M)				30124	42513	1465
OKA1(H)					110501	2748
OKA1(M)					56060	1372

Table AI.3 - New concentration (ppm) of spiked standards used in calibration of La, Ce, Nd, Sr, Ba and Th. (M) = single spiking, (H) = double spiking.

The analytical precision and possible drifts in calibration were monitored by replicate analysis of selected samples at different stages during the analytical run, and calculation of RSD (%) for each element. The accuracy of the method was assessed through the standard error of a least-squares regression between the recommended and observed values for each element in the international standards. The statistical parameters obtained are summarised in tables I.4 and I.5

	BHVO-1	W-2	XUXA	AGV-1
	RSD(%)	RSD(%)	RSD(%)	RSD(%)
Cr	2.38	3.10	1.80	4.91
Sc	3.24	7.21	8.39	9.61
Zr	2.91	2.01	1.05	0.95
Ni	2.36	4.30	1.70	9.11
Co	5.01	7.16	4.61	10.80
V	0.93	0.81	1.72	2.01
Nb	4.79	7.54	0.85	3.86
La	10.99	19.31	2.89	7.31
Ce	10.44	9.03	2.02	9.31
Nd	11.25	17.23	4.54	6.35
Y	5.06	5.56	3.59	2.66
Rb	4.69	3.20	1.59	1.60
Sr	2.07	1.80	1.30	0.94
Ba	1.65	4.13	0.16	1.14
Th	62.44	44.35	7.31	29.47

Table AI.4 - XRF trace-element analytical precision, expressed as relative standard deviation (RSD%) of repeated analysis of the same pellet throughout the analytical run

Element	Range	standard error (ppm)
Cr	3 - 635	0.66
Sc	0.24 - 55	1.99
Zr	16 - 1210	9.50
Ni	2 - 534	1.07
Co	0.5 - 87	1.84
V	8 - 526	1.68
Nb	0.03 - 3700	2.88
La	1.2 - 3778	9.43
Ce	2.1 - 7045	6.53
Nd	5 - 2536	2.03
Y	0.89 - 718	3.52
Rb	0.06 - 3600	2.52
Sr	5 - 89769	32.69
Ba	61 - 110501	60.7
Th	0.1 - 2932	4.77

Table AI.5 - Standard error of the regression of analytical results on recommended values for international standards

A1.2.4 - TRACE-ELEMENT ANALYSIS BY INDUCTIVELY COUPLED PLASMA MASS SPECTROMETRY (ICP-MS)

Sample preparation

Sample powders were dried for a minimum of 12 hours in an oven at 105° C. Screw-top Teflon vials were cleaned in Analar HNO_3 for 24 hours on a hot plate and rinsed thoroughly with MQ water before sample digestion.

A 0.1g aliquot of sample powder was transferred to the Teflon vial and then digested for 48 hours in a mixture of Aristar HNO_3 and HF on a hot-plate surface, at a temperature of 130-150° C. After digestion, the acid mixture was evaporated to a moist residue to remove HF and silicon as SiF_4. The residue was re-dissolved in dilute HNO_3 and checked for the presence of undissolved solids. Subsequently, the samples, blanks, and calibration standards were spiked with an internal standard solution containing known amounts of Rh and Re, and further diluted in 3.5% HNO_3. The final dilution factor of analysed solutions was 1/5000.

Samples showing petrographic evidence of mineral phases known to be refractory to HF - HNO_3 digestion (e.g. zircon) underwent an additional step in preparation. The samples and a set of international standards were mixed with Spectroflux 100 (lithium tetraborate) in a flux:sample ratio of 5:1, and fused according to the procedure described in section I.3.1. The fusion discs were ground manually with an agate pestle and mortar, and digested in the same way as the rock powders. The agate pestle and mortar were cleaned with quartz sand and thoroughly washed between runs.

Analytical procedure

The dissolved samples were analysed for Sc, Ti, V, Cr, Mn, Co, Ni, Cu, Zn, Ga, Rb, Sr, Y, Zr, Nb, Cs, Ba, La, Ce, Pr, Nd, Sm, Eu, Gd, Tb, Dy, Ho, Er, Tm, Yb, Lu, Hf, Ta, Pb, Th and U at the University of Durham, using a Perkin-Elmer Sciex Elan 6000 ICP Mass Spectrometer, equipped with a cross-flow nebuliser set at 1ml/min. The plasma was operated at 1100 to 1300 W. Analytical results were processed using software supplied by Sciex (version 2.0). Equipment performance was checked by daily quality control tests, and plasma temperature and sample flow rate were adjusted as necessary to ensure that oxides and double-charged ions were kept to less than 3 % of the total signal. A number of blanks was used to monitor possible contamination and international standards were used to set up calibration. Correction factors for several possible interferences were calculated from standard solutions and implemented in the analytical software, in addition to built-in corrections.. The use of the internal Rh and Re spike allowed compensation for signal fluctuation (caused by signal suppression in samples with complex matrices) and possible drifts in calibration.

Calibration and data quality assessment.

Blank concentrations were typically below 0.01 ppm, except for Sc, V, Cr, Ni, Cu, Zn. Standards used in calibration were BCR-1, AGV-1, W-2, BHVO-1, STM-1, ENDV, X-108 and K2/WI. Statistical parameters used to assess analysis precision and accuracy are reported in tables I.6 and I.7.

The statistical data illustrate the excellent precision and accuracy of this method for elements heavier than Ga, and in particular for the REE. Lighter elements, however, showed lower accuracy in table I.7. This is consistent with the lower precision and higher detection limits shown in table I.6, and with the higher blank values obtained for some of these elements during this research. The higher errors associated with light elements are either a result of contamination or interference during analysis.

From table I.7 it is also noteworthy that the analyses of fusion discs are usually less accurate than those conducted on the original sample powder. This is expected, since both samples and standards are considerably diluted by flux (dilution ratio = 1:5). Furthermore, the fusion discs consist of a different chemical matrix with the additional presence of excess boron and lithium. Presumably, potential interference caused by these elements would be compensated for by the use of fused blanks and calibration standards, but it must be stressed that this was not investigated in detail during this research.

Although several interferences can occur during ICP-MS analysis they can be readily monitored by the preparation of blanks and control standards, and many interferences can be compensated for with the use of correction factors. Potential interferences were additionally monitored by analyses of more than one isotope for some of the more susceptible elements (Cr, Sm, Eu, Dy, Er, Yb, Hf and Pb).

The most common interferences observed in this study comprise:

			Relative Standard Deviation (%)			
Element	Detection limit (ppm)	Quantitation limit (ppm)	K2/WI	STM1	XUXA	BHVO-1 (fusion)
Sc	6.8234	7.1782	5.78	21.68	1.10	14.67
Ti	0.9294	1.3294	3.12	3.51	3.81	1.64
V	1.9634	2.3585	2.60	9.97	1.03	1.53
Cr	9.0745	11.5507	4.46	9.71	1.02	1.38
Mn			4.78	3.12	1.36	1.15
Co	0.0422	0.0662	5.62	4.16	2.34	0.93
Ni	1.0470	1.3705	5.69	6.44	3.23	1.88
Cu	0.0722	0.1249	5.50	3.93	3.22	1.55
Zn			6.43	3.32	2.95	2.04
Ga	0.0314	0.0563	3.49	2.62	2.27	1.87
Rb	0.0178	0.0314	2.32	1.44	1.14	1.44
Sr	0.0473	0.0703	2.39	0.50	2.88	0.64
Y	0.0051	0.0084	0.78	0.58	0.42	0.97
Zr	0.0426	0.0560	0.72	0.85	0.08	0.74
Nb	0.0098	0.0158	0.75	0.50	0.03	0.65
Cs			2.39	0.93	0.98	11.52
Ba	0.1354	0.2167	2.27	0.86	4.91	1.46
La	0.0029	0.0043	3.18	1.79	2.63	1.63
Ce	0.0045	0.0062	2.96	1.97	2.92	0.66
Pr	0.0018	0.0033	2.68	1.70	2.66	0.74
Nd	0.0073	0.0133	2.78	1.71	2.44	1.29
Sm	0.0069	0.0138	1.89	1.26	2.17	3.08
Eu	0.0020	0.0039	1.68	1.05	2.15	0.81
Gd	0.0065	0.0137	2.65	1.40	1.99	0.82
Tb	0.0016	0.0030	1.61	0.67	1.25	0.49
Dy	0.0041	0.0082	0.92	1.00	1.40	3.03
Ho	0.0009	0.0018	1.28	0.74	1.80	1.32
Er	0.0021	0.0043	1.62	0.55	1.78	3.50
Tm	0.0009	0.0019	0.75	1.19	0.14	2.41
Yb	0.0022	0.0040	0.82	0.50	2.30	2.33
Lu	0.0011	0.0025	1.80	1.13	0.07	2.79
Hf	0.0051	0.0107	0.84	0.93	0.21	1.12
Ta	0.0050	0.0085	2.04	0.26	0.97	1.49
Pb			1.59	0.78	1.47	4.01
Th	0.0011	0.0023	2.85	1.12	1.80	1.24
U	0.0013	0.0027	2.96	1.67	2.05	1.49

Table AI.6 - ICP-MS analytical precision, expressed as relative standard deviation of repeated analysis of selected standards and control samples throughout the analytical run. Detection and quantitation limits are typical values obtained in the ICP-MS laboratory at the University of Durham, for the described analytical method.

	Powders		Fusions	
Element	Range (ppm)	Standard error (ppm)	Range (ppm)	Standard error (ppm)
Sc	12.1 - 35.9	0.62	12.1 - 42.8	2.66
Ti	0.14 - 2.71	0.018	0.14 - 2.71	0.019
V	50 - 358	2.85	50 - 358	2.93
Cr	12 .0 - 1240.0	20.80	12.0 - 1240.0	35.43
Mn	0.096 - 0.22	0.005	0.096 - 0.22	0.008
Co	0.9 - 61.55	1.14	0.9 - 61.55	1.04
Ni	13 - 798.3	9.42	17 - 798.3	14.87
Cu	19 - 136	2.54	17.0 - 136	5.30
Zn	66.12 - 129.5	6.21	66.12 - 105	3.87
Ga	9.19 - 36	0.37	9.19 - 36	0.47
Rb	9.6 - 158.4	0.30	9.6 - 158.4	0.70
Sr	85.47 - 662	2.34	85.47 - 662	8.61
Y	4.26 - 38	0.71	4.26 - 32.9	0.45
Zr	92.87 - 254.32	0.89	25.13 - 254.32	1.00
Nb	0.56 - 273-85	0.39	0.56 - 273-85	0.36
Cs	0.011 - 3.65	0.047	0.011 - 3.65	0.039
Ba	35.44 - 1221	3.20	35.44 - 1221	2.64
La	0.93 - 178.43	0.677	0.93 - 178.43	1.329
Ce	1.73 - 305.3	1.92	1.73 - 305.3	2.10
Pr	0.25 - 32.03	0.14	0.25 - 32.03	0.126
Nd	1.14 - 110.53	0.59	1.14 - 110.53	0.73
Sm	0.38 - 14.84	0.11	0.38 - 14.84	0.14
Eu	0.12 - 4.06	0.045	0.12 - 4.06	0.074
Gd	0.44 - 6.68	0.35	0.44 - 6.4	0.47
Tb	0.08 - 1.05	0.023	0.08 - 1.13	0.024
Dy	0.59 - 8.1	0.14	0.59 - 8.1	0.20
Ho	0.12 - 1.26	0.03	0.12 - 1.13	0.03
Er	0.48 - 4.2	0.08	0.48 - 4.2	0.097
Tm	0.09 - 0.56	0.017	0.09 - 0.69	0.015
Yb	0.68 - 3.38	0.028	0.68 - 3.06	0.034
Lu	0.11 - 0.6	0.023	0.11 - 0.6	0.025
Hf	0.69 - 28	0.11	0.69 - 28	0.19
Ta	0.052 - 9.38	0.041	0.052 - 9.38	0.060
Pb	1.62 - 36	0.71	1.62 - 36	0.389
Th	0.13 - 28.72	0.08	0.13 - 28.72	0.104
U	0.16 - 6.52	0.04	0.16 - 6.52	0.03

Table AI.7 - Standard error of the regression of ICP-MS analytical results on recommended values for international standards. Data shown separately for sample powder and fusion disc digestion.

(1) Contamination with extraneous material during sample preparation. This is difficult to correct, but it can be monitored through the preparation of blanks, and minimised by the use of a high-cleanliness laboratory and adequate precautions during preparation.

(2) Contamination from analytical reagents. This seems to be negligible for most analytes and can also be monitored by the preparation of blanks. The contamination is directly related to reagent grade, and was minimised by the use of high purity acids. Throughout this research sample digestion was done in Aristar (or equivalent grade) acids to ensure minimal contamination.

Contamination related to items (1) and/or (2) is reflected in the blank values for the elements Sc, V, Cr, Ni, Cu, Zn. All the other elements were negligible in the blanks, indicating very low levels of contamination.

More significant contamination affected samples that required fusion prior to analysis. This was observed in the blanks for Cr, Ni and Sc concentrations, and is at least partially linked to the Ni crucibles used to store and dry out the flux before the fusion was conducted. Fortunately, the affected elements can be reliably determined by XRF.

Furthermore, platinum crucibles used in the fusion process are a likely source of contamination in platinum-group elements (although these were not studied during this research). Finally, and perhaps more importantly, the flux used in the production of fusion discs was found to be a considerable source of La contamination. This was confirmed by analyses of pure flux, which revealed variable La concentrations (up to 20 ppm in Spectroflux 100 and up to 70 ppm in Spectroflux 100B, for the batches used in this research). This is likely to affect the lower range of the calibration line for La, as well as blank deductions. The impact of La contamination of this magnitude is small compared with the high concentrations of REE in most of the samples studied, although it could be substantial for comparatively REE-poor rocks.

(3) Polyatomic ions. Some of the elements present in the sample may combine with argon, fluorine, nitrogen, hydrogen or oxygen during the analysis. All the mentioned elements are readily available in the system: (a) hydrogen, oxygen and nitrogen are present in both the atmosphere and the diluted HNO_3 solution; (b) Argon is the medium for sample introduction in the system and is present in the plasma torch; (c)

fluorine should have been mostly removed as SiF_4 during sample preparation, but is still potentially present in the final analysed solution. Additionally carbon (or CO_2) may be present in some sample matrices. The use of HNO_3 instead of HCl for sample preparation is preferred, since atmospheric nitrogen would be an unavoidable potential interference in any case. The analysis of specially prepared standard solutions of single elements allows polyatomic interferences to be identified, quantified and corrected for.

Figure I.2 demonstrates the effect of the formation of barium oxide on the signal of other analytes. A standard synthetic solution containing 10 ppm Ba was analysed and produced spurious signals in the mass range 146 to 156, as a result of the combination of various barium and oxygen isotopes. Oxide formation during analysis is dependent on plasma temperature (the colder the plasma the higher the probability of oxide formation) and on sample flow rate, and can be minimised by careful adjustment of these parameters.

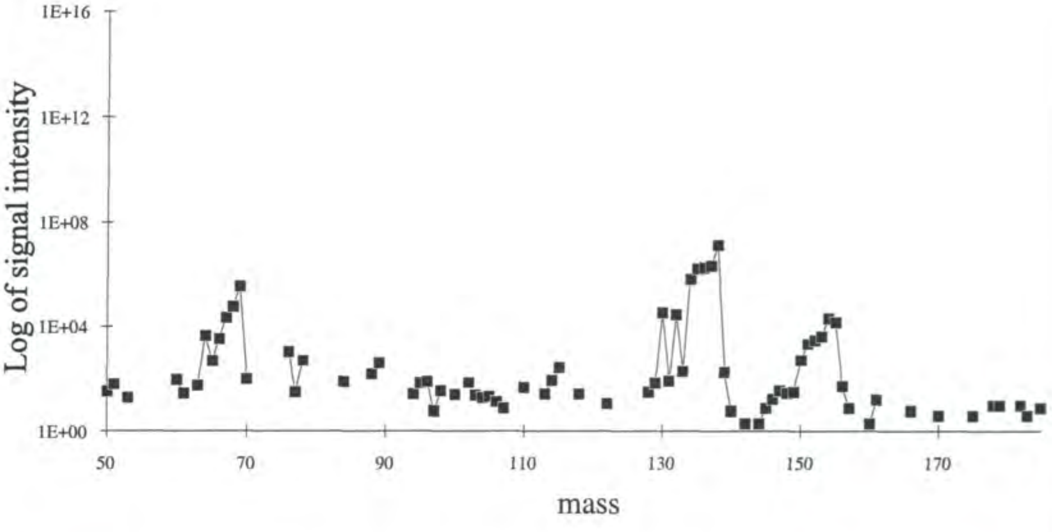

Figure AI. 2 - Effect of polyatomic and double-charged ions during ICP-MS analysis of a solution of 10 ppm Ba. False high signal intensities are produced in the mass ranges 65 to 69 (double-charged Ba) and 146 to 156 (combination of various Ba and O isotopes). Note that the intensity axis is log-scaled. Signal corrected for background

(4) Double-charged ions. When the sample is introduced in the plasma the atoms of the elements in solution are stripped of one electron, generating ions charged +1. Some elements, however, are more easily ionised, and can loose a second electron during analysis. Since signal intensity measurements in ICP-MS are made on

mass/charge ratios, the presence of a certain amount of double-charged ions of an element "E" will produce a spurious signal at half the mass of that element. For example, note in Figure AI.2 the spurious signals in the mass range 65 to 69 caused by various double-charged Ba isotopes. The formation of double-charged ions is dependent on the ionisation potential of the element and on the plasma temperature and sample flow rate. As in item (3), careful adjustment of the latter two parameters can minimise this type of interference. When necessary, correction factors were calculated and implemented in the analytical software.

(5) - Isobaric interferences are produced when different elements have isotopes with identical masses. In this case the signal from the two interfering isotopes can only be discriminated by high-resolution mass spectrometry. Therefore, an isotope free of isobaric interference was preferably chosen as the analyte whenever possible. The remaining, unavoidable isobaric interferences are corrected for by measuring the interfering element at an interference-free isotope. The applied correction factor is based on a constant ratio between isotopes.

Interferences related to items (3) to (5), if not corrected for, will result in the affected elements being reported with erroneously high concentrations.

(6) Incomplete digestion of refractory mineral phases in HF-HNO_3. This problem can be overcome by fusing the sample prior to HF digestion. During this study a series of digestion tests were carried out on samples where there was petrographic evidence of the presence of zircon. Figure I.3 illustrates the difference in results obtained for a Tapira syenite, prepared from both the original sample powder and a fusion disc. The diagram shows a remarkable difference, not only in the concentrations of Zr and Hf but also in the heavy rare-earth elements (HREE). This is consistent with the tendency of zircon to be enriched in HREE (e.g. Hinton and Upton, 1991).

The magnitude of the error related to partial digestion of zircon is not constant. The relative differences in Zr, Hf and HREE concentrations between fused and non-fused powder vary substantially from sample to sample, although in the zircon-bearing rocks from Tapira and Salitre some degree of partial digestion was always observed. However, not all Zr-rich samples show this effect, as illustrated (figure I.4) by tests carried out on the international standard STM-1 (Zr = 1210 ppm). The reasons for this may be differences in the grain size of the powder, variation of temperature during digestion or, alternatively and perhaps more likely, differences in the composition of zircon. Kresten *et al.* (1975) and Belousova *et al.* (1998) described kimberlite zircons as typically U- and Th-poor. Presumably, the crystal structure of this type of zircon would be less prone to have suffered radiation damage and therefore harder to destroy during acid digestion. Even if that is the case, the existence and magnitude of the divergence in the heaviest REE patterns would still depend on their actual enrichment factors in zircons of different origins.

Finally, the use of fused samples for ICP-MS analysis poses an additional concern, regarding the chemical homogeneity of the fusion disc itself. To assess this problem, several parts of a single disc (standard K2/WI) were independently digested and analysed. The relative standard deviations obtained are reported in table I.8 and suggest that, apart from Sc, Cr and Ni, there was no substantial heterogeneity in the fusion discs.

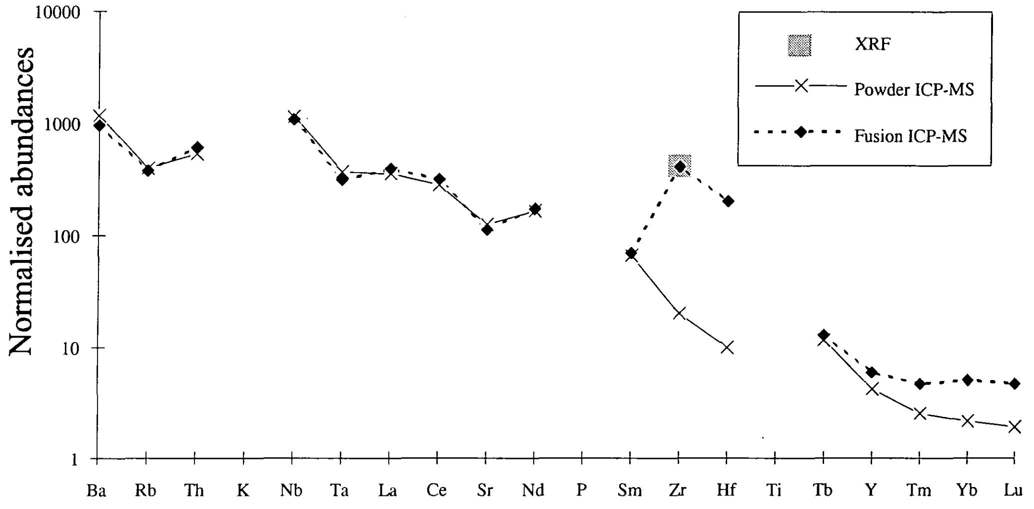

Figure AI.3 - Comparison of results of ICP-MS analysis on fused and non-fused syenite from Tapira. Note the differences in Zr, Hf, Y and the heaviest REE (Tm, Yb, Lu). Also noticeable is the agreement between Zr results obtained from fusion disc and independent Zr by XRF. Normalising factors from Thompson et al. (1984).

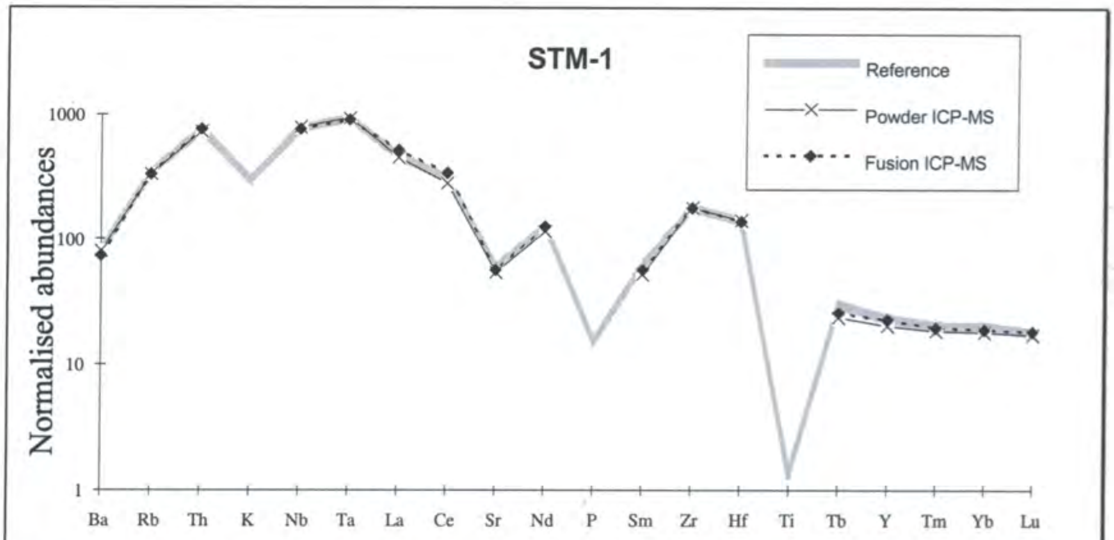

Figure AI.4 - ICP-MS results obtained from fused and non-fused starting materials for international standard STM-1, compared to recommended concentrations. The diagram shows that there are no significant differences between the two preparation methods and that both are in good agreement with the recommended values for this standard. Reference values from Potts et al. (1992) and Normalising factors from Thompson et al. (1984).

	RSD (%)		RSD (%)		RSD (%)
Sc	7.94	Y	0.69	Tb	2.49
Ti	0.79	Zr	1.07	Dy	1.37
V	2.55	Nb	0.89	Ho	0.88
Cr	14.21	Cs	0.36	Er	2.52
Mn	0.47	Ba	0.67	Tm	5.28
Co	0.89	La	0.86	Yb	2.51
Ni	48.13	Ce	0.54	Lu	3.88
Cu	0.94	Pr	0.61	Hf	1.72
Zn	3.48	Nd	0.68	Ta	0.53
Ga	1.98	Sm	0.98	Pb	1.12
Rb	0.46	Eu	0.88	Th	0.32
Sr	0.48	Gd	1.44	U	0.44

Table AI.8 - Relative standard deviation in the analysis of different portions of a single fusion disc by ICP-MS

Comparison of ICP-MS and XRF results.

The availability of trace-element data from two independent analytical techniques allowed cross-checking of results, and assisted in calibrating each method. For instance, Zr results from XRF can be used to evaluate incomplete acid digestion and

La, Ce and Nd from XRF can be checked against the more-accurate ICP-MS results. Figure I.5 shows the compared results for selected elements.

A1.2.5. CARBON AND SULPHUR ANALYSIS

Sample preparation

The method does not require special sample preparation other than previously drying the sample powders at 105°C to remove moisture.

Analytical procedure

An aliquot of 0.2 g of sample powder was weighed into a ceramic container and transferred to a furnace at 1375 °C. Carbon and sulphur are analysed by infrared absorption on separate aliquots, using independent furnaces in which the adequate detectors are installed. The samples were analysed at the University of Brasília using LECO CR-12 (carbon) and SC-132 (sulphur) furnaces. Oxygen (99.99%) was the carrier gas. Analytical results are reported together with the whole-rock data in Appendix 3.

Calibration and data quality assessment

Calibration of the analytical method is very simple and can be done with a small number of standards. Carbon calibration was based in pure $CaCO_3$ (LECO ref 501-034) and for sulphur a set of LECO calibration standards (coal samples) was used. The detection range of the method is 0.001 to 99.99% for carbon and sulphur. Typical accuracy is ± 1% of the actual content and sensitivity is 0.001 %. Analytical precision was determined by replication of analysis of a given sample and a calibration standard throughout the analytical run. Typical RSD (%) values obtained were 2.45 for carbon and 5.44 for sulphur.

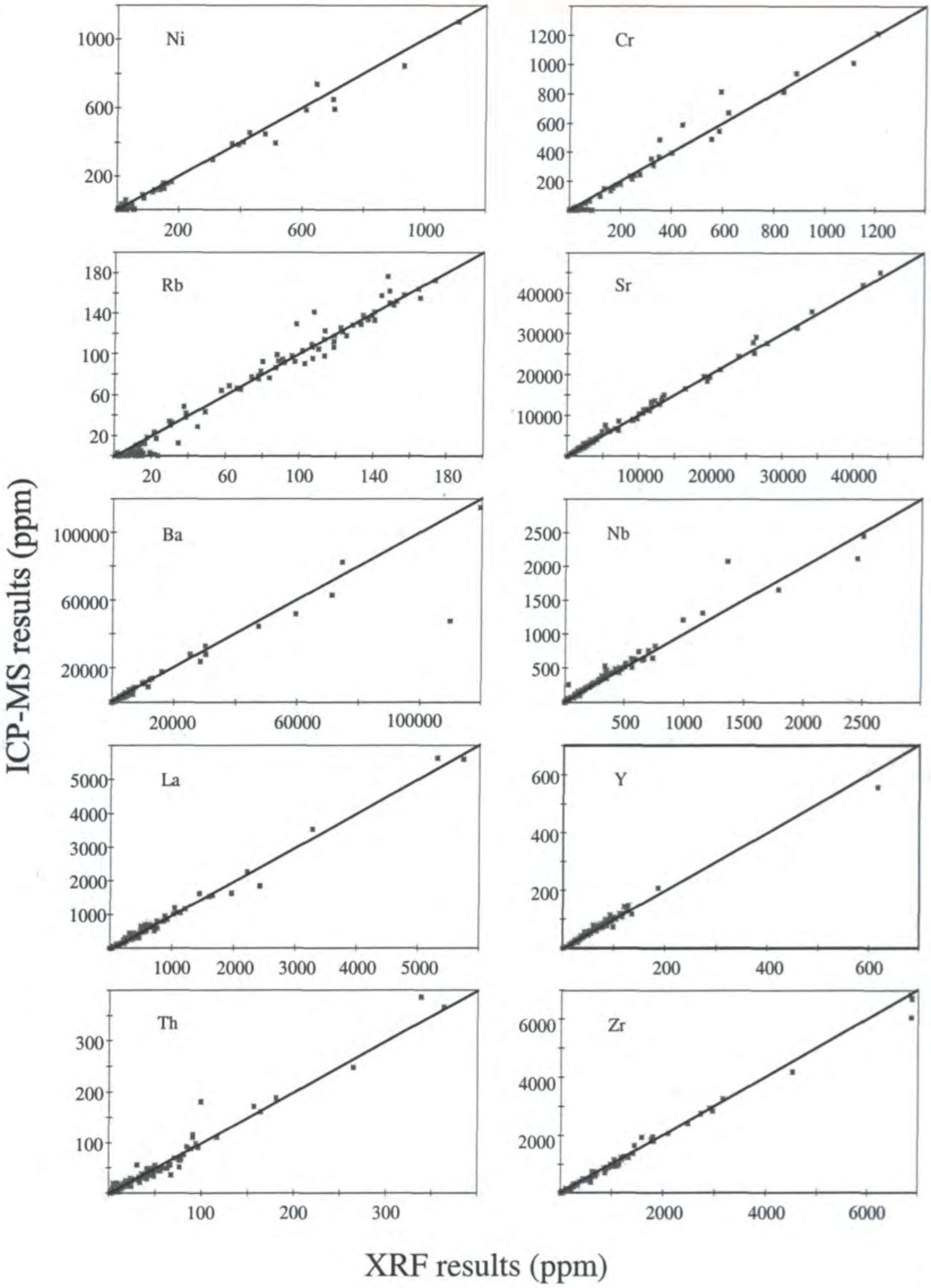

Figure AI.5 - Comparison of XRF and ICP-MS results for selected elements

A1.2.6. FERROUS IRON ANALYSIS

Ferrous iron was determined by titration. The analyses were kindly performed by Dr. Geraldo R. Boaventura, at the University of Brasília. Sample preparation and analytical procedures were according to the method of Wilson (1955), modified by Whipple (1974). As stressed by Whipple (1974), one major difficulty of this method is posed by the presence of sulphides in the sample. In this case, S^{2-} will tend to reduce various ions in the solution and consequently overestimate Fe^{2+} results. Caution must therefore be exercised in interpreting FeO results in sulphur-rich samples.

A1.2.7. SR AND ND ISOTOPE ANALYSIS

Sample preparation

Sample preparation was carried out in the Geochronology Laboratory at the University of Brasília

Teflon vials were cleaned in a mixture of HF, HCl and HNO_3 An aliquot of approximately 0.02g of sample powder was used for analysis. The powder and an internal spike solution were accurately weighed into the Teflon vials. Sample digestion was carried out on a hot plate according to the following successive steps: (1) digestion in HF and HNO_3; (2) evaporation; (3) re-dissolution in HF and HNO_3; (4) evaporation; (5) dissolution in 6N HCl; (6) evaporation; (7) final dissolution in 2.5N HCl. The solutions were passed through ion-exchange columns and Sr, Sm and Nd were separately collected for analysis. All steps of sample preparation were carried out in a high cleanliness laboratory, under positive atmospheric pressure. All reagents were distilled for maximum purity.

Analytical procedure

The analyses were kindly performed by Dr. Márcio M. Pimentel, at the geochronology laboratory of the University of Brasília. Analytical results are given in Appendix 3.

A1.3. MINERAL ANALYSIS

Chemical composition of several individual mineral phases in various rocks from Tapira and Salitre was investigated by the following techniques: (a) electron microprobe; (b) carbon and oxygen stable-isotope analysis and (c) trace-element analysis by ICP-MS.

A1.3.1 - ELECTRON MICROPROBE ANALYSIS

Electron microprobe analyses were carried out at the Universities of Brasília and Cambridge.

Sample preparation

Thin sections of selected samples were polished and coated in carbon under vacuum.

Analytical procedure

Analyses at both Cambridge and Brasilia were carried out with a CAMECA SX-50 electron microprobe, equipped with three WD spectrometers and a LINK ED system.

Silicates were primarily analysed by EDS at 20 nA and 20 kV, but F, Zr and Ba were determined by simultaneous WDS at 20 nA and 20 kV.

To minimise sample damage, analyses of carbonate were performed at 20 kV and 3 nA, with the beam size set to 15 microns. Lead was determined by WDS and all other elements by EDS.

For perovskite, all elements were determined by WDS. Operating conditions were 20 kV and variable current (20 - 100 nA), adjusted to optimise trace-element detection in specific cases.

Analytical data and calculated mineral formulae are reported in Appendix 2.

Calibration and data quality assessment

Standards used in calibration comprised pure elements, oxides and minerals. Analytical data were processed with LINK SPECTA. According to Reed (1996), typical detection limits are 0.1 % for EDS analysis and 50 ppm for WDS analysis. Counting precision is typically ± 1% and typical accuracy is between ± 1% and ± 2%.

A1.3.2 - CARBON AND OXYGEN STABLE ISOTOPE ANALYSIS

Sample preparation

Calcite- and dolomite-carbonatites from Tapira and Salitre were disaggregated and sieved to produce a size-limited concentrate, compatible with the average grain-size of the rock. The disaggregated sample was fed through a Frantz isodynamic magnetic separator, to remove magnetically susceptible minerals such as magnetite and phlogopite. The non-magnetic portion of the sample comprised mainly carbonates and apatite, from which the carbonate was then separated by hand-picking under a binocular microscope. The type of carbonate present in each sample (calcite, dolomite or a mixture of both) was determined by X-ray diffractometry and its composition further confirmed by qualitative EDS electron microprobe analysis. The final mineral separate was stored in labelled self-sealing bags for future isotope analysis.

An aliquot (usually 10 to 15 mg) of carbonate was accurately weighed and loaded into a reaction tube. The sample was reacted under vacuum with 100% phosphoric acid at 25 °C, to produce CO_2, as illustrated (for calcite) by the following reaction:

$$\boxed{3CaCO_3 + 2H_3PO_4 \Leftrightarrow 3CO_2 + Ca_3(PO_4)_2 + H_2O}$$

The resulting gas phase was then extracted into an evacuated system and distilled through a dry-ice trap to remove H_2O. CO_2 was subsequently collected in a liquid nitrogen trap. Vacuum in the extraction line was carefully controlled at all stages, to monitor potential leakage and consequent gas loss or atmospheric contamination.

As calcite and dolomite react at different rates (Epstein *et al.*, 1964; Walters *et al.*, 1972), it is possible to obtain separate CO_2 fractions for each mineral, in calcite-dolomite mixtures, by carefully timing the extraction. CO_2 evolved from calcite was extracted 1 hour after the initiation of reaction, when most of the calcite had been consumed, but dolomite had not yet started to react. The gas produced between 1 and 8 hours of reaction was discarded to remove any remaining CO_2 evolved from calcite. CO_2 produced thereafter should be derived only from dolomite and this was finally extracted after 24 hours of the initiation of reaction. For either pure calcite or pure dolomite CO_2 extraction is much simpler and was made after reaction completion.

The fine grain size of carbonates in the groundmass of silicate-carbonate rocks (phlogopite-picrites and low-Cr dykes) precluded analysis of pure carbonate separates. Instead, the analysis was carried out on the whole-rock powder, adjusting the sample aliquot to produce an amount of CO_2 equivalent to that obtained from carbonate separates. Most dyke samples were analysed on aliquots of 100 to 200 mg, and yielded acceptable amounts of CO_2. Reaction and gas extraction procedures were identical to those described for carbonate separates.

Analytical procedure

Carbon and oxygen isotopic compositions of calcites and dolomites from carbonatites, phlogopite-picrites and low-Cr dykes were determined by mass spectrometry at the University of Brasília and the Technical University of Munich. Oxygen isotopic composition was corrected to calcite and dolomite by applying the fractionation factors of 1.01025 and 1.0111, respectively. Results were expressed in the usual delta per mil (δ‰) notation, which represents the deviation of the analysed sample from a reference composition. The value of δ is calculated by:

$$\boxed{\delta = \left(\frac{R\ sample}{R\ reference} - 1 \right) x\, 10^3}$$

where R is the isotope ratio (i.e. $^{18}O/^{16}O$ for oxygen, $^{13}C/^{12}C$ for carbon). The reference value for $\delta^{18}O$ is Standard Mean Ocean Water (SMOW) and for $\delta^{13}C$ is the Pee Dee Belemnite (PDB). Analytical results are reported in Appendix 3.

Calibration and data quality assessment.

Total analytical error is estimated as 0.01 ‰. Replicate samples used to test consistency between the two laboratories show good agreement, as illustrated by table. I.9. Also shown is the result for the internal standard used in Brasília.

	Brasília		Munich	
Sample	$\delta^{18}O$	$\delta^{13}C$	$\delta^{18}O$	$\delta^{13}C$
at060a	7.60	-7.35	7.96	-7.33
at050	7.95	-7.65	8.37	-7.65
at047	8.17	-7.26	8.05	-7.23
	Read		Expected	
internal standard	12.48	-6.69	12.09	-7.00

Table AI.9 - Comparative results for $\delta^{18}O$ *and* $\delta^{13}C$ *in replicate samples analysed by independent laboratories*

A1.3.3 - ANALYSIS OF INDIVIDUAL MINERALS BY ICP-MS

Samples were disaggregated with a rock splitter and crushed to match the grain size of the target minerals in each rock. The sample was then fed through a Frantz isodynamic magnetic separator. Each fraction was subsequently washed in MQ pure water, and very fine-grained fractions were discarded to produce a roughly size-limited concentrate. The final mineral separates were purified by careful hand-picking under a binocular microscope, checked for purity by X-ray diffraction, and then ground manually with an agate pestle and mortar. Sample digestion, analytical procedures and statistical assessment are the same as those described in section I.5. Analytical results can be found in Appendix 2.

APPENDIX 2 – MINERAL CHEMISTRY DATA

Abbreviations used in the data tables	
php	phlogopite-picrite
beb	bebedourite
syen	syenite
wehrl	wehrlite
lcr	low-Cr dyke
cbt	carbonatite
fen	fenite
bre	breccia
gli or RR	reaction rock
tr x,y	microprobe traverse along a single grain. x = traverse number, y =analysis number
i	inclusion
g	groundmass
p	phenocryst
v	veinlet
n.a.	not analysed
* in carbonate analyses, 1 and 2 denote first and second generation of carbonate	

Table A.1 - Olivine analyses

Sample	at013	at013	at013	at013	at013	at013	at013	at013	at013	at013	at013	at013	at013	at013	at013	at013
Unit	php	php	php	php	php	php	php	php	php	php	php	php	php	php	php	php
Remarks	tr1,1	tr1,2	tr1,3	tr1,4	tr1,5	tr1,6	tr1,7	tr1,8	tr1,9	tr1,10	tr1,11	tr2,1	tr2,2	tr2,3	tr2,4	tr2,5
SiO2	40.155	40.085	39.798	40.009	39.824	39.972	40.167	40.321	40.097	39.722	39.448	39.336	39.639	39.851	39.961	39.809
TiO2	0.031	0.027	0.022	0.036	0.061	0.025	0.023	0.019	0.002	0.036	0.039	0.038	b.d.	0.026	0.034	0.038
Al2O3	b.d.	b.d.	b.d.	0.075	b.d.	b.d.	b.d.	b.d.	b.d.	b.d.	b.d.	b.d.	b.d.	b.d.	b.d.	0.013
FeO	11.770	11.520	11.032	10.623	10.770	10.791	10.653	10.813	10.887	11.371	12.575	11.519	10.983	11.124	11.674	11.956
MnO	0.183	0.162	0.156	0.125	0.154	0.235	0.163	0.074	0.113	0.142	0.214	0.210	0.094	0.139	0.137	0.118
MgO	46.696	47.077	47.417	47.277	47.188	47.538	47.705	47.727	47.598	46.719	45.729	46.659	46.831	47.342	47.293	46.766
CaO	0.220	0.242	0.146	0.135	0.103	0.098	0.146	0.171	0.147	0.206	0.312	0.228	0.097	0.178	0.129	0.033
NiO	0.196	0.189	0.359	0.357	0.346	0.374	0.422	0.378	0.338	0.347	0.117	0.279	0.368	0.278	0.375	0.327
Total	99.46	99.69	99.24	98.84	98.79	99.43	99.66	99.92	99.38	98.87	98.69	98.67	98.50	99.27	100.08	99.39
O=4																
Si	1.000	0.995	0.992	0.997	0.996	0.994	0.994	0.996	0.995	0.995	0.995	0.989	0.993	0.993	0.991	0.993
Al	0.000	0.000	0.000	0.002	0.000	0.000	0.000	0.000	0.000	0.000	0.000	0.000	0.000	0.000	0.000	0.000
Ti	0.001	0.001	0.000	0.001	0.001	0.000	0.000	0.000	0.000	0.001	0.001	0.001	0.000	0.000	0.001	0.001
Fe	0.245	0.239	0.230	0.221	0.225	0.224	0.221	0.223	0.226	0.238	0.265	0.242	0.230	0.232	0.242	0.250
Mn	0.004	0.003	0.003	0.003	0.003	0.005	0.003	0.002	0.002	0.003	0.005	0.004	0.002	0.003	0.003	0.002
Mg	1.733	1.743	1.761	1.756	1.759	1.762	1.760	1.758	1.761	1.744	1.719	1.749	1.749	1.758	1.748	1.740
Ca	0.006	0.006	0.004	0.004	0.003	0.003	0.004	0.005	0.004	0.006	0.008	0.006	0.003	0.005	0.003	0.001
Ni	0.004	0.004	0.007	0.007	0.007	0.007	0.008	0.008	0.007	0.007	0.002	0.006	0.007	0.006	0.007	0.007
Total	2.993	2.991	2.997	2.991	2.994	2.995	2.990	2.992	2.995	2.994	2.995	2.997	2.984	2.997	2.995	2.994

Table A.1 - Olivine analyses

Sample	at013	at013	at013	at013	at013	at013	at013	at013	at013	at013	at013	at013	at013	at013	at014a	at014a
Unit	php	php	php	php	php	php	php	php	php	php	php	php	php	php	php	php
Remarks	tr2,6	tr2,7	tr2,8	tr2,9	tr2,10	tr2,11	tr2,12	tr2,13	tr2,14	tr2,15	tr2,16	tr2,17	tr2,18	tr2,19	rim	core
SiO2	40.051	39.805	40.146	39.922	39.813	40.154	39.745	39.706	39.611	40.328	40.166	39.886	39.887	39.914	40.030	39.850
TiO2	0.078	0.031	0.031	b.d.	0.062	b.d.	0.015	0.078	0.049	0.006	0.004	0.071	b.d.	b.d.	0.040	0.020
Al2O3	b.d.	b.d.	b.d.	b.d.	b.d.	0.028	b.d.	b.d.	b.d.	b.d.	b.d.	b.d.	b.d.	b.d.	0.020	0.010
FeO	12.354	12.465	12.551	12.556	12.480	12.340	12.417	12.482	12.083	12.002	11.500	10.910	11.026	11.299	11.200	10.710
MnO	0.121	0.179	0.116	0.194	0.184	0.192	0.119	0.110	0.191	0.210	0.168	0.086	0.112	0.176	0.210	0.090
MgO	46.363	46.408	46.664	46.564	46.522	46.581	46.316	46.578	47.153	46.631	47.196	47.932	47.530	47.108	47.140	47.500
CaO	0.015	0.103	0.109	0.110	0.104	0.065	0.097	0.055	0.088	0.035	0.074	0.124	0.106	0.275	0.210	0.070
NiO	0.216	0.368	0.367	0.413	0.344	0.300	0.336	0.418	0.348	0.345	0.402	0.428	0.341	0.222	0.360	0.380
Total	99.49	99.60	100.32	100.01	99.87	99.99	99.31	99.88	99.98	99.96	99.86	99.82	99.37	99.35	99.43	99.05
O=4																
Si	0.999	0.994	0.995	0.993	0.992	0.998	0.994	0.990	0.986	1.000	0.996	0.987	0.991	0.995	0.995	0.993
Al	0.000	0.000	0.000	0.000	0.000	0.001	0.000	0.000	0.000	0.000	0.000	0.000	0.000	0.000	0.001	0.000
Ti	0.001	0.001	0.001	0.000	0.001	0.000	0.000	0.001	0.001	0.000	0.000	0.001	0.000	0.000	0.001	0.000
Fe	0.258	0.260	0.260	0.261	0.260	0.256	0.260	0.260	0.251	0.249	0.238	0.226	0.229	0.235	0.233	0.223
Mn	0.003	0.004	0.002	0.004	0.004	0.004	0.003	0.002	0.004	0.004	0.004	0.002	0.002	0.004	0.004	0.002
Mg	1.725	1.728	1.723	1.726	1.729	1.725	1.727	1.731	1.749	1.723	1.744	1.769	1.760	1.750	1.747	1.765
Ca	0.000	0.003	0.003	0.003	0.003	0.002	0.003	0.001	0.002	0.001	0.002	0.003	0.003	0.007	0.006	0.002
Ni	0.004	0.007	0.007	0.008	0.007	0.006	0.007	0.008	0.007	0.007	0.008	0.009	0.007	0.004	0.007	0.008
Total	2.990	2.997	2.991	2.995	2.996	2.992	2.994	2.993	3.000	2.984	2.992	2.997	2.992	2.995	2.994	2.993

Table A.1 - Olivine analyses

Sample	at014a	at014a	at016	at016	at016	at016	at016	at021	at021	at021	at021	at021	at021	at022	at022	at022
Unit	php	php	B1	B1	B1	B1	B1	php	php	php	php	php	php	php	php	php
Remarks	rim	core	rim	core	rim	core	core							tr3,1	tr3,2	tr3,3
SiO2	39.450	39.880	39.566	39.741	40.426	39.869	39.784	40.351	40.722	40.233	39.994	40.494	40.471	39.770	39.869	40.313
TiO2	0.050	b.d.	b.d.	b.d.	0.042	0.046	0.005	0.008	b.d.	0.085	0.018	0.038	0.045	0.037	0.047	0.067
Al2O3	b.d.	b.d.	b.d.	b.d.	b.d.	0.067	b.d.	b.d.	0.031	0.038	b.d.	b.d.	b.d.	b.d.	b.d.	0.058
FeO	11.760	11.220	13.173	13.436	13.609	13.686	13.871	11.577	10.848	11.833	13.356	11.959	11.707	12.025	11.894	11.143
MnO	0.150	0.090	0.543	0.617	0.563	0.534	0.581	0.077	0.106	0.132	0.222	0.193	0.211	0.157	0.240	0.177
MgO	46.530	46.900	45.496	45.398	45.978	45.185	44.937	47.268	47.801	47.237	45.464	47.057	46.989	46.689	46.497	47.364
CaO	0.180	0.130	0.414	0.422	0.502	0.453	0.429	0.094	0.142	0.122	0.143	0.033	0.206	0.267	0.209	0.160
NiO	0.310	0.330	0.000	0.034	0.005	0.021	0.012	0.401	0.348	0.397	0.259	0.249	0.284	0.133	0.241	0.239
Total	98.70	98.71	99.57	99.95	101.42	100.24	99.94	99.86	100.31	100.36	99.63	100.27	100.01	99.39	99.28	99.83
O=4																
Si	0.990	0.996	0.993	0.995	0.996	0.996	0.997	0.999	1.001	0.994	1.002	1.000	1.002	0.993	0.997	0.997
Al	0.000	0.000	0.000	0.000	0.000	0.002	0.000	0.000	0.001	0.001	0.000	0.000	0.000	0.000	0.000	0.002
Ti	0.001	0.000	0.000	0.000	0.001	0.001	0.000	0.000	0.000	0.002	0.000	0.001	0.001	0.001	0.001	0.001
Fe	0.247	0.234	0.277	0.281	0.280	0.286	0.291	0.240	0.223	0.244	0.280	0.247	0.242	0.251	0.249	0.231
Mn	0.003	0.002	0.012	0.013	0.012	0.011	0.012	0.002	0.002	0.003	0.005	0.004	0.004	0.003	0.005	0.004
Mg	1.741	1.747	1.702	1.695	1.689	1.682	1.679	1.745	1.751	1.739	1.697	1.733	1.734	1.738	1.733	1.747
Ca	0.005	0.003	0.011	0.011	0.013	0.012	0.012	0.002	0.004	0.003	0.004	0.001	0.005	0.007	0.006	0.004
Ni	0.006	0.007	0.000	0.001	0.000	0.000	0.000	0.008	0.007	0.008	0.005	0.005	0.006	0.003	0.005	0.005
Total	2.993	2.989	2.995	2.996	2.991	2.990	2.991	2.996	2.989	2.994	2.993	2.991	2.994	2.996	2.996	2.991

Table A.1 - Olivine analyses

Sample	at022	at022	at022	at022	at022	at022	at022	at022	at022	at022	at022	at022	at022	at022	at022	at022
Unit	php	php	php	php	php	php	php	php	php	php	php	php	php	php	php	php
Remarks	tr3,4	tr3,5	tr4,1	tr4,2	tr4,3	tr4,4	tr4,5	tr4,6	tr4,7	tr4,8	tr5,1	tr5,2	tr5,3	tr5,4	tr5,5	tr5,6
SiO2	40.037	39.968	39.723	40.134	40.144	40.143	39.863	40.154	40.435	39.944	40.070	39.902	39.669	39.566	39.555	39.256
TiO2	0.044	b.d.	0.011	0.008	0.033	0.117	0.080	0.062	b.d.	0.061	0.090	0.050	0.061	0.107	0.063	0.035
Al2O3	b.d.	b.d.	b.d.	b.d.	b.d.	b.d.	b.d.	b.d.	0.010	b.d.	b.d.	b.d.	b.d.	0.010	b.d.	b.d.
FeO	10.449	9.977	12.930	10.618	9.763	9.577	9.687	11.069	9.702	11.338	12.743	13.362	14.662	13.935	13.487	14.479
MnO	0.095	0.214	0.283	0.157	0.126	0.123	0.123	0.148	0.103	0.175	0.221	0.224	0.164	0.182	0.278	0.222
MgO	47.921	48.089	45.311	47.998	48.346	48.334	47.713	47.274	48.778	47.591	46.496	45.875	44.884	45.081	45.590	44.293
CaO	0.124	0.139	0.498	0.167	0.124	0.182	0.118	0.168	0.148	0.207	0.365	0.299	0.309	0.304	0.298	0.323
NiO	0.328	0.385	0.193	0.319	0.359	0.460	0.294	0.225	0.420	0.197	0.183	0.152	0.056	0.171	0.179	0.166
Total	99.20	99.07	99.17	99.87	99.14	99.14	98.14	99.38	99.97	99.79	100.66	100.27	100.33	99.62	99.62	98.97
O=4																
Si	0.994	0.992	1.000	0.991	0.994	0.994	0.997	0.998	0.994	0.990	0.992	0.993	0.994	0.994	0.992	0.996
Al	0.000	0.000	0.000	0.000	0.000	0.000	0.000	0.000	0.000	0.000	0.000	0.000	0.000	0.000	0.000	0.000
Ti	0.001	0.000	0.000	0.000	0.001	0.002	0.002	0.001	0.000	0.001	0.002	0.001	0.001	0.002	0.001	0.001
Fe	0.217	0.207	0.272	0.219	0.202	0.198	0.203	0.230	0.199	0.235	0.264	0.278	0.307	0.293	0.283	0.307
Mn	0.002	0.004	0.006	0.003	0.003	0.003	0.003	0.003	0.002	0.004	0.005	0.005	0.003	0.004	0.006	0.005
Mg	1.773	1.779	1.700	1.767	1.784	1.783	1.780	1.752	1.787	1.759	1.716	1.703	1.676	1.689	1.705	1.675
Ca	0.003	0.004	0.013	0.004	0.003	0.005	0.003	0.004	0.004	0.005	0.010	0.008	0.008	0.008	0.008	0.009
Ni	0.007	0.008	0.004	0.006	0.007	0.009	0.006	0.004	0.008	0.004	0.004	0.003	0.001	0.003	0.004	0.003
Total	2.997	2.994	2.995	2.990	2.994	2.994	2.994	2.992	2.994	2.998	2.993	2.991	2.990	2.993	2.999	2.996

Table A.1 - Olivine analyses

Sample	at022	at022	at022	at022	at022	at022	at022	at022	at022	at022	at022	at022	at022	at022	at022	at022
Unit	php	php	php	php	php	php	php	php	php	php	php	php	php	php	php	php
Remarks	tr5,7	tr5,8	tr5,9	tr6,1	tr6,2	tr6,3	tr6,4	tr6,5	tr6,6	tr6,7	tr6,8	tr6,9	tr6,10	tr6,11	tr6,12	tr6,13
SiO2	39.215	38.984	39.241	39.839	39.962	39.845	40.012	40.138	40.034	39.855	40.203	40.138	40.002	40.120	40.157	40.076
TiO2	0.048	0.005	0.091	0.023	0.008	0.005	0.026	0.054	0.021	0.043	b.d.	0.040	0.044	0.080	0.042	b.d.
Al2O3	b.d.	b.d.	b.d.	b.d.	b.d.	b.d.	b.d.	b.d.	b.d.	b.d.	0.002	b.d.	b.d.	b.d.	b.d.	b.d.
FeO	16.553	15.948	13.697	12.380	10.628	10.514	9.905	9.646	9.910	9.949	10.234	10.398	10.462	10.157	10.229	10.042
MnO	0.303	0.257	0.223	0.207	0.134	0.126	0.097	0.090	0.142	0.207	0.112	0.076	0.157	0.110	0.119	0.118
MgO	42.928	43.252	44.969	46.370	47.454	47.517	48.186	48.267	48.065	47.952	47.878	47.684	47.830	47.892	47.417	47.576
CaO	0.339	0.326	0.311	0.403	0.202	0.138	0.147	0.103	0.061	0.082	0.119	0.109	0.104	0.058	0.079	0.099
NiO	0.142	0.059	0.116	0.029	0.265	0.346	0.393	0.442	0.382	0.330	0.364	0.412	0.360	0.429	0.504	0.394
Total	99.91	99.13	98.73	99.83	98.98	98.87	98.92	99.01	98.83	98.81	99.08	99.08	99.25	99.26	98.80	98.80
O=4																
Si	0.996	0.994	0.993	0.993	0.996	0.994	0.992	0.995	0.996	0.993	0.997	0.997	0.994	0.995	1.001	0.998
Al	0.000	0.000	0.000	0.000	0.000	0.000	0.000	0.000	0.000	0.000	0.000	0.000	0.000	0.000	0.000	0.000
Ti	0.001	0.000	0.002	0.000	0.000	0.000	0.000	0.001	0.000	0.001	0.000	0.001	0.001	0.001	0.001	0.000
Fe	0.351	0.340	0.290	0.258	0.221	0.219	0.205	0.200	0.206	0.207	0.212	0.216	0.217	0.211	0.213	0.209
Mn	0.007	0.006	0.005	0.004	0.003	0.003	0.002	0.002	0.003	0.004	0.002	0.002	0.003	0.002	0.003	0.002
Mg	1.625	1.644	1.697	1.722	1.763	1.767	1.781	1.783	1.783	1.780	1.770	1.766	1.771	1.770	1.762	1.767
Ca	0.009	0.009	0.008	0.011	0.005	0.004	0.004	0.003	0.002	0.002	0.003	0.003	0.003	0.002	0.002	0.003
Ni	0.003	0.001	0.002	0.001	0.005	0.007	0.008	0.009	0.008	0.007	0.007	0.008	0.007	0.009	0.010	0.008
Total	2.992	2.994	2.997	2.989	2.993	2.994	2.992	2.993	2.998	2.994	2.991	2.993	2.996	2.990	2.992	2.987

Table A.1 - Olivine analyses

Sample	at022	at022	at022	at022	at022	at022	at022	at022	at025	at025	at025	at025	at025	at025	at025	at025
Unit	php	php	php	php	php	php	php	php	B1	B1	B1	B1	B1	B1	B1	B1
Remarks	tr6,14	tr6,15	tr6,16	tr6,17	tr6,18	tr6,19	tr6,20	tr6,21		rim	core	rim	core		rim	core
SiO2	40.122	40.268	39.922	39.929	40.224	40.304	40.004	39.948	40.007	40.297	39.728	40.022	40.034	39.876	39.998	40.171
TiO2	0.042	0.051	b.d.	0.038	b.d.	0.022	0.005	0.031	b.d.	b.d.	0.035	0.088	0.045	b.d.	0.054	b.d.
Al2O3	b.d.	0.002	b.d.	b.d.	b.d.	b.d.	b.d.	b.d.	b.d.	b.d.	b.d.	b.d.	0.052	b.d.	b.d.	b.d.
FeO	10.038	9.838	9.716	9.664	9.483	9.858	10.425	10.680	12.753	12.046	11.849	12.049	12.226	12.162	12.219	12.396
MnO	0.130	0.137	0.157	0.140	0.154	0.223	0.119	0.134	0.829	0.827	0.887	0.829	0.752	0.878	0.608	0.560
MgO	48.183	48.235	48.281	48.373	48.352	47.824	47.610	47.401	45.911	46.627	46.253	46.265	46.456	46.307	46.176	46.463
CaO	0.128	0.078	0.110	0.110	0.096	0.137	0.212	0.182	0.470	0.408	0.357	0.401	0.462	0.478	0.413	0.544
NiO	0.422	0.442	0.338	0.438	0.517	0.470	0.345	0.209	0.149	0.187	0.139	0.157	0.093	0.169	0.128	0.120
Total	99.42	99.40	98.81	99.01	99.27	99.14	99.00	98.97	100.46	100.87	99.58	100.17	100.45	100.24	99.92	100.67
O=4																
Si	0.993	0.995	0.991	0.991	0.995	0.998	0.995	0.995	0.994	0.994	0.992	0.995	0.992	0.991	0.996	0.994
Al	0.000	0.000	0.000	0.000	0.000	0.000	0.000	0.000	0.000	0.000	0.000	0.000	0.002	0.000	0.000	0.000
Ti	0.001	0.001	0.000	0.001	0.000	0.000	0.000	0.001	0.000	0.000	0.001	0.002	0.001	0.000	0.001	0.000
Fe	0.208	0.203	0.202	0.201	0.196	0.204	0.217	0.222	0.265	0.249	0.248	0.250	0.253	0.253	0.255	0.256
Mn	0.003	0.003	0.003	0.003	0.003	0.005	0.002	0.003	0.017	0.017	0.019	0.017	0.016	0.018	0.013	0.012
Mg	1.778	1.777	1.787	1.790	1.783	1.766	1.765	1.760	1.700	1.715	1.722	1.714	1.717	1.716	1.715	1.714
Ca	0.003	0.002	0.003	0.003	0.003	0.004	0.006	0.005	0.013	0.011	0.010	0.011	0.012	0.013	0.011	0.014
Ni	0.008	0.009	0.007	0.009	0.010	0.009	0.007	0.004	0.003	0.004	0.003	0.003	0.002	0.003	0.003	0.002
Total	2.994	2.990	2.993	2.998	2.990	2.986	2.992	2.990	2.992	2.990	2.995	2.992	2.995	2.994	2.994	2.992

Table A.1 - Olivine analyses

Sample	at025	at025	at025	at025	at025	at025	at120	at120	at120	at120	at120	at120	at120	at204	at204	at204
Unit	B1	B1	B1	B1	B1	B1	php	php	php	php	php	php	php	php	php	php
Remarks	tr7,1	tr7,2	tr7,3	tr7,4	tr7,5	tr7,6										
SiO2	40.001	40.065	40.550	40.182	40.070	40.545	40.148	40.187	40.189	40.228	40.057	39.655	40.249	40.190	40.110	39.660
TiO2	0.034	0.036	b.d.	b.d.	0.088	0.074	0.077	b.d.	0.056	0.061	b.d.	0.032	0.030	0.057	0.040	0.030
Al2O3	0.020	b.d.	b.d.	0.001	b.d.	b.d.	b.d.	b.d.	b.d.	b.d.	0.013	b.d.	b.d.	b.d.	0.010	b.d.
FeO	11.705	11.952	12.171	11.956	11.915	11.774	11.665	11.854	11.597	12.811	11.982	12.500	10.281	10.980	10.240	10.420
MnO	0.884	0.873	0.905	0.939	0.834	0.878	0.193	0.176	0.184	0.192	0.143	0.262	0.133	0.180	0.170	0.120
MgO	46.252	46.096	46.129	46.160	46.302	47.083	46.949	47.009	47.104	46.572	46.832	46.149	48.032	47.343	47.850	47.420
CaO	0.393	0.380	0.543	0.446	0.393	0.403	0.226	0.250	0.264	0.377	0.304	0.273	0.139	0.166	0.110	0.140
NiO	0.150	0.212	0.153	0.216	0.160	0.134	0.204	0.168	0.234	0.085	0.063	0.244	0.381	0.372	0.410	0.440
Total	99.93	100.01	100.89	100.43	100.24	101.26	99.65	100.08	99.85	100.88	99.56	99.35	99.61	99.61	99.00	98.28
O=4																
Si	0.996	0.998	1.001	0.996	0.996	0.995	0.997	0.996	0.997	0.993	0.996	0.994	0.994	0.997	0.996	0.994
Al	0.001	0.000	0.000	0.000	0.000	0.000	0.000	0.000	0.000	0.000	0.000	0.000	0.000	0.000	0.000	0.000
Ti	0.001	0.001	0.000	0.000	0.002	0.001	0.001	0.000	0.001	0.001	0.000	0.001	0.001	0.001	0.001	0.001
Fe	0.244	0.249	0.251	0.248	0.248	0.242	0.242	0.246	0.240	0.265	0.249	0.262	0.212	0.228	0.213	0.218
Mn	0.019	0.018	0.019	0.020	0.018	0.018	0.004	0.004	0.004	0.004	0.003	0.006	0.003	0.004	0.004	0.003
Mg	1.717	1.711	1.697	1.706	1.715	1.722	1.738	1.737	1.741	1.714	1.736	1.724	1.768	1.751	1.772	1.772
Ca	0.010	0.010	0.014	0.012	0.010	0.011	0.006	0.007	0.007	0.010	0.008	0.007	0.004	0.004	0.003	0.004
Ni	0.003	0.004	0.003	0.004	0.003	0.003	0.004	0.003	0.005	0.002	0.001	0.005	0.008	0.007	0.008	0.009
Total	2.991	2.991	2.985	2.986	2.992	2.992	2.992	2.993	2.995	2.989	2.993	2.999	2.990	2.992	2.997	3.001

Table A.1 - Olivine analyses

Sample	at204	at204	at204	at206	at206	at206	at206	at206	at206	at206	at206	at206	at206	at217	at217	at217
Unit	php	php	php	php	php	php	php	php	php	php	php	php	php	B1	B1	B1
Remarks																
SiO2	39.140	39.740	39.800	39.912	40.582	39.754	40.501	40.588	39.778	39.638	40.178	40.563	40.277	40.194	40.504	40.366
TiO2	0.020	b.d.	0.010	b.d.	0.049	0.055	0.059	0.021	0.071	b.d.	b.d.	0.017	0.014	b.d.	0.005	b.d.
Al2O3	b.d.	b.d.	b.d.	0.007	0.071	b.d.	b.d.	0.212	b.d.	0.054	b.d.	b.d.	0.020	b.d.	0.003	0.039
FeO	13.560	13.190	11.510	14.145	12.077	14.421	9.803	11.457	14.182	16.101	10.978	9.644	9.706	12.698	11.585	12.517
MnO	0.170	0.100	0.110	0.212	0.201	0.239	0.134	0.143	0.209	0.345	0.125	0.100	0.126	1.017	0.904	0.925
MgO	45.040	45.450	46.590	45.665	47.243	44.743	48.503	47.673	44.912	43.273	47.677	48.717	48.738	45.714	46.992	46.342
CaO	0.090	0.090	0.140	0.114	0.209	0.147	0.116	0.123	0.146	0.211	0.078	0.091	0.115	0.569	0.132	0.284
NiO	0.300	0.310	0.300	0.259	0.184	0.117	0.501	0.266	0.269	0.250	0.293	0.484	0.395	0.067	0.060	b.d.
Total	98.35	99.00	98.46	100.48	100.76	99.69	99.81	100.79	99.72	100.11	99.57	99.87	99.51	100.44	100.47	100.85
O=4																
Si	0.994	1.000	0.998	0.995	0.998	1.000	0.997	0.996	0.999	1.001	0.997	0.997	0.994	0.999	1.000	0.998
Al	0.000	0.000	0.000	0.000	0.002	0.000	0.000	0.006	0.000	0.002	0.000	0.000	0.001	0.000	0.000	0.001
Ti	0.000	0.000	0.000	0.000	0.001	0.001	0.001	0.000	0.001	0.000	0.000	0.000	0.000	0.000	0.000	0.000
Fe	0.288	0.277	0.241	0.295	0.248	0.303	0.202	0.235	0.298	0.340	0.228	0.198	0.200	0.264	0.239	0.259
Mn	0.004	0.002	0.002	0.004	0.004	0.005	0.003	0.003	0.004	0.007	0.003	0.002	0.003	0.021	0.019	0.019
Mg	1.704	1.704	1.741	1.697	1.732	1.677	1.780	1.744	1.682	1.630	1.763	1.785	1.793	1.694	1.730	1.708
Ca	0.002	0.002	0.004	0.003	0.005	0.004	0.003	0.003	0.004	0.006	0.002	0.002	0.003	0.015	0.003	0.008
Ni	0.006	0.006	0.006	0.005	0.004	0.002	0.010	0.005	0.005	0.005	0.006	0.010	0.008	0.001	0.001	0.000
Total	2.998	2.991	2.992	2.999	2.994	2.992	2.996	2.992	2.993	2.991	2.999	2.994	3.002	2.994	2.992	2.993

Table A.1 - Olivine analyses

Sample	at217	at217	at217	at217	at217	at217	at217	at217	at217	tap1b	tap1b	tap1b
Unit	B1	B1	B1	B1	B1	B1	B1	B1	B1	C2	C2	C2
Remarks												
SiO2	40.170	40.192	40.237	40.023	40.388	39.943	40.155	40.002	40.142	39.830	39.583	40.993
TiO2	0.070	b.d.	b.d.	b.d.	0.023	0.078	b.d.	0.050	b.d.	0.043	b.d.	b.d.
Al2O3	b.d.	0.003	b.d.	b.d.	0.004	b.d.	b.d.	b.d.	b.d.	0.011	0.031	0.004
FeO	12.553	12.594	12.664	12.550	12.372	12.473	12.857	12.544	12.576	15.762	15.860	8.882
MnO	1.002	1.008	0.917	0.758	0.897	0.965	0.689	0.950	1.022	0.485	0.521	0.537
MgO	45.870	45.678	45.634	45.710	45.977	45.999	45.751	45.934	45.686	44.060	43.953	49.897
CaO	0.520	0.584	0.609	0.701	0.441	0.474	0.504	0.574	0.587	0.077	0.089	0.062
NiO	b.d.	0.010	0.115	0.110	0.127	0.003	0.081	b.d.	0.072	0.033	b.d.	b.d.
Total	100.42	100.38	100.39	99.92	100.51	100.23	100.24	100.36	100.37	100.54	100.31	100.66
O=4												
Si	0.998	0.999	1.001	0.999	1.001	0.995	0.999	0.995	0.999	1.000	0.997	0.996
Al	0.000	0.000	0.000	0.000	0.000	0.000	0.000	0.000	0.000	0.000	0.001	0.000
Ti	0.001	0.000	0.000	0.000	0.000	0.001	0.000	0.001	0.000	0.001	0.000	0.000
Fe	0.261	0.262	0.263	0.262	0.256	0.260	0.268	0.261	0.262	0.331	0.334	0.180
Mn	0.021	0.021	0.019	0.016	0.019	0.020	0.015	0.020	0.022	0.010	0.011	0.011
Mg	1.699	1.693	1.692	1.701	1.699	1.707	1.698	1.704	1.695	1.648	1.650	1.807
Ca	0.014	0.016	0.016	0.019	0.012	0.013	0.013	0.015	0.016	0.002	0.002	0.002
Ni	0.000	0.000	0.002	0.002	0.003	0.000	0.002	0.000	0.001	0.001	0.000	0.000
Total	2.994	2.991	2.993	2.999	2.990	2.996	2.995	2.996	2.995	2.993	2.995	2.996

Table A2.2 - Clinopyroxene analyses

Sample	at003	at003	at003	at003	at003	at003	at003	at003	at003	at003	at003	at003	at003	at003	at009
Unit	B1	B1	B1	B1	B1	B1	B1	B1	B1	B1	B1	B1	B1	B1	B1
Rock Type	beb	beb	beb	beb	beb	beb	beb	beb	beb	beb	beb	beb	beb	beb	beb
Remarks				rim	rim	core		rim	core		rim	core	rim		rim
SiO2	54.449	54.040	54.380	53.065	53.813	52.423	54.014	53.522	53.856	52.886	53.484	53.355	52.971	53.050	53.162
TiO2	0.559	0.561	0.373	0.625	0.398	1.042	0.109	0.253	0.214	0.375	0.272	0.091	0.999	0.881	1.117
Al2O3	0.711	0.541	0.410	0.639	0.403	0.846	0.694	0.815	0.661	1.084	0.846	0.947	0.907	0.821	0.868
FeO	2.448	2.174	2.067	1.714	1.076	1.585	1.668	1.868	1.442	2.885	3.471	2.729	1.934	1.475	1.804
Fe2O3	0.809	1.427	0.875	1.761	2.211	2.625	1.455	2.732	1.602	2.954	1.731	1.914	2.258	2.368	2.443
Cr2O3	0.071	0.078	0.112	0.088	0.163	0.064	0.122	0.101	0.104	0.060	0.050	0.040	0.123	0.094	0.120
MnO	0.123	0.092	0.049	0.044	0.095	0.118	0.096	0.123	0.065	0.169	0.217	0.146	0.069	0.043	0.070
NiO	0.006	0.027	b.d.	b.d.	0.102	b.d.	b.d.	0.039	b.d.	b.d.	b.d.	b.d.	0.009	0.057	b.d.
MgO	16.412	16.233	16.605	16.066	16.438	15.929	16.427	15.653	16.407	14.585	15.272	15.231	15.738	16.075	15.914
CaO	25.192	25.000	25.299	24.876	25.064	24.640	25.163	24.690	25.268	24.466	24.542	24.821	24.697	24.861	24.741
Na2O	0.321	0.406	0.250	0.379	0.435	0.422	0.295	0.576	0.317	0.685	0.387	0.441	0.547	0.465	0.541
K2O	b.d.	b.d.	0.021	b.d.	b.d.	b.d.	0.013	b.d.	b.d.	b.d.	0.014	b.d.	b.d.	b.d.	0.039
Total	101.100	100.580	100.440	99.260	100.200	99.690	100.060	100.370	99.940	100.150	100.290	99.720	100.250	100.190	100.820
O = 6															
(IV)Si	1.969	1.966	1.977	1.957	1.963	1.931	1.971	1.957	1.968	1.949	1.964	1.966	1.939	1.940	1.936
(IV)Al	0.030	0.023	0.018	0.028	0.017	0.037	0.029	0.035	0.028	0.047	0.036	0.034	0.039	0.035	0.037
Sum	1.999	1.989	1.995	1.985	1.980	1.968	2.000	1.992	1.996	1.996	2.000	2.000	1.978	1.975	1.973
(VI)Al	0.000	0.000	0.000	0.000	0.000	0.000	0.001	0.000	0.000	0.000	0.000	0.007	0.000	0.000	0.000
(VI)Ti	0.015	0.015	0.010	0.017	0.011	0.029	0.003	0.007	0.006	0.010	0.008	0.003	0.028	0.024	0.031
(VI)Fe3+	0.022	0.039	0.024	0.049	0.061	0.073	0.040	0.075	0.044	0.082	0.048	0.053	0.062	0.065	0.067
(VI)Fe2+	0.074	0.066	0.063	0.053	0.033	0.049	0.051	0.057	0.044	0.089	0.107	0.084	0.059	0.045	0.055
(VI)Mg	0.885	0.881	0.900	0.883	0.894	0.874	0.894	0.853	0.894	0.801	0.836	0.837	0.859	0.877	0.864
(VI)Mn	0.004	0.003	0.001	0.001	0.003	0.004	0.003	0.004	0.002	0.005	0.007	0.005	0.002	0.001	0.002
(VI)Cr	0.002	0.002	0.003	0.003	0.005	0.002	0.004	0.003	0.003	0.002	0.001	0.001	0.004	0.003	0.003
(VI)Ni	0.000	0.001	0.000	0.000	0.003	0.000	0.000	0.001	0.000	0.000	0.000	0.000	0.000	0.002	0.000
(VI)Ca	0.976	0.975	0.985	0.983	0.980	0.972	0.984	0.967	0.989	0.966	0.965	0.980	0.969	0.974	0.965
(VI)Na	0.023	0.029	0.018	0.027	0.031	0.030	0.021	0.041	0.022	0.049	0.028	0.032	0.039	0.033	0.038
(VI)K	0.000	0.000	0.001	0.000	0.000	0.000	0.001	0.000	0.000	0.000	0.001	0.000	0.000	0.000	0.002
Sum	2.001	2.011	2.005	2.016	2.021	2.033	2.002	2.008	2.004	2.004	2.001	2.002	2.022	2.024	2.027

Table A2.2 - Clinopyroxene analyses

Sample	at009	at009	at009	at009	at009	at009	at009	at009	at009	at012	at012	at012	at012	at012	at012
Unit	B1	B1	B1	B1	B1	B1	B1	B1	B1						
Rock Type	beb	beb	beb	beb	beb	beb	beb	beb	beb	syen	syen	syen	syen	syen	syen
Remarks	core	rim	core	rim	rim	rim	core	rim	core	rim	core	rim	rim	core	rim
SiO2	53.052	53.408	51.974	54.412	54.026	53.919	53.067	53.462	52.984	51.652	51.635	50.992	50.990	51.195	51.301
TiO2	1.104	0.840	1.578	0.314	0.427	0.581	1.216	0.755	1.218	0.341	0.453	0.228	0.242	0.195	0.229
Al2O3	0.789	0.862	1.216	0.125	0.440	0.432	0.863	0.736	0.598	0.341	0.463	0.711	0.568	0.548	0.502
FeO	1.675	1.842	2.043	1.896	1.804	1.977	1.416	2.373	2.492	4.607	5.085	6.970	6.662	7.286	5.316
Fe2O3	2.664	2.961	2.703	1.961	2.077	2.197	3.073	1.941	1.798	17.830	17.680	15.016	14.876	13.687	15.079
Cr2O3	0.095	0.105	0.078	0.098	0.090	0.081	0.131	0.144	0.023	0.125	0.159	0.084	0.090	0.083	0.115
MnO	0.044	0.035	0.089	0.050	0.062	0.128	0.025	0.090	0.053	0.398	0.425	0.731	0.777	0.536	0.552
NiO	b.d.	b.d.	0.088	0.038	0.109	0.028	0.006	b.d.	b.d.	0.009	b.d.	b.d.	b.d.	b.d.	b.d.
MgO	15.928	15.544	15.176	16.126	16.033	16.030	15.882	15.644	15.834	5.143	4.916	4.819	5.312	5.599	6.055
CaO	24.729	24.590	24.565	24.617	24.761	24.724	24.554	24.736	24.648	10.608	10.964	13.086	13.790	14.557	13.360
Na2O	0.569	0.756	0.613	0.656	0.580	0.567	0.718	0.556	0.451	7.387	7.294	6.058	5.736	5.374	5.978
K2O	b.d.	0.005	b.d.	0.007	0.007	b.d.	b.d.	b.d.	b.d.	0.014	b.d.	0.008	b.d.	0.000	0.014
Total	100.650	100.950	100.120	100.300	100.420	100.660	100.950	100.440	100.100	98.450	99.070	98.700	99.040	99.060	98.500
O = 6															
(IV)Si	1.935	1.943	1.913	1.984	1.970	1.963	1.930	1.954	1.945	1.998	1.990	1.985	1.977	1.983	1.985
(IV)Al	0.034	0.037	0.053	0.005	0.019	0.019	0.037	0.032	0.026	0.002	0.010	0.015	0.023	0.017	0.015
Sum	1.969	1.980	1.966	1.989	1.989	1.982	1.967	1.986	1.971	2.000	2.000	2.000	2.000	2.000	2.000
(VI)Al	0.000	0.000	0.000	0.000	0.000	0.000	0.000	0.000	0.000	0.014	0.011	0.017	0.003	0.008	0.008
(VI)Ti	0.030	0.023	0.044	0.009	0.012	0.016	0.033	0.021	0.034	0.010	0.013	0.007	0.007	0.006	0.007
(VI)Fe3+	0.073	0.081	0.075	0.054	0.057	0.060	0.084	0.053	0.050	0.519	0.513	0.440	0.434	0.399	0.439
(VI)Fe2+	0.051	0.056	0.063	0.058	0.055	0.060	0.043	0.072	0.077	0.149	0.164	0.227	0.216	0.236	0.172
(VI)Mg	0.866	0.843	0.833	0.877	0.871	0.870	0.861	0.852	0.866	0.297	0.282	0.280	0.307	0.323	0.349
(VI)Mn	0.001	0.001	0.003	0.002	0.002	0.004	0.001	0.003	0.002	0.013	0.014	0.024	0.026	0.018	0.018
(VI)Cr	0.003	0.003	0.002	0.003	0.003	0.002	0.004	0.004	0.001	0.004	0.005	0.003	0.003	0.003	0.004
(VI)Ni	0.000	0.000	0.003	0.001	0.003	0.001	0.000	0.000	0.000	0.000	0.000	0.000	0.000	0.000	0.000
(VI)Ca	0.966	0.959	0.969	0.962	0.967	0.965	0.957	0.969	0.969	0.440	0.453	0.546	0.573	0.604	0.554
(VI)Na	0.040	0.053	0.044	0.046	0.041	0.040	0.051	0.039	0.032	0.554	0.545	0.457	0.431	0.404	0.449
(VI)K	0.000	0.000	0.000	0.000	0.000	0.000	0.000	0.000	0.000	0.001	0.000	0.000	0.000	0.000	0.001
Sum	2.030	2.019	2.036	2.012	2.011	2.018	2.034	2.013	2.031	2.001	2.000	2.001	2.000	2.001	2.001

Table A2.2 - Clinopyroxene analyses

Sample	at012	at012	at012	at012	at012	at012	at016	at016	at016	at016	at021	at021	at021	at021	at024
Unit							B1	B1	B1	B1					
Rock Type	syen	syen	syen	syen	syen	syen	wehrl	wehrl	wehrl	wehrl	php	php	php	php	lcr
Remarks		core			rim	core									
SiO2	51.880	51.824	51.343	52.105	50.836	51.309	53.087	53.063	51.845	52.799	54.436	54.431	54.246	54.746	52.601
TiO2	0.165	0.249	0.284	0.224	0.259	0.157	0.405	0.931	1.060	0.873	0.527	0.594	0.553	0.567	1.377
Al2O3	0.373	0.308	0.367	0.226	0.458	0.343	0.746	0.983	1.214	0.775	0.144	0.218	0.155	0.224	0.878
FeO	4.956	4.328	6.006	4.259	5.058	6.648	2.325	1.381	1.712	1.391	2.870	3.033	2.535	2.106	3.191
Fe2O3	16.419	16.437	14.726	15.450	16.149	14.463	4.439	2.376	2.333	2.120	1.051	0.761	0.695	1.791	2.533
Cr2O3	0.092	0.082	0.068	0.100	0.112	0.066	0.052	0.134	0.028	0.158	0.170	0.072	0.154	0.093	0.052
MnO	0.529	0.496	0.619	0.471	0.580	0.734	0.279	b.d.	0.094	0.053	0.123	0.124	0.146	0.112	0.135
NiO	b.d.	0.031	0.039	0.031	b.d.	b.d.	0.047	b.d.	b.d.	0.018	0.012	b.d.	b.d.	b.d.	0.020
MgO	5.573	6.159	5.991	6.810	5.406	5.552	14.857	16.094	15.495	16.071	16.024	16.142	16.372	16.355	15.138
CaO	11.630	12.539	13.993	13.765	12.634	14.395	23.933	24.951	24.581	24.727	24.671	24.703	24.757	24.580	24.063
Na2O	6.870	6.522	5.686	6.020	6.375	5.556	0.873	0.482	0.438	0.461	0.512	0.438	0.360	0.662	0.642
K2O	b.d.	0.018	0.005	0.015	b.d.	b.d.	b.d.	0.008	b.d.	b.d.	0.003	b.d.	0.038	0.011	b.d.
Total	98.490	98.990	99.130	99.480	97.860	99.220	101.040	100.400	98.800	99.450	100.540	100.520	100.010	101.250	100.630
O = 6															
(IV)Si	2.004	1.990	1.981	1.988	1.984	1.984	1.942	1.936	1.927	1.944	1.984	1.983	1.983	1.978	1.930
(IV)Al	0.000	0.010	0.017	0.010	0.016	0.016	0.032	0.042	0.053	0.034	0.006	0.009	0.007	0.010	0.038
Sum	2.004	2.000	1.998	1.998	2.000	2.000	1.974	1.978	1.980	1.978	1.990	1.992	1.990	1.988	1.968
(VI)Al	0.017	0.004	0.000	0.000	0.005	0.000	0.000	0.000	0.000	0.000	0.000	0.000	0.000	0.000	0.000
(VI)Ti	0.005	0.007	0.008	0.006	0.008	0.005	0.011	0.026	0.030	0.024	0.014	0.016	0.015	0.015	0.038
(VI)Fe3+	0.477	0.475	0.428	0.444	0.474	0.421	0.122	0.065	0.065	0.059	0.029	0.021	0.019	0.049	0.070
(VI)Fe2+	0.160	0.139	0.194	0.136	0.165	0.215	0.071	0.042	0.053	0.043	0.088	0.093	0.077	0.064	0.098
(VI)Mg	0.321	0.353	0.345	0.387	0.315	0.320	0.810	0.875	0.858	0.882	0.871	0.877	0.892	0.881	0.828
(VI)Mn	0.017	0.016	0.020	0.015	0.019	0.024	0.009	0.000	0.003	0.002	0.004	0.004	0.005	0.003	0.004
(VI)Cr	0.003	0.002	0.002	0.003	0.003	0.002	0.002	0.004	0.001	0.005	0.005	0.002	0.004	0.003	0.002
(VI)Ni	0.000	0.001	0.001	0.001	0.000	0.000	0.001	0.000	0.000	0.001	0.000	0.000	0.000	0.000	0.001
(VI)Ca	0.481	0.516	0.579	0.563	0.528	0.597	0.938	0.975	0.979	0.975	0.963	0.964	0.970	0.951	0.946
(VI)Na	0.515	0.486	0.425	0.445	0.482	0.417	0.062	0.034	0.032	0.033	0.036	0.031	0.026	0.046	0.046
(VI)K	0.000	0.001	0.000	0.001	0.000	0.000	0.000	0.000	0.000	0.000	0.000	0.000	0.002	0.001	0.000
Sum	1.996	2.000	2.002	2.001	1.999	2.001	2.026	2.021	2.021	2.024	2.010	2.008	2.010	2.013	2.033

Table A2.2 - Clinopyroxene analyses

Sample	at024	at024	at024	at024	at024	at024	at024	at024	at024	at025	at025	at025	at025	at025	at025
Unit										B1	B1	B1	B1	B1	B1
Rock Type	lcr	lcr	lcr	lcr	lcr	lcr	lcr	lcr	lcr	wehrl	wehrl	wehrl	wehrl	wehrl	wehrl
Remarks												rim	core	rim	core
SiO2	52.312	52.444	52.553	52.991	52.301	52.449	52.663	53.090	52.411	53.671	52.623	52.109	52.558	54.673	52.986
TiO2	1.463	1.305	1.297	1.303	1.439	1.505	1.345	1.247	1.509	0.936	1.287	1.317	1.016	0.393	0.992
Al2O3	0.839	0.613	0.747	0.969	1.228	0.980	0.774	0.772	1.034	0.426	0.962	0.940	0.569	0.256	0.654
FeO	3.559	3.944	3.765	4.179	4.433	3.680	3.814	3.995	3.857	2.179	2.656	1.330	1.175	0.397	0.920
Fe2O3	2.301	1.675	2.020	1.342	1.510	2.425	2.137	1.565	2.053	1.445	1.368	2.812	2.756	2.059	2.776
Cr2O3	0.072	0.089	0.090	0.167	0.123	0.045	0.080	0.047	0.060	0.099	0.195	0.145	0.123	0.109	0.129
MnO	0.099	0.131	0.110	0.148	0.028	0.157	0.145	0.084	0.140	0.068	0.084	0.003	0.031	0.151	0.061
NiO	b.d.	0.003	b.d.	0.009	b.d.	b.d.	b.d.	0.028	0.002	0.006	b.d.	0.007	0.061	0.049	0.038
MgO	15.024	14.948	15.221	15.178	15.021	15.002	15.133	15.095	15.057	16.317	15.878	15.755	16.041	16.997	16.428
CaO	23.886	23.975	23.920	23.949	23.678	23.720	23.965	24.118	23.568	24.534	24.688	24.829	24.760	25.542	24.680
Na2O	0.602	0.507	0.507	0.514	0.476	0.652	0.544	0.569	0.648	0.484	0.268	0.477	0.459	0.457	0.503
K2O	0.011	0.031	0.004	0.024	0.020	0.026	0.002	0.019	b.d.	b.d.	0.052	0.013	0.019	b.d.	b.d.
Total	100.170	99.660	100.230	100.770	100.250	100.640	100.600	100.630	100.340	100.170	100.060	99.730	99.570	101.080	100.170
O = 6															
(IV)Si	1.930	1.944	1.937	1.941	1.928	1.927	1.935	1.947	1.929	1.961	1.933	1.920	1.936	1.970	1.936
(IV)Al	0.036	0.027	0.032	0.042	0.053	0.042	0.034	0.033	0.045	0.018	0.042	0.041	0.025	0.011	0.028
Sum	1.966	1.971	1.969	1.983	1.981	1.969	1.969	1.980	1.974	1.979	1.975	1.961	1.961	1.981	1.964
(VI)Al	0.000	0.000	0.000	0.000	0.000	0.000	0.000	0.000	0.000	0.000	0.000	0.000	0.000	0.000	0.000
(VI)Ti	0.041	0.036	0.036	0.036	0.040	0.042	0.037	0.034	0.042	0.026	0.036	0.036	0.028	0.011	0.027
(VI)Fe3+	0.064	0.047	0.056	0.037	0.042	0.067	0.059	0.043	0.057	0.040	0.038	0.078	0.076	0.056	0.076
(VI)Fe2+	0.110	0.123	0.116	0.128	0.137	0.113	0.117	0.122	0.119	0.067	0.082	0.041	0.036	0.012	0.028
(VI)Mg	0.826	0.826	0.836	0.829	0.826	0.822	0.829	0.825	0.826	0.889	0.869	0.865	0.881	0.913	0.895
(VI)Mn	0.003	0.004	0.003	0.005	0.001	0.005	0.005	0.003	0.004	0.002	0.003	0.000	0.001	0.005	0.002
(VI)Cr	0.002	0.003	0.003	0.005	0.004	0.001	0.002	0.001	0.002	0.003	0.006	0.004	0.004	0.003	0.004
(VI)Ni	0.000	0.000	0.000	0.000	0.000	0.000	0.000	0.001	0.000	0.000	0.000	0.000	0.002	0.001	0.001
(VI)Ca	0.944	0.952	0.944	0.940	0.935	0.934	0.943	0.948	0.930	0.960	0.972	0.980	0.977	0.986	0.966
(VI)Na	0.043	0.036	0.036	0.037	0.034	0.046	0.039	0.040	0.046	0.034	0.019	0.034	0.033	0.032	0.036
(VI)K	0.001	0.001	0.000	0.001	0.001	0.001	0.000	0.001	0.000	0.000	0.002	0.001	0.001	0.000	0.000
Sum	2.034	2.028	2.030	2.018	2.020	2.031	2.031	2.018	2.026	2.021	2.027	2.039	2.039	2.019	2.035

Table A2.2 - Clinopyroxene analyses

Sample	at025	at025	at025	at025	at025	at025	at025	at025	at025	at029	at029	at029	at029	at029	at029
Unit	B1	B1	B1	B1	B1	B1	B1	B1	B1	B2	B2	B2	B2	B2	B2
Rock Type	wehrl	wehrl	wehrl	wehrl	wehrl	wehrl	wehrl	wehrl	wehrl	beb	beb	beb	beb	beb	beb
Remarks	rim	core	rim	core	rim	core	rim	core							
SiO2	54.932	54.502	53.865	53.012	54.680	53.702	54.193	53.981	53.364	51.836	50.991	52.227	53.401	52.737	52.513
TiO2	0.463	0.429	0.478	1.006	0.160	0.811	0.347	0.845	0.918	0.955	1.283	0.921	0.192	0.849	0.807
Al2O3	0.282	0.458	0.252	0.638	0.096	0.366	0.052	0.308	0.604	0.973	1.786	1.158	0.165	1.213	0.869
FeO	1.157	0.927	1.494	2.307	0.914	1.544	1.001	1.877	1.736	5.203	3.646	3.749	4.726	4.413	4.054
Fe2O3	1.249	1.471	1.083	1.589	1.053	2.226	1.256	1.720	1.965	2.980	5.594	3.593	3.145	2.128	3.713
Cr2O3	0.060	0.069	0.116	0.129	0.120	0.169	0.155	0.096	0.156	0.090	0.107	0.034	0.073	0.058	0.114
MnO	0.100	0.105	0.041	0.054	0.057	0.023	0.088	0.033	0.074	0.238	0.279	0.154	0.269	0.146	0.259
NiO	0.076	b.d.	b.d.	0.075	0.008	0.064	0.023	0.000	0.063	0.015	b.d.	b.d.	0.034	b.d.	b.d.
MgO	17.207	17.097	16.687	16.070	17.148	16.417	17.001	16.420	16.228	13.165	12.729	13.962	13.552	14.203	13.602
CaO	25.205	25.241	25.247	24.684	25.405	24.844	25.485	24.848	24.611	23.335	23.410	23.692	23.195	24.002	23.687
Na2O	0.385	0.369	0.256	0.343	0.310	0.474	0.225	0.490	0.498	0.870	1.175	0.886	1.090	0.692	0.995
K2O	b.d.	b.d.	0.007	b.d.	0.001	0.010	b.d.	0.005	b.d.	b.d.	0.026	0.013	0.018	b.d.	b.d.
Total	101.120	100.670	99.520	99.900	99.950	100.650	99.830	100.620	100.220	99.660	101.030	100.390	99.860	100.440	100.610
O = 6															
(IV)Si	1.977	1.970	1.974	1.947	1.988	1.954	1.978	1.963	1.950	1.940	1.888	1.931	1.986	1.944	1.941
(IV)Al	0.012	0.020	0.011	0.028	0.004	0.016	0.002	0.013	0.026	0.043	0.078	0.050	0.007	0.053	0.038
Sum	1.989	1.990	1.985	1.975	1.992	1.970	1.980	1.976	1.976	1.983	1.966	1.981	1.993	1.997	1.979
(VI)Al	0.000	0.000	0.000	0.000	0.000	0.000	0.000	0.000	0.000	0.000	0.000	0.000	0.000	0.000	0.000
(VI)Ti	0.013	0.012	0.013	0.028	0.004	0.022	0.010	0.023	0.025	0.027	0.036	0.026	0.005	0.024	0.022
(VI)Fe3+	0.034	0.040	0.030	0.044	0.029	0.061	0.035	0.047	0.054	0.084	0.156	0.100	0.088	0.059	0.103
(VI)Fe2+	0.035	0.028	0.046	0.071	0.028	0.047	0.031	0.057	0.053	0.163	0.113	0.116	0.147	0.136	0.125
(VI)Mg	0.923	0.922	0.912	0.880	0.930	0.890	0.925	0.890	0.884	0.734	0.703	0.769	0.751	0.781	0.749
(VI)Mn	0.003	0.003	0.001	0.002	0.002	0.001	0.003	0.001	0.002	0.008	0.009	0.005	0.008	0.005	0.008
(VI)Cr	0.002	0.002	0.003	0.004	0.003	0.005	0.004	0.003	0.004	0.003	0.003	0.001	0.002	0.002	0.003
(VI)Ni	0.002	0.000	0.000	0.002	0.000	0.002	0.001	0.000	0.002	0.000	0.000	0.000	0.001	0.000	0.000
(VI)Ca	0.972	0.978	0.991	0.971	0.990	0.968	0.997	0.968	0.964	0.936	0.929	0.938	0.924	0.948	0.938
(VI)Na	0.027	0.026	0.018	0.024	0.022	0.033	0.016	0.035	0.035	0.063	0.084	0.064	0.079	0.049	0.071
(VI)K	0.000	0.000	0.000	0.000	0.000	0.000	0.000	0.000	0.000	0.000	0.001	0.001	0.001	0.000	0.000
Sum	2.011	2.011	2.014	2.026	2.008	2.029	2.022	2.024	2.023	2.018	2.034	2.020	2.006	2.004	2.019

Table A2.2 - Clinopyroxene analyses

Sample	at029	at029	at029	at029	at029	at029	at029	at029	at033	at033	at033	at033	at033	at033	at033
Unit	B2	B2	B2	B2	B2	B2	B2	B2	B2	B2	B2	B2	B2	B2	B2
Rock Type	beb	beb	beb	beb	beb	beb	beb	beb	beb	beb	beb	beb	beb	beb	beb
Remarks												rim	core	rim	
SiO2	52.121	52.231	51.766	51.046	52.596	52.460	51.837	52.013	53.546	53.743	53.673	53.185	53.450	53.627	53.339
TiO2	0.782	0.799	0.970	1.272	0.668	0.794	0.715	0.740	0.441	0.493	0.344	0.416	0.319	0.266	0.545
Al2O3	0.854	0.869	1.374	1.533	1.009	0.938	0.923	0.995	0.569	0.673	0.554	0.440	0.450	0.322	0.657
FeO	5.568	5.266	5.314	4.138	6.229	4.711	4.606	4.753	4.412	4.957	3.658	4.294	5.767	4.963	4.289
Fe2O3	3.165	2.997	2.881	4.634	2.391	3.120	5.119	4.818	2.451	2.029	4.355	3.158	1.424	4.037	3.214
Cr2O3	0.124	0.112	0.073	0.122	0.089	0.072	0.128	0.046	0.037	0.099	0.092	0.119	0.117	0.143	0.182
MnO	0.249	0.247	0.238	0.186	0.252	0.181	0.217	0.305	0.256	0.175	0.267	0.202	0.239	0.199	0.191
NiO	b.d.	b.d.	b.d.	b.d.	b.d.	b.d.	b.d.	0.062	b.d.	b.d.	0.013	b.d.	0.032	0.062	0.161
MgO	12.866	13.256	12.993	12.956	12.831	13.547	12.528	12.525	14.013	14.262	13.891	13.770	13.574	13.164	13.844
CaO	23.369	23.348	23.488	23.335	23.033	23.499	22.782	22.786	23.603	23.614	23.524	23.523	23.388	23.030	23.734
Na2O	0.934	0.888	0.857	1.027	0.999	0.925	1.354	1.343	0.967	0.838	1.220	1.034	0.862	1.331	0.980
K2O	b.d.	b.d.	b.d.	0.034	b.d.	b.d.	b.d.	b.d.	0.020	b.d.	b.d.	b.d.	b.d.	b.d.	b.d.
Total	100.030	100.010	99.950	100.280	100.100	100.250	100.210	100.390	100.310	100.880	101.590	100.140	99.620	101.140	101.140
O = 6															
(IV)Si	1.947	1.947	1.932	1.902	1.960	1.946	1.935	1.938	1.976	1.972	1.961	1.970	1.991	1.975	1.959
(IV)Al	0.038	0.038	0.060	0.067	0.040	0.041	0.041	0.044	0.024	0.028	0.024	0.019	0.009	0.014	0.028
Sum	1.985	1.985	1.992	1.969	2.000	1.987	1.976	1.982	2.000	2.000	1.985	1.989	2.000	1.989	1.987
(VI)Al	0.000	0.000	0.000	0.000	0.005	0.000	0.000	0.000	0.000	0.001	0.000	0.000	0.010	0.000	0.000
(VI)Ti	0.022	0.022	0.027	0.036	0.019	0.022	0.020	0.021	0.012	0.014	0.009	0.012	0.009	0.007	0.015
(VI)Fe3+	0.089	0.084	0.081	0.130	0.067	0.087	0.144	0.135	0.068	0.056	0.120	0.088	0.040	0.112	0.089
(VI)Fe2+	0.174	0.164	0.166	0.129	0.194	0.146	0.144	0.148	0.136	0.152	0.112	0.133	0.180	0.153	0.132
(VI)Mg	0.716	0.737	0.723	0.720	0.713	0.749	0.697	0.696	0.771	0.780	0.756	0.760	0.754	0.723	0.758
(VI)Mn	0.008	0.008	0.008	0.006	0.008	0.006	0.007	0.010	0.008	0.005	0.008	0.006	0.008	0.006	0.006
(VI)Cr	0.004	0.003	0.002	0.004	0.003	0.002	0.004	0.001	0.001	0.003	0.003	0.003	0.003	0.004	0.005
(VI)Ni	0.000	0.000	0.000	0.000	0.000	0.000	0.000	0.002	0.000	0.000	0.000	0.000	0.001	0.002	0.005
(VI)Ca	0.935	0.932	0.939	0.932	0.920	0.934	0.911	0.909	0.933	0.929	0.921	0.934	0.933	0.909	0.934
(VI)Na	0.068	0.064	0.062	0.074	0.072	0.067	0.098	0.097	0.069	0.060	0.086	0.074	0.062	0.095	0.070
(VI)K	0.000	0.000	0.000	0.002	0.000	0.000	0.000	0.000	0.001	0.000	0.000	0.000	0.000	0.000	0.000
Sum	2.016	2.014	2.008	2.033	2.001	2.013	2.025	2.019	1.999	2.000	2.015	2.010	2.000	2.011	2.014

Table A2.2 - Clinopyroxene analyses

Sample	at033	at033	at033	at033	at033	at033	at033	at033	at033	at033	at033	at033	at033	at035	at035
Unit	B2	B2	B2	B2	B2	B2	B2	B2	B2	B2	B2	B2	B2	B1	B1
Rock Type	beb	beb	beb	beb	beb	beb	beb	beb	beb	beb	beb	beb	beb	beb	beb
Remarks	core			rim	core	rim	core	rim	core	rim	core	rim	core		
SiO2	53.183	53.661	53.764	53.010	53.435	53.306	53.457	53.263	53.456	52.455	53.127	53.372	53.579	53.384	53.694
TiO2	0.557	0.395	0.308	0.421	0.401	0.405	0.494	0.114	0.557	0.446	0.561	0.463	0.511	0.680	0.490
Al2O3	0.596	0.594	0.384	0.443	0.533	0.513	0.529	0.093	0.499	0.542	0.628	0.641	0.475	0.791	0.559
FeO	4.833	4.005	4.939	4.625	4.720	5.790	5.001	4.882	4.801	4.246	4.102	4.785	4.885	3.516	1.895
Fe2O3	2.148	2.641	2.655	2.784	2.641	1.895	3.031	3.902	2.055	2.626	3.194	2.192	2.208	1.737	2.033
Cr2O3	0.160	0.154	0.115	0.060	0.139	0.079	0.128	0.132	0.093	0.128	0.108	0.026	0.079	0.128	0.172
MnO	0.199	0.271	0.269	0.225	0.247	0.254	0.261	0.310	0.247	0.259	0.197	0.240	0.239	0.094	0.073
NiO	0.034	0.081	b.d.	0.031	b.d.	b.d.	0.010	0.040	b.d.	b.d.	0.009	0.005	0.048	0.015	0.010
MgO	13.771	14.446	13.751	13.678	13.822	13.449	13.487	12.933	14.221	13.858	13.769	13.878	14.013	15.267	16.035
CaO	23.740	23.835	23.541	23.687	23.503	23.388	23.309	22.529	23.571	23.834	23.781	23.785	23.548	24.401	24.701
Na2O	0.877	0.835	0.985	0.892	0.982	0.883	1.120	1.420	0.803	0.728	0.997	0.859	0.904	0.506	0.514
K2O	b.d.	b.d.	0.034	0.001	b.d.	0.005	0.003	0.018	0.034	b.d.	0.030	0.003	0.009	b.d.	0.016
Total	100.100	100.920	100.750	99.860	100.420	99.970	100.830	99.640	100.340	99.120	100.500	100.250	100.500	100.520	100.190
O = 6															
(IV)Si	1.971	1.967	1.981	1.971	1.973	1.982	1.971	1.990	1.973	1.963	1.961	1.973	1.976	1.956	1.963
(IV)Al	0.026	0.026	0.017	0.019	0.023	0.018	0.023	0.004	0.022	0.024	0.027	0.027	0.021	0.034	0.024
Sum	1.997	1.993	1.998	1.990	1.996	2.000	1.994	1.994	1.995	1.987	1.988	2.000	1.997	1.990	1.987
(VI)Al	0.000	0.000	0.000	0.000	0.000	0.004	0.000	0.000	0.000	0.000	0.000	0.001	0.000	0.000	0.000
(VI)Ti	0.016	0.011	0.009	0.012	0.011	0.011	0.014	0.003	0.015	0.013	0.016	0.013	0.014	0.019	0.013
(VI)Fe3+	0.060	0.073	0.074	0.078	0.073	0.053	0.084	0.110	0.057	0.074	0.089	0.061	0.061	0.048	0.056
(VI)Fe2+	0.150	0.123	0.153	0.144	0.145	0.180	0.154	0.153	0.148	0.133	0.127	0.148	0.150	0.108	0.058
(VI)Mg	0.761	0.790	0.755	0.758	0.761	0.745	0.741	0.720	0.783	0.773	0.758	0.765	0.770	0.834	0.874
(VI)Mn	0.006	0.008	0.008	0.007	0.008	0.008	0.008	0.010	0.008	0.008	0.006	0.008	0.007	0.003	0.002
(VI)Cr	0.005	0.004	0.003	0.002	0.004	0.002	0.004	0.004	0.003	0.004	0.003	0.001	0.002	0.004	0.005
(VI)Ni	0.001	0.002	0.000	0.001	0.000	0.000	0.000	0.001	0.000	0.000	0.000	0.000	0.001	0.000	0.000
(VI)Ca	0.942	0.936	0.929	0.944	0.930	0.932	0.921	0.902	0.932	0.956	0.941	0.942	0.930	0.958	0.967
(VI)Na	0.063	0.059	0.070	0.064	0.070	0.064	0.080	0.103	0.057	0.053	0.071	0.062	0.065	0.036	0.036
(VI)K	0.000	0.000	0.002	0.000	0.000	0.000	0.000	0.001	0.002	0.000	0.001	0.000	0.000	0.000	0.001
Sum	2.004	2.006	2.003	2.010	2.002	1.999	2.006	2.007	2.005	2.014	2.012	2.001	2.000	2.010	2.012

Table A2.2 - Clinopyroxene analyses

Sample	at035	at035	at038	at038	at038	at038	at038	at038	at038	at038	at038	at038	at038	at038	at038
Unit	B1	B1	B2	B2	B2	B2	B2	B2	B2	B2	B2	B2	B2	B2	B2
Rock Type	beb	beb	beb	beb	beb	beb	beb	beb	beb	beb	beb	beb	beb	beb	beb
Remarks			rim		core				rim			core			
SiO2	53.469	53.342	52.525	52.928	51.248	52.417	52.388	53.217	54.302	54.097	52.507	51.653	51.622	52.058	51.904
TiO2	0.850	0.777	0.590	0.347	1.016	0.804	0.638	0.573	0.170	0.211	0.668	0.874	0.969	0.873	0.790
Al2O3	0.572	0.607	0.763	0.895	1.874	1.432	1.125	1.050	0.192	0.222	0.852	1.477	1.441	1.313	1.302
FeO	3.915	1.836	3.329	2.882	3.367	3.555	3.527	2.923	2.633	2.780	3.067	3.751	3.791	2.370	2.093
Fe2O3	0.906	3.169	3.160	3.276	4.174	3.226	2.985	3.942	4.205	3.781	3.050	2.992	2.928	3.535	3.650
Cr2O3	0.085	0.025	0.050	0.168	0.128	0.071	0.045	0.074	0.118	0.148	b.d.	0.143	0.006	0.055	0.059
MnO	0.157	0.168	0.162	0.128	0.214	0.176	0.216	0.194	0.254	0.164	0.196	0.153	0.218	0.207	0.121
NiO	b.d.	0.017	0.031	0.109	0.058	b.d.	0.017	0.014	b.d.	0.009	b.d.	0.051	b.d.	0.045	b.d.
MgO	15.281	15.762	14.583	14.670	13.594	14.255	14.255	14.527	14.575	14.509	14.557	13.988	14.071	14.492	14.598
CaO	24.544	24.473	24.252	24.248	23.828	24.247	24.121	24.190	23.460	23.562	24.306	23.970	23.893	24.403	24.297
Na2O	0.400	0.624	0.595	0.706	0.822	0.690	0.680	0.891	1.327	1.265	0.638	0.638	0.629	0.708	0.737
K2O	0.032	0.036	b.d.	b.d.	b.d.	b.d.	b.d.	b.d.	b.d.	b.d.	0.028	b.d.	b.d.	0.012	b.d.
Total	100.210	100.840	100.040	100.360	100.320	100.870	100.000	101.600	101.230	100.750	99.870	99.690	99.570	100.070	99.550
O = 6															
(IV)Si	1.965	1.945	1.943	1.948	1.900	1.926	1.940	1.938	1.979	1.980	1.944	1.922	1.923	1.923	1.924
(IV)Al	0.025	0.026	0.033	0.039	0.082	0.062	0.049	0.045	0.008	0.010	0.037	0.065	0.063	0.057	0.057
Sum	1.990	1.971	1.976	1.987	1.982	1.988	1.989	1.983	1.987	1.990	1.981	1.987	1.986	1.980	1.981
(VI)Al	0.000	0.000	0.000	0.000	0.000	0.000	0.000	0.000	0.000	0.000	0.000	0.000	0.000	0.000	0.000
(VI)Ti	0.023	0.021	0.016	0.010	0.028	0.022	0.018	0.016	0.005	0.006	0.019	0.024	0.027	0.024	0.022
(VI)Fe3+	0.025	0.087	0.088	0.091	0.116	0.089	0.083	0.108	0.115	0.104	0.085	0.084	0.082	0.098	0.102
(VI)Fe2+	0.120	0.056	0.103	0.089	0.104	0.109	0.109	0.089	0.080	0.085	0.095	0.117	0.118	0.073	0.065
(VI)Mg	0.837	0.857	0.804	0.805	0.751	0.781	0.787	0.789	0.792	0.792	0.803	0.776	0.781	0.798	0.807
(VI)Mn	0.005	0.005	0.005	0.004	0.007	0.005	0.007	0.006	0.008	0.005	0.006	0.005	0.007	0.006	0.004
(VI)Cr	0.002	0.001	0.001	0.005	0.004	0.002	0.001	0.002	0.003	0.004	0.000	0.004	0.000	0.002	0.002
(VI)Ni	0.000	0.000	0.001	0.003	0.002	0.000	0.000	0.000	0.000	0.000	0.000	0.002	0.000	0.001	0.000
(VI)Ca	0.967	0.956	0.961	0.956	0.946	0.954	0.957	0.944	0.916	0.924	0.964	0.956	0.953	0.966	0.965
(VI)Na	0.028	0.044	0.043	0.050	0.059	0.049	0.049	0.063	0.094	0.090	0.046	0.046	0.045	0.051	0.053
(VI)K	0.002	0.002	0.000	0.000	0.000	0.000	0.000	0.000	0.000	0.000	0.001	0.000	0.000	0.001	0.000
Sum	2.009	2.029	2.022	2.013	2.017	2.011	2.011	2.017	2.013	2.010	2.019	2.014	2.013	2.020	2.020

Table A2.2 - Clinopyroxene analyses

Sample	at038	at038	at043	at043	at043	at043	at043	at043	at043	at043	at043	at043	at043	at043	at043
Unit	B2	B2	C3	C3	C3	C3	C3	C3	C3	C3	C3	C3	C3	C3	C3
Rock Type	beb	beb	cbt	cbt	cbt	cbt	cbt	cbt	cbt	cbt	cbt	cbt	cbt	cbt	cbt
Remarks	rim	core													
SiO2	53.388	52.146	50.779	50.844	51.501	51.421	52.316	50.762	52.505	52.795	51.699	51.367	52.395	51.083	52.638
TiO2	0.350	0.886	0.989	0.833	0.764	0.826	0.302	1.099	0.431	0.208	0.705	0.775	0.501	0.850	0.147
Al2O3	0.615	1.568	1.206	1.303	0.976	0.875	0.186	1.454	0.428	0.360	0.809	0.908	0.604	1.034	0.295
FeO	2.358	3.470	3.076	4.064	3.771	4.238	5.013	4.180	4.385	5.260	3.798	3.137	3.907	2.916	3.727
Fe2O3	4.586	3.749	3.348	2.801	2.430	1.815	2.172	2.780	2.276	1.796	1.970	3.204	2.562	3.381	4.318
Cr2O3	0.123	0.070	0.064	0.043	0.111	0.077	0.096	0.079	0.057	0.008	0.081	0.078	0.098	0.093	0.081
MnO	0.186	0.234	0.246	0.265	0.231	0.192	0.260	0.260	0.265	0.299	0.228	0.189	0.229	0.169	0.241
NiO	0.000	0.051	0.034	b.d.	0.027	0.009	b.d.	b.d.	b.d.	0.033	b.d.	b.d.	0.012	0.041	0.005
MgO	14.144	13.958	14.106	13.694	14.210	14.036	13.489	13.661	14.093	13.650	14.360	14.279	14.159	14.188	13.104
CaO	23.412	24.010	23.422	23.413	23.461	23.589	22.909	23.421	23.632	22.556	23.760	23.568	23.715	23.672	21.507
Na2O	1.381	0.809	0.649	0.600	0.598	0.523	0.886	0.611	0.671	0.971	0.515	0.671	0.708	0.658	1.751
K2O	b.d.	b.d.	0.032	0.007	0.027	0.040	0.015	0.018	0.009	b.d.	b.d.	0.008	0.017	0.024	0.023
Total	100.540	100.950	97.950	97.870	98.110	97.640	97.640	98.320	98.750	97.940	97.920	98.180	98.910	98.110	97.840
O = 6															
(IV)Si	1.961	1.918	1.921	1.929	1.943	1.950	1.988	1.918	1.970	1.996	1.952	1.936	1.961	1.928	1.991
(IV)Al	0.027	0.068	0.054	0.058	0.043	0.039	0.008	0.065	0.019	0.004	0.036	0.040	0.027	0.046	0.009
Sum	1.988	1.986	1.975	1.987	1.986	1.989	1.996	1.983	1.989	2.000	1.988	1.976	1.988	1.974	2.000
(VI)Al	0.000	0.000	0.000	0.000	0.000	0.000	0.000	0.000	0.000	0.012	0.000	0.000	0.000	0.000	0.004
(VI)Ti	0.010	0.025	0.028	0.024	0.022	0.024	0.009	0.031	0.012	0.006	0.020	0.022	0.014	0.024	0.004
(VI)Fe3+	0.126	0.104	0.095	0.080	0.069	0.052	0.062	0.079	0.064	0.051	0.056	0.091	0.072	0.096	0.123
(VI)Fe2+	0.072	0.107	0.097	0.129	0.119	0.135	0.159	0.132	0.137	0.166	0.120	0.099	0.122	0.092	0.118
(VI)Mg	0.774	0.765	0.795	0.774	0.799	0.794	0.764	0.770	0.788	0.769	0.808	0.802	0.790	0.798	0.739
(VI)Mn	0.006	0.007	0.008	0.009	0.007	0.006	0.008	0.008	0.008	0.010	0.007	0.006	0.007	0.005	0.008
(VI)Cr	0.004	0.002	0.002	0.001	0.003	0.002	0.003	0.002	0.002	0.000	0.002	0.002	0.003	0.003	0.002
(VI)Ni	0.000	0.001	0.001	0.000	0.001	0.000	0.000	0.000	0.000	0.001	0.000	0.000	0.000	0.001	0.000
(VI)Ca	0.921	0.946	0.949	0.952	0.948	0.958	0.933	0.948	0.950	0.914	0.961	0.952	0.951	0.957	0.872
(VI)Na	0.098	0.058	0.048	0.044	0.044	0.038	0.065	0.045	0.049	0.071	0.038	0.049	0.051	0.048	0.128
(VI)K	0.000	0.000	0.002	0.000	0.001	0.002	0.001	0.001	0.000	0.000	0.000	0.000	0.001	0.001	0.001
Sum	2.011	2.015	2.025	2.013	2.013	2.011	2.004	2.016	2.010	2.000	2.012	2.023	2.011	2.025	1.999

Table A2.2 - Clinopyroxene analyses

Sample	at043	at043	at043	at043	at043	at043	at043	at043	at043	at043	at043	at043	at043	at043	at043
Unit	C3	C3	C3	C3	C3	C3	C3	C3	C3	C3	C3	C3	C3	C3	C3
Rock Type	cbt	cbt	cbt	cbt	cbt	cbt	cbt	cbt	cbt	cbt	cbt	cbt	cbt	cbt	cbt
Remarks														core	
SiO2	52.051	51.320	51.897	51.594	51.711	50.496	49.072	50.401	50.095	52.860	52.890	53.879	51.850	53.612	52.753
TiO2	0.438	0.378	0.413	0.424	0.220	0.714	0.725	0.686	0.670	0.839	0.555	0.324	0.871	0.395	0.661
Al2O3	0.358	0.557	0.506	0.534	0.266	1.034	0.980	0.861	0.807	1.112	0.777	0.319	1.397	0.427	0.933
FeO	4.928	4.677	3.385	3.408	5.158	4.080	3.165	3.521	2.795	5.595	4.193	6.023	5.245	5.914	4.972
Fe2O3	2.177	2.044	1.723	2.174	2.362	2.493	4.235	2.770	3.141	0.572	1.577	0.788	1.457	0.536	1.543
Cr2O3	0.101	b.d.	b.d.	b.d.	b.d.	b.d.	b.d.	b.d.	b.d.	b.d.	b.d.	0.003	0.006	0.000	0.005
MnO	0.198	0.362	0.210	0.228	0.257	0.245	0.260	0.227	0.241	0.206	0.243	0.278	0.218	0.236	0.229
NiO	0.028	0.020	b.d.	b.d.	0.057	0.011	b.d.	b.d.	b.d.	b.d.	b.d.	b.d.	b.d.	b.d.	b.d.
MgO	13.641	13.321	14.738	14.287	12.908	13.598	13.019	13.833	13.889	13.967	14.411	13.843	13.613	13.938	13.740
CaO	23.425	24.035	24.258	24.513	23.451	23.929	23.541	24.025	24.144	24.568	24.946	24.069	24.467	24.480	24.797
Na2O	0.677	0.451	0.323	0.339	0.760	0.383	0.551	0.364	0.384	0.385	0.359	0.624	0.370	0.451	0.476
K2O	0.003	b.d.	b.d.	b.d.	b.d.	b.d.	b.d.	b.d.	b.d.	b.d.	b.d.	b.d.	b.d.	b.d.	b.d.
Total	98.020	97.165	97.452	97.502	97.149	96.983	95.548	96.689	96.167	100.103	99.950	100.149	99.493	99.989	100.108
O = 6															
(IV)Si	1.972	1.964	1.964	1.957	1.982	1.935	1.915	1.934	1.931	1.958	1.958	1.996	1.937	1.989	1.957
(IV)Al	0.016	0.025	0.023	0.024	0.012	0.047	0.045	0.039	0.037	0.042	0.034	0.004	0.061	0.011	0.041
Sum	1.988	1.989	1.987	1.981	1.994	1.982	1.960	1.973	1.968	2.000	1.992	2.000	1.998	2.000	1.998
(VI)Al	0.000	0.000	0.000	0.000	0.000	0.000	0.000	0.000	0.000	0.007	0.000	0.009	0.000	0.007	0.000
(VI)Ti	0.012	0.011	0.012	0.012	0.006	0.021	0.021	0.020	0.019	0.023	0.015	0.009	0.024	0.011	0.018
(VI)Fe3+	0.062	0.059	0.049	0.062	0.068	0.072	0.124	0.080	0.091	0.016	0.044	0.022	0.041	0.015	0.043
(VI)Fe2+	0.156	0.150	0.107	0.108	0.165	0.131	0.103	0.113	0.090	0.174	0.130	0.187	0.164	0.184	0.154
(VI)Mg	0.770	0.760	0.831	0.808	0.737	0.777	0.757	0.791	0.798	0.771	0.795	0.764	0.758	0.771	0.760
(VI)Mn	0.006	0.012	0.007	0.007	0.008	0.008	0.009	0.007	0.008	0.006	0.008	0.009	0.007	0.007	0.007
(VI)Cr	0.003	0.000	0.000	0.000	0.000	0.000	0.000	0.000	0.000	0.000	0.000	0.000	0.000	0.000	0.000
(VI)Ni	0.001	0.001	0.000	0.000	0.002	0.000	0.000	0.000	0.000	0.000	0.000	0.000	0.000	0.000	0.000
(VI)Ca	0.951	0.986	0.984	0.996	0.963	0.982	0.984	0.988	0.997	0.975	0.990	0.955	0.980	0.973	0.985
(VI)Na	0.050	0.033	0.024	0.025	0.056	0.028	0.042	0.027	0.029	0.028	0.026	0.045	0.027	0.032	0.034
(VI)K	0.000	0.000	0.000	0.000	0.000	0.000	0.000	0.000	0.000	0.000	0.000	0.000	0.000	0.000	0.000
Sum	2.011	2.012	2.014	2.018	2.005	2.019	2.040	2.026	2.032	2.000	2.008	2.000	2.001	2.000	2.001

Table A2.2 - Clinopyroxene analyses

Sample	at043	at043	at043	at043	at043	at043	at043	at043	at043	at043	at043	at060b	at060b	at113	at113
Unit	C3	C3	C3	C3	C3	C3	C3	C3	C3	C3	C3	C3	C3	B1	B1
Rock Type	cbt	cbt	cbt	cbt	cbt	cbt	cbt	cbt	cbt	cbt	cbt	cbt	cbt	beb	beb
Remarks		rim		core			rim							rim	
SiO2	52.260	52.349	53.742	53.313	52.712	52.942	53.633	52.349	53.589	51.823	52.206	53.829	54.098	52.486	52.298
TiO2	0.778	0.698	0.558	0.532	0.650	0.652	0.476	0.826	0.610	1.041	0.977	0.146	0.363	0.991	1.004
Al2O3	1.055	0.960	0.632	0.595	0.933	1.019	0.665	1.009	0.644	1.440	1.281	0.087	0.185	0.783	0.944
FeO	4.623	5.158	5.019	4.579	5.334	5.402	5.261	5.148	5.492	4.608	5.392	5.112	5.282	2.934	3.205
Fe2O3	1.962	1.175	1.051	1.408	1.357	1.402	0.938	1.173	0.289	2.364	1.427	0.751	1.297	2.615	2.661
Cr2O3	0.001	0.000	0.000	0.030	0.018	0.001	0.000	0.009	b.d.	0.001	0.012	b.d.	0.007	0.092	b.d.
MnO	0.249	0.191	0.190	0.223	0.209	0.241	0.225	0.191	0.228	0.202	0.203	0.322	0.313	0.205	0.106
NiO	b.d.	b.d.	b.d.	b.d.	b.d.	b.d.	b.d.	b.d.	b.d.	b.d.	b.d.	0.012	0.009	0.073	b.d.
MgO	13.884	13.678	14.473	14.494	13.601	13.800	14.108	13.818	14.392	13.779	13.482	14.601	14.446	14.928	14.580
CaO	24.633	24.613	24.932	24.817	24.651	24.655	24.924	24.556	24.897	24.736	24.606	23.252	23.539	24.049	23.991
Na2O	0.433	0.424	0.393	0.391	0.485	0.445	0.428	0.410	0.291	0.397	0.464	0.699	0.752	0.649	0.735
K2O	b.d.	b.d.	b.d.	b.d.	b.d.	b.d.	b.d.	b.d.	b.d.	b.d.	b.d.	b.d.	b.d.	b.d.	b.d.
Total	99.877	99.245	100.989	100.382	99.951	100.557	100.658	99.488	100.432	100.389	100.050	98.811	100.291	99.800	99.520
O = 6															
(IV)Si	1.943	1.958	1.970	1.966	1.960	1.956	1.975	1.953	1.976	1.921	1.941	2.009	1.995	1.941	1.941
(IV)Al	0.046	0.042	0.027	0.026	0.040	0.044	0.025	0.044	0.024	0.063	0.056	0.000	0.005	0.034	0.041
Sum	1.989	2.000	1.997	1.992	2.000	2.000	2.000	1.997	2.000	1.984	1.997	2.009	2.000	1.975	1.982
(VI)Al	0.000	0.000	0.000	0.000	0.000	0.000	0.004	0.000	0.003	0.000	0.000	0.004	0.003	0.000	0.000
(VI)Ti	0.022	0.020	0.015	0.015	0.018	0.018	0.013	0.023	0.017	0.029	0.027	0.004	0.010	0.028	0.028
(VI)Fe3+	0.055	0.033	0.029	0.039	0.038	0.039	0.026	0.033	0.008	0.066	0.040	0.021	0.036	0.073	0.074
(VI)Fe2+	0.144	0.161	0.154	0.141	0.166	0.167	0.162	0.161	0.169	0.143	0.168	0.159	0.163	0.091	0.099
(VI)Mg	0.770	0.763	0.791	0.797	0.754	0.760	0.774	0.769	0.791	0.761	0.747	0.812	0.794	0.823	0.807
(VI)Mn	0.008	0.006	0.006	0.007	0.007	0.008	0.007	0.006	0.007	0.006	0.006	0.010	0.010	0.006	0.003
(VI)Cr	0.000	0.000	0.000	0.001	0.001	0.000	0.000	0.000	0.000	0.000	0.000	0.000	0.000	0.003	0.000
(VI)Ni	0.000	0.000	0.000	0.000	0.000	0.000	0.000	0.000	0.000	0.000	0.000	0.000	0.000	0.002	0.000
(VI)Ca	0.981	0.986	0.979	0.981	0.982	0.976	0.983	0.982	0.983	0.982	0.980	0.930	0.930	0.953	0.954
(VI)Na	0.031	0.031	0.028	0.028	0.035	0.032	0.031	0.030	0.021	0.029	0.033	0.051	0.054	0.047	0.053
(VI)K	0.000	0.000	0.000	0.000	0.000	0.000	0.000	0.000	0.000	0.000	0.000	0.000	0.000	0.000	0.000
Sum	2.011	2.000	2.002	2.009	2.001	2.000	2.000	2.004	1.999	2.016	2.001	1.991	2.000	2.026	2.018

Table A2.2 - Clinopyroxene analyses

Sample	at113	at113	at113	at113	at113	at113	at113	at113	at202	at202	at202	at202	at202	at202	at202
Unit	B1	B1	B1	B1	B1	B1	B1	B1							
Rock Type	beb	beb	beb	beb	beb	beb	beb	beb	lcr	lcr	lcr	lcr	lcr	lcr	lcr
Remarks			core			rim	core	core							
SiO2	52.391	51.821	52.188	52.736	52.521	52.412	52.315	52.653	51.917	52.710	53.386	51.626	51.324	49.789	51.630
TiO2	0.960	1.190	1.095	0.946	0.681	0.606	1.226	0.944	0.241	0.133	0.109	0.713	0.849	1.147	0.616
Al2O3	0.907	1.069	1.016	0.818	0.607	0.771	0.755	0.854	0.459	0.414	0.468	1.303	1.296	1.444	1.005
FeO	3.663	2.777	3.001	4.087	2.479	3.506	3.434	2.443	9.391	7.759	6.176	6.358	5.882	8.785	6.743
Fe2O3	2.090	3.410	2.941	1.645	3.649	3.074	3.959	3.295	6.889	5.597	4.289	5.077	5.649	5.886	4.574
Cr2O3	0.104	b.d.	0.078	0.140	0.028	0.081	0.107	0.068	0.094	0.057	0.085	0.073	0.141	0.130	0.105
MnO	0.122	0.107	0.158	0.132	0.226	0.122	0.156	0.162	0.619	0.546	0.555	0.401	0.317	0.513	0.430
NiO	b.d.	b.d.	b.d.	0.013	0.013	0.007	0.104	0.025	b.d.	0.068	0.062	b.d.	0.037	0.025	0.002
MgO	14.500	14.500	14.552	14.514	14.376	14.311	13.946	14.986	8.332	10.141	11.831	11.244	11.447	8.862	11.250
CaO	23.980	23.904	24.028	24.046	24.019	23.681	22.389	24.375	19.321	20.729	21.968	22.395	22.323	21.327	22.226
Na2O	0.684	0.792	0.758	0.648	0.927	0.806	1.387	0.697	2.729	2.185	1.685	1.485	1.488	1.728	1.395
K2O	b.d.	b.d.	b.d.	b.d.	b.d.	b.d.	b.d.	b.d.	0.011	b.d.	0.028	b.d.	b.d.	0.036	0.032
Total	99.400	99.570	99.810	99.720	99.530	99.380	99.780	100.500	100.000	100.340	100.640	100.670	100.750	99.670	100.010
O = 6															
(IV)Si	1.947	1.924	1.932	1.954	1.950	1.951	1.942	1.934	1.983	1.987	1.987	1.932	1.920	1.912	1.946
(IV)Al	0.040	0.047	0.044	0.036	0.027	0.034	0.033	0.037	0.017	0.013	0.013	0.057	0.057	0.065	0.045
Sum	1.987	1.971	1.976	1.990	1.977	1.985	1.975	1.971	2.000	2.000	2.000	1.989	1.977	1.977	1.991
(VI)Al	0.000	0.000	0.000	0.000	0.000	0.000	0.000	0.000	0.004	0.005	0.007	0.000	0.000	0.000	0.000
(VI)Ti	0.027	0.033	0.030	0.026	0.019	0.017	0.034	0.026	0.007	0.004	0.003	0.020	0.024	0.033	0.017
(VI)Fe3+	0.058	0.095	0.082	0.046	0.102	0.086	0.111	0.091	0.198	0.159	0.120	0.143	0.159	0.170	0.130
(VI)Fe2+	0.113	0.086	0.093	0.127	0.077	0.109	0.107	0.075	0.300	0.245	0.192	0.199	0.184	0.282	0.213
(VI)Mg	0.803	0.803	0.803	0.802	0.796	0.794	0.772	0.820	0.475	0.570	0.656	0.627	0.638	0.507	0.632
(VI)Mn	0.004	0.003	0.005	0.004	0.007	0.004	0.005	0.005	0.020	0.017	0.018	0.013	0.010	0.017	0.014
(VI)Cr	0.003	0.000	0.002	0.004	0.001	0.002	0.003	0.002	0.003	0.002	0.002	0.002	0.004	0.004	0.003
(VI)Ni	0.000	0.000	0.000	0.000	0.000	0.000	0.003	0.001	0.000	0.002	0.002	0.000	0.001	0.001	0.000
(VI)Ca	0.955	0.951	0.953	0.955	0.955	0.944	0.891	0.959	0.791	0.837	0.876	0.898	0.895	0.878	0.897
(VI)Na	0.049	0.057	0.054	0.047	0.067	0.058	0.100	0.050	0.202	0.160	0.122	0.108	0.108	0.129	0.102
(VI)K	0.000	0.000	0.000	0.000	0.000	0.000	0.000	0.000	0.001	0.000	0.001	0.000	0.000	0.002	0.002
Sum	2.012	2.028	2.022	2.011	2.024	2.014	2.026	2.029	2.001	2.001	1.999	2.010	2.023	2.023	2.010

Table A2.2 - Clinopyroxene analyses

Sample	at202	at202	at202	at202	at202	at202	at202	at205	at205	at205	at205	at205	at205	at205	at205
Unit															
Rock Type	lcr	lcr	lcr	lcr	lcr	lcr	lcr	lcr	lcr	lcr	lcr	lcr	lcr	lcr	lcr
Remarks								rim					core		
SiO2	52.708	52.593	51.845	52.947	53.041	53.299	53.328	52.589	52.966	49.850	50.147	49.668	49.247	49.369	49.135
TiO2	0.325	0.319	0.306	0.140	0.213	0.120	0.068	0.447	0.391	1.477	1.499	1.682	1.817	1.783	1.890
Al2O3	0.627	0.536	0.837	0.640	0.483	0.428	0.423	0.193	0.357	1.562	1.730	1.758	1.804	1.805	2.252
FeO	6.509	7.508	8.807	8.203	7.289	7.448	5.483	2.224	3.033	5.359	5.729	5.469	6.274	6.065	6.111
Fe2O3	4.703	3.218	5.453	3.653	4.881	4.584	4.301	5.980	5.414	4.625	4.397	5.517	4.811	5.029	5.040
Cr2O3	0.027	0.107	0.101	0.055	0.026	0.096	0.045	0.127	0.164	0.092	0.087	0.121	0.092	0.113	0.043
MnO	0.419	0.539	0.555	0.441	0.605	0.500	0.549	0.403	0.438	0.290	0.344	0.293	0.284	0.348	0.209
NiO	0.002	b.d.	0.016	0.004	b.d.	0.020	0.049	b.d.	b.d.	b.d.	0.001	b.d.	0.030	b.d.	0.035
MgO	11.490	11.412	9.409	10.865	10.744	10.945	12.608	13.183	13.028	12.050	11.901	11.384	11.199	11.181	11.670
CaO	22.132	22.651	20.557	21.819	21.120	21.230	22.500	23.233	22.844	23.011	23.078	22.650	22.467	22.436	21.728
Na2O	1.615	1.211	2.107	1.611	2.049	1.975	1.381	1.595	1.658	0.936	0.962	1.255	1.119	1.191	1.156
K2O	0.020	0.046	b.d.	b.d.	b.d.	0.001	0.012	b.d.	0.013	b.d.	b.d.	b.d.	b.d.	0.014	0.035
Total	100.580	100.140	99.990	100.380	100.450	100.650	100.740	99.970	100.310	99.250	99.870	99.800	99.140	99.330	99.310
O = 6															
(IV)Si	1.970	1.977	1.971	1.988	1.989	1.993	1.978	1.955	1.963	1.890	1.890	1.879	1.878	1.879	1.866
(IV)Al	0.028	0.023	0.029	0.012	0.011	0.007	0.018	0.008	0.016	0.070	0.077	0.078	0.081	0.081	0.101
Sum	1.998	2.000	2.000	2.000	2.000	2.000	1.996	1.963	1.979	1.960	1.967	1.957	1.959	1.960	1.967
(VI)Al	0.000	0.001	0.008	0.016	0.010	0.012	0.000	0.000	0.000	0.000	0.000	0.000	0.000	0.000	0.000
(VI)Ti	0.009	0.009	0.009	0.004	0.006	0.003	0.002	0.012	0.011	0.042	0.042	0.048	0.052	0.051	0.054
(VI)Fe3+	0.132	0.091	0.156	0.103	0.138	0.129	0.120	0.167	0.151	0.132	0.125	0.157	0.138	0.144	0.144
(VI)Fe2+	0.203	0.236	0.280	0.257	0.229	0.233	0.170	0.069	0.094	0.170	0.181	0.173	0.200	0.193	0.194
(VI)Mg	0.640	0.640	0.533	0.608	0.601	0.610	0.697	0.731	0.720	0.681	0.669	0.642	0.637	0.634	0.661
(VI)Mn	0.013	0.017	0.018	0.014	0.019	0.016	0.017	0.013	0.014	0.009	0.011	0.009	0.009	0.011	0.007
(VI)Cr	0.001	0.003	0.003	0.002	0.001	0.003	0.001	0.004	0.005	0.003	0.003	0.004	0.003	0.003	0.001
(VI)Ni	0.000	0.000	0.000	0.000	0.000	0.001	0.001	0.000	0.000	0.000	0.000	0.000	0.001	0.000	0.001
(VI)Ca	0.886	0.912	0.837	0.878	0.848	0.850	0.894	0.925	0.907	0.935	0.932	0.918	0.918	0.915	0.884
(VI)Na	0.117	0.088	0.155	0.117	0.149	0.143	0.099	0.115	0.119	0.069	0.070	0.092	0.083	0.088	0.085
(VI)K	0.001	0.002	0.000	0.000	0.000	0.000	0.001	0.000	0.001	0.000	0.000	0.000	0.000	0.001	0.002
Sum	2.002	1.999	1.999	1.999	2.001	2.000	2.002	2.036	2.022	2.041	2.033	2.043	2.041	2.040	2.033

Table A2.2 - Clinopyroxene analyses

Sample	at205	at205	at205	at205	at205	at205	at205	at205	at212	at212	at212	at212	at212	at212	at212
Unit									C2	C2	C2	C2	C2	C2	C2
Rock Type	lcr	lcr	lcr	lcr	lcr	lcr	lcr	lcr	cbt,dk	cbt,dk	cbt,dk	cbt,dk	cbt,dk	cbt,dk	cbt,dk
Remarks						core	rim	core	rim	core	core				
SiO2	50.427	50.059	49.861	49.278	48.920	49.434	50.146	51.353	53.808	53.854	53.648	53.553	54.009	53.318	54.284
TiO2	1.336	1.442	1.567	1.806	2.340	2.141	1.852	1.042	0.445	0.599	0.710	0.323	0.458	0.473	0.500
Al2O3	1.475	1.527	1.580	1.983	1.822	1.818	2.007	1.085	0.139	0.279	0.241	0.352	0.083	0.614	0.147
FeO	5.478	4.501	6.016	4.216	4.805	5.811	5.745	4.953	3.499	1.994	2.939	5.028	2.153	4.186	2.028
Fe2O3	4.636	5.672	4.936	5.848	5.445	4.562	4.362	3.634	0.468	1.926	0.682	1.361	1.124	1.431	1.163
Cr2O3	0.088	0.095	b.d.	0.127	0.090	0.113	0.047	0.032	0.144	0.140	0.126	0.052	0.165	0.098	0.080
MnO	0.249	0.289	0.251	0.151	0.192	0.231	0.205	0.327	0.112	0.209	0.141	0.205	0.128	0.194	0.077
NiO	b.d.	b.d.	0.020	0.059	b.d.	0.008	0.073	0.044	b.d.	b.d.	0.086	0.106	0.055	b.d.	b.d.
MgO	12.252	11.992	11.328	12.346	11.888	11.794	11.911	12.883	15.646	15.993	16.140	14.121	16.354	14.398	16.394
CaO	23.039	22.896	22.480	22.974	22.930	23.017	22.760	23.038	24.846	24.794	24.842	24.229	24.824	23.707	24.997
Na2O	0.953	1.219	1.242	1.003	1.075	0.965	1.127	0.978	0.301	0.526	0.217	0.598	0.365	0.814	0.433
K2O	b.d.	0.005	0.000	0.013	0.018	b.d.	b.d.	b.d.	0.004	0.009	b.d.	b.d.	b.d.	b.d.	b.d.
Total	99.930	99.700	99.280	99.800	99.520	99.890	100.230	99.370	99.410	100.320	99.770	99.930	99.720	99.230	100.100
O = 6															
(IV)Si	1.897	1.888	1.895	1.857	1.854	1.868	1.882	1.930	1.987	1.968	1.972	1.985	1.981	1.981	1.981
(IV)Al	0.065	0.068	0.071	0.088	0.081	0.081	0.089	0.048	0.006	0.012	0.010	0.015	0.004	0.019	0.006
Sum	1.962	1.956	1.966	1.945	1.935	1.949	1.971	1.978	1.993	1.980	1.982	2.000	1.985	2.000	1.987
(VI)Al	0.000	0.000	0.000	0.000	0.000	0.000	0.000	0.000	0.000	0.000	0.000	0.000	0.000	0.008	0.000
(VI)Ti	0.038	0.041	0.045	0.051	0.067	0.061	0.052	0.029	0.012	0.016	0.020	0.009	0.013	0.013	0.014
(VI)Fe3+	0.131	0.161	0.141	0.166	0.155	0.130	0.123	0.103	0.013	0.053	0.019	0.038	0.031	0.040	0.032
(VI)Fe2+	0.172	0.142	0.191	0.133	0.152	0.184	0.180	0.156	0.108	0.061	0.091	0.156	0.066	0.130	0.062
(VI)Mg	0.687	0.674	0.642	0.694	0.671	0.664	0.666	0.722	0.861	0.871	0.884	0.780	0.894	0.797	0.892
(VI)Mn	0.008	0.009	0.008	0.005	0.006	0.007	0.007	0.010	0.004	0.006	0.004	0.006	0.004	0.006	0.002
(VI)Cr	0.003	0.003	0.000	0.004	0.003	0.003	0.001	0.001	0.004	0.004	0.004	0.002	0.005	0.003	0.002
(VI)Ni	0.000	0.000	0.001	0.002	0.000	0.000	0.002	0.001	0.000	0.000	0.003	0.003	0.002	0.000	0.000
(VI)Ca	0.929	0.925	0.915	0.928	0.931	0.932	0.915	0.928	0.983	0.971	0.978	0.962	0.975	0.944	0.978
(VI)Na	0.070	0.089	0.092	0.073	0.079	0.071	0.082	0.071	0.022	0.037	0.015	0.043	0.026	0.059	0.031
(VI)K	0.000	0.000	0.000	0.001	0.001	0.000	0.000	0.000	0.000	0.000	0.000	0.000	0.000	0.000	0.000
Sum	2.038	2.044	2.035	2.057	2.065	2.052	2.028	2.021	2.007	2.019	2.018	1.999	2.016	2.000	2.013

Table A2.2 - Clinopyroxene analyses

Sample	at217	at217	at217	at217	at217	at217	at217	at217	at217	at217	at217	at219	at219	rja	rja
Unit	B1	B1	B1	B1	B1	B1	B1	B1	B1	B1	B1	C2	C2		
Rock Type	wehrl	wehrl	wehrl	wehrl	wehrl	wehrl	wehrl	wehrl	wehrl	wehrl	wehrl	cbt,dk	cbt,dk	fen	fen
Remarks															
SiO2	53.742	53.990	54.548	54.518	53.736	53.531	54.236	54.522	54.700	54.816	53.167	53.052	53.122	53.553	53.909
TiO2	0.630	0.621	0.375	0.393	0.586	0.604	0.514	0.398	0.397	0.365	0.671	0.935	1.037	1.068	0.947
Al2O3	0.888	0.832	0.250	0.275	0.646	0.883	0.769	0.332	0.619	0.240	1.311	0.971	0.905	0.782	0.816
FeO	1.841	1.256	2.052	2.057	1.602	1.739	1.356	1.630	1.469	1.415	2.079	2.443	2.572	4.366	4.116
Fe2O3	1.352	1.837	0.442	0.111	1.635	1.641	1.507	0.850	1.188	0.936	1.320	1.919	1.556	12.463	13.472
Cr2O3	0.127	0.063	0.105	0.146	0.113	0.113	0.095	0.111	0.173	0.069	0.139	0.105	0.091	0.064	0.130
MnO	0.060	0.041	0.090	0.111	0.105	b.d.	0.044	0.088	0.118	0.163	0.064	0.122	0.060	0.410	0.395
NiO	0.079	b.d.	b.d.	0.123	0.054	0.001	0.089	b.d.	0.066	b.d.	b.d.	0.013	0.058	b.d.	b.d.
MgO	16.401	16.648	16.973	16.924	16.599	16.524	16.658	16.887	17.060	17.223	16.220	15.704	15.819	7.874	7.620
CaO	24.954	24.997	25.132	25.188	24.949	24.839	25.178	25.237	25.218	25.170	24.922	24.528	24.665	12.956	12.637
Na2O	0.354	0.456	0.181	0.158	0.308	0.306	0.398	0.298	0.291	0.272	0.262	0.493	0.408	6.378	6.690
K2O	0.006	0.005	0.044	0.035	0.018	0.040	0.018	0.009	0.011	0.032	b.d.	b.d.	0.020	0.003	0.001
Total	100.430	100.750	100.190	100.040	100.350	100.220	100.860	100.360	101.310	100.700	100.150	100.280	100.310	99.920	100.730
O = 6															
(IV)Si	1.956	1.955	1.984	1.986	1.957	1.952	1.962	1.979	1.968	1.981	1.942	1.943	1.944	2.008	2.006
(IV)Al	0.038	0.035	0.011	0.012	0.028	0.038	0.033	0.014	0.026	0.010	0.056	0.042	0.039	0.000	0.000
Sum	1.994	1.990	1.995	1.998	1.985	1.990	1.995	1.993	1.994	1.991	1.998	1.985	1.983	2.008	2.006
(VI)Al	0.000	0.000	0.000	0.000	0.000	0.000	0.000	0.000	0.000	0.000	0.000	0.000	0.000	0.035	0.036
(VI)Ti	0.017	0.017	0.010	0.011	0.016	0.017	0.014	0.011	0.011	0.010	0.018	0.026	0.029	0.030	0.027
(VI)Fe3+	0.037	0.050	0.012	0.003	0.045	0.045	0.041	0.023	0.032	0.025	0.036	0.053	0.043	0.352	0.377
(VI)Fe2+	0.056	0.038	0.062	0.062	0.049	0.053	0.041	0.049	0.044	0.042	0.063	0.075	0.079	0.137	0.128
(VI)Mg	0.890	0.899	0.920	0.919	0.901	0.898	0.898	0.914	0.915	0.928	0.883	0.857	0.863	0.440	0.423
(VI)Mn	0.002	0.001	0.003	0.003	0.003	0.000	0.001	0.003	0.004	0.005	0.002	0.004	0.002	0.013	0.012
(VI)Cr	0.004	0.002	0.003	0.004	0.003	0.003	0.003	0.003	0.005	0.002	0.004	0.003	0.003	0.002	0.004
(VI)Ni	0.002	0.000	0.000	0.004	0.002	0.000	0.003	0.000	0.002	0.000	0.000	0.000	0.002	0.000	0.000
(VI)Ca	0.973	0.970	0.979	0.983	0.974	0.970	0.976	0.982	0.972	0.975	0.975	0.962	0.967	0.520	0.504
(VI)Na	0.025	0.032	0.013	0.011	0.022	0.022	0.028	0.021	0.020	0.019	0.019	0.035	0.029	0.464	0.483
(VI)K	0.000	0.000	0.002	0.002	0.001	0.002	0.001	0.000	0.000	0.001	0.000	0.000	0.001	0.000	0.000
Sum	2.006	2.009	2.004	2.002	2.016	2.010	2.006	2.006	2.005	2.007	2.000	2.015	2.018	1.993	1.994

Table A2.2 - Clinopyroxene analyses

Sample	rja	rja	rja	rja	rja	rja	rja	rja	rja	rja	tap1b	tap1b	tap1b	tap1b	tap1b
Unit											C2	C2	C2	C2	C2
Rock Type	fen	fen	fen	fen	fen	fen	fen	fen	fen	fen	cbt,bre	cbt,bre	cbt,bre	cbt,bre	cbt,bre
Remarks															
SiO2	53.607	52.877	53.038	53.466	53.269	53.003	53.366	53.040	53.097	53.488	53.813	54.335	52.269	52.197	51.938
TiO2	1.090	1.401	1.209	1.143	1.203	1.322	1.113	1.284	1.306	0.872	0.598	0.411	0.404	0.195	0.334
Al2O3	0.781	0.638	0.801	0.817	0.809	0.792	0.738	0.846	0.820	0.928	0.464	0.342	2.570	1.483	2.222
FeO	4.064	3.235	3.283	3.664	3.398	2.845	2.952	2.398	3.260	2.148	3.270	3.937	7.530	8.029	7.793
Fe2O3	12.412	14.662	14.730	14.286	14.779	16.489	16.469	15.843	15.276	17.521	2.943	1.121	8.759	9.027	8.414
Cr2O3	0.076	b.d.	b.d.	0.094	0.060	0.080	0.112	0.034	0.056	0.076	0.019	0.074	0.079	0.031	0.103
MnO	0.398	0.376	0.402	0.393	0.351	0.369	0.391	0.445	0.376	0.320	0.166	0.123	0.557	0.641	0.549
NiO	b.d.	b.d.	0.071	0.058	0.013	0.098	0.078	b.d.	b.d.	b.d.	0.003	0.052	0.104	b.d.	b.d.
MgO	8.078	7.165	7.333	7.495	7.472	6.661	6.797	7.092	7.118	6.580	14.868	15.360	7.726	7.690	7.727
CaO	13.371	12.202	12.331	12.622	12.491	11.622	11.753	12.110	12.142	10.686	23.994	24.414	17.011	17.416	17.455
Na2O	6.270	7.004	6.865	6.751	6.833	7.429	7.366	7.214	7.066	7.948	0.887	0.540	4.125	3.843	3.866
K2O	b.d.	b.d.	0.021	b.d.	b.d.	0.019	0.025	0.042	0.011	b.d.	0.029	0.022	b.d.	0.029	b.d.
Total	100.150	99.560	100.080	100.790	100.680	100.730	101.160	100.350	100.530	100.570	101.050	100.730	101.130	100.580	100.400
O = 6															
(IV)Si	2.004	1.994	1.990	1.992	1.987	1.982	1.987	1.984	1.986	1.995	1.965	1.985	1.957	1.974	1.961
(IV)Al	0.000	0.006	0.010	0.008	0.013	0.018	0.013	0.016	0.014	0.005	0.020	0.015	0.043	0.026	0.039
Sum	2.004	2.000	2.000	2.000	2.000	2.000	2.000	2.000	2.000	2.000	1.985	2.000	2.000	2.000	2.000
(VI)Al	0.034	0.022	0.026	0.028	0.023	0.017	0.019	0.022	0.022	0.036	0.000	0.000	0.070	0.040	0.060
(VI)Ti	0.031	0.040	0.034	0.032	0.034	0.037	0.031	0.036	0.037	0.024	0.016	0.011	0.011	0.006	0.009
(VI)Fe3+	0.349	0.416	0.416	0.400	0.415	0.464	0.462	0.446	0.430	0.492	0.081	0.031	0.247	0.257	0.239
(VI)Fe2+	0.127	0.102	0.103	0.114	0.106	0.089	0.092	0.075	0.102	0.067	0.100	0.121	0.236	0.254	0.246
(VI)Mg	0.450	0.403	0.410	0.416	0.416	0.371	0.377	0.396	0.397	0.366	0.809	0.836	0.431	0.434	0.435
(VI)Mn	0.013	0.012	0.013	0.012	0.011	0.012	0.012	0.014	0.012	0.010	0.005	0.004	0.018	0.021	0.018
(VI)Cr	0.002	0.000	0.000	0.003	0.002	0.002	0.003	0.001	0.002	0.002	0.001	0.002	0.002	0.001	0.003
(VI)Ni	0.000	0.000	0.002	0.002	0.000	0.003	0.002	0.000	0.000	0.000	0.000	0.002	0.003	0.000	0.000
(VI)Ca	0.536	0.493	0.496	0.504	0.499	0.466	0.469	0.485	0.486	0.427	0.939	0.955	0.682	0.706	0.706
(VI)Na	0.454	0.512	0.499	0.488	0.494	0.539	0.532	0.523	0.512	0.575	0.063	0.038	0.299	0.282	0.283
(VI)K	0.000	0.000	0.001	0.000	0.000	0.001	0.001	0.002	0.001	0.000	0.001	0.001	0.000	0.001	0.000
Sum	1.996	2.000	2.000	1.999	2.000	2.001	2.000	2.000	2.001	1.999	2.015	2.001	1.999	2.002	1.999

Table A.2.3 - Phlogopite analyses

Sample	at003	at003	at003	at003	at003	at003	at009	at009	at009	at009	at009	at009
Unit	B1	B1	B1	B1	B1	B1	B1	B1	B1	B1	B1	B1
Rock type												
Remarks	rim	core	rim	core	rim	core	rim, tr1,1	rim, tr1,2	core, tr1,3	core, tr1,4	core, tr1,5	core, tr1,6
SiO2	37.647	37.370	37.305	37.663	37.588	37.285	40.173	40.048	38.560	38.653	38.272	38.387
TiO2	1.531	1.659	1.578	1.622	1.513	1.563	1.465	1.574	2.326	2.500	2.659	2.517
Al2O3	11.562	12.464	11.960	12.240	11.677	12.186	10.924	11.013	12.667	12.628	12.761	12.631
Cr2O3	0.005	0.034	0.013	b.d	b.d	b.d	0.071	0.030	0.007	b.d	0.051	0.075
FeO	11.925	12.358	12.188	12.289	11.677	11.950	6.065	5.901	6.814	6.823	6.859	6.415
Fe2O3	2.407	1.196	1.554	1.602	2.128	1.660	2.585	2.727	1.488	1.647	1.705	1.955
MnO	0.232	0.213	0.224	0.212	0.174	0.223	0.101	0.093	0.018	0.122	0.080	0.058
MgO	18.887	18.463	18.434	18.685	18.951	18.737	22.960	23.006	21.963	21.812	21.703	22.060
BaO	0.488	0.581	0.608	0.609	0.544	0.518	0.218	0.168	0.487	0.503	0.444	0.603
CaO	0.016	0.016	0.031	0.082	0.034	0.029	0.008	0.037	0.050	0.061	0.023	0.000
Na2O	0.298	0.291	0.274	0.335	0.356	0.460	0.587	0.708	0.569	0.643	0.538	0.654
K2O	10.008	10.029	9.814	9.970	9.943	9.890	9.895	9.909	9.761	9.671	9.663	9.702
F	n.a.	n.a.	n.a.	n.a.	n.a.	n.a.	n.a.	n.a.	n.a.	n.a.	n.a.	n.a.
Cl	b.d	b.d	0.012	0.007	0.022	b.d	0.023	b.d	b.d	b.d	0.018	0.012
H2O	3.980	3.970	3.940	3.990	3.960	3.960	4.120	4.130	4.090	4.110	4.090	4.100
Total	98.990	98.640	97.940	99.310	98.570	98.460	99.190	99.340	98.800	99.170	98.870	99.170
O=24												
(IV)Si	5.674	5.645	5.677	5.654	5.679	5.640	5.844	5.817	5.649	5.645	5.608	5.610
(IV)Al	2.052	2.217	2.143	2.164	2.078	2.171	1.871	1.884	2.185	2.172	2.202	2.174
(IV)Fe3+	0.273	0.136	0.178	0.181	0.242	0.189	0.283	0.298	0.164	0.181	0.188	0.215
Sum	7.999	7.998	7.998	7.999	7.999	8.000	7.998	7.999	7.998	7.998	7.998	7.999
(VI)Al	0.000	0.000	0.000	0.000	0.000	0.000	0.000	0.000	0.000	0.000	0.000	0.000
(VI)Ti	0.174	0.189	0.181	0.183	0.172	0.178	0.160	0.172	0.256	0.275	0.293	0.277
(VI)Fe2+	1.503	1.561	1.551	1.543	1.476	1.512	0.738	0.717	0.835	0.833	0.841	0.784
(VI)Cr	0.001	0.004	0.002	0.000	0.000	0.000	0.008	0.003	0.001	0.000	0.006	0.009
(VI)Mn	0.030	0.027	0.029	0.027	0.022	0.029	0.012	0.011	0.002	0.015	0.010	0.007
(VI)Mg	4.244	4.158	4.182	4.182	4.269	4.225	4.979	4.981	4.796	4.749	4.741	4.806
Sum	5.952	5.939	5.945	5.935	5.939	5.944	5.897	5.884	5.890	5.872	5.891	5.883
Ba	0.029	0.034	0.036	0.036	0.032	0.031	0.012	0.010	0.028	0.029	0.025	0.035
Ca	0.003	0.003	0.005	0.013	0.006	0.005	0.001	0.006	0.008	0.010	0.004	0.000
Na	0.087	0.085	0.081	0.098	0.104	0.135	0.166	0.199	0.162	0.182	0.153	0.185
K	1.924	1.933	1.905	1.910	1.917	1.908	1.836	1.836	1.824	1.802	1.806	1.809
Sum	2.043	2.055	2.027	2.057	2.059	2.079	2.015	2.051	2.022	2.023	1.988	2.029
F	0.000	0.000	0.000	0.000	0.000	0.000	0.000	0.000	0.000	0.000	0.000	0.000
Cl	0.000	0.000	0.003	0.002	0.006	0.000	0.006	0.000	0.000	0.000	0.005	0.003
OH	4.000	4.000	3.997	3.998	3.994	4.000	3.994	4.000	4.000	4.000	3.996	3.997

Table A.2.3 - Phlogopite analyses

Sample	at009	at009	at009	at012	at012	at013	at013	at013	at013	at013	at013	at013
Unit	B1	B1	B1	syenite	syenite	php	php	php	php	php	php	php
Rock type												
Remarks	core, tr1,7	core, tr1,8	rim, tr1,9			rim, tr3,1	rim, tr3,2	core, tr3,3	core, tr3,4	core, tr3,5	core, tr3,6	core, tr3,7
SiO2	38.527	38.215	38.973	37.230	36.220	38.134	37.456	36.989	36.557	37.526	37.628	37.825
TiO2	2.435	2.596	1.081	2.600	2.830	1.214	1.787	3.176	3.538	3.720	3.312	3.261
Al2O3	12.495	12.616	10.322	10.060	9.860	7.755	7.874	11.896	12.278	11.870	11.395	11.674
Cr2O3	0.039	b.d	b.d	0.020	0.010	0.033	0.014	0.023	0.000	0.049	0.020	0.043
FeO	6.675	6.642	4.919	18.188	19.366	14.819	16.465	8.384	6.923	7.159	6.444	7.032
Fe2O3	1.805	1.827	4.378	3.370	4.139	6.452	6.587	3.009	3.814	3.708	3.459	3.324
MnO	0.127	0.113	0.010	1.130	1.270	0.348	0.286	0.066	0.196	0.138	0.206	0.146
MgO	21.815	21.833	24.474	12.850	11.640	16.711	15.050	19.768	20.320	20.314	20.703	20.561
BaO	0.541	0.565	0.253	0.030	0.200	0.212	0.277	0.813	1.224	1.071	0.811	0.721
CaO	0.000	0.008	0.080	0.080	0.030	0.249	0.200	0.130	0.432	0.085	0.085	0.152
Na2O	0.724	0.518	0.567	0.300	0.280	0.330	0.342	0.257	0.428	0.424	0.451	0.490
K2O	9.681	9.598	8.681	9.870	9.930	9.342	9.547	9.501	9.712	9.695	9.414	9.689
F	n.a.	n.a.	n.a.	0.290	0.200	n.a.	n.a.	n.a.	n.a.	n.a.	n.a.	n.a.
Cl	0.024	b.d	0.004	0.010	0.020	0.012	0.006	b.d	0.008	0.017	0.009	0.028
H2O	4.090	4.080	4.080	3.730	3.720	3.900	3.870	3.990	4.040	4.070	4.020	4.050
Total	98.980	98.610	97.820	99.760	99.720	99.510	99.760	98.000	99.470	99.850	97.960	99.000
O=24												
(IV)Si	5.643	5.614	5.730	5.768	5.685	5.852	5.796	5.554	5.425	5.527	5.609	5.594
(IV)Al	2.155	2.183	1.787	1.836	1.823	1.402	1.435	2.104	2.146	2.059	2.000	2.033
(IV)Fe3+	0.199	0.202	0.484	0.393	0.488	0.744	0.766	0.340	0.425	0.411	0.388	0.370
Sum	7.997	7.999	8.001	7.997	7.996	7.998	7.997	7.998	7.996	7.997	7.997	7.997
(VI)Al	0.000	0.000	0.000	0.000	0.000	0.000	0.000	0.000	0.000	0.000	0.000	0.000
(VI)Ti	0.268	0.287	0.120	0.303	0.334	0.140	0.208	0.359	0.395	0.412	0.371	0.363
(VI)Fe2+	0.818	0.816	0.605	2.357	2.542	1.902	2.131	1.053	0.859	0.882	0.803	0.870
(VI)Cr	0.005	0.000	0.000	0.002	0.001	0.004	0.002	0.003	0.000	0.006	0.002	0.005
(VI)Mn	0.016	0.014	0.001	0.148	0.169	0.045	0.037	0.008	0.025	0.017	0.026	0.018
(VI)Mg	4.764	4.781	5.364	2.968	2.724	3.823	3.472	4.425	4.495	4.460	4.600	4.533
Sum	5.871	5.898	6.090	5.778	5.770	5.914	5.850	5.848	5.774	5.777	5.802	5.789
Ba	0.031	0.033	0.015	0.002	0.012	0.013	0.017	0.048	0.071	0.062	0.047	0.042
Ca	0.000	0.001	0.013	0.013	0.005	0.041	0.033	0.021	0.069	0.013	0.014	0.024
Na	0.206	0.148	0.162	0.090	0.085	0.098	0.103	0.075	0.123	0.121	0.130	0.141
K	1.809	1.799	1.628	1.951	1.988	1.829	1.885	1.820	1.839	1.822	1.790	1.828
Sum	2.046	1.981	1.818	2.056	2.090	1.981	2.038	1.964	2.102	2.018	1.981	2.035
F	0.000	0.000	0.000	0.142	0.100	0.000	0.000	0.000	0.000	0.000	0.000	0.000
Cl	0.006	0.000	0.001	0.003	0.006	0.003	0.002	0.000	0.002	0.004	0.003	0.007
OH	3.994	4.000	3.999	3.855	3.895	3.997	3.998	4.000	3.998	3.996	3.998	3.993

Table A.2.3 - Phlogopite analyses

Sample	at013	at013	at013	at013	at013	at013	at013	at014a	at014a	at014a	at014a	at016
Unit	php	php	php	php	php	php	php	php	php	php	php	wehrlite
Rock type												
Remarks	core, tr3,8	core, tr3,9	core, tr3,10	core, tr3,11	core, tr3,12	rim, tr3,13	rim, tr3,14					rim
SiO2	37.708	37.415	37.271	36.876	36.960	36.347	35.360	37.650	36.550	36.360	36.720	40.184
TiO2	3.281	3.362	3.464	3.683	3.064	2.865	2.562	3.590	3.630	4.060	4.070	0.887
Al2O3	11.404	11.151	11.318	11.458	11.266	8.275	7.475	10.870	11.230	11.630	11.530	11.512
Cr2O3	0.037	b.d	b.d	b.d	0.027	0.048	0.011	b.d	b.d	0.030	0.070	b.d
FeO	6.541	6.425	6.463	7.776	9.433	16.818	16.596	6.694	8.074	6.717	6.015	3.586
Fe2O3	3.540	3.976	4.047	3.588	3.468	6.722	7.413	4.063	3.897	4.060	3.873	2.153
MnO	0.081	0.142	0.148	0.108	0.207	0.412	0.463	0.120	0.150	0.150	0.060	0.051
MgO	20.987	20.808	20.742	19.496	18.772	13.681	13.080	20.010	18.830	19.550	19.940	25.127
BaO	0.790	0.965	0.965	0.777	0.561	0.316	0.504	0.860	0.840	1.160	1.120	0.345
CaO	0.092	0.061	0.154	0.112	0.198	0.159	0.489	0.130	0.210	0.230	0.110	0.146
Na2O	0.277	0.373	0.311	0.282	0.349	0.242	0.345	0.470	0.420	0.380	0.440	0.800
K2O	9.326	9.192	9.321	9.454	9.623	9.567	9.174	9.800	9.870	9.670	9.760	9.702
F	n.a.	n.a.	n.a.	n.a.	n.a.	n.a.	n.a.	0.550	0.480	0.480	0.480	n.a.
Cl	b.d	b.d	b.d	0.005	0.018	b.d	b.d	b.d	0.040	b.d	0.010	0.007
H2O	4.030	4.010	4.020	3.980	3.960	3.840	3.730	3.750	3.720	3.760	3.760	4.150
Total	98.090	97.880	98.220	97.590	97.910	99.290	97.200	98.560	97.940	98.240	97.960	98.650
O=24												
(IV)Si	5.605	5.589	5.556	5.557	5.594	5.682	5.684	5.626	5.545	5.474	5.517	5.807
(IV)Al	1.996	1.962	1.987	2.033	2.008	1.524	1.415	1.913	2.006	2.062	2.040	1.959
(IV)Fe3+	0.396	0.446	0.454	0.406	0.395	0.790	0.896	0.456	0.444	0.459	0.437	0.234
Sum	7.997	7.997	7.997	7.996	7.997	7.996	7.995	7.995	7.995	7.995	7.994	8.000
(VI)Al	0.000	0.000	0.000	0.000	0.000	0.000	0.000	0.000	0.000	0.000	0.000	0.000
(VI)Ti	0.367	0.378	0.388	0.417	0.349	0.337	0.310	0.404	0.414	0.460	0.460	0.096
(VI)Fe2+	0.813	0.803	0.806	0.980	1.194	2.199	2.231	0.837	1.024	0.846	0.756	0.433
(VI)Cr	0.004	0.000	0.000	0.000	0.003	0.006	0.001	0.000	0.000	0.004	0.008	0.000
(VI)Mn	0.010	0.018	0.019	0.014	0.027	0.055	0.063	0.015	0.019	0.019	0.008	0.006
(VI)Mg	4.650	4.634	4.610	4.380	4.236	3.189	3.135	4.458	4.258	4.388	4.466	5.413
Sum	5.844	5.833	5.823	5.791	5.809	5.786	5.740	5.714	5.715	5.717	5.698	5.948
Ba	0.046	0.056	0.056	0.046	0.033	0.019	0.032	0.050	0.050	0.068	0.066	0.020
Ca	0.015	0.010	0.025	0.018	0.032	0.027	0.084	0.021	0.034	0.037	0.018	0.023
Na	0.080	0.108	0.090	0.082	0.102	0.073	0.108	0.136	0.124	0.111	0.128	0.224
K	1.768	1.752	1.773	1.818	1.858	1.908	1.881	1.868	1.910	1.857	1.871	1.789
Sum	1.909	1.926	1.944	1.964	2.025	2.027	2.105	2.075	2.118	2.073	2.083	2.056
F	0.000	0.000	0.000	0.000	0.000	0.000	0.000	0.260	0.231	0.229	0.228	0.000
Cl	0.000	0.000	0.000	0.002	0.005	0.000	0.000	0.000	0.011	0.000	0.003	0.002
OH	4.000	4.000	4.000	3.999	3.995	4.000	4.000	3.740	3.759	3.771	3.769	3.998

Table A.2.3 - Phlogopite analyses

Sample	at016	at016	at016	at016	at016	at021	at021	at021	at021	at021	at021	at021
Unit	wehrlite	wehrlite	wehrlite	wehrlite	wehrlite	php	php	php	php	php	php	php
Rock type												
Remarks	core		rim	core		core	rim	core	rim	core	rim	core
SiO2	39.943	38.154	39.524	37.680	38.356	38.527	39.138	38.652	39.478	38.505	39.947	40.049
TiO2	0.877	1.101	0.925	2.702	1.525	3.481	2.119	3.054	1.987	3.359	1.257	2.635
Al2O3	11.975	11.685	12.035	12.953	12.602	10.949	5.143	10.912	5.781	11.056	5.158	9.201
Cr2O3	b.d	b.d	b.d	b.d	0.021	0.047	b.d	b.d	0.028	b.d	b.d	0.004
FeO	3.901	3.892	3.489	4.501	4.094	5.978	6.193	5.012	5.785	5.605	9.461	4.640
Fe2O3	1.457	1.915	1.522	1.693	1.628	4.500	10.366	4.429	9.461	4.712	9.702	5.475
MnO	0.120	0.109	0.088	0.029	0.075	0.155	0.328	0.160	0.305	0.205	0.749	0.126
MgO	24.834	23.958	25.087	23.039	24.341	21.495	21.172	22.474	21.531	21.945	20.029	23.178
BaO	0.432	0.469	n.a.	n.a.	n.a.	0.791	0.207	0.671	0.231	0.945	0.271	0.491
CaO	0.084	0.125	0.014	0.025	0.015	0.117	0.128	0.087	0.302	0.047	0.120	0.093
Na2O	0.801	0.644	0.728	0.579	0.636	0.343	0.105	0.364	0.270	0.376	0.118	0.235
K2O	9.738	9.314	9.823	9.625	9.565	9.394	9.593	9.374	9.574	9.551	9.443	8.864
F	n.a.	n.a.	n.a.	n.a.	n.a.	0.341	0.441	0.354	0.398	0.504	0.276	0.277
Cl	0.014	0.032	n.a.	n.a.	n.a.	n.a.	n.a.	n.a.	n.a.	n.a.	n.a.	n.a.
H2O	4.130	3.990	4.110	4.060	4.080	3.950	3.760	3.940	3.810	3.890	3.870	3.990
Total	98.310	95.390	97.340	96.890	96.940	100.070	98.690	99.480	98.940	100.700	100.400	99.260
O=24												
(IV)Si	5.794	5.720	5.765	5.560	5.638	5.624	5.909	5.642	5.914	5.596	5.993	5.826
(IV)Al	2.046	2.063	2.067	2.251	2.182	1.882	0.914	1.876	1.020	1.892	0.911	1.576
(IV)Fe3+	0.159	0.216	0.167	0.188	0.180	0.494	1.177	0.486	1.065	0.515	1.094	0.599
Sum	7.999	7.999	7.999	7.999	8.000	8.000	8.000	8.004	7.999	8.003	7.998	8.001
(VI)Al	0.000	0.000	0.000	0.000	0.000	0.000	0.000	0.000	0.000	0.000	0.000	0.000
(VI)Ti	0.096	0.124	0.101	0.300	0.169	0.382	0.241	0.335	0.224	0.367	0.142	0.288
(VI)Fe2+	0.473	0.488	0.426	0.555	0.503	0.730	0.782	0.612	0.725	0.681	1.187	0.564
(VI)Cr	0.000	0.000	0.000	0.000	0.002	0.005	0.000	0.000	0.003	0.000	0.000	0.000
(VI)Mn	0.015	0.014	0.011	0.004	0.009	0.019	0.042	0.020	0.039	0.025	0.095	0.016
(VI)Mg	5.370	5.355	5.455	5.068	5.334	4.677	4.765	4.891	4.808	4.754	4.480	5.027
Sum	5.954	5.981	5.993	5.927	6.017	5.813	5.830	5.858	5.799	5.827	5.904	5.895
Ba	0.025	0.028	0.000	0.000	0.000	0.045	0.012	0.038	0.014	0.054	0.016	0.028
Ca	0.013	0.020	0.002	0.004	0.002	0.018	0.021	0.014	0.048	0.007	0.019	0.014
Na	0.225	0.187	0.206	0.166	0.181	0.097	0.031	0.103	0.078	0.106	0.034	0.066
K	1.802	1.782	1.828	1.812	1.794	1.749	1.848	1.746	1.830	1.771	1.807	1.645
Sum	2.065	2.017	2.036	1.982	1.977	1.909	1.912	1.901	1.970	1.938	1.876	1.753
F	0.000	0.000	0.000	0.000	0.000	0.158	0.211	0.164	0.189	0.232	0.131	0.128
Cl	0.004	0.008	0.000	0.000	0.000	0.000	0.000	0.000	0.000	0.000	0.000	0.000
OH	3.997	3.992	4.000	4.000	4.000	3.843	3.789	3.837	3.811	3.768	3.869	3.873

Table A.2.3 - Phlogopite analyses

Sample	at021	at022	at022	at022	at022	at022	at022	at024	at024	at024	at024	at024
Unit	php	php	php	php	php	php	php	lcr	lcr	lcr	lcr	lcr
Rock type												
Remarks	rim	rim	core	rim	core	core, tr4,5	rim, tr4,6	rim, tr5,1	core, tr5,2	core. tr5,3	core, tr5,4	core, tr5,5
SiO2	39.239	38.641	37.283	38.256	36.980	37.867	39.150	38.256	37.968	38.141	38.715	37.958
TiO2	2.744	3.071	4.067	3.336	4.000	3.366	2.729	3.533	4.592	4.645	4.740	4.770
Al2O3	9.283	9.249	12.424	9.889	11.960	12.364	9.079	12.180	12.849	12.930	12.787	12.832
Cr2O3	b.d	0.025	b.d	0.012	0.014	b.d	0.065	0.033	0.330	0.349	0.233	0.339
FeO	5.943	6.298	5.348	5.117	5.246	5.137	6.487	5.415	6.886	7.000	6.813	6.794
Fe2O3	5.968	5.862	3.166	5.139	3.724	3.046	5.333	2.914	2.427	2.374	2.516	2.606
MnO	0.228	0.126	0.085	0.103	0.105	0.081	0.118	0.092	b.d	0.078	0.057	0.090
MgO	21.839	21.063	21.309	21.367	21.264	22.238	20.986	21.768	19.998	20.037	20.342	19.956
BaO	0.491	n.a.	n.a.	n.a.	n.a.	0.792	0.263	0.847	0.315	0.352	0.269	0.363
CaO	0.104	0.119	0.076	0.054	0.052	0.080	0.073	0.038	0.054	b.d	0.035	b.d
Na2O	0.289	0.353	0.433	0.432	0.281	0.373	0.369	0.407	0.405	0.313	0.421	0.329
K2O	9.737	9.806	9.935	10.052	9.946	9.657	9.787	9.709	9.794	9.766	9.821	9.863
F	0.395	n.a.	n.a.	n.a.	n.a.	n.a.	n.a.	0.536	0.505	0.385	0.405	0.466
Cl	n.a.	n.a.	n.a.	n.a.	n.a.	0.010	0.000	n.a.	n.a.	n.a.	n.a.	n.a.
H2O	3.910	4.050	4.070	4.030	4.040	4.100	4.040	3.850	3.880	3.950	3.980	3.910
Total	100.170	98.660	98.200	97.790	97.610	99.110	98.480	99.580	100.000	100.320	101.130	100.280
O=24												
(IV)Si	5.745	5.728	5.491	5.689	5.490	5.534	5.814	5.584	5.529	5.532	5.561	5.516
(IV)Al	1.600	1.615	2.155	1.732	2.091	2.128	1.588	2.094	2.203	2.208	2.163	2.196
(IV)Fe3+	0.657	0.653	0.351	0.575	0.416	0.335	0.595	0.320	0.266	0.259	0.272	0.285
Sum	8.002	7.996	7.997	7.996	7.997	7.997	7.997	7.998	7.998	7.999	7.996	7.997
(VI)Al	0.000	0.000	0.000	0.000	0.000	0.000	0.000	0.000	0.000	0.000	0.000	0.000
(VI)Ti	0.302	0.342	0.451	0.373	0.447	0.370	0.305	0.388	0.503	0.507	0.512	0.521
(VI)Fe2+	0.728	0.781	0.659	0.636	0.651	0.628	0.806	0.661	0.839	0.849	0.818	0.826
(VI)Cr	0.000	0.003	0.000	0.001	0.002	0.000	0.008	0.004	0.038	0.040	0.026	0.039
(VI)Mn	0.028	0.016	0.011	0.013	0.013	0.010	0.015	0.011	0.000	0.010	0.007	0.011
(VI)Mg	4.766	4.655	4.679	4.737	4.706	4.845	4.646	4.737	4.341	4.332	4.356	4.323
Sum	5.824	5.797	5.800	5.760	5.819	5.853	5.780	5.801	5.721	5.738	5.719	5.720
Ba	0.028	0.000	0.000	0.000	0.000	0.045	0.015	0.048	0.018	0.020	0.015	0.021
Ca	0.016	0.019	0.012	0.009	0.008	0.013	0.012	0.006	0.008	0.000	0.005	0.000
Na	0.082	0.101	0.124	0.125	0.081	0.106	0.106	0.115	0.114	0.088	0.117	0.093
K	1.819	1.855	1.867	1.907	1.884	1.801	1.854	1.808	1.819	1.807	1.800	1.829
Sum	1.945	1.975	2.003	2.041	1.973	1.965	1.987	1.977	1.959	1.915	1.937	1.943
F	0.183	0.000	0.000	0.000	0.000	0.000	0.000	0.248	0.233	0.177	0.184	0.214
Cl	0.000	0.000	0.000	0.000	0.000	0.003	0.000	0.000	0.000	0.000	0.000	0.000
OH	3.817	4.000	4.000	4.000	4.000	3.998	4.000	3.753	3.767	3.823	3.816	3.786

Table A.2.3 - Phlogopite analyses

Sample	at024	at024	at024	at024	at024	at024	at025	at025	at025	at025	at025	at025
Unit	lcr	lcr	lcr	lcr	lcr	lcr	wehrlite	wehrlite	wehrlite	wehrlite	wehrlite	wehrlite
Rock type												
Remarks	core, tr5,6	rim, tr5,7	rim, tr6,2	core, tr6,3	core, tr6,4	rim, tr6,5	rim, tr7,1	core, tr7,2	core, tr7,3	core, tr7,4	core, tr7,5	rim, tr7,6
SiO2	38.009	37.856	38.173	38.626	37.759	38.883	39.966	38.772	38.281	38.197	38.770	38.462
TiO2	4.728	4.612	4.770	4.793	4.692	3.118	0.710	2.777	2.780	3.378	3.043	1.899
Al2O3	12.827	12.532	12.606	11.738	12.458	11.021	10.743	12.800	12.711	12.874	13.082	12.357
Cr2O3	0.276	0.119	0.458	0.050	0.286	0.023	0.048	0.031	0.116	0.091	0.014	0.063
FeO	6.915	7.099	5.885	7.269	7.099	4.945	3.547	3.905	3.793	3.275	4.163	3.829
Fe2O3	2.428	3.018	2.774	3.228	2.772	3.897	2.895	2.167	2.397	2.697	2.141	2.793
MnO	0.056	b.d	0.064	0.095	b.d	0.101	0.094	0.098	0.063	0.107	0.051	0.128
MgO	19.939	19.929	20.327	19.578	19.555	22.349	25.235	23.694	23.563	23.485	23.594	24.310
BaO	0.241	0.359	0.212	0.330	0.326	0.697	0.222	0.401	0.500	0.514	0.542	0.628
CaO	b.d	0.139	0.047	0.051	0.033	0.034	0.084	0.052	0.042	0.037	0.054	0.109
Na2O	0.317	0.486	0.486	0.388	0.402	0.326	0.483	0.416	0.379	0.451	0.382	0.577
K2O	9.855	9.730	9.715	9.667	9.719	9.714	9.485	10.144	10.017	10.110	10.071	9.790
F	0.451	0.348	0.423	0.360	0.449	0.593	n.a.	n.a.	n.a.	n.a.	n.a.	n.a.
Cl	n.a.	n.a.	n.a.	n.a.	n.a.	n.a.	b.d	0.013	0.033	b.d	0.007	0.026
H2O	3.910	3.950	3.930	3.950	3.870	3.830	4.110	4.160	4.120	4.150	4.180	4.130
Total	99.950	100.180	99.870	100.120	99.420	99.530	97.620	99.430	98.800	99.370	100.090	99.100
O=24												
(IV)Si	5.533	5.516	5.541	5.628	5.541	5.675	5.835	5.590	5.562	5.515	5.559	5.582
(IV)Al	2.199	2.151	2.155	2.014	2.153	1.894	1.847	2.173	2.175	2.189	2.209	2.112
(IV)Fe3+	0.266	0.331	0.303	0.354	0.306	0.428	0.318	0.235	0.262	0.293	0.231	0.305
Sum	7.998	7.998	7.999	7.996	8.000	7.997	8.000	7.998	7.999	7.997	7.999	7.999
(VI)Al	0.000	0.000	0.000	0.000	0.000	0.000	0.000	0.000	0.000	0.000	0.000	0.000
(VI)Ti	0.518	0.506	0.521	0.525	0.518	0.342	0.078	0.301	0.304	0.367	0.328	0.207
(VI)Fe2+	0.842	0.865	0.714	0.886	0.871	0.604	0.433	0.471	0.461	0.395	0.499	0.465
(VI)Cr	0.032	0.014	0.052	0.006	0.033	0.003	0.006	0.004	0.013	0.010	0.002	0.007
(VI)Mn	0.007	0.000	0.008	0.012	0.000	0.012	0.012	0.012	0.008	0.013	0.006	0.016
(VI)Mg	4.327	4.329	4.398	4.252	4.278	4.863	5.493	5.092	5.104	5.055	5.043	5.260
Sum	5.726	5.714	5.693	5.681	5.700	5.824	6.022	5.880	5.890	5.840	5.878	5.955
Ba	0.014	0.020	0.012	0.019	0.019	0.040	0.013	0.023	0.028	0.029	0.030	0.036
Ca	0.000	0.022	0.007	0.008	0.005	0.005	0.013	0.008	0.007	0.006	0.008	0.017
Na	0.089	0.137	0.137	0.110	0.114	0.092	0.137	0.116	0.107	0.126	0.106	0.162
K	1.830	1.809	1.799	1.797	1.820	1.809	1.767	1.866	1.857	1.862	1.842	1.813
Sum	1.933	1.988	1.955	1.934	1.958	1.946	1.930	2.013	1.999	2.023	1.986	2.028
F	0.208	0.161	0.194	0.166	0.209	0.274	0.000	0.000	0.000	0.000	0.000	0.000
Cl	0.000	0.000	0.000	0.000	0.000	0.000	0.000	0.003	0.008	0.000	0.002	0.007
OH	3.792	3.840	3.806	3.834	3.792	3.726	4.000	3.997	3.992	4.000	3.998	3.994

Table A.2.3 - Phlogopite analyses

Sample	at025	at029	at029	at029	at029	at029	at029	at033	at033	at033	at033	at033
Unit	wehrlite	B2	B2	B2	B2	B2	B2	B2	B2	B2	B2	B2
Rock type												
Remarks	rim, tr7,7				rim	rim		rim	core	rim	core	rim
SiO2	38.353	36.886	37.456	37.110	38.584	38.708	36.839	36.879	37.903	37.782	37.120	37.706
TiO2	2.265	2.654	1.940	2.532	1.608	1.846	2.433	2.821	2.494	2.122	2.826	2.175
Al2O3	12.393	11.726	10.508	11.388	9.685	10.119	11.226	10.883	10.025	9.620	10.867	10.178
Cr2O3	0.045	b.d	0.017	b.d	b.d	0.053	0.037	b.d	0.021	0.051	0.054	b.d
FeO	4.204	13.790	13.569	13.554	12.445	12.548	13.852	15.252	14.651	16.154	15.648	14.456
Fe2O3	2.383	2.781	3.597	2.888	3.988	3.625	3.263	3.541	3.790	2.969	3.009	3.587
MnO	0.066	0.347	0.424	0.289	0.231	0.320	0.377	0.443	0.417	0.336	0.365	0.374
MgO	23.659	16.779	17.124	16.939	18.239	17.996	16.610	15.464	15.986	14.673	15.153	16.410
BaO	0.564	0.377	0.410	0.543	0.144	0.131	0.712	0.325	0.173	0.207	0.170	0.230
CaO	0.005	b.d	b.d	b.d	0.036	0.076	b.d	0.093	0.096	0.043	0.049	0.022
Na2O	0.423	0.226	0.267	0.157	0.410	0.301	0.299	0.242	0.297	0.107	0.085	0.158
K2O	9.880	9.980	9.972	9.925	9.803	10.189	9.898	9.612	9.569	9.664	9.711	9.773
F	n.a.	n.a.	n.a.	n.a.	n.a.	n.a.	n.a.	n.a.	n.a.	n.a.	n.a.	n.a.
Cl	b.d	0.015	0.011	b.d	0.023	0.017	0.041	0.006	0.002	b.d	b.d	b.d
H2O	4.100	3.950	3.940	3.950	3.970	4.000	3.930	3.920	3.940	3.850	3.910	3.930
Total	98.340	99.510	99.230	99.270	99.170	99.930	99.520	99.480	99.360	97.580	98.970	99.000
O=24												
(IV)Si	5.605	5.588	5.702	5.632	5.824	5.803	5.610	5.634	5.767	5.885	5.689	5.757
(IV)Al	2.133	2.092	1.884	2.035	1.722	1.786	2.013	1.958	1.796	1.765	1.961	1.830
(IV)Fe3+	0.262	0.317	0.412	0.330	0.453	0.409	0.374	0.407	0.434	0.348	0.347	0.412
Sum	8.000	7.997	7.998	7.997	7.999	7.998	7.997	7.999	7.997	7.998	7.997	7.999
(VI)Al	0.000	0.000	0.000	0.000	0.000	0.000	0.000	0.000	0.000	0.000	0.000	0.000
(VI)Ti	0.249	0.302	0.222	0.289	0.183	0.208	0.279	0.324	0.285	0.249	0.326	0.250
(VI)Fe2+	0.514	1.747	1.728	1.720	1.571	1.573	1.764	1.948	1.864	2.104	2.006	1.846
(VI)Cr	0.005	0.000	0.002	0.000	0.000	0.006	0.004	0.000	0.003	0.006	0.007	0.000
(VI)Mn	0.008	0.045	0.055	0.037	0.030	0.041	0.049	0.057	0.054	0.044	0.047	0.048
(VI)Mg	5.154	3.790	3.886	3.833	4.104	4.022	3.771	3.522	3.626	3.407	3.462	3.735
Sum	5.930	5.884	5.893	5.879	5.888	5.850	5.867	5.851	5.832	5.810	5.848	5.879
Ba	0.032	0.022	0.024	0.032	0.009	0.008	0.042	0.019	0.010	0.013	0.010	0.014
Ca	0.001	0.000	0.000	0.000	0.006	0.012	0.000	0.015	0.016	0.007	0.008	0.004
Na	0.120	0.066	0.079	0.046	0.120	0.087	0.088	0.072	0.088	0.032	0.025	0.047
K	1.842	1.929	1.937	1.922	1.888	1.949	1.923	1.873	1.857	1.920	1.899	1.903
Sum	1.995	2.017	2.040	2.000	2.023	2.056	2.053	1.979	1.971	1.972	1.942	1.968
F	0.000	0.000	0.000	0.000	0.000	0.000	0.000	0.000	0.000	0.000	0.000	0.000
Cl	0.000	0.004	0.003	0.000	0.006	0.005	0.011	0.002	0.001	0.000	0.000	0.000
OH	4.000	3.996	3.997	4.000	3.994	3.996	3.989	3.998	3.999	4.000	4.000	4.000

Table A.2.3 - Phlogopite analyses

Sample	at033	at035	at035	at038	at038	at038	at038	at038	at038	at038	at038	at042
Unit	B2	B1	B1	B2	B2	B2	B2	B2	B2	B2	B2	C1
Rock type												
Remarks	core			rim	core	rim	core	rim	core	rim	core	
SiO2	37.796	39.373	37.269	37.120	37.015	38.216	36.499	37.574	36.834	37.469	37.960	39.973
TiO2	2.352	1.731	2.805	2.041	2.012	1.318	2.087	1.873	1.885	1.802	1.607	0.199
Al2O3	10.499	11.079	11.457	12.485	12.742	10.892	12.652	11.352	12.300	12.344	12.533	0.143
Cr2O3	0.031	b.d	0.013	0.003	b.d	b.d	0.006	b.d	b.d	0.049	0.038	0.014
FeO	15.263	7.194	8.593	12.735	13.438	10.943	13.042	12.279	12.817	12.281	13.097	5.372
Fe2O3	3.408	2.951	3.143	1.694	1.465	3.012	1.751	2.877	1.784	1.918	1.394	14.675
MnO	0.365	0.189	0.266	0.215	0.287	0.301	0.229	0.275	0.300	0.274	0.284	0.057
MgO	15.877	22.344	19.677	18.068	17.885	19.558	17.648	18.236	17.950	18.723	18.623	22.551
BaO	0.192	0.589	0.441	0.477	0.505	0.315	0.618	0.403	0.595	0.434	0.430	0.151
CaO	0.056	0.078	0.180	0.089	0.011	0.073	0.052	0.113	0.046	0.109	0.098	0.073
Na2O	0.247	0.462	0.432	0.339	0.215	0.415	0.512	0.515	0.310	0.316	0.148	0.059
K2O	9.924	9.002	9.347	9.960	9.881	10.009	9.876	9.918	9.799	9.879	9.985	8.304
F	n.a.	0.163	0.058	n.a.	n.a.	n.a.	n.a.	n.a.	n.a.	n.a.	n.a.	0.003
Cl	b.d	n.a.	n.a.	b.d	0.015	0.024	0.020	b.d	0.014	0.009	0.023	0.002
H2O	3.950	4.020	3.950	3.980	3.980	3.990	3.950	3.980	3.940	4.000	4.020	3.830
Total	99.960	99.180	97.630	99.210	99.450	99.070	98.940	99.400	98.570	99.610	100.240	95.410
O=24												
(IV)Si	5.734	5.765	5.613	5.592	5.574	5.734	5.538	5.659	5.595	5.607	5.648	6.249
(IV)Al	1.876	1.910	2.032	2.215	2.259	1.925	2.261	2.013	2.200	2.175	2.196	0.026
(IV)Fe3+	0.389	0.325	0.356	0.192	0.166	0.340	0.200	0.326	0.204	0.216	0.156	1.725
Sum	7.999	8.000	8.001	7.999	7.999	7.999	7.999	7.998	7.999	7.998	8.000	8.000
(VI)Al	0.000	0.000	0.000	0.000	0.000	0.000	0.000	0.000	0.000	0.000	0.000	0.000
(VI)Ti	0.268	0.191	0.318	0.231	0.228	0.149	0.238	0.212	0.215	0.203	0.180	0.023
(VI)Fe2+	1.936	0.881	1.082	1.604	1.692	1.373	1.655	1.547	1.628	1.537	1.630	0.702
(VI)Cr	0.004	0.000	0.002	0.000	0.000	0.000	0.001	0.000	0.000	0.006	0.004	0.002
(VI)Mn	0.047	0.023	0.034	0.027	0.037	0.038	0.029	0.035	0.039	0.035	0.036	0.008
(VI)Mg	3.590	4.877	4.418	4.058	4.015	4.375	3.992	4.094	4.065	4.177	4.131	5.255
Sum	5.845	5.972	5.854	5.920	5.972	5.935	5.915	5.888	5.947	5.958	5.981	5.990
Ba	0.011	0.034	0.026	0.028	0.030	0.019	0.037	0.024	0.035	0.025	0.025	0.009
Ca	0.009	0.012	0.029	0.014	0.002	0.012	0.008	0.018	0.007	0.017	0.016	0.012
Na	0.073	0.131	0.126	0.099	0.063	0.121	0.151	0.150	0.091	0.092	0.043	0.018
K	1.921	1.681	1.796	1.914	1.898	1.916	1.912	1.906	1.899	1.886	1.895	1.656
Sum	2.014	1.858	1.977	2.055	1.993	2.068	2.108	2.098	2.032	2.020	1.979	1.695
F	0.000	0.076	0.028	0.000	0.000	0.000	0.000	0.000	0.000	0.000	0.000	0.002
Cl	0.000	0.000	0.000	0.000	0.004	0.006	0.005	0.000	0.004	0.003	0.006	0.001
OH	4.000	3.925	3.972	4.000	3.996	3.994	3.995	4.000	3.996	3.998	3.994	3.998

Table A.2.3 - Phlogopite analyses

Sample	at042	at042	at042	at042	at042	at042	at042	at043	at043	at043	at043	at043
Unit	C1	C1	C1	C1	C1	C1	C1	C3	C3	C3	C3	C3
Rock type												
Remarks												
SiO2	40.616	41.360	43.106	41.617	42.476	41.202	41.203	36.756	36.656	37.410	37.534	37.225
TiO2	0.197	0.150	0.191	0.190	0.261	0.162	0.162	3.013	3.132	3.075	2.857	2.643
Al2O3	0.113	0.106	0.065	0.065	0.077	0.082	0.082	11.065	11.697	11.824	12.530	12.479
Cr2O3	b.d	0.007	b.d	b.d	b.d	b.d	b.d	b.d	0.018	b.d	b.d	b.d
FeO	5.137	5.567	5.553	5.879	5.925	6.170	6.162	11.586	11.663	12.011	12.756	12.861
Fe2O3	15.586	14.686	14.468	15.398	15.090	15.774	15.783	2.973	2.172	1.082	1.184	1.408
MnO	0.098	0.045	0.064	0.099	0.031	0.111	0.111	0.355	0.371	0.288	0.264	0.221
MgO	23.326	22.773	23.740	23.332	23.612	23.420	23.420	17.069	17.079	17.055	17.486	17.539
BaO	0.108	0.220	b.d	0.094	0.022	b.d	b.d	n.a.	n.a.	0.423	0.152	0.316
CaO	0.072	0.079	0.049	0.003	0.006	b.d	b.d	0.122	0.039	b.d	b.d	0.011
Na2O	0.082	0.077	0.081	0.075	0.073	0.064	0.064	0.309	0.268	0.075	0.057	0.038
K2O	8.808	9.207	8.646	8.737	8.580	8.395	8.395	9.865	9.762	9.288	9.970	10.008
F	0.193	0.263	0.229	0.147	0.108	0.158	0.224	n.a.	n.a.	0.157	0.160	0.185
Cl	0.023	0.012	b.d	0.002	0.005	0.005	0.006	n.a.	n.a.	0.010	0.010	b.d
H2O	3.840	3.810	3.940	3.920	3.990	3.910	3.880	3.900	3.900	3.830	3.910	3.880
Total	98.200	98.360	100.130	99.560	100.260	99.450	99.490	97.010	96.760	96.530	98.870	98.810
O=24												
(IV)Si	6.193	6.298	6.378	6.250	6.303	6.201	6.201	5.650	5.630	5.737	5.645	5.620
(IV)Al	0.020	0.019	0.011	0.011	0.013	0.015	0.015	2.003	2.116	2.136	2.219	2.219
(IV)Fe3+	1.786	1.681	1.609	1.738	1.683	1.785	1.786	0.344	0.251	0.125	0.134	0.160
Sum	7.999	7.998	7.998	7.999	7.999	8.001	8.002	7.997	7.997	7.998	7.998	7.999
(VI)Al	0.000	0.000	0.000	0.000	0.000	0.000	0.000	0.000	0.000	0.000	0.000	0.000
(VI)Ti	0.023	0.017	0.021	0.021	0.029	0.018	0.018	0.348	0.362	0.355	0.323	0.300
(VI)Fe2+	0.655	0.709	0.687	0.738	0.735	0.777	0.776	1.489	1.498	1.540	1.604	1.624
(VI)Cr	0.000	0.001	0.000	0.000	0.000	0.000	0.000	0.000	0.002	0.000	0.000	0.000
(VI)Mn	0.013	0.006	0.008	0.013	0.004	0.014	0.014	0.046	0.048	0.037	0.034	0.028
(VI)Mg	5.302	5.169	5.237	5.224	5.223	5.254	5.254	3.911	3.911	3.899	3.920	3.947
Sum	5.993	5.902	5.953	5.996	5.991	6.063	6.062	5.794	5.821	5.831	5.881	5.899
Ba	0.006	0.013	0.000	0.006	0.001	0.000	0.000	0.000	0.000	0.025	0.009	0.019
Ca	0.012	0.013	0.008	0.000	0.001	0.000	0.000	0.020	0.006	0.000	0.000	0.002
Na	0.024	0.023	0.023	0.022	0.021	0.019	0.019	0.092	0.080	0.022	0.017	0.011
K	1.713	1.789	1.632	1.674	1.624	1.612	1.612	1.934	1.913	1.817	1.913	1.927
Sum	1.755	1.838	1.663	1.702	1.647	1.631	1.631	2.046	1.999	1.864	1.939	1.959
F	0.093	0.127	0.107	0.070	0.051	0.075	0.107	0.000	0.000	0.076	0.076	0.089
Cl	0.006	0.003	0.000	0.001	0.002	0.002	0.002	0.000	0.000	0.003	0.003	0.000
OH	3.901	3.870	3.893	3.930	3.948	3.924	3.892	4.000	4.000	3.921	3.921	3.912

Table A.2.3 - Phlogopite analyses

Sample	at043	at043	at043	at043	at044	at044	at044	at044	at044	at044	at047	at047
Unit	C3	C3	C3	C3	C1	C1	C1	C1	C1	C1	C2	C2
Rock type												
Remarks					rim	core	rim	core	rim	core		
SiO2	37.322	37.513	37.152	37.565	39.600	40.080	39.580	39.830	39.490	40.980	41.349	41.444
TiO2	3.140	3.031	3.113	3.036	0.080	0.130	0.110	0.110	0.110	0.200	0.102	0.174
Al2O3	12.430	11.608	11.976	11.371	0.020	0.090	b.d	0.070	0.200	0.250	7.990	8.120
Cr2O3	0.000	0.011	0.004	0.009	0.010	b.d	b.d	b.d	b.d	0.010	b.d	b.d
FeO	12.158	12.465	12.120	11.350	5.237	5.031	4.762	4.753	5.149	4.493	1.464	2.091
Fe2O3	1.553	1.986	1.990	2.493	15.784	15.380	16.212	15.966	16.060	15.156	5.355	5.739
MnO	0.292	0.318	0.285	0.305	0.130	0.140	0.080	0.100	0.120	0.150	0.045	0.076
MgO	17.529	17.086	17.373	17.778	22.290	22.330	22.810	22.860	22.550	23.110	26.525	26.479
BaO	0.181	0.021	0.211	0.042	0.020	0.040	0.060	0.050	b.d	0.070	0.220	0.185
CaO	0.013	0.046	0.000	0.036	0.090	0.040	0.100	b.d	0.190	b.d	0.266	0.156
Na2O	0.030	0.042	0.049	0.041	0.210	0.380	0.200	0.220	0.180	0.210	0.034	0.032
K2O	10.003	9.832	9.876	9.966	10.090	10.090	10.020	10.130	10.120	10.190	10.095	10.359
F	0.206	0.161	0.200	0.197	0.150	0.190	0.260	0.190	0.190	0.290	0.102	0.064
Cl	0.009	0.002	0.009	0.002	b.d	b.d	0.040	b.d	0.010	b.d	0.002	0.016
H2O	3.880	3.870	3.860	3.870	3.790	3.790	3.750	3.800	3.790	3.810	4.060	4.110
Total	98.750	97.990	98.220	98.060	97.500	97.710	97.980	98.080	98.160	98.920	97.610	99.040
O=24												
(IV)Si	5.618	5.695	5.632	5.686	6.150	6.194	6.115	6.136	6.097	6.222	6.037	5.992
(IV)Al	2.204	2.076	2.138	2.027	0.004	0.016	0.000	0.013	0.036	0.045	1.374	1.383
(IV)Fe3+	0.176	0.227	0.227	0.284	1.843	1.787	1.883	1.849	1.864	1.730	0.588	0.624
Sum	7.998	7.998	7.997	7.997	7.997	7.997	7.998	7.998	7.997	7.997	7.999	7.999
(VI)Al	0.000	0.000	0.000	0.000	0.000	0.000	0.000	0.000	0.000	0.000	0.000	0.000
(VI)Ti	0.356	0.346	0.355	0.346	0.009	0.015	0.013	0.013	0.013	0.023	0.011	0.019
(VI)Fe2+	1.531	1.583	1.537	1.437	0.680	0.650	0.615	0.612	0.665	0.571	0.179	0.253
(VI)Cr	0.000	0.001	0.000	0.001	0.001	0.000	0.000	0.000	0.000	0.001	0.000	0.000
(VI)Mn	0.037	0.041	0.037	0.039	0.017	0.018	0.010	0.013	0.016	0.019	0.006	0.009
(VI)Mg	3.934	3.867	3.926	4.012	5.161	5.145	5.254	5.250	5.191	5.231	5.774	5.708
Sum	5.858	5.838	5.855	5.835	5.868	5.828	5.892	5.888	5.885	5.845	5.970	5.989
Ba	0.011	0.001	0.013	0.002	0.001	0.002	0.004	0.003	0.000	0.004	0.013	0.010
Ca	0.002	0.007	0.000	0.006	0.015	0.007	0.017	0.000	0.031	0.000	0.042	0.024
Na	0.009	0.012	0.014	0.012	0.063	0.114	0.060	0.066	0.054	0.062	0.010	0.009
K	1.921	1.904	1.910	1.925	1.999	1.989	1.975	1.991	1.993	1.974	1.880	1.911
Sum	1.943	1.924	1.937	1.945	2.078	2.112	2.056	2.060	2.078	2.040	1.945	1.954
F	0.098	0.078	0.096	0.095	0.074	0.093	0.127	0.093	0.093	0.140	0.047	0.030
Cl	0.003	0.001	0.003	0.001	0.000	0.000	0.011	0.000	0.003	0.000	0.001	0.004
OH	3.900	3.922	3.902	3.905	3.926	3.907	3.862	3.907	3.905	3.861	3.952	3.967

Table A.2.3 - Phlogopite analyses

Sample	at047	at047	at047	at047	at047	at047	at047	at050	at050	at052	at052	at052
Unit	C2	C2	C2	C2	C2	C2	C2	C2	C2	C1	C1	C1
Rock type												
Remarks												
SiO2	40.456	40.742	40.659	40.012	39.887	42.073	42.238	41.840	41.553	40.007	39.760	41.106
TiO2	0.258	0.387	0.240	0.141	0.136	0.191	0.118	0.594	0.217	0.139	0.129	0.271
Al2O3	8.325	5.661	0.045	0.040	0.047	0.023	8.259	11.556	7.712	1.095	0.105	0.078
Cr2O3	b.d	0.010	0.047	0.023	0.021	0.031	0.045	b.d	b.d	0.067	b.d	0.059
FeO	2.123	2.393	4.092	4.975	5.078	4.504	1.613	3.740	2.788	7.178	5.964	6.634
Fe2O3	5.459	9.451	14.918	15.653	15.644	15.042	5.372	1.294	6.498	14.808	16.637	15.195
MnO	0.070	0.103	0.087	0.073	0.057	0.037	0.042	0.041	0.042	0.173	0.148	0.136
MgO	25.832	25.586	23.042	22.740	22.761	23.609	27.301	26.092	26.281	22.164	22.832	22.504
BaO	0.177	0.376	b.d	0.026	0.001	b.d	0.252	0.817	0.334	b.d	0.116	0.028
CaO	0.256	0.141	0.087	0.205	0.020	0.102	0.145	0.027	0.231	0.009	b.d	b.d
Na2O	0.058	0.030	0.065	0.061	0.070	0.036	0.020	0.180	0.203	0.073	0.075	0.088
K2O	10.342	10.353	9.715	9.614	9.642	9.813	9.818	9.575	9.660	9.276	9.636	8.421
F	0.108	0.059	0.254	0.228	0.146	0.157	0.120	0.133	0.905	0.409	0.274	0.328
Cl	0.016	0.008	b.d	0.012	0.007	0.016	0.003	0.007	b.d	0.007	b.d	0.020
H2O	4.020	4.060	3.770	3.770	3.810	3.930	4.140	4.160	3.730	3.730	3.800	3.780
Total	97.500	99.360	97.020	97.570	97.330	99.560	99.490	100.060	100.150	99.140	99.480	98.650
O=24												
(IV)Si	5.952	5.979	6.262	6.175	6.170	6.301	6.034	5.932	5.987	6.106	6.070	6.251
(IV)Al	1.443	0.978	0.008	0.007	0.009	0.004	1.390	1.930	1.309	0.197	0.019	0.014
(IV)Fe3+	0.604	1.043	1.727	1.816	1.819	1.694	0.577	0.138	0.704	1.699	1.910	1.737
Sum	7.999	8.000	7.997	7.998	7.998	7.999	8.001	8.000	8.000	8.002	7.999	8.002
(VI)Al	0.000	0.000	0.000	0.000	0.000	0.000	0.000	0.000	0.000	0.000	0.000	0.000
(VI)Ti	0.029	0.043	0.028	0.016	0.016	0.022	0.013	0.063	0.024	0.016	0.015	0.031
(VI)Fe2+	0.261	0.294	0.527	0.642	0.657	0.564	0.193	0.443	0.336	0.916	0.762	0.844
(VI)Cr	0.000	0.001	0.006	0.003	0.003	0.004	0.005	0.000	0.000	0.008	0.000	0.007
(VI)Mn	0.009	0.013	0.011	0.010	0.007	0.005	0.005	0.005	0.005	0.022	0.019	0.018
(VI)Mg	5.666	5.597	5.290	5.232	5.249	5.271	5.814	5.515	5.645	5.043	5.197	5.102
Sum	5.965	5.948	5.862	5.903	5.932	5.866	6.030	6.026	6.010	6.005	5.993	6.002
Ba	0.010	0.022	0.000	0.002	0.000	0.000	0.014	0.045	0.019	0.000	0.007	0.002
Ca	0.040	0.022	0.014	0.034	0.003	0.016	0.022	0.004	0.036	0.001	0.000	0.000
Na	0.017	0.009	0.019	0.018	0.021	0.010	0.006	0.049	0.057	0.022	0.022	0.026
K	1.941	1.938	1.909	1.893	1.903	1.875	1.789	1.732	1.776	1.806	1.877	1.634
Sum	2.008	1.991	1.942	1.947	1.927	1.901	1.831	1.830	1.888	1.829	1.906	1.662
F	0.051	0.028	0.124	0.112	0.072	0.075	0.054	0.060	0.413	0.198	0.133	0.158
Cl	0.004	0.002	0.000	0.003	0.002	0.004	0.001	0.002	0.000	0.002	0.000	0.005
OH	3.946	3.971	3.876	3.886	3.927	3.922	3.945	3.939	3.588	3.801	3.868	3.837

Table A.2.3 - Phlogopite analyses

Sample	at052	at055	at055	at055	at055	at055	at055	at055	at056	at056	at056	at056
Unit	C1	C1	C1	C1	C1	C1	C1	C1	C2	C2	C2	C2
Rock type												
Remarks		rim, tr8,1	rim, tr8,2	core, tr8,3	core, tr8,4	rim, tr8,5	rim	core	rim			
SiO2	39.394	38.417	38.809	38.511	39.471	38.622	39.262	38.914	41.772	40.122	40.685	41.618
TiO2	0.113	0.139	0.147	0.119	0.181	0.170	0.199	0.164	0.079	0.665	0.225	0.188
Al2O3	0.155	0.273	0.137	0.240	b.d	0.089	0.078	0.436	9.289	6.068	7.784	5.838
Cr2O3	0.076	b.d	0.036	0.024	b.d	b.d	0.023	0.021	b.d	0.003	b.d	b.d
FeO	6.423	4.861	5.254	5.084	5.020	5.188	4.745	5.265	1.114	3.643	2.279	1.833
Fe2O3	16.609	16.957	16.827	16.334	16.146	16.565	16.154	16.063	4.317	7.414	6.159	8.123
MnO	0.095	0.149	0.219	0.156	0.190	0.204	0.104	0.211	0.028	0.080	0.079	0.080
MgO	22.491	23.020	22.683	22.459	22.595	22.380	22.556	22.447	27.452	23.496	25.894	25.990
BaO	0.044	n.a.	n.a.	n.a.	n.a.	n.a.	n.a.	n.a.	0.216	0.266	0.229	0.095
CaO	0.085	0.136	0.041	b.d	0.029	b.d	0.134	b.d	0.105	0.404	0.183	0.242
Na2O	0.030	0.218	0.122	0.182	0.139	0.256	0.237	0.299	0.027	0.099	0.046	0.028
K2O	9.291	9.515	9.869	9.933	9.897	9.853	9.994	9.934	10.695	9.804	10.194	10.166
F	0.286	n.a.	n.a.	n.a.	n.a.	n.a.	n.a.	n.a.	0.142	0.172	0.049	0.122
Cl	0.043	n.a.	n.a.	n.a.	n.a.	n.a.	n.a.	n.a.	0.013	0.014	0.008	b.d
H2O	3.750	3.860	3.870	3.830	3.870	3.840	3.860	3.860	4.120	3.880	4.060	4.040
Total	98.880	97.550	98.010	96.870	97.540	97.170	97.350	97.610	99.370	96.130	97.870	98.360
O=24												
(IV)Si	6.056	5.969	6.014	6.032	6.117	6.036	6.098	6.043	5.972	6.072	5.974	6.097
(IV)Al	0.028	0.050	0.025	0.044	0.000	0.016	0.014	0.080	1.564	1.081	1.346	1.007
(IV)Fe3+	1.919	1.981	1.960	1.923	1.881	1.946	1.886	1.875	0.464	0.843	0.680	0.895
Sum	8.003	8.000	7.999	7.999	7.998	7.998	7.998	7.998	8.000	7.996	8.000	7.999
(VI)Al	0.000	0.000	0.000	0.000	0.000	0.000	0.000	0.000	0.000	0.000	0.000	0.000
(VI)Ti	0.013	0.016	0.017	0.014	0.021	0.020	0.023	0.019	0.008	0.076	0.025	0.021
(VI)Fe2+	0.826	0.632	0.681	0.666	0.651	0.678	0.616	0.684	0.133	0.461	0.280	0.225
(VI)Cr	0.009	0.000	0.004	0.003	0.000	0.000	0.003	0.003	0.000	0.000	0.000	0.000
(VI)Mn	0.012	0.020	0.029	0.021	0.025	0.027	0.014	0.028	0.003	0.010	0.010	0.010
(VI)Mg	5.154	5.332	5.240	5.244	5.220	5.214	5.222	5.196	5.851	5.301	5.668	5.676
Sum	6.014	6.000	5.971	5.948	5.917	5.939	5.878	5.930	5.995	5.848	5.983	5.932
Ba	0.003	0.000	0.000	0.000	0.000	0.000	0.000	0.000	0.012	0.016	0.013	0.005
Ca	0.014	0.023	0.007	0.000	0.005	0.000	0.022	0.000	0.016	0.066	0.029	0.038
Na	0.009	0.066	0.037	0.055	0.042	0.078	0.071	0.090	0.007	0.029	0.013	0.008
K	1.822	1.886	1.951	1.985	1.957	1.965	1.980	1.968	1.951	1.893	1.910	1.900
Sum	1.848	1.975	1.995	2.040	2.004	2.043	2.073	2.058	1.986	2.004	1.965	1.951
F	0.139	0.000	0.000	0.000	0.000	0.000	0.000	0.000	0.064	0.083	0.023	0.057
Cl	0.011	0.000	0.000	0.000	0.000	0.000	0.000	0.000	0.003	0.004	0.002	0.000
OH	3.850	4.000	4.000	4.000	4.000	4.000	4.000	4.000	3.933	3.914	3.975	3.943

Table A.2.3 - Phlogopite analyses

Sample	at059	at059	at059	at059	at059	at059	at059	at060a	at060a	at060a	at060a	at060a
Unit	C1	C1	C1	C1	C1	C1	C1	C3	C3	C3	C3	C3
Rock type												
Remarks							rim	rim	core	rim	core	rim
SiO2	39.513	39.336	39.127	40.486	38.227	38.380	40.596	41.534	38.929	41.107	38.923	39.780
TiO2	0.687	0.723	3.029	0.670	0.331	0.130	0.608	0.530	2.812	1.853	2.700	1.682
Al2O3	8.479	10.909	10.928	5.613	4.053	3.166	7.780	7.308	11.943	10.675	12.096	10.660
Cr2O3	b.d	0.004	0.004	0.009	0.002	b.d	b.d	0.004	b.d	0.005	0.000	0.000
FeO	12.853	12.538	10.227	9.878	12.063	14.237	13.891	4.983	7.325	4.040	6.944	4.978
Fe2O3	3.885	1.182	2.470	7.325	9.901	11.345	4.988	6.344	1.622	2.464	1.599	2.720
MnO	0.367	0.428	0.534	0.486	0.415	0.269	0.195	0.186	0.104	0.117	0.133	0.133
MgO	18.199	18.829	18.557	19.631	17.765	17.024	18.499	24.584	20.965	23.956	21.301	23.190
BaO	b.d	0.095	b.d	0.013	b.d	0.303	0.197	0.084	0.068	b.d	0.128	0.171
CaO	0.089	0.076	0.044	0.125	0.335	0.198	0.072	0.116	0.028	0.154	0.053	0.067
Na2O	b.d	0.102	0.157	0.094	0.041	0.055	0.049	0.052	0.101	0.077	0.124	0.078
K2O	10.124	10.107	9.997	9.978	9.629	9.380	9.584	9.205	10.150	10.454	10.283	10.189
F	0.387	0.486	0.282	0.405	0.332	0.170	0.399	0.205	0.249	0.304	0.289	0.179
Cl	0.006	0.017	0.012	0.003	0.001	0.024	0.019	0.012	0.005	0.014	0.010	0.000
H2O	3.750	3.740	3.900	3.750	3.620	3.710	3.820	4.020	3.950	4.020	3.940	3.990
Total	98.340	98.570	99.270	98.470	96.720	98.390	100.700	99.170	98.250	99.240	98.520	97.820
O=24												
(IV)Si	6.029	5.929	5.809	6.155	6.061	6.064	6.069	6.051	5.743	5.920	5.725	5.851
(IV)Al	1.524	1.936	1.911	1.005	0.757	0.589	1.370	1.254	2.075	1.810	2.095	1.847
(IV)Fe3+	0.446	0.134	0.276	0.837	1.180	1.348	0.561	0.695	0.180	0.267	0.177	0.301
Sum	7.999	7.999	7.996	7.997	7.998	8.001	8.000	8.000	7.998	7.997	7.997	7.999
(VI)Al	0.000	0.000	0.000	0.000	0.000	0.000	0.000	0.000	0.000	0.000	0.000	0.000
(VI)Ti	0.079	0.082	0.338	0.077	0.039	0.015	0.068	0.058	0.312	0.201	0.299	0.186
(VI)Fe2+	1.640	1.580	1.270	1.256	1.599	1.881	1.737	0.607	0.904	0.487	0.854	0.612
(VI)Cr	0.000	0.000	0.000	0.001	0.000	0.000	0.000	0.000	0.000	0.001	0.000	0.000
(VI)Mn	0.047	0.055	0.067	0.063	0.056	0.036	0.025	0.023	0.013	0.014	0.017	0.017
(VI)Mg	4.140	4.231	4.107	4.449	4.199	4.010	4.123	5.339	4.611	5.143	4.671	5.085
Sum	5.906	5.948	5.782	5.846	5.893	5.942	5.953	6.027	5.840	5.846	5.841	5.900
Ba	0.000	0.006	0.000	0.001	0.000	0.019	0.012	0.005	0.004	0.000	0.007	0.010
Ca	0.015	0.012	0.007	0.020	0.057	0.034	0.012	0.018	0.004	0.024	0.008	0.011
Na	0.000	0.030	0.045	0.028	0.013	0.017	0.014	0.015	0.029	0.022	0.035	0.022
K	1.971	1.943	1.894	1.935	1.948	1.891	1.828	1.711	1.910	1.921	1.930	1.912
Sum	1.986	1.991	1.946	1.984	2.018	1.961	1.866	1.749	1.947	1.967	1.980	1.955
F	0.187	0.232	0.133	0.195	0.167	0.085	0.189	0.095	0.116	0.139	0.135	0.084
Cl	0.002	0.005	0.003	0.001	0.001	0.007	0.005	0.003	0.002	0.004	0.003	0.000
OH	3.812	3.764	3.865	3.805	3.833	3.909	3.807	3.903	3.883	3.858	3.863	3.917

Table A.2.3 - Phlogopite analyses

Sample	at060a	at060b	at060b	at060b	at060b	at060b	at060b	at060b	at060b	at103	at103	at103
Unit	C3	C3	C3	C3	C3	C3	C3	C3	C3	C5	C5	C5
Rock type												
Remarks	core					rim	core	rim	core		core	rim
SiO2	40.238	38.246	38.426	38.447	39.573	39.364	38.413	39.885	38.573	41.110	40.736	39.229
TiO2	1.700	1.897	2.003	2.030	1.843	2.477	2.857	2.413	2.722	0.206	0.154	0.080
Al2O3	10.890	5.781	4.984	6.474	6.000	10.572	11.783	10.372	11.111	b.d	b.d	b.d
Cr2O3	0.000	0.049	0.025	0.018	0.002	0.016	0.012	0.016	0.000	b.d	0.005	0.029
FeO	3.718	9.765	10.212	10.138	10.264	9.279	9.765	8.860	9.516	4.462	4.948	5.669
Fe2O3	2.787	8.091	9.548	6.757	7.829	2.804	1.609	2.197	2.225	15.576	15.603	16.226
MnO	0.123	0.176	0.178	0.159	0.171	0.141	0.149	0.161	0.145	0.102	0.146	0.094
MgO	24.358	18.437	18.285	18.191	18.899	19.749	19.108	19.799	19.300	23.353	22.972	22.364
BaO	0.060	0.144	0.034	0.222	b.d	0.026	0.174	0.000	0.208	b.d	0.032	b.d
CaO	0.068	0.314	0.243	0.176	0.259	0.182	0.064	0.146	0.075	0.094	b.d	b.d
Na2O	0.095	0.123	0.152	0.149	0.161	0.067	0.116	0.118	0.100	0.129	0.222	0.117
K2O	10.304	8.809	9.029	8.660	9.079	10.057	9.971	9.904	9.724	9.914	9.812	9.797
F	0.284	0.083	0.163	0.178	0.144	0.334	0.252	0.236	0.221	0.215	0.135	0.088
Cl	0.028	0.019	0.016	0.012	0.012	b.d	0.005	0.011	0.011	n.a.	n.a.	n.a.
H2O	3.990	3.790	3.780	3.750	3.870	3.890	3.890	3.920	3.890	3.860	3.870	3.810
Total	98.640	95.720	97.080	95.360	98.110	98.960	98.170	98.040	97.820	99.020	98.640	97.500
O=24												
(IV)Si	5.835	5.981	5.969	6.011	6.025	5.838	5.742	5.933	5.784	6.225	6.210	6.101
(IV)Al	1.860	1.065	0.912	1.192	1.076	1.846	2.074	1.817	1.962	0.000	0.000	0.000
(IV)Fe3+	0.304	0.951	1.115	0.794	0.896	0.313	0.181	0.246	0.251	1.773	1.788	1.897
Sum	7.999	7.997	7.996	7.997	7.997	7.997	7.997	7.996	7.997	7.998	7.998	7.998
(VI)Al	0.000	0.000	0.000	0.000	0.000	0.000	0.000	0.000	0.000	0.000	0.000	0.000
(VI)Ti	0.185	0.223	0.234	0.239	0.211	0.276	0.321	0.270	0.307	0.023	0.018	0.009
(VI)Fe2+	0.451	1.277	1.327	1.326	1.307	1.151	1.221	1.102	1.193	0.565	0.631	0.737
(VI)Cr	0.000	0.006	0.003	0.002	0.000	0.002	0.001	0.002	0.000	0.000	0.001	0.004
(VI)Mn	0.015	0.023	0.023	0.021	0.022	0.018	0.019	0.020	0.018	0.013	0.019	0.012
(VI)Mg	5.265	4.298	4.235	4.240	4.290	4.366	4.258	4.391	4.314	5.271	5.221	5.185
Sum	5.916	5.827	5.822	5.828	5.830	5.813	5.820	5.785	5.832	5.872	5.890	5.947
Ba	0.003	0.009	0.002	0.014	0.000	0.002	0.010	0.000	0.012	0.000	0.002	0.000
Ca	0.011	0.053	0.040	0.029	0.042	0.029	0.010	0.023	0.012	0.015	0.000	0.000
Na	0.027	0.037	0.046	0.045	0.048	0.019	0.034	0.034	0.029	0.038	0.066	0.035
K	1.906	1.757	1.789	1.727	1.763	1.903	1.901	1.880	1.860	1.915	1.908	1.944
Sum	1.947	1.856	1.877	1.815	1.853	1.953	1.955	1.937	1.913	1.968	1.976	1.979
F	0.130	0.041	0.080	0.088	0.070	0.157	0.119	0.111	0.105	0.103	0.065	0.044
Cl	0.007	0.005	0.004	0.003	0.003	0.000	0.002	0.003	0.003	0.000	0.000	0.000
OH	3.863	3.954	3.916	3.909	3.928	3.843	3.880	3.886	3.892	3.897	3.935	3.957

Table A.2.3 - Phlogopite analyses

Sample	at104	at104	at104	at104	at104	at104	at104	at104	at104	at104	at104	at113
Unit	gli	gli	gli	gli	gli	gli	gli	gli	gli	gli	gli	B1
Rock type												
Remarks	rim, tr9,1	rim, tr9,2	core, tr9,3	core, tr9,4	core, tr9,5	core, tr9,6	core, tr9,7	rim, tr9,8	rim, tr9,9	rim, tr9,10	rim, tr9,11	rim
SiO2	39.318	39.533	39.579	38.808	38.500	38.742	39.365	39.422	39.420	39.508	39.244	38.593
TiO2	0.334	0.186	1.148	1.204	1.384	1.477	1.048	0.213	0.252	0.180	0.281	2.157
Al2O3	1.961	1.743	11.390	11.614	11.624	10.814	11.441	1.423	2.124	2.395	2.209	11.601
Cr2O3	b.d	0.060	0.035	0.040	0.004	0.002	b.d	b.d	0.012	0.009	0.001	b.d
FeO	5.947	5.911	3.731	3.732	3.785	3.248	3.694	5.552	6.288	6.206	5.869	8.341
Fe2O3	14.141	14.580	2.602	2.409	2.544	3.945	2.378	14.859	13.947	13.353	13.695	2.753
MnO	0.127	0.059	0.086	0.062	0.116	0.088	0.120	0.158	0.128	0.144	0.154	0.129
MgO	22.560	22.816	24.819	24.591	24.318	24.695	24.808	22.630	22.352	22.499	22.519	20.991
BaO	n.a.	n.a.	n.a.	n.a.	n.a.	n.a.	n.a.	n.a.	n.a.	n.a.	n.a.	0.567
CaO	0.006	0.022	0.008	b.d	b.d	b.d	b.d	0.080	0.045	0.057	0.244	0.109
Na2O	0.104	0.189	0.340	0.186	0.340	0.442	0.345	0.393	0.357	0.242	0.229	0.599
K2O	9.934	9.966	10.320	10.280	10.070	10.034	10.180	9.960	9.922	9.854	9.467	9.548
F	n.a.	n.a.	n.a.	n.a.	n.a.	n.a.	n.a.	n.a.	n.a.	n.a.	n.a.	n.a.
Cl	n.a.	n.a.	n.a.	n.a.	n.a.	n.a.	n.a.	n.a.	n.a.	n.a.	n.a.	b.d
H2O	3.920	3.940	4.120	4.070	4.060	4.080	4.090	3.920	3.930	3.930	3.910	4.070
Total	98.350	99.010	98.180	97.000	96.750	97.570	97.470	98.610	98.780	98.380	97.820	99.460
O=24												
(IV)Si	6.018	6.018	5.762	5.718	5.693	5.693	5.765	6.032	6.016	6.034	6.020	5.682
(IV)Al	0.354	0.312	1.953	2.015	2.024	1.871	1.973	0.256	0.382	0.431	0.399	2.011
(IV)Fe3+	1.627	1.668	0.285	0.267	0.283	0.436	0.262	1.709	1.600	1.533	1.579	0.305
Sum	7.999	7.998	8.000	8.000	8.000	8.000	8.000	7.997	7.998	7.998	7.998	7.998
(VI)Al	0.000	0.000	0.000	0.000	0.000	0.000	0.000	0.000	0.000	0.000	0.000	0.000
(VI)Ti	0.038	0.021	0.126	0.133	0.154	0.163	0.115	0.025	0.029	0.021	0.032	0.239
(VI)Fe2+	0.761	0.752	0.454	0.460	0.468	0.399	0.452	0.710	0.803	0.793	0.753	1.027
(VI)Cr	0.000	0.007	0.004	0.005	0.000	0.000	0.000	0.000	0.001	0.001	0.000	0.000
(VI)Mn	0.016	0.008	0.011	0.008	0.015	0.011	0.015	0.020	0.017	0.019	0.020	0.016
(VI)Mg	5.148	5.178	5.386	5.402	5.361	5.410	5.416	5.162	5.086	5.123	5.150	4.607
Sum	5.963	5.966	5.981	6.008	5.998	5.983	5.998	5.917	5.936	5.957	5.955	5.889
Ba	0.000	0.000	0.000	0.000	0.000	0.000	0.000	0.000	0.000	0.000	0.000	0.033
Ca	0.001	0.004	0.001	0.000	0.000	0.000	0.000	0.013	0.007	0.009	0.040	0.017
Na	0.031	0.056	0.096	0.053	0.097	0.126	0.098	0.117	0.106	0.072	0.068	0.171
K	1.940	1.935	1.917	1.932	1.900	1.881	1.902	1.944	1.932	1.920	1.853	1.793
Sum	1.972	1.995	2.014	1.985	1.997	2.007	2.000	2.074	2.045	2.001	1.961	2.014
F	0.000	0.000	0.000	0.000	0.000	0.000	0.000	0.000	0.000	0.000	0.000	0.000
Cl	0.000	0.000	0.000	0.000	0.000	0.000	0.000	0.000	0.000	0.000	0.000	0.000
OH	4.000	4.000	4.000	4.000	4.000	4.000	4.000	4.000	4.000	4.000	4.000	4.000

Table A.2.3 - Phlogopite analyses

Sample	at113	at113	at113	at113	at113	at113	at120	at120	at120	at120	at120	at120
Unit	B1	B1	B1	B1	B1	B1	php	php	php	php	php	php
Rock type												
Remarks		rim	core	core			rim, tr12,1	rim, tr12,2	core, tr12,3	core, tr12,4	core, tr12,5	core, tr12,6
SiO2	38.863	36.678	37.308	39.592	37.101	41.079	40.517	39.402	39.339	38.743	38.184	38.305
TiO2	2.391	3.515	3.457	0.009	2.940	0.463	0.418	0.764	2.224	2.649	2.804	2.577
Al2O3	12.182	12.721	12.833	10.815	12.321	9.585	5.991	7.201	10.298	11.323	12.051	11.095
Cr2O3	0.068	0.016	b.d	0.002	b.d	b.d	b.d	0.068	0.014	0.006	b.d	0.014
FeO	7.654	9.969	9.695	9.511	10.263	6.342	7.610	9.347	5.864	5.479	5.253	4.298
Fe2O3	2.328	2.555	2.229	1.719	2.341	4.091	9.180	7.688	4.502	3.836	3.205	3.927
MnO	0.152	0.174	0.238	0.244	0.235	0.186	0.397	0.358	0.134	0.127	0.125	0.123
MgO	21.412	18.586	19.122	21.559	18.848	23.904	22.614	20.802	22.476	22.693	22.623	23.192
BaO	0.457	0.706	0.589	0.255	0.562	0.122	0.164	0.266	0.407	0.646	0.812	0.816
CaO	0.092	0.079	0.077	0.062	0.026	0.138	0.120	0.315	0.096	0.046	0.114	0.050
Na2O	0.633	0.859	0.668	0.562	0.627	0.607	0.221	0.337	0.383	0.293	0.361	0.297
K2O	9.821	9.394	9.442	9.675	9.436	9.702	9.992	9.806	10.027	9.787	9.670	9.276
F	n.a.	n.a.	n.a.	n.a.	n.a.	n.a.	n.a.	n.a.	n.a.	n.a.	n.a.	n.a.
Cl	0.011	0.010	0.022	b.d	0.009	0.023	0.021	b.d	b.d	b.d	b.d	b.d
H2O	4.120	4.020	4.050	4.020	4.000	4.150	4.080	4.020	4.110	4.120	4.110	4.070
Total	100.180	99.280	99.730	98.020	98.710	100.390	101.330	100.370	99.870	99.750	99.310	98.040
O=24												
(IV)Si	5.655	5.474	5.515	5.907	5.560	5.927	5.950	5.873	5.736	5.638	5.574	5.640
(IV)Al	2.088	2.236	2.234	1.900	2.174	1.629	1.036	1.264	1.768	1.940	2.072	1.924
(IV)Fe3+	0.255	0.287	0.248	0.193	0.264	0.444	1.013	0.861	0.493	0.420	0.352	0.435
Sum	7.998	7.997	7.997	8.000	7.998	8.000	7.999	7.998	7.997	7.998	7.998	7.999
(VI)Al	0.000	0.000	0.000	0.000	0.000	0.000	0.000	0.000	0.000	0.000	0.000	0.000
(VI)Ti	0.262	0.395	0.384	0.001	0.331	0.050	0.046	0.086	0.244	0.290	0.308	0.285
(VI)Fe2+	0.931	1.244	1.199	1.187	1.286	0.765	0.935	1.165	0.715	0.667	0.641	0.529
(VI)Cr	0.008	0.002	0.000	0.000	0.000	0.000	0.000	0.008	0.002	0.001	0.000	0.002
(VI)Mn	0.019	0.022	0.030	0.031	0.030	0.023	0.049	0.045	0.017	0.016	0.015	0.015
(VI)Mg	4.645	4.135	4.214	4.795	4.211	5.141	4.951	4.622	4.885	4.923	4.924	5.091
Sum	5.865	5.798	5.827	6.014	5.858	5.979	5.981	5.926	5.863	5.897	5.888	5.922
Ba	0.026	0.041	0.034	0.015	0.033	0.007	0.009	0.016	0.023	0.037	0.046	0.047
Ca	0.014	0.013	0.012	0.010	0.004	0.021	0.019	0.050	0.015	0.007	0.018	0.008
Na	0.179	0.249	0.191	0.163	0.182	0.170	0.063	0.097	0.108	0.083	0.102	0.085
K	1.823	1.788	1.781	1.842	1.804	1.786	1.872	1.865	1.865	1.817	1.801	1.743
Sum	2.042	2.091	2.018	2.030	2.023	1.984	1.963	2.028	2.011	1.944	1.967	1.883
F	0.000	0.000	0.000	0.000	0.000	0.000	0.000	0.000	0.000	0.000	0.000	0.000
Cl	0.003	0.003	0.006	0.000	0.003	0.006	0.005	0.000	0.000	0.000	0.000	0.000
OH	3.997	3.997	3.994	4.000	3.998	3.994	3.995	4.000	4.000	4.000	4.000	4.000

Table A.2.3 - Phlogopite analyses

Sample	at120	at120	at120	at120	at120	at120	at120	at120	at122	at122	at122	at122
Unit	php	php	php	php	php	php	php	php	syenite	syenite	syenite	syenite
Rock type												
Remarks	core, tr12,7	core, tr12,8	core, tr12,9	ore, tr12,10	ore, tr12,11	ore, tr12,12	rim, tr12,13	rim, tr12,14	rim, tr14,1	rim, tr14,2	core, tr14,3	core, tr14,4
SiO2	38.213	38.339	38.014	36.996	36.054	38.304	37.748	38.447	37.520	37.467	37.042	37.295
TiO2	2.567	2.585	2.620	2.234	2.024	1.846	0.870	0.056	2.637	2.562	2.446	2.473
Al2O3	11.702	11.434	11.403	9.531	9.329	8.667	7.258	1.227	11.038	11.154	10.869	10.761
Cr2O3	b.d	0.083	0.038	0.020	b.d	b.d	0.014	b.d	0.029	0.026	0.005	b.d
FeO	5.408	5.627	5.511	3.245	2.847	6.049	10.997	6.596	16.309	16.060	16.344	16.161
Fe2O3	3.077	3.378	3.923	6.584	7.465	6.243	7.519	15.337	2.041	1.796	2.199	2.517
MnO	0.108	0.062	0.108	0.068	0.094	0.152	0.505	0.621	0.525	0.443	0.486	0.440
MgO	22.288	22.105	22.351	22.657	21.271	21.788	18.950	21.603	14.546	14.731	14.464	14.635
BaO	0.594	0.652	0.718	0.630	0.418	0.302	0.348	0.200	n.a.	n.a.	n.a.	n.a.
CaO	0.100	0.055	0.128	1.713	3.884	0.129	0.172	0.206	b.d	0.002	0.013	0.054
Na2O	0.444	0.394	0.368	0.271	0.546	0.373	0.342	0.251	0.292	0.266	0.246	0.395
K2O	9.917	10.011	9.741	8.996	9.176	9.914	9.729	9.704	9.871	9.922	9.870	9.966
F	n.a.	n.a.	n.a.	n.a.	n.a.	n.a.	n.a.	n.a.	n.a.	n.a.	n.a.	n.a.
Cl	b.d	b.d	b.d	0.023	0.036	b.d	0.006	0.006	n.a.	n.a.	n.a.	n.a.
H2O	4.070	4.070	4.080	3.980	3.940	3.990	3.890	3.850	3.900	3.900	3.860	3.890
Total	98.490	98.800	99.000	96.950	97.080	97.760	98.350	98.100	98.710	98.330	97.840	98.590
O=24												
(IV)Si	5.627	5.642	5.590	5.564	5.472	5.757	5.812	5.980	5.764	5.767	5.753	5.750
(IV)Al	2.029	1.982	1.975	1.688	1.667	1.534	1.316	0.225	1.997	2.022	1.988	1.954
(IV)Fe3+	0.341	0.374	0.434	0.744	0.852	0.705	0.870	1.793	0.236	0.208	0.257	0.292
Sum	7.997	7.998	7.999	7.996	7.991	7.996	7.998	7.998	7.997	7.997	7.998	7.996
(VI)Al	0.000	0.000	0.000	0.000	0.000	0.000	0.000	0.000	0.000	0.000	0.000	0.000
(VI)Ti	0.284	0.286	0.290	0.253	0.231	0.209	0.101	0.007	0.305	0.297	0.286	0.287
(VI)Fe2+	0.666	0.693	0.678	0.408	0.361	0.760	1.416	0.858	2.095	2.067	2.123	2.084
(VI)Cr	0.000	0.010	0.004	0.002	0.000	0.000	0.002	0.000	0.004	0.003	0.001	0.000
(VI)Mn	0.013	0.008	0.013	0.009	0.012	0.019	0.066	0.082	0.068	0.058	0.064	0.057
(VI)Mg	4.893	4.850	4.900	5.079	4.813	4.882	4.350	5.009	3.331	3.380	3.349	3.364
Sum	5.856	5.847	5.885	5.751	5.417	5.870	5.935	5.956	5.803	5.805	5.823	5.792
Ba	0.034	0.038	0.041	0.037	0.025	0.018	0.021	0.012	0.000	0.000	0.000	0.000
Ca	0.016	0.009	0.020	0.276	0.632	0.021	0.028	0.034	0.000	0.000	0.002	0.009
Na	0.127	0.112	0.105	0.079	0.161	0.109	0.102	0.076	0.087	0.079	0.074	0.118
K	1.863	1.880	1.827	1.726	1.777	1.901	1.911	1.926	1.935	1.948	1.955	1.960
Sum	2.040	2.039	1.993	2.118	2.595	2.049	2.062	2.048	2.022	2.027	2.031	2.087
F	0.000	0.000	0.000	0.000	0.000	0.000	0.000	0.000	0.000	0.000	0.000	0.000
Cl	0.000	0.000	0.000	0.006	0.010	0.000	0.002	0.002	0.000	0.000	0.000	0.000
OH	4.000	4.000	4.000	3.994	3.991	4.000	3.998	3.998	4.000	4.000	4.000	4.000

Table A.2.3 - Phlogopite analyses

Sample	at122	at122	at122	at131	at131	at131	at131	at131	at131	at134	at134	at134
Unit	syenite	syenite	syenite	C4	C4	C4	C4	C4	C4	C1	C1	C1
Rock type												
Remarks	core, tr14,5	rim, tr14,6	rim, tr14,7	rim	core	rim	core					
SiO2	37.515	37.063	37.126	40.650	41.070	40.860	40.570	39.770	39.460	39.761	41.142	41.676
TiO2	2.874	2.857	2.486	0.160	0.160	0.140	0.180	0.070	0.330	0.162	0.284	0.200
Al2O3	10.802	11.014	10.903	9.300	9.480	9.960	9.640	b.d	0.530	0.001	0.069	0.080
Cr2O3	b.d	0.035	0.070	b.d	b.d	0.020	0.060	0.030	b.d	0.050	0.014	b.d
FeO	15.741	16.333	16.383	1.910	2.027	2.255	2.163	1.159	3.133	7.047	6.089	6.496
Fe2O3	2.492	2.287	2.266	4.012	3.626	3.095	3.720	17.005	15.766	16.229	14.914	14.598
MnO	0.493	0.480	0.523	0.040	0.030	0.050	0.050	0.050	0.060	0.088	0.113	0.049
MgO	14.646	14.180	14.437	26.150	26.240	26.170	26.110	25.780	23.570	21.603	21.853	21.868
BaO	n.a.	n.a.	n.a.	0.150	0.140	0.190	0.100	b.d	0.050	0.031	0.056	0.016
CaO	0.004	0.043	0.004	b.d	b.d	b.d	0.040	0.110	0.770	0.079	0.123	0.152
Na2O	0.259	0.267	0.264	0.300	0.180	0.260	0.260	0.320	0.300	0.289	0.387	0.375
K2O	10.081	9.963	9.891	10.550	10.750	10.520	10.420	9.050	9.040	9.727	9.767	9.757
F	n.a.	n.a.	n.a.	0.430	0.370	0.440	0.380	b.d	0.070	0.303	0.386	0.313
Cl	n.a.	n.a.	n.a.	0.010	b.d	b.d	b.d	0.010	0.030	n.a.	n.a.	n.a.
H2O	3.910	3.880	3.870	3.890	3.940	3.910	3.920	3.940	3.850	3.750	3.750	3.810
Total	98.820	98.400	98.220	97.550	98.010	97.870	97.610	97.290	96.960	99.120	98.950	99.390
O=24												
(IV)Si	5.757	5.727	5.746	5.954	5.977	5.952	5.931	6.054	6.077	6.121	6.276	6.319
(IV)Al	1.952	2.004	1.987	1.604	1.625	1.709	1.660	0.000	0.096	0.000	0.012	0.014
(IV)Fe3+	0.287	0.266	0.264	0.442	0.397	0.339	0.409	1.946	1.825	1.878	1.710	1.664
Sum	7.996	7.997	7.997	8.000	7.999	8.000	8.000	8.000	7.998	7.999	7.998	7.997
(VI)Al	0.000	0.000	0.000	0.000	0.000	0.000	0.000	0.000	0.000	0.000	0.000	0.000
(VI)Ti	0.332	0.332	0.289	0.018	0.018	0.015	0.020	0.008	0.038	0.019	0.033	0.023
(VI)Fe2+	2.020	2.110	2.120	0.234	0.247	0.275	0.264	0.148	0.403	0.907	0.777	0.824
(VI)Cr	0.000	0.004	0.009	0.000	0.000	0.002	0.007	0.004	0.000	0.006	0.002	0.000
(VI)Mn	0.064	0.063	0.069	0.005	0.004	0.006	0.006	0.006	0.008	0.011	0.015	0.006
(VI)Mg	3.350	3.266	3.331	5.710	5.693	5.683	5.691	5.850	5.411	4.958	4.970	4.943
Sum	5.766	5.775	5.818	5.967	5.962	5.981	5.988	6.016	5.860	5.901	5.797	5.796
Ba	0.000	0.000	0.000	0.009	0.008	0.011	0.006	0.000	0.003	0.002	0.003	0.001
Ca	0.001	0.007	0.001	0.000	0.000	0.000	0.006	0.018	0.127	0.013	0.020	0.025
Na	0.077	0.080	0.079	0.085	0.051	0.073	0.074	0.094	0.090	0.086	0.114	0.110
K	1.973	1.964	1.953	1.971	1.996	1.955	1.943	1.758	1.776	1.910	1.901	1.887
Sum	2.051	2.051	2.033	2.065	2.055	2.039	2.029	1.870	1.996	2.011	2.038	2.023
F	0.000	0.000	0.000	0.199	0.171	0.203	0.176	0.000	0.034	0.148	0.186	0.150
Cl	0.000	0.000	0.000	0.003	0.000	0.000	0.000	0.003	0.008	0.000	0.000	0.000
OH	4.000	4.000	4.000	3.798	3.830	3.797	3.824	3.997	3.958	3.852	3.814	3.850

Table A.2.3 - Phlogopite analyses

Sample	at134	at134	at134	at134	at136	at136	at136	at136	at136	at136	at136	at136
Unit	C1	C1	C1	C1	C1	C1	C1	C1	C1	C1	C1	C1
Rock type												
Remarks			core	rim	tr15,01	tr15,01	tr15,02	tr15,03	tr15,04	tr15,05	tr15,06	tr15,07
SiO2	40.431	40.399	38.926	39.676	40.028	39.839	40.119	38.955	39.151	41.233	40.152	39.052
TiO2	0.197	0.167	0.108	0.136	0.150	0.168	0.148	0.227	0.157	0.237	0.188	0.234
Al2O3	0.107	0.036	0.042	b.d	b.d	0.015	0.185	0.096	b.d	0.120	0.094	b.d
Cr2O3	b.d	0.039	b.d	0.034	b.d	b.d	b.d	0.047	0.003	b.d	0.042	0.007
FeO	6.788	6.836	7.948	7.303	6.239	6.366	6.348	10.038	8.506	7.243	7.773	9.182
Fe2O3	15.456	15.779	16.875	16.061	16.102	15.755	15.507	15.418	16.137	13.991	15.958	15.795
MnO	0.126	0.113	0.120	0.122	0.114	0.173	0.167	0.164	0.168	0.119	0.094	0.150
MgO	21.630	21.777	21.193	21.302	22.078	21.802	21.893	19.220	20.532	20.948	21.378	19.855
BaO	0.056	b.d	0.058	b.d	b.d	b.d	b.d	b.d	b.d	b.d	b.d	b.d
CaO	b.d	0.048	0.017	0.155	0.137	0.142	0.032	0.193	0.095	0.110	0.174	0.082
Na2O	0.464	0.293	0.256	0.178	0.359	0.255	0.411	0.259	0.234	0.375	0.303	0.253
K2O	9.754	9.861	9.875	9.917	9.773	9.571	9.754	9.100	9.562	9.500	9.364	9.433
F	0.275	0.225	0.030	0.223	0.448	0.384	0.446	0.328	0.344	0.440	0.382	0.290
Cl	n.a.	n.a.	n.a.	n.a.	n.a.	n.a.	n.a.	n.a.	n.a.	n.a.	n.a.	n.a.
H2O	3.780	3.820	3.860	3.770	3.700	3.690	3.690	3.640	3.680	3.680	3.740	3.680
Total	99.060	99.390	99.310	98.880	99.130	98.160	98.700	97.680	98.570	98.000	99.640	98.010
O=24												
(IV)Si	6.198	6.178	6.028	6.132	6.140	6.163	6.171	6.151	6.107	6.354	6.146	6.135
(IV)Al	0.019	0.006	0.008	0.000	0.000	0.003	0.034	0.018	0.000	0.022	0.017	0.000
(IV)Fe3+	1.781	1.814	1.964	1.866	1.857	1.832	1.793	1.830	1.892	1.621	1.836	1.865
Sum	7.998	7.998	8.000	7.998	7.997	7.998	7.998	7.999	7.999	7.997	7.999	8.000
(VI)Al	0.000	0.000	0.000	0.000	0.000	0.000	0.000	0.000	0.000	0.000	0.000	0.000
(VI)Ti	0.023	0.019	0.013	0.016	0.017	0.020	0.017	0.027	0.018	0.027	0.022	0.028
(VI)Fe2+	0.870	0.874	1.029	0.944	0.800	0.824	0.817	1.326	1.110	0.933	0.995	1.206
(VI)Cr	0.000	0.005	0.000	0.004	0.000	0.000	0.000	0.006	0.000	0.000	0.005	0.001
(VI)Mn	0.016	0.015	0.016	0.016	0.015	0.023	0.022	0.022	0.022	0.016	0.012	0.020
(VI)Mg	4.943	4.964	4.893	4.908	5.049	5.028	5.020	4.524	4.774	4.813	4.879	4.650
Sum	5.852	5.877	5.951	5.888	5.881	5.895	5.876	5.905	5.924	5.789	5.913	5.905
Ba	0.003	0.000	0.004	0.000	0.000	0.000	0.000	0.000	0.000	0.000	0.000	0.000
Ca	0.000	0.008	0.003	0.026	0.023	0.024	0.005	0.033	0.016	0.018	0.029	0.014
Na	0.138	0.087	0.077	0.053	0.107	0.076	0.123	0.079	0.071	0.112	0.090	0.077
K	1.908	1.924	1.951	1.955	1.913	1.889	1.914	1.833	1.903	1.868	1.829	1.890
Sum	2.049	2.019	2.035	2.034	2.043	1.989	2.042	1.945	1.990	1.998	1.948	1.981
F	0.134	0.109	0.015	0.109	0.218	0.188	0.217	0.164	0.170	0.215	0.185	0.144
Cl	0.000	0.000	0.000	0.000	0.000	0.000	0.000	0.000	0.000	0.000	0.000	0.000
OH	3.867	3.891	3.985	3.891	3.783	3.812	3.783	3.836	3.830	3.786	3.815	3.856

Table A.2.3 - Phlogopite analyses

Sample	at136	at136	at136	at201	at201	at201	at201	at201	at201	at201	at201	at201
Unit	C1	C1	C1	lcr	lcr	lcr	lcr	lcr	lcr	lcr	lcr	lcr
Rock type												
Remarks	tr15,08	tr15,09	tr15,10	tr16,1	tr16,2	tr16,3	tr16,4	tr16,5	core	rim	core	core
SiO2	38.681	40.462	39.818	38.582	37.433	37.726	38.402	39.228	39.205	37.599	39.013	38.864
TiO2	0.204	0.163	0.145	3.730	4.798	4.850	4.854	3.083	3.915	5.040	3.536	3.955
Al2O3	0.111	b.d	0.172	10.329	12.845	12.638	12.577	10.571	9.262	4.639	9.988	8.981
Cr2O3	0.029	0.012	0.042	b.d	0.599	0.237	0.210	b.d	0.030	b.d	b.d	b.d
FeO	9.750	6.695	7.115	6.080	6.110	6.611	7.225	7.085	5.095	18.103	6.528	4.600
Fe2O3	15.612	15.341	15.895	5.137	2.788	2.809	2.900	4.648	6.399	9.503	4.973	6.950
MnO	0.256	0.097	0.071	0.190	0.042	0.002	0.018	0.199	0.203	1.018	0.216	0.192
MgO	19.597	21.638	21.550	20.988	19.861	19.947	19.836	21.119	21.079	8.784	20.526	21.226
BaO	b.d	0.025	0.000	0.745	0.298	0.268	0.261	0.724	1.017	0.376	0.895	0.869
CaO	0.236	0.149	0.129	0.091	0.124	0.093	0.014	0.094	0.163	0.371	0.205	0.206
Na2O	0.062	0.335	0.329	0.419	0.441	0.424	0.516	0.612	0.572	0.986	0.466	0.670
K2O	8.711	9.521	9.689	9.521	9.743	9.575	9.763	9.689	9.638	9.335	9.560	9.624
F	0.217	0.393	0.404	0.521	0.340	0.270	0.341	0.487	0.645	0.278	0.478	0.556
Cl	n.a.	n.a.	n.a.	n.a.	n.a.	n.a.	n.a.	n.a.	n.a.	n.a.	n.a.	n.a.
H2O	3.690	3.710	3.700	3.850	3.940	3.980	3.990	3.910	3.810	3.640	3.860	3.840
Total	97.160	98.540	99.060	100.180	99.360	99.430	100.910	101.450	101.030	99.670	100.240	100.530
O=24												
(IV)Si	6.123	6.225	6.129	5.650	5.479	5.513	5.546	5.686	5.709	5.983	5.723	5.685
(IV)Al	0.021	0.000	0.031	1.781	2.214	2.175	2.139	1.805	1.588	0.869	1.725	1.547
(IV)Fe3+	1.858	1.774	1.839	0.565	0.307	0.309	0.315	0.507	0.701	1.137	0.548	0.764
Sum	8.002	7.999	7.999	7.996	8.000	7.997	8.000	7.998	7.998	7.989	7.996	7.996
(VI)Al	0.000	0.000	0.000	0.000	0.000	0.000	0.000	0.000	0.000	0.000	0.000	0.000
(VI)Ti	0.024	0.019	0.017	0.411	0.528	0.533	0.527	0.336	0.429	0.603	0.390	0.435
(VI)Fe2+	1.291	0.861	0.916	0.745	0.748	0.808	0.873	0.859	0.621	2.409	0.801	0.563
(VI)Cr	0.004	0.001	0.005	0.000	0.069	0.027	0.024	0.000	0.003	0.000	0.000	0.000
(VI)Mn	0.034	0.013	0.009	0.024	0.005	0.000	0.002	0.024	0.025	0.137	0.027	0.024
(VI)Mg	4.625	4.962	4.945	4.582	4.334	4.346	4.270	4.564	4.576	2.084	4.488	4.628
Sum	5.978	5.856	5.892	5.762	5.684	5.714	5.696	5.783	5.654	5.233	5.706	5.650
Ba	0.000	0.002	0.000	0.043	0.017	0.015	0.015	0.041	0.058	0.023	0.051	0.050
Ca	0.040	0.025	0.021	0.014	0.019	0.015	0.002	0.015	0.025	0.063	0.032	0.032
Na	0.019	0.100	0.098	0.119	0.125	0.120	0.144	0.172	0.162	0.304	0.133	0.190
K	1.759	1.869	1.903	1.779	1.819	1.785	1.799	1.792	1.791	1.895	1.789	1.796
Sum	1.818	1.996	2.022	1.955	1.980	1.935	1.960	2.020	2.036	2.285	2.005	2.068
F	0.109	0.191	0.197	0.242	0.158	0.125	0.156	0.223	0.297	0.140	0.222	0.257
Cl	0.000	0.000	0.000	0.000	0.000	0.000	0.000	0.000	0.000	0.000	0.000	0.000
OH	3.891	3.809	3.803	3.759	3.843	3.875	3.844	3.777	3.703	3.860	3.778	3.743

Table A.2.3 - Phlogopite analyses

Sample	at202	at202	at202	at202	at202	at202	at204	at204	at204	at204	at204	at204
Unit	lcr	lcr	lcr	lcr	lcr	lcr	php	php	php	php	php	php
Rock type												
Remarks							rim	core			rim	core
SiO2	37.365	38.193	37.811	36.930	38.558	37.503	35.899	37.858	38.020	38.160	37.120	37.870
TiO2	2.288	2.131	2.137	2.268	2.063	2.187	2.302	2.484	2.610	2.730	3.000	2.940
Al2O3	11.733	11.362	11.281	11.525	11.280	11.396	8.677	10.834	11.260	11.040	12.030	11.530
Cr2O3	0.008	0.026	0.011	0.061	0.003	0.002	b.d	0.030	0.060	0.060	b.d	0.050
FeO	16.020	15.221	15.042	15.431	15.073	15.314	18.960	8.252	6.468	5.854	6.079	5.931
Fe2O3	1.726	1.677	1.804	1.969	2.030	1.789	6.027	3.346	3.203	3.363	2.980	2.822
MnO	0.428	0.386	0.350	0.475	0.442	0.440	0.537	0.173	0.060	0.110	0.120	0.110
MgO	15.508	16.172	16.054	15.336	16.517	15.741	12.786	19.894	21.290	21.480	21.270	21.190
BaO	0.422	0.230	0.291	0.367	0.103	0.476	0.145	0.450	0.520	0.740	0.840	0.850
CaO	0.043	b.d	0.079	0.217	b.d	0.196	0.305	0.348	b.d	b.d	0.060	0.020
Na2O	0.138	0.198	0.268	0.189	0.330	0.119	0.178	0.284	0.320	0.130	0.210	0.250
K2O	9.815	9.780	9.682	9.907	9.983	9.631	9.402	9.762	10.070	10.110	9.990	9.960
F	0.180	0.278	0.500	0.234	0.361	0.310	n.a.	n.a.	0.440	0.330	0.410	0.530
Cl	n.a.	n.a.	n.a.	n.a.	n.a.	n.a.	b.d	0.001	0.010	b.d	0.010	b.d
H2O	3.850	3.830	3.700	3.790	3.830	3.770	3.800	3.980	3.810	3.870	3.820	3.770
Total	99.520	99.480	99.010	98.700	100.570	98.870	99.020	97.700	98.140	97.980	97.940	97.820
O=24												
(IV)Si	5.694	5.783	5.766	5.682	5.779	5.739	5.668	5.698	5.663	5.684	5.546	5.653
(IV)Al	2.106	2.026	2.026	2.088	1.991	2.054	1.613	1.920	1.975	1.937	2.117	2.027
(IV)Fe3+	0.198	0.191	0.207	0.228	0.229	0.206	0.715	0.379	0.359	0.377	0.335	0.317
Sum	7.998	8.000	7.999	7.998	7.999	7.999	7.996	7.997	7.997	7.998	7.998	7.997
(VI)Al	0.000	0.000	0.000	0.000	0.000	0.000	0.000	0.000	0.000	0.000	0.000	0.000
(VI)Ti	0.262	0.243	0.245	0.262	0.233	0.252	0.273	0.281	0.292	0.306	0.337	0.330
(VI)Fe2+	2.042	1.927	1.918	1.985	1.889	1.960	2.504	1.039	0.806	0.729	0.760	0.740
(VI)Cr	0.001	0.003	0.001	0.007	0.000	0.000	0.000	0.004	0.007	0.007	0.000	0.006
(VI)Mn	0.055	0.050	0.045	0.062	0.056	0.057	0.072	0.022	0.008	0.014	0.015	0.014
(VI)Mg	3.523	3.651	3.649	3.517	3.690	3.591	3.010	4.463	4.727	4.770	4.737	4.715
Sum	5.883	5.874	5.858	5.833	5.868	5.860	5.859	5.809	5.840	5.826	5.849	5.805
Ba	0.025	0.014	0.017	0.022	0.006	0.029	0.009	0.027	0.030	0.043	0.049	0.050
Ca	0.007	0.000	0.013	0.036	0.000	0.032	0.052	0.056	0.000	0.000	0.010	0.003
Na	0.041	0.058	0.079	0.056	0.096	0.035	0.054	0.083	0.092	0.038	0.061	0.072
K	1.908	1.889	1.883	1.945	1.909	1.880	1.894	1.874	1.914	1.921	1.904	1.897
Sum	1.981	1.961	1.992	2.059	2.011	1.976	2.009	2.040	2.036	2.002	2.024	2.022
F	0.087	0.133	0.241	0.114	0.171	0.150	0.000	0.000	0.208	0.156	0.194	0.250
Cl	0.000	0.000	0.000	0.000	0.000	0.000	0.000	0.001	0.003	0.000	0.003	0.000
OH	3.913	3.867	3.759	3.886	3.829	3.850	4.000	4.000	3.790	3.845	3.804	3.750

Table A..2.3 - Phlogopite analyses

Sample	at201	at201	at201	at201	at201	at201	at201	at201	at201	at202	at202	at202
Rock type	lcr	lcr	lcr	lcr	lcr	lcr	lcr	lcr	lcr	lcr	lcr	lcr
Remarks	tr16,1	tr16,2	tr16,3	tr16,4	tr16,5	core	rim	core	core			
SiO2	38.582	37.433	37.726	38.402	39.228	39.205	37.599	39.013	38.864	37.365	38.193	37.811
TiO2	3.730	4.798	4.850	4.854	3.083	3.915	5.040	3.536	3.955	2.288	2.131	2.137
Al2O3	10.329	12.845	12.638	12.577	10.571	9.262	4.639	9.988	8.981	11.733	11.362	11.281
Cr2O3	b.d	0.599	0.237	0.210	b.d	0.030	b.d	b.d	b.d	0.008	0.026	0.011
FeO	6.080	6.110	6.611	7.225	7.085	5.095	18.103	6.528	4.600	16.020	15.221	15.042
Fe2O3	5.137	2.788	2.809	2.900	4.648	6.399	9.503	4.973	6.950	1.726	1.677	1.804
MnO	0.190	0.042	0.002	0.018	0.199	0.203	1.018	0.216	0.192	0.428	0.386	0.350
MgO	20.988	19.861	19.947	19.836	21.119	21.079	8.784	20.526	21.226	15.508	16.172	16.054
BaO	0.745	0.298	0.268	0.261	0.724	1.017	0.376	0.895	0.869	0.422	0.230	0.291
CaO	0.091	0.124	0.093	0.014	0.094	0.163	0.371	0.205	0.206	0.043	b.d	0.079
Na2O	0.419	0.441	0.424	0.516	0.612	0.572	0.986	0.466	0.670	0.138	0.198	0.268
K2O	9.521	9.743	9.575	9.763	9.689	9.638	9.335	9.560	9.624	9.815	9.780	9.682
F	0.521	0.340	0.270	0.341	0.487	0.645	0.278	0.478	0.556	0.180	0.278	0.500
Cl	n.a.	n.a.	n.a.	n.a.	n.a.	n.a.	n.a.	n.a.	n.a.	n.a.	n.a.	n.a.
H2O	3.850	3.940	3.980	3.990	3.910	3.810	3.640	3.860	3.840	3.850	3.830	3.700
Total	100.180	99.360	99.430	100.910	101.450	101.030	99.670	100.240	100.530	99.520	99.480	99.010
O=24												
(IV)Si	5.650	5.479	5.513	5.546	5.686	5.709	5.983	5.723	5.685	5.694	5.783	5.766
(IV)Al	1.781	2.214	2.175	2.139	1.805	1.588	0.869	1.725	1.547	2.106	2.026	2.026
(IV)Fe3+	0.565	0.307	0.309	0.315	0.507	0.701	1.137	0.548	0.764	0.198	0.191	0.207
Sum	7.996	8.000	7.997	8.000	7.998	7.998	7.989	7.996	7.996	7.998	8.000	7.999
(VI)Al	0.000	0.000	0.000	0.000	0.000	0.000	0.000	0.000	0.000	0.000	0.000	0.000
(VI)Ti	0.411	0.528	0.533	0.527	0.336	0.429	0.603	0.390	0.435	0.262	0.243	0.245
(VI)Fe2+	0.745	0.748	0.808	0.873	0.859	0.621	2.409	0.801	0.563	2.042	1.927	1.918
(VI)Cr	0.000	0.069	0.027	0.024	0.000	0.003	0.000	0.000	0.000	0.001	0.003	0.001
(VI)Mn	0.024	0.005	0.000	0.002	0.024	0.025	0.137	0.027	0.024	0.055	0.050	0.045
(VI)Mg	4.582	4.334	4.346	4.270	4.564	4.576	2.084	4.488	4.628	3.523	3.651	3.649
Sum	5.762	5.684	5.714	5.696	5.783	5.654	5.233	5.706	5.650	5.883	5.874	5.858
Ba	0.043	0.017	0.015	0.015	0.041	0.058	0.023	0.051	0.050	0.025	0.014	0.017
Ca	0.014	0.019	0.015	0.002	0.015	0.025	0.063	0.032	0.032	0.007	0.000	0.013
Na	0.119	0.125	0.120	0.144	0.172	0.162	0.304	0.133	0.190	0.041	0.058	0.079
K	1.779	1.819	1.785	1.799	1.792	1.791	1.895	1.789	1.796	1.908	1.889	1.883
Sum	1.955	1.980	1.935	1.960	2.020	2.036	2.285	2.005	2.068	1.981	1.961	1.992
F	0.242	0.158	0.125	0.156	0.223	0.297	0.140	0.222	0.257	0.087	0.133	0.241
Cl	0.000	0.000	0.000	0.000	0.000	0.000	0.000	0.000	0.000	0.000	0.000	0.000
OH	3.759	3.843	3.875	3.844	3.777	3.703	3.860	3.778	3.743	3.913	3.867	3.759

Table A..2.3 - Phlogopite analyses

Sample	at202	at202	at202	at204	at204	at204	at204	at204	at204	at205	at205	at205	at205
Rock type	lcr	lcr	lcr	php	php	php	php	php	php	lcr	lcr	lcr	lcr
Remarks				rim	core			rim	core	im, tr17,1	im, tr17,2	ore, tr17,3	ore, tr17,4
SiO2	36.930	38.558	37.503	35.899	37.858	38.020	38.160	37.120	37.870	38.906	37.968	37.993	38.095
TiO2	2.268	2.063	2.187	2.302	2.484	2.610	2.730	3.000	2.940	2.766	2.925	2.932	3.161
Al2O3	11.525	11.280	11.396	8.677	10.834	11.260	11.040	12.030	11.530	11.541	11.780	12.203	12.670
Cr2O3	0.061	0.003	0.002	b.d	0.030	0.060	0.060	b.d	0.050	b.d	0.031	b.d	b.d
FeO	15.431	15.073	15.314	18.960	8.252	6.468	5.854	6.079	5.931	7.617	7.233	7.054	7.010
Fe2O3	1.969	2.030	1.789	6.027	3.346	3.203	3.363	2.980	2.822	3.136	3.049	2.815	2.387
MnO	0.475	0.442	0.440	0.537	0.173	0.060	0.110	0.120	0.110	0.190	0.162	0.120	0.118
MgO	15.336	16.517	15.741	12.786	19.894	21.290	21.480	21.270	21.190	21.058	20.933	21.245	21.290
BaO	0.367	0.103	0.476	0.145	0.450	0.520	0.740	0.840	0.850	0.568	0.604	0.912	0.970
CaO	0.217	b.d	0.196	0.305	0.348	b.d	b.d	0.060	0.020	0.054	0.037	0.091	0.059
Na2O	0.189	0.330	0.119	0.178	0.284	0.320	0.130	0.210	0.250	0.496	0.356	0.395	0.324
K2O	9.907	9.983	9.631	9.402	9.762	10.070	10.110	9.990	9.960	9.882	9.814	9.719	9.832
F	0.234	0.361	0.310	n.a.	n.a.	0.440	0.330	0.410	0.530	n.a.	n.a.	n.a.	n.a.
Cl	n.a.	n.a.	n.a.	b.d	0.001	0.010	b.d	0.010	b.d	0.022	0.008	0.007	0.016
H2O	3.790	3.830	3.770	3.800	3.980	3.810	3.870	3.820	3.770	4.110	4.060	4.080	4.110
Total	98.700	100.570	98.870	99.020	97.700	98.140	97.980	97.940	97.820	100.350	98.960	99.570	100.040
O=24													
(IV)Si	5.682	5.779	5.739	5.668	5.698	5.663	5.684	5.546	5.653	5.672	5.609	5.577	5.559
(IV)Al	2.088	1.991	2.054	1.613	1.920	1.975	1.937	2.117	2.027	1.981	2.049	2.110	2.177
(IV)Fe3+	0.228	0.229	0.206	0.715	0.379	0.359	0.377	0.335	0.317	0.344	0.339	0.311	0.262
Sum	7.998	7.999	7.999	7.996	7.997	7.997	7.998	7.998	7.997	7.997	7.997	7.998	7.998
(VI)Al	0.000	0.000	0.000	0.000	0.000	0.000	0.000	0.000	0.000	0.000	0.000	0.000	0.000
(VI)Ti	0.262	0.233	0.252	0.273	0.281	0.292	0.306	0.337	0.330	0.303	0.325	0.324	0.347
(VI)Fe2+	1.985	1.889	1.960	2.504	1.039	0.806	0.729	0.760	0.740	0.929	0.894	0.866	0.855
(VI)Cr	0.007	0.000	0.000	0.000	0.004	0.007	0.007	0.000	0.006	0.000	0.004	0.000	0.000
(VI)Mn	0.062	0.056	0.057	0.072	0.022	0.008	0.014	0.015	0.014	0.023	0.020	0.015	0.015
(VI)Mg	3.517	3.690	3.591	3.010	4.463	4.727	4.770	4.737	4.715	4.577	4.610	4.649	4.631
Sum	5.833	5.868	5.860	5.859	5.809	5.840	5.826	5.849	5.805	5.832	5.853	5.854	5.848
Ba	0.022	0.006	0.029	0.009	0.027	0.030	0.043	0.049	0.050	0.032	0.035	0.052	0.055
Ca	0.036	0.000	0.032	0.052	0.056	0.000	0.000	0.010	0.003	0.008	0.006	0.014	0.009
Na	0.056	0.096	0.035	0.054	0.083	0.092	0.038	0.061	0.072	0.140	0.102	0.112	0.092
K	1.945	1.909	1.880	1.894	1.874	1.914	1.921	1.904	1.897	1.838	1.850	1.820	1.830
Sum	2.059	2.011	1.976	2.009	2.040	2.036	2.002	2.024	2.022	2.018	1.993	1.998	1.986
F	0.114	0.171	0.150	0.000	0.000	0.208	0.156	0.194	0.250	0.000	0.000	0.000	0.000
Cl	0.000	0.000	0.000	0.000	0.001	0.003	0.000	0.003	0.000	0.006	0.002	0.002	0.004
OH	3.886	3.829	3.850	4.000	4.000	3.790	3.845	3.804	3.750	3.995	3.998	3.998	3.996

Table A..2.3 - Phlogopite analyses

Sample	at205	at205	at205	at205	at205	at205	at205	at205	at205	at205	at205	at205	at205	at205	at206
Rock type	lcr	lcr	lcr	lcr	lcr	lcr	lcr	lcr	lcr	lcr	lcr	lcr	lcr	lcr	php
Remarks	ore, tr17,5	ore, tr17,6	ore, tr17,7	ore, tr17,8	im, tr17,9	im, tr18,1	ore, tr18,2	ore, tr18,3	ore, tr18,4	ore, tr18,5	ore, tr18,6	ore, tr18,7	im, tr18,8	im, tr18,9	
SiO2	37.553	37.624	38.107	38.164	38.293	38.205	37.676	38.270	37.933	37.639	37.978	36.772	38.790	38.767	37.674
TiO2	3.136	3.067	3.188	3.065	2.745	2.828	3.224	3.268	3.325	3.014	3.376	3.218	2.894	2.837	4.641
Al2O3	12.241	12.305	12.414	12.578	11.346	10.985	11.758	12.008	11.708	11.964	11.900	12.701	10.315	9.880	13.002
Cr2O3	b.d	0.026	0.034	0.010	b.d	0.041	b.d	b.d	b.d	b.d	0.066	0.057	0.072	0.033	0.040
FeO	6.556	6.314	6.338	6.637	7.343	7.564	6.320	6.558	6.191	6.507	6.346	6.619	7.907	7.891	9.984
Fe2O3	2.897	2.540	2.467	2.347	3.084	3.596	3.548	3.111	3.372	2.884	3.294	2.968	4.379	4.802	1.355
MnO	0.103	0.115	0.159	0.151	0.182	0.090	0.124	0.101	0.124	0.130	0.135	0.041	0.147	0.136	0.057
MgO	21.229	21.219	21.425	21.523	20.782	20.451	21.176	21.303	21.158	21.135	21.261	21.179	20.431	20.271	17.810
BaO	0.879	1.655	1.011	1.112	0.360	0.568	1.047	0.929	0.971	0.776	0.985	1.419	0.296	0.329	0.297
CaO	b.d	b.d	0.019	0.011	0.090	0.089	0.032	0.055	0.008	0.058	0.015	0.015	0.052	0.145	0.042
Na2O	0.421	0.287	0.364	0.343	0.326	0.410	0.373	0.399	0.364	0.364	0.176	0.349	0.286	0.278	0.687
K2O	9.790	9.679	9.776	9.731	10.013	9.930	9.896	9.856	9.923	9.826	9.822	9.595	9.949	10.005	9.226
F	n.a.	n.a.	n.a.	n.a.	n.a.	n.a.	n.a.	n.a.	n.a.	n.a.	n.a.	n.a.	n.a.	n.a.	0.335
Cl	b.d	b.d	0.003	b.d	b.d	0.034	0.021	0.023	0.010	b.d	0.011	0.012	b.d	b.d	n.a.
H2O	4.060	4.050	4.090	4.100	4.050	4.030	4.060	4.100	4.070	4.040	4.080	4.040	4.070	4.050	3.890
Total	98.870	98.880	99.400	99.770	98.610	98.820	99.260	99.980	99.160	98.340	99.440	98.990	99.590	99.420	99.040
O=24															
(IV)Si	5.546	5.569	5.583	5.575	5.674	5.674	5.560	5.590	5.591	5.585	5.576	5.450	5.720	5.739	5.579
(IV)Al	2.129	2.145	2.142	2.164	1.980	1.921	2.043	2.065	2.032	2.091	2.058	2.217	1.791	1.723	2.268
(IV)Fe3+	0.322	0.283	0.272	0.258	0.344	0.401	0.394	0.342	0.374	0.322	0.364	0.331	0.485	0.534	0.151
Sum	7.997	7.997	7.997	7.997	7.998	7.996	7.997	7.997	7.997	7.998	7.998	7.998	7.996	7.996	7.998
(VI)Al	0.000	0.000	0.000	0.000	0.000	0.000	0.000	0.000	0.000	0.000	0.000	0.000	0.000	0.000	0.000
(VI)Ti	0.348	0.341	0.351	0.337	0.306	0.316	0.358	0.359	0.369	0.336	0.373	0.359	0.321	0.316	0.517
(VI)Fe2+	0.810	0.782	0.777	0.811	0.910	0.939	0.780	0.801	0.763	0.807	0.779	0.820	0.975	0.977	1.236
(VI)Cr	0.000	0.003	0.004	0.001	0.000	0.005	0.000	0.000	0.000	0.000	0.008	0.007	0.008	0.004	0.005
(VI)Mn	0.013	0.014	0.020	0.019	0.023	0.011	0.015	0.012	0.015	0.016	0.017	0.005	0.018	0.017	0.007
(VI)Mg	4.674	4.682	4.679	4.687	4.591	4.528	4.659	4.638	4.649	4.675	4.654	4.680	4.491	4.474	3.932
Sum	5.845	5.822	5.831	5.855	5.830	5.799	5.812	5.810	5.796	5.834	5.831	5.871	5.813	5.788	5.697
Ba	0.051	0.096	0.058	0.064	0.021	0.033	0.061	0.053	0.056	0.045	0.057	0.082	0.017	0.019	0.017
Ca	0.000	0.000	0.003	0.002	0.014	0.014	0.005	0.009	0.001	0.009	0.002	0.002	0.008	0.023	0.007
Na	0.121	0.082	0.103	0.097	0.094	0.118	0.107	0.113	0.104	0.105	0.050	0.100	0.082	0.080	0.197
K	1.845	1.828	1.827	1.814	1.893	1.881	1.863	1.836	1.866	1.860	1.840	1.814	1.872	1.890	1.743
Sum	2.017	2.006	1.991	1.977	2.022	2.046	2.036	2.011	2.027	2.019	1.949	1.998	1.979	2.012	1.964
F	0.000	0.000	0.000	0.000	0.000	0.000	0.000	0.000	0.000	0.000	0.000	0.000	0.000	0.000	0.157
Cl	0.000	0.000	0.001	0.000	0.000	0.009	0.006	0.006	0.003	0.000	0.003	0.003	0.000	0.000	0.000
OH	4.000	4.000	3.999	4.000	4.000	3.991	3.995	3.994	3.998	4.000	3.997	3.997	4.000	4.000	3.843

Table A..2.3 - Phlogopite analyses

Sample	at206	at206	at206	at206	at206	at207	at207	at207	at207	at207	at207	at207	at207	at208	at209a
Rock type	php	php	php	php	php	lcr	lcr	lcr	lcr	lcr	lcr	lcr	lcr	lcr	lcr
Remarks						core	rim	core	rim	core	rim	core	rim		
SiO2	39.186	38.221	39.543	37.344	38.521	38.502	38.317	38.818	38.186	38.767	39.106	39.215	38.794	40.736	39.726
TiO2	4.918	4.180	3.176	4.275	3.897	4.626	3.630	3.615	2.449	3.766	3.440	3.498	3.024	3.089	1.525
Al2O3	12.781	13.350	8.862	14.042	11.857	13.572	11.041	10.951	8.192	10.213	10.188	9.215	9.456	6.200	8.519
Cr2O3	0.079	1.194	0.021	b.d	0.013	0.666	b.d	b.d	b.d	b.d	b.d	0.003	b.d	b.d	0.006
FeO	5.931	4.567	5.636	5.660	7.705	5.408	5.784	5.243	7.316	5.672	6.317	6.176	6.280	8.204	6.230
Fe2O3	2.306	1.538	5.808	1.837	2.568	2.057	4.480	4.369	7.351	4.957	4.743	5.769	5.743	7.683	5.567
MnO	0.097	b.d	0.087	0.110	0.047	0.053	0.132	0.069	0.223	0.124	0.131	0.156	0.181	0.216	0.236
MgO	20.763	21.218	21.428	21.567	19.947	21.292	21.541	21.926	20.253	21.235	21.165	20.835	21.236	19.028	22.167
BaO	0.303	0.294	0.248	1.324	0.120	0.261	0.578	0.742	0.286	0.601	0.593	0.408	0.455	0.351	0.296
CaO	0.004	0.026	b.d	0.042	b.d	0.025	0.118	0.079	0.759	0.006	0.117	0.108	0.166	0.323	0.090
Na2O	0.548	0.381	0.319	0.435	0.554	0.393	0.232	0.190	0.326	0.299	0.179	0.212	0.240	0.505	0.350
K2O	9.718	9.555	9.703	9.426	9.594	9.689	9.533	9.717	9.683	9.601	9.605	9.895	9.740	9.200	9.863
F	0.390	0.312	0.487	0.473	0.424	0.482	0.447	0.633	0.555	0.497	0.484	0.555	0.534	0.316	0.297
Cl	n.a.	n.a.	n.a.	n.a.	n.a.	n.a.	n.a.	n.a.	n.a.	n.a.	n.a.	n.a.	n.a.	n.a.	n.a.
H2O	4.010	3.980	3.840	3.920	3.880	3.970	3.890	3.820	3.740	3.850	3.870	3.820	3.810	3.880	3.900
Total	101.030	98.820	99.160	100.460	99.130	101.000	99.720	100.170	99.320	99.590	99.940	99.860	99.660	99.730	98.770
O=24															
(IV)Si	5.601	5.549	5.821	5.405	5.661	5.498	5.605	5.646	5.724	5.685	5.722	5.765	5.720	6.055	5.889
(IV)Al	2.151	2.282	1.536	2.393	2.052	2.282	1.902	1.876	1.446	1.764	1.755	1.595	1.642	1.085	1.487
(IV)Fe3+	0.248	0.168	0.643	0.200	0.284	0.221	0.493	0.478	0.828	0.546	0.522	0.638	0.637	0.859	0.620
Sum	8.000	7.999	8.000	7.998	7.997	8.001	8.000	8.000	7.998	7.995	7.999	7.998	7.999	7.999	7.996
(VI)Al	0.000	0.000	0.000	0.000	0.000	0.000	0.000	0.000	0.000	0.000	0.000	0.000	0.000	0.000	0.000
(VI)Ti	0.529	0.456	0.352	0.465	0.431	0.497	0.399	0.395	0.276	0.415	0.379	0.387	0.335	0.345	0.170
(VI)Fe2+	0.709	0.554	0.694	0.685	0.947	0.646	0.708	0.638	0.917	0.696	0.773	0.759	0.774	1.020	0.772
(VI)Cr	0.009	0.137	0.002	0.000	0.002	0.075	0.000	0.000	0.000	0.000	0.000	0.000	0.000	0.000	0.001
(VI)Mn	0.012	0.000	0.011	0.013	0.006	0.006	0.016	0.009	0.028	0.015	0.016	0.019	0.023	0.027	0.030
(VI)Mg	4.424	4.592	4.703	4.654	4.370	4.532	4.697	4.754	4.526	4.642	4.617	4.566	4.668	4.216	4.899
Sum	5.683	5.739	5.762	5.817	5.756	5.756	5.820	5.796	5.747	5.768	5.785	5.731	5.800	5.608	5.872
Ba	0.017	0.017	0.014	0.075	0.007	0.015	0.033	0.042	0.017	0.035	0.034	0.024	0.026	0.020	0.017
Ca	0.001	0.004	0.000	0.007	0.000	0.004	0.018	0.012	0.122	0.001	0.018	0.017	0.026	0.051	0.014
Na	0.152	0.107	0.091	0.122	0.158	0.109	0.066	0.054	0.095	0.085	0.051	0.060	0.069	0.146	0.101
K	1.772	1.770	1.822	1.741	1.799	1.765	1.779	1.803	1.852	1.796	1.793	1.856	1.832	1.745	1.865
Sum	1.942	1.898	1.927	1.945	1.964	1.893	1.896	1.911	2.086	1.917	1.896	1.957	1.953	1.962	1.997
F	0.177	0.143	0.227	0.217	0.197	0.218	0.207	0.291	0.263	0.231	0.224	0.258	0.249	0.149	0.139
Cl	0.000	0.000	0.000	0.000	0.000	0.000	0.000	0.000	0.000	0.000	0.000	0.000	0.000	0.000	0.000
OH	3.824	3.857	3.773	3.783	3.803	3.782	3.793	3.709	3.737	3.770	3.776	3.742	3.751	3.851	3.861

Table A..2.3 - Phlogopite analyses

Sample	at209a	at209a	at209a	at209a	at209a	at209b	at209b	at209b	at209b	at209b	at211	at211	at211	at211	at217
Rock typ	lcr	lcr	lcr	lcr	lcr	php	php	php	php	php	lcr	lcr	lcr	lcr	wehrlite
Remarks						tr19,1	tr19,2	tr19,3	tr19,4	tr19,5	rim	core	core	rim	
SiO2	37.089	36.521	38.462	37.958	39.909	37.440	37.570	37.370	37.720	37.870	37.550	36.675	36.707	39.022	39.557
TiO2	3.173	3.637	2.648	3.328	2.145	4.170	4.070	4.190	4.130	3.190	0.513	2.790	3.461	0.022	1.534
Al2O3	10.664	11.653	9.608	9.001	8.511	12.910	12.870	13.040	12.860	11.620	9.310	8.577	10.946	10.654	11.671
Cr2O3	0.007	b.d	b.d	b.d	0.058	1.160	0.960	1.150	0.790	0.230	0.033	0.052	b.d	b.d	b.d
FeO	7.805	7.157	6.531	6.907	7.149	4.566	4.215	4.331	4.767	5.055	13.915	11.968	8.557	9.473	3.644
Fe2O3	5.130	4.710	5.763	6.502	6.266	2.016	2.373	2.177	2.070	3.295	4.052	6.018	4.414	2.092	3.155
MnO	0.223	0.130	0.183	0.275	0.217	0.050	0.070	0.080	0.040	0.030	0.751	0.501	0.185	0.555	0.127
MgO	19.887	20.327	21.273	20.004	21.601	20.610	21.120	20.750	20.880	21.730	17.163	16.520	19.074	21.113	25.057
BaO	1.637	1.710	1.054	0.837	0.620	0.370	0.400	0.380	0.430	0.540	0.084	0.685	0.885	0.133	0.612
CaO	0.144	0.047	0.208	0.073	0.046	0.040	b.d	b.d	0.020	b.d	0.329	0.159	0.087	0.240	0.056
Na2O	0.331	0.178	0.214	0.281	0.347	0.190	0.500	0.480	0.340	0.230	0.295	0.112	0.279	0.221	0.315
K2O	9.437	9.498	9.746	9.770	9.485	10.100	10.100	10.100	10.040	10.160	9.915	9.355	9.658	10.148	9.914
F	0.270	0.221	0.219	0.189	0.207	0.290	0.300	0.390	0.330	0.420	n.a.	n.a.	n.a.	n.a.	0.341
Cl	n.a.	n.a.	n.a.	n.a.	n.a.	b.d	b.d	b.d	0.010	b.d	0.013	0.014	0.004	b.d	n.a.
H2O	3.880	3.920	3.950	3.920	4.000	3.920	3.950	3.890	3.920	3.850	3.860	3.840	3.970	3.980	4.010
Total	99.680	99.710	99.860	99.050	100.560	97.830	98.500	98.330	98.350	98.220	97.780	97.270	98.230	97.650	99.990
O=24															
(IV)Si	5.547	5.437	5.687	5.684	5.842	5.527	5.511	5.495	5.542	5.605	5.826	5.717	5.547	5.874	5.686
(IV)Al	1.878	2.043	1.673	1.587	1.467	2.244	2.223	2.258	2.225	2.025	1.701	1.574	1.948	1.889	1.976
(IV)Fe3+	0.577	0.527	0.641	0.732	0.690	0.224	0.262	0.241	0.229	0.367	0.473	0.705	0.501	0.237	0.341
Sum	8.002	8.007	8.001	8.003	7.999	7.995	7.996	7.994	7.996	7.997	8.000	7.996	7.996	8.000	8.003
(VI)Al	0.000	0.000	0.000	0.000	0.000	0.000	0.000	0.000	0.000	0.000	0.000	0.000	0.000	0.000	0.000
(VI)Ti	0.357	0.407	0.295	0.375	0.236	0.463	0.449	0.463	0.456	0.355	0.060	0.327	0.393	0.002	0.166
(VI)Fe2+	0.976	0.891	0.808	0.865	0.875	0.564	0.517	0.533	0.586	0.626	1.805	1.560	1.081	1.193	0.438
(VI)Cr	0.001	0.000	0.000	0.000	0.007	0.135	0.111	0.134	0.092	0.027	0.004	0.006	0.000	0.000	0.000
(VI)Mn	0.028	0.016	0.023	0.035	0.027	0.006	0.009	0.010	0.005	0.004	0.099	0.066	0.024	0.071	0.015
(VI)Mg	4.434	4.511	4.689	4.466	4.714	4.536	4.618	4.549	4.573	4.795	3.970	3.839	4.297	4.738	5.369
Sum	5.796	5.825	5.815	5.741	5.859	5.704	5.704	5.689	5.712	5.807	5.938	5.798	5.795	6.004	5.988
Ba	0.096	0.100	0.061	0.049	0.036	0.021	0.023	0.022	0.025	0.031	0.005	0.042	0.052	0.008	0.034
Ca	0.023	0.007	0.033	0.012	0.007	0.006	0.000	0.000	0.003	0.000	0.055	0.027	0.014	0.039	0.009
Na	0.096	0.051	0.061	0.082	0.098	0.054	0.142	0.137	0.097	0.066	0.089	0.034	0.082	0.065	0.088
K	1.800	1.804	1.838	1.866	1.771	1.902	1.890	1.895	1.882	1.918	1.962	1.860	1.862	1.949	1.818
Sum	2.015	1.962	1.993	2.009	1.912	1.983	2.055	2.054	2.007	2.015	2.111	1.963	2.010	2.061	1.949
F	0.128	0.104	0.103	0.090	0.096	0.136	0.139	0.182	0.154	0.197	0.000	0.000	0.000	0.000	0.155
Cl	0.000	0.000	0.000	0.000	0.000	0.000	0.000	0.000	0.003	0.000	0.004	0.004	0.001	0.000	0.000
OH	3.872	3.896	3.898	3.911	3.904	3.865	3.861	3.819	3.844	3.803	3.997	3.996	3.999	4.000	3.845

Table A..2.3 - Phlogopite analyses

Sample	at217	at217	at217	at217	at217	at217	at217	at217	at302	at302	at302	at302	at302
Rock type	wehrlite	wehrlite	wehrlite	wehrlite	wehrlite	wehrlite	wehrlite	wehrlite	syenite	syenite	syenite	syenite	syenite
Remarks			core	rim									
SiO2	40.235	40.787	39.948	40.967	39.717	38.409	38.862	40.479	36.466	35.867	36.308	35.881	36.044
TiO2	1.195	1.007	1.123	0.774	1.273	1.770	1.485	1.089	3.647	3.518	3.687	3.693	3.135
Al2O3	12.115	11.896	12.183	10.731	10.944	12.869	13.373	11.141	12.927	13.482	11.787	12.553	13.389
Cr2O3	0.036	0.033	0.033	0.005	0.003	b.d	0.028	b.d	0.037	b.d	0.027	0.054	0.082
FeO	4.045	4.154	4.707	3.430	3.853	4.922	4.857	3.513	18.578	19.621	18.672	19.862	20.242
Fe2O3	1.915	1.772	1.567	3.280	3.710	1.816	1.049	2.864	0.747	0.249	1.500	1.103	0.163
MnO	0.140	0.094	0.139	0.131	0.124	0.140	0.126	0.113	0.595	0.597	0.541	0.601	0.443
MgO	25.080	25.348	24.650	25.792	24.974	23.915	24.582	25.300	12.782	12.275	12.058	11.558	12.163
BaO	0.483	0.437	0.448	0.229	0.607	0.766	0.523	0.477	0.004	b.d	0.004	0.063	0.042
CaO	0.036	0.005	0.061	0.037	0.097	0.055	0.054	0.021	b.d	0.092	b.d	0.068	0.002
Na2O	0.344	0.339	0.273	0.433	0.423	0.409	0.366	0.268	0.207	0.230	0.241	0.223	0.287
K2O	10.117	9.967	9.905	10.059	9.622	9.504	9.478	10.163	9.836	9.573	9.688	9.706	9.767
F	0.291	0.350	0.290	0.427	0.267	0.247	0.239	0.444	0.373	0.269	0.365	0.171	0.301
Cl	n.a.	n.a.	n.a.	n.a.	n.a.	n.a.	n.a.	n.a.	n.a.	n.a.	n.a.	n.a.	n.a.
H2O	4.050	4.040	4.020	4.000	4.030	4.000	4.040	3.970	3.740	3.760	3.680	3.780	3.750
Total	100.080	100.230	99.350	100.300	99.640	98.820	99.060	99.840	99.940	99.530	98.560	99.320	99.810
O=24													
(IV)Si	5.755	5.813	5.761	5.846	5.736	5.596	5.614	5.812	5.581	5.526	5.657	5.572	5.556
(IV)Al	2.041	1.997	2.069	1.803	1.861	2.208	2.275	1.884	2.330	2.446	2.163	2.296	2.431
(IV)Fe3+	0.206	0.190	0.170	0.352	0.403	0.199	0.114	0.309	0.086	0.029	0.176	0.129	0.019
Sum	8.002	8.000	8.000	8.001	8.000	8.003	8.003	8.005	7.997	8.001	7.996	7.997	8.006
(VI)Al	0.000	0.000	0.000	0.000	0.000	0.000	0.000	0.000	0.000	0.000	0.000	0.000	0.000
(VI)Ti	0.129	0.108	0.122	0.083	0.138	0.194	0.161	0.118	0.420	0.408	0.432	0.431	0.363
(VI)Fe2+	0.484	0.495	0.568	0.409	0.465	0.600	0.587	0.422	2.378	2.528	2.433	2.579	2.609
(VI)Cr	0.004	0.004	0.004	0.001	0.000	0.000	0.003	0.000	0.004	0.000	0.003	0.007	0.010
(VI)Mn	0.017	0.011	0.017	0.016	0.015	0.017	0.015	0.014	0.077	0.078	0.071	0.079	0.058
(VI)Mg	5.348	5.385	5.299	5.487	5.377	5.195	5.294	5.415	2.917	2.819	2.801	2.676	2.795
Sum	5.982	6.003	6.010	5.996	5.995	6.006	6.060	5.969	5.796	5.833	5.740	5.772	5.835
Ba	0.027	0.024	0.025	0.013	0.034	0.044	0.030	0.027	0.000	0.000	0.000	0.004	0.003
Ca	0.006	0.001	0.009	0.006	0.015	0.009	0.008	0.003	0.000	0.015	0.000	0.011	0.000
Na	0.095	0.094	0.076	0.120	0.118	0.116	0.103	0.075	0.061	0.069	0.073	0.067	0.086
K	1.846	1.812	1.822	1.831	1.773	1.767	1.747	1.861	1.921	1.882	1.926	1.923	1.921
Sum	1.974	1.931	1.932	1.970	1.940	1.936	1.888	1.966	1.982	1.966	1.999	2.005	2.010
F	0.132	0.158	0.132	0.193	0.122	0.114	0.109	0.202	0.181	0.131	0.180	0.084	0.147
Cl	0.000	0.000	0.000	0.000	0.000	0.000	0.000	0.000	0.000	0.000	0.000	0.000	0.000
OH	3.868	3.842	3.868	3.807	3.878	3.886	3.891	3.798	3.819	3.869	3.820	3.916	3.853

Table A2.4 - Perovskite analyses

Sample	at003	at003	at003	at003	at003	at003	at003	at003	at003	at003	at006	at006
Unit	B1	B1	B1	B1	B1	B1	B1	B1	B1	B1	B2	B2
Rock type	beb	beb	beb	beb	beb	beb	beb	beb	beb	beb	beb	beb
Remarks	tr1.2	tr1.3	tr1.4	tr3.2	tr3.3							
TiO2	56.230	57.158	57.255	56.909	57.059	55.462	54.632	54.747	54.653	54.572	54.802	55.314
CaO	38.839	39.039	38.578	39.136	39.181	39.296	39.274	39.058	39.255	40.256	37.324	37.736
MgO	0.008	0.007	0.011	0.002	0.007	n.a	n.a	n.a	n.a	n.a	n.a	n.a
FeO	0.907	0.966	0.632	1.038	1.009	1.781	1.482	1.320	0.896	1.287	1.665	1.540
MnO	0.022	0.028	0.031	0.014	0.018	n.a	n.a	n.a	n.a	n.a	n.a	n.a
Na2O	n.a	n.a	n.a	n.a	n.a	0.173	0.073	0.113	0.584	0.173	0.519	0.472
La2O3	0.435	0.537	0.490	0.494	0.492	0.545	0.441	0.464	0.863	0.625	1.100	0.976
Ce2O3	0.634	0.800	0.896	0.753	0.610	0.962	0.862	0.841	1.382	1.064	2.032	1.710
Pr2O3	0.114	0.063	0.090	0.128	0.094	0.095	0.086	0.094	n.a	n.a	0.185	0.169
Nd2O3	0.253	0.296	0.298	0.272	0.240	0.060	0.049	0.054	0.370	0.340	0.094	0.076
Sm2O3	0.024	0.037	0.064	0.058	0.055	0.051	0.039	0.058	0.044	0.050	0.080	0.072
Gd2O3	0.020	b.d	0.119	0.035	0.099	0.033	0.002	0.044	0.024	0.037	0.058	0.067
Y2O3	0.050	0.049	0.016	0.035	0.044	0.036	0.037	0.044	0.016	0.027	0.052	0.056
ThO2	n.a	n.a	n.a	n.a	n.a	n.a	n.a	n.a	n.a	n.a	n.a	n.a
ZrO2	0.049	0.047	0.004	0.051	0.044	0.096	0.119	0.110	n.a	n.a	0.100	0.097
SrO	0.816	0.832	1.238	0.930	0.940	0.477	0.451	0.458	0.616	0.359	0.806	0.967
Nb2O5	0.560	0.618	0.681	0.535	0.472	0.724	0.526	0.638	1.446	0.627	1.285	1.178
Ta2O5	0.031	0.045	b.d.	0.036	0.032	n.a	n.a	n.a	n.a	n.a	n.a	n.a
Total	98.993	100.521	100.401	100.427	100.396	99.791	98.073	98.043	100.150	99.418	100.102	100.430
O=3												
Ti	0.9811	0.9835	0.9874	0.9810	0.9828	0.9660	0.9658	0.9683	0.9554	0.9578	0.9621	0.9646
Ca	0.9652	0.9568	0.9476	0.9610	0.9613	0.9749	0.9890	0.9839	0.9774	1.0064	0.9333	0.9373
Mg	0.0003	0.0002	0.0004	0.0001	0.0003							
Fe	0.0176	0.0185	0.0121	0.0199	0.0193	0.0345	0.0291	0.0260	0.0174	0.0251	0.0325	0.0299
Mn	0.0004	0.0005	0.0006	0.0003	0.0003							
Na						0.0078	0.0033	0.0052	0.0263	0.0078	0.0235	0.0212
La	0.0037	0.0045	0.0041	0.0042	0.0041	0.0047	0.0038	0.0040	0.0074	0.0054	0.0095	0.0083
Ce	0.0054	0.0067	0.0075	0.0063	0.0051	0.0081	0.0074	0.0072	0.0117	0.0091	0.0173	0.0145
Pr	0.0010	0.0005	0.0007	0.0011	0.0008	0.0008	0.0007	0.0008			0.0016	0.0014
Nd	0.0021	0.0024	0.0024	0.0022	0.0020	0.0005	0.0004	0.0005	0.0031	0.0028	0.0008	0.0006
Sm	0.0002	0.0003	0.0005	0.0005	0.0004	0.0004	0.0003	0.0005	0.0004	0.0004	0.0006	0.0006
Gd	0.0002		0.0009	0.0003	0.0008	0.0003	0.0000	0.0003	0.0002	0.0003	0.0005	0.0005
Y	0.0006	0.0006	0.0002	0.0004	0.0005	0.0004	0.0005	0.0005	0.0002	0.0003	0.0006	0.0007
Th												
Zr	0.0006	0.0005		0.0006	0.0005	0.0011	0.0014	0.0013			0.0011	0.0011
Sr	0.0110	0.0110	0.0165	0.0124	0.0125	0.0064	0.0061	0.0062	0.0083	0.0049	0.0109	0.0130
Nb	0.0059	0.0064	0.0071	0.0055	0.0049	0.0076	0.0056	0.0068	0.0152	0.0066	0.0136	0.0123
Ta	0.0002	0.0003		0.0002	0.0002							

Table A2.4 - Perovskite analyses

Sample	at006	at009	at009	at009	at009	at009	at009	at009	at009	at013	at013	at013
Unit	B2	B1	B1	B1	B1	B1	B1	B1	B1			
Rock type	beb	beb	beb	beb	beb	beb	beb	beb	beb	php	php	php
Remarks			rim	core	rim	core	rim	rim	core			
TiO2	54.047	58.944	57.173	57.396	57.224	57.117	57.298	57.458	56.843	52.775	56.760	55.903
CaO	35.865	38.949	38.665	38.643	38.428	38.733	38.798	37.948	38.910	34.561	38.159	38.214
MgO	n.a	0.007	0.001	0.005	0.003	0.018	0.011	0.012	0.008	0.881	0.031	0.024
FeO	1.661	0.847	0.695	0.852	0.938	0.978	0.955	1.063	1.027	2.586	1.734	2.084
MnO	n.a	0.023	0.019	0.009	0.019	0.017	0.028	0.024	0.022	0.027	0.004	0.024
Na2O	0.565	n.a	n.a	n.a	n.a	n.a	n.a	n.a	n.a	n.a	n.a	n.a
La2O3	1.118	0.333	0.466	0.597	0.503	0.436	0.464	0.578	0.532	0.627	0.567	0.450
Ce2O3	2.074	0.297	0.768	0.856	1.033	1.049	0.962	1.036	0.768	1.349	1.379	0.998
Pr2O3	0.208	0.046	0.095	0.155	0.118	0.073	0.077	0.075	0.117	0.184	0.102	0.096
Nd2O3	0.098	0.101	0.322	0.345	0.320	0.278	0.329	0.323	0.310	0.498	0.403	0.366
Sm2O3	0.080	0.061	0.074	0.038	0.061	0.029	0.039	0.030	0.038	0.098	0.058	0.064
Gd2O3	0.053	0.026	0.065	0.050	0.038	0.038	0.001	0.031	b.d	0.001	0.042	0.007
Y2O3	0.046	0.074	0.046	0.038	0.043	0.043	0.026	0.050	0.035	0.004	0.013	0.016
ThO2	n.a	n.a	n.a	n.a	n.a	n.a	n.a	n.a	n.a	n.a	n.a	n.a
ZrO2	0.107	0.073	0.040	0.044	0.032	0.026	0.019	0.015	0.023	0.026	0.021	0.046
SrO	0.900	0.754	0.909	0.878	0.871	0.840	0.733	0.861	0.825	0.465	0.777	0.829
Nb2O5	1.290	0.051	0.482	0.460	0.502	0.422	0.418	0.418	0.415	0.294	0.327	0.321
Ta2O5	n.a	b.d	0.038	0.042	0.050	b.d	0.006	0.071	0.011	0.046	0.011	0.006
Total	98.112	100.588	99.858	100.408	100.182	100.096	100.165	99.991	99.883	94.423	100.387	99.448
O=3												
Ti	0.9678	1.0050	0.9898	0.9894	0.9888	0.9868	0.9885	0.9942	0.9849	0.9141	0.9815	0.9748
Ca	0.9148	0.9459	0.9535	0.9489	0.9458	0.9532	0.9534	0.9352	0.9603	0.8527	0.9399	0.9491
Mg		0.0002		0.0002	0.0001	0.0006	0.0004	0.0004	0.0003	0.0302	0.0010	0.0008
Fe	0.0331	0.0161	0.0134	0.0163	0.0180	0.0188	0.0183	0.0204	0.0198	0.0498	0.0333	0.0404
Mn		0.0004	0.0004	0.0002	0.0004	0.0003	0.0006	0.0005	0.0004	0.0005	0.0001	0.0005
Na	0.0261											
La	0.0098	0.0028	0.0040	0.0050	0.0043	0.0037	0.0039	0.0049	0.0045	0.0053	0.0048	0.0038
Ce	0.0181	0.0025	0.0065	0.0072	0.0087	0.0088	0.0081	0.0087	0.0065	0.0114	0.0116	0.0085
Pr	0.0018	0.0004	0.0008	0.0013	0.0010	0.0006	0.0006	0.0006	0.0010	0.0015	0.0009	0.0008
Nd	0.0008	0.0008	0.0026	0.0028	0.0026	0.0023	0.0027	0.0027	0.0025	0.0041	0.0033	0.0030
Sm	0.0007	0.0005	0.0006	0.0003	0.0005	0.0002	0.0003	0.0002	0.0003	0.0008	0.0005	0.0005
Gd	0.0004	0.0002	0.0005	0.0004	0.0003	0.0003	0.0000	0.0002			0.0003	0.0001
Y	0.0006	0.0009	0.0006	0.0005	0.0005	0.0005	0.0003	0.0006	0.0004	0.0001	0.0002	0.0002
Th												
Zr	0.0012	0.0008	0.0005	0.0005	0.0004	0.0003	0.0002	0.0002	0.0003	0.0003	0.0002	0.0005
Sr	0.0124	0.0099	0.0121	0.0117	0.0116	0.0112	0.0098	0.0115	0.0110	0.0062	0.0104	0.0111
Nb	0.0139	0.0005	0.0050	0.0048	0.0052	0.0044	0.0043	0.0043	0.0043	0.0031	0.0034	0.0034
Ta			0.0002	0.0003	0.0003			0.0004	0.0001	0.0003	0.0001	

Table A2.4 - Perovskite analyses

Sample	at013	at013	at014b	at014b	at014b	at015	at015	at015	at016	at016	at016	at016
Unit			B1	B1	B1	B1	B1	B1	B1	B1	B1	B1
Rock type	php	php	wehrl	wehrl	wehrl	wehrl	wehrl	wehrl	wehrl	wehrl	wehrl	wehrl
Remarks									tr11.1	tr11.2	tr11.3	tr11.4
TiO2	55.967	56.058	56.130	55.459	55.827	55.247	55.663	55.622	56.328	55.844	55.911	55.646
CaO	36.921	37.790	38.166	38.431	38.968	38.688	37.604	38.348	38.862	38.846	39.382	39.439
MgO	0.051	0.061	n.a	n.a	n.a	n.a	n.a	n.a	0.001	0.025	0.009	0.014
FeO	1.959	1.858	1.455	1.554	1.614	1.868	1.607	1.681	0.901	1.053	1.031	1.011
MnO	0.041	0.025	n.a	n.a	n.a	n.a	n.a	n.a	0.016	0.016	0.014	0.024
Na2O	n.a	n.a	0.230	0.248	0.233	0.142	0.312	0.285	n.a	n.a	n.a	n.a
La2O3	0.820	0.643	0.706	0.718	0.716	0.733	0.861	0.814	0.675	0.860	0.725	0.727
Ce2O3	2.055	1.423	1.615	1.658	1.560	1.609	1.831	1.820	1.361	1.541	1.217	1.336
Pr2O3	0.275	0.143	0.170	0.173	0.167	0.167	0.194	0.190	0.193	0.199	b.d	0.233
Nd2O3	0.809	0.532	0.084	0.088	0.092	0.089	0.099	0.092	0.479	0.508	0.440	0.411
Sm2O3	0.072	0.085	0.077	0.084	0.083	0.068	0.092	0.086	0.076	0.095	0.104	0.042
Gd2O3	0.092	b.d	0.046	0.058	0.052	0.049	0.052	0.061	0.075	0.007	0.039	0.068
Y2O3	0.021	0.031	0.036	0.039	0.041	0.037	0.039	0.040	0.061	0.057	0.055	0.063
ThO2	n.a	n.a	n.a	n.a	n.a	n.a	n.a	n.a	n.a	n.a	n.a	n.a
ZrO2	0.027	0.025	0.116	0.085	0.106	0.127	0.066	0.084	0.069	0.042	0.046	0.036
SrO	0.682	0.628	0.531	0.460	0.481	0.540	0.546	0.484	0.424	0.375	0.450	0.404
Nb2O5	0.329	0.383	0.526	0.568	0.630	0.572	0.664	0.607	0.611	0.630	0.738	0.678
Ta2O5	0.008	0.011	n.a	n.a	n.a	n.a	n.a	n.a	0.007	0.047	b.d	0.029
Total	100.128	99.696	99.888	99.623	100.570	99.936	99.630	100.214	100.138	100.143	100.161	100.159
O=3												
Ti	0.9785	0.9772	0.9777	0.9707	0.9681	0.9654	0.9756	0.9699	0.9778	0.9721	0.9705	0.9679
Ca	0.9194	0.9383	0.9469	0.9581	0.9626	0.9630	0.9388	0.9525	0.9609	0.9632	0.9737	0.9772
Mg	0.0018	0.0021								0.0009	0.0003	0.0005
Fe	0.0381	0.0360	0.0282	0.0302	0.0311	0.0363	0.0313	0.0326	0.0174	0.0204	0.0199	0.0195
Mn	0.0008	0.0005							0.0003	0.0003	0.0003	0.0005
Na			0.0103	0.0112	0.0104	0.0064	0.0141	0.0128				
La	0.0070	0.0055	0.0060	0.0062	0.0061	0.0063	0.0074	0.0070	0.0057	0.0073	0.0062	0.0062
Ce	0.0175	0.0121	0.0137	0.0141	0.0132	0.0137	0.0156	0.0154	0.0115	0.0130	0.0103	0.0113
Pr	0.0023	0.0012	0.0014	0.0015	0.0014	0.0014	0.0016	0.0016	0.0016	0.0017		0.0020
Nd	0.0067	0.0044	0.0007	0.0007	0.0008	0.0007	0.0008	0.0008	0.0039	0.0042	0.0036	0.0034
Sm	0.0006	0.0007	0.0006	0.0007	0.0007	0.0005	0.0007	0.0007	0.0006	0.0008	0.0008	0.0003
Gd	0.0007		0.0004	0.0005	0.0004	0.0004	0.0004	0.0005	0.0006	0.0001	0.0003	0.0005
Y	0.0003	0.0004	0.0004	0.0005	0.0005	0.0005	0.0005	0.0005	0.0007	0.0007	0.0007	0.0008
Th												
Zr	0.0003	0.0003	0.0013	0.0010	0.0012	0.0014	0.0007	0.0009	0.0008	0.0005	0.0005	0.0004
Sr	0.0092	0.0084	0.0071	0.0062	0.0064	0.0073	0.0074	0.0065	0.0057	0.0050	0.0060	0.0054
Nb	0.0035	0.0040	0.0055	0.0060	0.0066	0.0060	0.0070	0.0064	0.0064	0.0066	0.0077	0.0071
Ta		0.0001								0.0003		0.0002

Table A2.4 - Perovskite analyses

Sample	at016	at016	at016	at016	at016	at016	at016	at016	at016	at016	at016	at022
Unit	B1	B1	B1	B1	B1	B1	B1	B1	B1	B1	B1	
Rock type	wehrl	wehrl	wehrl	wehrl	wehrl	wehrl	wehrl	wehrl	wehrl	wehrl	wehrl	
Remarks	tr11.6	tr11.7	tr11.8	tr11.9	tr11.10	tr12.1	tr12.2	tr12.3	tr12.4	tr12.5	tr12.6	php
TiO2	55.722	55.642	55.556	55.717	55.579	55.514	55.238	55.624	55.612	55.434	56.037	52.948
CaO	38.752	39.102	39.264	38.884	38.966	38.827	38.765	38.768	39.366	38.682	39.745	37.284
MgO	0.007	0.022	0.007	0.012	0.004	0.001	0.009	0.014	0.014	0.013	0.011	0.056
FeO	1.104	1.088	0.997	1.124	0.932	1.151	1.152	1.174	1.022	1.207	0.920	1.612
MnO	0.016	0.027	0.016	0.021	0.012		0.007	0.018	0.016	0.014	0.002	0.038
Na2O	n.a	n.a	n.a	n.a	n.a	n.a	n.a	n.a	n.a	n.a	n.a	n.a
La2O3	0.889	0.723	0.790	0.873	0.857	0.975	0.943	0.843	0.714	0.924	0.593	0.749
Ce2O3	1.485	1.390	1.377	1.336	1.512	1.442	1.696	1.362	1.519	1.591	1.107	1.479
Pr2O3	0.157	0.101	0.175	0.198	0.180	0.152	0.159	0.143	0.130	0.195	0.066	0.147
Nd2O3	0.474	0.522	0.556	0.460	0.618	0.544	0.567	0.537	0.483	0.552	0.387	0.666
Sm2O3	0.088	0.048	0.065	0.103	0.078	0.043	0.079	0.054	0.082	0.090	0.051	0.075
Gd2O3	0.097	0.111	0.124	0.052	0.003	0.121	0.071	0.043	0.046	0.041	0.043	0.014
Y2O3	0.053	0.062	0.058	0.064	0.064	0.079	0.091	0.119	0.068	0.056	0.058	0.030
ThO2	n.a	n.a	n.a	n.a	n.a	n.a	n.a	n.a	n.a	n.a	n.a	n.a
ZrO2	0.040	0.051	0.040	0.072	0.071	0.091	0.052	0.116	0.032	0.076	0.034	0.017
SrO	0.487	0.519	0.468	0.508	0.506	0.448	0.450	0.500	0.380	0.492	0.336	1.005
Nb2O5	0.848	0.787	0.771	0.788	0.807	0.824	0.882	0.833	0.593	0.810	0.592	0.359
Ta2O5	0.046	0.031	b.d	0.032	0.033	0.069	0.056	0.042	0.059	0.042	0.061	0.009
Total	100.263	100.226	100.264	100.244	100.220	100.282	100.216	100.187	100.136	100.220	100.040	96.487
O=3												
Ti	0.9703	0.9683	0.9673	0.9695	0.9681	0.9671	0.9645	0.9685	0.9681	0.9668	0.9716	0.9616
Ca	0.9612	0.9692	0.9738	0.9637	0.9667	0.9634	0.9641	0.9614	0.9761	0.9610	0.9816	0.9645
Mg	0.0002	0.0007	0.0003	0.0004	0.0001		0.0003	0.0005	0.0005	0.0004	0.0004	0.0020
Fe	0.0214	0.0210	0.0193	0.0217	0.0180	0.0223	0.0224	0.0227	0.0198	0.0234	0.0177	0.0326
Mn	0.0003	0.0005	0.0003	0.0004	0.0002		0.0001	0.0003	0.0003	0.0003		0.0008
Na												
La	0.0076	0.0062	0.0067	0.0074	0.0073	0.0083	0.0081	0.0072	0.0061	0.0079	0.0050	0.0067
Ce	0.0126	0.0118	0.0117	0.0113	0.0128	0.0122	0.0144	0.0115	0.0129	0.0135	0.0093	0.0131
Pr	0.0013	0.0009	0.0015	0.0017	0.0015	0.0013	0.0013	0.0012	0.0011	0.0016	0.0006	0.0013
Nd	0.0039	0.0043	0.0046	0.0038	0.0051	0.0045	0.0047	0.0044	0.0040	0.0046	0.0032	0.0057
Sm	0.0007	0.0004	0.0005	0.0008	0.0006	0.0003	0.0006	0.0004	0.0007	0.0007	0.0004	0.0006
Gd	0.0007	0.0009	0.0010	0.0004	0.0000	0.0009	0.0006	0.0003	0.0004	0.0003	0.0003	0.0001
Y	0.0006	0.0008	0.0007	0.0008	0.0008	0.0010	0.0011	0.0015	0.0008	0.0007	0.0007	0.0004
Th												
Zr	0.0005	0.0006	0.0005	0.0008	0.0008	0.0010	0.0006	0.0013	0.0004	0.0009	0.0004	0.0002
Sr	0.0065	0.0070	0.0063	0.0068	0.0068	0.0060	0.0061	0.0067	0.0051	0.0066	0.0045	0.0141
Nb	0.0089	0.0082	0.0081	0.0082	0.0084	0.0086	0.0093	0.0087	0.0062	0.0085	0.0062	0.0039
Ta	0.0003	0.0002		0.0002	0.0002	0.0004	0.0004	0.0003	0.0004	0.0003	0.0004	0.0001

Table A2.4 - Perovskite analyses

Sample	at022	at022	at022	at022	at022	at022	at022	at022	at025	at025	at025	at025
Unit									B1	B1	B1	B1
Rock type	php	php	php	php	php	php	php	php	wehrl	wehrl	wehrl	wehrl
Remarks												
TiO2	54.996	55.735	54.637	55.139	52.422	55.765	54.871	54.216	53.438	53.641	56.824	55.474
CaO	35.932	37.996	35.205	35.727	34.745	36.721	36.109	35.721	36.270	35.620	38.436	35.912
MgO	0.503	0.027	0.074	0.054	0.846	0.045	0.045	0.051	0.013	0.023	0.012	0.037
FeO	1.678	1.736	1.535	1.569	3.031	1.490	1.616	1.560	2.050	2.268	1.080	1.277
MnO	0.016	0.004	0.034	0.019	0.044	0.027	0.024	0.009	0.021	0.015	0.007	0.029
Na2O	n.a	n.a	n.a	n.a	n.a	n.a	n.a	n.a	n.a	n.a	n.a	n.a
La2O3	0.817	0.577	1.018	1.016	0.805	0.799	0.978	0.890	1.525	1.868	0.538	1.126
Ce2O3	1.614	1.006	2.381	2.409	1.659	1.679	2.355	2.350	2.941	3.160	1.208	2.653
Pr2O3	0.235	0.144	0.291	0.279	0.219	0.156	0.233	0.257	0.308	0.269	0.071	0.380
Nd2O3	0.773	0.293	1.044	0.848	0.674	0.732	1.051	1.062	0.914	0.919	0.392	1.162
Sm2O3	0.076	0.032	0.085	0.110	0.055	0.071	0.098	0.125	0.169	0.114	0.071	0.179
Gd2O3	0.017	0.071	0.090	b.d	b.d	0.020	0.052	0.032	0.066	0.027	0.031	0.106
Y2O3	0.041	0.032	0.003	0.028	0.029	0.035	0.022	0.035	0.103	0.085	0.050	0.028
ThO2	n.a	n.a	n.a	n.a	n.a	n.a	n.a	n.a	n.a	n.a	n.a	n.a
ZrO2	0.025	0.037	0.014	0.021	0.025	0.021	0.024	0.021	0.121	0.128	0.026	0.024
SrO	1.026	1.074	0.813	0.881	0.841	0.904	0.889	0.869	0.857	0.903	0.803	0.673
Nb2O5	0.340	0.392	0.288	0.267	0.324	0.333	0.312	0.329	1.188	1.331	0.514	0.516
Ta2O5	0.041	0.028	0.004	0.046	0.056	0.050	0.077	0.073	0.056	0.026	0.110	0.118
Total	98.129	99.185	97.514	98.414	95.775	98.848	98.756	97.599	100.039	100.396	100.172	99.695
O=3												
Ti	0.9719	0.9771	0.9841	0.9837	0.9201	0.9843	0.9773	0.9776	0.9529	0.9549	0.9839	0.9816
Ca	0.9045	0.9489	0.9032	0.9079	0.8686	0.9232	0.9161	0.9175	0.9213	0.9032	0.9480	0.9052
Mg	0.0176	0.0009	0.0026	0.0019	0.0294	0.0016	0.0016	0.0018	0.0005	0.0008	0.0004	0.0013
Fe	0.0330	0.0338	0.0307	0.0311	0.0591	0.0292	0.0320	0.0313	0.0406	0.0449	0.0208	0.0251
Mn	0.0003	0.0001	0.0007	0.0004	0.0009	0.0005	0.0005	0.0002	0.0004	0.0003	0.0001	0.0006
Na												
La	0.0071	0.0050	0.0090	0.0089	0.0069	0.0069	0.0085	0.0079	0.0133	0.0163	0.0046	0.0098
Ce	0.0139	0.0086	0.0208	0.0209	0.0142	0.0144	0.0204	0.0206	0.0255	0.0273	0.0102	0.0228
Pr	0.0020	0.0012	0.0025	0.0024	0.0019	0.0013	0.0020	0.0022	0.0027	0.0023	0.0006	0.0033
Nd	0.0065	0.0024	0.0089	0.0072	0.0056	0.0061	0.0089	0.0091	0.0077	0.0078	0.0032	0.0098
Sm	0.0006	0.0003	0.0007	0.0009	0.0004	0.0006	0.0008	0.0010	0.0014	0.0009	0.0006	0.0015
Gd	0.0001	0.0006	0.0007			0.0002	0.0004	0.0003	0.0005	0.0002	0.0002	0.0008
Y	0.0005	0.0004		0.0003	0.0004	0.0004	0.0003	0.0005	0.0013	0.0011	0.0006	0.0004
Th												
Zr	0.0003	0.0004	0.0002	0.0002	0.0003	0.0002	0.0003	0.0002	0.0014	0.0015	0.0003	0.0003
Sr	0.0140	0.0145	0.0113	0.0121	0.0114	0.0123	0.0122	0.0121	0.0118	0.0124	0.0107	0.0092
Nb	0.0036	0.0041	0.0031	0.0029	0.0034	0.0035	0.0033	0.0036	0.0127	0.0142	0.0053	0.0055
Ta	0.0003	0.0002		0.0003	0.0004	0.0003	0.0005	0.0005	0.0004	0.0002	0.0007	0.0008

Table A2.4 - Perovskite analyses

Sample	at025	at025	at025	at027	at027	at027	at029	at029	at029	at029	at029	at033
Unit	B1	B1	B1	B1	B1	B1	B2	B2	B2	B2	B2	B2
Rock type	wehrl	wehrl	wehrl	beb	beb	beb	beb	beb	beb	beb	beb	beb
Remarks							rim	core	rim	core		
TiO2	55.380	54.629	54.189	54.878	56.368	56.484	56.639	55.788	56.223	56.899	56.970	53.133
CaO	37.525	39.210	38.683	38.631	38.677	39.283	37.240	36.419	37.240	37.161	37.073	31.603
MgO	0.020	n.a	n.a	n.a	n.a	n.a	b.d.	b.d.	0.007	0.005	b.d.	b.d.
FeO	1.519	1.412	1.749	1.226	1.215	1.217	0.774	1.151	0.737	0.727	0.726	0.912
MnO	0.009	n.a	n.a	n.a	n.a	n.a	0.024	0.033	0.035	0.032	0.041	0.008
Na2O	n.a	0.415	0.434	0.253	0.227	0.238	n.a	n.a	n.a	n.a	n.a	n.a
La2O3	1.358	0.712	1.286	0.358	0.430	0.465	0.802	1.230	0.683	0.618	0.656	1.653
Ce2O3	1.596	1.885	2.426	0.559	0.671	0.826	1.205	2.078	1.292	1.254	1.246	3.401
Pr2O3	0.154	n.a	n.a	0.048	0.058	0.077	0.165	0.244	0.112	0.253	0.182	0.237
Nd2O3	0.461	0.697	0.799	0.046	0.043	0.062	0.471	0.626	0.457	0.480	0.410	0.978
Sm2O3	0.085	0.084	0.081	0.039	0.043	0.046	0.103	0.083	0.072	0.041	0.092	0.040
Gd2O3	0.056	0.061	0.068	0.035	0.035	0.057	0.065	0.053	0.064	0.088	b.d	0.041
Y2O3	0.085	0.032	0.078	0.058	0.057	0.065	0.063	0.065	0.028	0.021	0.022	0.007
ThO2	n.a	n.a	n.a	n.a	n.a	n.a	n.a	n.a	n.a	n.a	n.a	n.a
ZrO2	0.106	n.a	n.a	0.106	0.099	0.107	0.021	0.020	0.014	0.016	0.009	0.004
SrO	0.923	0.296	0.372	0.802	0.812	0.844	1.764	1.920	2.623	2.556	2.516	3.274
Nb2O5	0.540	0.377	0.540	0.716	0.714	0.805	0.738	0.898	1.017	0.956	0.932	4.082
Ta2O5	0.002	n.a	n.a	n.a	n.a	n.a	0.045	0.080	0.035	b.d	0.004	0.119
Total	99.818	99.808	100.706	97.755	99.449	100.576	100.118	100.686	100.639	101.108	100.877	99.492
O=3												
Ti	0.9739	0.9606	0.9527	0.9623	0.9799	0.9717	0.9874	0.9779	0.9801	0.9858	0.9879	0.9614
Ca	0.9399	0.9821	0.9687	0.9648	0.9577	0.9626	0.9247	0.9093	0.9247	0.9171	0.9157	0.8145
Mg	0.0007								0.0002	0.0002		
Fe	0.0297	0.0276	0.0342	0.0239	0.0235	0.0233	0.0150	0.0224	0.0143	0.0140	0.0140	0.0183
Mn	0.0002						0.0005	0.0006	0.0007	0.0006	0.0008	0.0002
Na		0.0188	0.0197	0.0114	0.0102	0.0106						
La	0.0117	0.0061	0.0111	0.0031	0.0037	0.0039	0.0069	0.0106	0.0058	0.0052	0.0056	0.0147
Ce	0.0136	0.0161	0.0207	0.0048	0.0057	0.0069	0.0102	0.0177	0.0109	0.0106	0.0105	0.0299
Pr	0.0013			0.0004	0.0005	0.0006	0.0014	0.0021	0.0009	0.0021	0.0015	0.0021
Nd	0.0038	0.0058	0.0067	0.0004	0.0004	0.0005	0.0039	0.0052	0.0038	0.0039	0.0034	0.0084
Sm	0.0007	0.0007	0.0006	0.0003	0.0003	0.0004	0.0008	0.0007	0.0006	0.0003	0.0007	0.0003
Gd	0.0004	0.0005	0.0005	0.0003	0.0003	0.0004	0.0005	0.0004	0.0005	0.0007		0.0003
Y	0.0011	0.0004	0.0010	0.0007	0.0007	0.0008	0.0008	0.0008	0.0003	0.0003	0.0003	0.0001
Th												
Zr	0.0012			0.0012	0.0011	0.0012	0.0002	0.0002	0.0002	0.0002	0.0001	
Sr	0.0125	0.0040	0.0050	0.0108	0.0109	0.0112	0.0237	0.0259	0.0352	0.0341	0.0336	0.0457
Nb	0.0057	0.0040	0.0057	0.0075	0.0075	0.0083	0.0077	0.0095	0.0107	0.0100	0.0097	0.0444
Ta							0.0003	0.0005	0.0002			0.0008

Table A2.4 - Perovskite analyses

Sample	at033	at033	at033	at033	at033	at036	at036	at036	at038	at038	at038	at038
Unit	B2	B2	B2	B2	B2	B1	B1	B1	B2	B2	B2	B2
Rock type	beb	beb	beb	beb	beb	beb	beb	beb	beb	beb	beb	beb
Remarks		rim	core						tr6.3	tr6.4	tr6.5	tr6.6
TiO2	53.201	56.111	55.787	54.443	53.072	56.093	56.540	56.681	54.648	54.669	55.111	54.370
CaO	31.968	36.714	36.379	36.916	35.442	39.332	39.183	39.312	35.536	34.609	34.903	34.821
MgO	b.d.	0.000	b.d.	n.a	n.a	n.a	n.a	n.a	0.013	0.004	0.002	0.000
FeO	0.759	0.972	0.856	1.087	0.661	1.373	1.143	0.865	1.458	1.363	1.383	1.443
MnO	0.027	0.032	0.017	n.a	n.a	n.a	n.a	n.a	0.013	0.026	0.032	0.024
Na2O	n.a	n.a	n.a	0.907	1.514	0.216	0.256	0.256	n.a	n.a	n.a	n.a
La2O3	1.855	1.048	1.050	1.184	1.176	0.464	0.387	0.389	1:458	1.569	1.553	1.504
Ce2O3	3.543	1.851	1.784	2.383	2.594	0.810	0.736	0.673	2.838	3.077	3.016	3.477
Pr2O3	0.404	0.161	0.243	n.a	n.a	0.078	0.068	0.058	0.344	0.367	0.295	0.409
Nd2O3	0.949	0.609	0.622	0.771	0.860	0.061	0.049	0.045	1.003	1.249	1.019	1.230
Sm2O3	0.069	0.041	0.083	0.094	0.066	0.050	0.055	0.039	0.123	0.166	0.146	0.175
Gd2O3	0.016	0.041	0.059	0.069	0.033	0.048	0.049	0.035	0.079	0.067	0.106	0.084
Y2O3	b.d	0.067	0.043	0.049	0.000	0.051	0.046	0.056	0.047	0.051	0.057	0.042
ThO2	n.a	n.a	n.a	n.a	n.a	n.a	n.a	n.a	n.a	n.a	n.a	n.a
ZrO2	0.004	0.042	0.050	n.a	n.a	0.077	0.072	0.137	0.038	0.031	0.019	0.023
SrO	3.265	1.715	1.633	0.700	1.239	0.678	0.688	0.751	1.670	1.610	1.730	1.616
Nb2O5	3.719	1.081	1.121	1.409	2.719	0.638	0.580	0.636	1.019	1.145	1.050	0.975
Ta2O5	0.102	0.026	0.124	n.a	n.a	n.a	n.a	n.a	0.082	0.097	0.047	0.058
Total	99.882	100.512	99.851	100.012	99.377	99.969	99.852	99.933	100.370	100.099	100.468	100.251
O=3												
Ti	0.9609	0.9804	0.9814	0.9615	0.9489	0.9728	0.9738	0.9789	0.9691	0.974	0.976	0.9697
Ca	0.8224	0.9137	0.9115	0.9287	0.9026	0.9716	0.9613	0.9671	0.8976	0.8783	0.8804	0.8846
Mg									0.0005	0.0002	0.0001	
Fe	0.0152	0.0189	0.0167	0.0214	0.0131	0.0265	0.0219	0.0166	0.0288	0.027	0.0272	0.0286
Mn	0.0005	0.0006	0.0003						0.0003	0.0005	0.0006	0.0005
Na				0.0413	0.0698	0.0097	0.0114	0.0114				
La	0.0164	0.009	0.009	0.0102	0.0103	0.0039	0.0033	0.0033	0.0127	0.0137	0.0135	0.0131
Ce	0.0311	0.0157	0.0153	0.0205	0.0226	0.0068	0.0062	0.0057	0.0245	0.0267	0.026	0.0302
Pr	0.0035	0.0014	0.0021			0.0007	0.0006	0.0005	0.003	0.0032	0.0025	0.0035
Nd	0.0081	0.0051	0.0052	0.0065	0.0073	0.0005	0.0004	0.0004	0.0084	0.0106	0.0086	0.0104
Sm	0.0006	0.0003	0.0007	0.0008	0.0005	0.0004	0.0004	0.0003	0.001	0.0014	0.0012	0.0014
Gd	0.00013	0.00032	0.00045	0.00054	0.00026	0.00037	0.00037	0.00027	0.00062	0.00052	0.00082	0.00066
Y		0.0008	0.0005	0.0006		0.0006	0.0006	0.0007	0.0006	0.0006	0.0007	0.0005
Th												
Zr		0.0005	0.0006			0.0009	0.0008	0.0015	0.0004	0.0004	0.0002	0.0003
Sr	0.0455	0.0231	0.0221	0.0095	0.0171	0.0091	0.0091	0.01	0.0228	0.0221	0.0236	0.0222
Nb	0.0404	0.0114	0.0118	0.015	0.0292	0.0066	0.006	0.0066	0.0109	0.0123	0.0112	0.0105
Ta	0.0007	0.0002	0.0008						0.0005	0.0006	0.0003	0.0004

Table A2.4 - Perovskite analyses

Sample	at038	at038	at038	at038	at043	at113	at113	at113	at113	at113	at113
Unit	B2	B2	B2	B2	C3	B1	B1	B1	B1	B1	B1
Rock type	beb	beb	beb	beb	cbt	beb	beb	beb	beb	beb	beb
Remarks	tr6.7	rim	core					rim	core		
TiO2	54.470	54.571	54.922	55.221	42.766	56.947	56.837	56.622	56.478	55.312	55.305
CaO	34.572	35.965	35.491	35.476	18.664	38.601	38.236	37.973	38.476	39.850	39.824
MgO	0.001	0.013	b.d.	b.d.	n.a	b.d.	b.d.	0.006	b.d.	n.a	n.a
FeO	1.414	1.316	1.408	1.128	11.312	0.687	0.765	0.945	0.759	0.701	1.723
MnO	0.032	0.031	0.035	0.017	n.a	0.020	0.029	0.022	0.027	n.a	n.a
Na2O	n.a	n.a	n.a	n.a	3.616	n.a	n.a	n.a	n.a	0.394	0.335
La2O3	1.715	1.186	1.329	1.233	4.627	0.619	0.576	0.656	0.663	0.587	0.599
Ce2O3	3.323	2.305	2.483	2.979	10.300	0.746	0.846	0.872	0.946	0.912	0.904
Pr2O3	0.359	0.303	0.338	0.323	0.677	0.031	b.d	0.055	0.047	n.a	n.a
Nd2O3	1.314	0.861	0.876	1.013	2.892	0.226	0.241	0.198	0.247	0.249	0.236
Sm2O3	0.144	0.192	0.176	0.130	0.171	0.045	0.021	0.051	0.056	0.050	0.039
Gd2O3	0.130	0.124	0.061	0.028	0.102	b.d	0.031	0.016	0.023	0.047	0.035
Y2O3	0.058	0.091	0.095	0.039	0.042	0.040	0.049	0.043	0.040	0.047	0.042
ThO2	n.a	n.a	n.a	n.a	n.a	n.a	n.a	n.a	n.a	n.a	n.a
ZrO2	0.026	0.041	0.041	0.009	n.a	0.053	0.056	0.057	0.045	n.a	n.a
SrO	1.587	1.589	1.503	1.270	0.539	1.365	1.458	1.346	1.439	0.591	0.633
Nb2O5	0.978	1.073	1.325	1.273	0.447	0.972	0.879	0.974	0.997	0.898	0.945
Ta2O5	0.061	0.091	0.092	b.d	n.a	0.018	0.045	0.023	0.065	n.a	n.a
Total	100.182	99.751	100.174	100.139	96.15(*)	100.370	100.066	99.859	100.307	99.639	100.620
O=3											
Ti	0.9721	0.9685	0.9718	0.9771	0.8116	0.9832	0.9855	0.9839	0.9787	0.9653	0.9591
Ca	0.8789	0.9091	0.8945	0.8941	0.5045	0.9493	0.9443	0.9399	0.9498	0.9906	0.9837
Mg		0.0004						0.0002			
Fe	0.0281	0.026	0.0277	0.0222	0.2387	0.0132	0.0147	0.0183	0.0146	0.0136	0.0332
Mn	0.0006	0.0006	0.0007	0.0003		0.0004	0.0006	0.0004	0.0005		
Na					0.1769					0.0177	0.015
La	0.015	0.0103	0.0115	0.0107	0.043	0.0052	0.0049	0.0056	0.0056	0.005	0.0051
Ce	0.0288	0.0199	0.0214	0.0256	0.095	0.0063	0.0071	0.0074	0.008	0.0077	0.0076
Pr	0.0031	0.0026	0.0029	0.0028	0.0062	0.0003		0.0005	0.0004		
Nd	0.0111	0.0073	0.0074	0.0085	0.026	0.0019	0.002	0.0016	0.002	0.0021	0.0019
Sm	0.0012	0.0016	0.0014	0.0011	0.0015	0.0004	0.0002	0.0004	0.0004	0.0004	0.0003
Gd	0.00102	0.00096	0.00048	0.00022	0.00085		0.00023	0.00012	0.00017	0.00036	0.00026
Y	0.0007	0.0011	0.0012	0.0005	0.0006	0.0005	0.0006	0.0005	0.0005	0.0006	0.0005
Th											
Zr	0.0003	0.0005	0.0005	0.0001		0.0006	0.0006	0.0006	0.0005		
Sr	0.0218	0.0217	0.0205	0.0173	0.0079	0.0182	0.0195	0.018	0.0192	0.0079	0.0085
Nb	0.0105	0.0114	0.0141	0.0135	0.0051	0.0101	0.0092	0.0102	0.0104	0.0094	0.0098
Ta	0.0004	0.0006	0.0006			0.0001	0.0003	0.0001	0.0004		

(*)SiO2=5.0

Table A2.4 - Perovskite analyses

Sample	at120	at120	at120	at120	at120	at120	at120	at120	at120	at120	at120	at120
Unit												
Rock type	php	php	php	php	php	php	php	php	php	php	php	php
Remarks	tr16.3	tr16.5	tr16.7	tr16.9	tr16.10			tr19.1	tr19.3	tr19.5	tr19.6	
TiO2	56.085	56.001	55.587	55.956	55.642	56.069	56.009	55.694	56.363	56.146	54.628	56.494
CaO	36.146	36.516	36.258	36.332	35.825	36.851	36.378	36.748	36.606	37.351	35.716	36.503
MgO	0.038	0.037	0.046	0.041	0.082	0.033	0.033	0.031	0.025	0.018	0.927	0.050
FeO	1.352	1.331	1.372	1.364	1.413	1.326	1.353	1.405	1.338	1.451	1.661	1.519
MnO	0.010	0.017	0.025	0.024	0.032	0.021	0.022	0.026	0.034	0.020	0.006	0.016
Na2O	n.a	n.a	n.a	n.a	n.a	n.a	n.a	n.a	n.a	n.a	n.a	n.a
La2O3	0.864	0.925	1.051	0.984	1.056	0.992	0.930	0.922	0.854	0.781	0.677	0.859
Ce2O3	2.245	2.176	2.493	2.388	2.249	2.464	2.533	2.332	2.190	1.856	1.317	2.251
Pr2O3	0.287	0.290	0.442	0.286	0.307	0.177	0.220	0.327	0.235	0.198	0.073	0.198
Nd2O3	0.900	1.009	0.949	1.070	1.001	0.901	1.097	0.914	0.904	0.618	0.439	0.928
Sm2O3	0.088	0.089	0.133	0.092	0.132	0.116	0.153	0.107	0.071	0.073	0.069	0.078
Gd2O3	0.070	0.058	0.079	0.042	b.d	b.d	0.085	0.128	0.041	b.d	0.038	b.d
Y2O3	b.d	0.058	0.012	0.030	0.039	0.018	0.048	0.014	0.025	0.017	0.019	0.054
ThO2	n.a	n.a	n.a	n.a	n.a	n.a	n.a	n.a	n.a	n.a	n.a	n.a
ZrO2	0.020	0.025	0.013	0.018	0.013	0.017	0.022	0.020	0.025	0.030	0.032	0.021
SrO	0.776	0.757	0.737	0.765	0.747	0.719	0.733	0.750	0.776	0.859	0.972	0.754
Nb2O5	0.347	0.377	0.326	0.322	0.354	0.351	0.333	0.343	0.261	0.404	0.458	0.339
Ta2O5	0.075	0.050	0.068	0.039	0.028	0.022	0.043	0.091	0.090	0.017	0.019	0.072
Total	99.301	99.714	99.591	99.752	98.918	100.074	99.991	99.849	99.838	99.839	97.052	100.134
O=3												
Ti	0.9892	0.9847	0.9827	0.9850	0.9851	0.9831	0.9853	0.9801	0.9885	0.9822	0.9585	0.9874
Ca	0.9081	0.9146	0.9130	0.9110	0.9035	0.9203	0.9115	0.9211	0.9144	0.9307	0.8926	0.9087
Mg	0.0013	0.0013	0.0016	0.0014	0.0029	0.0011	0.0012	0.0011	0.0009	0.0006	0.0322	0.0017
Fe	0.0265	0.0260	0.0270	0.0267	0.0278	0.0258	0.0265	0.0275	0.0261	0.0282	0.0324	0.0295
Mn	0.0002	0.0003	0.0005	0.0005	0.0006	0.0004	0.0004	0.0005	0.0007	0.0004	0.0001	0.0003
Na												
La	0.0075	0.0080	0.0091	0.0085	0.0092	0.0085	0.0080	0.0079	0.0073	0.0067	0.0058	0.0074
Ce	0.0192	0.0186	0.0214	0.0204	0.0194	0.0210	0.0217	0.0200	0.0187	0.0158	0.0112	0.0191
Pr	0.0024	0.0025	0.0038	0.0024	0.0026	0.0015	0.0019	0.0028	0.0020	0.0017	0.0006	0.0017
Nd	0.0075	0.0084	0.0080	0.0089	0.0084	0.0075	0.0092	0.0076	0.0075	0.0051	0.0037	0.0077
Sm	0.0007	0.0007	0.0011	0.0007	0.0011	0.0009	0.0012	0.0009	0.0006	0.0006	0.0006	0.0006
Gd	0.0005	0.0005	0.0006	0.0003			0.0007	0.0010	0.0003		0.0003	
Y		0.0007	0.0002	0.0004	0.0005	0.0002	0.0006	0.0002	0.0003	0.0002	0.0002	0.0007
Th												
Zr	0.0002	0.0003	0.0001	0.0002	0.0002	0.0002	0.0003	0.0002	0.0003	0.0003	0.0004	0.0002
Sr	0.0106	0.0103	0.0100	0.0104	0.0102	0.0097	0.0099	0.0102	0.0105	0.0116	0.0131	0.0102
Nb	0.0037	0.0040	0.0035	0.0034	0.0038	0.0037	0.0035	0.0036	0.0028	0.0042	0.0048	0.0036
Ta	0.0005	0.0003	0.0004	0.0002	0.0002	0.0001	0.0003	0.0006	0.0006	0.0001	0.0001	0.0005

Table A2.4 - Perovskite analyses

Sample	at206	at206	at206	at217	at217	at217	at217	at217	at217	at217	at217
Unit				B1	B1	B1	B1	B1	B1	B1	B1
Rock type	php	php	php	wehrl	wehrl	wehrl	wehrl	wehrl	wehrl	wehrl	wehrl
Remarks	pheno	pheno	pheno								
TiO2	55.545	55.596	55.775	48.887	55.119	52.298	54.897	55.518	54.880	55.602	48.977
CaO	36.526	36.435	36.646	33.911	38.214	36.518	37.407	38.870	38.082	38.146	34.240
MgO	0.093	0.038	0.034	0.447	0.060	0.012	0.033	0.013	0.051	0.090	0.172
FeO	1.108	1.161	1.185	3.389	1.540	2.585	1.734	1.428	1.474	1.308	3.552
MnO	n.a.	n.a.	n.a.	n.a.	n.a.	n.a.	n.a.	n.a.	n.a.	n.a.	n.a.
Na2O	0.855	0.808	0.877	0.963	0.403	0.636	0.549	0.326	0.396	0.415	1.082
La2O3	1.169	1.084	1.118	1.904	0.992	1.456	1.137	0.920	1.090	0.898	1.902
Ce2O3	2.916	2.969	2.989	4.456	2.051	3.019	2.671	1.571	2.073	2.217	4.370
Pr2O3	n.a	n.a	n.a	n.a	n.a	n.a	n.a	n.a	n.a	n.a	n.a
Nd2O3	1.339	1.380	1.352	1.756	0.714	1.136	1.231	0.648	0.661	0.966	1.737
Sm2O3	n.a	n.a	n.a	n.a	n.a	n.a	n.a	n.a	n.a	n.a	n.a
Gd2O3	0.093	0.058	0.106	0.052	b.d	0.027	0.079	b.d	0.106	0.115	0.117
Y2O3	0.068	0.047	0.026	0.072	0.051	0.075	0.034	0.002	0.046	0.067	0.004
ThO2	0.393	0.348	0.323	0.116	0.095	0.145	0.418	0.025	0.148	0.213	0.181
ZrO2	0.039	0.079	0.047	0.339	0.289	0.290	0.162	0.258	0.142	0.037	0.516
SrO	0.297	0.313	0.321	0.368	0.395	0.367	0.304	0.452	0.404	0.329	0.309
Nb2O5	0.545	0.494	0.527	3.068	0.939	2.201	0.344	0.780	0.693	0.389	3.644
Ta2O5	0.116	0.076	0.056	0.029	0.034	0.001	b.d	0.021	0.057	b.d	b.d
Total	101.101	100.885	101.384	99.757	100.897	100.765	100.999	100.831	100.300	100.792	100.802
O=3											
Ti	0.9689	0.9702	0.9702	0.8848	0.9571	0.9244	0.9601	0.9588	0.9593	0.9658	0.8860
Ca	0.9075	0.9057	0.9080	0.8742	0.9451	0.9194	0.9318	0.9562	0.9482	0.9438	0.8822
Mg	0.0032	0.0013	0.0012	0.0160	0.0021	0.0004	0.0011	0.0004	0.0018	0.0031	0.0062
Fe	0.0215	0.0225	0.0229	0.0682	0.0297	0.0508	0.0337	0.0274	0.0286	0.0253	0.0714
Mn											
Na	0.0385	0.0363	0.0393	0.0449	0.0180	0.0290	0.0248	0.0145	0.0178	0.0186	0.0505
La	0.0100	0.0093	0.0095	0.0169	0.0084	0.0126	0.0097	0.0078	0.0093	0.0076	0.0169
Ce	0.0247	0.0252	0.0253	0.0392	0.0173	0.0259	0.0227	0.0132	0.0176	0.0187	0.0384
Pr											
Nd	0.0111	0.0114	0.0112	0.0151	0.0059	0.0095	0.0102	0.0053	0.0055	0.0080	0.0149
Sm											
Gd	0.0007	0.0005	0.0008	0.0004		0.0002	0.0006		0.0008	0.0009	0.0009
Y	0.0008	0.0006	0.0003	0.0009	0.0006	0.0009	0.0004		0.0006	0.0008	0.0001
Th	0.0021	0.0018	0.0017	0.0006	0.0005	0.0008	0.0022	0.0001	0.0008	0.0011	0.0010
Zr	0.0004	0.0009	0.0005	0.0040	0.0033	0.0033	0.0018	0.0029	0.0016	0.0004	0.0060
Sr	0.0040	0.0042	0.0043	0.0051	0.0053	0.0050	0.0041	0.0060	0.0054	0.0044	0.0043
Nb	0.0057	0.0052	0.0055	0.0334	0.0098	0.0234	0.0036	0.0081	0.0073	0.0041	0.0396
Ta	0.0007	0.0005	0.0004	0.0002	0.0002			0.0001	0.0004		

Table A2.5 - Spinel analyses

Sample	at003	at003	at003	at003	at003	at009	at009	at009	at009	at009	at013	at013
Unit	B1	B1	B1	B1	B1	B1	B1	B1	B1	B1		
Rock type	beb	beb	beb	beb	beb	beb	beb	beb	beb	beb	php	php
SiO2	0.20	0.25	0.17	0.16	0.15	0.50	0.23	0.17	0.92	0.15	0.24	0.27
TiO2	6.47	4.38	3.68	7.57	6.26	6.96	7.57	8.68	7.90	7.64	13.88	14.79
Al2O3	0.20	0.16	0.05	0.18	0.20	0.01	0.02	0.19	0.06	0.05	2.69	2.69
Cr2O3	0.00	0.00	0.07	0.02	0.03	0.05	0.02	0.01	0.00	0.01	0.00	5.57
FeO	35.19	33.77	32.84	36.18	34.46	35.78	36.63	35.59	34.97	36.28	31.14	38.50
Fe2O3	55.53	59.63	61.84	53.87	56.92	55.05	53.79	53.03	51.76	53.60	41.15	31.78
MnO	1.00	0.73	0.62	1.12	1.04	0.50	0.59	0.77	0.71	0.55	0.67	1.35
MgO	0.57	0.52	0.43	0.62	0.46	0.57	0.50	1.51	1.62	1.31	7.28	3.22
CaO	0.00	0.01	0.01	0.02	0.04	0.04	0.02	0.03	0.45	0.02	0.16	0.12
Total	99.16	99.45	99.71	99.73	99.56	99.46	99.36	99.97	98.39	99.61	97.21	98.28
O=32												
Si	0.06	0.08	0.05	0.05	0.05	0.15	0.07	0.05	0.28	0.04	0.07	0.08
Ti	1.49	1.01	0.85	1.73	1.44	1.59	1.74	1.96	1.81	1.74	3.02	3.27
Al	0.07	0.06	0.02	0.06	0.07	0.00	0.01	0.07	0.02	0.02	0.92	0.93
Cr	0.00	0.00	0.02	0.01	0.01	0.01	0.00	0.00	0.00	0.00	0.00	1.30
Fe2	9.01	8.62	8.38	9.17	8.78	9.11	9.35	8.93	8.89	9.20	7.53	9.48
Fe3	12.80	13.70	14.21	12.29	13.06	12.61	12.35	11.97	11.84	12.22	8.96	7.04
Mn	0.26	0.19	0.16	0.29	0.27	0.13	0.15	0.20	0.18	0.14	0.16	0.34
Mg	0.26	0.24	0.20	0.28	0.21	0.26	0.23	0.68	0.73	0.59	3.14	1.41
Ca	0.00	0.00	0.00	0.01	0.01	0.01	0.01	0.01	0.15	0.01	0.05	0.04
Total	23.96	23.88	23.88	23.88	23.89	23.87	23.90	23.85	23.90	23.96	23.86	23.88

Table A2.5 - Spinel analyses

Sample	at016	at016	at016	at016	at016	at016	at021	at021	at021	at021	at021	at021
Unit	B1	B1	B1	B1	B1	B1						
Rock type	wehrl	wehrl	wehrl	wehrl	wehrl	wehrl	php	php	php	php	php	php
SiO2	0.18	0.13	0.16	0.18	0.11	0.16	0.19	0.21	0.71	0.19	0.25	0.19
TiO2	4.40	8.61	7.96	3.85	5.49	6.46	5.40	15.88	14.95	15.77	12.20	14.97
Al2O3	0.12	0.91	0.72	0.13	0.04	0.03	8.09	2.74	2.69	2.51	2.09	2.62
Cr2O3	0.11	0.01	0.02	0.02	0.05	0.05	43.60	1.71	0.10	0.30	0.06	0.15
FeO	31.36	32.19	31.67	31.80	32.50	33.20	19.97	29.01	30.63	30.18	27.70	28.80
Fe2O3	59.82	52.75	54.61	60.74	57.61	55.50	9.23	38.38	39.85	39.26	46.52	41.54
MnO	0.62	0.72	0.74	0.79	0.55	0.74	0.43	0.58	0.56	0.48	0.58	0.59
MgO	1.78	3.86	3.58	0.84	2.08	2.27	11.64	9.95	8.90	9.51	8.45	9.52
CaO	0.13	0.00	0.00	0.13	0.04	0.03	0.06	0.22	0.21	0.25	0.51	0.33
Total	98.52	99.18	99.46	98.48	98.47	98.44	98.61	98.67	98.61	98.46	98.36	98.70
O=32												
Si	0.05	0.04	0.05	0.06	0.03	0.05	0.05	0.06	0.20	0.05	0.07	0.05
Ti	1.01	1.92	1.77	0.89	1.26	1.48	1.09	3.33	3.17	3.34	2.62	3.16
Al	0.04	0.32	0.25	0.05	0.01	0.01	2.55	0.90	0.89	0.83	0.70	0.87
Cr	0.03	0.00	0.01	0.01	0.01	0.01	9.20	0.38	0.02	0.07	0.01	0.03
Fe2	8.02	7.99	7.84	8.19	8.30	8.47	4.46	6.77	7.22	7.11	6.61	6.76
Fe3	13.76	11.78	12.16	14.08	13.25	12.74	1.86	8.06	8.45	8.32	9.98	8.77
Mn	0.16	0.18	0.19	0.21	0.14	0.19	0.10	0.14	0.13	0.12	0.14	0.14
Mg	0.81	1.71	1.58	0.39	0.95	1.03	4.64	4.14	3.74	3.99	3.59	3.98
Ca	0.04	0.00	0.00	0.04	0.01	0.01	0.02	0.07	0.06	0.08	0.15	0.10
Total	23.92	23.93	23.83	23.91	23.98	23.99	23.95	23.85	23.88	23.91	23.88	23.85

Table A2.5 - Spinel analyses

Sample	at021	at021	at021	at021	at022	at022	at022	at022	at022	at022	at022	at022
Unit												
Rock type	php	php	php	php	php	php	php	php	php	php	php	php
SiO2	0.24	0.24	0.21	0.16	0.18	0.18	0.18	0.16	0.21	0.19	0.11	0.18
TiO2	13.11	11.34	14.56	12.61	6.99	8.09	5.85	7.06	9.92	9.55	11.96	11.12
Al2O3	2.74	2.63	2.62	2.63	4.44	4.42	5.28	4.61	4.07	4.15	3.21	3.18
Cr2O3	0.02	0.00	0.06	0.02	38.33	34.84	40.43	37.78	27.21	27.53	20.12	22.11
FeO	29.41	28.08	29.07	27.72	22.60	22.38	21.40	22.68	24.81	24.90	27.76	27.05
Fe2O3	43.36	47.63	41.36	46.64	15.89	18.78	15.04	15.84	21.17	20.68	25.38	24.03
MnO	0.63	0.57	0.57	0.59	0.30	0.28	0.40	0.45	0.27	0.40	0.27	0.32
MgO	8.69	8.24	9.28	8.66	10.32	10.32	10.56	10.07	10.10	9.78	8.97	9.13
CaO	0.24	0.26	0.24	0.33	0.02	0.00	0.05	0.01	0.00	0.00	0.07	0.06
Total	98.44	98.98	97.98	99.37	99.06	99.29	99.18	98.66	97.77	97.17	97.85	97.18
O=32												
Si	0.07	0.07	0.06	0.05	0.05	0.05	0.05	0.04	0.06	0.05	0.03	0.05
Ti	2.80	2.42	3.11	2.66	1.44	1.65	1.20	1.45	2.07	2.01	2.53	2.37
Al	0.92	0.88	0.88	0.87	1.43	1.41	1.69	1.49	1.33	1.37	1.06	1.06
Cr	0.00	0.00	0.01	0.00	8.26	7.48	8.67	8.17	5.96	6.08	4.47	4.94
Fe2	7.00	6.67	6.90	6.51	5.16	5.09	4.86	5.19	5.75	5.82	6.53	6.40
Fe3	9.28	10.18	8.83	9.86	3.26	3.84	3.07	3.26	4.42	4.35	5.38	5.12
Mn	0.15	0.14	0.14	0.14	0.07	0.07	0.09	0.11	0.06	0.10	0.07	0.08
Mg	3.68	3.49	3.93	3.63	4.20	4.18	4.28	4.11	4.18	4.08	3.76	3.85
Ca	0.07	0.08	0.07	0.10	0.01	0.00	0.01	0.00	0.00	0.00	0.02	0.02
Total	23.98	23.91	23.93	23.82	23.86	23.76	23.91	23.84	23.82	23.85	23.86	23.89

Table A2.5 - Spinel analyses

Sample	at022	at022	at022	at022	at024	at024	at024	at024	at024	at024	at025	at025
Unit											B1	B1
Rock type	php	php	php	php	lcr	lcr	lcr	lcr	lcr	lcr	wehrl	wehrl
SiO2	0.18	0.20	0.17	0.09	0.22	0.19	0.32	0.23	0.28	0.23	0.13	0.28
TiO2	11.76	6.31	3.48	3.61	12.18	12.06	11.54	15.10	14.72	11.94	12.78	1.98
Al2O3	3.70	4.70	0.12	0.05	1.09	1.04	1.38	1.41	1.60	1.15	0.36	0.47
Cr2O3	23.25	36.96	0.06	0.09	0.00	0.03	0.08	0.03	0.05	0.04	1.65	0.91
FeO	26.21	22.45	26.67	26.93	32.46	31.27	31.58	37.39	40.81	31.73	32.58	29.65
Fe2O3	21.98	17.54	63.16	63.36	45.06	46.09	46.02	38.87	38.16	46.94	45.82	64.28
MnO	0.29	0.34	0.81	0.84	0.76	0.76	0.81	0.46	0.47	0.73	1.74	0.90
MgO	10.16	9.57	3.44	3.35	5.11	6.17	5.86	3.98	1.32	5.72	5.18	2.11
CaO	0.13	0.16	0.05	0.03	0.16	0.50	0.34	0.09	0.11	0.16	0.08	0.04
Total	97.67	98.23	97.95	98.34	97.04	98.10	97.93	97.56	97.52	98.65	100.33	100.59
O=32												
Si	0.05	0.06	0.05	0.03	0.07	0.06	0.09	0.07	0.09	0.07	0.04	0.08
Ti	2.46	1.31	0.79	0.82	2.73	2.66	2.55	3.38	3.36	2.62	2.77	0.44
Al	1.21	1.53	0.04	0.02	0.38	0.36	0.48	0.50	0.57	0.40	0.12	0.16
Cr	5.12	8.07	0.01	0.02	0.00	0.01	0.02	0.01	0.01	0.01	0.37	0.21
Fe2	6.11	5.19	6.76	6.80	8.10	7.67	7.76	9.31	10.34	7.74	7.84	7.38
Fe3	4.61	3.65	14.40	14.40	10.11	10.18	10.18	8.70	8.70	10.30	9.92	14.40
Mn	0.07	0.08	0.21	0.22	0.19	0.19	0.20	0.12	0.12	0.18	0.42	0.23
Mg	4.22	3.94	1.56	1.51	2.27	2.70	2.57	1.76	0.60	2.49	2.22	0.94
Ca	0.04	0.05	0.02	0.01	0.05	0.16	0.11	0.03	0.04	0.05	0.02	0.01
Total	23.89	23.87	23.83	23.82	23.90	23.97	23.95	23.87	23.82	23.86	23.73	23.86

Table A2.5 - Spinel analyses

Sample	at025	at025(*)	at025	at025	at025	at025	at025	at025	at025	at025	at025
Unit	B1	B1	B1	B1	B1	B1	B1	B1	B1	B1	B1
Rock type	wehrl	wehrl	wehrl	wehrl	wehrl	wehrl	wehrl	wehrl	wehrl	wehrl	wehrl
SiO2	0.27	0.10	1.63	0.15	0.18	0.14	0.21	0.21	0.21	0.14	0.19
TiO2	7.73	1.15	3.72	6.49	10.59	2.67	0.81	0.94	1.09	4.59	1.29
Al2O3	0.03	0.16	0.00	0.00	0.00	0.00	0.01	0.00	0.03	0.05	0.08
Cr2O3	1.46	1.80	1.23	1.45	1.63	1.55	1.44	1.92	1.68	1.81	1.51
FeO	31.86	30.48	28.97	32.14	32.53	29.40	29.09	29.08	30.02	28.70	29.13
Fe2O3	53.95	65.00	57.72	55.53	48.55	63.32	66.02	66.28	65.15	60.69	65.79
MnO	1.27	0.44	0.75	1.17	1.54	0.61	0.46	0.44	0.52	0.90	0.59
MgO	3.31	1.34	3.34	2.38	4.12	1.97	1.50	1.49	1.63	4.05	1.91
CaO	0.14	0.00	0.07	0.00	0.16	0.02	0.45	0.03	0.01	0.11	0.11
Total	100.02	100.48	97.42	99.30	99.30	99.68	99.97	100.39	100.33	101.03	100.60
O=32											
Si	0.08	0.03	0.49	0.05	0.05	0.04	0.06	0.06	0.06	0.04	0.06
Ti	1.72	0.26	0.84	1.47	2.35	0.61	0.18	0.21	0.25	1.01	0.29
Al	0.01	0.06	0.00	0.00	0.00	0.00	0.00	0.00	0.01	0.02	0.03
Cr	0.34	0.43	0.29	0.35	0.38	0.37	0.34	0.46	0.40	0.42	0.36
Fe2	7.90	7.71	7.32	8.11	8.01	7.40	7.36	7.30	7.54	7.03	7.31
Fe3	12.03	14.78	13.12	12.61	10.75	14.34	15.04	14.98	14.72	13.38	14.85
Mn	0.32	0.11	0.19	0.30	0.38	0.16	0.12	0.11	0.13	0.22	0.15
Mg	1.46	0.60	1.50	1.07	1.81	0.88	0.68	0.67	0.73	1.77	0.86
Ca	0.04	0.00	0.02	0.00	0.05	0.01	0.15	0.01	0.00	0.04	0.03
Total	23.91	23.99	23.78	23.95	23.78	23.79	23.93	23.80	23.84	23.92	23.93

(*) with exsolved ilmenite
(see Table A2.6)

Table A2.5 - Spinel analyses

Sample	at038	at038	at038	at038	at038	at038	at038	at038	at038	at043	at043	at043
Unit	B2	B2	B2	B2	B2	B2	B2	B2	B2	C3	C3	C3
Rock type	beb	beb	beb	beb	beb	beb	beb	beb	beb	cbt	cbt	cbt
SiO2	0.12	0.16	0.13	0.22	0.23	0.12	0.16	0.23	0.09	0.15	0.16	0.12
TiO2	0.97	1.61	2.15	0.35	0.64	1.85	1.83	1.82	4.43	4.03	4.73	3.82
Al2O3	0.04	0.00	0.05	0.00	0.03	0.03	0.03	0.08	0.00	0.06	0.00	0.01
Cr2O3	0.10	0.03	0.08	0.06	0.03	0.08	0.07	0.00	0.03	0.11	0.11	0.09
FeO	31.21	30.88	31.34	30.23	29.18	30.49	30.86	30.71	32.63	31.09	31.34	30.58
Fe2O3	68.02	66.23	64.73	67.39	68.62	66.06	65.63	65.56	60.80	58.47	56.38	58.34
MnO	0.28	0.62	0.87	0.48	0.50	0.82	0.88	0.87	1.53	1.12	1.30	1.08
MgO	0.29	0.18	0.25	0.12	0.33	0.28	0.28	0.28	0.41	0.44	0.49	0.39
CaO	0.00	0.22	0.12	0.41	0.36	0.15	0.13	0.05	0.02	0.02	0.03	0.01
Total	101.03	99.93	99.72	99.27	99.91	99.88	99.86	99.60	99.93	95.49	94.54	94.44
O=32												
Si	0.04	0.05	0.04	0.07	0.07	0.04	0.05	0.07	0.03	0.05	0.05	0.04
Ti	0.22	0.37	0.50	0.08	0.15	0.43	0.42	0.42	1.02	0.97	1.14	0.93
Al	0.01	0.00	0.02	0.00	0.01	0.01	0.01	0.03	0.00	0.02	0.00	0.00
Cr	0.02	0.01	0.02	0.02	0.01	0.02	0.02	0.00	0.01	0.03	0.03	0.02
Fe2	7.90	7.89	8.02	7.82	7.44	7.78	7.89	7.86	8.32	8.28	8.42	8.24
Fe3	15.49	15.23	14.91	15.68	15.74	15.17	15.10	15.10	13.95	14.02	13.63	14.14
Mn	0.07	0.16	0.23	0.13	0.13	0.21	0.23	0.23	0.39	0.30	0.35	0.29
Mg	0.13	0.08	0.11	0.06	0.15	0.13	0.13	0.13	0.19	0.21	0.24	0.19
Ca	0.00	0.07	0.04	0.14	0.12	0.05	0.04	0.02	0.01	0.01	0.01	0.00
Total	23.88	23.87	23.89	23.98	23.81	23.83	23.89	23.85	23.91	23.88	23.87	23.86

Table A2.5 - Spinel analyses

Sample	at043	at043	at043	at043	at043	at043	at044	at104	at104	at104	at104(*)	at113
Unit	C3	C3	C3	C3	C3	C3	C1					B1
Rock type	cbt	cbt	cbt	cbt	cbt	cbt	cbt	RR	RR	RR	RR	beb
SiO2	0.13	0.14	0.20	0.47	0.17	0.11	0.17	0.10	0.17	0.16	0.14	0.15
TiO2	5.03	4.09	7.44	3.68	3.73	5.18	5.77	3.73	0.78	0.76	0.97	6.07
Al2O3	0.02	0.02	0.00	0.00	0.07	0.10	0.84	0.00	0.00	0.00	0.09	0.13
Cr2O3	0.06	0.09	0.09	0.11	0.11	0.08	0.09	0.22	0.24	0.23	0.24	0.03
FeO	32.42	31.58	33.32	31.74	31.58	32.35	35.61	34.29	32.22	32.60	32.02	32.66
Fe2O3	55.74	58.40	51.64	58.14	58.32	56.28	56.01	62.49	68.20	67.59	66.83	58.09
MnO	1.25	1.10	2.11	1.05	1.06	1.30	0.28	0.17	0.05	0.07	0.00	1.16
MgO	0.44	0.51	0.71	0.45	0.38	0.57	0.35	0.30	0.15	0.22	0.19	0.97
CaO	0.01	0.00	0.15	0.07	0.05	0.02	0.15	0.01	0.03	0.01	0.05	0.00
Total	95.10	95.93	95.66	95.71	95.47	95.99	99.27	101.32	101.85	101.65	100.53	99.26
O=32												
Si	0.04	0.05	0.06	0.15	0.06	0.04	0.05	0.03	0.05	0.05	0.04	0.05
Ti	1.21	0.98	1.77	0.88	0.90	1.23	1.33	0.84	0.18	0.17	0.22	1.38
Al	0.01	0.01	0.00	0.00	0.03	0.04	0.30	0.00	0.00	0.00	0.03	0.05
Cr	0.02	0.02	0.02	0.03	0.03	0.02	0.02	0.05	0.06	0.06	0.06	0.01
Fe2	8.69	8.38	8.81	8.43	8.43	8.54	9.09	8.63	8.13	8.23	8.18	8.28
Fe3	13.44	13.95	12.29	13.89	14.02	13.38	12.86	14.14	15.49	15.36	15.36	13.25
Mn	0.34	0.30	0.57	0.28	0.29	0.35	0.07	0.04	0.01	0.02	0.00	0.30
Mg	0.21	0.24	0.34	0.21	0.18	0.27	0.16	0.13	0.07	0.10	0.09	0.44
Ca	0.00	0.00	0.05	0.02	0.02	0.01	0.05	0.00	0.01	0.00	0.02	0.00
Total	23.96	23.93	23.91	23.89	23.94	23.87	23.93	23.88	24.00	23.99	24.00	23.74

(*) with exsolved ilmenite
(see Table A2.6)

Table A2.5 - Spinel analyses

Sample	at113	at113	at113	at113	at113	at113	at120	at120	at120	at120	at120	at120
Unit	B1	B1	B1	B1	B1	B1						
Rock type	beb	beb	beb	beb	beb	beb	php	php	php	php	php	php
SiO2	0.20	0.14	0.11	0.14	0.17	0.25	0.22	0.16	0.13	0.14	0.21	0.30
TiO2	2.87	0.60	6.54	4.80	6.25	8.27	15.71	11.59	16.83	13.37	16.74	15.37
Al2O3	0.11	0.12	0.08	0.03	0.06	0.44	1.28	1.19	1.28	1.42	1.34	1.27
Cr2O3	0.01	0.04	0.04	0.00	0.00	0.05	0.02	0.03	0.11	0.05	0.02	0.05
FeO	32.75	30.69	34.65	33.46	34.91	36.21	36.68	33.73	35.97	34.49	33.06	36.51
Fe2O3	61.83	67.29	55.64	58.10	55.23	52.45	38.04	47.26	35.88	42.83	39.17	39.04
MnO	0.67	0.18	1.11	1.05	1.06	1.16	1.79	1.63	1.56	1.51	0.62	1.39
MgO	0.27	0.21	0.86	0.78	0.81	0.87	4.28	3.16	5.68	4.19	8.46	4.44
CaO	0.15	0.03	0.02	0.00	0.01	0.02	0.04	0.13	0.00	0.05	0.06	0.08
Total	98.86	99.29	99.04	98.36	98.50	99.71	98.06	98.89	97.43	98.05	99.68	98.45
O=32												
Si	0.06	0.04	0.03	0.04	0.05	0.08	0.06	0.05	0.04	0.04	0.06	0.09
Ti	0.67	0.14	1.50	1.12	1.45	1.88	3.49	2.57	3.72	2.98	3.55	3.40
Al	0.04	0.04	0.03	0.01	0.02	0.16	0.44	0.42	0.44	0.49	0.44	0.44
Cr	0.00	0.01	0.01	0.00	0.00	0.01	0.01	0.01	0.03	0.01	0.00	0.01
Fe2	8.48	7.92	8.86	8.64	8.99	9.13	9.05	8.32	8.84	8.53	7.81	8.98
Fe3	14.40	15.62	12.80	13.50	12.80	11.90	8.45	10.50	7.94	9.54	8.32	8.64
Mn	0.18	0.05	0.29	0.28	0.28	0.30	0.45	0.41	0.39	0.38	0.15	0.35
Mg	0.13	0.10	0.39	0.36	0.37	0.39	1.88	1.39	2.49	1.85	3.56	1.95
Ca	0.05	0.01	0.01	0.00	0.00	0.01	0.01	0.04	0.00	0.01	0.02	0.02
Total	24.00	23.92	23.92	23.95	23.97	23.85	23.85	23.70	23.88	23.83	23.91	23.88

Table A2.5 - Spinel analyses

Sample	at120	at120	at120	at120	at120	at131	at131	at131	at131	at201	at201	at204
Unit						C4	C4	C4	C4			
Rock type	php	php	php	php	php	cbt	cbt	cbt	cbt	lcr	lcr	php
SiO2	0.23	0.14	0.27	0.25	0.19	0.13	0.16	0.11	0.15	0.17	0.21	0.17
TiO2	16.21	16.21	16.51	16.20	15.42	3.05	2.99	3.23	3.36	12.16	12.36	6.07
Al2O3	1.17	1.41	1.16	1.27	1.00	0.06	0.15	0.10	0.25	0.97	1.12	7.57
Cr2O3	0.13	0.11	0.68	0.12	0.72	0.10	0.02	0.00	0.02	0.03	0.02	39.70
FeO	35.12	36.53	34.68	39.18	38.38	28.10	29.44	26.63	27.60	30.68	31.14	22.96
Fe2O3	38.43	37.58	37.38	36.80	37.77	63.59	62.27	63.70	62.62	46.17	46.25	11.88
MnO	1.19	1.94	1.62	2.76	2.66	0.94	0.72	1.21	1.32	0.95	0.70	0.60
MgO	6.06	4.07	5.61	2.34	1.88	2.63	2.10	3.33	3.19	5.99	5.86	9.47
CaO	0.00	0.03	0.10	0.06	0.14	0.08	0.13	0.09	0.06	0.28	0.21	0.14
Total	98.53	98.02	98.02	98.97	98.16	98.68	97.98	98.40	98.57	97.41	97.87	98.56
O=32												
Si	0.07	0.04	0.08	0.07	0.06	0.04	0.05	0.03	0.05	0.05	0.06	0.05
Ti	3.53	3.59	3.62	3.61	3.47	0.70	0.69	0.73	0.77	2.70	2.72	1.24
Al	0.40	0.49	0.40	0.44	0.35	0.02	0.05	0.04	0.09	0.34	0.39	2.43
Cr	0.03	0.03	0.16	0.03	0.17	0.02	0.01	0.00	0.01	0.01	0.00	8.53
Fe2	8.52	8.99	8.45	9.69	9.61	7.14	7.57	6.72	6.99	7.56	7.62	5.22
Fe3	8.38	8.32	8.19	8.19	8.51	14.53	14.40	14.46	14.27	10.24	10.18	2.43
Mn	0.29	0.48	0.40	0.69	0.68	0.24	0.19	0.31	0.34	0.24	0.17	0.14
Mg	2.62	1.79	2.44	1.03	0.84	1.19	0.96	1.50	1.44	2.63	2.55	3.84
Ca	0.00	0.01	0.03	0.02	0.05	0.03	0.04	0.03	0.02	0.09	0.07	0.04
Total	23.84	23.73	23.76	23.77	23.74	23.90	23.96	23.82	23.97	23.85	23.75	23.92

Table A2.5 - Spinel analyses

Sample	at204	at204	at204	at204	at204	at212	at212	at212	at212	at217	at217	at217
Unit						C2	C2	C2	C2	B1	B1	B1
Rock type	php	php	php	php	php	cbt,dk	cbt,dk	cbt,dk	cbt,dk	wehrl	wehrl	wehrl
SiO2	2.56	0.66	0.20	0.13	0.61	0.98	4.75	0.29	0.20	0.20	0.11	0.16
TiO2	15.62	13.63	14.32	9.81	15.49	10.03	8.13	10.70	11.04	4.48	1.60	3.03
Al2O3	0.94	1.21	1.59	0.63	1.38	0.48	0.55	0.77	0.42	0.06	0.00	0.00
Cr2O3	0.38	0.36	0.20	0.07	0.29	0.02	0.09	0.01	0.00	0.28	0.27	0.34
FeO	43.08	41.71	42.77	35.15	42.92	37.74	36.70	37.03	40.13	30.85	29.08	29.37
Fe2O3	31.47	38.09	36.43	48.57	34.20	47.61	43.29	37.35	45.12	60.47	66.06	63.31
MnO	0.45	0.62	0.80	0.79	0.84	0.40	0.31	0.38	0.56	1.10	0.53	1.12
MgO	1.52	0.38	0.18	2.09	0.42	0.40	1.55	0.23	0.15	1.79	1.24	1.61
CaO	0.00	0.30	0.12	0.16	0.14	0.66	1.07	1.24	0.52	0.00	0.06	0.04
Total	96.02	96.96	96.61	97.40	96.29	98.32	96.44	87.98	98.14	99.23	98.96	98.99
O=32												
Si	0.78	0.20	0.06	0.04	0.19	0.30	1.42	0.10	0.06	0.06	0.03	0.05
Ti	3.56	3.16	3.35	2.26	3.59	2.29	1.83	2.73	2.55	1.02	0.37	0.69
Al	0.34	0.44	0.58	0.23	0.50	0.17	0.19	0.31	0.15	0.02	0.00	0.00
Cr	0.09	0.09	0.05	0.02	0.07	0.00	0.02	0.00	0.00	0.07	0.07	0.08
Fe2	10.91	10.75	11.11	9.01	11.07	9.59	9.17	10.51	10.31	7.84	7.45	7.49
Fe3	7.17	8.83	8.51	11.20	7.94	10.88	9.73	9.54	10.43	13.82	15.23	14.53
Mn	0.12	0.16	0.21	0.21	0.22	0.10	0.08	0.11	0.15	0.28	0.14	0.29
Mg	0.69	0.17	0.08	0.96	0.19	0.18	0.69	0.11	0.07	0.81	0.57	0.73
Ca	0.00	0.10	0.04	0.05	0.05	0.21	0.34	0.45	0.17	0.00	0.02	0.01
Total	23.63	23.90	23.99	23.97	23.81	23.73	23.46	23.85	23.89	23.93	23.88	23.88

Table A2.5 - Spinel analyses

Sample	at217	at217	at217	at217	at217	at217	at217	at217	tap-1b	tap-1b	tap-1b
Unit	B1	B1	B1	B1	B1	B1	B1	B1	C2	C2	C2
Rock type	wehrl	wehrl	wehrl	wehrl	wehrl	wehrl	wehrl	wehrl	bre	bre	bre
SiO2	0.15	0.22	0.11	0.16	0.29	0.12	0.18	0.24	0.19	0.97	0.16
TiO2	11.02	1.11	2.97	4.67	3.16	4.58	19.00	13.19	5.62	9.35	4.12
Al2O3	0.00	0.06	0.00	0.01	0.02	0.02	0.00	0.05	0.16	0.06	0.26
Cr2O3	0.26	2.11	0.22	0.22	0.27	0.32	0.29	0.42	0.02	0.09	0.07
FeO	32.40	29.92	28.22	30.28	29.94	30.39	35.42	35.02	29.61	39.60	27.94
Fe2O3	49.31	63.49	63.11	60.21	62.75	60.37	35.85	42.39	59.11	50.25	62.30
MnO	1.98	0.60	1.06	1.54	1.03	1.24	2.40	2.45	0.61	0.25	0.49
MgO	4.58	1.17	1.86	1.96	1.52	1.85	6.59	3.64	3.41	0.10	3.45
CaO	0.05	0.03	0.00	0.07	0.03	0.02	0.01	0.03	0.01	0.03	0.02
Total	99.74	98.71	97.55	99.12	99.01	98.91	99.74	97.43	98.74	100.70	98.81
O=32											
Si	0.05	0.07	0.04	0.05	0.09	0.04	0.05	0.07	0.06	0.29	0.05
Ti	2.44	0.26	0.69	1.07	0.73	1.05	4.10	3.01	1.27	2.11	0.93
Al	0.00	0.02	0.00	0.01	0.01	0.01	0.00	0.02	0.06	0.02	0.09
Cr	0.06	0.51	0.05	0.05	0.06	0.08	0.07	0.10	0.00	0.02	0.02
Fe2	7.99	7.71	7.28	7.69	7.64	7.73	8.50	8.87	7.45	9.92	7.02
Fe3	10.94	14.72	14.66	13.76	14.40	13.82	7.74	9.66	13.38	11.33	14.08
Mn	0.49	0.16	0.28	0.40	0.27	0.32	0.58	0.63	0.16	0.06	0.12
Mg	2.01	0.54	0.86	0.89	0.69	0.84	2.82	1.64	1.53	0.04	1.54
Ca	0.01	0.01	0.00	0.02	0.01	0.01	0.00	0.01	0.01	0.01	0.01
Total	24.01	23.99	23.85	23.93	23.89	23.89	23.87	24.01	23.90	23.81	23.86

Table A2.6 -Ilmenite Analyses

Sample	at025(*)	at055	at055	at104(*)	at205	at205	at205	at205	at205	at205
Unit	B1	C1	C1							
Rock type	wehrl	cbt	cbt	RR	lcr	lcr	lcr	lcr	lcr	lcr
SiO2	0.18	0.25	0.11	0.13	0.40	0.21	0.14	0.20	0.25	0.09
TiO2	32.57	52.90	51.13	52.49	52.04	51.32	54.28	52.28	52.56	52.78
Al2O3	0.00	0.00	0.00	0.01	0.01	0.01	0.03	0.02	0.00	0.01
Cr2O3	1.65	0.03	0.00	0.10	0.00	0.00	0.04	0.03	0.02	0.04
FeO	5.44	36.47	40.56	41.32	45.77	45.77	45.20	45.98	46.56	46.43
Fe2O3	50.00	2.94	2.53	2.26	0.31	1.26	0.00	0.95	0.00	0.00
MnO	4.17	4.19	3.41	2.60	0.11	0.07	0.14	0.09	0.24	0.37
MgO	10.62	3.18	1.04	1.71	0.02	0.00	0.10	0.07	0.03	0.09
CaO	0.00	0.45	0.29	0.02	0.27	0.56	0.23	0.35	0.08	0.08
Total	104.63(**)	100.41	99.07	100.64	98.93	99.20	100.16	99.97	99.74	99.89
O=3										
Si	0.004	0.006	0.003	0.003	0.010	0.005	0.003	0.005	0.006	0.002
Ti	0.555	0.971	0.970	0.976	0.992	0.980	1.021	0.988	0.996	1.001
Al	0.000	0.000	0.000	0.000	0.000	0.000	0.001	0.001	0.000	0.000
Cr	0.029	0.001	0.000	0.002	0.000	0.000	0.001	0.001	0.000	0.001
Fe2	0.103	0.745	0.856	0.855	0.970	0.972	0.946	0.966	0.981	0.979
Fe3	0.852	0.054	0.048	0.042	0.006	0.024	0.000	0.018	0.000	0.000
Mn	0.080	0.086	0.072	0.055	0.002	0.002	0.003	0.002	0.005	0.008
Mg	0.359	0.116	0.039	0.064	0.001	0.000	0.004	0.003	0.001	0.003
Ca	0.000	0.012	0.008	0.001	0.007	0.015	0.006	0.009	0.002	0.002
Total	1.982	1.991	1.996	1.998	1.988	1.998	1.985	1.993	1.991	1.996

(*) = exsolution lamella in magnetite (see table A2.5)

(**) Anomalously high total probably results from beam overlap with the host

Table A2.7 - Garnet analyses

Sample	at202	at202	at202	at202	at202	at202	at202	at003	at003	at003	at003
Unit								B1	B1	B1	B1
Rock type	lcr	lcr	lcr	lcr	lcr	lcr	lcr	beb	beb	beb	beb
Remarks	rim	core	rim	core	core	core	rim				
SiO2	31.77	31.44	32.12	27.64	27.36	27.91	31.15	30.76	30.82	29.80	30.18
TiO2	9.03	9.59	8.43	16.44	17.18	15.28	9.68	9.98	9.60	11.22	10.46
Al2O3	0.88	0.87	0.71	0.92	1.05	0.91	0.81	1.12	1.16	1.51	1.15
Cr2O3	0.03	0.16	0.05	0.06	0.11	0.05	0.10	0.10	0.04	0.12	0.13
Fe2O3	21.95	21.54	21.82	15.10	14.36	17.71	21.54	21.09	22.43	21.57	21.84
FeO	2.82	2.24	2.79	4.80	4.60	3.11	2.14	2.79	2.10	2.00	2.94
MnO	0.32	0.28	0.31	0.20	0.36	0.36	0.31	0.11	0.19	0.19	0.15
MgO	0.67	0.82	0.68	1.48	1.65	1.28	0.81	1.15	0.78	1.09	0.88
CaO	31.71	31.82	31.75	31.11	31.17	31.26	31.83	32.24	32.18	32.03	31.66
ZrO2	0.98	0.87	0.98	1.71	2.10	1.68	0.93	0.05	0.15	n.a.	n.a.
NiO	0.08	0.06	n.a.	n.a.	0.03	0.09	0.06	0.03	0.06	0.00	0.00
La2O3	n.a.	0.020	0.023	0.035	n.a.	0.027	n.a.	n.a.	n.a.	n.a.	n.a.
Ce2O3	n.a.	0.019	0.036	0.076	0.072	0.036	0.098	n.a.	n.a.	n.a.	n.a.
Nd2O3	0.011	n.a.	n.a.	0.025	0.085	0.004	n.a.	n.a.	n.a.	n.a.	n.a.
Gd2O3	n.a.	0.104	n.a.	0.034	0.061	n.a.	0.104	n.a.	n.a.	n.a.	n.a.
Y2O3	0.028	0.012	0.023	0.025	0.082	0.053	n.a.	n.a.	n.a.	n.a.	n.a.
Nb2O5	n.a.	0.007	0.035	0.299	0.229	0.180	0.116	n.a.	n.a.	n.a.	n.a.
Total	100.26	99.86	99.75	99.96	100.50	99.95	99.67	99.41	99.52	99.53	99.39
O=12											
Dodecahedral											
Ca	2.860	2.878	2.876	2.842	2.831	2.849	2.889	2.934	2.926	2.901	2.889
Na	0.059	0.053	0.065	0.027	0.041	0.048	0.057	0.010	0.030	0.020	0.010
Mn	0.023	0.020	0.022	0.015	0.026	0.026	0.023	0.008	0.014	0.014	0.011
Mg	0.059	0.049	0.038	0.117	0.102	0.077	0.031	0.048	0.031	0.066	0.091
Tetrahedral											
Si	2.674	2.654	2.715	2.356	2.320	2.374	2.639	2.613	2.615	2.519	2.570
Ti	0.326	0.346	0.285	0.644	0.680	0.626	0.362	0.388	0.385	0.481	0.430
Octahedral											
Ti	0.246	0.263	0.251	0.410	0.415	0.352	0.255	0.251	0.227	0.233	0.240
Mg	0.026	0.054	0.047	0.071	0.106	0.086	0.071	0.098	0.068	0.072	0.021
Mn											
Ca											
Fe3+	1.389	1.367	1.387	0.968	0.915	1.132	1.372	1.347	1.430	1.371	1.398
Al	0.087	0.087	0.071	0.093	0.105	0.091	0.081	0.112	0.116	0.150	0.115
Fe2+	0.198	0.158	0.197	0.342	0.326	0.221	0.151	0.198	0.149	0.142	0.210
Cr	0.002	0.011	0.003	0.004	0.008	0.004	0.007	0.007	0.003	0.008	0.009

Table A2.7 - Garnet analyses

Sample	at003	at003	at003	at003	at003	at003	at003	at003	at021	at021	at021
Unit	B1	B1	B1	B1	B1	B1	B1	B1			
Rock type	beb	beb	beb	beb	beb	beb	beb	beb	php	php	php
Remarks			tr2.1	tr2.2	tr2.3	tr2.4				core	core
SiO2	29.72	28.84	30.67	30.51	30.69	30.46	30.25	28.97	30.99	28.23	32.49
TiO2	11.70	13.02	9.97	8.87	8.88	9.67	10.28	12.93	8.29	19.18	4.31
Al2O3	1.23	1.64	1.14	1.36	1.27	1.16	1.15	0.97	0.24	0.90	0.66
Cr2O3	0.08	0.04	0.13	0.07	0.06	0.15	0.12	0.13	0.16	0.12	0.11
Fe2O3	20.44	21.24	21.54	24.15	24.14	23.42	23.11	20.76	22.24	12.56	24.83
FeO	2.63	1.38	3.22	0.63	0.71	1.35	1.42	2.18	0.00	3.22	0.00
MnO	0.16	0.20	0.07	0.14	0.10	0.12	0.12	0.24	0.14	0.56	0.08
MgO	0.86	1.28	0.79	1.14	1.11	0.87	0.80	0.95	1.49	1.45	1.49
CaO	32.18	31.96	31.81	32.07	32.12	31.84	32.24	31.94	32.64	31.28	32.77
ZrO2	n.a.	n.a.	n.a.	n.a.	n.a.	n.a.	n.a.	n.a.	1.06	0.12	0.90
NiO	0.02	0.08	0.08	0.02	0.10	0.01	0.00	0.04	n.a.	0.04	0.09
La2O3	n.a.	n.a.	n.a.	n.a.	n.a.	n.a.	n.a.	n.a.	n.a.	n.a.	n.a.
Ce2O3	n.a.	n.a.	n.a.	n.a.	n.a.	n.a.	n.a.	n.a.	n.a.	n.a.	n.a.
Nd2O3	n.a.	n.a.	n.a.	n.a.	n.a.	n.a.	n.a.	n.a.	n.a.	n.a.	n.a.
Gd2O3	n.a.	n.a.	n.a.	n.a.	n.a.	n.a.	n.a.	n.a.	n.a.	n.a.	n.a.
Y2O3	n.a.	n.a.	n.a.	n.a.	n.a.	n.a.	n.a.	n.a.	n.a.	n.a.	n.a.
Nb2O5	n.a.	n.a.	n.a.	n.a.	n.a.	n.a.	n.a.	n.a.	n.a.	n.a.	n.a.
Total	99.03	99.68	99.42	98.98	99.18	99.04	99.49	99.10	97.25	97.67	97.73
O=12											
Dodecahedr:											
Ca	2.940	2.890	2.899	2.924	2.919	2.896	2.925	2.914	2.913	2.810	2.904
Na	0.018	0.049	0.006	0.020	0.026	0.047	0.041	0.044	0.087	0.190	0.096
Mn	0.012	0.014	0.005	0.010	0.007	0.009	0.009	0.018			
Mg	0.030	0.047	0.090	0.045	0.047	0.049	0.026	0.025			
Tetrahedral											
Si	2.534	2.434	2.608	2.597	2.603	2.585	2.561	2.467	2.674	2.396	2.789
Ti	0.466	0.566	0.392	0.403	0.397	0.415	0.439	0.533	0.326	0.604	0.211
Octahedral											
Ti	0.285	0.260	0.246	0.165	0.170	0.203	0.216	0.295	0.212	0.621	0.067
Mg	0.079	0.114	0.011	0.100	0.093	0.061	0.075	0.096	0.191	0.184	0.191
Mn									0.010	0.041	0.006
Ca									0.105	0.034	0.110
Fe3+	1.311	1.347	1.377	1.545	1.539	1.495	1.471	1.329	1.443	0.801	1.602
Al	0.124	0.163	0.114	0.137	0.127	0.116	0.115	0.097	0.025	0.090	0.067
Fe2+	0.188	0.098	0.229	0.045	0.050	0.096	0.101	0.155	0.000	0.229	0.000
Cr	0.005	0.003	0.009	0.005	0.004	0.010	0.008	0.008	0.011	0.008	0.007

Table A2.7 - Garnet analyses

Sample	at025	at025	at025	at025	at029	at029	at029	at029	at029	at029	at029
Unit	B1	B1	B1	B1	B2	B2	B2	B2	B2	B2	B2
Rock type	wehrl	wehrl	wehrl	wehrl	beb	beb	beb	beb	beb	beb	beb
Remarks		core									
SiO2	29.80	30.18	29.72	28.84	29.65	29.85	29.72	29.52	30.08	29.50	29.98
TiO2	11.22	10.46	11.70	13.02	13.45	12.71	13.33	14.51	12.65	13.90	11.91
Al2O3	1.51	1.15	1.23	1.64	0.36	0.38	0.54	0.36	0.60	0.31	0.27
Cr2O3	0.12	0.13	0.08	0.04	0.00	0.12	0.00	0.03	0.16	0.02	0.08
Fe2O3	21.59	21.85	20.45	21.21	20.12	20.35	19.94	18.41	19.79	17.82	22.14
FeO	1.99	2.93	2.63	1.40	3.41	3.54	2.79	4.00	3.48	5.12	2.64
MnO	0.19	0.15	0.16	0.20	0.42	0.52	0.34	0.46	0.46	0.54	0.48
MgO	1.09	0.88	0.86	1.28	0.69	0.63	0.83	0.65	0.57	0.59	0.87
CaO	32.03	31.66	32.18	31.96	31.50	31.61	32.16	31.58	31.89	31.36	31.68
ZrO2	n.a.	n.a.	n.a.	n.a.	n.a.	n.a.	n.a.	n.a.	n.a.	n.a.	n.a.
NiO	0.00	0.00	0.02	0.08	0.08	0.00	0.05	0.00	0.00	0.03	0.00
La2O3	n.a.	n.a.	n.a.	n.a.	n.a.	n.a.	n.a.	n.a.	n.a.	n.a.	n.a.
Ce2O3	n.a.	n.a.	n.a.	n.a.	n.a.	n.a.	n.a.	n.a.	n.a.	n.a.	n.a.
Nd2O3	n.a.	n.a.	n.a.	n.a.	n.a.	n.a.	n.a.	n.a.	n.a.	n.a.	n.a.
Gd2O3	n.a.	n.a.	n.a.	n.a.	n.a.	n.a.	n.a.	n.a.	n.a.	n.a.	n.a.
Y2O3	n.a.	n.a.	n.a.	n.a.	n.a.	n.a.	n.a.	n.a.	n.a.	n.a.	n.a.
Nb2O5	n.a.	n.a.	n.a.	n.a.	n.a.	n.a.	n.a.	n.a.	n.a.	n.a.	n.a.
Total	99.55	99.38	99.03	99.68	99.68	99.71	99.70	99.51	99.68	99.20	100.05
O=12											
Dodecahedr:											
Ca	2.901	2.889	2.940	2.890	2.864	2.879	2.916	2.871	2.897	2.874	2.875
Na	0.020	0.010	0.018	0.048	0.076	0.051	0.061	0.081	0.054	0.032	0.046
Mn	0.014	0.011	0.012	0.014	0.030	0.037	0.023	0.033	0.033	0.039	0.034
Mg	0.065	0.090	0.030	0.047	0.030	0.033		0.016	0.015	0.056	0.045
Tetrahedral											
Si	2.519	2.570	2.534	2.434	2.516	2.537	2.516	2.504	2.551	2.523	2.539
Ti	0.481	0.430	0.466	0.566	0.484	0.463	0.485	0.496	0.449	0.477	0.461
Octahedral											
Ti	0.232	0.240	0.285	0.261	0.375	0.350	0.364	0.430	0.358	0.417	0.298
Mg	0.072	0.022	0.079	0.114	0.057	0.047	0.105	0.067	0.057	0.020	0.065
Mn							0.002				
Ca											
Fe3+	1.372	1.399	1.311	1.346	1.284	1.300	1.269	1.174	1.262	1.146	1.410
Al	0.151	0.115	0.124	0.163	0.036	0.038	0.054	0.036	0.060	0.031	0.027
Fe2+	0.140	0.208	0.188	0.099	0.242	0.252	0.197	0.283	0.247	0.366	0.187
Cr	0.008	0.009	0.005	0.002	0.000	0.008	0.000	0.002	0.011	0.001	0.005

Table A2.7 - Garnet analyses

Sample	at033	at033	at033	at033	at038	at120	at120	at209	at209	at209	at209
Unit	B2	B2	B2	B2	B2						
Rock type	beb	beb	beb	beb	beb	php	php	lcr	lcr	lcr	lcr
Remarks											
SiO2	27.47	29.16	28.28	29.44	28.37	32.07	30.57	34.94	35.03	34.12	34.86
TiO2	18.69	14.46	16.81	14.54	14.31	6.28	11.24	3.30	3.03	5.33	2.77
Al2O3	0.48	0.30	0.29	0.47	0.91	0.30	0.14	0.85	0.99	0.78	1.29
Cr2O3	0.09	0.08	0.09	0.12	0.07	0.08	0.11	0.09	0.12	0.10	0.07
Fe2O3	14.29	18.22	17.28	18.38	20.39	24.14	20.06	25.54	25.88	22.86	25.36
FeO	5.07	4.41	4.47	4.16	2.33	0.00	0.00	0.00	0.00	1.18	0.18
MnO	0.38	0.25	0.31	0.23	0.20	0.05	0.31	0.15	0.23	0.11	0.20
MgO	0.99	0.79	0.83	0.82	1.27	1.61	1.31	1.54	1.45	1.46	1.23
CaO	31.07	31.33	31.17	31.45	31.51	32.80	33.69	32.77	32.69	33.05	32.88
ZrO2	0.63	n.a.	n.a.	n.a.	n.a.	n.a.	n.a.	0.11	0.15	0.12	0.08
NiO	n.a.	0.00	0.00	0.01	0.00	0.10	0.00	0.03	0.00	0.05	0.06
La2O3	n.a.	n.a.	n.a.	n.a.	n.a.	n.a.	n.a.	n.a.	n.a.	n.a.	n.a.
Ce2O3	n.a.	n.a.	n.a.	n.a.	n.a.	n.a.	n.a.	n.a.	n.a.	n.a.	n.a.
Nd2O3	n.a.	n.a.	n.a.	n.a.	n.a.	n.a.	n.a.	n.a.	n.a.	n.a.	n.a.
Gd2O3	n.a.	n.a.	n.a.	n.a.	n.a.	n.a.	n.a.	n.a.	n.a.	n.a.	n.a.
Y2O3	n.a.	n.a.	n.a.	n.a.	n.a.	n.a.	n.a.	n.a.	n.a.	n.a.	n.a.
Nb2O5	n.a.	n.a.	n.a.	n.a.	n.a.	n.a.	n.a.	n.a.	n.a.	n.a.	n.a.
Total	99.15	99.00	99.53	99.62	99.36	97.44	97.43	99.32	99.58	99.16	98.98
O=12											
Dodecahedr:											
Ca	2.839	2.870	2.821	2.849	2.860	2.972	2.929	2.944	2.931	2.984	2.969
Na	0.105	0.060	0.097	0.075	0.058	0.028	0.071	0.024	0.020	0.004	0.002
Mn	0.027	0.018	0.022	0.017	0.015			0.011	0.016	0.008	0.014
Mg	0.029	0.052	0.060	0.059	0.068			0.021	0.033	0.004	0.015
Tetrahedral											
Si	2.343	2.493	2.389	2.490	2.403	2.745	2.621	2.930	2.931	2.875	2.938
Ti	0.657	0.507	0.612	0.511	0.597	0.255	0.379	0.070	0.069	0.125	0.062
Octahedral											
Ti	0.542	0.423	0.457	0.414	0.315	0.149	0.346	0.138	0.122	0.213	0.113
Mg	0.097	0.049	0.044	0.045	0.092	0.206	0.168	0.171	0.148	0.179	0.140
Mn						0.004	0.023				
Ca						0.036	0.166				
Fe3+	0.916	1.171	1.097	1.168	1.298	1.553	1.293	1.610	1.628	1.448	1.606
Al	0.048	0.030	0.029	0.047	0.091	0.030	0.014	0.084	0.098	0.077	0.128
Fe2+	0.361	0.315	0.316	0.294	0.165	0.000	0.000	0.000	0.000	0.083	0.013
Cr	0.006	0.005	0.006	0.008	0.004	0.005	0.008	0.006	0.008	0.007	0.005

Table A2.7 - Garnet analyses

Sample	at209	at209	at209	at211	at211	at211	at211	at211	at211	at211	at211
Unit											
Rock type	lcr	lcr	lcr	lcr	lcr	lcr	lcr	lcr	lcr	lcr	lcr
Remarks				rim	core	rim	core	rim	core	rim	core
SiO2	33.52	34.52	34.07	35.71	28.12	34.43	28.59	33.25	28.53	33.46	29.44
TiO2	6.48	4.42	3.97	0.53	17.22	3.64	15.60	6.20	15.44	4.56	12.99
Al2O3	0.42	0.98	0.99	1.35	0.73	1.40	0.70	0.65	0.84	0.62	0.58
Cr2O3	0.10	0.08	0.05	0.16	0.02	0.00	0.05	0.12	0.08	0.16	0.03
Fe2O3	22.94	23.86	23.72	28.50	12.22	25.56	15.22	24.13	15.62	24.94	19.26
FeO	0.00	0.49	1.03	0.00	5.45	0.49	3.87	1.46	3.77	1.30	3.11
MnO	0.18	0.12	0.13	0.16	0.32	0.28	0.31	0.19	0.31	0.19	0.24
MgO	1.77	1.25	1.22	0.25	2.16	0.70	1.90	0.90	1.92	0.46	1.26
CaO	32.96	32.82	32.69	32.87	30.32	32.43	30.90	32.39	30.75	32.07	31.05
ZrO2	0.38	0.12	0.06	0.02	2.63	n.a.	n.a.	n.a.	n.a.	n.a.	n.a.
NiO	0.10	0.09	n.a.	n.a.	n.a.	0.07	0.06	0.03	0.00	0.09	0.02
La2O3	n.a.	n.a.	n.a.	n.a.	n.a.	n.a.	n.a.	n.a.	n.a.	n.a.	n.a.
Ce2O3	n.a.	n.a.	n.a.	n.a.	n.a.	n.a.	n.a.	n.a.	n.a.	n.a.	n.a.
Nd2O3	n.a.	n.a.	n.a.	n.a.	n.a.	n.a.	n.a.	n.a.	n.a.	n.a.	n.a.
Gd2O3	n.a.	n.a.	n.a.	n.a.	n.a.	n.a.	n.a.	n.a.	n.a.	n.a.	n.a.
Y2O3	n.a.	n.a.	n.a.	n.a.	n.a.	n.a.	n.a.	n.a.	n.a.	n.a.	n.a.
Nb2O5	n.a.	n.a.	n.a.	n.a.	n.a.	n.a.	n.a.	n.a.	n.a.	n.a.	n.a.
Total	98.86	98.74	97.94	99.56	99.20	99.01	97.21	99.32	97.26	97.86	97.99
O=12											
Dodecahedr											
Ca	2.965	2.966	2.990	2.958	2.774	2.921	2.824	2.922	2.807	2.948	2.839
Na	0.035	0.013	0.000	0.023	0.023	0.031	0.038	0.021	0.040	0.026	0.054
Mn		0.009	0.010	0.012	0.024	0.020	0.023	0.014	0.022	0.014	0.017
Mg		0.012	0.001	0.008	0.180	0.028	0.116	0.043	0.131	0.013	0.090
Tetrahedral											
Si	2.826	2.912	2.908	2.999	2.401	2.895	2.439	2.800	2.432	2.871	2.512
Ti	0.174	0.088	0.092	0.001	0.599	0.105	0.561	0.200	0.568	0.129	0.488
Octahedral											
Ti	0.237	0.192	0.163	0.033	0.507	0.125	0.440	0.193	0.422	0.166	0.346
Mg	0.222	0.145	0.154	0.024	0.095	0.060	0.126	0.070	0.113	0.047	0.071
Mn	0.013										
Ca	0.013										
Fe3+	1.454	1.513	1.522	1.799	0.785	1.616	0.976	1.528	1.001	1.609	1.236
Al	0.042	0.097	0.099	0.133	0.074	0.139	0.070	0.065	0.084	0.062	0.058
Fe2+	0.000	0.034	0.073	0.000	0.389	0.034	0.276	0.103	0.269	0.094	0.222
Cr	0.007	0.005	0.004	0.011	0.002	0.000	0.004	0.008	0.005	0.011	0.002

Table A2.8 - Feldspar analyses

Sample	at012	at012	at012	at012	at012	at012	at012	at024	at122	at122	at122	at122	at122
Unit													
Rock type	syen	syen	syen	syen	syen	syen	syen	lcr	syen	syen	syen	syen	syen
SiO2	62.275	62.700	63.026	62.226	62.219	62.205	62.922	64.787	63.646	62.948	62.462	64.120	63.484
Al2O3	18.659	18.761	18.615	18.737	18.790	18.409	18.982	17.054	18.719	18.671	19.479	18.806	18.828
Fe2O3	0.404	0.466	0.451	0.433	0.491	1.192	0.440	0.711	0.316	0.196	0.235	0.079	0.076
BaO	1.976	2.152	1.652	2.348	2.512	1.966	1.830	0.072	1.355	1.845	1.747	1.015	1.106
CaO	0.004	0.000	0.010	0.084	0.017	0.000	0.000	0.675	0.000	0.000	0.000	0.036	0.000
Na2O	0.099	0.186	0.120	0.083	0.239	0.012	0.139	0.102	0.169	0.210	0.500	0.160	0.214
K2O	16.076	15.945	16.175	15.888	15.793	15.914	16.134	14.212	16.362	16.000	15.503	16.644	16.425
Total	99.49	100.21	100.05	99.80	100.06	99.70	100.45	97.61	100.57	99.87	99.93	100.86	100.13
O=32													
Si	11.783	11.782	11.824	11.762	11.745	11.762	11.771	12.163	11.849	11.831	11.710	11.875	11.848
Al	4.158	4.152	4.113	4.171	4.177	4.099	4.182	3.771	4.104	4.133	4.301	4.102	4.138
Fe3	0.057	0.066	0.064	0.061	0.070	0.169	0.062	0.100	0.044	0.028	0.033	0.011	0.011
Ba	0.147	0.158	0.121	0.174	0.186	0.146	0.134	0.005	0.099	0.136	0.128	0.074	0.081
Ca	0.001	0.000	0.002	0.017	0.003	0.000	0.000	0.136	0.000	0.000	0.000	0.007	0.000
Na	0.036	0.068	0.044	0.030	0.087	0.004	0.050	0.037	0.061	0.076	0.182	0.057	0.077
K	3.880	3.822	3.871	3.831	3.803	3.839	3.851	3.404	3.886	3.836	3.708	3.932	3.911
Ab	0.90	1.70	1.10	0.80	2.20	0.10	1.30	1.00	1.50	1.90	4.70	1.40	1.90
An	0.00	0.00	0.10	0.40	0.10	0.00	0.00	3.80	0.00	0.00	0.00	0.20	0.00
Or	99.10	98.30	98.80	98.80	97.70	99.90	98.70	95.20	98.50	98.10	95.30	98.40	98.10

Table A2.8 - Feldspar analyses

Sample	at122	at122	at207	at219	at219	at301	at301	at301	at301	at301	at301	at301	at302
Unit				C2	C2								
Rock type	syen	syen	lcr	cbt,dk	cbt,dk	syen	syen	syen	syen	syen	syen	syen	syen
SiO2	63.473	63.711	62.649	64.269	65.676	63.952	62.452	63.273	62.472	64.344	63.018	63.850	63.482
Al2O3	18.694	18.896	16.552	17.344	18.231	18.524	18.991	18.972	18.757	18.495	18.769	18.544	18.558
Fe2O3	0.252	0.230	2.836	0.304	0.241	0.344	0.396	0.332	0.312	0.407	0.371	0.385	0.425
BaO	0.930	1.197	0.000	0.000	0.000	0.818	2.525	1.719	1.987	0.873	1.770	0.814	1.601
CaO	0.000	0.000	0.229	0.101	0.052	0.000	0.000	0.000	0.009	0.000	0.019	0.000	0.000
Na2O	0.176	0.326	0.045	0.027	0.061	0.417	0.232	0.335	0.238	0.209	0.573	0.210	0.481
K2O	16.442	16.374	14.799	15.088	15.699	15.295	14.949	15.988	16.094	16.474	15.547	16.485	14.897
Total	99.97	100.73	97.11	97.13	99.96	99.35	99.55	100.62	99.87	100.80	100.07	100.29	99.44
O=32													
Si	11.857	11.831	11.969	12.147	12.079	11.931	11.778	11.795	11.777	11.908	11.805	11.882	11.890
Al	4.112	4.132	3.724	3.861	3.949	4.070	4.218	4.165	4.164	4.031	4.140	4.064	4.093
Fe3	0.035	0.032	0.407	0.043	0.033	0.048	0.056	0.046	0.044	0.057	0.052	0.054	0.060
Ba	0.068	0.087	0.000	0.000	0.000	0.060	0.187	0.126	0.147	0.063	0.130	0.059	0.117
Ca	0.000	0.000	0.047	0.021	0.010	0.000	0.000	0.000	0.002	0.000	0.004	0.000	0.000
Na	0.064	0.117	0.017	0.010	0.022	0.151	0.085	0.121	0.087	0.075	0.208	0.076	0.175
K	3.918	3.879	3.607	3.638	3.684	3.640	3.597	3.802	3.871	3.890	3.715	3.913	3.559
Ab	1.60	2.90	0.50	0.30	0.60	4.00	2.30	3.10	2.20	1.90	5.30	1.90	4.70
An	0.00	0.00	1.30	0.60	0.30	0.00	0.00	0.00	0.10	0.00	0.10	0.00	0.00
Or	98.40	97.10	98.30	99.20	99.10	96.00	97.70	96.90	97.80	98.10	94.60	98.10	95.30

Table A2.8 - Feldspar analyses

Sample	at302	at302	at302	at302	at302	at302	at302	rja	rja	rja	rja	rja	rja
Unit													
Rock type	syen	syen	syen	syen	syen	syen	syen	fen	fen	fen	fen	fen	fen
SiO2	64.617	63.829	63.649	63.085	64.931	63.562	63.558	67.550	67.355	65.772	64.915	64.510	67.333
Al2O3	18.636	18.846	18.750	18.704	18.669	19.067	18.515	19.418	18.996	18.561	18.126	18.371	18.807
Fe2O3	0.365	0.064	0.142	0.364	0.378	0.356	0.285	0.112	0.555	0.451	0.789	0.424	0.589
BaO	0.438	0.906	1.187	1.673	0.548	1.568	0.451	0.085	0.053	0.195	0.302	0.331	0.059
CaO	0.000	0.020	0.016	0.000	0.011	0.022	0.000	0.012	0.004	0.000	0.000	0.000	0.000
Na2O	0.230	0.257	0.199	0.208	0.261	0.243	0.174	8.147	7.298	3.356	1.412	0.480	6.940
K2O	15.751	16.451	16.576	16.204	17.017	16.328	16.689	4.980	4.731	11.274	14.667	15.770	5.655
Total	100.04	100.37	100.52	100.24	101.81	101.15	99.67	100.30	98.99	99.61	100.21	99.89	99.38
O=32													
Si	11.949	11.863	11.851	11.816	11.898	11.789	11.882	11.964	12.038	12.000	11.965	11.958	12.041
Al	4.059	4.125	4.111	4.126	4.029	4.165	4.076	4.050	3.998	3.988	3.935	4.010	3.961
Fe3	0.051	0.009	0.020	0.051	0.052	0.050	0.040	0.015	0.075	0.062	0.109	0.059	0.079
Ba	0.032	0.066	0.087	0.123	0.039	0.114	0.033	0.006	0.004	0.014	0.022	0.024	0.004
Ca	0.000	0.004	0.003	0.000	0.002	0.004	0.000	0.002	0.001	0.000	0.000	0.000	0.000
Na	0.082	0.092	0.072	0.075	0.093	0.087	0.063	2.798	2.529	1.187	0.504	0.173	2.406
K	3.716	3.901	3.938	3.872	3.978	3.863	3.980	1.125	1.079	2.624	3.449	3.729	1.290
Ab	2.20	2.30	1.80	1.90	2.30	2.20	1.60	71.30	70.10	31.10	12.70	4.40	65.10
An	0.00	0.10	0.10	0.00	0.00	0.10	0.00	0.10	0.00	0.00	0.00	0.00	0.00
Or	97.80	97.60	98.10	98.10	97.70	97.70	98.40	28.70	29.90	68.90	87.30	95.60	34.90

Table A2.8 - Feldspar analyses

Sample	rja	rja	rja	rja	rja	rja	rja	rja	rja	rja	rja
Unit											
Rock type	fen	fen	fen	fen	fen	fen	fen	fen	fen	fen	fen
SiO2	64.764	67.943	64.361	64.705	65.533	64.649	66.980	66.270	64.833	65.053	67.954
Al2O3	18.539	19.348	18.295	18.539	18.535	18.350	18.990	18.888	18.448	18.580	19.261
Fe2O3	0.496	0.256	0.609	0.524	0.524	0.566	0.268	0.176	0.392	0.579	0.584
BaO	0.328	0.028	0.520	0.314	0.219	0.231	0.210	0.032	0.733	0.480	0.099
CaO	0.000	0.000	0.000	0.000	0.001	0.000	0.013	0.000	0.000	0.051	0.000
Na2O	2.554	8.044	1.414	1.205	0.543	0.914	8.120	4.742	2.008	1.711	11.133
K2O	12.344	3.925	14.412	15.155	16.646	15.846	4.871	10.198	14.160	14.665	0.786
Total	99.02	99.54	99.61	100.44	102.00	100.56	99.45	100.31	100.57	101.12	99.82
O=32											
Si	11.955	12.032	11.938	11.917	11.938	11.926	11.980	11.964	11.924	11.904	11.951
Al	4.030	4.035	3.996	4.021	3.976	3.987	4.000	4.016	3.996	4.004	3.989
Fe3	0.069	0.034	0.085	0.073	0.072	0.079	0.036	0.024	0.054	0.080	0.077
Ba	0.024	0.002	0.038	0.023	0.016	0.017	0.015	0.002	0.053	0.034	0.007
Ca	0.000	0.000	0.000	0.000	0.000	0.000	0.002	0.000	0.000	0.010	0.000
Na	0.914	2.762	0.509	0.430	0.192	0.327	2.816	1.660	0.716	0.607	3.796
K	2.907	0.887	3.410	3.561	3.868	3.729	1.111	2.349	3.322	3.424	0.176
Ab	23.90	75.70	13.00	10.80	4.70	8.10	71.70	41.40	17.70	15.00	95.60
An	0.00	0.00	0.00	0.00	0.00	0.00	0.10	0.00	0.00	0.20	0.00
Or	76.10	24.30	87.00	89.20	95.30	91.90	28.30	58.60	82.30	84.70	4.40

Table A2.9 - Calcite analyses

Sample	at009	at009	at013	at013	at013	at013	at022	at022	at042	at042	at042	at042	at042	at042
Unit	B1	B1							C1	C1	C1	C1	C1	C1
Rock type	beb	beb	php	php	php	php	php	php	cbt	cbt	cbt	cbt	cbt	cbt
Remarks	i	g	g	g	g	g	g	g		1	1	1	1	1
CaO	53.58	54.19	52.71	53.85	53.43	53.67	53.53	53.60	51.49	51.19	49.58	51.80	50.46	51.17
MgO	0.14	0.19	0.00	0.04	0.01	0.10	0.00	0.07	0.98	0.89	1.12	0.82	1.27	1.29
FeOt	0.25	0.10	0.18	0.19	0.13	0.11	0.19	0.23	0.25	0.20	0.21	0.20	0.11	0.18
MnO	0.06	0.00	0.01	0.01	0.00	0.00	0.03	0.00	0.16	0.13	0.13	0.11	0.14	0.11
SrO	1.96	1.27	2.46	1.38	1.80	1.59	1.30	0.46	3.51	2.97	3.95	2.51	3.93	3.60
BaO	0.35	0.35	0.71	0.22	0.58	0.83	0.45	0.83	0.53	0.53	0.89	0.36	0.95	0.66
CO2	43.40	43.52	43.09	43.45	43.34	43.37	43.23	43.02	43.38	42.77	42.26	42.91	43.09	43.47
Total	99.74	99.62	99.16	99.14	99.29	99.67	98.73	98.21	100.30	98.69	98.13	98.71	99.96	100.47
O=6														
Ca	1.935	1.950	1.915	1.941	1.932	1.941	1.932	1.927	1.863	1.879	1.841	1.895	1.838	1.848
Mg	0.007	0.010	0.000	0.002	0.001	0.005	0.000	0.004	0.049	0.046	0.058	0.042	0.065	0.065
Fe	0.007	0.003	0.005	0.005	0.004	0.003	0.005	0.006	0.007	0.006	0.006	0.006	0.003	0.005
Mn	0.002	0.000	0.000	0.000	0.000	0.000	0.001	0.000	0.005	0.004	0.004	0.003	0.004	0.003
Sr	0.038	0.025	0.048	0.027	0.035	0.031	0.025	0.009	0.069	0.059	0.079	0.050	0.077	0.070
Ba	0.005	0.005	0.009	0.003	0.008	0.011	0.006	0.011	0.007	0.007	0.012	0.005	0.013	0.009
Total	1.994	1.993	1.977	1.978	1.980	1.991	1.969	1.957	2.000	2.001	2.000	2.001	2.000	2.000

Sample	at042	at042	at043	at043	at043	at043	at043	at043	at043	at043	at043	at043	at043	at043
Unit	C1	C1	C3	C3	C3	C3	C3	C3	C3	C3	C3	C3	C3	C3
Rock type	cbt	cbt	cbt	cbt	cbt	cbt	cbt	cbt	cbt	cbt	cbt	cbt	cbt	cbt
Remarks	1	2		1	1	1	1	1	1	1	1	1	1	1
CaO	51.75	51.15	53.86	53.94	53.98	53.92	53.97	53.73	53.86	53.95	53.80	53.88	53.89	53.86
MgO	0.84	1.59	0.06	0.07	0.07	0.07	0.06	0.07	0.03	0.06	0.03	0.06	0.04	0.04
FeOt	0.23	0.21	0.10	0.05	0.03	0.06	0.01	0.02	0.07	0.04	0.07	0.00	0.07	0.03
MnO	0.12	0.13	0.07	0.03	0.06	0.05	0.06	0.08	0.05	0.05	0.06	0.03	0.02	0.04
SrO	3.27	1.93	2.23	2.22	2.11	2.20	2.20	2.30	2.25	2.05	2.14	2.35	2.25	2.23
BaO	0.37	0.35	0.33	0.21	0.24	0.20	0.19	0.38	0.24	0.32	0.39	0.26	0.26	0.33
CO2	43.23	43.01	43.49	43.48	43.48	43.47	43.48	43.41	43.42	43.45	43.40	43.45	43.44	43.42
Total	99.81	98.37	100.14	99.99	99.98	99.96	99.98	100.00	99.91	99.92	99.89	100.02	99.97	99.95
O=6														
Ca	1.879	1.867	1.944	1.947	1.948	1.947	1.948	1.943	1.947	1.949	1.946	1.946	1.947	1.947
Mg	0.042	0.081	0.003	0.004	0.004	0.003	0.003	0.004	0.002	0.003	0.002	0.003	0.002	0.002
Fe	0.007	0.006	0.003	0.001	0.001	0.002	0.000	0.001	0.002	0.001	0.002	0.000	0.002	0.001
Mn	0.003	0.004	0.002	0.001	0.002	0.002	0.002	0.002	0.002	0.001	0.002	0.001	0.000	0.001
Sr	0.064	0.038	0.043	0.043	0.041	0.043	0.043	0.045	0.044	0.040	0.042	0.046	0.044	0.044
Ba	0.005	0.005	0.004	0.003	0.003	0.003	0.003	0.005	0.003	0.004	0.005	0.003	0.003	0.004
Total	2.000	2.001	1.999	1.999	1.999	2.000	1.999	2.000	2.000	1.998	1.999	1.999	1.998	1.999

Table A2.9 - Calcite analyses

Sample	at043	at043	at043	at043	at043	at043	at043	at044	at044	at044	at044	at044	at044	at044
Unit	C3.	C3	C3	C3	C3	C3	C3	C1	C1	C1	C1	C1	C1	C1
Rock type	cbt	cbt	cbt	cbt	cbt	cbt	cbt	cbt	cbt	cbt	cbt	cbt	cbt	cbt
Remarks	1	1	1	1	1	1	1	1	1	1	1	1	1	1
CaO	53.83	53.98	53.89	53.87	53.77	53.85	53.92	51.25	50.09	50.94	50.28	51.14	50.98	50.78
MgO	0.06	0.05	0.06	0.06	0.04	0.04	0.04	0.99	1.10	0.88	0.99	0.80	0.76	0.92
FeOt	0.09	0.02	0.04	0.04	0.05	0.00	0.04	0.06	0.16	0.14	0.13	0.10	0.06	0.11
MnO	0.05	0.03	0.05	0.05	0.04	0.04	0.03	0.14	0.12	0.14	0.13	0.15	0.10	0.13
SrO	2.24	2.20	2.25	2.24	2.32	2.30	2.17	3.51	4.34	3.39	4.20	3.61	3.64	3.78
BaO	0.29	0.28	0.33	0.26	0.35	0.39	0.30	0.20	0.52	0.44	0.58	0.71	0.75	0.53
CO2	43.45	43.48	43.46	43.44	43.40	43.42	43.43	42.98	42.69	42.68	42.64	42.89	42.70	42.77
Total	100.01	100.04	100.07	99.96	99.97	100.04	99.93	99.13	99.02	98.63	98.94	99.40	99.00	99.02
O=6														
Ca	1.945	1.949	1.946	1.946	1.945	1.946	1.948	1.872	1.842	1.873	1.850	1.871	1.874	1.864
Mg	0.003	0.002	0.003	0.003	0.002	0.002	0.002	0.051	0.057	0.045	0.051	0.041	0.039	0.047
Fe	0.003	0.001	0.001	0.001	0.001	0.000	0.001	0.002	0.005	0.004	0.004	0.003	0.002	0.003
Mn	0.001	0.001	0.001	0.002	0.001	0.001	0.001	0.004	0.004	0.004	0.004	0.004	0.003	0.004
Sr	0.044	0.043	0.044	0.044	0.045	0.045	0.043	0.069	0.086	0.067	0.084	0.072	0.072	0.075
Ba	0.004	0.004	0.004	0.003	0.005	0.005	0.004	0.003	0.007	0.006	0.008	0.010	0.010	0.007
Total	2.000	2.000	1.999	1.999	1.999	1.999	1.999	2.001	2.001	1.999	2.001	2.001	2.000	2.000

Sample	at044	at044	at045	at045	at045	at045	at045	at045	at045	at045	at045	at045	at045	at045
Unit	C1	C1	C2	C2	C2	C2	C2	C2	C2	C2	C2	C2	C2	C2
Rock type	cbt	cbt	cbt	cbt	cbt	cbt	cbt	cbt	cbt	cbt	cbt	cbt	cbt	cbt
Remarks	2	2	1	1	1	1	1	1	1	1	1	1	1	1
CaO	55.23	54.81	52.45	52.84	51.85	51.50	52.61	51.63	52.05	52.53	52.19	52.25	53.06	52.28
MgO	0.29	0.25	0.88	0.64	0.89	0.70	0.72	0.84	0.75	0.81	0.84	0.80	0.64	0.78
FeOt	0.09	0.12	0.19	0.18	0.23	0.22	0.19	0.18	0.22	0.21	0.26	0.21	0.28	0.25
MnO	0.16	0.11	0.33	0.27	0.29	0.28	0.21	0.24	0.25	0.28	0.29	0.29	0.29	0.28
SrO	0.41	0.51	2.61	2.25	2.79	3.65	2.47	2.90	2.99	2.50	2.65	2.52	2.00	2.51
BaO	0.06	0.15	0.03	0.38	0.41	0.53	0.40	0.67	0.40	0.20	0.27	0.15	0.21	0.14
CO2	44.01	43.69	43.57	43.51	43.29	43.19	43.49	43.12	43.34	43.54	43.44	43.30	43.60	43.35
Total	100.25	99.64	100.06	100.07	99.76	100.07	100.08	99.57	100.01	100.08	99.93	99.52	100.08	99.59
O=6														
Ca	1.970	1.969	1.890	1.906	1.880	1.871	1.899	1.879	1.885	1.894	1.886	1.894	1.910	1.893
Mg	0.014	0.012	0.044	0.032	0.045	0.035	0.036	0.042	0.038	0.041	0.042	0.040	0.032	0.039
Fe	0.003	0.003	0.005	0.005	0.007	0.006	0.005	0.005	0.006	0.006	0.007	0.006	0.008	0.007
Mn	0.004	0.003	0.010	0.008	0.008	0.008	0.006	0.007	0.007	0.008	0.008	0.008	0.008	0.008
Sr	0.008	0.010	0.051	0.044	0.055	0.072	0.048	0.057	0.059	0.049	0.052	0.049	0.039	0.049
Ba	0.001	0.002	0.000	0.005	0.005	0.007	0.005	0.009	0.005	0.003	0.004	0.002	0.003	0.002
Total	2.000	1.999	2.000	2.000	2.000	1.999	1.999	1.999	2.000	2.001	1.999	1.999	2.000	1.998

Table A2.9 - Calcite analyses

Sample	at045	at045	at045	at045	at046	at046	at046	at046	at046	at046	at047	at047	at047	at047
Unit	C2	C2	C2	C2	C2	C2	C2	C2	C2	C2	C2	C2	C2	C2
Rock type	cbt	cbt	cbt	cbt	cbt	cbt	cbt	cbt	cbt	cbt	cbt	cbt	cbt	cbt
Remarks	1	2	2	2	1	1	1	2	2	2	1	1	1	1
CaO	52.32	52.68	53.06	53.66	52.54	51.38	52.71	53.54	52.74	53.76	53.34	53.59	53.39	53.56
MgO	0.73	1.07	0.62	0.50	0.86	0.96	0.19	0.35	0.80	0.69	0.47	0.51	0.48	0.47
FeOt	0.19	0.32	0.22	0.25	0.26	0.20	0.29	0.21	0.26	0.26	0.00	0.01	0.07	0.00
MnO	0.27	0.27	0.28	0.27	0.27	0.27	0.21	0.19	0.28	0.29	0.09	0.06	0.08	0.06
SrO	2.72	1.21	1.67	1.36	2.50	2.75	2.20	1.53	1.93	1.43	2.01	2.06	2.00	1.84
BaO	0.38	0.02	0.13	0.00	0.31	0.43	0.00	0.26	0.21	0.12	0.45	0.50	0.39	0.48
CO2	43.41	43.39	43.38	43.57	43.65	42.95	42.82	43.37	43.48	43.92	43.42	43.67	43.48	43.51
Total	100.02	98.95	99.37	99.61	100.38	98.94	98.42	99.45	99.70	100.47	99.79	100.39	99.89	99.93
O=6														
Ca	1.892	1.906	1.920	1.933	1.889	1.878	1.932	1.938	1.904	1.921	1.928	1.926	1.927	1.932
Mg	0.037	0.054	0.031	0.025	0.043	0.049	0.010	0.018	0.040	0.034	0.024	0.026	0.024	0.024
Fe	0.005	0.009	0.006	0.007	0.007	0.006	0.008	0.006	0.007	0.007	0.000	0.000	0.002	0.000
Mn	0.008	0.008	0.008	0.008	0.008	0.008	0.006	0.005	0.008	0.008	0.003	0.002	0.002	0.002
Sr	0.053	0.024	0.033	0.026	0.049	0.054	0.044	0.030	0.038	0.028	0.039	0.040	0.039	0.036
Ba	0.005	0.000	0.002	0.000	0.004	0.006	0.000	0.003	0.003	0.002	0.006	0.007	0.005	0.006
Total	2.000	2.001	2.000	1.999	2.000	2.001	2.000	2.000	2.000	2.000	2.000	2.001	1.999	2.000

Sample	at047	at047	at047	at047	at047	at047	at047	at047	at048	at048	at048	at048	at048	at048
Unit	C2	C2	C2	C2	C2	C2	C2	C2	C1	C1	C1	C1	C1	C1
Rock type	cbt	cbt	cbt	cbt	cbt	cbt	cbt	cbt	cbt	cbt	cbt	cbt	cbt	cbt
Remarks	1	1	1	2	2	2	2	2	1	1	1	1	1	2
CaO	53.15	53.52	53.33	54.77	54.22	54.98	54.36	54.76	54.67	53.51	53.44	53.64	53.71	54.84
MgO	0.48	0.49	0.48	0.34	0.32	0.60	0.64	0.25	0.16	0.13	0.25	0.14	0.17	0.21
FeOt	0.04	0.00	0.02	0.04	0.20	0.00	0.00	0.05	0.72	0.75	0.54	0.60	0.65	0.56
MnO	0.07	0.06	0.07	0.07	0.08	0.10	0.08	0.08	0.14	0.13	0.15	0.17	0.14	0.76
SrO	1.97	1.99	1.99	0.67	0.82	0.63	0.84	0.80	0.51	0.63	0.65	0.66	0.62	0.47
BaO	0.41	0.55	0.47	0.00	0.20	0.00	0.13	0.12	0.01	0.05	0.19	0.02	0.07	0.03
CO2	43.26	43.58	43.41	43.70	43.49	44.13	43.80	43.71	43.83	42.97	42.97	43.02	43.12	44.29
Total	99.37	100.18	99.78	99.58	99.34	100.44	99.86	99.77	100.05	98.17	98.19	98.26	98.48	101.16
O=6														
Ca	1.928	1.928	1.928	1.967	1.957	1.955	1.948	1.966	1.958	1.955	1.952	1.957	1.955	1.944
Mg	0.024	0.025	0.024	0.017	0.016	0.030	0.032	0.013	0.008	0.007	0.013	0.007	0.009	0.010
Fe	0.001	0.000	0.001	0.001	0.006	0.000	0.000	0.002	0.020	0.021	0.015	0.017	0.019	0.016
Mn	0.002	0.002	0.002	0.002	0.002	0.003	0.002	0.002	0.004	0.004	0.004	0.005	0.004	0.021
Sr	0.039	0.039	0.039	0.013	0.016	0.012	0.016	0.016	0.010	0.012	0.013	0.013	0.012	0.009
Ba	0.005	0.007	0.006	0.000	0.003	0.000	0.002	0.002	0.000	0.001	0.003	0.000	0.001	0.000
Total	1.999	2.001	2.000	2.000	2.000	2.000	2.000	2.001	2.000	2.000	2.000	1.999	2.000	2.000

Table A2.9 - Calcite analyses

Sample	at049	at049	at049	at049	at049	at049	at049	at049	at049	at049	at049	at050	at050	at050
Unit	C2	C2	C2	C2	C2	C2	C2	C2	C2	C2	C2	C2	C2	C2
Rock type	cbt	cbt	cbt	cbt	cbt	cbt	cbt	cbt	cbt	cbt	cbt	cbt	cbt	cbt
Remarks	1		1	1	1	1	1	1	1	2	2	1	1	1
CaO	51.65	52.03	53.33	52.83	51.78	52.34	52.52	52.10	52.31	54.36	53.18	53.92	53.97	54.01
MgO	1.13	1.00	0.68	0.79	0.73	0.92	0.87	0.96	0.84	0.48	0.90	0.35	0.42	0.40
FeOt	0.28	0.22	0.18	0.26	0.21	0.30	0.27	0.27	0.26	0.21	0.22	0.11	0.05	0.07
MnO	0.31	0.29	0.29	0.26	0.25	0.25	0.33	0.30	0.25	0.30	0.31	0.06	0.11	0.06
SrO	2.98	2.43	2.34	2.47	2.70	2.88	2.68	3.02	2.35	1.36	1.52	1.62	1.60	1.91
BaO	0.42	0.05	0.19	0.27	0.46	0.51	0.10	0.37	0.40	0.07	0.00	0.40	0.20	0.35
CO2	43.53	43.28	43.94	43.77	42.99	43.79	43.70	43.68	43.40	44.10	43.69	43.61	43.63	43.81
Total	100.30	99.30	100.95	100.65	99.12	100.99	100.47	100.71	99.82	100.87	99.82	100.07	99.97	100.61
O=6														
Ca	1.863	1.887	1.905	1.894	1.890	1.876	1.886	1.872	1.892	1.935	1.910	1.941	1.941	1.935
Mg	0.057	0.050	0.034	0.040	0.037	0.046	0.043	0.048	0.042	0.024	0.045	0.018	0.021	0.020
Fe	0.008	0.006	0.005	0.007	0.006	0.008	0.008	0.007	0.007	0.006	0.006	0.003	0.001	0.002
Mn	0.009	0.008	0.008	0.007	0.007	0.007	0.009	0.009	0.007	0.008	0.009	0.002	0.003	0.002
Sr	0.058	0.048	0.045	0.048	0.053	0.056	0.052	0.059	0.046	0.026	0.030	0.032	0.031	0.037
Ba	0.006	0.001	0.002	0.004	0.006	0.007	0.001	0.005	0.005	0.001	0.000	0.005	0.003	0.005
Total	2.001	2.000	1.999	2.000	1.999	2.000	1.999	2.000	1.999	2.000	2.000	2.001	2.000	2.001

Sample	at050	at050	at050	at050	at050	at050	at051	at051	at051	at051	at051	at051	at051	at052
Unit	C2	C2	C2	C2	C2	C2	C2	C2	C2	C2	C2	C2	C2	C1
Rock type	cbt	cbt	cbt	cbt	cbt	cbt	cbt	cbt	cbt	cbt	cbt	cbt	cbt	cbt
Remarks	1	1	1	1	1		p,1	p,1	p,1	g,1	g,1	g,1	g,1	c,1
CaO	53.47	54.02	54.11	53.69	54.08	53.37	53.35	52.70	53.02	52.99	52.69	52.96	52.56	53.14
MgO	0.38	0.44	0.38	0.39	0.39	0.43	0.54	0.53	0.53	0.63	0.54	0.66	0.63	0.79
FeOt	0.10	0.10	0.13	0.00	0.07	0.04	0.20	0.24	0.22	0.50	0.53	0.21	0.42	0.11
MnO	0.00	0.00	0.12	0.18	0.09	0.04	0.25	0.22	0.23	0.30	0.30	0.26	0.28	0.14
SrO	1.77	1.73	1.73	1.47	1.67	1.69	1.63	2.00	1.82	1.80	1.83	1.67	1.79	2.14
BaO	0.43	0.35	0.33	0.42	0.36	0.42	0.06	0.20	0.13	0.26	0.20	0.31	0.20	0.00
CO2	43.32	43.77	43.87	43.42	43.77	43.24	43.44	43.13	43.28	43.61	43.28	43.37	43.19	43.63
Total	99.47	100.41	100.67	99.58	100.43	99.22	99.46	99.02	99.24	100.09	99.36	99.44	99.07	99.95
O=6														
Ca	1.937	1.937	1.936	1.941	1.939	1.937	1.928	1.918	1.923	1.907	1.911	1.917	1.910	1.912
Mg	0.019	0.022	0.019	0.020	0.020	0.022	0.027	0.027	0.027	0.032	0.027	0.033	0.032	0.040
Fe	0.003	0.003	0.004	0.000	0.002	0.001	0.006	0.007	0.006	0.014	0.015	0.006	0.012	0.003
Mn	0.000	0.000	0.003	0.005	0.003	0.001	0.007	0.006	0.007	0.009	0.009	0.007	0.008	0.004
Sr	0.035	0.034	0.034	0.029	0.032	0.033	0.032	0.039	0.036	0.035	0.036	0.033	0.035	0.042
Ba	0.006	0.005	0.004	0.006	0.005	0.006	0.001	0.003	0.002	0.003	0.003	0.004	0.003	0.000
Total	2.000	2.001	2.000	2.001	2.001	2.000	2.001	2.000	2.001	2.000	2.001	2.000	2.000	2.001

Table A2.9 - Calcite analyses

Sample	at052	at052	at052	at052	at052	at055	at055	at055	at055	at055	at055	at055	at055	at055
Unit	C1	C1	C1	C1	C1	C1	C1	C1	C1	C1	C1	C1	C1	C1
Rock type	cbt	cbt	cbt	cbt	cbt	cbt	cbt	cbt	cbt	cbt	cbt	cbt	cbt	cbt
Remarks	1	1	2	2	2	1	1	1	1	1	1	1	1	1
CaO	51.53	51.54	53.69	55.58	54.66	53.36	53.55	53.25	53.16	53.36	53.43	53.58	53.22	53.34
MgO	1.02	0.68	0.33	0.12	0.11	0.49	0.45	0.48	0.49	0.52	0.47	0.50	0.46	0.43
FeOt	0.17	0.05	0.09	0.00	0.02	0.06	0.05	0.11	0.07	0.06	0.01	0.03	0.08	0.12
MnO	0.25	0.22	0.25	0.21	0.24	0.11	0.10	0.12	0.12	0.12	0.15	0.10	0.13	0.12
SrO	2.37	2.89	0.82	0.75	0.25	2.03	1.92	2.01	2.09	1.82	1.87	1.84	1.95	1.91
BaO	0.67	0.64	0.00	0.03	0.00	0.45	0.36	0.56	0.68	0.62	0.58	0.39	0.73	0.61
CO2	43.02	42.78	43.06	44.21	43.28	43.52	43.55	43.48	43.46	43.52	43.52	43.59	43.45	43.48
Total	99.04	98.80	98.24	100.91	98.56	100.02	99.98	100.01	100.07	100.01	100.04	100.03	100.02	100.01
O=6														
Ca	1.880	1.891	1.957	1.973	1.982	1.924	1.930	1.922	1.920	1.925	1.927	1.929	1.923	1.925
Mg	0.052	0.035	0.017	0.006	0.006	0.024	0.023	0.024	0.025	0.026	0.024	0.025	0.023	0.022
Fe	0.005	0.001	0.003	0.000	0.001	0.002	0.001	0.003	0.002	0.002	0.000	0.001	0.002	0.004
Mn	0.007	0.006	0.007	0.006	0.007	0.003	0.003	0.004	0.003	0.004	0.004	0.003	0.004	0.003
Sr	0.047	0.057	0.016	0.014	0.005	0.040	0.037	0.039	0.041	0.035	0.036	0.036	0.038	0.037
Ba	0.009	0.009	0.000	0.000	0.000	0.006	0.005	0.007	0.009	0.008	0.008	0.005	0.010	0.008
Total	2.000	1.999	2.000	1.999	2.001	1.999	1.999	1.999	2.000	2.000	1.999	1.999	2.000	1.999

Sample	at055	at055	at055	at055	at055	at055	at055	at055	at055	at055	at055	at055	at056	at056
Unit	C1	C1	C1	C1	C1	C1	C1	C1	C1	C1	C1	C1	C2	C2
Rock type	cbt	cbt	cbt	cbt	cbt	cbt	cbt	cbt	cbt	cbt	cbt	cbt	cbt	cbt
Remarks	1	1	1	1	1	1	1	1	1	1	1	2	1	1
CaO	53.39	53.38	53.48	53.42	53.29	53.65	53.63	53.25	53.42	53.38	53.56	54.35	53.45	52.83
MgO	0.40	0.41	0.41	0.40	0.61	0.39	0.38	0.59	0.46	0.43	0.36	0.31	0.47	0.47
FeOt	0.10	0.00	0.14	0.06	0.14	0.01	0.10	0.03	0.07	0.11	0.10	0.04	0.05	0.15
MnO	0.15	0.12	0.11	0.12	0.12	0.10	0.13	0.13	0.12	0.09	0.15	0.13	0.08	0.10
SrO	1.95	1.90	1.76	1.78	1.85	1.83	1.90	1.93	1.88	2.01	1.79	0.71	2.26	1.99
BaO	0.58	0.75	0.68	0.72	0.47	0.57	0.34	0.50	0.49	0.55	0.56	0.30	0.24	0.57
CO2	43.49	43.45	43.52	43.46	43.58	43.53	43.56	43.53	43.51	43.50	43.52	43.48	43.56	43.13
Total	100.05	100.01	100.09	99.97	100.05	100.08	100.05	99.95	99.95	100.06	100.04	99.31	100.10	99.23
O=6														
Ca	1.927	1.928	1.929	1.929	1.919	1.934	1.932	1.920	1.927	1.926	1.932	1.962	1.926	1.923
Mg	0.020	0.021	0.021	0.020	0.031	0.019	0.019	0.030	0.023	0.022	0.018	0.016	0.023	0.024
Fe	0.003	0.000	0.004	0.002	0.004	0.000	0.003	0.001	0.002	0.003	0.003	0.001	0.001	0.004
Mn	0.004	0.003	0.003	0.004	0.003	0.003	0.004	0.004	0.003	0.002	0.004	0.004	0.002	0.003
Sr	0.038	0.037	0.034	0.035	0.036	0.036	0.037	0.038	0.037	0.039	0.035	0.014	0.044	0.039
Ba	0.008	0.010	0.009	0.010	0.006	0.008	0.004	0.007	0.006	0.007	0.007	0.004	0.003	0.008
Total	2.000	1.999	2.000	2.000	1.999	2.000	1.999	2.000	1.998	1.999	1.999	2.001	1.999	2.001

Table A2.9 - Calcite analyses

Sample	at056	at056	at056	at056	at056	at056	at056	at056	at057	at057	at057	at057	at057	at057
Unit	C2	C2	C2	C2	C2	C2	C2	C2	C2	C2	C2	C2	C2	C2
Rock type	cbt	cbt	cbt	cbt	cbt	cbt	cbt	cbt	cbt	cbt	cbt	cbt	cbt	cbt
Remarks	1	1	1	1		2	2	2						
CaO	53.51	53.81	53.62	53.44	55.47	53.98	53.58	54.71	54.37	53.95	54.85	54.82	54.71	54.59
MgO	0.48	0.51	0.50	0.48	0.15	0.42	0.44	0.46	0.32	0.20	0.13	0.19	0.14	0.17
FeOt	0.03	0.09	0.07	0.08	0.33	0.02	0.03	0.00	0.19	0.14	0.34	0.18	0.60	0.26
MnO	0.06	0.02	0.09	0.07	0.02	0.04	0.10	0.11	0.21	0.10	0.19	0.21	0.28	0.15
SrO	2.07	2.11	2.12	2.11	0.38	1.03	1.66	1.26	0.69	1.18	0.39	0.41	0.24	0.54
BaO	0.46	0.35	0.50	0.42	0.09	0.20	0.06	0.17	0.21	0.38	0.10	0.10	0.01	0.00
CO2	43.59	43.84	43.77	43.58	44.10	43.35	43.34	44.09	43.69	43.45	43.77	43.75	43.79	43.65
Total	100.20	100.73	100.67	100.18	100.55	99.04	99.21	100.80	99.68	99.40	99.77	99.66	99.76	99.37
O=6														
Ca	1.927	1.926	1.923	1.925	1.974	1.954	1.941	1.948	1.953	1.949	1.967	1.966	1.961	1.963
Mg	0.024	0.025	0.025	0.024	0.007	0.021	0.022	0.023	0.016	0.010	0.007	0.010	0.007	0.009
Fe	0.001	0.002	0.002	0.002	0.009	0.001	0.001	0.000	0.005	0.004	0.010	0.005	0.017	0.007
Mn	0.002	0.001	0.003	0.002	0.001	0.001	0.003	0.003	0.006	0.003	0.005	0.006	0.008	0.004
Sr	0.040	0.041	0.041	0.041	0.007	0.020	0.032	0.024	0.013	0.023	0.008	0.008	0.005	0.011
Ba	0.006	0.005	0.007	0.006	0.001	0.003	0.001	0.002	0.003	0.005	0.001	0.001	0.000	0.000
Total	2.000	2.000	2.001	2.000	1.999	2.000	2.000	2.000	1.996	1.994	1.998	1.996	1.998	1.994

Sample	at057	at057	at057	at057	at057	at057	at057	at057	at057	at057	at057	at058b	at058b	at058b
Unit	C2	C2	C2	C2	C2	C2	C2	C2	C2	C2	C2	C5	C5	C5
Rock type	cbt	cbt	cbt	cbt	cbt	cbt	cbt	cbt	cbt	cbt	cbt	cbt	cbt	cbt
Remarks												1	1	1
CaO	54.46	55.09	54.77	54.43	54.47	53.90	54.09	53.62	54.35	50.69	51.80	55.05	55.32	55.05
MgO	0.37	0.15	0.22	0.22	0.15	0.47	0.59	0.68	0.54	2.56	1.51	0.14	0.07	0.12
FeOt	0.36	0.26	0.13	0.26	0.56	0.21	0.28	0.96	0.25	1.25	1.72	0.44	0.37	0.47
MnO	0.19	0.20	0.17	0.06	0.34	0.18	0.24	0.25	0.29	0.28	0.27	0.12	0.16	0.15
SrO	0.48	0.26	0.66	0.69	0.25	0.68	0.60	0.40	0.45	0.24	0.35	0.38	0.18	0.28
BaO	0.04	0.00	0.00	0.11	0.00	0.05	0.04	0.01	0.00	0.02	0.02	0.04	0.00	0.08
CO2	43.78	43.85	43.77	43.59	43.63	43.47	43.77	43.81	43.84	43.75	43.78	43.87	43.91	43.87
Total	99.67	99.79	99.72	99.36	99.40	98.96	99.59	99.74	99.72	98.79	99.45	100.04	100.00	100.00
O=6														
Ca	1.953	1.972	1.964	1.960	1.959	1.946	1.940	1.921	1.946	1.818	1.857	1.969	1.977	1.970
Mg	0.018	0.007	0.011	0.011	0.007	0.023	0.029	0.034	0.027	0.128	0.075	0.007	0.004	0.006
Fe	0.010	0.007	0.004	0.007	0.016	0.006	0.008	0.027	0.007	0.035	0.048	0.012	0.010	0.013
Mn	0.005	0.006	0.005	0.002	0.010	0.005	0.007	0.007	0.008	0.008	0.008	0.004	0.005	0.004
Sr	0.009	0.005	0.013	0.013	0.005	0.013	0.012	0.008	0.009	0.005	0.007	0.007	0.003	0.005
Ba	0.001	0.000	0.000	0.001	0.000	0.001	0.001	0.000	0.000	0.000	0.000	0.000	0.000	0.001
Total	1.996	1.997	1.997	1.994	1.997	1.994	1.997	1.997	1.997	1.994	1.995	1.999	1.999	1.999

Table A2.9 - Calcite analyses

Sample	at058b	at058b	at058b	at058b	at058b	at058b	at058b	at058b	at058b	at058b	at058b	at059	at059	at059
Unit	C5	C5	C5	C5	C5	C5	C5	C5	C5	C5	C5	C1	C1	C1
Rock type	cbt	cbt	cbt	cbt	cbt	cbt	cbt	cbt	cbt	cbt	cbt	cbt	cbt	cbt
Remarks	1	g	g	g	g	2	2	2	2	2	2		1	1
CaO	55.25	55.07	55.36	55.15	55.03	55.41	55.54	55.18	55.50	55.35	55.33	51.11	51.22	51.68
MgO	0.11	0.11	0.14	0.14	0.19	0.12	0.06	0.11	0.04	0.05	0.07	0.51	0.36	0.32
FeOt	0.39	0.40	0.28	0.37	0.32	0.18	0.25	0.25	0.19	0.30	0.24	0.32	0.28	0.21
MnO	0.09	0.15	0.11	0.12	0.15	0.12	0.12	0.16	0.11	0.11	0.18	0.56	0.43	0.34
SrO	0.30	0.47	0.19	0.37	0.37	0.19	0.17	0.43	0.31	0.33	0.33	3.27	3.75	3.53
BaO	0.00	0.00	0.06	0.02	0.09	0.07	0.00	0.00	0.00	0.04	0.02	0.50	0.50	0.75
CO2	43.91	43.88	43.94	43.90	43.88	43.93	43.95	43.88	43.92	43.90	43.91	42.75	42.77	42.97
Total	100.05	100.08	100.09	100.08	100.02	100.03	100.08	100.01	100.07	100.07	100.09	99.02	99.33	99.81
O=6														
Ca	1.975	1.970	1.977	1.972	1.968	1.980	1.983	1.974	1.983	1.979	1.978	1.877	1.880	1.888
Mg	0.005	0.006	0.007	0.007	0.009	0.006	0.003	0.006	0.002	0.002	0.004	0.026	0.018	0.016
Fe	0.011	0.011	0.008	0.010	0.009	0.005	0.007	0.007	0.005	0.008	0.007	0.009	0.008	0.006
Mn	0.003	0.004	0.003	0.003	0.004	0.003	0.003	0.005	0.003	0.003	0.005	0.016	0.013	0.010
Sr	0.006	0.009	0.004	0.007	0.007	0.004	0.003	0.008	0.006	0.006	0.006	0.065	0.075	0.070
Ba	0.000	0.000	0.001	0.000	0.001	0.001	0.000	0.000	0.000	0.000	0.000	0.007	0.007	0.010
Total	2.000	2.000	2.000	1.999	1.998	1.999	1.999	2.000	1.999	1.998	2.000	2.000	2.001	2.000

Sample	at059	at059	at059	at059	at059	at059	at059	at059	at060a	at060a	at060a	at060a	at060a	at060a
Unit	C1	C1	C1	C1	C1	C1	C1	C1	C3	C3	C3	C3	C3	C3
Rock type	cbt	cbt	cbt	cbt	cbt	cbt	cbt	cbt	cbt	cbt	cbt	cbt	cbt	cbt
Remarks	1	1	1	1	1	1	1	1	p	2	2	1	1	1
CaO	50.66	51.81	51.15	51.75	50.88	52.49	51.15	51.00	52.84	54.27	54.17	52.72	53.36	53.16
MgO	0.37	0.36	0.37	0.40	0.55	0.34	0.33	0.45	0.38	0.24	0.27	0.40	0.33	0.33
FeOt	0.45	0.41	0.34	0.35	0.27	0.20	0.31	0.42	0.03	0.03	0.12	0.10	0.10	0.07
MnO	0.53	0.46	0.31	0.76	0.43	0.45	0.48	0.44	0.09	0.11	0.09	0.12	0.13	0.11
SrO	3.85	2.94	4.07	3.33	3.77	2.37	3.33	3.74	2.32	1.60	1.66	2.16	2.18	2.03
BaO	0.75	0.36	0.83	0.46	0.76	0.45	0.94	1.08	0.34	0.12	0.03	0.40	0.30	0.22
CO2	42.62	42.94	42.92	43.29	42.79	43.10	42.69	42.95	43.05	43.64	43.65	42.98	43.40	43.12
Total	99.23	99.28	99.98	100.34	99.45	99.40	99.24	100.09	99.05	100.01	99.99	98.88	99.79	99.04
O=6														
Ca	1.866	1.894	1.871	1.876	1.866	1.911	1.881	1.864	1.927	1.952	1.948	1.925	1.930	1.935
Mg	0.019	0.018	0.019	0.020	0.028	0.017	0.017	0.023	0.019	0.012	0.014	0.020	0.017	0.017
Fe	0.013	0.012	0.010	0.010	0.008	0.006	0.009	0.012	0.001	0.001	0.003	0.003	0.003	0.002
Mn	0.015	0.013	0.009	0.022	0.013	0.013	0.014	0.013	0.003	0.003	0.003	0.004	0.004	0.003
Sr	0.077	0.058	0.081	0.065	0.075	0.047	0.066	0.074	0.046	0.031	0.032	0.043	0.043	0.040
Ba	0.010	0.005	0.011	0.006	0.010	0.006	0.013	0.014	0.005	0.002	0.000	0.005	0.004	0.003
Total	2.000	2.000	2.001	1.999	2.000	2.000	2.000	2.000	2.001	2.001	2.000	2.000	2.001	2.000

Table A2.9 - Calcite analyses

Sample	at060a	at060b	at060b	at060b	at061b	at061b	at120	at120	at120	at120	at120	at131	at131	at131
Unit	C3	C3	C3	C3	C5	C5						C4	C4	C4
Rock type	cbt	cbt	cbt	cbt	cbt	cbt	php	php	php	php	php	cbt	cbt	cbt
Remarks	2	1	1	1			g	g	g	g	g			
CaO	52.90	52.34	52.68	52.55	54.15	53.71	54.02	54.83	52.85	54.53	54.05	53.78	53.77	53.58
MgO	0.36	0.27	0.32	0.30	0.03	0.03	0.09	0.10	0.10	0.00	0.06	0.25	0.27	0.33
FeOt	0.12	0.14	0.19	0.18	0.47	0.28	0.03	0.06	0.11	0.06	0.14	0.04	0.00	0.27
MnO	0.07	0.18	0.11	0.15	0.12	0.24	0.08	0.00	0.07	0.06	0.09	0.08	0.07	0.04
SrO	1.75	2.20	2.33	2.18	0.19	0.02	1.81	1.07	2.80	1.30	1.77	1.82	1.66	1.72
BaO	0.24	0.40	0.46	0.20	0.02	0.04	0.22	0.07	0.59	0.25	0.07	0.38	0.30	0.21
CO2	42.84	42.62	43.00	42.75	42.99	42.53	43.45	43.67	43.15	43.53	43.48	43.50	43.49	43.52
Total	98.29	98.14	99.09	98.30	97.98	96.86	99.70	99.80	99.67	99.73	99.66	99.85	99.56	99.67
O=6														
Ca	1.938	1.928	1.923	1.929	1.977	1.982	1.947	1.967	1.920	1.962	1.947	1.939	1.938	1.930
Mg	0.019	0.014	0.016	0.015	0.002	0.002	0.005	0.005	0.005	0.000	0.003	0.013	0.014	0.017
Fe	0.003	0.004	0.005	0.005	0.013	0.008	0.001	0.002	0.003	0.002	0.004	0.001	0.000	0.008
Mn	0.002	0.005	0.003	0.004	0.004	0.007	0.002	0.000	0.002	0.002	0.003	0.002	0.002	0.001
Sr	0.035	0.044	0.046	0.043	0.004	0.000	0.035	0.021	0.055	0.025	0.035	0.036	0.032	0.034
Ba	0.003	0.005	0.006	0.003	0.000	0.001	0.003	0.001	0.008	0.003	0.001	0.005	0.004	0.003
Total	2.000	2.000	1.999	1.999	2.000	2.000	1.993	1.996	1.993	1.994	1.993	1.996	1.990	1.993

Sample	at131	at204	at204	at204	at205	at205	at205	at205	at205	at205	at205	at205	at205	at209a
Unit	C4													
Rock type	cbt	php	php	php	lcr	lcr	lcr	lcr	lcr	lcr	lcr	lcr	lcr	lcr
Remarks			g											
CaO	53.99	55.33	54.90	54.90	55.25	54.70	54.33	54.35	54.36	55.08	54.74	55.21	53.97	53.03
MgO	0.25	0.06	0.03	0.07	0.07	0.07	0.09	0.00	0.06	0.04	0.06	0.15	0.22	0.07
FeOt	0.00	0.08	0.09	0.11	0.38	0.23	0.70	0.06	0.03	0.06	0.11	0.32	0.99	1.01
MnO	0.00	0.04	0.00	0.14	0.12	0.05	0.08	0.12	0.06	0.03	0.09	0.11	0.11	0.02
SrO	1.74	0.54	0.93	0.55	0.06	1.12	0.93	1.43	1.29	0.78	1.13	0.06	0.74	0.00
BaO	0.21	0.00	0.07	0.09	0.00	0.00	0.01	0.29	0.39	0.02	0.00	0.15	0.02	0.34
CO2	43.55	43.81	43.67	43.71	43.83	43.68	43.64	43.53	43.54	43.70	43.66	43.82	43.70	42.89
Total	99.74	99.86	99.69	99.57	99.71	99.85	99.78	99.78	99.73	99.71	99.79	99.82	99.75	97.36
O=6														
Ca	1.943	1.980	1.969	1.967	1.974	1.963	1.950	1.958	1.958	1.974	1.965	1.974	1.937	1.899
Mg	0.013	0.003	0.001	0.003	0.003	0.003	0.004	0.000	0.003	0.002	0.003	0.007	0.011	0.003
Fe	0.000	0.002	0.003	0.003	0.011	0.006	0.020	0.002	0.001	0.002	0.003	0.009	0.028	0.028
Mn	0.000	0.001	0.000	0.004	0.003	0.001	0.002	0.003	0.002	0.001	0.003	0.003	0.003	0.001
Sr	0.034	0.010	0.018	0.011	0.001	0.022	0.018	0.028	0.025	0.015	0.022	0.001	0.014	0.000
Ba	0.003	0.000	0.001	0.001	0.000	0.000	0.000	0.004	0.005	0.000	0.000	0.002	0.000	0.004
Total	1.993	1.996	1.992	1.989	1.992	1.995	1.994	1.995	1.994	1.994	1.996	1.996	1.993	1.935

Table A2.9 - Calcite analyses

Sample	at209a	at211	at211	at211	at211	at211	at212	at212	at212	at212	at212	at212	at212	at212
Unit							C2	C2	C2	C2	C2	C2	C2	C2
Rock type	lcr	lcr	lcr	lcr	lcr	lcr	cbt,dk	cbt,dk	cbt,dk	cbt,dk	cbt,dk	cbt,dk	cbt,dk	cbt,dk
Remarks							p	p	p	p	p, rim	p, core	g	g
CaO	53.03	54.62	54.37	53.28	53.08	54.65	53.79	53.15	54.51	52.76	54.68	53.72	54.56	54.22
MgO	0.07	0.07	0.06	0.04	0.00	0.00	0.35	0.18	0.21	0.34	0.24	0.43	0.37	0.34
FeOt	1.01	0.10	0.12	0.03	0.23	0.11	0.58	0.17	0.61	0.38	0.20	0.49	0.39	0.38
MnO	0.02	0.48	0.00	0.02	0.04	0.41	0.10	0.04	0.12	0.07	0.41	0.50	0.30	0.20
SrO	0.00	0.49	1.26	1.71	1.69	0.68	0.95	2.55	0.50	1.84	0.32	0.93	0.38	0.68
BaO	0.34	0.09	0.15	1.13	1.58	0.29	0.18	0.43	0.06	0.43	0.05	0.05	0.00	0.36
CO2	42.89	43.66	43.58	43.21	43.06	43.61	43.60	43.29	43.74	43.08	43.78	43.70	43.83	43.69
Total	97.36	99.51	99.54	99.42	99.68	99.75	99.55	99.81	99.75	98.90	99.68	99.82	99.83	99.87
O=6														
Ca	1.899	1.958	1.955	1.933	1.930	1.964	1.932	1.925	1.953	1.904	1.957	1.927	1.951	1.946
Mg	0.003	0.003	0.003	0.002	0.000	0.000	0.017	0.009	0.010	0.017	0.012	0.021	0.018	0.017
Fe	0.028	0.003	0.003	0.001	0.007	0.003	0.016	0.005	0.017	0.011	0.006	0.014	0.011	0.011
Mn	0.001	0.014	0.000	0.001	0.001	0.012	0.003	0.001	0.003	0.002	0.012	0.014	0.008	0.006
Sr	0.000	0.010	0.025	0.034	0.033	0.013	0.018	0.050	0.010	0.036	0.006	0.018	0.007	0.013
Ba	0.004	0.001	0.002	0.015	0.021	0.004	0.002	0.006	0.001	0.006	0.001	0.001	0.000	0.005
Total	1.935	1.989	1.988	1.986	1.992	1.996	1.988	1.996	1.994	1.976	1.994	1.995	1.995	1.998

Sample	at212	at212	at212	at212	at212	at212	at212	at212	at212	at212
Unit	C2	C2	C2	C2	C2	C2	C2	C2	C2	C2
Rock type	cbt,dk	cbt,dk	cbt,dk	cbt,dk	cbt,dk	cbt,dk	cbt,dk	cbt,dk	cbt,dk	cbt,dk
Remarks	g	g	g	p,rim	p, rim	p,core	p	p	p	g
CaO	54.33	54.73	53.75	55.08	54.61	53.23	53.46	52.92	54.42	53.37
MgO	0.22	0.27	0.29	0.02	0.23	0.14	0.15	0.16	0.24	0.50
FeOt	0.16	0.18	0.76	0.08	0.22	0.19	0.21	0.37	0.42	0.76
MnO	0.48	0.43	0.09	0.63	0.41	0.01	0.03	0.07	0.14	0.29
SrO	0.21	0.27	0.42	0.22	0.35	2.17	1.89	2.22	0.69	0.86
BaO	0.64	0.00	0.90	0.00	0.04	0.39	0.55	0.42	0.10	0.11
CO2	43.65	43.79	43.52	43.79	43.76	43.20	43.34	43.12	43.69	43.60
Total	99.69	99.67	99.73	99.82	99.62	99.33	99.63	99.28	99.70	99.49
O=6										
Ca	1.950	1.958	1.935	1.971	1.954	1.926	1.933	1.916	1.951	1.917
Mg	0.011	0.013	0.015	0.001	0.011	0.007	0.008	0.008	0.012	0.025
Fe	0.004	0.005	0.021	0.002	0.006	0.005	0.006	0.010	0.012	0.021
Mn	0.014	0.012	0.003	0.018	0.012	0.000	0.001	0.002	0.004	0.008
Sr	0.004	0.005	0.008	0.004	0.007	0.042	0.037	0.043	0.013	0.017
Ba	0.008	0.000	0.012	0.000	0.001	0.005	0.007	0.006	0.001	0.001
Total	1.991	1.993	1.994	1.996	1.991	1.985	1.992	1.985	1.993	1.989

Table A2.10 - Dolomite analyses

Sample	at042	at042	at044	at044	at045	at045	at045	at045	at045	at046	at046	at046	at046	at046
Unit	C1	C1	C1	C1	C2	C2	C2	C2	C2	C2	C2	C2	C2	C2
Rock type	cbt	cbt	cbt	cbt	cbt	cbt	cbt	cbt	cbt	cbt	cbt	cbt	cbt	cbt
Remarks	v,1	v,1	1	1		1	1	1	1	1	1	2	2	2
CaO	28.91	28.80	33.11	33.83	28.99	28.91	29.10	29.03	29.75	29.44	29.65	29.70	29.97	29.31
MgO	20.10	20.14	18.04	18.78	19.21	19.31	19.26	19.19	20.04	19.45	19.41	19.67	19.83	19.70
FeOt	1.20	1.52	0.13	0.10	1.71	1.44	1.73	1.62	1.50	1.69	1.92	1.72	1.52	1.62
MnO	0.24	0.27	0.05	0.08	0.49	0.44	0.50	0.46	0.45	0.46	0.59	0.54	0.52	0.46
SrO	1.09	0.94	0.51	0.56	1.18	1.15	1.08	1.20	1.31	1.12	0.80	0.48	0.40	1.09
BaO	0.01	0.02	0.00	0.13	0.09	0.06	0.02	0.09	0.03	0.00	0.04	0.00	0.08	0.00
CO2	45.99	46.11	46.00	47.43	45.62	45.45	45.71	45.56	46.99	46.14	46.35	46.38	46.63	46.26
Total	97.54	97.81	97.83	100.91	97.29	96.76	97.40	97.17	100.05	98.31	98.76	98.49	98.96	98.46
O=6														
Ca	0.987	0.981	1.130	1.119	0.998	0.998	0.999	1.000	0.994	1.001	1.004	1.005	1.009	0.995
Mg	0.955	0.954	0.856	0.865	0.920	0.928	0.920	0.920	0.931	0.920	0.914	0.926	0.929	0.930
Fe	0.032	0.041	0.003	0.003	0.046	0.039	0.046	0.044	0.039	0.045	0.051	0.045	0.040	0.043
Mn	0.006	0.007	0.001	0.002	0.013	0.012	0.013	0.013	0.012	0.012	0.016	0.014	0.014	0.012
Sr	0.020	0.017	0.009	0.010	0.022	0.022	0.020	0.022	0.024	0.021	0.015	0.009	0.007	0.020
Ba	0.000	0.000	0.000	0.002	0.001	0.001	0.000	0.001	0.000	0.000	0.001	0.000	0.001	0.000
Total	2.000	2.000	1.999	2.001	2.000	2.000	1.998	2.000	2.000	1.999	2.001	1.999	2.000	2.000

Sample	at046	at049	at049	at049	at049	at049	at049	at049	at049	at052	at052	at053b	at053b	at053b
Unit	C2	C2	C2	C2	C2	C2	C2	C2	C2	C1	C1	C5	C5	C5
Rock type	cbt	cbt	cbt	cbt	cbt	cbt	cbt	cbt	cbt	cbt	cbt	cbt	cbt	cbt
Remarks	2	c, 1	1	1	1	1	1	1	1	v	v	1	1	1
CaO	29.47	29.81	29.34	29.76	29.79	29.81	29.37	29.63	29.56	32.88	32.84	29.59	29.74	29.68
MgO	19.63	19.84	19.62	19.76	19.49	19.96	19.67	19.76	19.50	17.26	17.78	20.34	19.91	20.05
FeOt	1.64	1.58	1.48	1.12	2.09	1.19	1.73	1.87	2.03	1.88	0.53	1.25	1.63	1.61
MnO	0.48	0.43	0.44	0.34	0.61	0.43	0.46	0.57	0.55	0.27	0.40	0.51	0.58	0.51
SrO	0.98	1.21	1.23	1.46	0.40	1.19	1.05	0.92	0.90	0.71	0.65	1.16	1.22	1.08
BaO	0.09	0.00	0.00	0.00	0.03	0.00	0.00	0.11	0.18	0.55	0.69	0.00	0.00	0.08
CO2	46.32	46.80	46.16	46.45	46.49	46.69	46.32	46.76	46.51	46.43	46.24	47.05	46.97	46.99
Total	98.62	99.66	98.28	98.88	98.90	99.27	98.60	99.63	99.23	99.99	99.14	99.90	100.05	100.00
O=6														
Ca	0.999	1.000	0.998	1.006	1.006	1.002	0.995	0.995	0.997	1.111	1.115	0.987	0.994	0.991
Mg	0.926	0.926	0.928	0.929	0.915	0.934	0.927	0.923	0.915	0.812	0.840	0.944	0.926	0.932
Fe	0.043	0.041	0.039	0.030	0.055	0.031	0.046	0.049	0.054	0.050	0.014	0.032	0.042	0.042
Mn	0.013	0.011	0.012	0.009	0.016	0.011	0.012	0.015	0.015	0.007	0.011	0.013	0.015	0.013
Sr	0.018	0.022	0.023	0.027	0.007	0.022	0.019	0.017	0.016	0.013	0.012	0.021	0.022	0.020
Ba	0.001	0.000	0.000	0.000	0.000	0.000	0.000	0.001	0.002	0.007	0.009	0.000	0.000	0.001
Total	2.000	2.000	2.000	2.001	1.999	2.000	1.999	2.000	1.999	2.000	2.001	1.997	1.999	1.999

Table A2.10 - Dolomite analyses

Sample	at053b	at053b	at053b	at053b	at053b	at053b	at053b	at053b	at053b	at053b	at053b	at053b	at053b	at053b
Unit	C5	C5	C5	C5	C5	C5	C5	C5	C5	C5	C5	C5	C5	C5
Rock type	cbt	cbt	cbt	cbt	cbt	cbt	cbt	cbt	cbt	cbt	cbt	cbt	cbt	cbt
Remarks	1	1	1	1	1	1	1	1	1	1	1	1	1	1
CaO	29.62	29.62	29.79	29.54	29.62	29.77	29.81	29.84	29.69	29.86	29.67	29.82	29.64	29.63
MgO	20.26	20.29	20.07	20.04	20.17	20.03	20.01	19.03	20.14	20.32	19.76	18.40	20.30	20.09
FeOt	1.53	1.48	1.56	1.68	1.38	1.39	1.48	2.69	1.47	1.33	1.78	3.21	1.20	1.59
MnO	0.51	0.55	0.50	0.59	0.61	0.51	0.56	0.71	0.54	0.48	0.71	0.89	0.54	0.54
SrO	1.02	1.03	1.06	1.17	1.09	1.00	1.00	0.99	1.04	0.94	1.10	1.02	1.16	0.98
BaO	0.00	0.00	0.00	0.08	0.00	0.07	0.00	0.00	0.05	0.00	0.00	0.00	0.00	0.00
CO2	47.08	47.09	47.04	46.98	47.00	46.93	46.97	46.73	47.02	47.15	46.89	46.50	47.04	46.99
Total	100.02	100.06	100.03	100.09	99.88	99.71	99.84	99.99	99.97	100.08	99.91	99.83	99.89	99.83
O=6														
Ca	0.988	0.987	0.994	0.987	0.989	0.996	0.996	1.002	0.991	0.994	0.993	1.007	0.989	0.990
Mg	0.940	0.941	0.932	0.931	0.937	0.932	0.930	0.889	0.935	0.941	0.920	0.864	0.943	0.934
Fe	0.040	0.038	0.041	0.044	0.036	0.036	0.039	0.070	0.038	0.035	0.046	0.085	0.031	0.042
Mn	0.014	0.015	0.013	0.016	0.016	0.014	0.015	0.019	0.014	0.013	0.019	0.024	0.014	0.014
Sr	0.018	0.019	0.019	0.021	0.020	0.018	0.018	0.018	0.019	0.017	0.020	0.019	0.021	0.018
Ba	0.000	0.000	0.000	0.001	0.000	0.001	0.000	0.000	0.001	0.000	0.000	0.000	0.000	0.000
Total	2.000	2.000	1.999	2.000	1.998	1.997	1.998	1.998	1.998	2.000	1.998	1.999	1.998	1.998

Sample	at053b	at053b	at054	at054	at054	at054	at054	at054	at054	at054	at104	at104	at104	at104
Unit	C5	C5	C5	C5	C5	C5	C5	C5	C5	C5				
Rock type	cbt	cbt	cbt	cbt	cbt	cbt	cbt	cbt	cbt	cbt	RR	RR	RR	RR
Remarks	1		1	1	1	1	1	1	v, 1	v, 1				
CaO	29.56	29.36	29.27	29.58	29.64	29.58	29.50	29.66	29.34	29.48	27.69	28.93	28.13	29.74
MgO	20.37	20.05	20.94	21.18	20.95	20.82	20.56	20.73	20.74	21.12	20.46	19.55	19.86	18.93
FeOt	1.40	0.97	0.81	0.70	0.75	0.78	1.24	0.84	0.83	0.60	1.10	0.91	1.42	1.60
MnO	0.55	0.39	0.27	0.21	0.21	0.20	0.22	0.26	0.25	0.20	0.04	0.12	0.11	0.27
SrO	0.95	0.99	1.22	0.86	1.11	0.86	0.93	1.18	1.20	1.06	2.24	1.96	2.26	1.32
BaO	0.00	0.00	0.17	0.01	0.05	0.00	0.04	0.00	0.06	0.14	1.59	1.66	1.71	1.39
CO2	47.08	46.21	47.07	47.27	47.22	46.92	46.91	47.09	46.87	47.17	46.40	46.24	46.28	46.30
Total	99.91	97.97	99.75	99.80	99.94	99.16	99.41	99.76	99.29	99.76	99.52	99.37	99.77	99.55
O=6														
Ca	0.985	0.997	0.976	0.982	0.985	0.989	0.987	0.989	0.983	0.981	0.935	0.980	0.954	1.007
Mg	0.945	0.948	0.972	0.979	0.969	0.969	0.957	0.961	0.967	0.978	0.962	0.921	0.937	0.892
Fe	0.036	0.026	0.021	0.018	0.019	0.020	0.032	0.022	0.022	0.015	0.029	0.024	0.038	0.042
Mn	0.014	0.010	0.007	0.006	0.006	0.005	0.006	0.007	0.007	0.005	0.001	0.003	0.003	0.007
Sr	0.017	0.018	0.022	0.015	0.020	0.016	0.017	0.021	0.022	0.019	0.041	0.036	0.041	0.024
Ba	0.000	0.000	0.002	0.000	0.001	0.000	0.000	0.000	0.001	0.002	0.020	0.021	0.021	0.017
Total	1.997	1.999	2.000	2.000	2.000	1.999	1.999	2.000	2.002	2.000	1.988	1.985	1.994	1.989

Table A2.10 - Dolomite analyses

Sample	at104	at104	at104	at104	at104	at104	at046	at051
Unit							C2	C2
Rock type	RR	RR	RR	RR	RR	RR	cbt	cbt
Remarks								g,1
CaO	28.81	31.12	32.40	30.81	31.05	28.63	30.35	28.92
MgO	19.14	17.84	18.09	19.55	18.06	19.19	17.32	17.46
FeOt	2.38	2.18	1.55	0.34	0.75	1.91	4.32	4.70
MnO	0.45	1.20	0.07	0.13	0.99	0.07	0.92	1.38
SrO	1.24	0.43	0.68	1.73	1.72	1.83	0.25	0.18
BaO	1.14	0.41	0.00	0.30	0.99	1.71	0.00	0.00
CO2	46.33	46.42	46.67	46.79	46.26	46.12	46.06	45.58
Total	99.49	99.60	99.46	99.65	99.82	99.46	99.22	98.22
O=6								
Ca	0.974	1.050	1.088	1.032	1.053	0.973	1.034	0.996
Mg	0.901	0.838	0.845	0.911	0.852	0.907	0.821	0.836
Fe	0.063	0.057	0.041	0.009	0.020	0.051	0.115	0.126
Mn	0.012	0.032	0.002	0.003	0.027	0.002	0.025	0.038
Sr	0.023	0.008	0.012	0.031	0.032	0.034	0.005	0.003
Ba	0.014	0.005	0.000	0.004	0.012	0.021	0.000	0.000
Total	1.987	1.990	1.988	1.990	1.996	1.988	2.000	1.999

Sample	at051	at051	at051	at051	at057	at057	at204
Unit	C2	C2	C2	C2	C2	C2	
Rock type	cbt	cbt	cbt	cbt	cbt	cbt	php
Remarks	g,1	g,1	g	g,1	1	2	v
CaO	28.89	29.00	32.66	28.91	31.34	30.21	28.69
MgO	16.85	16.77	14.14	18.19	15.19	15.72	17.82
FeOt	4.76	5.07	5.53	3.60	4.00	3.76	5.25
MnO	1.51	1.32	0.09	0.63	0.87	0.77	0.94
SrO	0.31	0.52	0.29	0.62	0.31	0.17	0.50
BaO	0.05	0.00	0.00	0.09	0.00	1.36	0.30
CO2	45.09	45.22	44.64	45.44	44.42	44.22	46.20
Total	97.46	97.90	97.36	97.47	96.12	96.22	99.70
O=6							
Ca	1.006	1.007	1.148	0.999	1.107	1.072	0.973
Mg	0.816	0.810	0.692	0.874	0.747	0.776	0.841
Fe	0.129	0.137	0.152	0.097	0.110	0.104	0.139
Mn	0.041	0.036	0.002	0.017	0.024	0.022	0.025
Sr	0.006	0.010	0.006	0.012	0.006	0.003	0.009
Ba	0.001	0.000	0.000	0.001	0.000	0.018	0.004
Total	1.999	2.000	2.000	2.000	1.994	1.995	1.991

Table A2.11 - Ankerite analyses

Sample	at042	at048	at048	at048	at057	at057	at057	at057	at204	at204	at204	at204	at205	at205
Unit	C1	C1	C1	C1	C2	C2	C2	C2						
Rock type	cbt	cbt	cbt	cbt	cbt	cbt	cbt	cbt	php	php	php	php	lcr	lcr
Remarks	v						2	1	v	v	v	v		
CaO	28.62	28.88	28.80	28.93	32.88	29.59	28.84	31.17	29.02	28.76	28.84	29.00	28.06	27.85
MgO	11.61	12.81	13.41	13.11	10.12	14.86	12.65	11.28	16.64	16.51	15.98	16.54	9.13	8.79
FeOt	13.47	10.19	10.57	10.88	11.13	8.05	11.04	10.00	7.11	7.40	8.03	7.16	17.65	18.61
MnO	0.69	2.16	0.80	0.75	0.67	0.81	0.67	0.65	0.59	0.61	0.67	0.74	0.76	0.57
SrO	0.01	0.15	0.62	0.60	0.15	0.25	0.17	0.17	0.28	0.20	0.35	0.13	0.26	0.20
BaO	0.09	0.02	0.06	0.00	0.00	0.00	0.01	0.00	0.14	0.00	0.01	0.08	0.09	0.00
CO2	43.85	44.31	44.50	44.41	44.23	45.11	43.78	43.47	45.92	45.87	45.71	45.89	43.60	43.49
Total	98.35	98.51	98.77	98.68	99.18	98.67	97.15	96.74	99.70	99.35	99.59	99.54	99.55	99.51
O=6														
Ca	1.024	1.023	1.016	1.022	1.167	1.029	1.034	1.126	0.991	0.981	0.989	0.989	1.008	1.003
Mg	0.578	0.631	0.658	0.645	0.500	0.719	0.631	0.566	0.790	0.784	0.762	0.785	0.456	0.440
Fe	0.376	0.282	0.291	0.300	0.308	0.219	0.309	0.282	0.189	0.197	0.215	0.191	0.495	0.523
Mn	0.019	0.060	0.022	0.021	0.019	0.022	0.019	0.019	0.016	0.016	0.018	0.020	0.022	0.016
Sr	0.000	0.003	0.012	0.011	0.003	0.005	0.003	0.003	0.005	0.004	0.006	0.002	0.005	0.004
Ba	0.001	0.000	0.001	0.000	0.000	0.000	0.000	0.000	0.002	0.000	0.000	0.001	0.001	0.000
Total	1.998	1.999	2.000	1.999	1.997	1.994	1.996	1.996	1.993	1.982	1.990	1.988	1.987	1.986

Sample	at205	at205	at207	at207	at212	at212	at212
Unit					C2	C2	C2
Rock type	lcr	lcr	lcr	lcr	cbt,dk	cbt,dk	cbt,dk
Remarks					p	g	g
CaO	27.99	28.85	28.44	28.80	28.36	34.05	34.28
MgO	9.59	8.04	17.05	15.80	10.94	10.37	10.60
FeOt	17.55	18.49	7.74	9.24	12.75	9.50	8.04
MnO	0.55	0.78	0.51	0.16	0.93	0.68	0.67
SrO	0.27	0.10	0.00	0.00	0.34	0.02	0.31
BaO	0.00	0.09	0.00	0.00	0.12	0.12	0.11
CO2	43.78	43.39	46.08	45.72	43.20	44.52	44.39
Total	99.73	99.74	99.82	99.72	96.64	99.26	98.40
O=6							
Ca	1.003	1.042	0.968	0.987	1.002	1.194	1.206
Mg	0.478	0.404	0.808	0.754	0.538	0.506	0.519
Fe	0.491	0.521	0.206	0.247	0.351	0.260	0.221
Mn	0.016	0.022	0.014	0.004	0.026	0.019	0.019
Sr	0.005	0.002	0.000	0.000	0.006	0.000	0.006
Ba	0.000	0.001	0.000	0.000	0.002	0.002	0.001
Total	1.993	1.992	1.996	1.992	1.925	1.981	1.972

Table A2.12 - Semi-quantitative strontianite analyses

Sample	at046	at046	at048	at051	at051	at051	at051	at051	at051	at059
Unit	C2	C2	C1	C2	C2	C2	C2	C2	C2	C1
Rock type	cbt	cbt	cbt	cbt	cbt	cbt	cbt	cbt	cbt	cbt
Remarks	i	i		i	i	i	i	i	i	i
CaO	8.14	12.15	10.13	15.75	14.74	18.44	16.47	14.56	13.17	14.52
MgO	0.01	0.02	0.02	0.00	0.00	0.01	0.00	0.01	0.00	0.00
FeOt	0.00	0.11	0.30	0.02	0.00	0.01	0.02	0.00	0.01	0.06
MnO	0.00	0.01	0.00	0.00	0.00	0.00	0.00	0.01	0.00	0.00
SrO	45.98	42.76	28.59	27.43	27.48	34.76	32.10	29.08	27.64	26.98
BaO	8.82	7.74	17.32	11.84	12.46	11.55	10.29	12.65	11.44	18.65
CO2	28.46	30.01	25.27	27.42	26.81	32.57	29.53	27.43	25.37	28.24
Total	91.41	92.80	81.63	82.46	81.49	97.33	88.42	83.74	77.63	88.46
O=6										
Ca	0.449	0.636	0.629	0.901	0.863	0.889	0.876	0.833	0.815	0.807
Mg	0.001	0.001	0.002	0.000	0.000	0.001	0.000	0.001	0.000	0.000
Fe	0.000	0.004	0.014	0.001	0.000	0.000	0.001	0.000	0.001	0.002
Mn	0.000	0.001	0.000	0.000	0.000	0.000	0.000	0.001	0.000	0.000
Sr	1.372	1.210	0.961	0.850	0.871	0.907	0.923	0.901	0.925	0.812
Ba	0.178	0.148	0.393	0.248	0.267	0.204	0.200	0.265	0.259	0.379
Total	2.000	2.000	1.999	2.000	2.001	2.001	2.000	2.001	2.000	2.000

Table A2.13 - ICP-MS analyses of mineral separates from the Tapira complex

	Apatite	Calcite	Phlogopite	Perovskite	Clinopyroxene
Cr	0.155	0.000	0.976	0.170	0.394
Ni	6.195	6.516	45.246	4.397	11.335
Co	0.631	0.909	69.415	2.079	23.026
Sc	0.000	0.000	5.671	0.000	111.595
V	19.112	0.350	39.632	122.722	45.853
Cu	0.014	1.083	12.302	245.290	7.272
Pb	2.716	5.676	1.128	6.435	2.165
Zn	0.000	0.508	94.409	655.752	30.102
Ba	95.214	2621.300	11407.000	45.160	142.956
Rb	0.094	0.389	244.880	0.778	1.680
Sr	16798.000	17031.400	65.350	4180.730	656.649
Cs	0.002	0.017	3.385	0.030	0.038
Ga	21.347	2.746	24.462	31.523	3.397
Nb	0.985	1.833	27.480	6048.540	18.490
Ta	0.040	0.152	0.284	240.068	0.214
Zr	2.480	5.195	64.364	1093.220	307.251
Hf	0.218	0.117	1.602	45.078	10.650
Y	285.762	71.130	0.368	551.918	12.689
Th	6.096	0.471	0.263	176.462	1.130
U	3.318	0.372	0.188	113.957	0.208
La	2890.610	461.097	3.485	5989.180	32.163
Ce	6929.760	936.320	6.603	11352.150	64.832
Pr	907.000	90.419	0.744	1186.070	7.695
Nd	3235.216	315.665	2.710	4279.560	29.831
Sm	459.576	40.162	0.361	624.110	4.988
Eu	108.181	10.974	n.a.	171.960	1.487
Gd	222.143	26.454	n.a.	385.560	3.834
Tb	24.162	3.131	0.013	48.172	0.509
Dy	85.955	13.621	0.049	191.435	2.498
Ho	11.143	2.152	0.011	26.038	0.406
Er	19.607	4.864	0.020	44.298	0.962
Tm	2.038	0.648	0.004	4.375	0.142
Yb	9.054	3.448	0.033	17.802	0.916
Lu	1.037	0.481	0.007	1.807	0.154

APPENDIX 3 – WHOLE-ROCK AND ISOTOPE GEOCHEMISTRY

Abbreviations used in the data tables	
php	phlogopite-picrite
beb	bebedourite
syen	syenite
wehrl	wehrlite
lcr	low-Cr dyke
cbt	carbonatite
fen	fenite
bre	breccia
RR	reaction rock
CR	country rock
n.a.	not analysed
b.d.	below detection

Table A3.1 - Major and trace-element XRF analyses

Sample	AT002	AT013	AT014	AT021a	AT021b	AT022	AT028	AT120a	AT203	AT204	AT206	AT207
Unit/Locality												
Rock type	php	php	php	php	php	php	php	php	php	php	php	lcr
Remarks												
SiO2	28.49	29.37	30.94	29.88	33.40	29.27	27.88	27.93	24.30	32.03	29.35	26.10
TiO2	4.50	4.63	4.10	3.80	5.01	5.37	4.76	5.29	3.32	4.59	3.24	5.21
Al2O3	3.97	4.49	3.47	3.48	3.44	2.89	4.11	3.24	1.63	2.25	3.34	2.82
Fe2O3(T)	13.51	12.95	13.47	12.98	14.44	13.84	12.63	13.59	10.85	15.18	12.32	13.63
MnO	0.22	0.19	0.19	0.20	0.16	0.20	0.24	0.22	0.22	0.21	0.18	0.21
MgO	11.32	12.92	19.42	18.87	21.34	19.17	8.73	11.13	14.77	17.76	18.07	9.98
CaO	17.96	16.79	13.45	13.30	9.31	13.51	17.52	19.41	15.93	13.48	11.31	17.61
Na2O	0.55	1.14	0.65	0.55	0.41	0.49	1.62	1.29	0.95	0.51	0.50	1.50
K2O	4.58	4.80	3.90	3.27	2.68	4.06	4.29	4.14	3.10	3.45	3.49	3.21
P2O5	3.98	2.56	2.00	2.18	2.19	2.34	2.70	3.48	2.15	1.57	1.74	3.76
LOI	10.82	9.94	7.86	10.84	7.63	7.87	13.77	9.34	21.95	9.37	16.22	14.90
BaO	0.41	0.39	0.31	0.34	0.33	0.37	0.66	0.27	0.45	0.32	0.34	0.26
SrO	0.42	0.33	0.25	0.41	0.19	0.37	0.59	0.45	0.31	0.25	0.26	0.45
Total	100.73	100.49	100.01	100.09	100.53	99.75	99.50	99.78	99.92	100.97	100.36	99.63
CO2	9.55	9.05	6.60	9.39	3.29	5.96	13.14	8.22	21.90	9.05	15.50	14.94
S	0.06	0.05	0.04	0.05	n.a.	0.02	0.17	0.03	0.33	0.04	0.18	0.25
FeO	6.58	6.31	7.42	n.a.	5.47	7.39	7.85	n.a.	9.88	6.84	8.07	8.67
Ba	3833.0	3594.1	2703.3	3233.0	3326.4	2519.9	5603.1	2496.0	4377.7	2731.3	2992.0	2280.1
Ce	692.9	406.8	370.5	425.0	n.a.	698.8	818.3	582.0	744.9	858.9	406.9	866.9
Co	48.0	56.1	76.4	67.6	n.a.	64.1	46.4	51.0	50.4	65.6	68.5	46.4
Cr	329.2	320.9	585.1	835.2	1110.4	555.8	136.6	162.0	276.3	350.5	619.6	181.7
La	293.3	232.4	224.5	251.0	n.a.	388.8	462.6	363.0	412.3	436.7	237.1	440.8
Nb	282.6	211.4	174.4	200.5	231.1	226.2	312.2	294.1	251.3	203.7	144.9	336.9
Nd	254.6	156.7	145.0	167.0	n.a.	268.0	433.1	297.0	288.7	363.8	165.0	320.7
Ni	162.5	309.7	646.1	704.0	932.0	512.5	82.3	149.0	478.9	700.2	611.6	121.7
Pb	21.7	18.3	20.5	69.0	45.8	23.7	52.8	69.0	18.8	32.4	24.9	24.1
Rb	140.5	151.0	122.0	118.5	79.9	144.3	101.4	113.0	79.0	123.2	106.5	95.8
Sc	34.9	29.4	25.3	35.7	21.2	28.8	32.5	51.0	26.2	14.8	23.9	28.9
Sr	3301.7	2611.1	2079.4	3645.0	1570.4	2315.0	4543.1	3648.0	2364.6	2099.7	2153.9	3313.5
Th	24.5	31.6	23.6	35.8	46.6	55.5	63.3	41.2	55.5	32.6	25.6	52.1
U	5.0	6.9	3.2	3.3	n.a.	5.5	2.5	1.7	4.1	2.7	3.7	5.1
V	287.2	337.0	249.3	201.0	n.a.	203.2	440.0	278.0	486.2	190.3	186.2	318.8
Y	55.3	44.0	34.1	50.8	41.9	36.5	52.0	65.0	56.3	29.5	31.2	58.9
Zr	1109.8	711.0	580.7	662.0	447.9	621.3	701.2	1054.0	712.0	621.0	474.7	1020.6

Table A3.1 - Major- and trace-element XRF analyses

Sample	AT209b	AT210	TP-90-4B	TP-90-4C	AT005	TP-90-4A	HS186i	HS186m	AT019	AT020	AT024	AT031
Unit/Locality							Araxa	Araxa				
Rock type	php	php	php	php	php	php	php	php	lcr	lcr	lcr	lcr
Remarks												
SiO2	27.47	27.17	28.23	31.62	30.09	28.60	35.71	34.82	29.00	22.43	29.23	28.38
TiO2	4.82	3.61	4.70	4.56	4.17	4.33	5.59	5.15	3.94	4.94	3.62	2.98
Al2O3	2.91	2.67	4.24	4.69	4.07	4.05	3.82	4.19	3.75	2.73	4.09	3.29
Fe2O3(T)	13.69	11.77	13.88	13.40	12.76	13.25	16.65	15.78	15.46	15.81	13.08	14.00
MnO	0.21	0.21	0.21	0.20	0.17	0.19	0.25	0.23	0.28	0.26	0.31	0.32
MgO	10.47	12.90	10.18	8.91	14.57	10.19	10.42	11.54	7.54	11.77	6.69	6.88
CaO	16.99	16.89	14.62	14.56	12.75	13.85	11.24	12.68	19.34	18.02	18.35	21.52
Na2O	0.55	1.14	0.45	0.67	0.85	0.83	0.59	0.99	1.71	0.44	0.45	1.68
K2O	5.50	2.99	5.53	5.87	5.20	5.36	3.91	2.54	4.10	4.09	5.95	3.57
P2O5	3.29	2.80	3.03	2.93	2.94	2.75	1.56	2.42	2.98	3.96	3.26	4.11
LOI	13.35	16.93	14.59	10.37	12.21	16.15	8.89	9.19	10.24	14.60	12.55	11.47
BaO	0.46	0.35	0.39	0.36	0.25	0.26	0.30	0.17	0.14	0.35	0.63	0.28
SrO	0.47	0.47	0.47	0.40	0.51	0.39	0.27	0.23	0.50	0.37	0.71	0.49
Total	100.19	99.90	100.52	98.54	100.53	100.20	99.19	99.93	98.97	99.76	98.92	98.96
CO2	13.10	17.23	14.24	12.29	9.99	16.24	n.a.	n.a.	10.90	13.80	12.50	11.70
S	0.08	0.22	0.10	0.16	0.21	0.15	n.a.	n.a.	0.10	0.09	0.37	0.43
FeO	6.58	8.18	8.99	8.34	7.75	9.20	n.a.	n.a.	8.02	8.02	9.80	5.98
Ba	3654.0	3045.9	3106.8	2836.8	2211.3	2324.2	2764.4	1676.4	1225.5	3140.3	4361.5	2485.9
Ce	896.7	849.1	680.7	623.5	450.7	590.5	455.0	393.3	508.6	1103.0	692.4	320.0
Co	44.2	51.7	51.9	44.8	58.3	51.7	66.7	67.8	48.4	53.6	36.0	42.6
Cr	200.3	401.0	254.7	170.5	531.0	256.3	441.9	590.6	7.8	245.5	18.0	6.8
La	441.3	471.2	347.2	320.7	250.6	311.3	254.3	200.1	288.9	580.1	385.4	228.3
Nb	251.3	307.0	234.8	231.8	290.5	247.5	173.6	146.3	379.8	309.1	360.0	346.4
Nd	317.3	366.3	262.4	232.5	198.2	232.6	153.5	141.3	165.8	412.7	236.7	90.6
Ni	145.2	409.0	175.7	115.9	406.7	191.9	428.6	372.1	16.8	86.7	23.4	20.6
Pb	37.5	13.8	33.0	28.6	20.9	27.5	14.1	8.6	8.9	38.5	38.8	29.3
Rb	164.5	90.8	152.4	148.7	214.8	125.3	107.6	98.0	102.5	147.6	134.3	104.6
Sc	28.0	24.8	24.6	27.8	29.3	23.1	29.8	33.2	26.6	24.6	32.0	33.2
Sr	3595.0	3597.1	3679.6	3131.2	4271.8	3282.8	2132.0	1861.5	4188.8	3197.4	4908.9	4112.1
Th	53.4	45.7	33.7	36.1	63.2	36.6	5.2	19.9	14.7	43.6	42.9	15.9
U	3.1	2.1	5.0	5.0	4.4	4.6	15.7	3.6	n.a.	5.0	n.a.	n.a.
V	342.5	337.0	326.6	359.0	264.8	341.6	309.7	294.5	368.5	345.4	314.6	354.4
Y	55.8	48.7	51.8	53.2	82.0	53.0	37.4	33.4	53.3	54.6	81.3	62.7
Zr	1145.4	938.4	879.6	1058.2	1002.3	1035.3	869.3	682.3	1604.4	1586.1	1805.0	2031.2

Table A3.1 - Major- and trace-element XRF analyses

Sample	AT041	AT201	AT202	AT205	AT208	AT209a	AT211	AT213	AT214	AT215	AT020b	AT106
Unit/Locality												
Rock type	lcr	lcr	lcr	lcr	lcr	lcr	lcr	lcr	lcr	lcr	lcr	lcr
Remarks												
SiO2	20.93	27.62	36.70	27.05	23.98	25.69	28.43	24.15	22.85	23.00	18.40	33.16
TiO2	1.92	4.65	3.98	3.29	5.26	2.38	3.16	3.75	3.30	1.25	4.34	2.88
Al2O3	2.33	3.61	7.41	2.96	2.04	2.49	3.89	2.11	2.56	4.36	3.30	4.71
Fe2O3(T)	12.75	14.02	15.95	10.80	13.65	12.61	13.66	14.18	13.58	10.51	12.77	15.16
MnO	0.40	0.27	0.25	0.16	0.26	0.29	0.31	0.36	0.34	0.31	0.23	0.36
MgO	7.08	7.40	6.04	9.54	8.50	8.86	7.37	7.01	6.93	2.99	9.57	3.82
CaO	26.20	18.21	19.38	24.98	19.31	24.72	22.86	22.66	17.92	26.03	25.22	17.73
Na2O	0.83	0.46	0.66	1.22	0.45	1.27	0.66	2.34	2.27	1.89	0.36	2.37
K2O	3.55	5.68	4.27	2.85	3.97	3.63	4.63	2.82	2.85	3.61	3.62	4.42
P2O5	6.34	3.69	2.04	6.02	4.56	5.57	4.12	3.49	2.78	2.37	4.29	2.38
LOI	16.83	12.34	1.98	10.34	14.50	11.45	10.12	16.14	21.51	19.97	16.29	10.99
BaO	0.59	0.53	0.27	0.30	0.41	0.45	0.41	0.36	0.40	0.53	0.45	0.47
SrO	0.71	0.49	0.23	0.46	0.38	0.54	0.47	0.43	0.48	1.35	0.70	0.63
Total	100.46	98.97	99.16	99.97	97.27	99.95	100.09	99.81	97.77	98.17	99.54	99.07
CO2	16.94	12.05	1.07	10.26	13.87	10.67	9.10	16.27	22.27	21.14	n.a.	n.a.
S	0.45	0.26	0.17	0.03	1.97	0.23	0.12	0.15	0.54	0.27	n.a.	n.a.
FeO	6.35	8.36	6.52	4.28	8.25	4.97	5.31	6.83	10.18	6.72	n.a.	n.a.
Ba	5295.0	4958.4	2799.4	3645.7	4235.7	4999.5	4281.2	4185.1	4618.2	5870.4	4027.1	4186.5
Ce	440.7	1105.0	242.3	833.4	1101.3	626.7	585.1	611.7	516.2	1218.1	1085.9	183.6
Co	35.4	34.9	32.1	22.9	33.7	26.3	32.0	21.3	34.5	12.4	38.7	36.5
Cr	14.8	36.4	27.0	21.0	29.5	27.8	30.3	20.9	28.8	33.3	176.6	11.1
La	332.4	556.3	135.3	473.5	510.3	305.0	225.7	349.0	330.3	702.3	543.1	136.4
Nb	334.0	391.4	270.5	275.9	387.7	212.4	403.5	338.7	501.3	450.8	297.8	262.9
Nd	113.7	375.3	85.5	239.4	360.0	121.1	99.5	210.2	155.0	332.4	445.9	56.1
Ni	22.1	24.5	12.5	5.1	35.2	2.7	32.3	17.7	25.8	8.4	74.5	15.1
Pb	58.3	38.0	4.9	27.5	29.7	40.8	11.9	10.8	19.0	60.9	9.8	99.4
Rb	137.5	133.1	83.6	77.6	139.3	107.1	136.7	88.3	29.6	57.7	117.2	91.7
Sc	29.8	25.0	22.0	63.5	35.6	51.4	35.4	40.2	35.0	34.7	29.7	22.2
Sr	5987.3	3889.7	1932.6	3369.4	2824.5	4146.5	3362.9	3297.3	3927.9	11143.9	5891.4	5290.6
Th	0.6	48.1	6.3	7.0	38.8	3.7	2.0	37.3	59.1	78.1	42.6	0.8
U	n.a.	6.7	3.9	6.5	8.3	5.4	4.0	21.6	1.8	16.3	n.a.	2.2
V	452.5	279.8	310.3	199.4	578.3	357.2	468.5	629.8	742.5	431.5	227.0	647.6
Y	94.5	78.1	84.5	84.5	77.7	111.8	93.2	75.5	52.8	116.1	61.6	59.1
Zr	1196.1	1326.3	2728.0	1821.1	468.4	2958.8	2480.0	590.5	4519.1	1792.1	593.6	1013.5

Table A3.1 - Major- and trace-element XRF analyses

Sample	AT216	AT218	AT016	AT025	AT126a	AT217	AT015	AT003	AT004	AT009	AT027	AT036
Unit/Locality			B1	B1	B2	B1	B1	B1	B1	B1	B1	B1
Rock type	lcr	lcr	wehrl	wehrl	wehrl,dk	wehrl	wehrl	beb	beb	beb	beb	beb
Remarks												
SiO2	24.27	29.84	18.67	32.86	29.23	31.45	12.69	34.46	30.76	29.80	36.95	33.06
TiO2	4.47	5.16	10.46	5.12	2.19	6.45	15.63	5.64	4.73	5.60	4.08	8.85
Al2O3	2.49	3.40	0.76	2.75	2.79	0.92	0.60	4.16	5.14	4.96	0.83	1.12
Fe2O3(T)	12.46	13.53	14.14	14.87	12.06	23.68	26.79	12.57	12.21	12.31	17.66	18.32
MnO	0.22	0.20	0.24	0.39	0.21	0.54	0.23	0.14	0.16	0.11	0.23	0.21
MgO	8.16	12.48	17.96	29.12	11.53	24.99	14.25	11.17	12.75	12.46	10.96	10.14
CaO	18.00	15.93	22.70	8.42	25.67	9.91	18.88	22.18	20.66	20.63	23.24	23.26
Na2O	1.25	1.43	0.46	0.48	0.13	0.45	0.49	0.46	0.53	0.55	0.63	0.83
K2O	3.88	2.56	0.48	2.18	2.88	0.88	0.39	2.86	3.36	3.27	0.39	0.54
P2O5	4.32	3.16	10.52	1.63	9.98	0.03	7.21	4.03	7.16	7.30	4.20	3.05
LOI	17.52	12.03	1.72	2.29	1.50	1.51	1.33	1.63	1.22	1.96	0.92	0.96
BaO	0.24	0.26	0.03	0.12	0.14	0.04	n.a.	0.14	0.29	0.17	0.01	0.03
SrO	0.39	0.22	0.33	0.09	0.23	0.07	0.22	0.19	0.25	0.19	0.24	0.22
Total	97.67	100.20	98.48	100.32	98.54	100.92	98.71	99.63	99.22	99.31	100.34	100.59
CO2	18.48	7.19	0.61	1.01	n.a.	1.04	1.24	1.10	1.07	1.83	0.09	0.27
S	0.55	0.02	0.05	0.04	n.a.	0.49	0.03	0.00	0.01	0.03	0.03	0.03
FeO	10.95	1.36	7.57	7.87	n.a.	9.58	10.91	4.06	5.41	5.45	7.85	7.56
Ba	2114.6	2342.2	372.2	1329.4	1078.7	341.0	n.a.	1363.2	2680.3	1666.5	161.2	480.2
Ce	790.9	522.8	2090.9	2143.2	539.9	2456.7	2639.4	619.7	985.6	672.5	337.2	480.9
Co	33.5	50.0	79.3	109.6	34.7	89.7	114.1	37.3	47.0	46.9	61.0	63.3
Cr	26.8	113.4	22.6	1205.7	18.3	352.6	8.9	3.6	3.4	3.7	4.5	3.0
La	397.0	295.0	1044.5	1031.0	417.1	1078.4	900.9	346.6	636.8	356.0	243.8	312.9
Nb	360.7	262.8	757.3	619.8	139.6	989.8	871.9	298.5	422.8	167.5	209.7	335.7
Nd	270.8	191.0	741.0	796.0	186.1	923.0	729.8	233.1	337.5	271.9	139.0	176.4
Ni	32.2	186.7	81.4	1111.5	7.5	393.3	n.a.	35.5	28.5	47.0	30.4	28.5
Pb	28.2	29.3	2.4	16.8	13.5	21.0	28.5	3.6	6.5	2.5	5.5	4.8
Rb	99.3	168.4	12.8	77.8	68.5	35.0	14.6	87.0	97.4	118.4	13.6	29.0
Sc	35.6	28.5	10.3	24.2	31.4	42.0	0.0	33.8	37.7	45.4	53.8	44.4
Sr	3330.1	1840.7	2357.8	738.6	1825.6	580.9	1897.6	1349.3	1982.3	1382.0	1992.2	1561.8
Th	72.6	35.0	45.1	70.7	14.7	88.9	82.5	8.5	5.4	14.1	7.6	10.3
U	7.4	7.1	n.a.	5.9	5.5	8.1	n.a.	n.a.	n.a.	n.a.	n.a.	n.a.
V	562.5	451.1	160.9	89.1	272.9	191.8	n.a.	146.6	111.0	148.7	206.6	247.9
Y	89.2	50.5	127.3	63.8	156.6	42.9	93.9	52.9	91.5	51.8	45.6	59.9
Zr	1925.6	1136.2	467.7	256.0	2155.7	438.9	314.3	225.7	238.9	145.7	268.1	330.2

Table A3.1 - Major- and trace-element XRF analyses

Sample	AT037	AT007	AT026	AT035	AT040	AT001	AT006	AT010	AT017	AT023	AT029	AT030
Unit/Locality	B1	B1	B1	B1	B1	B2	B2	B2	B2	B2	B2	B2
Rock type	beb	beb	beb	beb	beb	beb	beb	beb	beb	beb	beb	beb
Remarks												
SiO2	31.39	13.07	44.13	34.31	24.40	30.33	31.86	39.05	46.22	40.75	38.23	38.01
TiO2	7.64	18.48	1.57	6.72	13.39	5.13	5.17	7.02	0.62	0.94	5.28	2.94
Al2O3	4.71	1.36	2.49	1.45	2.68	1.53	2.00	1.04	4.06	3.62	1.52	4.91
Fe2O3(T)	14.51	20.39	8.59	18.72	16.41	16.18	17.25	12.07	9.28	6.01	16.27	11.63
MnO	0.16	0.19	0.16	0.24	0.16	0.19	0.21	0.16	0.31	0.18	0.25	0.23
MgO	11.95	5.52	13.28	11.38	9.36	9.37	10.63	12.55	10.48	16.45	9.76	9.92
CaO	18.88	27.04	24.22	20.67	23.35	26.10	22.85	24.46	22.26	19.61	23.12	20.72
Na2O	0.84	0.66	0.73	0.75	0.50	0.58	0.80	0.75	1.09	0.80	0.90	1.15
K2O	3.47	0.57	0.63	0.66	1.88	0.48	1.05	0.66	1.25	2.67	0.45	3.02
P2O5	4.54	8.41	2.69	1.25	5.28	7.34	5.35	1.48	2.04	6.88	3.04	4.92
LOI	1.33	0.92	2.19	2.75	0.98	1.43	2.02	1.43	1.91	1.52	1.11	2.80
BaO	0.16	0.07	0.06	0.08	0.11	0.02	0.08	0.03	0.16	0.08	0.02	0.23
SrO	0.23	0.27	0.16	0.14	0.17	0.29	0.22	0.16	0.19	0.23	0.26	0.29
Total	99.81	96.94	100.90	99.12	98.66	98.98	99.49	100.86	99.87	99.74	100.21	100.77
CO2	0.40	1.11	1.92	2.82	0.11	1.37	1.92	1.39	1.01	1.15	0.48	1.55
S	0.06	0.04	0.07	0.01	0.08	0.11	0.02	0.05	0.03	0.02	0.11	0.02
FeO	8.08	8.20	4.42	6.70	7.43	6.94	7.12	4.69	5.50	3.79	7.86	7.03
Ba	1563.7	617.4	536.8	710.6	971.9	272.0	784.4	351.7	1711.7	839.7	232.2	2058.2
Ce	721.6	2382.0	341.9	1152.5	1457.0	1514.7	1202.5	1186.3	579.2	651.1	1216.4	866.3
Co	57.1	62.7	43.5	63.0	57.2	51.2	52.9	60.6	41.3	16.4	54.1	43.9
Cr	3.5	4.9	3.2	1.9	23.5	2.4	58.6	1.4	7.1	884.6	2.6	1.5
La	378.3	1684.0	188.2	871.7	1027.0	764.5	767.0	562.0	272.4	260.7	647.0	445.2
Nb	343.9	823.7	77.6	736.4	619.7	461.8	507.0	358.5	43.8	56.8	590.1	196.2
Nd	273.7	905.0	163.0	382.4	540.0	704.2	417.3	431.9	312.5	393.0	459.9	362.2
Ni	35.8	69.0	29.5	33.9	57.1	35.0	37.0	37.9	17.7	138.7	34.1	33.4
Pb	3.2	2.1	5.6	10.2	4.9	6.6	7.9	5.1	5.4	2.0	3.8	7.3
Rb	113.5	17.4	11.5	17.3	59.5	10.9	25.5	12.1	16.5	74.0	12.8	66.1
Sc	29.4	3.8	42.5	58.7	23.9	53.6	52.6	53.1	29.3	83.6	39.1	39.1
Sr	1588.7	2243.7	1353.6	1206.4	1404.5	2243.0	1807.4	1012.5	1541.4	1749.2	1937.4	2250.6
Th	18.3	138.1	6.7	15.4	60.8	66.6	21.0	35.2	19.4	5.4	41.5	16.8
U	n.a.	n.a.	n.a.	n.a.	n.a.	n.a.	n.a.	n.a.	n.a.	n.a.	n.a.	n.a.
V	258.0	411.1	76.9	126.8	395.3	155.2	130.7	103.8	160.5	167.0	249.5	135.7
Y	67.6	122.2	40.4	89.0	98.3	85.6	82.4	49.8	38.5	38.3	50.0	61.1
Zr	326.6	677.5	422.9	2384.3	349.0	511.9	489.8	338.6	615.7	257.6	330.5	980.0

Table A3.1 - Major- and trace-element XRF analyses

Sample	AT032	AT033	AT034	AT038a	AT008	AT011	AT109b	TP-90-10	TP-90-11	TP-90-8	AT115	AT302
Unit/Locality	B2	B2	B2	B2	B2	B2	B2	B2	B2	B2		
Rock type	beb	beb	beb	beb	beb	beb	beb	beb	beb	beb	syen	syen
Remarks												
SiO2	45.40	41.93	31.98	40.07	39.36	31.40	42.03	37.79	37.12	32.00	55.81	55.42
TiO2	0.65	4.54	6.05	3.49	3.68	1.72	0.84	3.62	3.98	4.28	0.58	0.30
Al2O3	3.16	2.14	4.90	1.59	1.61	5.41	4.44	1.94	3.82	2.45	18.35	16.70
Fe2O3(T)	8.15	13.41	14.90	10.21	11.62	10.41	7.49	15.26	12.87	16.58	3.18	3.35
MnO	0.24	0.22	0.21	0.19	0.20	0.21	0.21	0.26	0.22	0.24	0.07	0.09
MgO	12.36	10.94	8.79	10.89	10.52	10.25	12.60	10.73	10.19	7.96	0.82	1.44
CaO	21.99	21.43	21.95	25.58	24.58	22.91	22.90	24.79	22.64	25.58	2.88	3.07
Na2O	0.86	0.93	0.57	0.67	0.87	0.60	0.66	0.42	0.64	0.60	0.44	0.43
K2O	1.68	1.61	3.31	0.49	0.71	3.81	2.32	1.10	2.49	1.16	13.99	13.48
P2O5	2.17	0.60	4.76	3.98	4.05	9.68	5.16	4.66	4.00	6.85	0.15	0.17
LOI	1.65	1.56	1.31	1.63	2.47	1.86	0.77	0.15	0.74	0.84	2.83	2.05
BaO	0.07	0.07	0.19	0.03	0.13	0.23	0.16	0.05	0.14	0.06	0.43	1.46
SrO	0.22	0.13	0.18	0.26	0.32	0.34	0.21	0.21	0.21	0.30	0.28	0.25
Total	98.60	99.51	99.10	99.09	100.12	98.83	99.79	100.98	99.06	98.89	99.81	98.22
CO2	0.47	0.23	0.66	1.29	2.26	1.51	n.a.	0.01	n.a.	0.10	2.40	2.92
S	0.00	0.00	0.02	0.03	0.07	0.35	n.a.	n.a.	n.a.	n.a.	0.05	0.67
FeO	5.86	8.83	6.80	4.96	5.68	7.66	n.a.	7.33	n.a.	7.50	n.a.	n.a.
Ba	1040.1	731.6	1800.9	369.2	1156.1	2073.2	1434.1	454.0	1276.6	523.1	3478.1	12141.7
Ce	277.2	481.7	318.1	1343.7	637.9	2037.8	999.3	1495.2	945.8	1266.7	258.1	820.8
Co	35.6	64.4	60.2	36.4	46.2	44.1	15.8	47.1	36.8	41.5	2.1	1.2
Cr	17.2	2.8	3.1	6.4	7.6	3.1	8.3	15.3	20.8	20.4	1.0	23.5
La	142.3	229.8	162.6	632.2	367.1	1000.0	427.3	754.6	503.4	697.4	103.1	394.0
Nb	30.0	514.2	287.5	319.4	223.7	153.4	51.6	435.3	269.3	315.0	216.2	212.2
Nd	122.3	262.1	153.0	579.2	266.4	780.3	468.9	491.4	330.5	451.0	82.6	224.8
Ni	34.1	29.0	23.2	26.4	32.0	24.9	4.9	29.3	9.1	30.4	8.3	30.9
Pb	3.1	8.1	3.6	3.5	9.1	3.2	15.7	6.4	18.7	4.7	8.0	20.7
Rb	47.5	44.3	107.0	12.1	15.0	88.2	74.2	25.1	70.0	30.4	128.7	125.2
Sc	39.4	44.0	27.0	45.9	47.3	29.6	32.0	34.6	33.9	35.8	3.8	9.3
Sr	1722.5	966.5	1439.1	1906.7	2675.9	2843.6	1803.8	1743.5	1748.2	2495.8	2405.4	2376.6
Th	5.7	19.0	2.9	50.1	15.0	30.6	27.1	60.5	42.1	38.9	22.0	65.3
U	n.a.	n.a.	n.a.	n.a.	n.a.	n.a.	6.7	n.a.	4.4	n.a.	1.6	10.0
V	142.2	199.6	207.1	113.3	188.0	150.7	154.1	178.6	226.6	191.4	77.9	81.1
Y	21.2	42.0	186.2	48.5	49.3	163.2	61.8	71.0	68.4	87.0	20.7	32.9
Zr	271.1	852.4	6864.2	434.8	370.3	1490.0	612.5	883.9	1155.6	1128.9	1197.7	6877.0

Table A3.1 - Major- and trace-element XRF analyses

Sample	AT303	AT304	AT012	AT018	AT039	AT119b	AT301	AT305	AT042	AT044	AT048	AT055
Unit/Locality									C1	C1	C1	C1
Rock type	syen	syen	syen	syen	syen	syen	syen	syen	cbt	cbt	cbt	cbt
Remarks												
SiO2	53.21	54.30	49.04	54.46	54.57	53.74	55.07	53.73	2.46	3.79	1.08	2.34
TiO2	0.46	0.30	2.21	0.38	0.68	0.76	0.61	0.42	0.06	0.20	0.03	0.09
Al2O3	16.03	18.88	10.61	16.33	17.51	15.82	16.07	17.14	0.01	0.11	0.19	0.18
Fe2O3(T)	4.24	2.71	10.51	5.66	5.54	3.71	3.65	4.25	2.54	5.18	2.50	1.09
MnO	0.14	0.07	0.22	0.13	0.11	0.10	0.10	0.11	0.14	0.14	0.27	0.13
MgO	2.33	1.41	2.48	0.79	3.41	1.75	1.94	3.12	1.86	2.68	1.67	1.28
CaO	4.09	3.64	9.16	3.35	1.62	5.17	3.80	2.71	47.51	41.99	46.24	49.14
Na2O	0.38	0.41	1.51	0.65	0.48	0.43	0.38	0.42	0.58	0.40	0.27	0.46
K2O	12.98	13.55	8.75	13.09	13.45	13.00	13.16	13.38	0.22	0.43	0.01	0.23
P2O5	0.02	0.03	0.35	0.04	0.10	0.78	0.05	0.39	0.48	1.39	0.02	0.79
LOI	3.18	3.34	4.14	3.15	2.03	3.41	4.22	2.32	38.58	34.32	42.09	40.11
BaO	1.56	0.84	0.57	0.51	0.84	0.96	1.32	0.91	0.66	1.98	1.19	0.44
SrO	0.27	0.24	0.26	0.15	0.09	0.14	0.48	0.18	3.28	2.90	2.29	1.52
Total	98.89	99.72	99.81	98.69	100.43	99.77	100.85	99.08	98.38	95.51	97.85	97.81
CO2	4.41	2.28	3.85	2.17	1.55	3.80	4.67	1.88	40.99	37.23	43.61	42.65
S	0.57	0.07	1.47	1.20	0.09	0.29	0.13	0.15	0.57	0.94	0.00	0.18
FeO	n.a.	n.a.	n.a.	n.a.	n.a.	n.a.	n.a.	n.a.	n.a.	n.a.	n.a.	n.a.
Ba	12906.9	6816.3	4702.6	3931.6	6263.4	7355.5	10523.0	6848.8	6159.6	16014.6	10285.8	3676.4
Ce	711.9	118.3	197.4	426.7	137.5	500.7	706.3	344.1	1185.3	1957.5	3901.2	458.1
Co	0.7	2.0	47.2	48.7	48.6	3.9	2.6	4.6	42.2	53.9	6.2	8.6
Cr	24.8	23.2	12.8	8.1	3.7	0.4	21.7	22.4	1.0	7.7	0.1	0.1
La	362.3	63.4	92.2	176.6	60.5	222.3	341.9	154.7	691.6	1099.7	1961.6	278.8
Nb	344.7	81.8	558.2	650.0	111.2	335.6	315.5	338.0	237.4	2451.8	9.1	130.9
Nd	220.7	30.6	94.6	116.2	47.4	199.3	243.0	138.5	405.2	622.6	1502.9	190.4
Ni	56.5	30.8	16.3	15.0	11.9	31.9	53.0	19.7	18.2	11.2	10.0	13.9
Pb	18.6	8.8	8.7	8.8	10.0	16.4	16.0	12.3	17.0	20.4	22.0	12.4
Rb	106.8	118.6	110.3	102.8	156.5	132.5	113.5	140.6	5.8	11.6	4.9	6.9
Sc	6.4	7.6	12.2	1.7	6.9	12.5	3.7	4.4	8.5	12.6	4.7	5.5
Sr	2462.7	2071.0	2334.3	1418.5	1078.3	1103.3	4180.7	1523.7	27887.1	23937.7	19732.3	12941.6
Th	55.0	14.3	3.0	76.4	4.9	35.9	52.5	24.8	94.1	363.1	49.3	24.2
U	9.3	21.7	n.a.	n.a.	n.a.	1.5	3.7	27.4	1.5	0.4	0.0	13.7
V	100.0	60.9	308.4	158.3	87.3	72.5	122.1	91.0	6.0	63.6	24.2	8.0
Y	21.4	13.7	38.1	29.6	7.7	28.5	12.8	15.1	79.6	105.3	135.8	47.0
Zr	3163.4	658.4	2103.6	6855.9	171.5	1186.4	369.5	2903.9	102.4	64.4	1.0	22.0

Table A3.1 - Major- and trace-element XRF analyses

Sample	AT059	AT102	AT136	AT138	AT140	AT052	AT134	AT139	AT045	AT046	AT047	AT049
Unit/Locality	C1	C1	C1	C1	C1	C1	C1	C1	C2	C2	C2	C2
Rock type	cbt	cbt	cbt	cbt	cbt	cbt	cbt	cbt	cbt	cbt	cbt	cbt
Remarks												
SiO2	4.24	2.06	5.01	0.60	2.19	1.50	2.41	2.15	1.31	0.86	1.73	1.05
TiO2	0.15	0.59	0.08	0.14	0.05	0.04	0.18	0.10	0.02	0.02	0.14	0.01
Al2O3	0.37	0.58	0.54	0.41	0.29	0.13	0.45	0.27	0.16	0.28	0.19	0.14
Fe2O3(T)	0.94	3.13	6.22	1.08	1.26	1.63	4.90	1.44	0.75	1.61	3.14	0.54
MnO	0.22	0.20	0.25	0.34	0.30	0.12	0.19	0.31	0.26	0.26	0.11	0.25
MgO	1.08	3.47	3.82	5.93	4.55	1.91	4.66	5.51	2.89	3.69	1.85	2.43
CaO	38.48	40.31	37.56	36.89	39.83	47.09	41.27	36.72	48.24	45.96	47.30	47.95
Na2O	0.37	0.40	0.45	0.40	0.31	0.35	0.39	0.45	0.31	0.50	0.44	0.25
K2O	0.08	0.25	0.89	0.02	0.03	0.16	0.54	0.07	0.01	0.03	0.11	0.01
P2O5	2.12	0.58	0.95	0.36	0.12	0.28	3.02	0.11	0.11	0.37	3.30	0.05
LOI	30.96	35.67	31.24	37.20	39.68	39.61	34.70	37.99	42.80	41.52	36.81	43.10
BaO	12.16	9.21	3.11	12.83	3.70	0.69	0.48	9.97	0.56	0.30	0.33	0.32
SrO	4.97	4.20	3.44	2.99	3.73	3.33	2.13	3.30	2.18	2.31	1.63	2.51
Total	96.14	100.65	93.56	99.18	96.03	96.83	95.32	98.39	99.60	97.71	97.07	98.61
CO2	32.54	35.62	35.01	38.37	42.87	41.08	37.78	39.76	42.54	42.73	38.84	44.49
S	0.00	0.10	0.94	0.00	0.16	0.00	0.46	0.00	0.10	0.33	0.27	0.00
FeO	n.a.	n.a.	n.a.	n.a.	n.a.	n.a.	n.a.	n.a.	n.a.	n.a.	n.a.	n.a.
Ba	109915.4	74355.7	25160.9	119505.5	29962.4	6138.1	4259.5	89303.4	4893.9	2571.8	2660.4	3124.4
Ce	4287.3	2075.8	1750.7	2257.9	3308.9	1141.1	1050.6	2503.4	1022.8	1090.8	1200.3	822.8
Co	0.1	3.2	47.1	1.8	2.9	18.3	9.9	0.3	10.0	10.9	12.6	5.5
Cr	56.4	74.7	20.5	24.1	21.8	0.1	9.5	23.2	1.8	0.1	0.1	0.1
La	3278.6	1441.6	1140.4	1655.6	2219.3	690.1	560.1	1766.4	551.1	591.1	593.6	472.8
Nb	10.9	2503.0	1788.5	127.2	149.1	121.5	2555.8	97.4	26.5	700.1	736.2	32.1
Nd	907.6	426.2	489.6	507.0	877.7	404.6	420.0	600.8	394.2	433.4	438.8	341.8
Ni	13.1	16.9	15.5	18.4	11.7	13.4	7.8	5.7	11.4	9.8	11.5	9.4
Pb	0.0	8.7	21.3	0.0	26.0	11.5	25.7	1.0	16.3	16.1	17.4	13.1
Rb	1.7	n.a.	27.6	4.8	7.5	6.3	5.8	4.2	4.7	1.5	2.3	4.0
Sc	14.1	15.3	15.3	16.8	11.3	8.5	13.3	15.6	5.7	6.1	9.8	5.5
Sr	41303.3	34117.4	26302.2	26127.4	32043.4	28150.1	18014.3	27939.6	19581.6	19084.9	13143.9	21372.4
Th	33.8	264.5	180.5	16.3	41.3	57.2	379.7	110.0	6.1	46.5	84.5	9.9
U	60.1	29.6	13.8	9.5	12.0	4.4	0.0	8.9	0.0	0.0	37.1	0.0
V	40.2	37.6	13.4	41.0	5.9	6.1	42.1	29.5	8.7	8.2	41.5	2.1
Y	93.2	70.8	112.6	66.5	96.4	79.2	81.4	97.3	78.1	84.5	77.6	71.9
Zr	17.0	27.1	12.5	11.8	7.5	72.0	5.6	12.4	4.1	27.7	114.0	8.9

Table A3.1 - Major and trace-element XRF analyses

Sample	AT050	AT051	AT056	AT058a	AT212	AT219	TAP-1B	AT053a	AT057	TP-90-2	AT043	AT060B
Unit/Locality	C2	C2	C2	C2	C2	C2	C2	C2	C2	C2	C3	C3
Rock type	cbt	cbt	cbt	cbt	cbt,dk	cbt,dk	cbt,bre	cbt	cbt	cbt,bre	cbt	cbt
Remarks												
SiO2	2.40	2.12	2.36	7.82	16.57	12.85	15.11	3.24	3.66	18.87	8.49	7.66
TiO2	0.20	0.08	0.17	0.63	2.02	1.51	2.24	0.54	0.73	2.60	0.89	0.54
Al2O3	0.28	0.06	0.17	0.29	1.63	1.18	1.42	0.44	0.36	2.43	1.69	2.16
Fe2O3(T)	2.99	1.22	3.30	5.03	11.07	8.72	19.01	4.91	9.70	18.76	7.98	3.21
MnO	0.10	0.31	0.11	0.27	0.28	0.28	0.24	0.15	0.45	0.24	0.15	0.11
MgO	1.70	3.89	1.88	3.69	8.56	7.76	12.39	1.33	6.22	11.17	2.96	3.62
CaO	46.37	45.21	45.56	37.99	27.52	28.79	21.38	45.90	35.42	20.38	41.66	42.98
Na2O	0.54	0.41	0.49	0.40	0.82	0.42	0.58	0.04	0.44	0.62	0.59	0.42
K2O	0.09	0.05	0.09	0.22	1.97	1.59	1.92	0.41	0.15	2.66	1.50	1.90
P2O5	2.29	0.27	3.11	3.49	6.75	6.03	6.81	4.87	5.31	5.77	7.72	3.47
LOI	38.37	42.09	36.90	33.00	18.85	25.78	17.33	34.50	32.22	15.49	23.79	31.26
BaO	0.30	0.80	0.33	1.24	0.53	1.00	0.21	0.18	0.94	0.31	0.18	0.25
SrO	1.33	2.30	1.71	1.78	0.76	1.02	0.43	1.57	1.00	0.44	1.33	1.61
Total	96.96	98.81	96.18	95.85	97.34	96.93	99.07	98.08	96.60	99.74	98.93	99.19
CO2	40.86	42.14	40.64	36.60	20.13	27.01	17.73	34.06	33.26	15.90	25.06	32.83
S	0.00	0.15	0.30	0.62	0.47	0.80	0.21	0.31	0.71	0.26	0.29	0.15
FeO	n.a.	n.a.	n.a.	n.a.	n.a.	n.a.	9.52	n.a.	n.a.	10.17	n.a.	n.a.
Ba	2494.6	5521.0	2658.9	9847.6	6656.7	11620.6	1917.5	1586.8	8386.5	2820.3	1517.9	2071.0
Ce	976.8	2490.8	1266.2	1090.1	1724.1	1622.7	1032.2	844.4	1744.1	912.5	1030.8	1301.3
Co	3.7	11.8	9.1	8.2	25.5	21.2	61.3	10.9	13.1	46.8	8.8	7.0
Cr	0.1	0.1	0.1	15.9	79.5	63.9	26.8	4.9	16.5	28.7	17.7	9.2
La	506.5	1607.7	633.0	566.3	925.9	868.5	539.6	445.8	860.0	573.1	564.7	721.7
Nb	62.1	33.4	662.5	351.2	564.5	477.4	253.9	177.7	356.7	276.5	159.1	132.1
Nd	308.5	859.0	450.6	346.4	542.8	496.4	414.7	328.6	413.8	446.6	405.0	608.5
Ni	9.7	16.8	9.9	7.7	48.4	48.7	34.5	12.3	5.8	15.6	21.5	18.5
Pb	14.0	25.8	19.2	53.9	62.5	85.6	15.9	8.1	44.2	15.9	10.6	9.2
Rb	4.1	6.0	1.8	5.5	61.9	37.5	68.1	7.7	3.4	76.7	30.3	34.5
Sc	9.6	27.3	10.5	17.9	33.4	35.6	45.8	13.0	23.9	40.1	15.7	11.9
Sr	11214.2	19909.7	13286.3	13544.6	5584.9	7235.9	3678.3	13287.6	8482.1	3706.5	11564.6	12255.2
Th	51.5	18.6	75.5	48.5	77.4	38.9	81.1	19.0	60.1	53.3	23.5	20.0
U	7.1	5.0	41.7	38.5	11.2	7.4	n.a.	30.5	43.8	4.9	50.4	42.6
V	38.4	8.8	43.5	150.5	324.8	333.7	336.0	135.6	387.7	316.6	195.6	49.7
Y	93.0	87.4	80.1	117.9	125.3	125.3	76.1	86.5	139.5	67.3	101.2	99.2
Zr	62.7	3.9	131.0	39.7	1772.8	1052.0	1444.7	647.0	60.3	1072.2	574.1	232.2

Table A3.1 - Major and trace-element XRF analyses

Sample	AT127	AT131	AT054	AT103	AT135	AT137	AT053b	AT104	RJAT3	AT412a	AT407	ASL003
Unit/Locality	C4	C4	C5	C5	C5	C5	C5					Salitre
Rock type	cbt	cbt	cbt	cbt	cbt	cbt	cbt	RR	fen	CR	CR	beb
Remarks												
SiO2	0.92	2.51	0.93	2.38	2.20	3.08	1.57	19.93	62.50	97.97	60.89	15.70
TiO2	0.02	0.20	0.02	0.08	0.06	0.11	0.06	7.49	0.28	0.05	0.88	24.37
Al2O3	0.40	0.63	0.14	0.55	0.60	0.51	0.20	1.02	14.96	1.14	21.43	0.97
Fe2O3(T)	0.50	7.15	1.70	6.19	3.18	2.31	4.64	21.73	5.15	0.58	4.49	23.70
MnO	0.07	0.10	0.35	0.52	0.58	0.35	0.74	0.29	0.10	0.00	0.03	0.21
MgO	0.66	1.83	19.46	9.60	16.92	8.91	19.19	13.02	1.65	0.09	1.51	17.81
CaO	49.74	46.37	29.62	28.40	26.26	31.13	29.41	14.78	2.19	0.01	0.09	15.52
Na2O	0.33	0.42	0.21	0.35	0.31	0.28	0.07	0.71	3.50	0.13	0.92	0.38
K2O	0.01	0.19	0.02	0.03	0.02	0.01	0.25	4.75	9.10	0.00	4.69	0.19
P2O5	0.07	5.87	0.74	1.13	0.27	0.57	3.00	8.27	0.13	0.02	0.03	0.01
LOI	42.87	30.98	45.37	31.76	41.65	35.99	39.57	5.92	0.64	0.39	4.90	0.08
BaO	0.28	0.18	0.04	5.78	4.98	7.04	0.06	0.70	0.33	0.00	0.08	0.08
SrO	1.96	1.44	1.07	3.29	1.58	5.35	0.88	0.76	0.06	0.00	0.01	0.09
Total	97.83	97.88	99.68	90.06	98.60	95.64	99.64	99.37	100.59	100.38	99.95	99.11
CO2	44.96	33.21	n.a.	35.97	43.72	37.01	n.a.	5.09	n.a.	n.a.	n.a.	n.a.
S	0.04	0.32	0.03	1.14	0.35	0.20	0.51	0.09	n.a.	n.a.	n.a.	n.a.
FeO	n.a.	n.a.	n.a.	n.a.	n.a.	n.a.	n.a.	n.a.	n.a.	n.a.	n.a.	n.a.
Ba	2310.1	1484.6	449.6	59428.6	47299.8	71228.5	530.2	5822.6	2903.6	1.9	801.5	742.5
Ce	613.3	963.8	244.2	11294.6	1467.0	8052.0	556.3	2674.0	128.0	2.9	85.2	4546.5
Co	0.3	26.1	1.8	33.8	1.1	3.4	15.6	47.9	5.9	n.a.	n.a.	92.0
Cr	0.1	6.4	0.1	43.3	15.1	89.4	0.1	239.0	20.3	1.9	121.5	45.5
La	377.3	497.6	226.0	5312.8	890.5	5740.6	383.6	1217.8	46.6	1.3	41.3	827.6
Nb	4.1	2.1	1.9	119.5	563.1	451.9	174.8	1153.9	54.4	2.8	18.6	1117.5
Nd	254.6	364.9	128.3	2567.7	356.0	1378.8	243.8	735.5	80.2	2.5	36.8	574.5
Ni	10.2	16.9	6.1	21.5	6.4	16.0	6.4	152.0	14.4	1.2	26.9	249.9
Pb	9.3	8.2	10.2	0.0	0.0	0.0	10.1	n.a.	33.7	7.3	21.7	19.0
Rb	3.8	4.2	4.6	10.3	13.3	0.9	7.0	87.6	91.3	0.4	148.7	8.4
Sc	4.7	12.2	17.5	10.1	20.3	16.7	18.4	25.6	39.5	1.8	10.5	*
Sr	16529.1	11831.0	9255.0	25903.5	11793.9	43756.0	7438.1	7203.2	527.3	31.4	128.9	747.3
Th	1.9	5.6	4.7	90.7	96.7	99.2	27.9	116.8	6.8	1.5	15.6	78.3
U	0.0	5.6	1.5	44.2	2.5	3.3	13.5	n.a.	1.2	3.8	3.3	1.5
V	7.0	83.1	11.9	8.2	17.0	20.3	7.8	219.0	164.9	4.3	129.2	460.6
Y	61.8	74.1	18.4	104.8	56.0	120.0	32.3	n.a.	17.5	1.2	24.7	83.8
Zr	12.8	102.5	5.0	5.9	9.1	10.7	6.4	203.6	114.6	75.8	264.5	339.5

Table A3.1 - Major- and trace-element XRF analyses

Sample	ASL005	ASL018	ASL021	ASL023	ASL026	ASL010	ASL011	ASL014	ASL015	ASL017	ASL020	ASL022
Unit/Locality	Salitre	Salitre	Salitre	Salitre	Salitre	Salitre	Salitre	Salitre	Salitre	Salitre	Salitre	Salitre
Rock type	beb	cbt	cbt	cbt	cbt	cbt	cbt	cbt	cbt	cbt	cbt	cbt
Remarks												
SiO2	24.73	0.91	1.33	0.56	0.79	0.29	0.42	0.64	1.19	1.46	0.75	0.44
TiO2	14.84	0.05	0.01	0.05	0.03	0.01	0.01	0.08	0.05	0.01	0.03	0.02
Al2O3	2.08	0.39	0.18	0.24	0.19	0.08	0.12	0.17	0.20	0.10	0.27	0.25
Fe2O3(T)	17.47	6.40	1.47	6.90	1.64	0.27	0.96	4.28	9.92	0.75	1.79	3.22
MnO	0.25	0.15	0.10	0.15	0.07	0.05	0.11	0.10	0.12	0.12	0.15	0.14
MgO	28.42	3.35	0.58	3.33	1.53	0.53	2.01	2.49	3.03	3.50	4.02	3.47
CaO	9.93	45.35	53.51	44.06	47.88	52.65	51.01	47.32	41.85	49.77	47.34	47.75
Na2O	0.25	0.21	0.10	0.10	0.13	0.12	0.08	0.12	0.10	0.13	0.17	0.10
K2O	0.34	0.04	0.00	0.06	0.11	0.01	0.05	0.07	0.05	0.09	0.07	0.06
P2O5	0.04	4.99	0.00	2.09	2.87	0.08	0.01	2.25	3.38	4.01	0.72	3.91
LOI	1.13	33.91	43.11	36.83	38.48	43.30	42.59	38.01	28.91	38.72	40.68	37.23
BaO	0.04	0.12	0.16	0.13	0.21	0.20	0.21	0.17	0.14	0.20	0.22	0.12
SrO	0.08	1.04	0.30	1.09	1.34	1.30	1.31	1.35	1.12	1.29	1.55	1.21
Total	99.60	96.92	100.85	95.59	95.27	98.89	98.88	97.05	90.06	100.15	97.76	97.92
CO2	n.a.	36.55	42.87	40.49	43.24	44.45	43.28	39.83	34.71	39.54	41.81	39.36
S	n.a.	0.25	0.03	0.29	0.28	0.16	0.19	0.16	0.91	0.09	0.28	0.09
FeO	n.a.	3.73	1.20	2.84	0.76	n.a.	0.60	1.98	n.a.	0.36	n.a.	1.03
Ba	356.8	1026.7	1307.7	1093.7	1692.8	1802.2	1838.6	1511.2	1208.9	1755.1	1980.2	1108.2
Ce	1869.5	573.2	8.1	530.6	568.5	473.4	503.9	652.3	658.2	631.2	761.4	595.1
Co	105.7	30.3	5.0	37.8	10.6	1.2	2.9	10.5	90.3	0.7	7.7	11.3
Cr	691.0	5.6	0.1	2.6	3.0	1.4	0.9	3.3	6.2	1.8	2.7	0.0
La	748.6	271.3	7.8	250.7	298.8	264.1	260.2	320.4	326.8	308.1	394.9	269.9
Nb	833.7	176.8	0.6	119.2	15.8	1.8	4.0	67.9	101.7	90.9	542.5	86.0
Nd	401.3	251.0	12.5	218.9	231.1	169.6	202.4	264.0	267.8	255.2	299.8	245.6
Ni	613.0	14.0	8.0	7.8	11.4	10.5	11.8	7.2	16.5	7.6	9.2	13.7
Pb	12.1	11.9	3.7	9.9	7.8	10.2	11.9	9.3	9.9	11.0	13.4	7.1
Rb	11.9	1.1	2.0	2.2	5.2	3.3	3.1	2.8	0.9	6.7	1.8	2.3
Sc	0.0	11.6	3.8	11.8	6.2	3.2	4.2	9.7	16.3	5.2	6.5	8.4
Sr	671.9	9165.4	2471.4	9802.3	10691.6	11007.9	11039.7	11433.2	9485.4	10927.2	13085.3	10190.9
Th	39.9	29.6	2.3	16.0	8.8	4.4	2.6	3.2	10.8	24.7	117.1	10.8
U	5.0	26.4	1.2	25.9	0.9	0.0	2.0	15.9	13.8	8.7	25.6	17.7
V	156.7	33.7	4.0	40.6	16.8	4.4	3.1	38.7	36.9	5.8	4.6	14.1
Y	80.4	55.1	3.4	51.4	57.9	46.7	56.0	56.0	50.4	63.5	68.3	53.7
Zr	268.6	29.8	2.7	12.9	18.8	9.0	2.8	84.1	114.2	16.1	25.6	17.4

Table A3.1 - Major- and trace-element XRF analyses

Sample	ASL028	ASL032	ASL035	ASL039	ASL012	ASL013	ASL024	ASL030	ASL016	ASL019	ASL027	ASL029
Unit/Locality	Salitre	Salitre	Salitre	Salitre	Salitre	Salitre	Salitre	Salitre	Salitre	Salitre	Salitre	Salitre
Rock type	cbt	cbt	cbt	cbt	cbt	cbt	cbt	cbt	cbt	cbt	cbt	cbt
Remarks												
SiO2	0.22	3.01	0.42	0.40	1.09	0.22	0.00	0.01	0.52	0.12	0.31	0.06
TiO2	0.06	0.15	0.01	0.01	0.08	0.17	0.12	0.01	0.03	0.02	0.05	0.03
Al2O3	0.29	0.29	0.19	0.15	0.24	0.17	0.35	0.17	0.09	0.15	0.28	0.25
Fe2O3(T)	4.74	4.73	0.66	0.54	2.70	3.62	4.78	1.21	2.04	1.74	2.55	2.12
MnO	0.16	0.12	0.15	0.09	0.58	0.39	0.24	0.34	0.25	0.26	0.22	0.23
MgO	5.04	3.81	5.17	1.52	11.54	18.48	18.77	20.07	18.58	19.37	17.66	17.93
CaO	44.26	47.73	46.11	49.55	35.70	25.13	30.41	30.08	30.00	31.03	31.89	32.54
Na2O	0.13	0.18	0.46	0.24	0.39	0.10	0.05	0.14	0.10	0.03	0.09	0.14
K2O	0.10	0.16	0.01	0.01	0.03	0.03	0.11	0.03	0.10	0.06	0.10	0.08
P2O5	2.37	8.14	0.00	0.43	7.24	0.43	2.18	0.12	1.82	1.46	4.78	4.24
LOI	37.07	30.56	43.66	42.47	33.41	43.12	41.65	46.68	43.07	44.03	39.82	41.21
BaO	0.12	0.15	0.16	0.20	3.14	2.66	0.02	0.06	0.00	0.00	0.00	0.02
SrO	1.24	1.07	1.38	1.38	0.72	1.23	0.74	1.25	0.62	0.77	0.74	0.82
Total	95.80	100.10	98.38	96.99	96.86	95.75	99.42	100.17	97.22	99.04	98.49	99.67
CO2	39.54	30.23	44.63	44.45	32.27	45.95	42.36	47.38	44.96	44.16	41.11	38.29
S	0.39	0.13	0.07	0.19	0.51	0.19	0.31	0.51	0.47	0.31	0.00	0.50
FeO	2.14	1.49	0.31	0.25	n.a.	n.a.	0.75	1.09	n.a.	n.a.	1.17	1.09
Ba	1100.6	1374.9	1448.7	1826.4	30102.3	28386.4	148.2	493.0	0.0	0.4	0.0	195.7
Ce	519.7	789.1	498.1	476.4	996.7	3668.3	203.3	194.9	197.4	166.3	408.3	324.2
Co	15.5	8.2	7.3	1.9	1.6	2.4	3.8	1.0	6.6	6.7	0.1	2.2
Cr	3.1	6.1	3.0	1.4	13.1	46.6	6.2	4.4	2.7	1.9	2.0	3.3
La	231.6	384.7	257.6	238.2	562.6	2115.2	84.5	91.7	93.6	62.4	148.9	120.6
Nb	668.5	69.6	9.3	2.5	95.7	77.3	111.7	2.1	1560.2	614.1	806.8	134.1
Nd	214.6	327.8	202.6	186.2	487.5	1376.6	100.9	73.7	83.2	75.2	184.5	149.3
Ni	9.3	11.9	11.0	2.5	8.8	13.9	3.4	3.9	0.0	0.3	0.1	7.2
Pb	14.3	10.7	9.4	10.2	11.0	68.0	9.5	11.7	15.8	13.1	14.5	10.7
Rb	1.3	4.9	3.0	4.3	0.0	15.3	6.3	17.0	2.8	5.0	3.7	8.2
Sc	9.7	10.4	5.5	4.5	17.4	27.1	20.0	16.3	16.1	15.8	14.7	14.5
Sr	10468.3	9059.9	11629.0	11628.7	5938.7	10095.5	5977.6	10656.7	5246.8	6510.5	6275.8	6940.1
Th	122.5	69.4	1.5	9.8	338.1	163.9	18.8	10.9	141.6	73.7	124.4	26.8
U	31.7	5.1	1.5	0.6	16.0	20.6	1.8	0.0	0.1	0.0	1.3	0.0
V	24.4	47.3	0.0	2.0	31.3	42.6	53.4	4.8	14.4	6.9	31.6	18.3
Y	52.7	85.3	53.6	49.0	617.1	66.5	14.4	17.9	24.0	18.9	28.7	28.9
Zr	29.8	165.3	6.4	4.8	243.0	4.2	6.3	11.3	25.8	11.1	17.5	6.7

Table A3.1 - Major- and trace-element XRF analyses

Sample	ASL031	ASL033	ASL034	ASL036	ASL037	ASL038	ASL042	ASL043	ASL040	ASL025	ASL041	91SB16
Unit/Locality	Salitre	Salitre	Salitre	Salitre	Salitre	Salitre	Salitre	Salitre	Salitre	Salitre	Salitre	Salitre
Rock type	cbt	cbt	cbt	cbt	cbt	cbt	cbt	cbt	cbt	cbt	cbt	syen dk
Remarks												
SiO2	0.33	0.38	0.02	0.24	0.93	0.00	0.00	0.85	0.00	6.49	4.69	54.59
TiO2	0.08	0.07	0.01	0.01	0.08	0.02	0.01	0.02	0.30	0.75	0.52	1.08
Al2O3	0.32	0.22	0.19	0.23	1.86	0.31	0.13	0.26	0.20	0.47	0.23	16.18
Fe2O3(T)	3.43	4.22	0.82	1.86	3.98	1.86	0.70	0.66	14.69	19.77	13.92	9.12
MnO	0.19	0.22	0.23	0.22	0.20	0.24	0.24	0.18	0.29	0.36	0.25	0.11
MgO	14.88	17.24	18.69	19.35	16.59	19.45	19.43	16.32	15.16	11.43	6.83	0.72
CaO	35.40	30.91	31.46	29.72	32.00	29.35	30.17	33.92	26.69	32.55	38.43	2.34
Na2O	0.19	0.49	0.45	0.50	0.62	0.48	0.27	0.38	0.30	0.16	0.36	5.02
K2O	0.05	0.05	0.03	0.16	0.20	0.12	0.01	0.15	0.07	0.33	0.22	8.01
P2O5	10.16	4.26	3.27	0.66	6.88	0.36	0.43	7.37	3.36	4.85	5.48	0.13
LOI	33.38	39.80	42.84	44.22	35.89	44.62	46.30	37.31	34.44	21.90	26.96	1.32
BaO	0.00	0.00	0.00	0.03	0.00	0.01	0.02	0.00	0.03	0.11	0.12	0.29
SrO	0.79	0.74	0.79	0.84	0.64	0.73	0.86	0.74	0.90	0.75	0.84	0.19
Total	99.20	98.60	98.80	98.04	99.87	97.55	98.58	98.16	96.44	99.92	98.85	99.10
CO2	33.44	41.11	43.86	45.22	36.37	45.91	46.94	38.15	36.24	22.17	28.13	n.a.
S	0.33	0.07	0.07	0.82	0.16	0.75	0.36	0.01	0.48	0.00	0.01	n.a.
FeO	1.36	2.18	0.73	n.a.	3.94	n.a.	n.a.	n.a.	5.77	5.72	4.11	n.a.
Ba	32.0	0.0	32.6	266.3	0.0	72.5	212.0	0.0	0.0	956.1	1065.9	2440.0
Ce	683.5	417.2	283.4	180.9	613.6	144.1	123.3	548.7	413.7	782.8	766.1	195.6
Co	3.2	1.8	0.9	6.7	5.3	9.8	1.1	0.8	13.7	18.7	11.1	12.5
Cr	3.4	5.7	4.2	2.9	5.9	4.2	0.3	4.4	10.3	10.2	6.8	22.4
La	263.7	160.0	107.3	85.1	230.4	57.5	56.8	214.8	164.1	354.5	381.9	104.3
Nb	628.9	1071.5	694.9	160.9	1667.9	727.6	63.6	907.3	1357.5	264.5	134.5	92.1
Nd	318.6	192.0	127.6	78.5	281.5	57.9	54.8	255.8	182.8	335.2	322.7	59.2
Ni	5.4	0.0	0.2	0.9	0.0	0.1	2.3	2.6	1.5	14.4	7.5	6.6
Pb	13.4	13.5	17.3	10.9	15.7	12.2	12.3	14.6	16.0	8.8	10.9	4.4
Rb	3.3	2.6	6.5	10.7	4.5	8.5	8.1	6.0	0.7	1.4	0.9	137.1
Sc	13.6	17.6	12.4	16.3	16.8	17.8	15.1	10.9	28.3	32.3	25.5	4.2
Sr	6682.6	6235.5	6660.8	7100.0	5429.5	6184.7	7312.1	6299.1	5361.1	6368.4	7109.4	1699.1
Th	1.5	145.0	80.2	20.5	175.7	89.6	11.1	97.4	156.5	76.8	60.6	11.3
U	1.7	0.9	34.5	2.4	3.6	0.0	0.0	28.4	9.4	14.0	11.4	2.3
V	38.3	42.4	3.2	3.3	42.9	9.5	2.1	9.4	162.4	188.9	150.3	170.7
Y	54.0	30.5	20.5	15.6	42.9	10.9	8.7	42.3	24.2	72.3	66.6	14.3
Zr	44.1	27.1	14.9	6.7	43.6	23.9	10.9	43.0	33.6	1089.2	614.7	1418.0

Table A3.1 - Major- and trace-element XRF analyses

Sample	SAL-2	SAL-3	SAL-3C	SAL-3D	SAL-3	SAL-1
Unit/Locality	Salitre	Salitre	Salitre	Salitre	Salitre	Salitre
Rock type	syen	syen	syen	syen	syen	fen
Remarks	dk	dk	dk	dk	dk	
SiO2	51.85	54.14	41.87	60.31	54.14	75.96
TiO2	1.06	2.76	4.82	1.00	2.76	0.49
Al2O3	17.96	10.30	10.36	14.51	10.30	9.82
Fe2O3(T)	8.97	9.72	13.18	7.20	9.72	3.72
MnO	0.14	0.17	0.19	0.09	0.17	0.02
MgO	0.61	2.82	4.04	0.69	2.82	1.76
CaO	2.10	6.67	8.61	1.74	6.67	0.14
Na2O	7.21	3.24	2.78	3.67	3.24	1.53
K2O	7.37	7.25	7.25	9.96	7.25	5.01
P2O5	0.13	0.97	1.17	0.03	0.97	0.04
LOI	0.46	0.75	3.80	0.35	0.75	0.47
BaO	0.41	n.a.	0.29	0.23	0.17	0.11
SrO	0.30	n.a.	0.23	0.08	0.13	0.01
Total	98.57	98.79	98.58	99.86	99.09	99.07
CO2	n.a.	n.a.	n.a.	n.a.	n.a.	n.a.
S	n.a.	n.a.	n.a.	n.a.	n.a.	n.a.
FeO	n.a.	n.a.	n.a.	n.a.	n.a.	n.a.
Ba	3580.4	1519.0	2519.4	1892.6	1519.0	941.2
Ce	556.2	361.3	476.8	126.1	361.3	43.0
Co	10.6	23.4	38.9	5.2	23.4	14.1
Cr	19.2	43.6	25.6	20.9	43.6	56.8
La	366.1	228.3	280.3	60.2	228.3	12.9
Nb	350.2	182.4	194.2	87.0	182.4	8.1
Nd	136.9	156.5	174.9	57.6	156.5	20.6
Ni	11.0	18.3	27.5	3.4	18.3	19.7
Pb	3.6	10.9	25.0	2.8	10.9	5.7
Rb	91.7	139.4	165.4	173.4	139.4	152.1
Sc	2.1	11.6	20.3	0.7	11.6	5.5
Sr	2827.8	1086.3	1965.8	648.3	1086.3	55.7
Th	18.4	0.4	16.5	11.2	0.4	5.1
U	1.7	1.8	2.2	0.0	1.8	1.0
V	116.5	226.6	331.2	148.4	226.6	53.0
Y	13.1	76.7	41.8	22.1	76.7	6.9
Zr	1238.8	959.9	892.0	896.6	959.9	182.7

Table A3.2 - Trace-element ICP-MS analyses

Sample	AT002	AT013	AT014	AT021a	AT021b	AT022	AT028	AT120a	AT203	AT204	AT206	AT207
Unit/Locality												
Rock type	php	php	php	php	php	php	php	php	php	php	php	lcr
Remarks												
Ba	3665.1	3458.8	2793.9	3000.3	2963.1	3337.4	5940.0	2426.9	3993.1	2838.1	3039.8	2297.4
Co	48.9	55.9	72.1	67.2	96.0	58.4	41.3	51.6	51.3	64.5	64.8	47.6
Cr	312.6	355.0	548.5	813.4	1012.3	492.4	149.1	134.4	247.5	370.5	672.6	175.5
Cs	n.a.	n.a.	2.269	2.716	2.452	2.189	0.728	1.795	n.a.	n.a.	n.a.	n.a.
Cu	73.0	77.1	54.9	69.2	58.4	92.3	62.5	78.3	75.8	61.5	52.5	66.2
Ga	19.408	16.955	16.788	12.347	15.241	20.416	22.604	16.431	12.703	15.603	12.502	18.279
Hf	23.03	16.039	10.584	15.428	11.724	15.659	15.698	23.061	14.502	12.115	10.95	20.002
Nb	306.9	234.3	200	229.1	271.4	257.1	342	326.7	276.3	224.21	167.6	359.4
Ni	154.8	300.1	739.3	595.2	845.6	395.8	90.4	158.6	449.4	650.6	586.7	119.4
Pb	21.2	13.4	10.3	16.2	12.7	20.9	32.3	15.5	17.2	19.5	12.4	17.5
Rb	141.4	148.3	125.9	106.8	92.4	157.4	102.9	114.3	83.1	121.5	109.2	97.9
Sc	28.11	28.89	23.38	23.57	23.07	22.44	22.45	36.91	17.42	16.73	20.93	24.72
Sr	3528.4	2755.7	2131.1	3441.1	1610.3	3091.8	4979.5	3772.5	2590.5	2121.1	2173.2	3770.5
Ta	13.187	12.462	10.275	12.203	19.849	15.365	14.566	17.21	13.046	21.86	10.484	17.991
Th	27.72	26.74	28.61	37.83	55.99	43.89	49.1	48.19	49.31	31.93	27.63	46.55
U	4.85	6.58	5.86	7.04	6.9	11.53	1.91	7.91	5.66	1.96	3.7	4.21
V	257.7	320.2	256.7	171	174.2	271.9	410.8	252.1	380.8	180.7	168.5	266.2
Y	58.91	42.49	33.11	44.73	46.12	42.2	49.3	59.28	59.79	28.73	33.11	61.7
Zn	144.7	118.2	86.6	122.2	135.5	103.8	100.4	176.5	103.3	132.9	103.5	144.0
Zr	944.6	693.9	552.6	680.5	476.4	749.9	725.9	917.7	697.6	561.6	483.1	940.8
La	349.293	282.57	263.1	320.93	498.4542	417.3	507.9	444.8	394.896	406.781	266.05	436.934
Ce	592.764	506.296	479	637.06	1018.856	752.53	898.5	923.6	753.613	869.04	497.9	805.131
Pr	70.3	60.9	60.01	69.95	112.772	92.79	110.61	99.7	87.6	105.5	57.7	96.006
Nd	261.4	226.8	221.8	256.17	410.5892	330.7	396.3	364.1	320.4	389	213.1	319.885
Sm	38.1	31.8	29.81	35.8	55.4	43.1	50.8	49.3	42.5	44.7	28.5	45.725
Eu	10.24	8.33	7.7	9.18	13.75	10.58	12.25	12.59	10.88	9.89	7.29	13.406
Gd	25.84	21.07	20.72	20.87	29.18	28.2	32.45	28.45	27.37	23.08	18.86	34.84
Tb	3.14	2.44	2.27	2.52	3.3894	3.07	3.48	3.38	3.15	2.27	2.02	3.9
Dy	13.72	10.38	9.35	10.55	13.0893	12.39	13.38	14.23	13.68	8.37	8.38	16.31
Ho	2.13	1.58	1.36	1.62	1.8632	1.75	1.99	2.15	2.18	1.13	1.25	2.38
Er	4.72	3.45	2.785	3.39	3.6222	3.588	4.345	4.5	5.17	2.43	2.72	5
Tm	0.556	0.413	0.335	0.413	0.4045	0.422	0.507	0.532	0.677	0.277	0.322	0.567
Yb	2.876	2.187	1.693	2.167	1.9612	2.073	2.696	2.755	4.042	1.6	1.762	3.032
Lu	0.353	0.279	0.214	0.276	0.2463	0.298	0.334	0.337	0.591	0.225	0.218	0.378

Table A3.2 - Trace-element ICP-MS analyses

Sample	AT209b	AT210	HS186i	HS186m	TP-90-4B	TP-90-4C	AT020	AT024	AT201	AT202	AT205	AT208
Unit/Locality			Araxa	Araxa								
Rock type	php	php	php	php	php	php	lcr	lcr	lcr	lcr	lcr	lcr
Remarks												
Ba	4160.6	3139.2	2660.6	1510.0	3495.8	3224.7	3128.6	5660.8	4725.4	2394.1	2673.1	3672.2
Co	44.5	56.5	69.7	65.6	47.9	42.1	43.5	38.9	36.7	31.9	30.0	42.1
Cr	181.9	398.0	590.4	816.1	243.8	156.0	218.1	8.5	17.8	8.5	6.1	12.0
Cs	n.a.	n.a.	18.8527	25.924	n.a.	n.a.	1.854	1.78	1.27	2.466	1.31	2.645
Cu	91.3	84.6	145.2	118.1	91.3	104.1	84.7	139.2	99.8	94.5	29.8	142.6
Ga	16.571	15.037	18.191	17.8143	18.675	19.243	27.524	17.944	18.607	17.981	15.283	16.344
Hf	19.43	20.692	15.6598	13.2458	20.121	22.919	30.924	33.016	25.897	64.571	47.744	13.264
Nb	275.7	334	208.1166	175.691	258.5	256.9	388	418	428.4	303.5	295.4	425.5
Ni	138.8	400.9	457.0	390.0	167.5	104.5	69.5	9.4	14.1	34.1	12.3	22.7
Pb	21.9	17.4	10.7	6.7	19.2	19.8	40.3	31.0	29.2	1.4	11.0	22.1
Rb	163.7	94.8	141.2	129.6	152.2	150.1	176.6	138.3	129.0	76.5	78.6	137.9
Sc	28.08	22.51	22.6161	26.9336	21.65	22.59	18.545	24.43	23.31	16.08	68.48	29.98
Sr	3989.5	3970.3	2254.633	1924.112	3972.6	3398.2	3090.6	6000.4	4157.1	1980.4	3894.2	3197.3
Ta	16.954	16.952	10.7198	13.1895	16.009	14.62	21.658	12.554	21.342	4.422	7.464	22.387
Th	45.59	36.44	18.9699	23.5111	36.03	32.91	48.82	37.48	41.29	2.63	9.06	31.13
U	3.59	2.08	2.8489	4.1601	5.32	6.06	4.95	10.99	9.73	3.99	6.14	16.77
V	300.7	280.1	337.6681	294.8232	293.4	323.3	361.5	338	283.9	429.4	190	515.5
Y	53.83	49.9	37.7726	30.9757	53.58	54.37	55.03	82.93	83.31	98.74	87.34	81.83
Zn	136.4	128.7	159.1	136.9	146.0	143.5	139.3	178.1	221.1	116.5	157.3	208.9
Zr	998.9	891.8	715.6	587.3	825.4	982.2	1946.7	1959.2	1229.1	2757.9	1813.2	469.2
La	440.502	419.738	205.0212	159.7959	357.977	329.98	654.117	343.9	540.5	121	420.7	471.4
Ce	833.3	791.338	402.8161	340.4609	671.061	603.577	1199.426	668.2	1095.2	203.8	697.1	991.1
Pr	97.9	93.2	46.823	41.6271	80.8	72.6	151.513	64.6	118	23.8	70.6	108.6
Nd	358.3	343	174.505	161.3238	299.8	270.4	554.145	236.5	430.5	94.3	254.4	392.8
Sm	47.2	44.9	24.8696	23.6315	41.5	38.1	70.96	38.8	58.5	19.5	41.8	51.3
Eu	11.98	11.15	6.7114	6.1904	10.76	9.96	16.895	11.52	15.05	6.58	12.35	12.87
Gd	30.22	27.35	15.7671	14.8082	27.18	25.35	44.218	28.13	34.67	20.25	32.12	28.79
Tb	3.29	2.98	1.8964	1.7742	3.05	2.96	4.84	3.7	4.16	2.91	4.1	3.58
Dy	13.36	12.26	8.3008	7.4211	13.08	12.72	18.626	16.91	18.28	15.96	18.72	16.27
Ho	1.99	1.83	1.2651	1.1075	2.02	2.02	2.489	2.66	2.92	3	3	2.78
Er	4.41	4.08	2.6775	2.2286	4.47	4.59	4.796	5.93	6.48	7.83	6.53	6.99
Tm	0.525	0.515	0.3408	0.2713	0.524	0.562	0.519	0.794	0.822	1.11	0.78	0.979
Yb	2.873	2.983	1.8028	1.3429	2.764	3.065	2.533	4.274	4.397	6.327	4.131	5.516
Lu	0.367	0.395	0.2258	0.1717	0.336	0.381	0.365	0.579	0.564	0.835	0.509	0.731

Table A3.2 - Trace-element ICP-MS analyses

Sample	AT209a	AT211	AT213	AT214	AT215	AT016	AT025	AT126a	AT217	AT003	AT004	AT009
Unit/Locality						B1	B1	B2	B1	B1	B1	B1
Rock type	lcr	lcr	lcr	lcr	lcr	wehrl	wehrl	wehrl,dk	wehrl	beb	beb	beb
Remarks												
Ba	4065.5	3630.3	3242.9	3554.7	4790.0	293.9	1051.6	1227.9	374.7	1253.6	2564.5	1512.2
Co	33.7	39.1	23.1	35.0	14.0	101.7	101.8	49.2	80.4	45.8	62.9	62.8
Cr	1.6	1.5	1.8	1.6	1.1	4.1	1211.7	12.3	490.0	2.6	9.0	2.5
Cs	1.909	1.642	1.39	0.134	1.26	0.227	1.227	1.304	0.605	1.033	1.333	1.291
Cu	45.4	205.0	152.3	162.2	50.2	45.6	38.9	0.6	41.9	25.8	30.1	23.0
Ga	14.529	19.137	15.774	16.83	17.907	13.862	17.665	15.184	18.372	18.598	18.074	16.234
Hf	61.211	52.258	12.906	49.458	31.415	13.01	10.877	3.451	19.057	5.776	8.038	5.174
Nb	232.7	441.3	374.4	520.7	446.7	824.6	740.8	120.3	1215.2	338.1	489.4	189.1
Ni	5.7	4.2	8.8	7.2	1.9	88.8	1106.9	43.5	387.1	23.7	17.1	42.1
Pb	20.0	18.4	11.1	14.2	27.3	1.6	2.1	0.7	1.6	1.5	6.1	1.7
Rb	108.1	133.5	93.1	34.4	64.6	11.6	75.6	68.8	30.4	86.1	92.5	112.5
Sc	43.97	24.27	26.97	21.44	7.49	7.79	26.73	27.73	42.99	38.51	46.18	54.64
Sr	4560.1	3980.1	3672.6	4052.8	11381.92	2829.7	744.4	1978.3	603	1606	2142.1	1591.6
Ta	1.762	4.435	9.879	9.135	6.092	46.36	26.734	1.035	33.57	12.433	13.443	12.678
Th	1.59	1.88	32.83	49.72	70.32	39.4	69.92	2.18	89.25	5.79	10.06	10.27
U	8.41	8.25	32.16	6.39	23.82	21	11.27	10.08	10.92	8.11	14.25	3.34
V	420.8	536	545.9	683.1	440.6	142.9	112.5	260.4	276.2	171.8	128.9	149.8
Y	120.1	102.31	79.62	58.36	109.44	146.94	73.33	181.96	55.06	54.95	94.79	49.19
Zn	159.7	169.8	199.7	217.7	192.2	233.6	238.0	119.0	316.5	213.8	120.1	127.3
Zr	2839.0	2410.9	360.3	4088.0	1908.3	490.1	303.0	211.2	492.9	202.8	213.3	141.7
La	330.5	238.6	329.8	307.6	614.8	1195.7	1009.7	438.5	1069.1	371.8	700	367.5
Ce	387.6	308.9	565	460.8	981.9	2239.8	2119.2	563.6	2452.8	599	1022.4	662.3
Pr	35.8	30.2	63.8	46.6	97.1	240.8	231.1	62.6	271.8	65.3	101.7	69.8
Nd	120.7	105.8	234.2	157.2	304.5	886.3	814.8	224.8	963.5	236	348.8	256.5
Sm	23.8	21.5	36.7	23.1	46.9	139.8	102.3	43	116.1	40.6	57.4	40.6
Eu	8.49	7.54	10.49	6.52	14.77	38.15	25.31	14.58	27.18	11.9	17.05	11.28
Gd	25.41	22.41	26.73	15.84	36.87	93.88	51.65	45.53	53.33	30.59	43.08	28.1
Tb	3.7	3.22	3.47	2.15	5.4	10.68	6.16	6.4	5.94	3.57	5.33	3.16
Dy	19.73	16.88	16.11	10.52	24.32	43.39	23.97	32.35	21.65	14.75	22.48	12.72
Ho	3.59	3.09	2.66	1.93	4.27	6.09	3.32	5.81	2.8	2.13	3.37	1.82
Er	8.87	7.72	6.29	5.01	8.89	11.51	6.48	13.3	5.04	4.01	6.69	3.42
Tm	1.243	1.059	0.852	0.73	1.154	1.176	0.677	1.986	0.482	0.427	0.816	0.354
Yb	7.165	5.901	4.513	4.35	6.317	5.305	3.1	10.734	2.279	1.946	3.868	1.678
Lu	0.949	0.773	0.58	0.551	0.792	0.571	0.34	1.53	0.24	0.221	0.5	0.194

Table A3.2 - Trace-element ICP-MS analyses

Sample	AT027	AT036	AT037	AT001	AT006	AT010	AT017	AT023	AT029	AT030	AT032	AT033
Unit/Locality	B1	B1	B1	B2	B2	B2	B2	B2	B2	B2	B2	B2
Rock type	beb	beb	beb	beb	beb	beb	beb	beb	beb	beb	beb	beb
Remarks												
Ba	111.1	225.6	1444.6	219.7	696.9	283.0	1446.8	730.3	177.1	2031.6	630.9	620.8
Co	66.9	55.0	62.5	66.4	64.6	102.5	48.6	23.7	62.9	55.5	23.1	79.5
Cr	0.6	1.6	1.3	3.5	6.5	166.7	7.0	942.8	2.6	2.2	10.3	2.9
Cs	0.399	0.547	1.23	0.215	0.409	0.142	3.342	1.128	0.185	2.674	1.252	0.786
Cu	24.7	38.0	44.0	32.3	33.6	n.a.	6.6	11.7	49.5	23.3	39.7	442.9
Ga	8.171	10.148	16.012	14.246	13.72	11.973	12.349	13.78	10.607	15.89	7.357	12.328
Hf	9.027	11.286	8.148	16.704	15.897	10.662	7.098	11.629	9.865	27.585	6.602	28.962
Nb	223.8	531.4	470.4	507.1	559.7	354.4	51.7	67.7	633.2	222.8	25.8	571.7
Ni	12.2	13.4	26.7	18.9	22.1	221.9	6.1	120.4	14.5	17.4	19.0	13.9
Pb	0.5	1.9	1.5	1.6	3.9	3.4	2.1	1.7	1.8	3.9	0.8	3.9
Rb	12.5	18.3	98.2	10.1	23.4	9.7	17.3	77.5	11.4	66.4	43.6	42.1
Sc	44.48	50.88	41.66	49.2	58.6	40.09	41	145.83	35.36	42.85	40.16	59.72
Sr	1998.7	1873.7	1974.4	2488	1869.2	1311.1	1603.6	1909.9	2216.4	2449.4	1839	1131.9
Ta	6.341	23.531	24.564	35.13	16.473	23.252	3.097	3.665	24.497	7.499	1.548	20.421
Th	6.7	10.94	18.37	56.9	21.03	27.05	18.25	8.13	41.74	18.99	4.45	14.63
U	5.61	13.7	10.36	11.42	11.64	11.01	5.83	4.55	13.03	5.78	2.55	10.26
V	259.7	264.3	256	195.4	179.2	123.4	211.6	196	319.8	164.6	188.1	279.3
Y	49.8	79.84	77.33	91.4	88.29	54.35	39.56	36.32	56.37	65.75	18.79	46.55
Zn	135.6	193.8	171.1	158.8	128.2	160.9	95.4	65.3	147.8	133.3	89.0	150.8
Zr	241.6	309.9	264.9	475.2	442.6	298.8	643.8	256.2	329.7	1005.5	291.0	867.7
La	235.8	433.1	442.9	794.2	792.8	621	199.6	210.4	636.5	416.8	110.8	234.5
Ce	350.6	662.7	844	1721.4	1253.6	1023	419.2	511.1	1193.4	791.2	223.1	503.5
Pr	35.8	65.2	79.5	199	126.7	120.8	49.8	66.5	121.8	83.6	26.7	62.7
Nd	125.2	232.9	287.9	733	434.5	432	188	261.9	431.8	304	101.9	245.3
Sm	22.5	45.2	48.9	99.6	67.3	63.6	27.6	38.4	62.2	45	14	40.4
Eu	6.98	14.23	14.3	24.86	19.02	16.61	7.26	9.58	16.07	12.41	3.6	11.08
Gd	20.09	38.26	36.08	56.32	45.57	45.14	17.65	22.35	34.72	30.63	8.42	26.65
Tb	2.57	4.96	4.59	6.42	5.68	5.01	1.96	2.53	4.16	3.59	0.96	3.13
Dy	11.97	22.14	19.86	25.5	23.12	19.2	8.11	10.16	16.54	15.2	4.04	13.29
Ho	1.87	3.31	2.89	3.63	3.47	2.6	1.31	1.45	2.31	2.35	0.64	1.93
Er	3.88	6.63	5.54	6.94	6.78	4.97	2.94	2.98	4.46	4.94	1.44	3.87
Tm	0.426	0.694	0.587	0.725	0.803	0.513	0.419	0.361	0.478	0.572	0.194	0.441
Yb	2.07	3.221	2.69	3.48	3.924	2.356	2.502	1.94	2.409	3.057	1.244	2.284
Lu	0.253	0.354	0.309	0.4	0.546	0.28	0.417	0.282	0.308	0.4	0.199	0.303

Table A3.2 - Trace-element ICP-MS analyses

Sample	AT034	AT038a	AT115	AT302	AT303	AT304	AT012	AT018	AT039	AT119b	AT301	AT305
Unit/Locality	B2	B2										
Rock type	beb	beb	syen	syen	syen	syen	syen	syen	syen	syen	syen	syen
Remarks												
Ba	1660.2	305.0	3878.7	13114.4	13973.2	7499.0	5127.5	4551.5	7491.1	8634.5	11811.9	8160.3
Co	69.8	48.0	3.0	3.9	3.3	4.2	59.5	7.5	9.1	6.3	3.3	5.5
Cr	4.1	9.0	2.1	8.1	7.1	2.9	4.7	6.6	3.3	3.3	4.8	1.4
Cs	1.273	0.207	0.881	0.749	1.008	1.208	1.439	0.578	1.907	0.838	0.585	1.595
Cu	31.4	14.5	3.0	20.3	12.9	2.0	107.5	34.3	3.2	4.5	3.2	3.1
Ga	21.053	10.24	21.61	26.887	27.244	23.95	30.3	31.829	24.707	20.909	22.098	26.273
Hf	142.611	13.234	27.249	113.089	57.579	17.462	41.457	98.785	2.291	22.475	9.044	39.912
Nb	332.3	367.7	239.8	240.6	388.2	90.1	640	612.8	109.4	369.7	354.3	359.3
Ni	9.0	11.4	2.0	5.1	5.1	0.7	7.9	4.1	0.2	0.3	1.0	1.0
Pb	1.3	1.9	3.5	16.6	9.7	3.7	4.4	9.0	2.0	5.2	6.4	11.1
Rb	95.5	12.2	128.5	117.6	106.6	118.1	104.9	90.0	158.5	131.2	122.6	133.2
Sc	72.36	37.04	3.4	14.97	16.04	2.11	19.52	29.14	3.45	4.41	2.89	3.53
Sr	1518.9	2236.3	2334.2	2131.8	2288.1	2051.2	2156.8	1290.9	798.5	1168.4	4089.2	1523.1
Ta	6.418	25.187	13.572	10.048	19.263	7.471	7.676	15.534	2.99	8.299	4.523	7.074
Th	2.29	54.69	20.14	55.62	46.94	9.43	4.75	51.54	7.79	37.04	48.51	25.18
U	5.78	9.37	2.37	15.85	15.2	29.56	4.17	113.71	3.12	4.61	6.9	35.62
V	275.1	152.6	77.3	74.3	91.6	54.1	338.9	86.8	73.4	68.5	105.4	86.2
Y	208.98	52.37	17.05	28.93	19.6	10.49	34.97	21.3	5.2	23.92	11.37	11.65
Zn	129.3	87.4	46.1	66.6	89.9	52.7	149.3	60.5	133.5	62.1	49.8	117.1
Zr	6052.5	430.6	1169.7	6706.8	3263.2	682.0	2076.3	6845.9	105.8	1239.8	397.7	2942.3
La	144	631.2	87.2	294.9	269.3	53.6	67.6	128.4	52	180.3	274.8	120.3
Ce	202.3	1353.9	180.4	544	507.1	92.1	159.3	250.3	100.4	393.2	549.2	260.2
Pr	22.9	143.6	20.2	58.2	54.6	9.2	21	25.9	10.5	44.6	58.6	29.7
Nd	96.6	530.2	66.6	196	192.6	29.7	85.2	88	33.4	149.4	190.8	102.7
Sm	26.6	69.7	9.1	22	22.5	4.7	17.2	12	4.6	19.4	23.8	13.5
Eu	10.39	17.05	2.42	5.29	5.31	1.24	5.26	3.12	1	4.81	5.95	3.23
Gd	34.04	38.26	5.42	9.28	9.56	3.53	12.18	6.66	2.68	9.73	11.93	6.48
Tb	5.94	4.21	0.76	1.1	1.04	0.5	1.69	0.86	0.34	1.18	1.25	0.74
Dy	33.56	16.16	3.48	5.23	4.1	2.17	7.86	3.92	1.31	4.6	3.74	2.87
Ho	6.62	2.21	0.67	1.02	0.7	0.4	1.27	0.69	0.21	0.91	0.48	0.47
Er	17.06	4.21	1.6	3.21	1.71	0.9	2.93	1.9	0.47	2.43	0.86	1.1
Tm	2.517	0.44	0.26	0.573	0.292	0.131	0.439	0.332	0.06	0.407	0.099	0.161
Yb	13.942	2.312	1.7	3.791	1.896	0.886	2.568	2.45	0.326	2.691	0.718	1.139
Lu	1.894	0.299	0.271	0.588	0.314	0.123	0.398	0.42	0.047	0.388	0.106	0.154

Table A3.2 - Trace-element ICP-MS analyses

Sample	AT042	AT044	AT048	AT055	AT059	AT102	AT136	AT138	AT140	AT045	AT046	AT047
Unit/Locality	C1	C1	C1	C1	C1	C1	C1	C1	C1	C2	C2	C2
Rock type	cbt	cbt	cbt	cbt	cbt	cbt	cbt	cbt	cbt	cbt	cbt	cbt
Remarks												
Ba	5895.8	17761.7	10657.6	3975.8	47593.9	82495.0	27872.1	114871.4	33104.6	5023.2	2693.5	2942.2
Co	43.8	57.9	8.4	7.6	4.6	12.0	58.5	2.9	5.6	13.9	20.0	17.1
Cr	0.4	1.3	1.7	0.2	0.0	4.3	2.8	0.1	0.9	1.9	0.8	0.8
Cs	0.127	0.233	0.008	0.185	0.058	0.311	0.661	0.04	0.058	0.024	0.021	0.056
Cu	198.9	127.3	0.1	21.4	16.2	8.3	50.5	5.0	7.8	1.6	5.6	57.4
Ga	3.582	6.341	11.802	1.966	11.15	6.637	7.943	7.049	8.427	3.236	3.857	5.092
Hf	2.482	2.215	0.026	0.284	0.149	0.532	0.292	0.118	0.083	0.202	0.275	2.653
Nb	285.7	2120.7	19	134.3	11.9	2450.3	1661.1	108.5	164	51.1	758.7	647.8
Ni	6.1	3.3	6.4	6.9	3.4	7.8	9.4	3.9	5.9	5.7	9.2	4.9
Pb	11.3	13.8	22.3	9.3	25.0	25.0	23.2	24.7	32.5	16.6	13.1	9.2
Rb	4.7	10.0	0.3	7.1	2.9	12.6	28.8	0.5	1.5	0.7	0.5	2.6
Sc	7.05	8.26	3.07	5.59	0	5.88	12.43	13.79	8.19	11.52	9.84	21.02
Sr	27756	24514.7	19376.8	12873.5	42017.6	35525.4	29114	25249.7	31513	18460	19493.9	13743
Ta	0.67	0.498	0.101	1.899	0.14	3.031	1.111	0.202	0.177	0.381	1.763	5.262
Th	98.16	366.37	46.74	14.13	21.87	247.79	187.8	13.18	29.23	12.68	48.98	92.33
U	0.52	0.28	0.51	12.96	3.38	1.21	0.18	0.11	0.18	0.28	1.99	47.29
V	19.4	61.9	30.3	2.4	5.7	15.2	14	1	3	4.5	4.5	42.1
Y	75.66	100.09	118.26	46.87	114.95	79.11	114.03	71.55	93.08	72.28	80.47	78.54
Zn	8.1	21.9	15.9	7.7	10.8	27.2	26.6	17.9	6.8	7.4	6.8	29.9
Zr	138.7	54.8	1.4	11.3	3.5	12.3	7.0	0.9	3.0	6.0	5.1	77.1
La	673.7	1067.7	1628.2	276.1	3541.1	1624.5	1052.1	1575.9	2274	496.2	536.5	651.1
Ce	1254	2132.6	3617.3	490.8	4605.9	2233.5	1840.5	2491.6	3399.5	1068.2	1156.5	1360.9
Pr	122	211.8	422.2	55.8	354.2	172.8	177.1	218.9	272.9	110.3	123.9	140.4
Nd	418.1	709.7	1587.1	200.2	1121.9	515.7	586.6	658.9	831.6	393.8	451.9	507.6
Sm	53.1	82.6	212.6	28.2	136.2	54.5	74.6	63.3	84.6	51.8	59.9	65.3
Eu	13.74	20.73	50.39	7.33	36.99	17.43	19.58	17.2	21.94	13.51	15.55	16.58
Gd	31.2	42.24	99.95	18.21	79.84	31.19	41.28	30.67	46.67	31.56	35.27	36
Tb	3.98	5.53	9.33	2.22	8.64	3.85	5.44	3.88	5.53	3.89	4.34	4.27
Dy	17.38	23.79	32.23	9.84	30.63	15.8	24.12	16.07	21.39	16.87	18.75	17.78
Ho	2.74	3.7	4.57	1.62	4.28	2.52	3.88	2.59	3.15	2.73	2.96	2.72
Er	6.22	8.12	10.11	3.78	8.72	5.8	8.96	6.07	6.82	6.21	6.49	5.97
Tm	0.798	1.017	1.252	0.509	1.038	0.799	1.191	0.814	0.916	0.818	0.824	0.76
Yb	4.325	5.511	7.208	2.903	5.57	4.446	6.58	4.736	5.026	4.649	4.512	4.077
Lu	0.596	0.713	0.867	0.416	0.745	0.623	0.874	0.651	0.688	0.636	0.603	0.537

Table A3.2 - Trace-element ICP-MS analyses

Sample	AT049	AT050	AT051	AT056	AT058a	AT212	AT219	TAP-1B	AT043	AT060B	AT127	AT131
Unit/Locality	C2	C2	C2	C2	C2	C2	C2	C2	C3	C3	C4	C4
Rock type	cbt	cbt	cbt	cbt	cbt	cbt,dk	cbt,dk	cbt,bre	cbt	cbt	cbt	cbt
Remarks												
Ba	2904.7	2707.9	7133.9	2984.2	11142.6	4782.6	8998.2	1920.3	1635.1	2218.9	2476.8	1632.4
Co	1.6	11.9	1.3	20.5	14.0	32.5	26.8	46.4	12.9	6.7	2.1	26.3
Cr	0.4	1.3	0.4	1.2	2.8	65.0	48.0	23.2	2.1	3.6	0.1	0.0
Cs	0.027	0.096	0.045	0.065	0.028	1.007	0.515	1.229	0.729	0.874	0.024	0.084
Cu	1.3	0.8	0.8	68.1	58.8	214.1	216.2	49.8	26.7	5.3	3.3	20.5
Ga	2.647	4.572	8.03	4.62	4.936	14.923	12.144	11.283	11.28	8.384	2.177	4.604
Hf	0.16	1.486	0.089	2.547	0.664	39.57	25.965	31.28	6.668	4.429	0.145	1.871
Nb	259.5	67	41.6	638.2	350.9	596	486.4	276.1	175.5	144.9	10.7	10.3
Ni	6.6	6.3	4.5	11.9	6.6	21.9	16.4	22.3	5.1	6.0	5.9	4.6
Pb	11.3	8.3	20.6	9.4	69.8	34.4	45.6	10.9	4.4	4.8	4.7	2.4
Rb	1.0	4.6	1.2	2.6	3.3	68.9	48.7	65.4	33.1	38.0	0.8	6.0
Sc	6.22	15.77	12.5	18.98	5.35	20.44	17.09	30.05	2.32	3.79	0	4.89
Sr	21196.8	11259.2	19450.2	14472.7	15010.9	6448	8604.9	3629.2	11204.3	13655	16564.6	12212.7
Ta	0.924	1.987	0.319	5.274	4.98	12.647	9.151	22.363	11.853	12.54	0.756	1.443
Th	11.91	45.24	20.64	66.25	34.2	64.84	36.05	75.97	23.67	24.84	2.32	7.64
U	0.46	5.1	3.98	41.77	26.43	19.89	12.11	13.72	68.73	22.24	2.14	0.93
V	4	40.7	6.1	46.7	142.2	311.3	302.3	386.6	213.8	55.9	5.1	108.1
Y	69.37	92.12	77.71	79.72	121.1	132.22	129.14	81.38	107.01	72.55	61.63	76.12
Zn	3.8	36.1	14.7	35.8	154.8	169.0	148.9	163.7	78.8	40.9	1.9	41.6
Zr	4.8	52.2	2.8	110.4	30.1	1852.9	1165.5	1646.0	543.9	223.5	7.5	120.3
La	408.7	649.6	1530.9	697.7	688.1	842.4	797	494.9316	597.1	508.7	333.3	553.9
Ce	937.1	1134.4	2689.6	1397.5	1114	1527.8	1397.2	1105.547	1195.9	1150.4	697.2	1155.7
Pr	91.9	113.3	270.3	131.8	100.4	158.5	142.7	133.4	131.2	128	68.7	123.3
Nd	324	396	920.9	465.8	343.4	566.5	514.1	509.5	497.6	480.8	247.3	465.9
Sm	43.7	51.5	103.1	59.8	48.1	81.9	76.1	71.2	72.4	63.6	34.1	64.1
Eu	11.54	13.68	23.32	15.56	14.15	22.59	20.98	18.12	19.63	16.11	9.45	16.67
Gd	27.49	31.9	45.84	36.11	33.3	53.21	50.01	42.71	49.97	37.2	23.3	40.29
Tb	3.43	4.02	5.14	4.17	4.55	6.67	6.3	5	5.76	4.19	2.8	4.45
Dy	14.77	18.4	19.86	17.11	22.12	29.1	28.28	20.9	24.56	17.45	12.25	17.79
Ho	2.34	3.08	2.99	2.57	3.83	4.55	4.54	3.14	3.81	2.64	1.97	2.58
Er	5.13	7.1	6.64	5.52	9.38	9.76	10.17	6.68	8.17	5.75	4.33	5.12
Tm	0.706	0.934	0.858	0.704	1.338	1.147	1.255	0.802	0.955	0.675	0.565	0.599
Yb	3.874	5.106	4.759	3.795	7.234	5.913	6.551	4.357	4.777	3.531	2.991	2.999
Lu	0.546	0.688	0.658	0.513	0.947	0.726	0.823	0.543	0.582	0.438	0.423	0.391

Table A3.2 - Trace-element ICP-MS analyses

Sample	AT054	AT103	AT135	AT137	AT104	RJAT3	AT412a	AT407	ASL018	ASL021	ASL023	ASL026
Unit/Locality	C5	C5	C5	C5					Salitre	Salitre	Salitre	Salitre
Rock type	cbt	cbt	cbt	cbt	RR	fen	CR	CR	cbt	cbt	cbt	cbt
Remarks												
Ba	397.8	51755.4	44581.5	63048.3	6275.3	2955.8	4.8	691.0	1102.1	1412.3	1176.9	1846.2
Co	5.2	59.0	1.2	6.3	31.5	5.9	n.a.	34.4	28.4	0.4	39.9	12.0
Cr	0.3	4.7	4.6	0.2	238.0	19.5	4.7	95.5	b.d	1.0	3.2	b.d.
Cs	0.014	0.028	0.069	0.014	2.455	0.744	0.023	6.114	0.023	0.001	0.018	0.074
Cu	19.8	46.7	0.0	22.2	27.5	3.0	2.1	11.8	50.4	n.a.	18.2	91.3
Ga	1.602	31.945	4.312	21.573	18.481	17.265	1.142	25.408	4.646	0.081	4.401	2.881
Hf	0.091	0.269	0.224	0.178	6.141	4.179	1.212	6.195	0.997	0.017	0.452	1.054
Nb	7.6	97.7	515.4	434.8	1317.7	73.1	0.9	23.6	201.6	0.5	144.8	57.4
Ni	1.5	8.1	3.3	1.6	125.2	9.3	3.3	29.5	b.d.	6.1	0.0	b.d.
Pb	4.3	11.6	8.8	14.8	2.7	5.3	2.3	23.1	4.1	n.a.	1.7	3.7
Rb	0.3	0.4	2.5	0.1	99.3	91.8	0.2	162.4	1.2	0.0	1.2	3.9
Sc	10.86	18.4	17.14	17.61	10.71	49.92	0	24.72	24.77	1.67	16.63	4.95
Sr	9088.7	27791.7	13336.4	45224.8	6423.7	543.2	29.7	117	8811.5	2544.8	9202	11360.4
Ta	0.215	0.22	0.209	0.62	32.683	0.579	1.584	1.876	56.798	0.02	40.535	2.803
Th	9.59	110.57	91.14	181.32	110.6	9.55	0.93	17.35	27.46	0.19	15.69	19.89
U	0.75	1.1	0.42	0.64	10.37	0.6	0.25	2.23	34.08	0.29	36.28	2.38
V	4.4	16.3	5.7	8.6	249.4	166.6	4.3	107.4	42.7	0.1	54.1	19.1
Y	17.58	105.26	58.23	144.26	104.76	12.08	1.28	28.43	52.21	2.61	49.48	59.88
Zn	9.9	17.2	17.6	16.7	196.0	74.6	1.6	66.1	38.7	3.0	37.6	9.4
Zr	5.5	19.9	5.4	4.9	121.1	150.4	49.9	235.7	26.4	1.0	13.1	52.6
La	134.2	5623.4	947.9	5599.1	1167.5	52.9	1.9	29.6	317.2	10.7	269.5	359.4
Ce	286.4	9482.7	1443.6	7099.3	2556.7	143.2	3.9	71.2	712.6	17.8	591.9	849.1
Pr	33.5	927.8	125.7	597.6	272	20.5	0.5	8.5	87.9	2.1	70.8	88.7
Nd	124.2	2785.5	376.8	1613.5	954.4	90.3	1.9	31.8	336.9	8.2	267.9	327.9
Sm	17.4	198	38.3	118.4	118.5	15.5	0.4	5.9	47.2	1.4	38.3	44.1
Eu	4.51	38.14	10.13	27.84	28.46	3.91	0.07	1.14	12.45	0.46	10.17	11.58
Gd	10.17	73.75	19.24	66.31	56.24	7.13	0.29	5.15	28.68	1.23	23.92	26.74
Tb	1.19	7.37	2.79	7.51	6.72	0.74	0.05	0.84	3.32	0.14	2.84	3.12
Dy	4.81	24.45	12.62	29.91	26.96	2.66	0.26	4.94	13.24	0.58	11.88	13.01
Ho	0.71	3.78	2.14	5.01	3.9	0.38	0.04	0.98	2	0.08	1.86	1.95
Er	1.4	8.13	5.27	12.18	8.55	0.81	0.12	2.75	4.01	0.16	3.89	4.07
Tm	0.182	1.058	0.669	1.677	1.053	0.127	0.02	0.475	0.493	0.014	0.52	0.5
Yb	0.9	4.983	3.009	7.708	5.376	0.894	0.137	2.877	2.56	0.058	2.717	2.648
Lu	0.121	0.63	0.314	0.894	0.609	0.15	0.02	0.486	0.362	0.007	0.394	0.355

Table A3.2 - Trace-element ICP-MS analyses

Sample	ASL012	ASL013	ASL024	ASL030	ASL040	91SB16	SAL-2	SAL-3C	SAL-3D
Unit/Locality	Salitre	Salitre	Salitre	Salitre	Salitre	Salitre	Salitre	Salitre	Salitre
Rock type	cbt	cbt	cbt	cbt	cbt	syen	syen	syen	syen
Remarks						dk	dk	dk	dk
Ba	28111.7	23840.1	214.6	566.0	284.0	2607.8	3661.1	2555.3	2044.5
Co	2.3	4.4	7.7	0.9	14.5	6.7	4.4	37.9	2.8
Cr	4.0	25.9	1.8	0.5	1.1	7.4	6.0	17.9	8.2
Cs	0.035	0.021	0.04	0.085	0.059	6.599	1.696	2.043	0.876
Cu	18.3	24.4	19.2	n.a.	2.4	14.5	13.2	161.8	7.3
Ga	5.387	13.101	2.892	0.739	5.167	25.943	25.257	23.58	29.569
Hf	10.355	0.239	0.181	0.063	1.368	30.094	29.88	19.046	21.485
Nb	89.9	70.2	158.9	8.2	2082	121.3	466.4	227.7	112.1
Ni	5.3	7.0	0.7	2.5	3.0	5.0	3.9	57.2	5.0
Pb	4.9	36.9	1.0	3.0	2.3	6.8	2.8	18.8	2.9
Rb	0.7	1.2	2.2	2.9	2.8	134.9	91.7	154.6	172.5
Sc	30.38	55.11	16.69	10.36	10.08	15.89	13	24.73	23.48
Sr	6077.9	10402.1	6229.4	10533.1	7651	1566.5	2561.6	1913.3	648.9
Ta	0.463	1.133	4.445	0.033	24.805	4.949	17.829	12.611	3.794
Th	387.19	161.1	25.23	16.65	171.73	8.82	22.02	14.21	2.71
U	16.96	3.82	3.43	1.01	7.06	4.34	2.35	3.67	0.68
V	21.8	38.9	54.6	0.2	169.1	188.6	125.7	316.4	157.8
Y	557.1	59.93	14.3	17.56	25.23	14.19	12.63	38.82	20.21
Zn	21.0	195.1	42.7	12.7	131.6	62.5	40.2	145.4	50.0
Zr	211.9	7.7	4.6	4.2	35.4	1376.1	1264.5	842.9	902.1
La	591.6	1845.7	109	100.1	169.8	106.5	376.2	234.2	57.5
Ce	1134.8	3485.8	266	208.9	437.8	203	637.2	453.1	134
Pr	139.2	400	33.2	23	55.1	21.2	56.9	51.2	16.5
Nd	565.1	1451.6	128.3	80.5	212.7	71.3	160.5	184.3	57.3
Sm	133.1	202.3	17.9	9.8	29.5	9.4	14.5	26.7	8.6
Eu	52.26	55.36	4.58	2.56	7.3	2.49	3.43	7.07	2.31
Gd	164.03	125.26	10.48	6.21	17.27	5.71	5.92	16.53	5.57
Tb	26.86	10.34	1.11	0.78	1.83	0.73	0.81	2.13	0.81
Dy	131.12	26.04	4.2	3.79	7.04	3.28	3.16	9.31	3.78
Ho	20.86	2.73	0.58	0.67	0.93	0.53	0.5	1.5	0.68
Er	44.72	4.91	1.1	1.58	1.77	1.28	1.3	3.35	1.73
Tm	5.774	0.695	0.134	0.205	0.185	0.209	0.251	0.455	0.263
Yb	27.714	4.835	0.665	1.108	0.881	1.587	2.04	2.438	1.762
Lu	3.621	0.795	0.085	0.139	0.106	0.342	0.411	0.365	0.339

Table A3.3 - Carbon and oxygen isotopic composition for various rock-types from Tapira and Salitre

Sample	Unit/Locality	Rock type	Mineral	CO2	d18O	d13C
asl017	Salitre	cbt	calcite	39.54	7.4	-7.0
asl018	Salitre	cbt	calcite	36.55	7.8	-6.9
asl022	Salitre	cbt	calcite	39.36	6.9	-7.1
asl023	Salitre	cbt	calcite	40.49	7.3	-6.9
asl024	Salitre	cbt	dolomite	42.36	8.1	-6.5
asl026	Salitre	cbt	calcite	43.24	7.3	-7.2
asl028	Salitre	cbt	calcite	39.54	7.4	-6.9
asl030	Salitre	cbt	dolomite	47.38	8.6	-6.4
asl032	Salitre	cbt	calcite	30.23	7.3	-7.2
asl035	Salitre	cbt	calcite	44.63	7.2	-7.0
asl039	Salitre	cbt	calcite	44.45	7.3	-7.1
asl040	Salitre	cbt	dolomite	36.24	8.0	-6.6
at013		php	calcite	9.05	9.8	-5.8
at014		php	calcite	6.60	10.9	-6.1
at021b		php	calcite	2.90	19.0	-8.9
at021b		php	calcite	2.90	17.7	-8.8
at022		php	calcite	5.96	9.3	-6.2
at024		lcr	calcite	12.50	14.7	-6.4
at028		lcr	calcite	13.14	9.4	-5.8
at028		lcr	dolomite	13.14	8.7	-5.1
at042	C1	cbt	calcite		9.6	-6.8
at043	C3	cbt	calcite	25.06	7.8	-7.6
at044	C1	cbt	calcite	37.23	11.5	-6.5
at045am	C2	cbt	calcite	42.54	11.9	-6.5
at045am	C2	cbt	dolomite	42.54	8.2	-6.4
at045b	C2	cbt	calcite	42.54	8.8	-7.1
at045b	C2	cbt	dolomite	42.54	7.8	-7.1
at046a	C2	cbt	calcite	42.73	8.8	-7.0
at046a	C2	cbt	dolomite	42.73	7.9	-7.0
at046bm	C2	cbt	calcite	42.73	8.8	-6.8
at046bm	C2	cbt	dolomite	42.73	7.6	-6.6
at047	C2	cbt	calcite	38.84	8.0	-7.2
at048am	C1	cbt	calcite	43.61	8.4	-5.8
at048am	C1	cbt	dolomite	43.61	6.3	-5.6
at048b	C1	cbt	calcite	43.61	7.3	-5.8
at048b	C1	cbt	dolomite	43.61	5.4	-5.6
at049	C2	cbt	calcite	44.49	8.7	-7.1
at049	C2	cbt	dolomite	44.49	8.4	-7.1
at050	C2	cbt	calcite	40.86	8.4	-7.6
at051	C2	cbt	calcite	42.14	8.1	-7.0
at051	C2	cbt	calcite	42.14	8.1	-7.6
at051	C2	cbt	dolomite	42.14	7.8	-7.6
at053b	C5	cbt	dolomite	34.06	8.6	-6.4
at054	C5	cbt	dolomite		9.1	-6.3
at055	C1	cbt	calcite	42.65	8.9	-7.1
at056	C2	cbt	calcite	40.64	8.7	-7.0
at057	C2	cbt	calcite	33.26	12.8	-4.9
at058a	C2	cbt	calcite	36.60	11.4	-4.9
at059	C1	cbt	calcite	32.54	9.4	-7.6
at060a	C3	cbt	calcite		8.0	-7.3
at060b	C3	cbt	calcite	32.83	8.0	-7.3

Table A3.3 - Carbon and oxygen isotopic composition for various rock-types from Tapira and Salitre

at102	C1	cbt	calcite	35.62	9.2	-7.6
at104		RR	dolomite	5.09	19.6	-6.1
at120		php	calcite	4.10	9.7	-7.4
at127	C4	cbt	calcite	44.96	7.5	-8.1
at131	C4	cbt	calcite	33.21	7.0	-8.3
at140	C1	cbt	calcite	42.87	11.4	-7.2
at201		lcr	calcite	12.05	15.0	-6.5
at204		php	calcite	9.05	12.4	-5.5
at205		lcr	calcite	10.26	8.0	-6.0
at208		lcr	calcite	13.87	11.0	-4.3
at209a		lcr	calcite	10.67	8.5	-6.2
at210		lcr	calcite	17.23	12.6	-5.5
at210		lcr	dolomite	17.23	9.6	-4.9
at211		lcr	calcite	9.10	10.0	-5.7
at212	C2	cbt,dk	calcite	20.13	9.3	-6.0
at212	C2	cbt,dk	dolomite	20.13	11.1	-5.3
at213		lcr	calcite	16.27	10.9	-6.8
at219	C2	cbt,dk	calcite	27.01	13.8	-4.3
at219	C2	cbt,dk	dolomite	27.01	14.7	-3.5
at301		syenite	calcite	4.67	12.1	-6.1
tap1b	C2	cbt,bre	calcite	17.73	13.2	-5.4
tap1b	C2	cbt,bre	dolomite	17.73	12.5	-4.5
tp90 2	C2	cbt,bre	calcite	15.90	11.5	-5.7
tp90 4b		php	calcite	14.24	12.9	-5.5

Table A3.4 - Sr and Nd isotopic ratios of selected Tapira samples

Sample	Unit	Rock type	Sm(ppm)	Nd(ppm)	143Sm/144Nd	143Nd/144Nd(+/-2SE)	End	87Sr/86Sr(+/-2SE)
at003	B1	beb	37.853	210.320	0.109	0.512312(06)	-6.3	0.70555(01)
at014		php	28.562	204.280	0.085	0.512268(05)	-7.2	0.70637(02)
at025	B1	wehrl	97.130	745.000	0.079	0.512281(04)	-6.9	0.70551(02)
at033	B2	beb	41.317	242.320	0.103	0.512288(05)	-6.8	0.70531(01)
at038	B2	beb	68.618	510.220	0.081	0.512267(05)	-7.2	0.70517(01)
at039		syen	5.029	36.865	0.083	0.512272(04)	-7.1	0.70620(01)
at042	C1	cbt	52.924	408.840	0.078	0.51224(05)	-7.7	0.70518(01)
at043	C3	cbt	70.548	469.890	0.091	0.512291(05)	-6.7	0.70519(01)
at045	C2	cbt	52.167	388.530	0.081	0.512295(05)	-6.7	0.7052(01)
at201		lcr	55.873	396.700	0.085	0.512272(05)	-7.1	0.70545(01)
at212	C2	cbt,dk	78.914	527.440	0.090	0.512296(04)	-6.6	0.70534(01)
at305		syen	15.935	118.620	0.081	0.512281(06)	-6.9	0.70584(02)
at412a		CR	0.365	1.823		0.511672(25)	-19.03	0.73314(7)

APPENDIX 4 - MODAL COMPOSITION OF SPS

ULTRAMAFIC ROCKS

The modal composition of wehrlites, bebedourites and apatite- and perovskite-rich cumulates of the Tapira Silicate Plutonic Series (SPS) were determined on thin - sections, using an automatic point-counter. On average, 1000 points were determined per sample. The spacing between points was adjusted to suit the grainsize of the sample. Results are given in Table A4.1.

Table A4.1 - Modal composition of SPS ultramafic rocks

B1										
Sample	Olivine	Diopside	Phlogopite	Perovskite	Apatite	Sphene	Garnet	Opaques	Carbonate	Feldspar(?)
at001		56.8	6.4	5.2	14.8	3.4		11.6	1.8	
at003		36.2	24.2	8.4	11.0		15.0	5.2		
at004		30.1	41.0	8.1	17.8			3.0		
at006		59.2	5.6	10.2	15.8	0.4		8.2	0.6	
at007		26.5	6.3	28.5	18.3			20.4		
at009		36.0	26.0	10.4	16.0			11.6		
at010		53.8	8.8	15.6	13.6			8.2		
at014b	5.0	2.9	40.0	12.9	19.2			20.0		
at015	21.8		6.0	30.2	18.4			23.6		
at016	30.8	7.6	2.8	23.8	31.0			4.0		
at025	40.2	11.4	26.8	12.4	4.6			4.6		
at026		70.2	15.0	4.9	5.5		0.4	2.4	1.6	
at027f		64.8	4.0	1.4	9.2		0.6	20.0		
at027g		51.8	4.6	19.4	11.0			13.2		
at034a		25.6	30.4	0.2	12.0		31.0	0.8		
at035		73.8	7.2	12.0	4.0	0.6		1.0	1.4	
at036a		49.0	7.0	16.6	14.6			12.8		
at036b		26.8	33.6		9.0		30.0	0.6		
at037		38.4	28.0	14.4	10.0			9.2		
at040		30.4	19.0	12.4	11.4		25.6	1.2		
at101a	21.4	19.4	28.8	12.6	7.6			10.2		
at101b	29.8	14.0	23.0	12.0	9.2			12.0		
at111b		60.8	4.4	9.4	7.4			18.0		
at111c		64.6	0.4	9.2	8.0			17.8		
at112a		55.6	5.2	8.4	13.6	0.6		16.6		
at113		61.0	7.6	5.8	14.4	0.8		10.4		
at114		60.0	16.3	12.8	5.3			4.7	0.9	
at118		48.6	8.8	9.0	12.4			20.0	1.2	
at126c		48.2	9.0	12.6	15.9			14.3		
at126d		46.2	6.6	9.9	19.0	0.3		16.0	2.0	
at129		69.2	2.2	9.0	9.0			10.6		
at217	43.2	23.2	12.8	10.0	1.0			9.8		
B2										
Sample	Olivine	Diopside	Phlogopite	Perovskite	Apatite	Sphene	Garnet	Opaques	Carbonate	Feldspar(?)
at008		70.8	7.4		9.6	3.4		6.0	2.8	
at011		28.4	34.3		24.0		10.2		3.1	
at017		82.0	2.1	0.2	2.6	0.5	3.2			9.4
at023		50.0	35.0		15.0		0.0			
at029		67.4	7.2	3.6	9.0	5.6	6.0	1.2		
at030		63.2	21.6		13.0	1.0			1.2	
at032		72.8	4.2		6.5				7.2	9.3
at033		53.8	22.8	5.2	2.4	0.8	14.2	0.8		
at038a		63.0	8.4	5.8	12.0	3.2	4.0	1.6	2.0	
at038b		65.0	4.8	4.1	11.9	6.0	3.8	1.8	2.6	
at105		66.8	2.8	7.4	16.4		6.6			
at109b		37.2	43.2		15.4		4.0	0.2		
at110a		46.8	5.6	1.4	11.6	1.2	21.8	11.6		
at110b		43.4	9.2		16.4		30.4	0.2	0.4	
at114b		61.6	22.4	2.0	8.4			3.0	2.6	
at114c		68.0	20.0	2.5	5.5			3.8	0.2	
at125		24.0	38.0		9.8	0.6	24.4		3.2	
at126a	6.2	30.0	18.2	0.2	17.8		16.4	9.8	1.4	
at126b	24.2	23.6	19.0		14.4		13.2	4.2	1.4	